JOURNAL OF THE MYANMAR ACADEMY OF ARTS AND SCIENCE

Chemistry, Physics, Zoology, Botany and Marine Science, Geology

Vol. XX, No.1, October, 2023

Myanmar Academy of Arts and Science

Journal of the Myanmar Academy of Arts and Science

Vol. XX, No.1

Contents

Section (i), Chemistry

Section (ii), Physics

Section (iii), Zoology

Section (iv), Botany

Section (v), Marine Science

Section (vi), Geology

Edition
2023, October, 275 Copies

Published by

Dr Maung Kyaw (00322) Vice-President,
Myanmar Academy of Arts and Science

ISSN 2520-0186
LCCN 2003-323143

Universities Press, Yangon, Myanmar

FOREWORD

The Myanmar Academy of Arts and Science (MAAS) was constituted on August-16, 1999 with five Aims and Eight Tasks. These involve four major fields of endeavour, namely:

(a) Introduction to Modern Methods of Teaching and Learning
(b) Promotion of Research Activities and Laying Down of Research Guidelines
(c) Dissemination of Knowledge and Learning
(d) Production of New Experts and Academics

In pursuance of these endeavours the MAAS has, since the year 2001, held Research Conferences and published research papers in the Journal of the Myanmar Academy of Arts and Science.

At the Research Conference held on 27- 29 December 2021, a total of about (93) research papers were read. These papers have been published in volume XX as follows:

Vol. XX, No.1	Chemistry, Physics, Zoology, Botany, Marine Science and Geology
Vol. XX, No.2	Myanmar, Geography, History, Anthropology and Law
Vol. XX, No.3	Educational Psychology, Curriculum and Methodology

The executive members of Myanmar Academy of Arts and Science had been reconstituted on 4 August 2022, by the Ministry of Education with the Approval of the Government of the Union of Myanmar. The primary mission of the academy is to develop and promote Higher Education in preparing future generations to meet the challenges of the new millennium. The Publication Committee along with the Editorial Board have been formed.

The majority of the papers in these issues represent findings of research conducted by Ph.D. and Master's candidates in partial or total fulfillment of requirement for these degrees. We, the members of MAAS, do appreciate the editing work done by senior professors and scholars of high standing. Accordingly, these papers should prove useful, not only for other candidates for such degrees, but also for all those who are interested in the results of systematic research and inquiry. Due to the outbreak of covid-19 pandemic; a delay in the date of publication might occur.

Dr Thet Lwin
President
The Myanmar Academy of Arts and Science

Editorial Board

Chief Editor	-	Professor Dr Daw Kyi Kyi Hla
Editors	-	Professor U Thi Ha
		Professor Dr Maung Kyaw
		Professor Dr Hla Pe
		Professor Dr U Win
		Professor Dr Maung Thin

Editors

(Chemistry, Physics, Zoology, Botany and Marine Science, Geology)

Chemistry

Dr Saw Hla Myint, Professor and Head (Retd.), Department of Chemistry, Yangon University
Dr Daw Hla Ngwe, Professor and Head (Retd.), Department of Chemistry, Yangon University
Dr Aye Aye Myint, Professor, Department of Chemistry, Yangon University
Dr Ni Ni Sein, Professor, Department of Chemistry, University of Yangon
Dr Hlaing Hlaing Oo, Professor and Head (Retd.), Department of Chemistry, West Yangon University
Dr Hnin Hnin Than, Professor and Head, Department of Chemistry, Dagon University
Dr Yu Yu Myo, Professor and Head, Department of Chemistry, Yangon University of Distance Education
Dr Ni Ni Than, Professor and Head, Department of Chemistry, University of Yangon
Dr Yi Yi Myint, Professor and Head, Department of Chemistry, Mandalay University

Physics

Dr Khin Khin Win, Professor & Head (Retd.), Department of Physics, Yangon University
Dr Chit Shwe, Professor & Head (Retd.), Department of Physics, Monywa University
Dr Min Maung Maung, Professor, Department of Physics, Yangon University
Dr Yin Maung Maung, Professor & Head, Department of Physics, Yangon University
Dr Kalayar Thwe, Professor & Head, Department of Physics, Mandalay University

Zoology

Dr May Thet Oo, Professor and Head (Retd.), Department of Zoology, Yangon University of Distance Education
Dr Zaw Win Myint, Lecturer (Retd.), Department of Zoology, Yangon University
Dr Aye Mi San, Professor and Head(Retd.), Department of Zoology, Yangon University
Dr Kay Lwin Tun, Professor and Head, Department of Zoology, Yangon University
Dr Thant Zin, Professor and Head, Department of Zoology, Mandalay University

Botany

Dr Thidar Htoo, Professor (Retd.), Department of Botany, Yangon University
Dr Soe Soe Aung, Professor, Department of Botany, Mandalay University
Dr Thet Thet Mar Win, Professor, Department of Botany, Yangon University
Dr Aye Phe, Professor and Head, Department of Botany, Yangon University
Dr Nu Nu Yee, Professor and Head, Department of Botany, Mandalay University

Marine Science

U Saw Han Shein, Rector (Retd.), Mawlamying University
Dr Hla Tint, Rector (Retd.), Yangon University of Distance Education
Dr Cherry Aung, Professor and Head, Myeik University
Dr Aye Phe, Professor and Head, Department of Botany, Yangon University
Dr Nyo Nyo Tun, Professor and Head, Department of Botany, Mawlamying University

Geology

Dr U Thein, Professor and Head (Retd), Department of Geology, University of Yangon
U Hla Kyi, Professor and Head (Retd), Department of Geology, Dagon University
U Maung Ko, Professor and Head (Retd.), Department of Geology, East Yangon University
Dr Cho Cho Aye, Professor and Head (Retd.), Department of Geology, East Yangon University
Dr Min Aung, Part-Time Professor, Department of Geology, Mandalay University
Dr Ohn Thwin, Part-Time Professor, Department of Geology, Yangon University
Dr Phyu Phyu Lwin, Part-Time Professor, Department of Geology, Dagon University
Dr Daywa Aung, Professor and Head, Department of Geology, Yangon University
Dr Kyi Kyi Lin, Professor and Head, Department of Geology, Mandalay University

MOLECULAR CONFIRMATION OF THE SOIL BACTERIAL *PSEUDOMONAS AERUGINOSA* AND EVALUATION OF SOME BIOACTIVE SECONDARY METABOLITES*

Su Swe Su[1], Nwet Nwet Win[2], Daw Hla Ngwe[3], Saw Hla Myint[4], Ni Ni Than[5]

Abstract

This research focuses on the molecular confirmation of *Pseudomonas aeruginosa* isolated from the clinical soil sample collected from Insein General Hospital, Yangon Region, and evaluation of some bioactive secondary metabolites from it. The isolated *P. aeruginosa* strain characterized by microscopic examination and biochemical tests was confirmed by 16S rRNA sequencing technique. The chloroform extract was prepared from the *P. aeruginosa* culture in a large scale for the investigation of the chemical constituents. According to silica gel chromatographic separation on the chloroform extract, five nitrogeneous compounds such as 1-hydroxyphenazine, phenazine-1-carboxylic acid, cyclo-(L-Leu-L-Pro), cyclo-(D-Pro-D-Leu) and cyclo-(D-Pro-L-Val) were isolated. These isolated secondary metabolites were structurally identified by using modern NMR spectroscopic techniques such as ^{1}H NMR, ^{13}C NMR, COSY, HSQC, ROESY, HMBC spectroscopies, and mass spectrometry. The two isolated phenazines: 1-hydroxyphenazine and phenazine-1-carboxylic acid were found to be potent in antimicrobial activity with the inhibition zone diameters ranged between (21 ~ 32 mm) and (15 ~ 31 mm), whereas the remaining three diketopiperazines showed mild antimicrobial activity (inhibition zone diameters between 12 mm ~ 14 mm). In addition, 1-hydroxyphenazine (IC_{50} = 14.12 µg/mL) and phenazine-1-carboxylic acid (IC_{50} = 15.0 µg/mL) were found to exhibit good antiproliferative activity against human breast cancer cell MCF7 and the remaining three compounds: cyclo(L-Leu-L-Pro) (IC_{50} = 176.4 µg/mL), cyclo(D-Pro-D-Leu) (IC_{50} = 87.7 µg/mL) and cyclo(D-Pro-L-Val) (IC_{50} = 196.5 µg /mL) have mild antiproliferative activity.

Keywords: *Pseudomonas aeruginosa*, 16S rRNA sequencing technique, phenazines, diketopiperazines, antimicrobial activity, antiproliferative activity

Introduction

Pathogenic microscopic organisms can cause extreme and lethal sicknesses in humans, animals and plants. With increase in prevalence of drug resistant pathogenic bacteria, the search for novel antibacterial agents is of most extreme significance. Several microorganisms are known to suppress the growth of pathogenic bacteria and fungi due to production of bioactive compounds. Soil is a broadly investigated natural specialty for sources of microorganisms that produce useful biologically active compounds. Among these microbes, bacteria are prolific source of novel compounds with fascinating antimicrobial activity. *Pseudomonas* is a genus of gram-negative, aerobic bacteria that can cause disease in animals, including humans. *Pseudomonas aeruginosa* bacteria had a potential to produce bioactive compounds belong to the gamma proteobacteria class with these characteristics: gram-negative, rod-shaped, motile, forming smooth spherical colonies with greenish fluorescent colour, wide spread in the environment. These bacteria produce pyocyanin pigment which is soluble in water, chloroform and n-butanol. *Pseudomonas* is a large group of free-living bacteria that live primarily in soil, seawater, and fresh water. In the previous research work, it has been reported that the chloroform extract from *P. aeruginosa* isolated from soil possesses some biological activities such as antimicrobial activity, antioxidant activity, cytotoxic effect and antiproliferative activity (Su Swe Su *et al.,* 2020) and the isolated bacteria was

[1] Dr, Lecturer, Department of Chemistry, University of Yadanabon
[2] Institute of Natural Medicine, University of Toyama, 2630-Sugitani, Toyama 930-0194, Japan
[3] Dr, Professor and Head (Retd.,), Department of Chemistry, University of Yangon
[4] Dr, Part-time Professor , Department of Chemistry, University of Yangon
[5] Dr, Professor and Head Department of Chemistry, University of Yangon
[*] Best Paper Award Winning Paper in Chemistry (2021)

characterized as a rod shaped and gram-negative bacteria according to the observations from the microscopic examination and biochemical tests (Su Swe Su *et al.*, 2018). Baron and Rowe (1981) reported that some compounds present in *P. aeruginosa*, like phenazines (pyocyanin, 1-hydroxy-phenazine, phenazine-1-carboxamide and phenazine-1-carboxylic acid) serve as electron shuttles in reduction and solubilization of Fe(III) function as antibiotics. In the present work, the *P. aeruginosa* bacteria isolated from clinical soil is identified by using DNA sequencing technique. In addition, some bioactive secondary metabolites such as two phenazines and three diketopiperazines are isolated from the chloroform extract of *P. aeruginosa* and structurally identified by modern spectroscopic techniques. Furthermore, some biological activities such as antimicrobial activity and antiproliferative activity of the isolated compounds are also investigated.

Materials and Methods

Sample Collection

Soil samples were collected from the Insein General Hospital, Yangon Region. Bacteriological analyses were started within three days after collecting the samples. *P. aeruginosa* was then isolated from the soil sample and cultured in a large scale of nutrient ager medium and chloroform extract was prepared from the isolated bacteria culture according to the reported method (Su Swe Su *et al.*, 2020).

Identification of the Isolated *P. aeruginosa* by DNA Sequencing Technique

The isolated bacteria *P. aeruginosa* was identified by DNA sequencing technique using bacterial 16S rRNA primer and compared with the reported data (Amuth and Kokila, 2014).

Firstly, about 25 mL of nutrient broth medium at pH 7 was prepared and inoculated with two loops full culture of the isolated bacteria in 250 mL conical flask. It was then incubated at 37 °C in an incubated shaker for overnight providing the bacteria solution. Secondly, the DNA of the *P. aeruginosa* was extracted using Genomic DNA extraction kit (Real Genomics, Canada) according to the bacterial genomic DNA isolation protocol and the purity of the extracted genomic DNA was checked by using agarose gel electrophoresis (Amutha and Kokila, 2014). This experiment was performed in the Pharmaceutical Research Department, Insein, Yangon. Thirdly, the extracted genomic DNA was used as a template in PCR amplification which was carried out in 0.2 mL PCR tubes with 10 µL of reaction mixture volume with the composition as shown in Table 1.

Table 1 Composition of PCR Reaction Mixture

Reaction mixture	**Volume (µL)**
PCR buffer (10X) with $MgCl_2$ (1.5 mM)	2.5
dNTPs mixture (0.5 mM each)	2.0
Taq DNA polymerase (5U/ µL)	0.3
Primer F (10 nM)	0.6
Primer R (10 nM)	0.6
Template DNA (the extracted DNA from *P. aeruginosa*)	4.0
Total	**10.0**

Table 2 PCR Program Used to Amplify 16S rRNA

Stage of PCR		Time (min)	Temperature (°C)	No. of cycle
Pre-PCR	Hot start	3	95	1
PCR	Denaturation	0.5	95	35
	Annealing	0.5	50	
	Extension	2	72	
Post –PCR	Final extension	10	72	1
Hold			4	

The polymerase chain reaction was performed using PCR thermal cycler and a temperature profile standardized for 16S rRNA gene amplification. The PCR program used to amplify the 16S rRNA is shown in Table 2. The PCR products were separated by agarose gel the products obtained through amplification with two universal targeting 16S rRNA primers 27F (5'-AGAGTTTGATCMTGGCTCAG-3') (M = C or A) and 1492R (5'-GGYTACCTTGTTACGACTT-3') (Y = C or T) were subjected to sequencing using same upstream and downstream primers (Amutha and Kokila, 2014) and the present work was carried out in Bio Basic Lab, Singapore. Finally, molecular confirmation of the isolated bacteria was carried out by BLAST (Basic Local Alignment Search Tool) against the (National Center for Biotechnology Information) NCBI data.

Isolation and Identification of Bioactive Compounds from Chloroform Extract of *P. aeruginosa* by Column Chromatography

P. aeruginosa chloroform extract (5 g) was separated with different polarities of solvent systems of PE:EA in the ratios of 9:1, 4:1, 7:3, 3:2 and 1:1 v/v by using silica gel column chromatographic method. On the chromatographic separation, six main fractions (F-I to F-VI) were collected after examining on the precoated TLC plates. Among the fractions, from the sub-fraction F2b2 of fraction F-II, compound **1** was obtained as a yellow crystal in 12 mg (0.24 % yield based on chloroform extract), whereas from the sub-fraction F3b of fraction F-III, 34.6 mg of compound **2** was obtained as a yellow amorphous powder in 0.72 % yield. In addition, two colourless solid compounds: **3** (17 mg, 0.34 % yield) and **4** (4.5 mg, 0.09 % yield) were respectively isolated. Moreover, the sub-fractions F5b and F6a of fractions F-V and F-VI gave compound **5** as a colourless powder (10.4 mg, 0.18 % yield). Some physical properties of these isolated compounds, such as melting points, R_f values and solubility in some solvents such as petroleum ether, ethyl acetate, methanol, ethanol and acetone were determined. The structures of these isolated secondary metabolites were identified by using modern NMR spectroscopic techniques such as ^{1}H NMR, ^{13}C NMR, COSY, HSQC, HMBC, ROESY and Mass spectroscopies, and by comparing with the reported data. The NMR and Mass spectra of the isolated compounds were measured at Division of Natural Product Chemistry, Institute of Natural Medicine, University of Toyama, Japan.

Screening of Antimicrobial Activity of the Isolated Compounds by Agar Disc Diffusion Method

The screening of antimicrobial activity of isolated compounds (**1** to **5**) was carried out by agar disc diffusion method (Perez *et al*., 1990) at Pharmaceutical Research Department (PRD), Yangon, Myanmar and Department of Chemistry, Yangon University, Myanmar. Seven species of microorganisms: *Agrobacterium tumerfaceins* (N.I.T.E -09678), *Bacillus subtilis* (N.C.T.C-8236), *Bacillus pumilus* (N.C.I.B-8982), *Candida albicans* (-), *Escherichia coli* (N.C.I.B-8134) *Pseudomonas aeruginosa* (6749) and *Staphylococcus aureus* (N.C.P.C-6371) were used in this test.

Investigation of Antiproliferative Activity of the Isolated Compounds against Human Breast Cancer Cell Line Using CCK-8 Assay

Antiproliferative activity of the five isolated compounds (**1** to **5**) from chloroform extract of *P. aeruginosa* was investigated in *in vitro* by using CCK-8 assay at Division of Natural Product Chemistry, Institute of Natural Medicine, and University of Toyama, Japan. The cell line used was MCF 7 (human breast cancer cell line). K562 µ-Minimum essential medium with L-glutamine and phenol red (α-MEM, Wako) were used for cell cultures. All media were supplemented with 10 % fetal bovine serum (FBS, Sigma) and 1% of antibiotic antimycotic solution (Sigma). For MCF 7 cell, 1 % of 0.1 M non-essential amino acid (NEAA, Gibco) and 1 % of 1 mM sodium pyruvate (Gibco) were also supplemented. The *in vitro* antiproliferative activity of the isolated compound was determined by the procedure described by (Win *et al.*, 2015). Briefly, each cell line was seeded in 96-well plates (2×10^3 per well) and incubated in the respective medium at 37 °C under 5 % of CO_2 and 95 % of air for 24 h. After the cells were washed with PBS (Nissui Pharmaceuticals), serial diluted solutions of the tested samples were added. After 72 h incubation, the cells were washed with PBS, and 100 µL of medium containing 10 % of WST-8 cell counting kit (Dojindo; Kumamoto, Japan) solution was added into the wells. After 2 h incubation, the absorbance at 450 nm was measured. The concentrations of the crude extracts were 200, 100, 20, 10 µg/ mL were prepared by serial dilution. Cell viability was calculated from the mean values of the data from three wells using the equation below and antiproliferative activity was expressed as the IC_{50} (50 % inhibitory concentration) value. 5-Fluorouracil (5FU) was used as positive control.

$$\% \text{ Cell viability} = \left[\frac{A_{\text{test sample}} - A_{\text{blank}}}{A_{\text{control}} - A_{\text{blank}}} \right] \times 100$$

where, $A_{\text{test sample}}$ = absorbance of test sample solution

A_{control} = absorbance of DMSO

A_{blank} = absorbance of CCK–8 reagent

Results and Discussion

In this study, *P. aeruginosa*, a rod shaped and gram negative bacteria isolated from one of the clinical soil sample collected from the Insein General Hospital, Yangon Region was identified by using DNA sequencing technique. The isolated *P. aeruginosa* strain characterized and identified by microscopic examination and biochemical tests (Su Swe Su *et al*., 2018) was used in the present research work. For the molecular confirmation using DNA sequencing technique, genomic DNA was extracted from the isolated *P. aeruginosa* and subjected to check the purity by using agarose gel electrophoresis. It can be clearly seen that the extracted genomic DNA was highly pure and it can also be estimated that the size of DNA may have 10000 bp compared with control as shown in Figure 1 (a). The extracted pure genomic DNA of the isolated *P. aeruginosa* bacteria was used as a template in the molecular confirmation by PCR amplification with two universal 16S rRNA primers: 27F (5'-AGAGTTTGATCMTGGCTCAG-3') (M = C or A) as forward primer F and 1492R (5'-GGYTACCTTGTTACGACTT- 3') (Y = C or T) as reverse primer R according to the reported method (Amutha and Kokila, 2014). The PCR products were photographed under ultraviolet light machine (Transillumnator;Uvite, UK) to detect the specific amplified product by comparing it with 1000 base pairs standard DNA ladder (Figure 1 (b)).

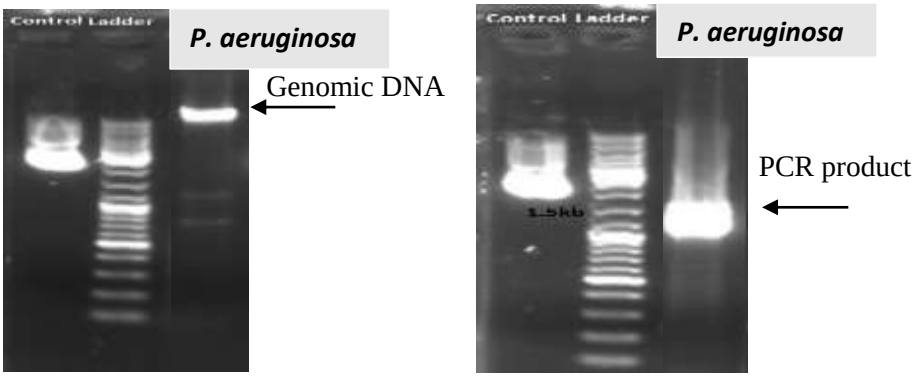

(a) (b)

Figure 1 Agarose gel electrophoresis of genomic DNA and PCR products after amplification of the 16S rRNA gene (a) Gel image showing genomic DNA extracted from the isolated *P. aeruginosa* (250 - 10000 bp) DNA Ladder (b) PCR product

From the PCR result, it can be clearly seen that the size of the PCR product of genomic DNA might be expected to have 1500 bp. The DNA sequence was compared with NCBI gene bank database using BLAST algorithm. Figure 2 shows the consensus nucleotide sequence of the PCR product, amplified segment of 16S rRNA gene of *P. aeruginosa*. The result showed a data gave high similarity (99-100 %) homology of the search sequence with *P. aeruginosa* strain S 04 16S rRNA (accession number MT 626658.1). Therefore the results of phenotypic tests and biochemical tests (Su Swe Su *et al*., 2018) and genotypic confirmation, the isolated bacterial strain was finally identified as a strain of *P. aeruginosa.*

ATGCAAGTCGAGCGGATGAAGGGAGCTTGCTCCTGGATTCAGCGGCGGACGGGTGA
GTAATGCCTAGGAATCTGCCTGGTAGTGGGGGATAACGTCCGGAAACGGGCGCTAAT
ACCGCATACGTCCTGAGGGAGAAAGTGGGGGATCTTCGGACCTCACGCTATCAGATG
AGCCTAGGTCGGATTAGCTAGTTGGTGGGGTAAAGGCCTACCAAGGCGACGATCCGT
AACTGGTCTGAGAGGATGATCAGTCACACTGGAACTGAGACACGGTCCAGACTCCTA
CGGGAGGCAGCAGTGGGGAATATTGGACAATGGGCGAAAGCCTGATCCAGCCATGC
CGCGTGTGTGAAGAAGGTCTTCGGATTGTAAAGCACTTTAAGTTGGGAGGAAGGGCA
GTAAGTTAATACCTTGCTGTTTTGACGTTACCAACAGAATAAGCACCGGCTAACTTCG
TGCCAGCAGCCGCGGTAATACGAAGGGTGCAAGCGTTAATCGGAATTACTGGGCGTA
AAGCGCGCGTAGGTGGTTCAGCAAGTTGGATGTGAAATCCCCGGGCTCAACCTGGGA
ACTGCATCCAAAACTACTGAGCTAGAGTACGGTAGAGGGTGGTGGAATTTCCTGTGT
AGCGGTGAAATGCGTAGATATAGGAAGGAACACCAGTGGCGAAGGCGACCACCTGG
ACTGATACTGACACTGAGGTGCGAAAGCGTGGGGAGCAAACAGGATTAGATACCCT
GGTAGTCCACGCCGTAAACGATGTCGACTAGCCGTTGGGATCCTTGAGATCTTAGTG
GCGCAGCTAACGCGATAAGTCGACCGCCTGGGGAGTACGGCCGCAAGGTTAAAACT
CAAATGAATTGACGGGGGCCCGCACAAGCGGTGGAGCATGTGGTTTAATTCGAAGCA
ACGCGAAGAACCTTACCTGGCCTTGACATGCTGAGAACTTTCCAGAGATGGATTGGT
GCCTTCGGGAACTCAGACACAGGTGCTGCATGGCTGTCGTCAGCTCGTGTCGTGAGA
TG

Figure 2 Nucleotide sequence of the amplified segment of 16S rRNA gene of *P. aeruginosa*

Some Secondary Metabolites of the Isolated *P. aeruginosa*

Five secondary metabolites (**1** to **5**) including two phenazines (**1** and **2**) and three cyclopeptides, diketopiperazines (**3**, **4** and **5**) were isolated from the chloroform extract of *P. aeruginosa* by using silica gel coloumn chromatographic separation technique. Their structures were elucidated using 1D (^{1}H and ^{13}C NMR) and 2D NMR (HSQC, ^{1}H-^{1}H COSY, HMBC, ROESY) spectroscopic techniques. All of these compounds are the chemical constituents found in *P. aeruginosa* (David *et al*., 1986; Kwon *et al*., 2001 and Muhanna *et al*., 2017).

Compound 1: It was obtained as a yellow crystal with melting point of 152-157 °C and has R_f value of 0.6 (PE:EA, 4:1 v/v). It is soluble in all polar and non-polar organic solvents (pet ether, ethyl acetate, methanol, ethanol and acetone) tested. According to the 1D (^{1}H, ^{13}C) and 2D (HSQC, COSY, HMBC) NMR spectroscopic data (Table 3), compound 1 was observed to contain eight protons including seven *sp* alkenic methine protons (=CH) and one OH proton together with twelve carbons including seven *sp* alkenic methine carbons (=CH-), one *sp* alkenic methine carbon bearing OH group and four *sp* alkenic quarternary carbons (=C-) resulting the partial molecular formula of $C_{12}H_8O$ with molecular weight of *m/z* 168. The ESI-MS mass spectrum indicated that the molecular weight of compound **1** was *m/z* 196. Consequently, the remaining mass is 28, and it must contain two nitrogen atoms. Thus, the complete structural formula of compound **1** must be assigned as $C_{12}H_8N_2O$ with the molecular weight 196. Since the DBE (Double Bond Equivalent) equal to 10, there will be three rings and seven double bonds present in compound **1**. The COSY and HMBC correlations finally gave the complete structure of compound **1** as described in Figure 3. It was found that the observed NMR data of compound **1** were similar to the reported data of 1- hydroxy phenazine (Sinha *et. al*., 2015) (Table 3). In addition, the melting point (152-157 ºC) of compound **1** was observed to be identical with the reported data of 1-hydroxyphenazine (mpt.156 – 159 ºC) (Tokyo Chemical Industry), one of the constituents of *P. aeruginosa* (Sinha *et. al*., 2015). On the basis of the above information, the compound **1** was identified as 1-hydroxyphenazine.

Table 3 1D and 2D NMR Spectral Data of 1-Hydroxy phenazine and the Reported Data

Carbon Position	1-Hydroxy phenazine ($CDCl_3$)				*Reported data (DMSO)	
	δ_C(ppm) HSQC	δ_H(ppm) (*J* H_z)	COSY	HMBC	δ_C(ppm)	δ_H(ppm) (*J* H_z)
1	151.76, =C-OH	-	-	-	153.9,COH	-
2	108.97, =CH -	7.26,*dd* (2.1,6.5)	H-3	1,3,4a,10a	110.8 CH	7.20,*dd* (1.0,7.5)
3	120.01, =CH -	7.77,*dd* (2.1,8.1)	H-2	1,2,4a,10a	119.4 CH	7.69,*dd* (1.0,8.5)
4	131.92, =CH -	7.87, *m*	H-3	2,4a,10a	132.3 CH	7.97, *m*
4a	143.89, =C(qC)	-	-	-	143.4 qC	-
5a	144.2, =C(qC)	-	-	-	144.1 qC	-
6	130.85, =CH -	7.86, *m*	H-7	5a,9,9a	131.4 CH	7.91, *m*
7	129.25, =CH -	8.26,*dd* (2.3,7.7)	H-6	4,4a,6	129.5 CH	8.22,*dd* (2.5,6.0)
8	130.55, =CH -	7.84,*dd* (6.6,9.5)	H-9	5a,9a,9	130.8 CH	7.79,*dd* (7.5,8.5)
9	129.77, =CH -	8.31,*dd* (2.2,7.8)	H-8	8	129.8 CH	8.27,*dd* (2.5,6.0)
9a	141.25, =C(qC)	-	-	-	141.5 qC	-
10a	134.76, =C(qC)	-	-	-	136.1 qC	-
OH		8.26			-	8.24

*Sinha *et.al*. 2015

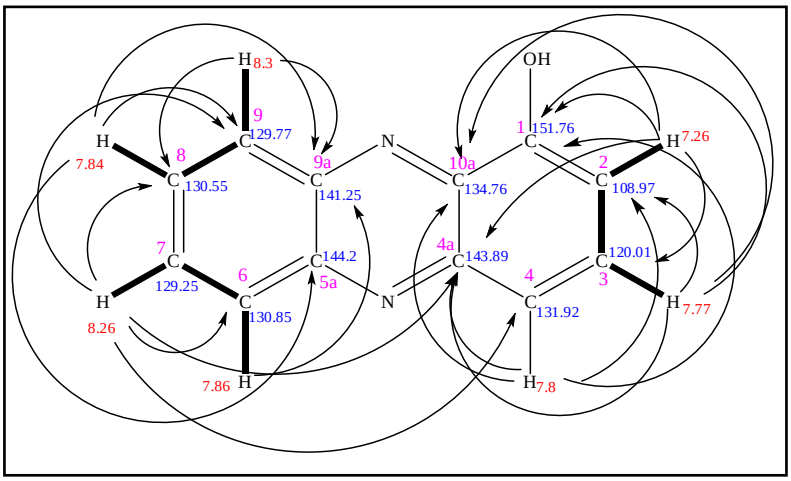

Figure 3 Structure of 1-hydroxyphenazine(1) [COSY (▬) and HMBC (H→C) correlation]

Compound 2: It was obtained as a yellow amorphous powder with melting point of 240- 246 °C and has R_f value of 0.27 (PE:EA, 4:1 v/v). It is also soluble in all polar and non-polar organic solvents tested. It was also found to be a derivative of phenzazine, i.e., phenazine-1-carboxylic acid. Hence, the structure of compound **2** is similar to compound **1** and they differ to each other only in the substituents at C-1. All of the 1D and 2D NMR spectral data were found to be identical with those of the reported data of phenazine-1-carboxylic acid (Sayed *et al*., 2008) (Table 4). The COSY and HMBC correlations gave the complete structure of compound **2** as illustrated in Figure 4. In addition, the melting point of compound **2** ($C_{13}H_8N_2O_2$, m/z = 224 confirmed by mass spectrum) was also observed to be consistent with that of phenazine-1-carboxylic acid (239 ~ 245 °C, $C_{13}H_8N_2O_2$, mol. wt. = 224) (Syn Quest Labs).

Table 4 1D and 2D NMR Spectral Data of Phenazine-1-carboxylic Acid and the Reported Data

Carbon position	Phenazine-1-carboxylic acid ($CDCl_3$)				*Reported data (CD_3OD)	
	δ_C(ppm) HSQC	δ_H(ppm) (*J*,Hz)	COSY	HMBC	δ_H(ppm)	δ_C(ppm)
1	125.04, = C	-	-	2,3	-	124.9 C
2	137.5, = CH	8.99,*dd* (1.44,7.07)	3	1,4,10a,	8.99,*dd* (1.5,7.3)	137.4 CH
3	130.3, = CH	8.05, *m*	COOH		8.05, *m*	130.3 CH
4	135.2, = CH	8.55,*dd* (1.46,8.5)	2,4	1,2,4a	8.54,*dd* (1.5,8.8)	135.1 CH
4a	143.4, = C	-	3	2,10a	-	143.4 C
5a	144.2, = C	-	-	3	-	144.1 C
6	128.0, = CH	8.30,*dd* (1.9,8.3)	-	6,7	8.29,*dd* (1.8,7.7)	128.0 CH
7	133.3, = CH	7.99, *m*	7	5a,8	7.99, *m*	133.2 CH
8	131.8, = CH	8.03, *m*	6	5a	8.03, *m*	131.7 CH
9	130.1, = CH	8.35,*dd* (1.9,8.3)	9	9a	8.35,*dd* (2.6,7.3)	130.1 CH
9a	139.9, = C	-	8	7,9a	-	139.8 C
10a	140.1, = C	-	-	8,9	-	140.1 C
COOH	166.0, C=O	-	-	2,4	-	165.9 C

* Sayed *et al*., 2008

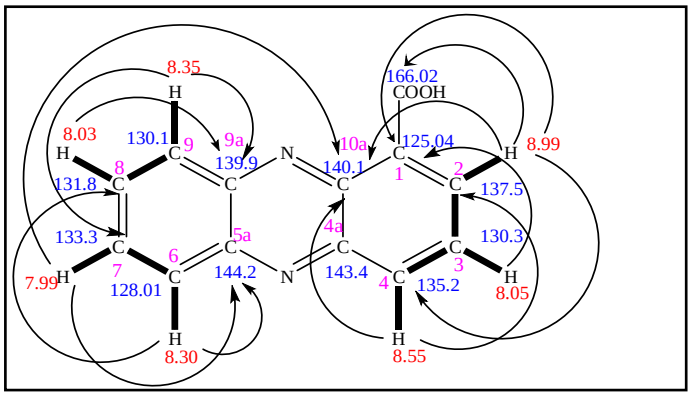

Figure 4 Structure of phenazine-1-carboxylic acid (2) [COSY (▬) and HMBC (H→C) correlation]

Compound 3: It was obtained as a colourless powder (0.34 % yield based on the chloroform extract) with melting point of 161~164 °C and has R_f value of 0.45 (PE:EA, 7:3 v/v). It is soluble in chloroform, ethyl acetate, methanol, ethanol and acetone, and insoluble in non-polar solvent pet ether. 1D and 2D NMR spectral data (Table 5) indicated the presence of 18 protons and eleven carbons related to two sp^3 methyl groups (-CH_3), four sp^3 methylene groups (-CH_2-), three sp^3 methine groups (-CH-), one NH group and two carbonyl groups (C=O). From the NMR and ESI-MS spectroscopic analyses, compound **3** was assigned as a nitrogeneous compound having the molecular formula $C_{11}H_{18}N_2O_2$ with *m/z* 210. These NMR spectral data of compound **3** was observed to be consistent with the reported data of cyclo-(L-Leu-L-Pro) (Youn *et. al.*, 2016) (Table 5) and its melting point was identical with the reported data (mpt. 163 – 165 °C) (ChemSpider). The COSY and HMBC correlationships (Figure **5**) and all of the above observations confirmed the compound **3** as cyclo-(L-Leu-L-Pro), a cyclodipeptide. The ROESY spectral data confirmed the stereochemical configuration of compound **3**, i.e., the beta hydrogens (δ_H 4.11 ppm and 4.01 ppm) on C-6 and C-9 (Table 5).

Table 5 1D and 2D NMR Spectral Data of Cyclo-(L-Leu-L-Pro) and the Reported Data

Carbon position	Cyclo-(L-Leu-L-Pro) (CDCl₃)					*Reported data (CDCl₃)	
	δ_C(ppm) HSQC	δ_H(ppm)	COSY	HMBC	ROESY	δ_C(ppm)	δ_H(ppm)
1	166.21, C=O	-	-	-		168.9(CO)	-
3	45.45, $CH_2(sp^3)$	3.56 (*m*)	4	4,5,6		45.4(CH_2)	3.56(*m*)
4	22.70, $CH_2(sp^3)$	2.02 (*m*)	3,5	4,7		23.6(CH_2)	2.01(*m*)
5	28.04, $CH_2(sp^3)$	2.34 (*m*)	6	4,3,6	6(CHβ)	29.1(CH_2)	2.30, 2.31(*m*)
6	58.93, CH(sp^3)	4.11 (t,8.2)	5	7,5		60.3(CH)	4.27(*dt*,9.3,1.5)
7	170.3, C=O	-	-	-		172.8(CO)	-
8	-	6.36(1H,s, NH)	-	-		-	6.36(1H,*s*,NH)
9	53.35, CH(sp^3)	4.01 (*m*)	10	1,10,11		54.6(CH)	4.13(*m*)
10	38.50, $CH_2(sp^3)$	1.52 (*m*)	11	1,12	9(CHβ)	39.4(CH_2)	1.53(*m*)
11	24.58, CH(sp^3)	1.77 (*m*)	10,1, 12'	10,12		25.8(CH)	1.88(*m*)
12	23.23, $CH_3(sp^3)$	0.99 (*d*,6.59)	11	10,11		23.3(CH_3)	0.99(*d*,6.59)
12'	21.18, $CH_3(sp^3)$	0.94 (*d*,6.52)	11	10,11		22.2(CH_3)	0.95(*d*,6.52)

* Youn *et. al.*, 2016

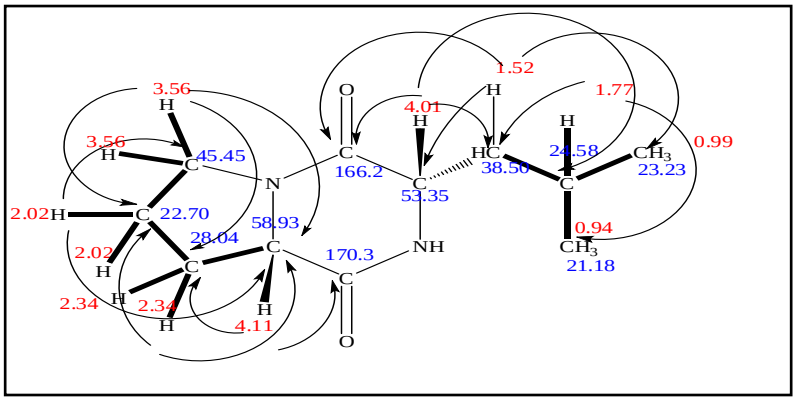

Figure 5 Structure of cyclo-(L-Leu-L-Pro)(3) [COSY (▬) and HMBC (H→C) correlation]

Compound 4: It was obtained as a colourless powder and has R_f value of 0.36 (PE:EA, 7:3 v/v). It is soluble in only in ethyl acetate, methanol, ethanol and acetone, and insoluble in non-polar pet ether solvent. It is also a cyclodipeptide, i.e., a diketopiperazine and structurally elucidated as cyclo-(D-Pro-D-Leu) with the molecular formula $C_{11}H_{18}N_2O_2$ (m/z = 210) by ESI-MS. All of the 1D and 2D NMR spectral data of this compound were found to be similar to the reported data (Youn *et. al.*, 2016) (Table 6). Figure 6 shows the ^{1}H-^{1}H COSY and HMBC correlations of this compound. ROESY spectral analysis on stereochemical configuration confirmed that both hydrogens at δ_H 2.36 and 1.53 ppm respectively attached to C-5 and C-10 were observed to be in alpha positions. Compounds **3** and **4** were found to be the stereoisomers of cyclodipeptide of proline and leucine amino acids.

Table 6 1D and 2D NMR Spectral Data of Cyclo-(D-Pro-D-Leu) and the Reported Data

Carbon position	Cyclo-(D-Pro-D-Leu) ($CDCl_3$)					*Reported data ($CDCl_3$)	
	δ_C(ppm) HSQC	δ_H(ppm)	COSY	HMBC	ROESY	δ_C(ppm)	δ_H(ppm)
1	166.2, C=O	-	-	-		168.9(CO)	-
3	45.49, $CH_2(sp^3)$	3.58 (*m*)	4	4,5,6		45.4(CH_2)	3.56(*m*)
4	22.72, $CH_2(sp^3)$	2.08 (*m*)	3,5	1,4,6,7		23.6(CH_2)	2.01(*m*)
5	28.10,$CH_2(sp^3)$	2.36 (*m*)	6	4,3,6	6(CH,α)	29.1(CH_2)	2.30,2.31(*m*)
6	58.97, $CH(sp^3)$	4.12 (*t*, 8.2)	5	7,5		60.3 (CH)	4.27(*dt*,9.3,1.5)
7	170.3, C=O	-	-	-		172.8(CO)	-
8	-	5.92 (1H, *s*, NH)	-	-		-	6.36 (1H,*s*,NH)
9	53.36, $CH(sp^3)$	4.03(*dd*, 3.29, 3.87)	10	1,10		54.6 (CH)	4.13(*m*)
10	38.61, $CH_2(sp^3)$	1.53 (*m*)	11	1,12	9(CH,α)	39.4(CH_2)	1.53(*m*)
11	24.70, $CH(sp^3)$	1.76 (*m*)	10,12	10,12		25.8 (CH)	1.88(*m*)
12	23.27, $CH_3(sp^3)$	1.01 (*d*,6.59)	11	10,11		23.3(CH_3)	0.99 (*d*,6.59)
12'	21.17, $CH_3(sp^3)$	0.96 (*d*,6.52)	11	10,11		22.2(CH_3)	0.95 (*d*,6.52)

* Youn *et al*., 2016

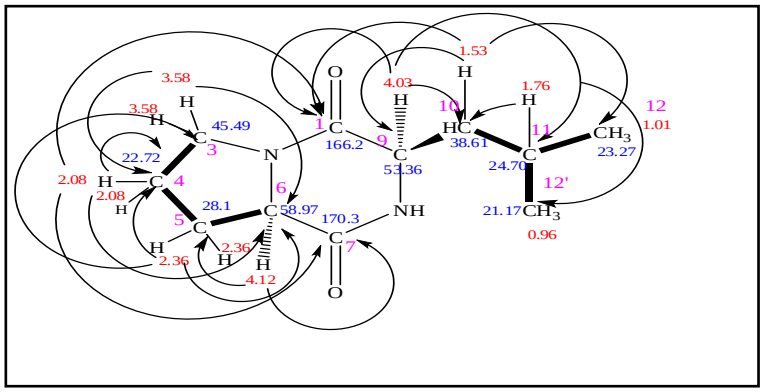

Figure 6 Structure of cyclo-(D-Pro-D-Leu) (4) [COSY (▬) and HMBC (H→C) correlation]

Compound 5: It was obtained as a yellow oil and has R_f value of 0.6 (Hexane:EtOAc:MeOH, 1.8:8:0.2, v/v/v). It is soluble in only in ethyl acetate, methanol, ethanol and acetone, and insoluble in chloroform and pet ether. It is also a cyclodipeptide, i.e., a diketopiperazine and structurally elucidated as cyclo-(D-Pro-L-Val) with the molecular formula $C_{10}H_{16}N_2O_2$ (m/z = 196) by ESI-MS. All of the 1D and 2D NMR spectral data of this compound were found to be similar to the reported data (Kwon *et. al*., 2001) (Table 7). Figure 7 shows the ^{1}H-^{1}H COSY and HMBC correlations of this compound. ROESY spectral analysis on stereochemical configuration confirmed that both hydrogens at δ_H 3.94 and 4.08 ppm respectively attached to C-3 and C-6 were observed to be in alpha positions.

Antimicrobial Activity of the Isolated Compounds (1 to 5)

In the screening of antimicrobial activity on the five isolated compounds (**1** to **5**) against seven different pathogenic microbes such as *A. tumefacines, B. subtilis, B. pumilus, C. albicans, E. coli, P. aeruginosa* and *S. aureus* using agar well diffusion method, compound **1** (1-hydroxyphenazine) was observed to exhibit high activity against all of the tested microorganisms with the inhibition zone diameters ranged above 20 mm. The compound **2** (phenazine-1-carboxylic acid) was observed medium activity against the tested microorganisms. The remaining three isolated diketoperazines: cyclo(L-Leu-L-Pro) (**3)**, cyclo(D-Pro-D-Leu) (**4)** and cyclo(D-Pro-L- Val) (**5**) showed mild antimicrobial activity with the inhibition zone diameters between 12 mm ~ 14 mm but inactive against all of the tested microorganisms. The results are shown in Table 8.

Table 7 1D and 2D NMR Spectral Data of Cyclo-(D-Pro-L-Val) and the Reported Data

Carbon position	Cyclo-(D-Pro-L-Val) ($CDCl_3$)					*Reported data ($CDCl_3$)	
	δ_C(ppm) HSQC	δ_H(ppm)	COSY	HMBC	ROESY	δ_C(ppm)	δ_H(ppm)
1	170.03, C=O	-	-	8		169.9(CO)	-
3	60.36, -CH(sp^3)	3.94 (*m*)	-	4,10,1, 12	3 (CH,α)	60.3(CH)	3.94(1H,m)
4	164.89, C=O	-	-	3		164.8(CO)	-
6	58.79, -CH(sp^3)	4.08(*m*)	7,8	7,1	6 (CH,α)	58.7(CH)	4.09 (1H,*m*)
7	28.50,-CH_2(sp^3)	2.08(*m*),Ha	6,8	6,8,9		28.3(CH_2)	2.05 (1Ha,*m*)
		2.3(*m*),Hb					2.39 (1Hb,*m*)
8	22.33,-CH_2(sp^3)	1.91(*m*),Ha	7,9	7,9		22.2(CH_2)	1.90 (1Ha,*m*)
		2.02(*m*),Hb		1,6,7,8		22.2(CH_2)	2.05 (1Hb,*m*)
9	45.12,-CH_2(sp^3)	3.55(*m*),Ha	8	7,8		44.9(CH_2)	3.55, (1Ha,*m*)
		3.65(*m*),Hb					3.65, (1Hb,*m*)
10	28.33, CH(sp^3)	2.64 (*m*)	11	3,11,12		28.4(CH)	2.64(2H,*m*)
11	16.02,-CH_3(sp^3)	0.92 (*d*,6.9)	10,12	10,12		15.9(CH_3)	0.92 (3H,*d*,6.9)
12	19.21, CH_3(sp^3)	1.07 (*d*,7.5)	11	10,11		19.2(CH_3)	1.07 (3H,*d*,7.5)

* Kwon *et. al*. 2001

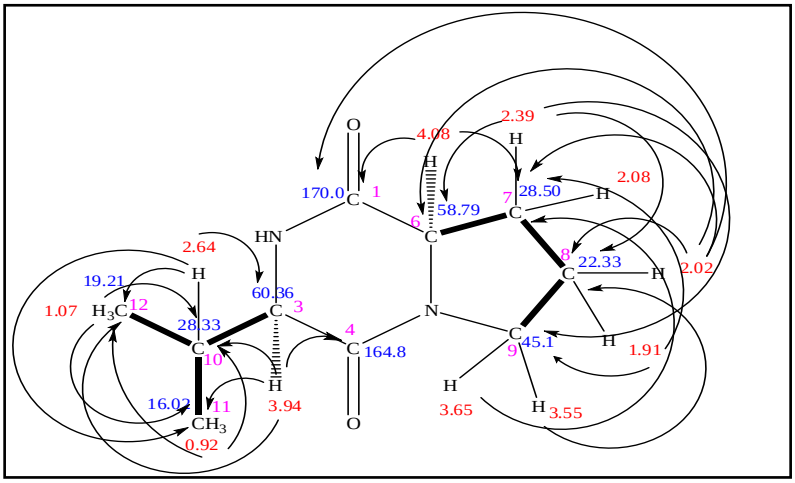

Figure 7 Structure of cyclo-(D-Pro-L-Val) (5) [COSY (▬) HMBC (H→C) correlation]

Antiproliferative Activity of the Isolated Compounds (1 to 5) against Human Breast Cancer MCF7 Cells

The antiproliferative activities of the isolated compounds were investigated with MCF7 (human breast cancer cell line). Antiproliferative activity was expressed as the IC_{50} (50 % inhibitory concentration) value. 5-Fluorouracil was used as positive control. The results are summarized in Table 9. It was observed that the two isolated phenazines: 1-hydroxyphenazine (**1**, IC_{50}=14.1 µg/mL) and phenazine-1-carboxylic acid (**2**, IC_{50}=15.0 µg/mL) exhibited high antiproliferative activity against MCF 7 cell line whereas the remaining three isolated diketoperirazines: cyclo(L-Leu-L-Pro) (**3**, IC_{50} = 176.4 µg/mL), cyclo(D-Pro-D-Leu) (**4**, IC_{50} = 87.7 µg/mL) and cyclo(D-Pro-L-Val) (**5**, IC_{50} = 196.5 µg /mL) showed mild antiproliferative activity. The compounds **1** and **2** were found to be comparable with the standard 5-fluorouracil (IC_{50} = 11.50 µg/mL) in antiproliferative activity against MCF7 human breast cancer cell line.

Table 8 Inhibition Zone Diameters of the Isolated Compounds of *P. aeruginosa* against Seven Microorganisms by Agar Well Diffusion Method

Microorganisms	Inhibition zone diameters (mm) of the isolated compounds					
	1	**2**	**3**	**4**	**5**	**Control**
A. tumefacines	28(+++)	26(+++)	12(+)	-	-	-
B. pumilus	30(+++)	27(+++)	-	14(+)	14(+)	-
B. subtilis	32(+++)	26(+++)	12(+)	-	14(+)	-
E. coli	32(+++)	20(+++)	12(+)	12(+)	-	-
C. albicans	28(+++)	31(+++)	14(+)	-	-	-
P. aeruginosa	21(+++)	18(++)	14(+)	12(+)	12(+)	-
S. aureus	23(+++)	15(++)	14(+)	12(+)	-	-

Agar well –10 mm, 10 mm ~ 14 mm = (+) low activity, 15 mm ~ 19 mm = (++) medium activity, 20 mm and above = (+++) high activity, 1 = 1-hydroxyphenazine, **2** = phenazine-1-carboxylicacid, **3** = cyclo(L-Leu-L-Pro), **4** = cyclo(D-Pro-D-Leu), **5** = cyclo(D-Pro-L- Val)

Table 9 Antiproliferative Activity of the Isolated Compounds and Standard 5 Fluorouracil against Human Breast Cancer Cell MCF7

Isolated compounds	% Cell survival in different concentrations of each sample				IC_{50} (µg/mL)
	10	**20**	**100**	**200**	
1	51.94 ± 2.40	47.22 ± 1.77	10.29 ± 0.07	9.13 ± 0.14	14.1
2	74.86 ± 0.64	45.55 ± 1.20	13.49 ± 0.07	12.81 ± 0.35	15.0
3	87.97 ± 0.49	77.66 ± 7.92	66.50 ± 0.71	44.93 ± 0.57	176.4
4	78.97 ± 1.48	59.90 ± 3.11	48.21 ± 0.99	44.64 ± 0.64	87.7
5	102.90 ± 3.39	94.28 ± 6.28	67.20 ± 9.97	49.38 ± 1.27	196.5
***5-Fluorouracil	61.94 ± 0.8	37.22 ± 0.7	10.29 ± 1.0	8.42 ± 0.2	11.5

1 = 1-hydroxyphenazine , **2** = phenazine-1-carboxylic acid, **3** = cyclo(L-Leu-L-Pro)

4 = cyclo(D-Pro-D-Leu), **5** = cyclo(D-Pro-L- Val)) * standard

Conclusion

The present study reveals that *P. aeruginosa* bacterial strain isolated from the clinical soil sample of Insein General Hospital, Yangon Region was successfully confirmed by the DNA sequencing technique using PCR amplification of 16S rRNA. In addition, two phenazine derivatives such as 1-hydroxyphenazine (0.24 % based on chloroform extract, m.pt 152-157 °C) and phenazine-1-carboxylic acid (0.7 %, m.pt 240-246 °C) together with three cyclopeptides, diketopiperazines such as cyclo(L-Leu-L-Pro (0.34 %, m.pt 164- 164 °C), cyclo(D-Pro-D-Leu) (0.09 %) and cyclo(D-Pro-L-Val) (0.18 %) could be isolated from the chloroform extract of the isolated *P. aeruginosa* strain. These isolated compounds were structurally elucidated by 1D and 2D NMR spectroscopic techniques and ESI-MS spectrometry, and also by comparing with their respective reported data. Moreover, it can be also evaluated that the two isolated phenazines exhibit high antimicrobial activity against all tested microorganisms with the inhibition zone diameter ranged between 15 ~ 40 mm. The remaining three isolated diketopiperazines showed mild antimicrobial activity with the inhibition zone diameters ranged between 12 mm ~ 14 mm. Furthermore, 1-hydroxyphenazine (IC_{50} = 14.12 µg/mL) and phenazine-1-carboxylic acid (IC_{50} = 15.0 µg/mL) were also found to possess good antiproliferative activity against human breast cancer MCF7 whereas cyclo(L-Leu-L-Pro) (IC_{50} = 176.4 µg/mL), cyclo(D-Pro- D-Leu) (IC_{50} = 87.7 µg/mL) and cyclo(D-Pro-L-Val) (IC_{50} = 196.5 µg /mL) have mild activity. From the present work, it can be inferred that the isolated compounds especially 1-hydroxyphenazine and phenazine-1-carboxylic acid may be useful in the formulation of antibacterial and antifungal agents for the treatment of the diseases infected by the tested microorganisms and may be useful in the formulation of anticancer agents for the treatment of human breast cancer cell. Hence, the finding of this research work will contribute to some extend in the development of antimicrobial agents and anticancer agents from the source of soil bacteria *P. aeruginosa.*

Acknowledgements

The authors would like to express their profound gratitude to the Department of Higher Education, Ministry of Education, Yangon, Myanmar, for providing the opportunity to do this research and to Dr Saw Hla Myint, Dr Ni Ni Than for their Super Vision.

References

Amutha, K., and V. Kokila. (2014). "PCR Amplification, Sequencing of 16S rRNA Genes with Universal Primers and Phylogenetic Analysis of *Pseudomonas aeruginosa*". *Journal of Science and Research*, vol. 3 (8), pp. 2-6

Baron, S. S., and J. J. Rowe. (1981). "Antibiotic Action of Pyocyanin". *Journal of Antimicrobial Agents and Chemotherapy*, vol. 20 (6), pp. 814–820

ChemSpider, ChemSpider.com/Chemical-Structure 5428292. html

David, W., M. John, W. Robert, C. Peter, and W.T. Graham. (1986) "Purification and Structural Analysis of Pyocyanin and 1- Hydroxyphenazine". *Journal of Biochemistry*. vol. 159, pp. 309–313

Kwon, O. S., P. Sang Ho, Y. Bong-Sik, P. Yu-Ryang, and K. Chang-Jin. (2001). "Cyclo (D-Pro-L-Val), a Specific /3-Glucosidase Inhibitor Produced by *Aspergillus* sp. F70609". *Journal of Antibiotics*, vol. 54, pp. 179-181

Muhanna, M. A. N. M., J. Juriyati, S. M. Nik, J. A. Siti, K. Nurkhalida, and E. E. Ru Angelie. (2017). "Isolation, Purification and Characterization of Five Active Diketopiperazine Derivatives from Endophytic Streptomyces SUK 25 with Antimicrobial and Cytotoxic Activities". *Journal of Microbiol Biotechnol*, vol. 27 (7), pp. 1249-1256

Perez, C., M. Paul, and P. Bezique. (1990). *An Antibiotic Assay by Agar Well Diffusion Method*. Alta Biomed., Group Experiences, vol. 15**,** pp. 133-155

Sayed, W. El., M. Abd El-Megeed, A. B. Abd El-Razik, K.H. Soliman, and S. A. Ibrahim. (2008). "Isolation and Identification of Phenazine-1-Carboxylic acid from different *Pesudomonas* Isolates and its Biological Activity Against *Alternaria Solani*". *Journal of Agriculture and Biological Sciences*, vol. 4 (6), pp. 892-901

Sinha, S., X. Shen, F. Gallazzi, Q. Li, J. W. Zmijewski, J. R. Lancaster, and K. S. Gates. (2015). "Generation of Reactive Oxygen Species Mediated by 1-Hydroxyphenazine, a Virulence Factor of *Pseudomonas Aeruginosa*". *Journal of Chemistry Research Toxicol*ogy, vol.28(2), pp. 175-181

Su Swe Su, Khine Zar Wynn Lae, and Daw Hla Ngwe. (2018). "Isolation and Identification of *Pseudomonas Aeruginosa* from the Clinical Soil". *Journal of Research University of Yangon*, vol. 8, pp. 271-275

Su Swe Su, Khine Zar Wynn Lae, Nwet Nwet Win, and Daw Hla Ngwe. (2019). "Investigation of Chemical Composition and Some Biological Properties of Chloroform Extract of *Pseudomonas Aeruginosa*". *Jour. Myan. Acad. Arts & Sc*, vol. 18 (1A), pp. 545-560

Syn Quest Labs. http://synquestlabs.com/product/id/68826.html

Tokyo Chemical Industry. http//: www. tcichemicals.com/US/en/p/H0289#docoments Section PDP

Win, N. N., T. Ito, S. Aimaiti, H. Imagawa, H. Ngwe, I. Abe, and H. Morita. (2015). "Kaempulchraols A–H, Diterpenoids from the Rhizomes of *Kaempferia pulchra* Collected in Myanmar". *J. Nat. Prod.*, vol. 78, pp. 1113–1118

Youn, U. J., M. J. Kim, S. J. Han and J. H. Yim. (2016). "Isolation of Secondary Metabolites from an Arctic Bacterium, *Pseudomonas Aeruginosa* and their Antimicrobial activities". *Journal of Microbiology*, vol. 52(4), pp. 415-420

ANALYSIS AND SOME BIOACTIVITIES OF THE ESSENTIAL OIL AND SOME SOLVENT EXTRACTS OF CARROT SEEDS

Sandar Moe[1], Kay Thi[2], Ya Min Thuzar[3], Myint Myint Khin[4], Khine Khine Lin[5], Cho Cho Nyein[6]

Abstract

A readily available local carrot seeds was selected for the investigation of some bioactivities of essential oil. The essential oil of carrot seeds was extracted by steam distillation using Clevenger's apparatus; the yield % of 0.96 was obtained, and GC-MS analysis showed twenty-one compounds and by comparison of the mass spectra of eluted compound against respective standards showed mono- and sesquiterpenes/terpenoids and a phenol dimer in the oil extracted. Screening of antimicrobial activity by agar well diffusion method showed highest activity for the essential oil (20-25 mm), lower activity for the alcohol extracts (10-16 mm), and no activity for watery and petroleum ether extracts. Antioxidant activity of the essential oil was higher (IC_{50} 0.9 μg/mL) than ascorbic acid standard (IC_{50} 1.17 μg/mL) by DPPH assay method, with lower activities for the crude extracts (in H_2O and EtOH).

Keywords: Carrot seeds, essential oil, GC-MS, terpenoids, antimicrobial activity, antioxidant activity

Introduction

Carrot is biennial flowering plant belonging to Apiaceae family and genus *Daucus* and it is widely distributed and commonly cultivated for its edible root. To collect seeds the plant is not harvested in the first season. Carrot plant possessed plenty of beneficial skin care properties and very popular in the personal care industry (Kulkarni, 2017). Nowadays, most people prefer natural foods, herbal medicines, herbal cosmetics and natural curing practices for healthy life. The production and usage of synthetic based products and their derived products cause human health hazard (Kapoor, 2005). Carrot seed essential oil is obtained from carrot seeds by steam distillation. Mono- and sesquiterpenes/terpenoids are the main constituents of carrot seed essential oil in which carotol and daucol were the main compounds (Kaur *et al*., 2018). The oil has also gained more attraction for its anti-inflammatory, antifungal, and antioxidant properties (Whenlan, 2019). It significantly improves psychological and physical health and well-being and is also used in perfumery, cosmetics, food and medicine (Smigielski *et al*., 2014). Carrot seed essential oil is not yet widely used in Myanmar, an agriculture country, where carrot plants are abundantly grown, so it would be beneficial to find a domestic market and earn foreign income through it. The aim of the present study is thus to investigate the chemical composition, and antimicrobial and antioxidant activities of the local carrot seed essential oil.

Materials and Methods

Sample Collection and Preparation

Carrot seeds were collected in the 1999-20 from La Mine village at Kalaw Township, Southern Shan State and the collected sample was identified at Department of Botany, Taunggyi University. Carrot seeds were dried and then ground into powder by using electric blender and stored in air tight container to prevent moisture and other contamination.

[1] Professor, Department of Chemistry, Kyaing Tong University
[2] Demonstrator, Department of Chemistry, Taunggyi University
[3] Demonstrator, Department of Chemistry, Kyaing Tong University
[4,5] Associate Professors, Department of Chemistry, Kyaing Tong University
[6] Professor and Head, Department of Chemistry, Kyaing Tong University

Preliminary Phytochemical Tests of Carrot Seeds

In order to find out the type of organic constituents present in the selected sample of carrot seeds, preliminary phytochemical investigation was carried out by the appropriate methods.

Extraction of Essential Oil of Carrot Seeds

The dried powdered sample of carrot seeds (100 g) and distilled water (200 mL) were placed in the round bottomed flask (250 mL). The flask was fitted with a Clevenger's apparatus which was joined to water condenser. After boiling the water in the flask for 4 h, the condensed oil and water were collected in the receiver of the apparatus. The oil was then extracted with petroleum ether (60-80 ºC) in a separating funnel. The petroleum ether layer was also dried over anhydrous sodium sulphate, filtered and evaporated to get a weight of essential oil. The extraction in the same manner was made for ten batches altogether and the combined extracts placed in a bottle and stored in refrigerator at 4 ºC for further investigation. The percentage yield of essential oil is calculated using the formula:

$$\text{Percent yield of oil (w/w)} = \frac{\text{Weight of oil in gram}}{\text{Weight of the sample in gram}} \times 100\ \%$$

GC-MS Analysis

The chemical constituents of the carrot seed essential oil are volatile and gas chromatography – mass spectrometry (GC-MS) is usually used for their identification. The compounds eluted at different retention times from GC were identified by comparing their mass spectra with data bank by software.

Screening of Antimicrobial Activity of Crude Extracts and Essential Oil of Carrot Seeds

Wells (8 mm in diameter) were punched with a sterile cork borer through test agar plates inoculated with test organisms (0.2 mL) and filled with the sample (50 µL: neat sample for essential oil or 0.1 g/mL solution in respective solvents for the solvent extracts) and the Petri dishes were incubated at room temperature for 24 h. After incubation, the diameters of the growth inhibition zones surrounding the agar wells were measured in mm, which indicate the antimicrobial activities of the tested samples (Collin and Lyne, 1964).

Screening of Antioxidant Activity of Crude Extracts and Essential Oil of Carrot Seeds

Antioxidant activity of the essential oil, water and ethanol crude extracts was determined by DPPH free radical scavenging assay method. In this experiment, six different concentrations (0.625, 1.25, 2.5, 5, 10 and 20 µg/mL) of essential oil and crude extracts (ethanol and watery) were prepared by serial dilution. The control solution was prepared by mixing 1.5 mL of 60 μM DPPH solution and 1.5 mL of ethanol. The test sample solution was also prepared by mixing 1.5 mL of DPPH solution and 1.5 mL of test sample solution. The mixture solutions were allowed to stand at room temperature for 30 min. Then, the absorbance of these solutions was measured at 517 nm on a UV-2550 spectrophotometer. Absorbance measurements were determined in triplicate for each concentration and the mean value so obtained were used to calculate percent inhibition of oxidation. IC_{50} value was calculated by linear regression using Microsoft Excel software.

Results and Discussion

Preliminary Phytochemical Screening of Carrot Seeds

The preliminary qualitative analysis of phytochemical investigation showed the presence of alkaloids, flavonoids, glycosides, polyphenols, saponins, terpenes, protein, α-amino acids,

carbohydrates, phenolic compounds, starch and reducing sugars whereas tannins and resins are absent in the carrot seeds.

Identification of Essential Oil Components by GC-MS

The extracted essential oil (yield 0.96 %) is pale yellow in colour and it has a characteristic odour. The chemical composition of the essential oil from carrot seeds was investigated by gas chromatography-mass spectroscopy (GC-MS). MS analysis of compounds and library matching with standard mass spectra indicated the presence of 21 compounds: ten each of mono- and sesquiterpenes and a phenol dimer (Figures 1 to 22 and Table 1). Therefore, it may be concluded that the carrot seeds essential oil contained predominantly mono- and sesquiterpenes/terpenoids. These findings justify its use for human health both as part of a balanced diet and as pharmaceutical agents due to their potential for the treatment of cardiovascular disease and cancer.

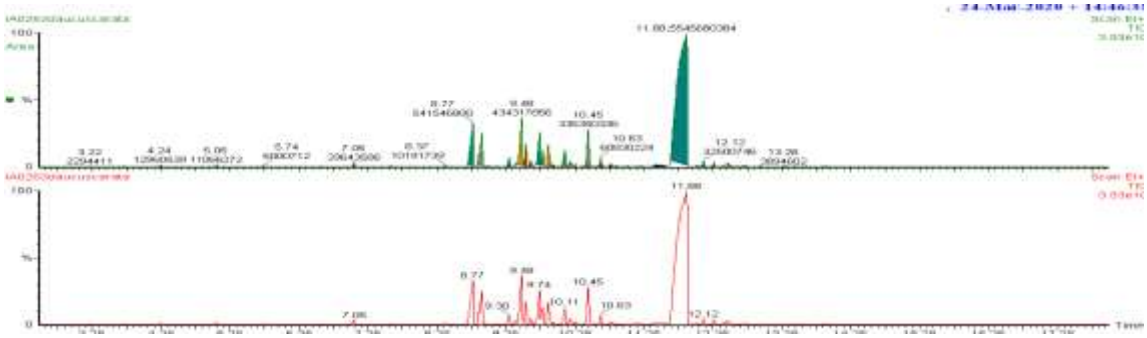

Figure 1 Gas chromatograms of essential oil from carrot seeds

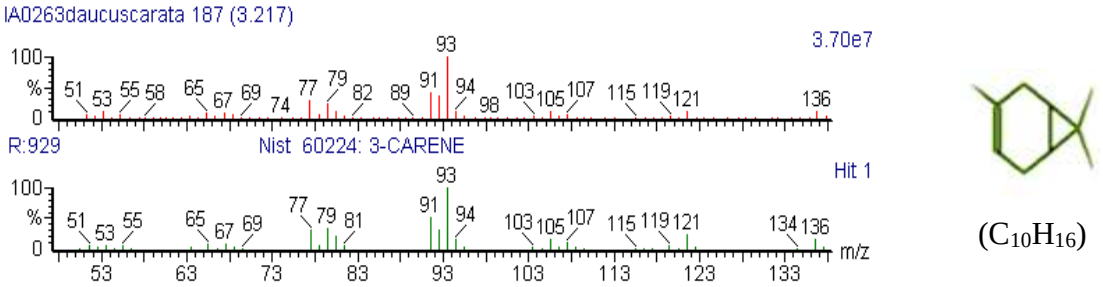

Figure 2 Comparison of the mass spectra of eluted compound RT 3.217 min and standard 3-carene

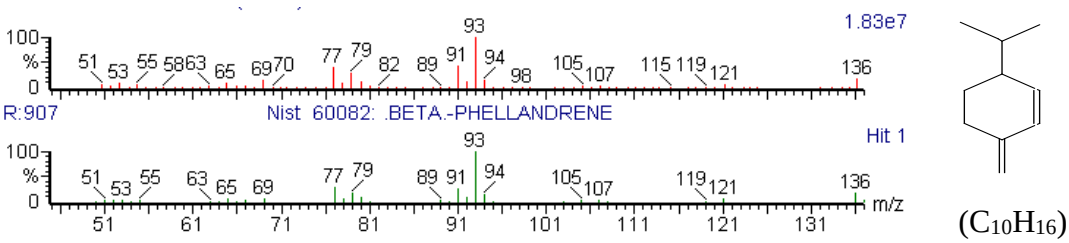

Figure 3 Comparison of the mass spectra of eluted compound RT 3.600 min and standard beta-phellandrene

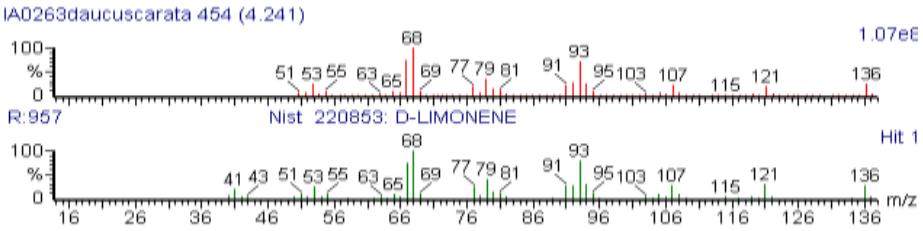

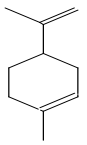

($C_{10}H_{16}$)

Figure 4 Comparison of the mass spectra of eluted compound RT 4.241 min and standard D-limonene

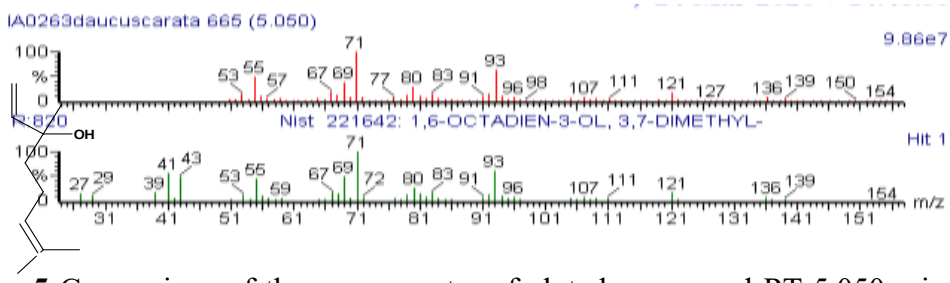

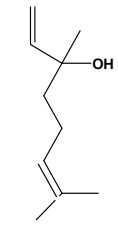

($C_{10}H_{18}O$)

Figure 5 Comparison of the mass spectra of eluted compound RT 5.050 min and standard 3,7-dimethyl-1,6-octadien-3-ol

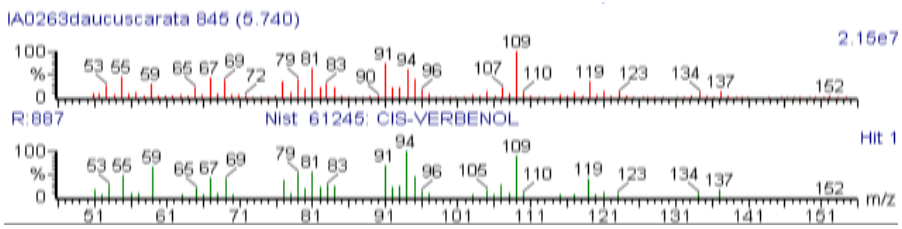

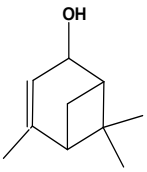

($C_{10}H_{16}O$)

Figure 6 Comparison of the mass spectra of eluted compound RT 5.740 min and standard *cis*-verbenol

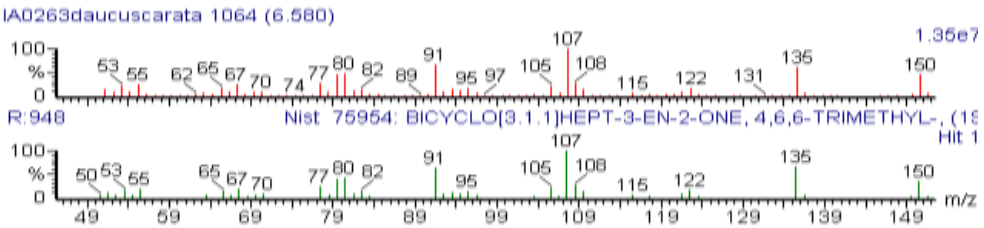

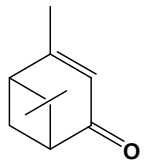

($C_{10}H_{14}O$)

Figure 7 Comparison of the mass spectra of eluted compound RT 6.580 min and standard 4,6,6-trimethylbicyclo[3.1.1]hept-3-en-2- one

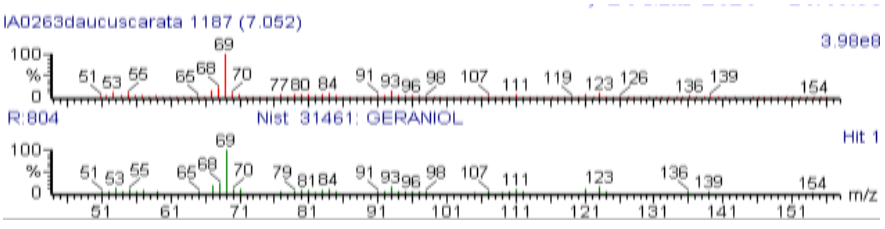

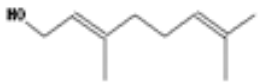

($C_{10}H_{18}O$)

Figure 8 Comparison of the mass spectra of eluted compound RT 7.052 min and standard geraniol

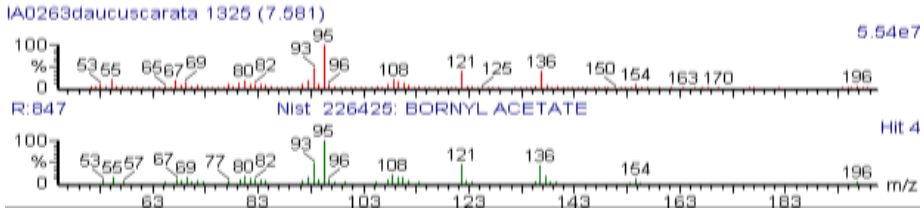

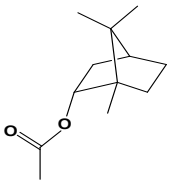

($C_{12}H_{20}O_2$)

Figure 9 Comparison of the mass spectra of eluted compound RT 7.581 min and standard bornyl acetate

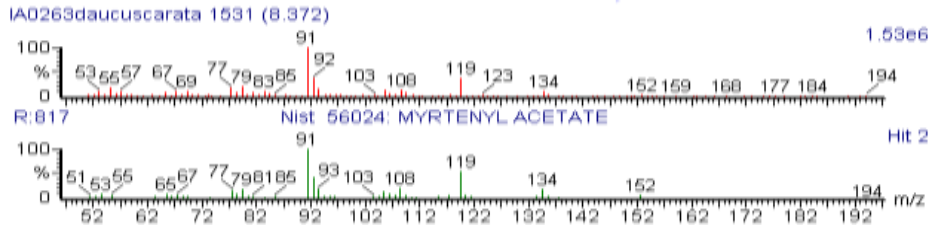

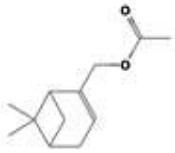

($C_{12}H_{18}O_2$)

Figure 10 Comparison of the mass spectra of eluted compound RT 8.372 min and standard myrtenyl acetate

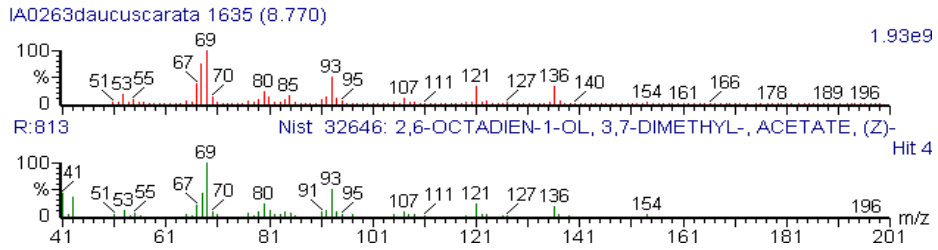

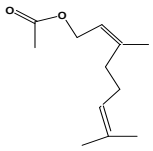

($C_{12}H_{20}O_2$)

Figure 11 Comparison of the mass spectra of eluted compound RT 8.770 min and standard 3,7-dimethylocta-2,6-dien-1-yl acetate

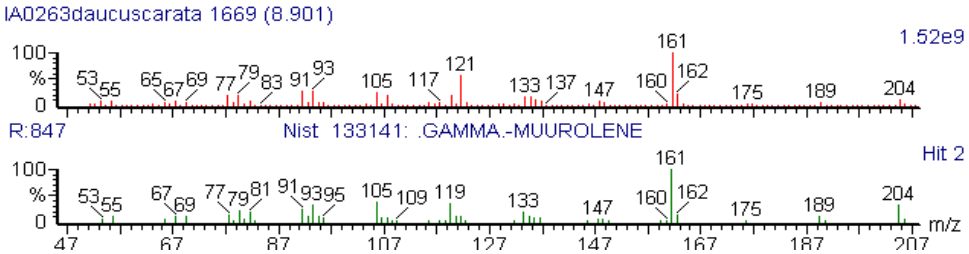

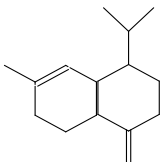

($C_{15}H_{24}$)

Figure 12 Comparison of the mass spectra of eluted compound RT 8.901 min and standard gamma-muurolene

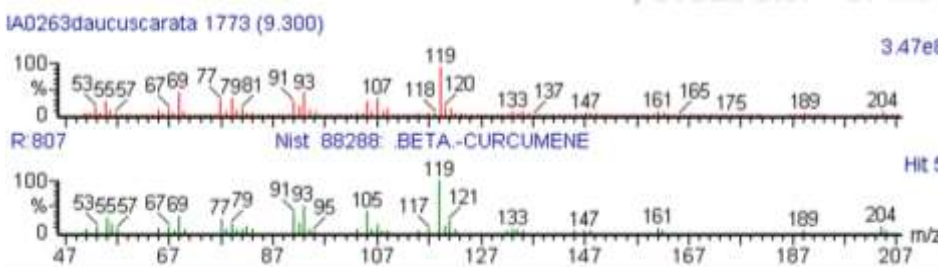

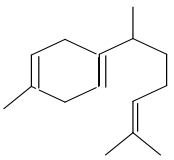

($C_{15}H_{24}$)

Figure 13 Comparison of the mass spectra of eluted compound RT 9.300 min and standard beta-curcumene

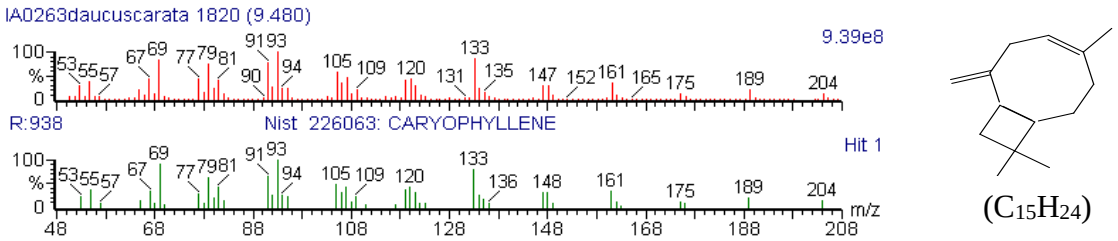

Figure 14 Comparison of the mass spectra of eluted compound RT 9.480 min and standard caryophyllene

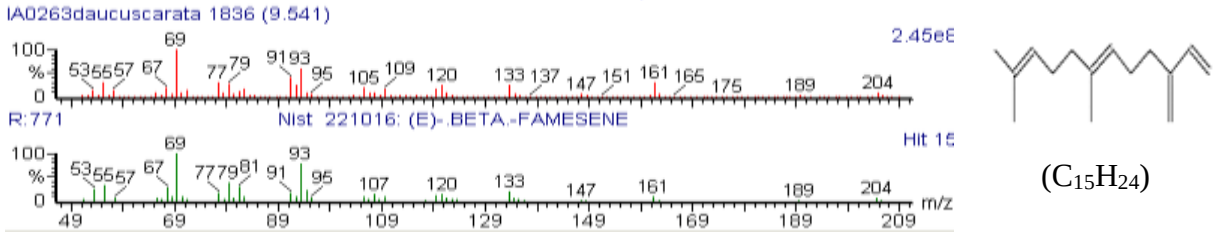

Figure 15 Comparison of the mass spectra of eluted compound RT 9.541 min and standard (E)-beta-famesene

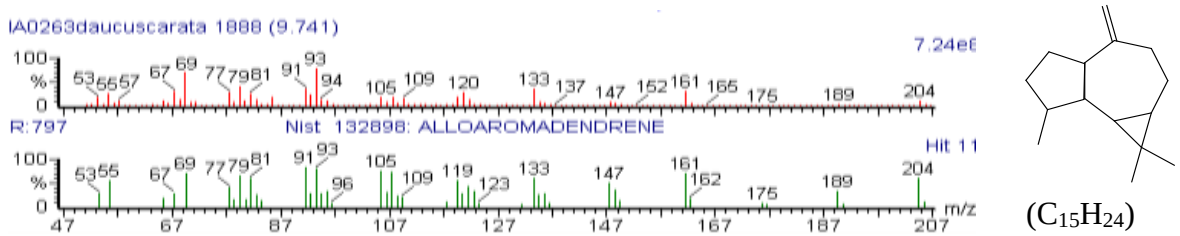

Figure 16 Comparison of the mass spectra of eluted compound RT 9.741 min and standard alloaromadendrene

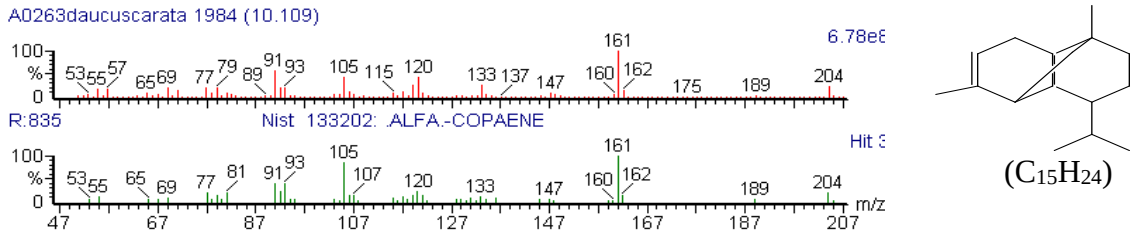

Figure 17 Comparison of the mass spectra of eluted compound RT 10.109 min and standard Alpha copaene

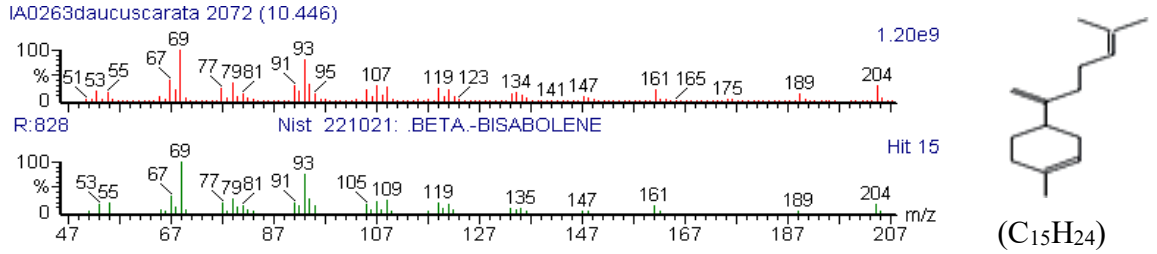

Figure 18 Comparison of the mass spectra of eluted compound RT 10.446 min and standard beta-bisabolene

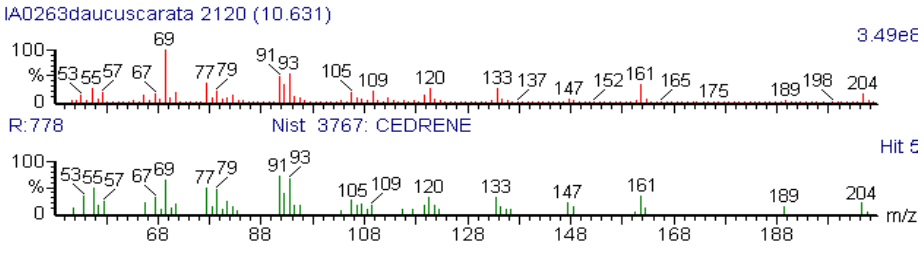

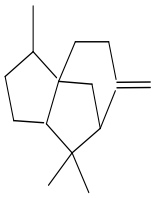

($C_{15}H_{24}$)

Figure 19 Comparison of the mass spectra of eluted compound RT 10.631 min and standard cedrene

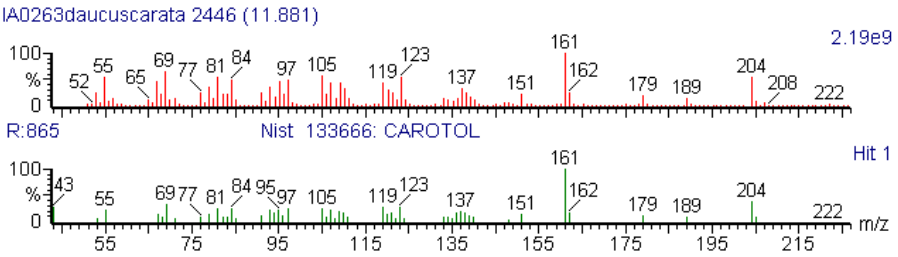

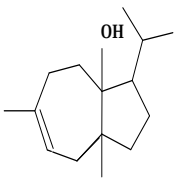

($C_{15}H_{26}O$)

Figure 20 Comparison of the mass spectra of eluted compound RT 11.881 min and standard carotol

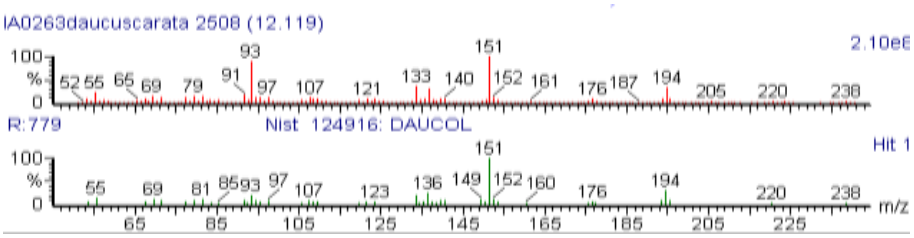

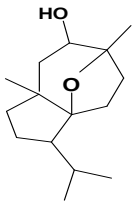

($C_{15}H_{26}O$)

Figure 21 Comparison of the mass spectra of eluted compound RT 12.119 min and standard daucol

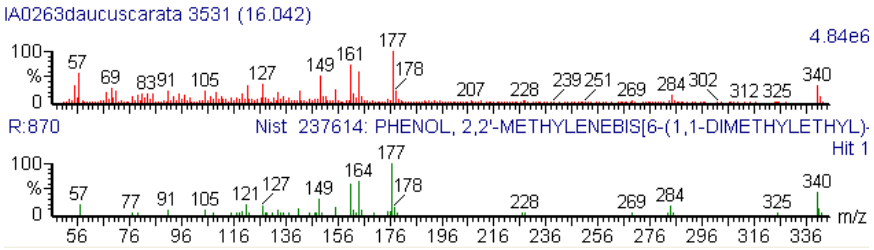

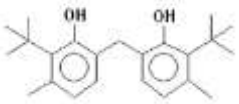

($C_{23}H_{32}O_2$)

Figure 22 Comparison of the mass spectra of eluted compound RT 16.042 min and standard 6,6′-methylenebis(2-(tert-butyl)-3-methyl phenol)

Table 1 Chemical Composition of the Essential Oil of Carrot Seeds

No.	Retention time (min)	Compound name	Molecular formula	Molecular weight	Figure number
1	3.217	3-Carene	$C_{10}H_{16}$	136	2
2	3.600	β- Phellandrene	$C_{10}H_{16}$	136	3
3	4.241	D- Limonene	$C_{10}H_{16}$	136	4
4	5.050	3,7-Dimethyl-1,6-octadien-3-ol	$C_{10}H_{18}O$	154	5
5	5.740	*cis*-Verbenol	$C_{10}H_{16}O$	152	6
6	6.580	4,6,6-Trimethyl bicycle [3.1.1] hept-3-en-2- one	$C_{10}H_{14}O$	150	7
7	7.052	Geraniol	$C_{10}H_{18}O$	154	8
8	7.581	Bornyl acetate	$C_{12}H_{20}O_2$	196	9
9	8.372	Myrtenyl acetate	$C_{12}H_{18}O_2$	194	10
10	8.770	3,7-Dimethylocta-2,6-dien-1-yl acetate	$C_{12}H_{20}O_2$	196	11
11	8.901	γ-Muurolene	$C_{15}H_{24}$	204	12
12	9.300	β-Curcumene	$C_{15}H_{24}$	204	13
13	9.480	Caryophyllene	$C_{15}H_{24}$	204	14
14	9.541	(E)-β-Famesene	$C_{15}H_{24}$	204	15
15	9.741	Alloaromadendrene	$C_{15}H_{24}$	204	16
16	10.109	α-Copaene	$C_{15}H_{24}$	204	17
17	10.446	β-Bisabolene	$C_{15}H_{24}$	204	18
18	10.631	Cedrene	$C_{15}H_{24}$	204	19
19	11.881	Carotol	$C_{15}H_{26}O$	222	20
20	12.119	Daucol	$C_{15}H_{26}O$	222	21
21	16.042	6,6′-Methylenebis(2-(tert-butyl)-3-methylphenol)	$C_{23}H_{32}O_2$	340	22

Antimicrobial Activity of Essential Oil and Crude Extracts from Carrot Seeds

Screening of antimicrobial activity for essential oil and crude extracts (in methanol, ethanol, water and petroleum ether) was done by agar well diffusion method. The results are summarized in Table 2 and Figure 23. The essential oil of carrot seeds had very high activity against *C. albicans, E. coli, M. furfur, S. typhi* and *S. aureus*. Water and petroleum ether extracts were inactive on all tested microorganisms. Methanol and ethanol extracts had high activity against *B. subtilis, C. albicans, M. furfur, S. typhi and S. aureus* but they possess weak activity on *E. coli*. Therefore, the essential oil in carrot seeds possesses a high antimicrobial activity.

Table 2 Antimicrobial Activity of Crude Extracts and Essential Oil from Carrot Seeds by Agar Well Diffusion Method

No.	Samples	Diameter of zone of inhibition (mm)					
		B. subtilis	***C. albicans***	***E. coli***	***M. furfur***	***S. typhi***	***S. aureus***
1	Methanol extract	14	14	10	13	15	13
2	Watery extract	-	-	-	-	-	-
3	Ethanol extract	13	15	10	15	16	15
4	Petroleum ether extract	-	-	-	-	-	-
5	Essential oil	-	25	20	23	20	25

10 -12 mm = weak activity, 13 - 18 mm = high activity, >18 mm = very high activity (well size = 8 mm)

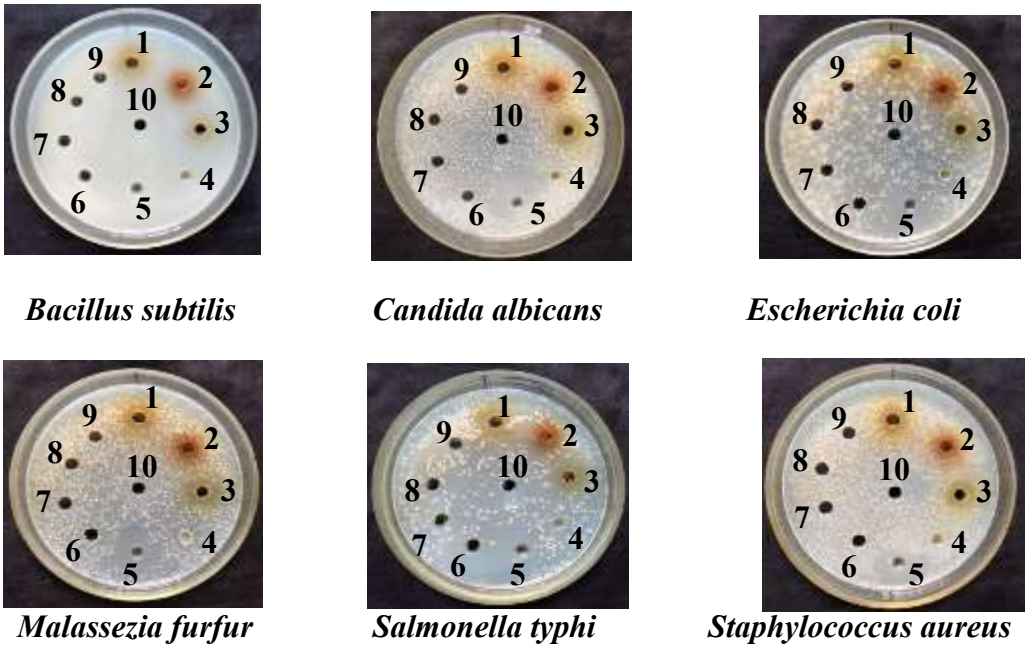

Bacillus subtilis ***Candida albicans*** ***Escherichia coli***

Malassezia furfur ***Salmonella typhi*** ***Staphylococcus aureus***

1= Methanol extract, 2 = Watery extract, 3 = Ethanol extract, 4 = Petroleum ether extract,

5 = Essential oil; 6, 7, 8, 9 and 10 = Control (solvents)

Figure 23 Antimicrobial screening of essential oil and crude extracts of carrot seeds

Antioxidant Activity of Essential Oil and Crude Extracts of Carrot Seeds

The antioxidant activity of the essential oil, ethanol and watery extracts of carrot seeds was studied by DPPH free radical scavenging assay method. DPPH free radical scavenging method is widely used method to evaluate the free radical scavenging ability of various samples. In this study, six different concentrations (20, 10, 5, 2.5, 1.25 and 0.625 μg/mL) of essential oil and crude extracts (EtOH and H_2O) were prepared by serial dilution. Ascorbic acid was used as standard. Ethanol without crude or essential oil was employed as control. Absorbance was measured at λ_{max} 517 nm using UV-visible spectrophotometer, UV-2550. The resultant average % RSA of essential oil and crude extracts (in H_2O and EtOH) with different concentrations (20, 10, 5, 2.5, 1.25 and

0.62 µg/mL) were tabulated in Table 3 and Figure 24. According to these data, the IC_{50} values of essential oil, watery extract and ethanol extract were comparable to that of standard ascorbic acid. Essential oil (IC_{50} 0.9 µg/mL) has even higher radical scavenging potency than ascorbic acid, followed by watery extract (IC_{50} 6.62 µg/mL) and ethanol extract (IC_{50} 8.37 µg/mL). Thus, the essential oil of carrot seeds may reduce the risk of oxidative stress related diseases.

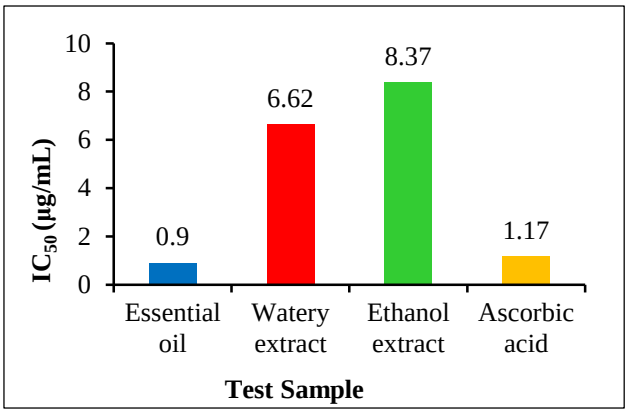

Figure 24 IC_{50} values of essential oil, crude extracts and standard ascorbic acid

Table 3 Radical Scavenging Activity (% RSA) of Essential Oil and Crude Extracts of Carrot Seeds

Test sample	Percent oxidative inhibition in different concentrations (µg/mL)						IC_{50} (µg/mL)
	0.625	1.25	2.5	5	10	20	
Essential oil	42.86 ± 0.004	59.23 ± 0.000	77.23 ± 0.002	88.24 ± 0.002	91.22 ± 0.002	93.58 ± 0.000	0.9
Watery extract	17.53 ± 0.63	33.38 ± 0.37	41.35 ± 2.47	47.07 ± 3.93	56.12 ± 3.77	80.11 ± 0.001	6.62
Ethanol extract	14.09 ± 0.01	15.83 ± 0.03	33.39 ± 0.02	47.78 ± 0.03	61.29 ± 0.000	78.58 ± 0.000	8.37
Standard ascorbic acid	14.04 ± 2.09	54.83 ± 2.48	72.44 ± 3.87	77.13 ± 1.47	87.40 ± 2.37	89.25 ± 3.81	1.17

Conclusion

The overall assessment of this research work, the carrot seeds showed the presence of alkaloids, flavonoids, glycosides, polyphenols, saponins, terpenes, protein, α-amino acids, carbohydrates, phenolic compounds, starch and reducing sugars while tannins and resins were absent. A pale-yellow essential oil with strong aromatic fragrance (0.96 % yield on dry weight basis) was obtained by steam distillation using a Clevenger's apparatus. GC-MS analysis indicates twenty one compounds with retention times between 3.217 and 16.042 min for 10 each of mono- and sesquiterpenes/terpenoids plus a phenol dimer in the carrot seeds essential oil. Moreover, the results of the antimicrobial activities showed very high activity of the essential oil against *C. albicans*, *E. coli, M. furfur, S. typhi* and *S. aureus*. Water and petroleum ether extracts were inactive against all tested microorganisms. Methanol and ethanol extracts were highly active against *B. subtilis, C. albicans, M. furfur, S. typhi* and *S. aureus* but they have weak activity on *E. coli*. Also, the essential oil (IC_{50} 0.9 µg/mL) showed a very high radical scavenging activity

with lower activities for the watery and ethanol extracts (IC_{50}: 6.62 and 8.37 µg/mL), suggesting that the essential oil may better prevent oxidative stress related diseases.

Acknowledgements

The authors are grateful to the Board of Editors of Myanmar Academy of Arts and Science for kindly allowing to present this paper.

References

Collin, C. H., and P. M. Lyne. (1964). *Microbiological Methods*, London: 1st Ed., Butterworth-Heinemann Co. Ltd.

Kapoor, V. P. (2005). "Herbal Cosmetic for Skin and Hair Care". *Natural Product Radiance*, vol. 4(4), pp. 306-314

Kaur, A., K. K. Chahal, D. Kataria, A. Kumar, and B. Urvashi. (2018). "Assessment of Carrot Seed Essential Oil and Its Chemical Constituents Against *Meloidogyne incognita*". *Journal of Pharmacognosy and Phytochemistry*, vol.**7** (1), pp. 896-903

Kulkarni, C. P. (2017). "Phytochemical Analysis and Total Phenol Content in *Daucus carota* Linn.". *International Journal of Advanced Science and Research*, vol. 2 (6), pp. 74-76

Smigielski, K. B., M. Majewska, A. Kunicka-Styczynska, M. Szczesan-Antczak, R. Gruska, and E. Stanc. (2014). "The Effect of Enzyme-Assisted Meceration on Bioactivity, Quality and Yield of Essential Oil from Waste Carrot (*Daucus carota* L*.) Seeds". Journal of Food Quality*, vol. 37, pp. 219-222

Whenlan. C. (2019). "*The Benefit of Carrot Seeds Essential Oil*". https://www.healthline.com>health

(Accessed: 23 January 2020)

COMPARISON OF RADON EXPLORATION IN DIFFERENT ENVIRONMENTAL SAMPLES BY USING LR-115 TYPE II DETECTOR

Win Ko[1], Hnin Hnin Than[2]

Abstract

This work investigated the interaction of LR-115 type II Solid State Nuclear Track Detectors (SSNTDs) with various radiations (neutron, alpha, and gamma). After irradiation, the tracks formed were etched with alkaline solution 10 % NaOH at 60 °C for 90 min. The etched tracks in irradiated LR-115 type II were observed by using an optical microscope. In this study, radon exploration in different environmental samples such as coal, bottom ash, volcanic ash, mud volcano, Crown cement, and tobacco were carried out by using an LR-115 type II (an alpha sensitive plastic track detector). It indicates radon's existence as an alpha emitter in all different environmental samples. Among them, the radon concentration in the volcanic ash sample was found to be the highest value (105.5511 Bq/m^3) and exceed the national reference level (100 Bq/m^3) whereas in the coal sample, was found to be the second-highest value (100.6902 Bq/m^3).

Keywords: LR-115, radon, alpha track, environmental samples

Introduction

Radon is a colourless, odourless natural radioactive gas that is the most common source of radiation exposure in humans. Radon is the most common source of radiation exposure in our environment during a person's lifetime (Aziz *et al*., 2016).

The present study used SSNTDs in the track etches technique due to their simplicity, low cost, non-destructive, small size, and having the integrating capability for large scale studies for the measurement of radon concentration and radon exhalation rates studies in the environmental samples. It is of great interest in estimating the radiation risk to the public from radon and its daughters (Dorschel *et al.*, 2003).

LR-115 is a 12 μm thick red-dyed cellulose nitrate emulsion coated on a 100 μm thick inert polyester base. A high enough linear energy transfer has the highest sensitivity for alpha particles, fission fragments, and ionizing particles. Ionizing radiation passes through insulating solids, leaving narrow trails of intense damage on an atomic scale. These trails are known as 'Tracks'. They can be seen under an optical microscope after being treated with a suitable chemical etchant (Siems *et al.*, 2001).

Materials and Methods

This section mainly consists of three parts. The first part is related to the study on the effect of etching times with alpha irradiated LR-115. The second part is concerned with the interaction of LR-115 detectors by using neutron, gamma, and alpha radiations standard sources. The final part is concerned with the applications of LR-115 for radon level measurement from environmental samples; coal, bottom ash, volcanic ash, mud volcano, Crown cement, and tobacco.

Treatment of LR-115 Detector with Standard Sources

LR-115 detectors were cut into small pieces of 1 cm × 1 cm. These samples were irradiated with neutron from Am(Be) source, gamma from Co-60 source, and alpha from Am-241 source. The LR-115 was removed from the sources and etched chemically in 10% NaOH solution at 60 °C

[1] Dr, Associate Professor, Department of Chemistry, Monywa University
[2] Dr, Professor, Department of Chemistry, Dagon University

for 90 min in an oven. The etched tracks on the detectors were scanned, using an optical microscope (OLYMPUS BX-51). It was also concerned with examining the composition of SSNTDs before and after irradiation by using other auxiliary methods such as FT IR.

Detection of Radon via Alpha Particles in Different Environmental Samples

In this work, LR-115 detectors were used for measuring radon via alpha particles in the environmental samples. Each sample (100 g) was placed in the cylindrical "Can". The LR-115 detectors were fixed on the top inside of the "Can" for three months. The plastic "Can" is 7.5 cm in height and 8.0 cm in diameter. During this time the alpha particles from radon and its daughter would leave tracks on the detector. The LR-115 was removed from the plastic "Can" and etched chemically in the above procedure.

The track density of environmental samples was calculated by dividing the number of tracks by the microscope view area (19.635 10^{-4} cm^2) and exposure time (90 days). The radon activity was calculated using the track density and a calibration factor of 0.21 tracks/cm^2d (Eappen and Mayya, 2004). Radon activity was used to calculate the radon exhalation rate (Anil Sharma1 *et al*., 2014). The radon concentration in environmental samples was then computed using an exhalation rate (Abd-Elzaher, 2012).

Results and Discussion

Effect of Etching Parameters on LR-115 Detectors

Six LR-115 detectors were irradiated with Am-241 alpha radiation for 15 min. These detectors were etched in 10 % NaOH solution with different etching times (50, 60, 70, 80, 90, and 100 min) at 60 °C. The etching time (90 min) was chosen optimum condition for this research.

Observation of Tracks with Standard Sources

The detection of LR-115 with a neutron, gamma, and alpha radiations was studied. In this, the detector can not detect neutron and gamma radiations. LR-115 can detect especially for alpha. From the study on different alpha irradiation times (15, 30, 60, 90 min), the greater the irradiation times, the higher the track density on LR-115. But it will be damaged at irradiation time over 60 min. It was used for radon level measurement from the environmental samples.

Examination of Effect of Radiation on LR-115 by Using FT IR Method

From the FT IR spectra of the neutron, gamma, and alpha irradiated LR-115 detectors, it was found that the wavenumbers of functional groups in all irradiated detectors of different irradiation times do not differ before and after irradiation. The observations suggested that the potentiality of LR-115 can be used as dosimeters.

Observation of Radon via Alpha Particles from Environmental Samples

According to the experimental results, the LR-115 detector is more effective in alpha detection. Hence, it was used for observation of radon via alpha particles emitting environmental samples.

Each LR-115 detector was fixed at the top of inside each "Can" according to facing the detector and α-emitted via radon in coal, bottom ash, volcanic ash, mud volcano, Crown cement, and tobacco samples. After the exposure period of three months, they were etched in 10 % NaOH at 60 °C for 90 min.

The experimental results revealed that the whole tracks were found in all the LR-115 detectors placed in these environmental samples. The shape of the track observed agrees with the literature and it indicates that this is due to an interaction between detectors and alpha particles via radon present in it (Figures 1, 2, 3, 4, 5 and 6).

From Table 1, the track density was found to be between 1131.7658 and 1397.7308 track/ cm^2 in all detectors in the coal sample. The average value was found to be 1312.8484 track/cm^2. According to the observed track density, the radon activity was found to be between 5389.3611 and 6655.8610 Bq/m^3. The average was 6251.6589 Bq/m^3. The calculated radon exhalation rate values were between 0.4063 and 0.5018 Bq/m^2h and the mean value was 0.4713 Bq/m^2h. Therefore, the radon concentration in the coal sample was found to be 100.6902 Bq/m^3. Therefore, the annual effective dose equivalent rate of the Thitchauk coal mine lies within the intervention limit for mine workers. The mine workers in the Thitchauk coal mine are safe from health hazards from radon.

From Table 2, the track density was found to be between 38.1971 and 89.1266 track/cm^2 in all detectors in the bottom ash sample. The average value was found to be 66.2083 track/cm^2. According to the observed track density, the radon activity was found to be between 181.8909 and 424.4122 Bq/m^3. The average was 315.2776 Bq/m^3. The calculated radon exhalation rate values were between 0.0149 and 0.0348 Bq/m^2h and the mean value was 0.0258 Bq/m^2h. Therefore, the radon concentration in the bottom ash sample was found to be 5.5281Bq/m^3. As a byproduct of coal combustion, massive amounts of fly ash, and bottom ash are manufactured, which typically contain radioactive materials. Radon health effects adhere to the respiratory tract and lung areas in the factory environment, becoming a permanent source of radioactivity within the body and eventually causing lung cancer and bronchial tissue damage.

From Table 3, the track density was found to be between 1352.4602 and 1426.0250 track/ cm^2 in all detectors in the volcanic ash sample. The average value was found to be 1376.2270 track/ cm^2. According to the observed track density, the radon activity was found to be between 6440.2866 and 6790.5950 Bq/m^3. The average was 6553.4630 Bq/m^3. The calculated radon exhalation rate values were between 0.4855 and 0.5119 Bq/m^2h and the mean value was 0.4941Bq/m^2h. Therefore, the average radon concentration in the volcanic ash sample was found to be 105.5511 Bq/m^3. The people living around the volcano area should be noticed that health risk from radon and volcanic ash usually contains radon and other radioactive nuclides.

From Table 4, the track density was found to be between 16.9765 and 59.4177 track/cm^2 in all detectors in the mud volcano sample. The average value was found to be 32.2553 track/cm^2. According to the observed track density, the radon activity was found to be between 80.8404 and 282.9415 Bq/m^3. The average was 153.5968 Bq/m^3. The calculated radon exhalation rate values were between 0.0063 and 0.0221 Bq/m^2h and the mean value was 0.0120 Bq/m^2h. Therefore, the average radon concentration in the mud volcano sample was found to be 2.5573 Bq/m^3. Therefore, the average radon concentrations of mud volcanoes lie below the intervention limit for people.

From Table 5, the track density was found to be between 50.9295 and 89.1266 track/cm^2 in all detectors in Crown cement sample. The average value was found to be 68.7548 track/cm^2. According to the observed track density, the radon activity was found to be between 242.5213 and 424.4122 Bq/m^3. The average was 327.4037 Bq/m^3. The calculated radon exhalation rate values were between 0.0199 and 0.0348 Bq/m^2h and the mean value was 0.0269 Bq/m^2h. Therefore, the average radon concentration in Crown brands cement sample was found to be 5.7407 Bq/m^3. Although the measured radon concentration values in cement samples are below the recommended action level, cement usually contains radon. Therefore, the construction worker should be noticed the health risk from radon exposure.

From Table 6, the track density was found to be between 25.4647 and101.8589 track/cm^2 in all detectors in the tobacco sample. The average value was found to be 53.4759 track/cm^2. According to the observed track density, the radon activity was found to be between 121.2606 and 485.0425 Bq/m^3. The average was 254.6473 Bq/m^3. The calculated radon exhalation rate values were between 0.0100 and 0.0398 Bq/m^{2}h and the mean value was 0.0209 Bq/m^{2}h. Therefore, the average radon concentration in the tobacco sample was found to be 4.4650 Bq/m^3. The vast majority of radon-related lung cancer deaths occur in current and former smokers, and radon exposure raises the risk of lung cancer in everyone, whether they are current, former, or non-smokers. The majority of countries have an active anti-smoking public information campaign. Anti-smoking leaflets and information are available in health centers and hospitals. Lung health and cancer organizations are frequently involved in public awareness campaigns.

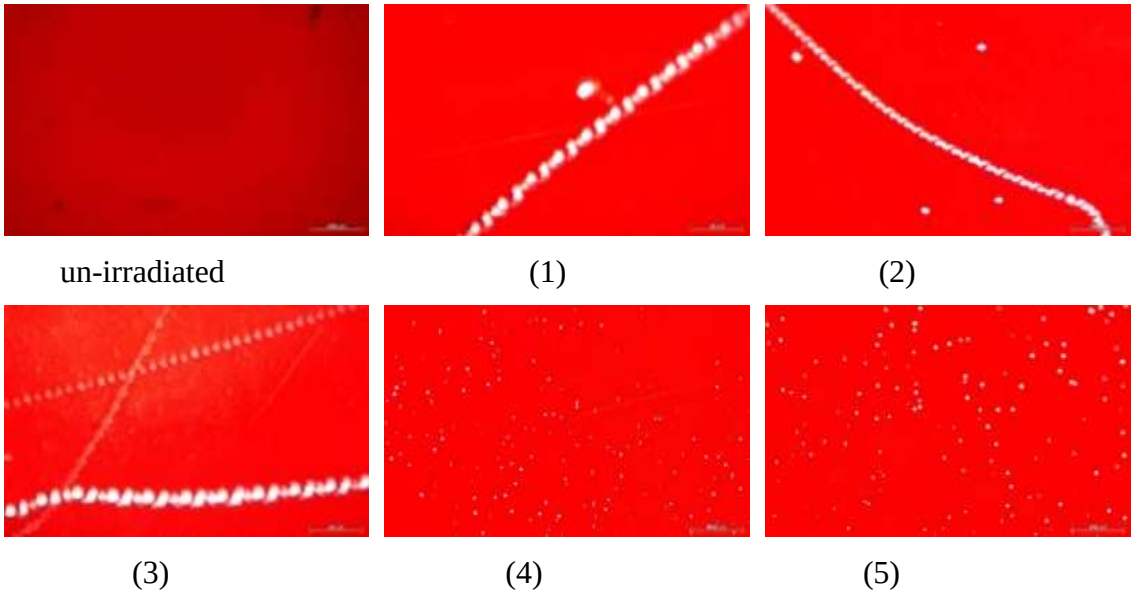

Figure 1 Photomicrographs (1 to 5) for the revelation of the alpha particle tracks in LR-115 detectors for coal sample from Thitchauk coal mine

Table 1 Measurement of Track Density, Radon Activity, Radon Exhalation Rate, and Radon Concentration from Coal Sample

LR-115	Track density (tracks/cm^{2}d)	Radon activity (Bq/m^3)	Radon exhalation rate (Bq/m^{2}h)	Radon concentration (Bq/m^3)	Annual effective dose (mSv/y)
1	1131.7658	5389.3611	0.4063	86.8019	2.4371
2	1329.8249	6332.4993	0.4774	101.9922	2.8636
3	1346.8013	6413.3397	0.4835	103.2942	2.9001
4	1358.1190	6467.2334	0.4876	104.1622	2.9245
5	1397.7308	6655.8610	0.5018	107.2003	3.0098
Mean Value ± SD	1312.8484 ±93.2592	6251.6589 ±444.0912	0.4713 ±0.0335	100.6902 ±7.1526	2.8270 ±0.2008

* International reference level of radon concentration = 100 Bq/m^3

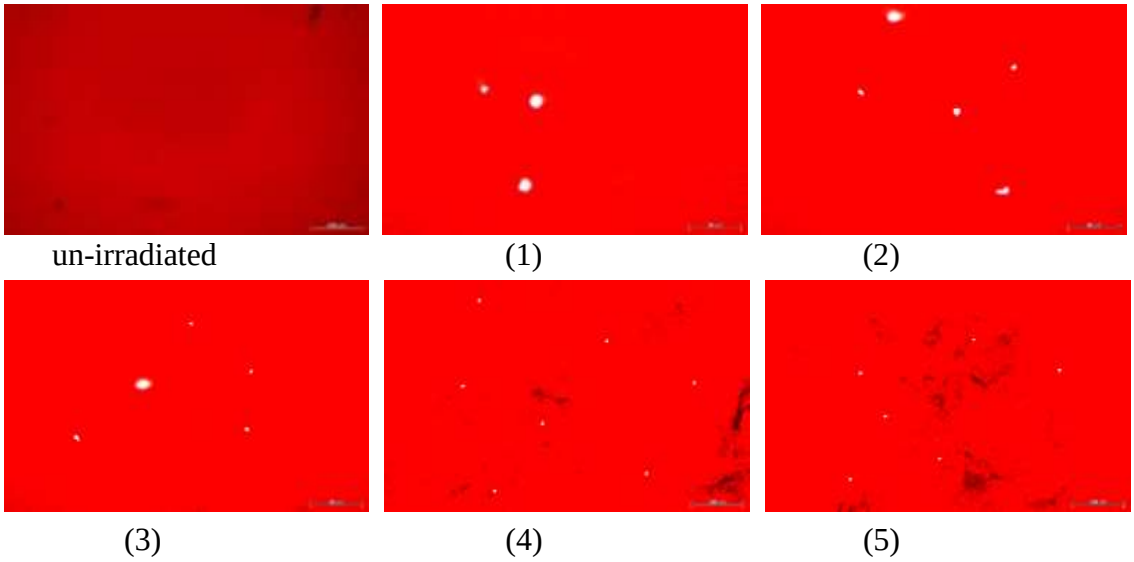

Figure 2 Photomicrographs (1 to 5) for the revelation of the alpha particle tracks in LR-115 detectors for bottom ash sample from Hom Pan Tile Factory, Sagaing

Table 2 Measurement of Track Density, Radon Activity, Radon Exhalation Rate and Radon Concentration from Bottom Ash Sample

LR-115	Track density (tracks/cm^{2}d)	Radon activity (Bq/m^3)	Radon exhalation rate (Bq/m^{2}h)	Radon concentration (Bq/m^3)
1	38.1971	181.8909	0.0149	3.1893
2	63.6618	303.1516	0.0249	5.3155
3	63.6618	303.1516	0.0249	5.3155
4	76.3942	363.7819	0.0299	6.3786
5	89.1266	424.4122	0.0348	7.4417
Mean Value ± SD	66.2083 ±16.8914	315.2776 ±80.4352	0.0258 ±0.0066	5.5281 ±1.4104

* International reference level of radon concentration = 100 Bq/m^3

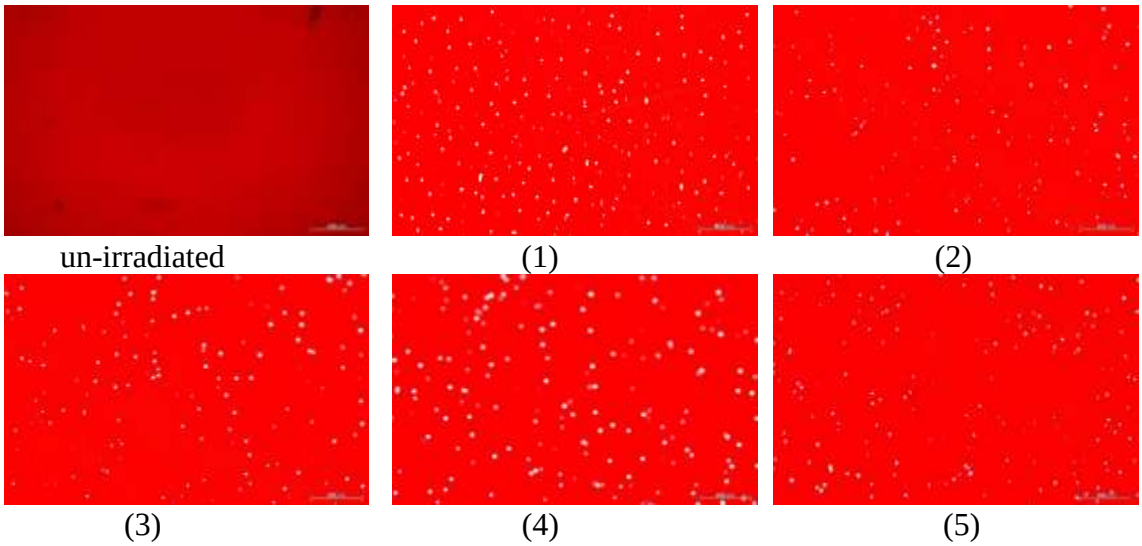

Figure 3 Photomicrographs (1 to 5) for the revelation of the alpha particle tracks in LR-115 detectors for volcanic ash sample from Kyaukphyu township

Table 3 Measurement of Track Density, Radon Activity, Radon Exhalation Rate and Radon Concentration from Volcanic Ash

LR-115	Track density (tracks/cm^{2}d)	Radon activity (Bq/m^3)	Radon exhalation rate (Bq/m^{2}h)	Radon concentration (Bq/m^3)
1	1352.4602	6440.2866	0.4855	103.7282
2	1358.1190	6467.2334	0.4876	104.1622
3	1369.4367	6521.1270	0.4916	105.0303
4	1375.0955	6548.0738	0.4937	105.4643
5	1426.0250	6790.5950	0.5119	109.3703
Mean Value ± SD	1376.2270 ±26.1534	6553.4630 ±124.5397	0.4941 ±0.0094	105.5511 ±2.0058

* International reference level of radon concentration = 100 Bq/m^3

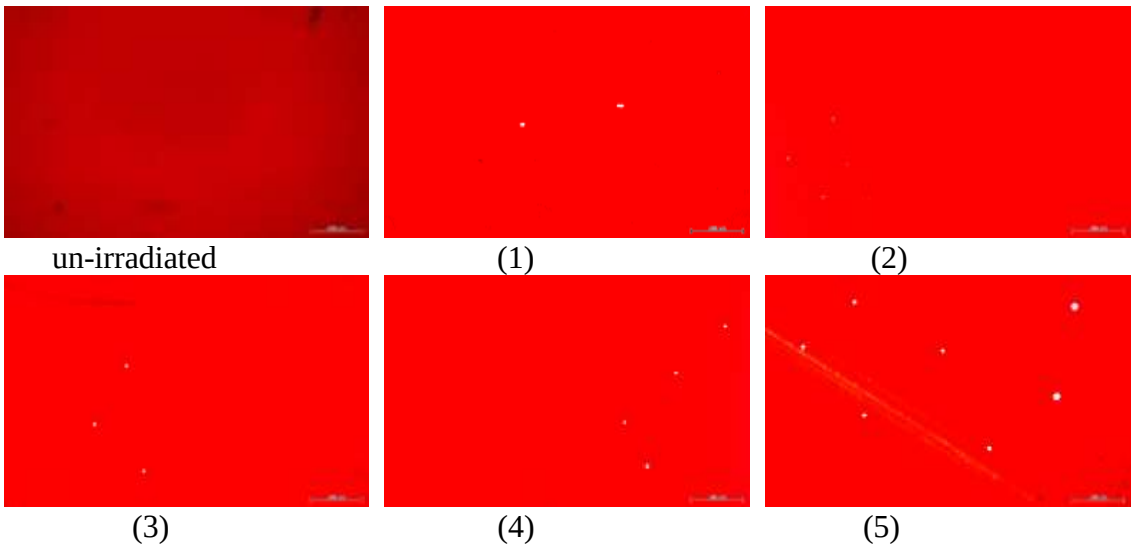

Figure 4 Photomicrographs (1 to 5) for the revelation of the alpha particle tracks in LR-115 detectors for mud volcano sample from Nagarpwattaung, Minbu township

Table 4 Measurement of Track Density, Radon Activity, Radon Exhalation Rate, and Radon Concentration from Mud Volcano

LR-115	Track density (tracks/cm^{2}d)	Radon activity (Bq/m^3)	Radon exhalation rate (Bq/m^{2}h)	Radon concentration (Bq/m^3)
1	16.9765	80.8404	0.0063	1.3459
2	25.4647	121.2606	0.0095	2.0189
3	25.4647	121.2606	0.0095	2.0189
4	33.9530	161.6808	0.0126	2.6919
5	59.4177	282.9415	0.0221	4.7108
Mean Value ± SD	32.2553 ±14.6037	153.5968 ±69.5416	0.0120 ±0.0054	2.5573 ±1.1578

* International reference level of radon concentration = 100 Bq/m^3

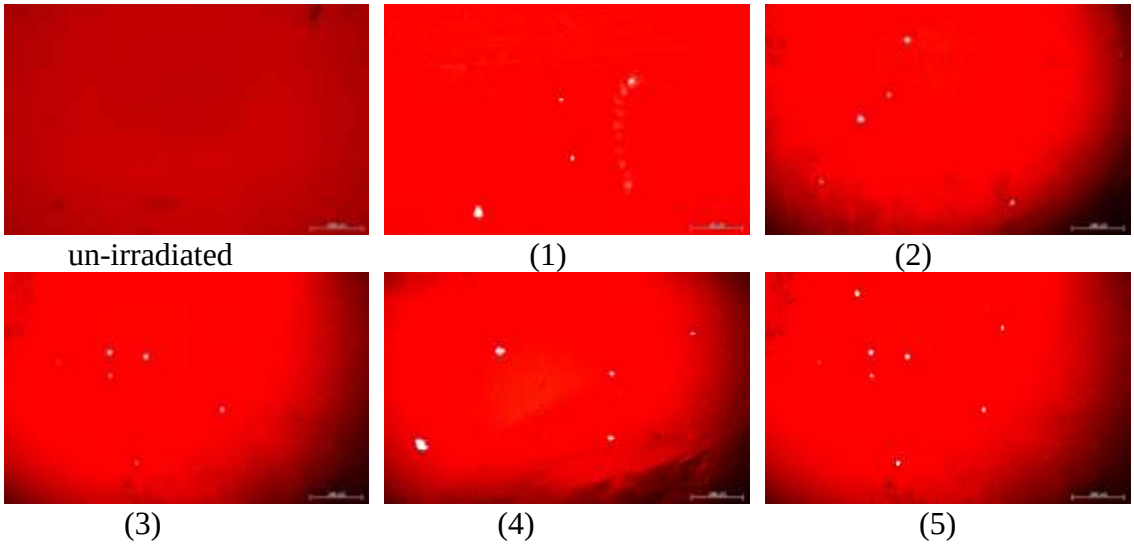

Figure 5 Photomicrographs (1 to 5) for the revelation of the alpha particle tracks in LR-115 detectors for crown brands cement

Table 5 Measurement of Track Density, Radon Activity, Radon Exhalation Rate, and Radon Concentration from Crown Cement

LR-115	Track density (tracks/cm^{2}d)	Radon activity (Bq/m^3)	Radon exhalation rate (Bq/m^{2}h)	Radon concentration (Bq/m^3)
1	50.9295	242.5213	0.0199	4.2524
2	63.6618	303.1516	0.0249	5.3155
3	63.6618	303.1516	0.0249	5.3155
4	76.3942	363.7819	0.0299	6.3786
5	89.1266	424.4122	0.0348	7.4417
Mean Value ± SD	68.7548 ±12.9845	327.4037 ±61.8310	0.0269 ±0.0051	5.7407 ±1.0842

* International reference level of radon concentration = 100 Bq/m^3

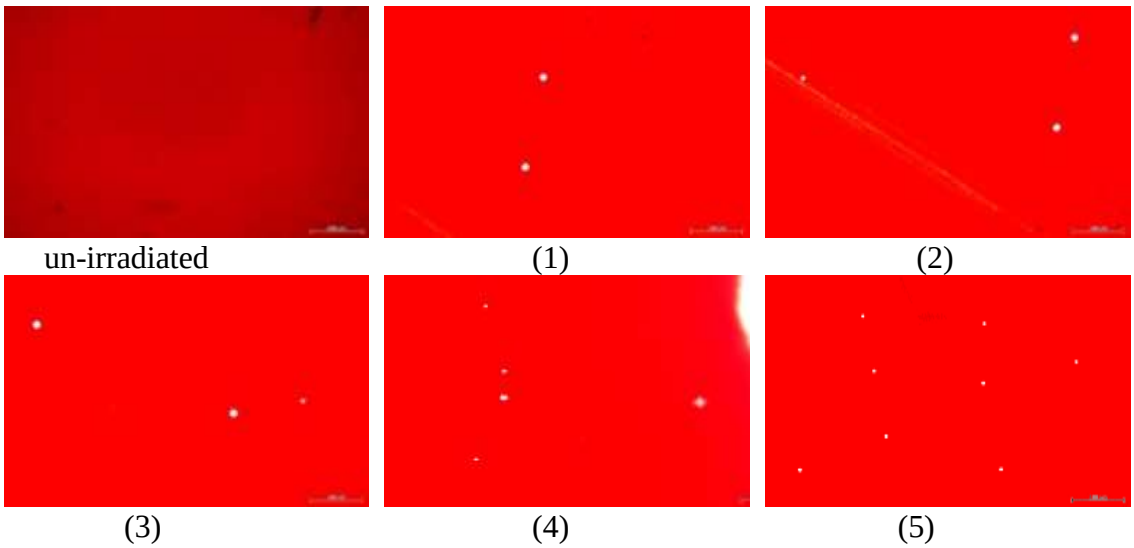

Figure 6 Photomicrographs (1 to 5) for the revelation of the alpha particle tracks in LR-115 detectors for tobacco sample

Table 6 Measurement of Track Density, Radon Activity, Radon Exhalation Rate and Radon Concentration from Tobacco Sample

LR-115	Track density (tracks/cm^{2}d)	Radon activity (Bq/m^3)	Radon exhalation rate (Bq/m^{2}h)	Radon concentration (Bq/m^3)
1	25.4647	121.2606	0.0100	2.1262
2	38.1971	181.8909	0.0149	3.1893
3	38.1971	181.8909	0.0149	3.1893
4	63.6618	303.1516	0.0249	5.3155
5	101.8589	485.0425	0.0398	8.5049
Mean Value ± SD	53.4759 ±27.1889	254.6473 ±129.4709	0.0209 ±0.0106	4.4650 ±2.2702

* International reference level of radon concentration = 100 Bq/m^3

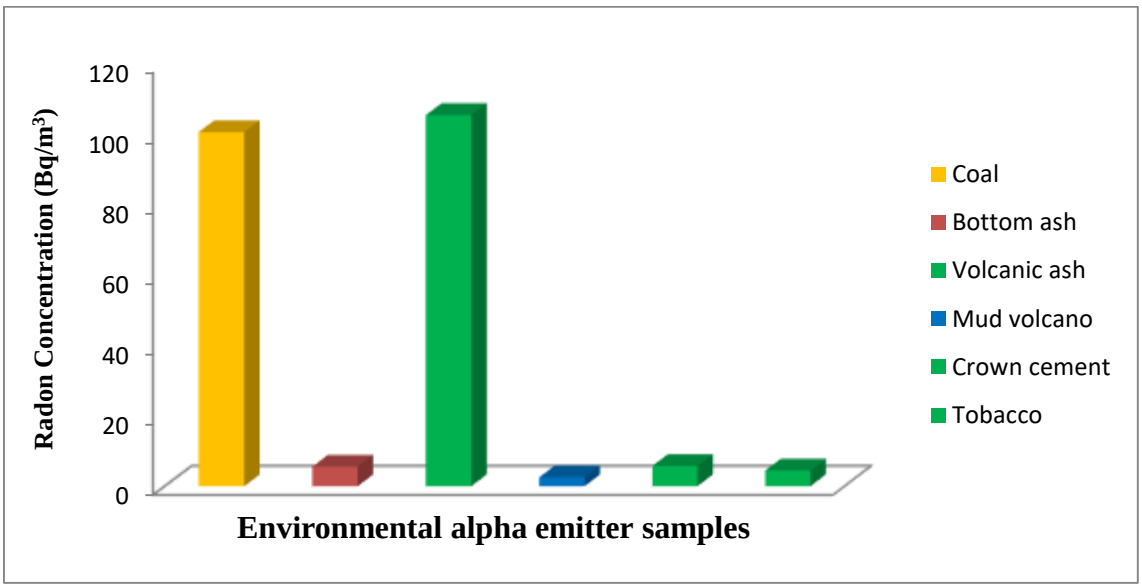

Figure 7 Average radon concentration of different environmental samples

From this figure, radon was found to be present in all these samples. Whether its concentration is low or high, it should be aware of the risk for people.

Conclusion

In this research work, most of the radon is trapped in coal and volcanic ash samples. Therefore, mine workers and people living around the volcano area should be concerned about their health due to radon exposure. The average radon concentrations of mud volcanoes lie below the intervention limit for people. The people living around Minbu are safe from health hazard from radon. Although the measured radon concentration values in the cement sample are below the recommended action level, cement usually contains radon. Therefore, the construction worker should be noticed the health risk from radon exposure. In addition, this risk seems to apply even at low radon concentrations, which is below the reference levels applied in several countries. Furthermore, active smokers have a significantly higher risk of lung cancer than nonsmokers.

Overall, radon has been discovered in environmental samples, and whether the concentration is low or high, it should be considered a risk to human health.

Acknowledgments

We would like to thank Dr. Thura Oo, Rector of Monywa University, for his permission to conduct this research as well as his invaluable suggestions. We are also grateful to Professor Dr. Ni Ni Aung, Head of the Chemistry Department at Monywa Univ ersity, for her kind assistance and suggestions. We also wanted to thank Professor Dr. Ni Ni Than, Head of the Chemistry Department at the University of Yangon.

References

Abd-Elzaher, M. (2012). "An Overview on Studying 222Rn Exhalation Rates Using Passive Technique Solid-State Nuclear Track Detectors". *American Journal of Applied Sciences*, vol. 9 (10), pp.1653-1659

Anil Sharma1, Ajay Kumar Mahur, R. G. Sonkawade, A. C. Sharma, Raj Kumar, and Rajendra Prasad. (2014). "Radon Exhalation in Some Building Construction Materials and the Effect of Plastering and Paints on the Radon Exhalation Rate Using Fired Bri**cks".** *Advances in Applied Science Research*, vol. 5(2), pp.382-386.

Aziz, B., B. Laila, A. Khadija, and N. Hamid. (2016). "Measurement of Natural Radioactivity and Radon Exhalation Rate in Coal Ash Samples from a Thermal Power Plant". *World Journal of Nuclear Science and Technology*, vol. 6, pp. 153-160.

Dörschel, B., D. Hermsdorf, S. Pieck, S. Starke, H. Thiele, and F. Weickert. (2003). "Studies of SSNTDs Made from LR-115 Given Their Applicability in Radiobiological Experiments with Alpha Particles". *Nuclear Instruments and Methods in Physics Research Section B: Beam Interactions with Materials and Atoms*, vol. 207(2), pp.154-164.

Eappen, K. P., and Y. S. Mayya, (2004). "Calibration factors for LR-115 (type-II) Based Radon Thoron Discriminating Dosimeter". *Radiation Measurements*, vol. 38(1), pp.5-17.

Siems, M., K. Freyer, H. C. Treutler, G. Jönsson, and W. Enge. (2001). "Experimental Study on the Aging Process of the LR-115 Cellulose Nitrate Radon Detector". *Radiation Measurements*, vol. 34(1-6), pp.81-84

INVESTIGATION OF BIOACTIVE SUBSTANCES CONTENTS AND *IN VITRO* FREE RADICAL SCAVENGING ACTIVITY OF *MICHELIA CHAMPACA* L. (SAGAWA) FLOWER

Myint Myint Khin[1], Mai Linda Smith Len[2], Kyin Kyin Win[3], Sandar Moe[4]

Abstract

The objective of this study was to examine the yield percent of organic solvent extractable matter, the content of bioactive substances (total phenolic contents and total flavonoids contents) and free radical scavenging activity of ethanolic and watery extracts of *Michelia champaca* L. (Sagawa flower). The results indicated that *M. champaca* was more soluble in polar solvent and it had pronounced effects on both phenolic compound levels and antioxidant potential. Ethanolic extract contained the higher amounts of bioactive compounds and exhibited the better antioxidant activity than watery extract. The evaluation of antioxidant activity of both extracts revealed highly significant correlation between anti-radical ability and total phenolic and total flavonoid contents.

Keywords: *Michelia champaca* L., total phenolic contents, total flavonoids contents, antioxidant activity

Introduction

Michelia champaca L. (Figure 1) is commonly known as Sagawa in Myanmar and it is a tall tree with yellow fragrant blossoms. It is commonly used in many traditional herbal preparations. The plant is also reported to have significant wound healing, antimicrobial, antidiabetic, antitumor, anti-inflammatory, antioxidant and anti-infective properties. Phenolics possess a good spectrum of biochemical activities like antioxidant, anti-mutagenic, anti-carcinogenic likewise ability to change the organic phenomenon (Sulaiman, 2014). Phenolics are the biggest group of phytochemicals that account for many of the antioxidant activity in plants or plant products. Since the phenolic compounds possess the strong evidence of biological activities, Biju *et al.* (2013) focused on determination of total phenolic content in the selected medicinal plant. Sagawa flower could also be a crucial herbal drug with some important marker useful to treat some challenging diseases to marking in future life. The herbal or traditional medicine involves the use of different types of organic extracts or bioactive chemical constituents. This type of biochemical investigation provides health care at an affordable cost. So, the Sagawa flower had been chosen to investigate some bioactivities in this research paper.

Figure 1 Photographs of plant and flowers of *Michelia champaca* L. (Sagawa)

[1] Dr, Associate Professor, Department of Chemistry, Kyaing Tong University
[2] MSc Candidate, Department of Chemistry, University of Yangon
[3] Lecturer, Department of Chemistry, Kyaing Tong University
[4] Dr, Professor, Department of Chemistry, Kyaing Tong University

Materials and Methods

Sample Collection and Preparation of *M. champaca* (Sagawa) Flower

Flowers of *M. champaca* (Sagawa) were collected from Mandalay Region in June, 2017. Then, the sample was authenticated at the Department of Botany, University of Yangon. The collected sample was washed with water and dried in an oven at 50 °C. The dried pieces were made into powder by using grinding machine. The powdered sample was stored in air-tight container to prevent moisture changes and other contaminations.

Preparation of Different Extracts of *M. champaca* (Sagawa) Flower

The powdered sample was extracted by cold maceration for 72 h at 37 ℃ with occasional shaking with different solvents like petroleum ether, ethyl acetate and ethanol to ensure complete extraction. After this, the extracts were filtered through Whatman filter paper and the extracts were collected and stored at 4 ℃ in the refrigerator. Watery extract was prepared by boiling 100 g of sample with 500 mL of distilled water for 6 h and filtered. It was repeated three times and the filtrates were combined, followed by heating on water bath and sand bath to obtain watery extract. The percentage yield of various extracts of the flower of *M. champaca* was calculated.

Determination of Total Phenolic Contents of *M. champaca* (Sagawa) Flower by FCR Method

One of the antioxidative factors, total phenolic contents (TPC) of watery and ethanol extracts were measured spectrophotometrically according to the Folin-Ciocalteu method (Saxena *et al.,* 2013). Firstly, the sample solution was prepared by dissolving 2 mg of each extract in 100 mL of distilled water respectively. 0.5 mL of each of the sample solution and these solutions were mixed with 0.5 mL of methanol. 5 mL of FCR reagent (1:10) was added to each of the sample solution and these solutions were incubated for 5 min. 4 mL of 1 M sodium carbonate solution was added to each tube and kept at room temperature for 2 h. Then, the UV absorbance of reaction mixture was read at λ_{max} 765 nm. The blank solution was prepared as the above procedure by using distilled water instead of sample solution. Total phenolic content was estimated as μg gallic acid equivalents per mg of different extracts (μg GAE/ mg).

Determination of Total Flavonoids Contents by Aluminium Chloride Colorimetric Assay

The total flavonoids contents (TFC) of the samples were determined by UV spectrophotometer according to the aluminium chloride colorimetric assay (Zhishen *et al.,* 1999). Each extract (10 mg) was mixed with 20 mL of distilled water to get 500 μg/mL solution. Each extract solution (0.5 mL) was mixed with 1.5 mL of methanol, 0.1 mL of 1 % aluminium chloride solution, 0.1 mL of 1 M potassium acetate and 2.8 mL of distilled water. The resultant mixture was allowed to stand for 30 min at room temperature. Absorbance of the resulting solution was measured against reagent blank solution at 415 nm by using a spectrophotometer (UV-7504, China). The experiment was done in triplicate. The concentration of quercetin equivalent (QE) in the dried flower extracts was calculated by using the linear regression equation from standard calibration curve of quercetin. Total flavonoids contents (TFC) of the dried flower sample were expressed as mg quercetin equivalent per 1 g dried flower extract (mg of QE/g).

Determination of Antioxidant Activity by DPPH Free Radical Scavenging Assay

The free radical scavenging activity of watery and ethanol extracts of *M. champaca* (Sagawa) flower was measured by using DPPH free radical scavenging assay (Marinova and Batchvarov, 2011). The control solution was prepared by mixing 1.5 mL of 0.002 % DPPH solution and 1.5 mL of ethanol in the brown bottle. The sample solution was also prepared by mixing 1.5 mL of 0.002 % DPPH solution and 1.5 mL of test sample solution. These bottles were incubated

at room temperature and were shaken on shaker for 30 min. After 30 min, the absorbance of different concentrations (12.5, 25, 50, 100, 200 and 400 μg/mL) of tested sample was measured at 517 nm using UV-7504 spectrophotometer. Absorbance measurements were done in three times for each concentration and the mean value so obtained were used to calculate percentage of radical scavenging activity as shown in Table 4. The antioxidant power (IC_{50}) is expressed as the concentration (μg/mL) of test substances that results in a 50 % reduction of initial absorbance of DPPH solution. IC_{50} (50 % inhibition concentration) values were calculated by linear regressive excel program.

Results and Discussion

The phytochemical constituents possess varying degrees of antioxidant activity. Hence, they can be assumed as health protective agents. It has been reported the presence of alkaloids, α-amino acids, carbohydrates, organic acids, flavonoids, glycosides, phenolic compounds, reducing sugars, saponin, starch, steroids, tannins and terpenoids, except harmful cyanogenic glycosides, and ten compounds present in essential oil extracted from Sagawa flower identified by GC-MS analysis (Myint Myint Khin, 2021).

Percentage Yields of Different Extracts of *M. champaca* (Sagawa) Flower

Extraction involves the use of an inert solvent which actively separates the molecules from the plant's parts. The extracts obtained with various solvents such as petroleum ether, ethyl acetate, ethanol and distilled water were weighed and their percentage yields were calculated as compared to the initial weight of the plant material to get the extractive values. The experimental data are presented in Table 1. The present study revealed that the yield of watery extract (11.49 %) showed the highest value, followed by the yield of ethanol extract (6.81 %), ethyl acetate extract (2.08 %) and petroleum ether extract (0.78 %). The resulted data suggested that the extractable matter contents increase with increase in polarity of the solvents. These data indicated that the amounts of polar constituents were higher than that of non-polar constituents in the Sagawa flower.

Table 1 Percentage Yields of Different Extracts of *M. champaca* (Sagawa) Flower

No.	Samples	Percentage yields (%)
1.	Watery extract	11.49
2.	Ethanol extract	6.81
3.	Ethyl acetate extract	2.08
4.	Petroleum ether extract	0.78

Total Phenolic Contents of Crude Extracts of *M. champaca* (Sagawa) Flower

The phenolic compounds are plant metabolites characterized by the presence of several phenol groups. Some of them are very reactive in neutralizing free radical by donating a hydrogen atom or an electron (Almey *et al.,* 2010). Phenolic compounds have antioxidant properties of protective against degenerative disease like heart diseases and cancer. The total phenolic contents of water and ethanol crude extracts of flowers of Sagawa were evaluated with spectrophotometric method using Folin-Ciocalteu reagent. The principle of this method is based on the reduction ability of the phenol functional group. Phenols react with an oxidizing agent phosphomolybdate in Folin-Ciocalteu reagent under alkaline conditions resulting in the formation of blue coloured complex (Dudonee *et al.,* 2009).

The reduction of complex will increase when the extracts contain more phenolic compounds. Thus, the colour will be darker and the absorbance will be higher. The absorbance can be measured at UV 765 nm. Gallic acid (3, 4, 5-trihydroxybenzoic acid) was used to construct standard calibration curve. Total phenolic content was expressed as microgram gallic acid equivalent per milligram (µg GAE/mg) of crude extract (Saxena *et al.,* 2013). In this study, high phenol contents have been found to exert high antioxidant potential. The study shows a direct relation between antioxidant activity and total phenol contents. According to the results as shown in Table 2, the higher TPC (µg GAE/mg) was detected in ethanol extract (508.95 µg GAE/mg) than watery (328.55 µg GAE/mg) extract of Sagawa flowers. This means that phenolic compounds were more soluble in ethanol. Comparison of TPC in watery and ethanol extracts of Sagawa flower is represented by a bar graph in Figure 2.

Table 2 Total Phenolic Contents in Watery and Ethanol Extracts of *M. champaca* (Sagawa) Flower

Extracts	TPC (µg GAE/mg ± SD)
Watery	328.55 ± 0.0052
Ethanol	508.95 ± 0.0043

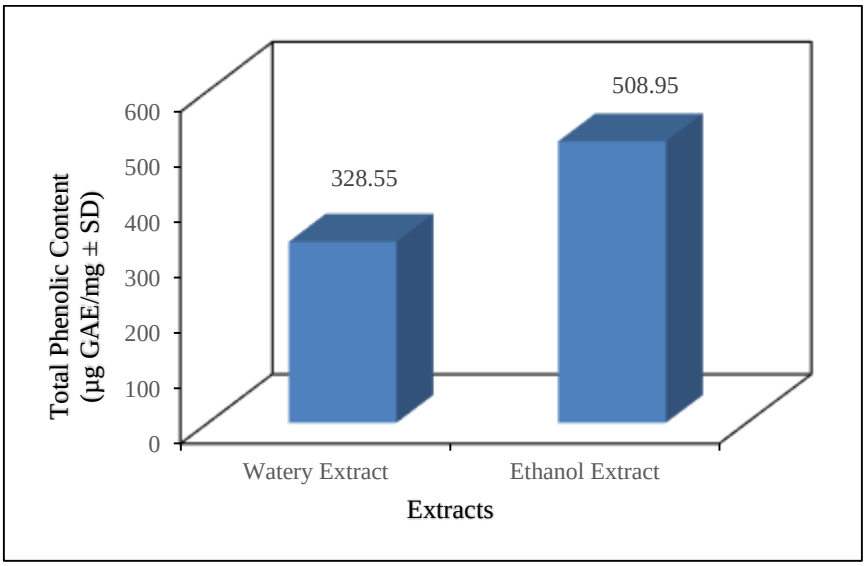

Figure 2 Total phenolic contents of watery and ethanol extracts of *M. champaca* -(Sagawa) Flower

Total Flavonoids Contents of Crude Extracts of *M. champaca* (Sagawa) Flower

The total flavonoids contents of the watery and ethanol crude extracts of the flowers of Sagawa were evaluated with spectrophotometric method using aluminium chloride reagent. As shown in Table 3 and Figure 3, the higher TFC (mg GAE/g) was detected in ethanol (9.63 mg QE/g) than watery (0.88 mg QE/g) extracts of Sagawa flower. This means that flavonoid compounds were more soluble in ethanol. In this study, high phenol contents have been found to exert high flavonoid content. Similar to phenolic content, ethanolic extract had higher flavonoid content compared to watery extract.

Table 3 Total Flavonoids Contents of Watery and Ethanol Extracts *M. champaca* (Sagawa) Flower

Extracts	TFC (mg of QE/ g of extract ± SD)
Watery	0.88 ± 0.002
Ethanol	9.63 ± 0.001

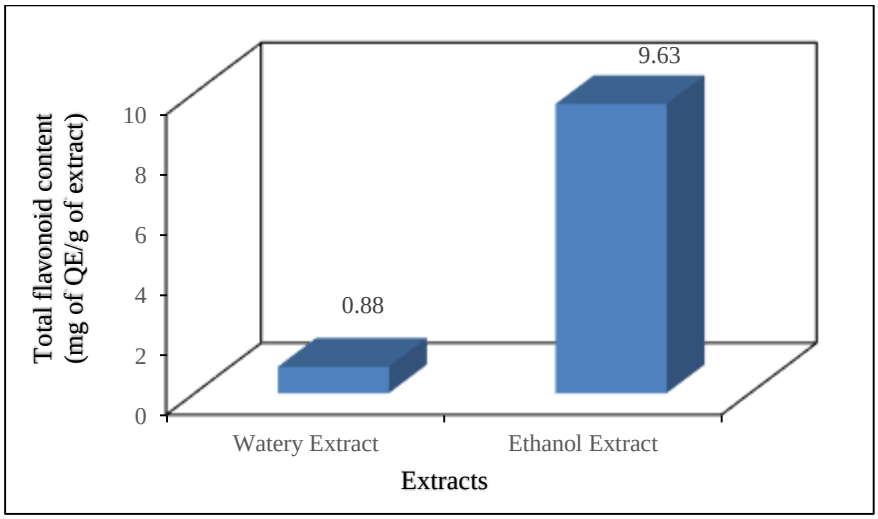

Figure 3 Total flavonoids contents of watery and ethanol extracts of *M. champaca* (Sagawa) Flower

Radical Scavenging Activity of Crude Extracts of Flower of *M. champaca* (Sagawa) Flower by DPPH Radical Scavenging Assay

Antioxidant compounds in plant play an important role as a health-protecting factor. Scientific evidence suggests that antioxidants reduce the risk for chronic diseases including cancer and heart disease. The antioxidant activity of watery and ethanol crude extracts of Sagawa flowers was evaluated by the DPPH (2,2-diphenyl-1 -picrylhydrazyl) radical scavenging assay. Butylated hydroxytoluene was used as a standard. Colorimetry with DPPH, a stable free radical, has been reported as a simple method for evaluation of the free radical scavenging activity. It tends to capture hydrogen from the antioxidant due to its free radical. The ethanolic DPPH solution is violet, and its maximum absorption wavelength is 517 nm.

The colour changes upon neutralization of this free radical from violet to pale yellow by daylight. The decolouration of the initial colour is proportional to the test substances having anti-radicalizing power. The absorbance of different concentrations (12.5, 25, 50, 100, 200 and 400 µg/ mL) of tested sample was measured at 517 nm by using UV-7504 spectrophotometer. It was found that as the concentrations were increased, the absorbance values decreased. The percent radical scavenging activity of crude extracts and standard BHT are tabulated in Table 4. The greater the % RSA, the greater the antioxidant activity. In contrast, the lower the IC_{50} indicates the more effective antioxidant activity. From the experimental results, flowers of Sagawa were found to have antioxidant activity. IC_{50} values of ethanol and watery extracts are 26.408 and 51.755 µg/mL, respectively.

According to the result, the ethanol extract was found to be more antioxidant potency than watery extract. The antioxidant potency of ethanol and watery extracts was concluded to be weak when compared with the potency of standard butylated hydroxytoluene (IC_{50} = 22.51 µg/mL). The

IC_{50} values of ethanol and water crude extracts of Sagawa flowers and standard butylated hydroxytoluene are shown in Table 5 and Figure 4.

The scavenging capacity against DPPH used for determining antioxidant activity has been proven to exhibit a positive linear correlation with phenolic compounds and flavonoid compounds, stating that these compounds contribute to the antioxidant capacity of ethanol and watery extracts of Sagawa flower. The results revealed a highly significant correlation between antioxidant activity and total phenolic and total flavonoids contents.

Table 4 Radical Scavenging Activity of Watery and Ethanol Extracts from *M. champaca* (Sagawa) Flower and Standard BHT

Samples	% RSA±SD of different concentrations (µg/mL)					
	12.5	**25**	**50**	**100**	**200**	**400**
Watery extract	11.35 ± 0.005	39.30 ± 0.035	48.68 ± 0.006	86.02 ± 0.011	91.04 ± 0.002	100.65 ± 0.016
Ethanol extract	21.12 ± 0.009	49.39 ± 0.014	60.18 ± 0.002	73.40 ± 0.002	88.90 ± 0.0007	93.01 ± 0.018
BHT (Std.)	34.36 ± 0.004	53.86 ± 0.002	62.38 ± 0.003	66.87 ± 0.004	72.75 ± 0.001	80.65 ± 0.005

Table 5 IC_{50} Values of Crude Extracts from *M. champaca* (Sagawa) Flower and Standard BHT

Samples	**IC_{50} (µg/mL)**
Watery extract	51.76
Ethanol extract	26.41
BHT (Std.)	22.51

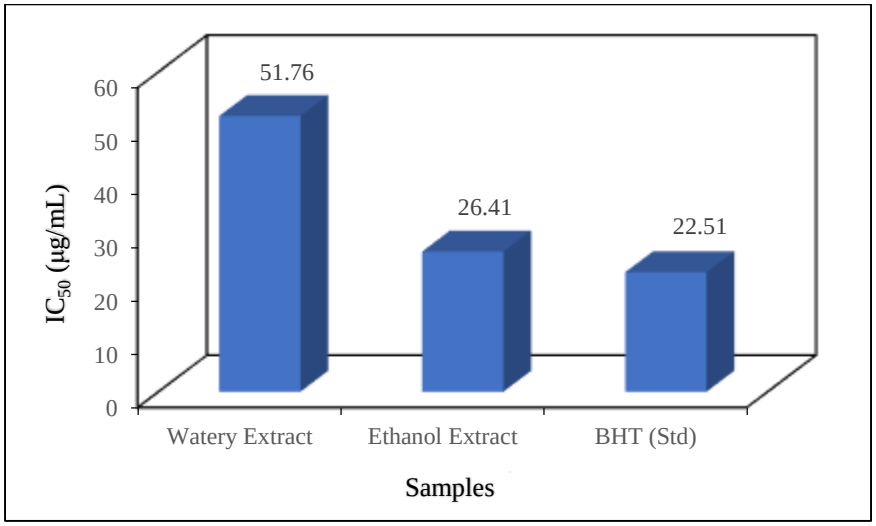

Figure 4 IC_{50} values of watery and ethanol extracts from *M. champaca* (Sagawa) flower and standard BHT

Conclusion

The present study revealed that the extraction yield of watery extract (11.49 %) showed the highest value, followed by the yield of ethanol extract (6.81 %), ethyl acetate extract (2.08 %) and petroleum ether extract (0.78 %). Among the crude extracts, yield percent of watery extract found to be the highest and petroleum ether soluble matter was the lowest in the selected sample. Therefore, *M. champaca* was more soluble in polar solvent. Total phenolic content in ethanol extract (508.95 µg GAE/mg) is higher than that in the watery extract (328.55 µg GAE/mg). In this study, high phenol contents have been found to exert high flavonoids content. The total flavonoids content of watery and ethanol extracts of Sagawa flower was detected to be higher in ethanol extract (9.63 mg QE/g) than watery extract (0.88 mg QE/g). This means that flavonoid compounds were more soluble in ethanol. The antioxidant potential of ethanol extract (IC_{50} = 26.41 µg/mL) is more potent than the watery extract (IC_{50} = 51.76 µg/mL), but weaker activity than standard butylated hydroxytoluene (BHT) (IC_{50} = 22.51 µg/mL). These results might suggest a higher medicinal suitability of alcoholic extracts in various antioxidant applications. The current investigation confirmed that Sagawa flower can be considered as a potential natural source of bioactive phytochemicals such as phenolic compounds and flavonoids that play a major role in human health as free radical scavenger. The ethanolic extract which exhibited the strong antioxidant activity contained the high level of phenolic compounds as well as flavonoids. The results showed significant activities for both phenolic content and antioxidant potential of Sagawa flower. Thus, the natural bioactive compounds from Sagawa flower can be used as the synthetic antioxidant in food, pharmaceutical and cosmetic products.

Acknowledgements

The authors are grateful to the Department of Higher Education, Ministry of Education, Yangon, Myanmar, for the permission of doing this research and also to the Myanmar Academy of Arts and Science for allowing the present of this paper. We also thank to Professor and Head, Dr Cho Cho Nyein, Department of Chemistry, Kyaing Tong University for her kind interest and encouragement this paper.

References

Almey, A. A. A., C. A. J. Khan, I. S. Zahar, K. M. Suleiman, M. R. Aisyah, and K. K. Rahim. (2010). "Total Phenolic Content and Primary Antioxidant Activity of Methanolic and Ethanolic Extracts of Aromatic Plants Leaves". *International Food Research Journal*, vol. 17, pp. 1077-1084

Biju, T., C. T. Sulaiman, S. George, and V. R. Reddy. (2013). *"Total Phenolics and Flavonoids in Selected Medical Plants from Kerala". International Journal of Pharmacy and Pharmaceutical Sciences, vol. 6 (1), pp. 406-408*

Dudonne, S., X. Vitrac, P. Coutiere, M. Woillez, and J. M. Merillon. (2009). "Comparative Study of Antioxidant Properties and Total Phenolic Contents of 30 Plant Extracts of Industrial Interest Using DPPH, ABTS, FRAP, SOD and ORAC Assays". *J. Agric. Food Chem*, vol. 57 (5), pp. 1768-1774

Marinova, G., and V. Batchvarov. (2011). "Evaluation of the Methods for Determination of the Free Radical Scavenging Activity by DPPH". Bulgarian *Journal of Agricultural Science*, vol. 17 (1), pp. 11-24

Myint Myint Khin, Mai Linda Smith Len, and Phyoe Ei San. (2021). "Extraction of Essential Oil and Investigation of Anti-arthritic Activity of *Michelia champaca* L. (Sagawa Flower)". *Kyaing Tong University Research Journal*, vol. 12 (1)

Saxena, M., J. Saxena, R. Nema, D. Singh, and A. Gupta. (2013). "Phytochemical of Medicinal Plants". *Journal of Pharmacognosy and Phytochemistry*, vol. 1 (6), pp. 168-172

Sulaiman, C. T., and G. Satheesh. (2014). "Total phenolics and flavonoids in selected medicinal plants from Kerala". *International Journal of Pharmaceutical Sciences*, vol. 6 (1), pp. 406-408

Zhishen, J., T. Mengcheng, and W. Jianming. (1999). "The Determination of Flavonoid Contents in Mulberry and Their Scavenging Effects on Superoxide Radicals". *Food Chem*., vol. 64, pp. 555-559

PHOTOCATALYTIC ACTIVITIES OF SYNTHESIZED TIN(IV) OXIDE NANOPARTICLES BY USING AQUEOUS EXTRACT OF *CITRUS AURANTIFOLIA* LEAVES

Khine Yee Htoo[1], Yee Mun Than[2], Ye Myint Aung[3]

Abstract

Citrus aurantifolia leaves aqueous extract was used to synthesize tin(IV) oxide nanoparticles utilizing a straightforward, environmentally friendly, and inexpensive approach. Aqueous leaves extract of *C. aurantifolia* was utilized as a reducing agent, while tin(II) chloride dihydrate was utilized as the starting material. SnO_2 NPs were produced at 600 °C, according to an X-ray diffractogram (XRD) examination, and their crystallite size was 28.7 nm when they were made with an aqueous leaf extract. The distinctive peak of SnO_2 was visible in the 450–790 cm^{-1} range according to the results of the FT IR investigation. SEM examination revealed SnO_2 NPs with very minor agglomerations. The average crystallite size of SnO_2 NPs was determined by TEM examination to be consistent with the XRD results. For the commercial dye, methyl violet, which serves as a representative organic dye pollutant, the produced SnO_2 NPs demonstrated outstanding degrading efficiency. The ideal conditions for the photocatalytic degradation of 10 ppm of methyl violet were achieved using 0.5 g of SnO_2 NPs in the sunlight for 8 h.

Keywords: *Citrus aurantifolia*, tin(IV) oxide nanoparticles, methyl violet, photocatalytic degradation

Introduction

Water pollution is one of the biggest problems today, which increases every year causing serious and irreparable damage to the planet (Luquea *et al*., 2020). Water pollution is a serious threat to human health and aquatic life all over the world (Paramarta *et al*., 2017). Among various industrial effluents, the effluents are one of the most toxic by-products of the textile industry. These toxic effluents are responsible for many hazardous health effects such as cancer, skin irritation, and allergic response. Industrial wastewater may contain poisonous chemicals such as insecticides and organic dyes. Dyes cause allergies, dermatitis, skin irritation, cancer, etc, in humans. Methyl violet (MV) is a water-soluble dye, used in textile industries, paper dyeing, paints, and printing ink. MV is also used as a disinfectant and is found very poisonous to animals (Archita *et al*., 2015). Methyl violet dye is a highly toxic, carcinogenic dye. Contamination with water causes long-term adverse effects on the aquatic environment and is a real threat to aquatic life (Bhattacharjee *et al*., 2014). These organic dyes can be degraded photochemically by the use of nanostructure semiconductor oxide which acts as an excellent photocatalyst in the degradation process. The SnO_2 is an important n-type semiconductor having a bandgap of 3.6 eV, exhibits unique size and shape-dependent properties including optical, electronic, electrochemical, and catalytic properties (Fu *et al*., 2015).

Using plant parts to synthesize nanoparticles is known as green synthesis. These nanomaterials are advantageous due to easy handling, non-toxic, environment-friendly, and economical nature. Leaves extract of *Citrus aurantifolia* was used in the present work for preparation of SnO_2 NPs. The extract obtained from plants serves the purpose of reducing agents. Photocatalytic degradation of the dyes namely methyl violet in the presence of synthesized SnO_2 NPs acts as a catalyst. This method does not cause secondary pollution and has attracted increasing attention as cleaner and greener technology for the removal of toxic organic and inorganic pollutants in water and wastewater. The synthesized SnO_2 NPs using aqueous extract of *Citrus*

[1] 3 PhD Candidate, Department of Chemistry, University of Yangon
[2] Lecturer, Department of Chemistry, University of Yangon
[3] Professor, Department of Chemistry, University of Yangon

aurantifolia leaves were characterized by XRD, FT IR, TG-DTA, SEM, and TEM. Then these NPs were used for photocatalytic degradation of the methyl violet dye.

Materials and Methods

Materials

The *C. aurantifolia* leaves were collected from Moattama village, Mawlamyine Township, Mon State. Ethanol and 98 % pure tin(II) chloride ($SnCl_2$. $2H_2O$) from BDH were used. To evaluate the photocatalytic activity, methyl violet was obtained from Sigma- Aldrich.

Preparation of the Leaves Aqueous Extracts of *C. aurantifolia*

The collected *C. aurantifolia* leaves were washed thoroughly with deionized water to remove the dust particles. Next, 10 g of the sample was mixed with 100 mL of deionized water and the mixture was ground by using a motor and pestle. Eventually, the solution was filtered with Whatman filter paper to obtain the green-colored leaves extract.

Preparation of SnO_2 NPs

The desired SnO_2 NPs were prepared by mixing 40 mL of $SnCl_2.2H_2O$ (0.02 M) with 100 mL of aqueous extract of *C. aurantifolia* leaves sample solution in a 250 mL beaker and then mixed thoroughly by a magnetic stirrer at 80 ˚C. The greenish gel was washed with deionized water and ethanol. The residue obtained was then collected in a porcelain crucible and heated in air at 80 ˚C. The grey-colored powder was obtained for *C. aurantifolia* leaves. It was cooled at room temperature and was calcined at a temperature of 600 ˚C in the muffle furnace for 3 h. SnO_2 NPs were carefully collected and packed for characterization purposes.

Characterization of SnO_2 Nanoparticles

The prepared SnO_2 nanoparticles were characterized by powder X-ray diffraction (XRD) method using MultiFlex 2kW Type, Rigaku. D/max 2200, Japan diffractometer with CuK_α radiation of wavelength 1.5418 Aº. The surface morphology of the prepared SnO_2 NPs was studied by Scanning electron microscope. The surface morphology and particles size distribution of each of the prepared sample was studied by transmission electron microscope (TEM, JEOL TEM-3010). An infrared spectrum was recorded in the wavenumber range of 400 to 4000 cm^{-1} by using an FT IR spectrometer.

Photocatalytic Activity of Synthesized SnO_2 Nanoparticles

The photocatalytic potential of the prepared SnO_2 NPs was investigated by the decomposition of methyl violet dye under sunlight. Effects of contact time, the dosage of SnO_2 NPs, and the initial concentration of methyl violet dye on the photocatalytic degradation of dye were studied. Briefly, to 25 mL of 50 ppm methyl violet solution in separate 150 mL capacity of clean and dry conical flasks, 0.05 g of the prepared SnO_2 NPs was added. The solution mixture was stirred for 30 min in dark for the equilibrium of the adsorption and desorption process of methyl violet with nanoparticles. After stirring, the conical flasks were placed in sunlight. After stirring for 1, 2, 3, 4, 5, 6, 7, and 8 h under sunlight, the conical flasks were taken out and filtered off the filtrate. Afterward, the absorbance values of filtrates were measured at 590 nm by using a spectrophotometer.

Results and Discussion

Characterization of the SnO_2 Nanoparticles Prepared by Green Synthesis Method

SnO_2 nanoparticle was prepared by using aqueous leaves extracts of *C. aurantifolia* by reaction with $SnCl_2.2H_2O$. The formation of black Sn $(OH)_2$ gel was observed at 80 ˚C. The grey-colored powder was obtained for *C. aurantifolia* leaves. It was cooled at room temperature and was calcined at a temperature of 600 ˚C in the muffle furnace for 3 h.

XRD studies

The X-ray diffraction pattern of the NPs obtained by means of the green synthesis is presented in Figure 1. The XRD pattern was recorded in order to investigate the crystal structure, purity, and crystalline nature of synthesized SnO_2 nanoparticles. The XRD pattern of SnO_2 nanoparticles at 600 ˚C shows the diffraction peaks at 2θ values of 26.12˚, 33.40˚, 37.49˚, and 51.30˚ which correspond to the (110), (101), (200), and (211) planes respectively. The diffraction peaks of SnO_2 were indexed to the tetragonal structure with lattice parameters a= 4.8207 Å and c= 3.2250 Å (JCPDS Card No. PDF 99-0024). From the XRD data, pure and crystallite SnO_2 NPs become gradually sharper and the full width at half maximum (FWHM) is reduced by increasing in calcination temperature to 600 ˚C. The average crystallite size was estimated by using the reflections of characteristic planes (110), and the average crystallite size was 28.7 nm in aqueous leaves extract for samples prepared at 600 ˚C. There is the absence of some other phase that does not correspond to SnO_2 NPs confirming the purity of the sample.

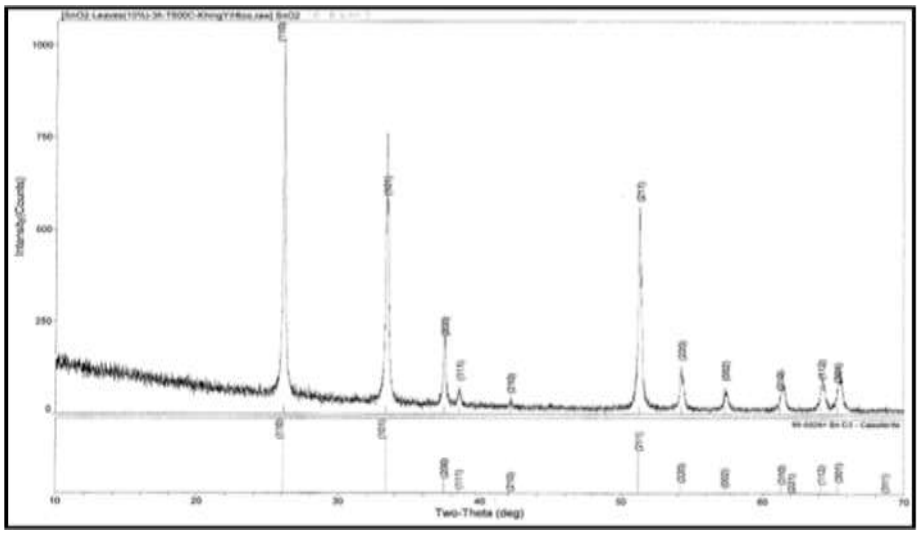

Figure 1 X-ray diffractogram of SnO_2 NPs by using aqueous extract of *C. aurantifolia* leaves at 600 ˚C

TG-DTA analysis

The thermal stability of the prepared SnO_2 NPs sample before calcination was investigated by TG-DTA. The thermogram of SnO_2 NPs is shown in Figure 2 and the corresponding thermal data are presented in Table 1. Two endothermic peaks and one exothermic peak were observed in the thermogram of SnO_2 NPs obtained by using an aqueous extract of *C. aurantifolia* leaves. The first endothermic peak was due to the removal of physically adsorbed water. The second endothermic peak was due to the removal of chemisorbed water. The exothermic peak appeared at 504.89 ˚C in SnO_2 NPs by using aqueous leaves extract was due to oxidation of SnO to SnO_2. Thus, thermal analysis data confirmed the calcination temperature of 600 ˚C for the preparation of SnO_2 NPs.

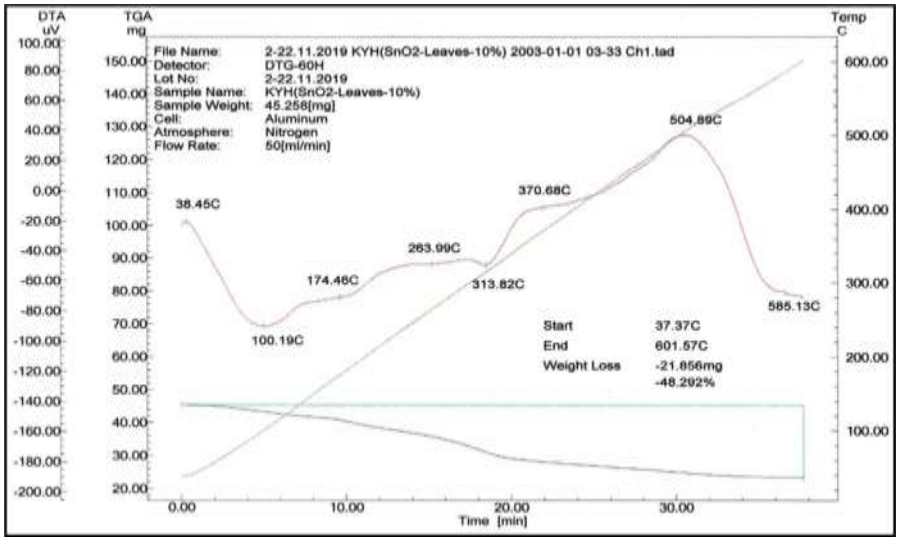

Figure 2 TG-DTA thermogram of SnO_2 NPs prepared by using aqueous extract of *C. aurantifolia* leaves (before calcination)

Table 1 TG-DTA Data of SnO_2 NPs prepared by Using Aqueous Extract of *C. aurantifolia* Leaves (before calcination)

No.	Temperature range (˚C)	Weight loss (%)	Break-in temp: (˚C)	Nature of peak	Remark
1.	36.45-200	12.779	100.19	Endothermic peak	Desorption of physically adsorbed water molecules
2.	200-400	19.885	313.82	Endothermic peak	Removal of chemisorbed water
3.	400-601.57	6.628	504.89	Exothermic peak	Oxidation of SnO to SnO_2

FT IR analysis

The structural information was further evidenced by the FT IR spectrum for the prepared SnO_2 NPs obtained at 600 ˚C (Figure 3). The characteristic peaks of SnO_2 due to stretching vibration were observed at 479 cm^{-1} and 609 cm^{-1}. The absorption peaks between 450-790 cm^{-1} were attributed to the vibration of SnO_2 stretching and indicated the formation of SnO_2 NPs.

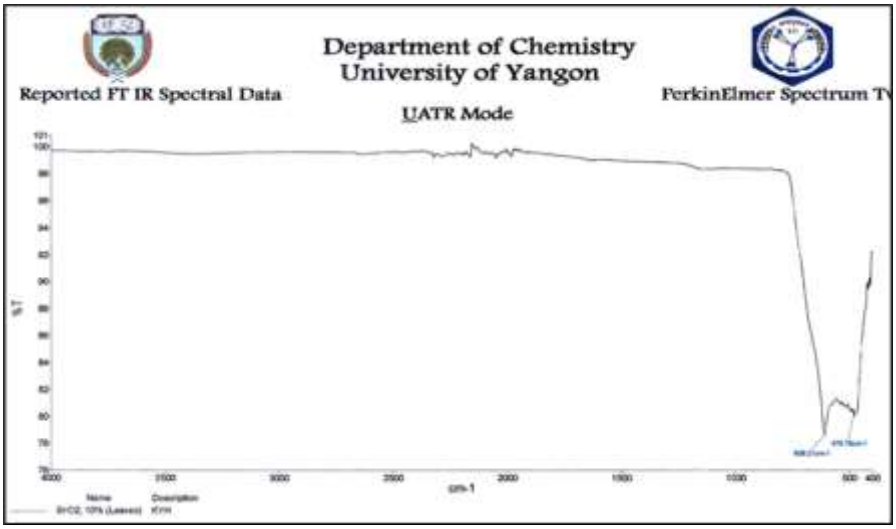

Figure 3 FT IR spectrum of the prepared SnO_2 NPs by using aqueous extract of *C. aurantifolia* leaves

Surface morphology of the prepared SnO_2 NPs by scanning electron microscopy

The surface morphology of the prepared SnO_2 NPs was studied by using SEM. SEM image of the prepared SnO_2 NPs by using aqueous extract of *C. aurantifolia* leaves.is depicted in Figure 4. The SEM images showed slightly agglomerated particles with a tetragonal shape was observed in SnO_2 NPs using an aqueous extract of *C. aurantifolia* leaves.

Surface morphology of the prepared SnO_2 NPs by transmission electron microscopy

TEM images are used to study the shape and size of the nanoparticles. Figure 5 shows the TEM picture of the SnO_2 NPs sample and it was mainly consisting of tetragonal shaped along with large agglomerated particles with an average diameter of around 28.1 nm. These values are well-matched with the grain size calculated from XRD results and confirm the SnO_2 nature with a tetragonal rutile type structure.

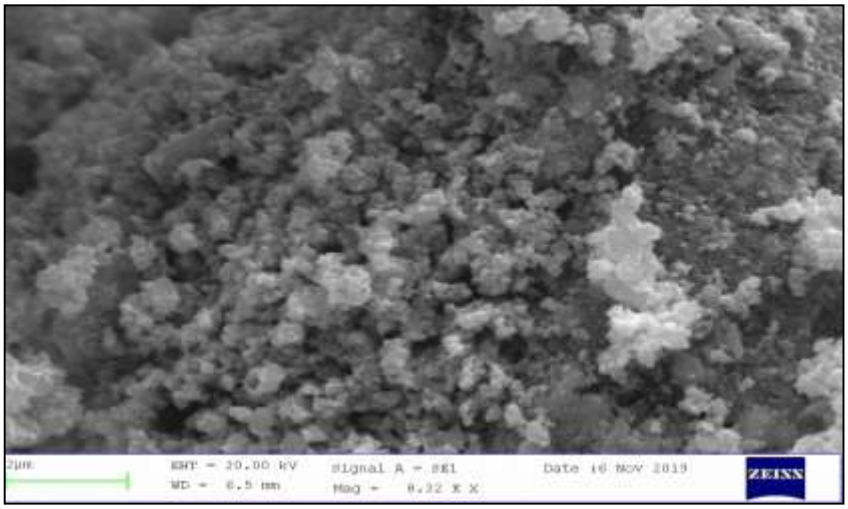

Figure 4 SEM image of the SnO_2 NPs prepared by using aqueous extract of *C. aurantifolia* leaves

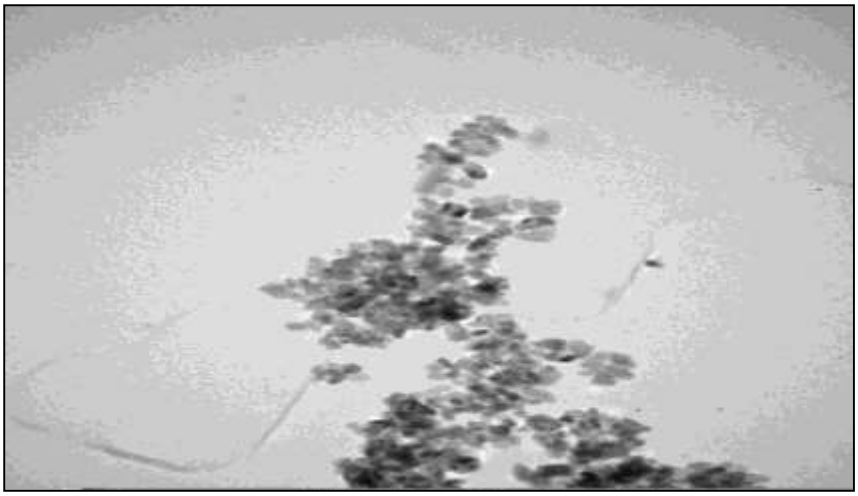

Figure 5 TEM image of the SnO_2 NPs prepared by using aqueous extract of *C. aurantifolia* leaves

The wavelength of Maximum Absorption of Methyl Violet Solution and its Calibration Curve

In quantitative analysis of substance by spectroscopic method, the standard plot techniques require the Lambert-Beers' law to be obeyed in the first place. In this work, the absorption spectra of methyl violet were recorded in the wavelength range of 400-800 nm, and was found that the wavelength of maximum absorption occurred at 590 nm (Figure 6). The standard calibration curve for methyl violet was plotted using five different concentrations (10, 30, 50, 70, and 90 ppm) at a fixed wavelength (λ_{max}) at 590 nm. The curve became a straight line and passed through the origin, which indicated Beer's Law was well obeyed (Table 2 and Figure 7).

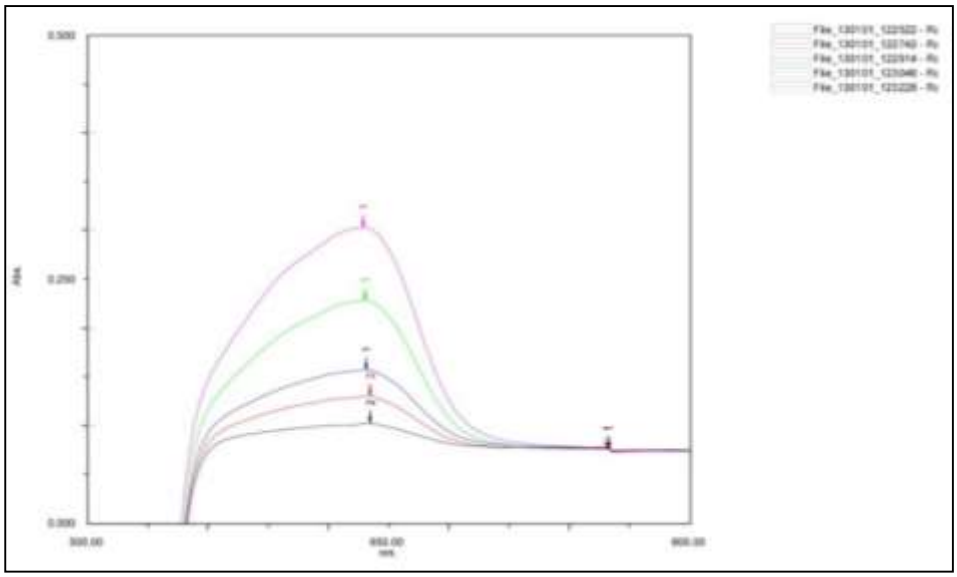

Figure 6 Overlay absorption spectra of various concentrations of methyl violet dye solution

Table 2 Relationship between Absorbance and Concentration of Methyl Violet Solution

No.	The concentration of methyl violet (ppm)	Absorbance at 590 nm
1.	10	0.148
2.	30	0.403
3.	50	0.618
4.	70	0.828
5.	90	1.021

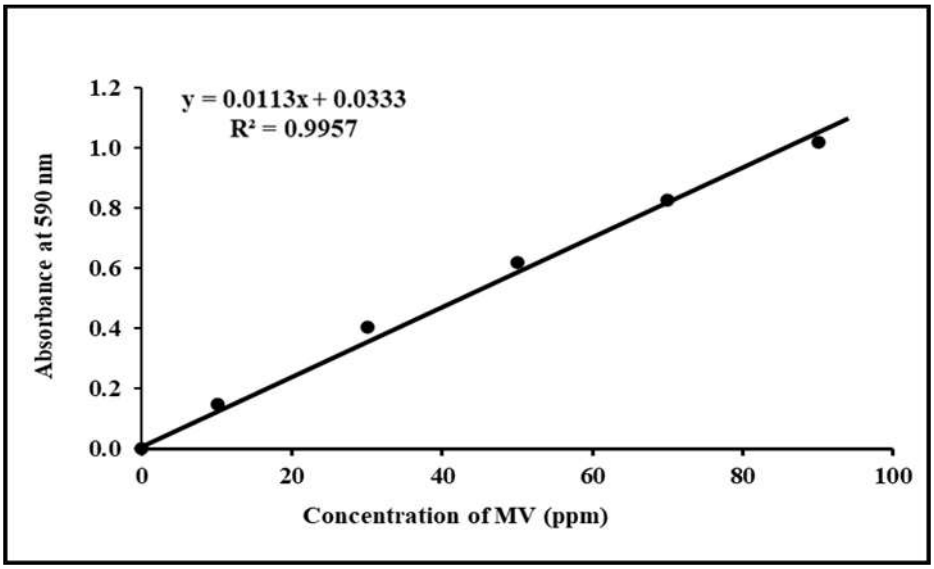

Figure 7 Calibration curve of methyl violet solution

Photocatalytic Degradation of Methyl Violet by the Prepared SnO_2 NPs under Sunlight

Effect of contact time for degradation of methyl violet solution

The effect of optimum contact time on photodegradation was performed with varying contact times ranging from 1-8 h, as shown in Table 3 and Figure 8. After 1 h of contact time, the degradation percent of methyl violet was 39.95 % by using prepared SnO_2 NPs in the presence of aqueous leaves extract. As the contact time increased, the degradation percentages of dye solution were also found to increase. After 8 h, it was observed that the degradation percent was found to be 99.13 % using SnO_2 NPs. Then, degradation processes proceed gradually and became nearly constant. This hindrance in further degradation of methyl violet may be due to the fact that the surface of the nanoparticles gets saturated so no active site is available for further photodegradation of methyl violet. Therefore, the optimum contact time for the degradation study was chosen as 8 h for these dyes.

Table 3 Degradation Percentage of Methyl Violet by the Prepared SnO_2 NPs Using Aqueous Leaves Extract of *C. aurantifolia* with Different Contact Times

No.	Contact time (h)	Absorbance after degradation	Degradation percent (%)
1.	1	0.481	39.95
2.	2	0.380	52.55
3.	3	0.289	63.92
4.	4	0.188	75.52
5.	5	0.149	81.39
6.	6	0.068	91.51
7.	7	0.019	97.62
8.	8	0.007	99.13

Initial absorbance = 0.801

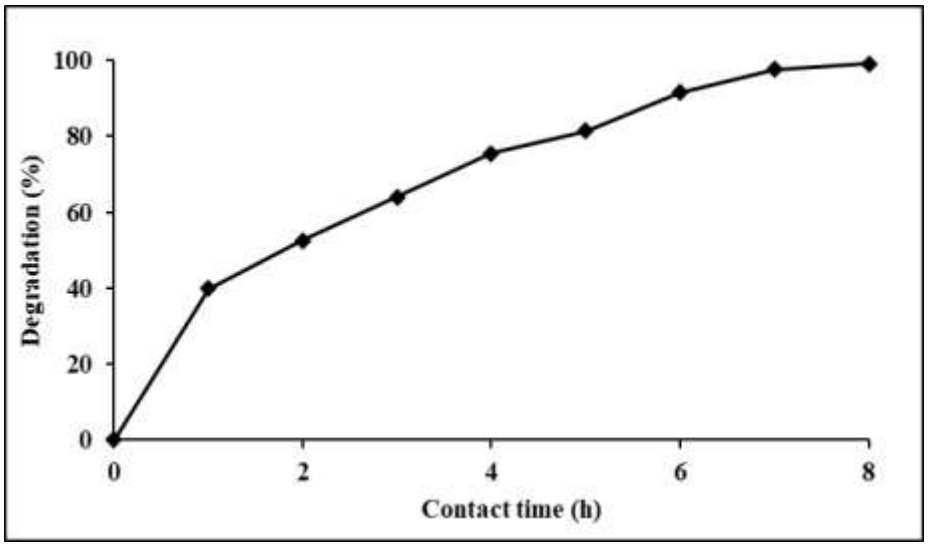

Figure 8 Degradation percentage of dye by the prepared SnO_2 NPs using aqueous extract of *C. aurantifolia* leaves as a function of contact time (dosage = 0.05 g, the volume of dye solution = 25 mL, and dye concentration = 50 ppm)

Effect of dosage of the prepared SnO_2 NPs for degradation of dyes solutions

The degradation percentage of methyl violet dye using the prepared SnO_2 NPs with different dosages ranging from 0.1 to 0.5 g was studied under sunlight and the results are shown in Table 4 and Figure 9. By using 0.1 g of SnO_2 NPs obtained from leaves extract, 94.69 % was degraded, after 8 h of contact time. The maximum percentage of photodegradation was obtained at 0.5 g of SnO_2 NPs, i.e., 99.81 % which can provide the highest absorption of light. At higher dosages loading, the dosages particles also scatter the incident photons, and hence the availability of the photon flux to the solution has increased. Thus, photocatalytic degradation increased.

Table 4 Degradation Percentage of Methyl Violet by the Prepared SnO_2 NPs Using Aqueous Leaves Extract of *C. aurantifolia* with Different Dosages

No.	Dosages (g)	The absorbance of methyl violet after degradation	Degradation percent (%)
1.	0.1	0.015	94.69
2.	0.2	0.007	99.11
3.	0.3	0.007	99.39
4.	0.4	0.005	99.59
5.	0.5	0.003	99.81

Initial absorbance = 0.801

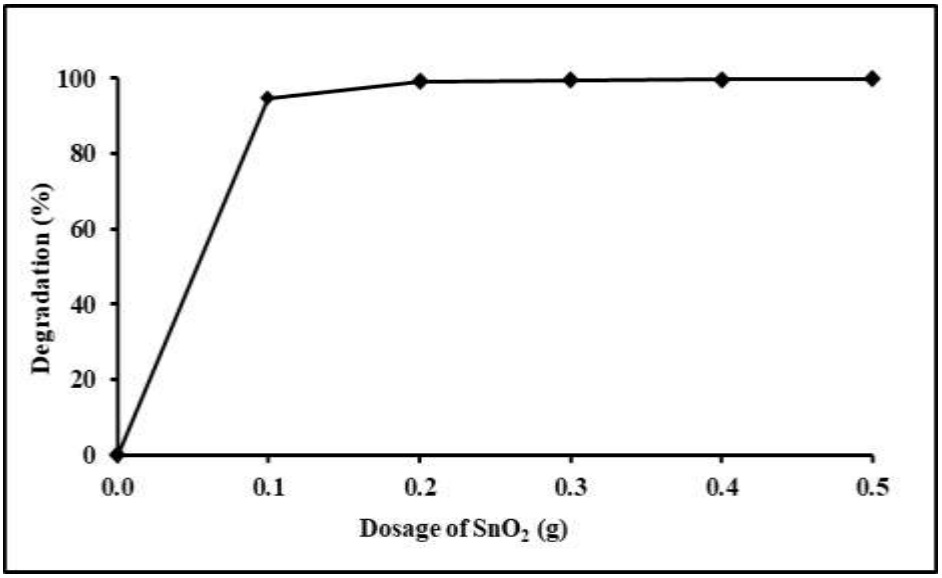

Figure 9 Degradation percentage of methyl violet by the prepared SnO_2 NPs using aqueous extract of *C. aurantifolia* leaves as a function of dosages (contact time = 8 h, the volume of dye solution = 25 mL, and dye concentration = 50 ppm)

Effect of initial concentration of dye solutions

To investigate the effect of the initial concentration of methyl violet, photodegradation studies were performed with varying concentrations of methyl violet solution of 10, 30, 50, 70, and 90 ppm. The results are described in Table 5 and plotted in Figure 10. For a 10 ppm concentration of methyl violet dye, the degradation percent was 98.80 % by using SnO_2 NPs from an aqueous extract of leaves. When the initial concentration of the dye reached 90 ppm, 96.82 % of methyl violet dye was degraded. The rate of photocatalytic degradation gradually decreased with the increase of the initial concentration dye. This behavior is due to the decrease of the concentration OH^- adsorbed on catalyst surface with the increase of dye concentration, that the active sites are covered the methyl violet dye molecules (Hazin *et al*., 2015). As a result, the degradation percent of the dyes decreased.

Table 5 Degradation Percentage of Methyl Violet by the Prepared SnO_2 NPs Using Aqueous Extract of *C. aurantifolia* Leaves with Different Concentrations of Dye

No.	Concentration (ppm)	The absorbance of methyl violet after degradation	Degradation percent (%)
1.	10	0.009	98.80
2.	30	0.012	98.78
3.	50	0.015	98.70
4.	70	0.015	98.47
5.	90	0.019	96.82

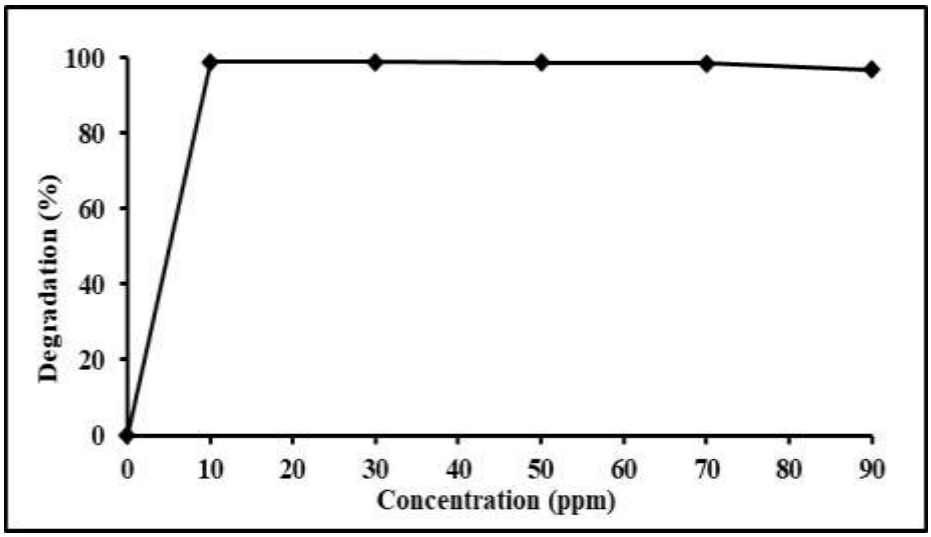

Figure 10 Degradation percentage of methyl violet by the prepared SnO_2 NPs using aqueous extract of *C. aurantifolia* leaves as a function of different concentrations (contact time = 8 h, the volume of dye solution = 25 mL, and dosage = 0.05 g)

Conclusion

A simple, eco-friendly, and efficient synthesis of SnO_2 was conducted by using aqueous leaves extract *C. aurantifolia* with acts as a reducing agent. XRD pattern confirmed the tetragonal structure of prepared SnO_2 NPs using aqueous leaves extract and the average crystallite size was found to be 28.7 nm. The Crystallite size of SnO_2 NPs from leaves was confirmed by the crystallite size and morphology by TEM analysis. SEM images showed slightly agglomerates. Thermal analysis of SnO_2 NPs indicated that SnO_2 was almost thermally stable at 600 ˚C. The purity of SnO_2 NPs was checked through FT IR analysis. Photocatalytic degradation of synthesized SnO_2 NPs was studied using methyl violet dye solution. High degradation percentage of methyl violet was attained at 99.13 % in 8 h contact time. The maximum photocatalytic degradation percent was found to be 99.81 % using a 0.5 g dosage of SnO_2 NPs. The maximum degradation percentage was found to be 98.80 % using a 10 ppm quantity of methyl violet color.

Acknowledgments

The authors are thankful to the Department of Chemistry, University of Yangon, and East Yangon University for providing the research and analytical instrument facilities. Special thanks are also due to Defense Services Science and Technology Research Center, Pyin Oo Lwin for SEM imaging and TEM imaging to Science and Technology Research Equipment Centre in Chulalongkorn University, Thailand.

References

Archita, B., M. Ahmaruzzaman, T. D. Babita, and N. Jayashree. (2016). "Photodegradation of Methyl Violet 6B and Methylene Blue using Tin-Oxide Nanoparticles (Synthesized via a Green Route)". *Journal of Photochemistry and Photobiology A: Chemistry*, vol. 325, pp. 116-124

Bhattacharjee, A., M. Ahmaruzzaman, and T. Sinha. (2014). "A Novel Approach for the Synthesis of SnO_2 Nanoparticles and its Application as a Catalyst in the Reduction and Photodegradation of Organic Compounds". *Spectrochimica Acta Part A: Molecular and Biomolecular Spectroscopy*, vol. 136 (B), pp. 751-760

Fu, L., Y. Zheng, Q. Ren, A. Wang, and B. Deng. (2015). "Green Biosynthesis of SnO_2 Nanoparticles by *Plectrathus amboinicus* Leaf Extract Their Photocatalytic Activity toward Rhodamine B Degradation". *Journal of Ovonic Research*, vol. 11 (1), pp. 21-26

Hazim, Y., A. Gubury and S. A. Ghadeer. (2015). "Photocatalytic Decolorization of Brilliant Cresyl Blue using Zinc Oxide". *International Journal of Pharm Tech Research*, vol. 8 (2), pp. 289-297

Luquea, P. A., O. Navaa, C. A. Soto-Roblese, M. J. Chinchillas-Chinchillasa, H. E. Garrafa-Galvezb, Y. A. Baez-Lopeza, K. P. Valdez-Nunezc, A. R. Vilchis-Nestord, and A. Castro-Baltranb. (2020). "Improved Photocatalytic Efficiency of SnO_2 Nanoparticles through Green Synthesis". *International Journal for Light and Electron Optics*, vol. 206, pp. 1-8

Paramarta. V., A. Taufik, L. Munisa, and R. Saleh. (2017). "Sono- and Photocatalytic Activities of SnO_2 Nanoparticles for Degradation of Cation and Anionic Dyes". *AIP Conference Proceedings*, vol. 1788, pp. 1-9

IRON OXIDE PARTICLES ASSISTED PHYTOREMEDIATION OF SOIL CONTAMINATED WITH CYPERMETHRIN RESIDUE

Swe Sint[1], Phyu Phyu Myint[2], Saw Hla Myint[3]

Abstract

Cypermethrin is one of the most widely used pyrethroid insecticides against different pests, and its use causes soil contamination. The removal of 3-phenoxybenzoic acid (3-PBA), a secondary metabolite of cypermethrin, from contaminated soil by phytoremediation with four plants species: Peanut (*Arachis hypogaea* L.), Sesame (*Sesamum indicum* L.), Aster (*Callistephus chinensis* (L.) Nees) and Bermuda grass (*Cynodon dactylon* L. Pers.) was investigated in the absence and presence of iron oxide particles (0.01 g/kg of soil). The insecticide residue percent in the soil samples was determined by UV-Vis and GC-MS. The results showed that presence of iron oxide particles is important in the removal of cypermethrin. Good phytoremediation was demonstrated only by Aster and Bermuda grass (64.19 % and 96.7 % PBA removal) in 12 weeks period. Furthermore, the activities of soil urease (mg NH_4^+-N g^{-1} soil h^{-1}) and dehydrogenase (µg TPF g^{-1} soil h^{-1}) also increased in the treated soil samples as determined by phenol-hypochlorite colorimetric method and Triphenyl Tetrazolium Chloride (TTC) assay method: Aster (4.45 ± 0.17) and Bermuda grass (4.68 ± 0.04) compared to uncultivated soil (S_0) (3.74 ± 0.03), and (0.0017 ± 1.547 x 10^{-4}) and (0.0016 ± 1.516 x 10^{-4}) compared to S_0 (0.0008 ± 0.424 x 10^{-4}), respectively. The results demonstrated that Aster and Bermuda grass showed great promising potential as Phyto remediating agents.

Keywords: phytoremediation, iron oxide particles, Peanut, Sesame, Aster, Bermuda grass, insecticide-contaminated soil

Introduction

Soil pollution involves the contamination of soil by various anthropogenic activities which involve the addition of nutrients, pesticides, and sediments to soil (Srivastava *et al.,* 2019). In recent years, the phasing out of organophosphate products such as diazinon and chlorpyrifos has prompted an increased use of pyrethroid insecticides for agricultural pest control. Cypermethrin is classed as a type II pyrethroid and is commonly found in rivers, sediments, soils, and even foodstuff (Bootharaju and Pradeep, 2012). 3-PBA is a vital step for remediation of cypermethrin pollution because it is a common secondary metabolite of the synthetic pyrethroid insecticides. Cypermethrin and its metabolite 3-phenoxybenzoic acid (PBA) have exerted adverse biological impacts on the environment; therefore, it is critically important to develop different methods to enhance their degradation (Xie *et al*., 2008).

Environmental applications of nanoparticles such as cleanup of pollutants from air, water and soil have been done by various approaches, known as remediation. If living plants are involved in the remediation process, that is known as phytoremediation. Phytoremediation is the use of plants directly or indirectly to degrade contaminants from soil and water. Phytoremediation is an effective, nonintrusive and inexpensive of remediating soils (Srivastava *et al.,* 2019). Iron oxides form naturally through the weathering of Fe-containing rocks both on land and in the oceans. They have attracted much attention due to their fine magnetic properties and applications in modern science (Fernandez-Garcia and Rodriguez, 2007).

Enzymes produced by soil microorganisms are natural catalysts of many important processes that occur in soils. For this reason, enzymes may be useful in monitoring the effects of pollution on the soil environment (Malachowska-Jutsz and Matyja, 2019). A reliable assessment

[1] Lecturer, Department of Chemistry, University of Yangon
[2] Pro-rector, Loikaw University
[3] Part-Time Professor, Department of Chemistry, University of Yangon

of soil quality contaminated with organic products is possible by testing the activity of lipase, dehydrogenase, catalases, and ureases. In this study, it focuses on the determination of urease and dehydrogenase activities of soil microorganisms. The aim of this research is to study the iron oxide particles assisted phytoremediation in the soil contamination by cypermethrin residues and its effect on enzymatic activities.

Materials and Methods

Soil Sample Collection

Soil sample was collected from the surface layer (0-20 cm depth) of an agricultural field located in Hpya Thee Village (21º 48' N latitude and 94º 57' E longitude), Myaing Township, Pakokku District, and Magway Region (Figure 1). This field is usually cropped with a chili and tomato rotation without treatment of any pyrethroids insecticide (including cypermethrin) for several years.

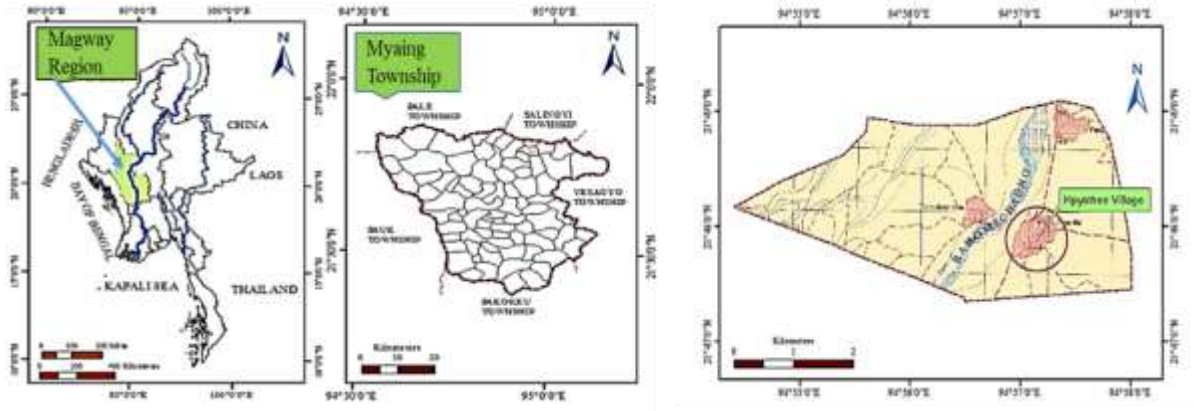

Figure 1 Sample collection site (Hpya Thee Village, Myaing Township, Magway Region)

Determination of Physicochemical Properties of Soil Sample

The moisture content of the soil sample was determined according to the oven dry method, pH value by pH meter, electrical conductivity (EC) value by electrical conductivity meter, organic matter content by Walkley and Black method based upon the oxidizable organic matter content, total nitrogen N content by Kjeldahl's method, cation exchange capacity by the method of Kappen (Jaremko and Kalembasa, 2014*)*, total phosphorus (P) content by spectrophotometric method of Olsen for neutral and alkaline soil, potassium content by ammonium acetate extraction method using flame photometer, and the elemental analysis of the soil sample by EDXRF.

Experimental Design for Determination of Insecticide Degradation in Soil

The experiment was conducted under natural light conditions. The collected soil sample (1 kg) was placed in each plastic pot. In this study, iron oxide particles were synthesized by green method, by adding 0.01 M $FeCl_3.6H_2O$ solution to the tea extract in a 1:1 volume ratio and vacuum filtered to separate the black iron oxide particles from the liquid phase. The sizes and shapes of the iron oxide particles were determined by XRD, FT IR, TG-DTA and FESEM-EDX analyses.

The experimental pots were arranged according to a random design that consists of nine treatments: (1) S_0: only cypermethrin contaminated soil, (2) S_{Fe}: cypermethrin contaminated soil with iron oxide particles (3) S_{0p}: S_0 with Peanut plant (4) S_{0s}: S_0 with Sesame plant (5) S_{0a}: S_0 with

Aster plant (6) S_{0b}: S_0 with Bermuda grass plant (7) S_{Fep}: S_{Fe} with Peanut plant (8) S_{Fes}: S_{Fe} with Sesame plant (9) S_{Fea}: S_{Fe} with Aster plant and (10) S_{Feb}: S_{Fe} with Bermuda grass plant.

For S_0, dried soil samples (10 g) and H_2O (1 mL) were placed in a 150 mL cup. For S_{Fe}, dried soil samples (10 g) and H_2O (1 mL) and 1% Fe_3O_4 (1 mL) were placed in a 150 mL cup. To each cup, 1 mL each of 0.0001 % cypermethrin solution was thoroughly mixed. In this way 45 cups each of S_0 and S_{Fe} were prepared. All the containers were covered with perforated aluminum foil to ensure gas exchange and then incubated at 25 ºC. Ninety pots were used for all treatments, each treatment has 9 pots for three different times of sample collection, at 0, 2 and 12 weeks (with three replicates for each time) from the time of exposure to determine the amount of secondary metabolite of cypermethrin (3-phenoxy- benzoic acid, 3-PBA) formed and urease and dehydrogenase enzyme activities. Thus each treatment was amended with cypermethrin insecticide concentration of 100 µg/g soil.

Extraction and Characterization of Insecticide Residue

In brief, PBA was extracted from 10 g of soil samples using methanol and dichloromethane (3:1, v/v) and placed in shaker at 150 rpm for 30 min. The supernatant liquid was centrifuged at 5000 rpm for 15 min in three times. The residual insecticide (as its metabolite 3-PBA) in extracted soil samples from the experimental plot was examined by using UV-Vis spectrophotometer and GC-MS.

Determination of the Urease Enzyme Activity

The activity of the urease enzyme (mg NH_4^+-N g^{-1} soil h^{-1}) was measured by colorimetric methods (Guo and Cai, 2012). A 10 g of fresh soil was placed in a 100 mL volumetric flask and treated with 1 mL of toluene, 10 mL buffer (pH-7) and 5 mL of 10 % urea solution (freshly prepared). After a thorough mixing, the flask was incubated for 3 h at 37 ºC in dark. After incubation, the volume was made up to 100 mL with distilled water. The ammonia released as a result of urease activity was measured by indophenol blue method with the spectrophotometer at 630 nm.

Determination of the Dehydrogenase Enzyme Activity

Dehydrogenase enzyme activity was assayed by modified 2,3,5 triphenyl tetrazolium chloride (TTC) reduction technique (Casida *et al.,* 1964). Five grams of soil was placed in a test tube (15 x 2 cm) and carefully mixed with 0.1 g of $CaCO_3$ and 1.5 mL of distilled water added into the mixture. Then, 1 mL of 1 % TTC solution was added and the tubes were incubated at 30 ºC for 24 h after plugging with cotton. The resulting slurry was filtered and triphenyl formazan (TPF) was extracted with successive aliquots of methanol in a 50 mL volumetric flask. The absorption of the pink colour was read out with spectrophotometer at 485 nm.

Results and Discussion

Physicochemical Properties of Soil Sample

The soil has the sandy loam texture. This research used a soil with low nitrogen, very low organic carbon, humus and electrical conductivity (EC), high K_2O and very high phosphorus (P) contents in order to scientifically investigate on the degradation of cypermethrin. The moisture content of the contaminated soil was found to be 2.34 %. The pH value of the contaminated soil was found to be 8.79, it can be considered as a moderately alkaline type of soil. The pH of the soil is important because it can alter the availability of nutrients to the plants, thereby affecting the activity of the roots and microbes. The electrical conductivity value of the contaminated soil was

found to be 0.09 mS/cm. The electrical conductivity of soil informs the ionic nature of the soluble compound to supply the needs of plants. The organic carbon content of the contaminated soil was found to be 0.36 % and humus content was 0.62 %. Humus contains every element absorbed by growing plants, but not in the same proportions as in plant. The microbes become a part of the soil humus, along with materials that have partially or entirely resisted the process of decomposition. Humus is a very important part of the ability of the soil to supply the needs to plant.

The nitrogen content of the contaminated soil was found to be the lowest value 0.13 %. Nitrogen helps plants make the proteins they need to produce new tissues. In nature, nitrogen is often in short supply, so plants have evolved to take up as much nitrogen as possible, even if it means not taking up other necessary elements. If too much nitrogen is available, the plant may grow abundant foliage but not produce fruit or flower. The cation exchangeable capacity (CEC) content of the soil was found to be 21.06 meq/100 g. The CEC is an essential measurement in agronomy and soil science to estimate the physicochemical state of a soil, which may be a good indicator of soil quality and productivity to supply the three important plant nutrients: calcium, magnesium and potassium. CEC is important for maintaining adequate quantities of plant available calcium (Ca^{2+}), magnesium (Mg^{2+}), and potassium (K^{+}), respectively. The highest phosphorus content of the contaminated soil was found to be 45.03 ppm. Phosphorus stimulates root growth, helps the plant set buds and flowers, improves vitality and increases seed size. It does this by helping transfer energy from one part of the plant to another. Organic matter and the activity of soil organisms also increase the availability of the phosphorus.

Table 1 Characteristics of the Soil Sample

Test Parameter	**Content**
Texture	Sandy loam
Moisture (%)	2.34
pH	8.79
Electrical Conductivity (mS/cm)	0.09
Organic carbon (%)	0.36
Humus (%)	0.62
Total Nitrogen (%)	0.13
CEC (meq/100 g)	21.06
Phosphorus (ppm)	45.03
K_2O (mg/100g)	20.27
Exchangeable Ca^{2+} (meq/100 g)	19.10
Exchangeable Mg^{2+} (meq/100 g)	0.68
Exchangeable K^{+} (meq/100 g)	0.43
Exchangeable Na^{+}(meq/100 g)	0.85

The K_2O content of the contaminated soil was found to be 20.27 mg/100 g. Potassium is one of the three major fertilizer elements. In fertilizer and soil analyses, however, potash signifies the hypothetical potassium oxide although K_2O is not absorbed by plants. Plant roots absorb most of their potassium as potassium ions K^{+}. The exchangeable calcium content of the contaminated soil was found to be 19.10 meq/100 g. Calcium is used by plants in cell membranes, at their growing points and to neutralize toxic materials. In addition, calcium improves soil structure and helps to bind organic and inorganic particles together. The exchangeable magnesium content of the contaminated soil was found to be 0.68 meq/100 g. Magnesium is the only metallic component of

chlorophyll. Without it, chlorophyll cannot capture sun energy needed for photosynthesis. The exchangeable potassium content of the contaminated soil was found to be (0.43) meq/100 g. Potassium improves overall vigor of the plant. It helps the plants make carbohydrates and provides disease resistance. It also helps regulate metabolic activities. The exchangeable sodium content of the contaminated soil was found to be 0.85 meq/100 g. Sodium cations (Na^+) are not plant nutrient, so are not wanted by the plants. When exchangeable sodium is present in quantities greater than above 5% of (CEC), it makes the clay particles unstable in rainwater. This shows up as dispersion or cloudiness in water. Dispersive soils have poor water entry and drainage and set hard on drying. This study gives information about nature of soil and nutrients present in soil, so that farmer can arrange the quantity of fertilizers and nutrients needed by the soil for increased crop yield (Table 1).

EDXRF Analysis

The relative abundances of some elemental contents: Si, Fe, K, Ca, Ti, Mn, Cr, Ni, Sr, Zn, Y and Rb in insecticide-contaminated soil are shown by EDXRF (Figure 2 and Table 2). The insecticide-contaminated soil contained silicon (Si) as the major constituent and iron (Fe) as the second major constituent and other trace constituents are: potassium (K), calcium (Ca), titanium (Ti), manganese (Mn), chromium (Cr), strontium (Sr), nickel (Ni), zinc (Zn), yttrium (Y) and rubidium (Rb). All of the insecticide-contaminated soil contained high amounts of Si, Fe, K, Ca, and Ti.

Table 2 Elemental Analysis of the Soil Sample

Element	Relative Abundance (%)
Silicon (Si)	54.729
Iron (Fe)	25.643
Potassium (K)	8.398
Calcium (Ca)	7.198
Titanium (Ti)	2.451
Manganese (Mn)	0.627
Chromium (Cr)	0.372
Nickel (Ni)	0.266
Strontium (Sr)	0.169
Zinc (Zn)	0.074
Yttrium (Y)	0.039
Rubidium (Rb)	0.034

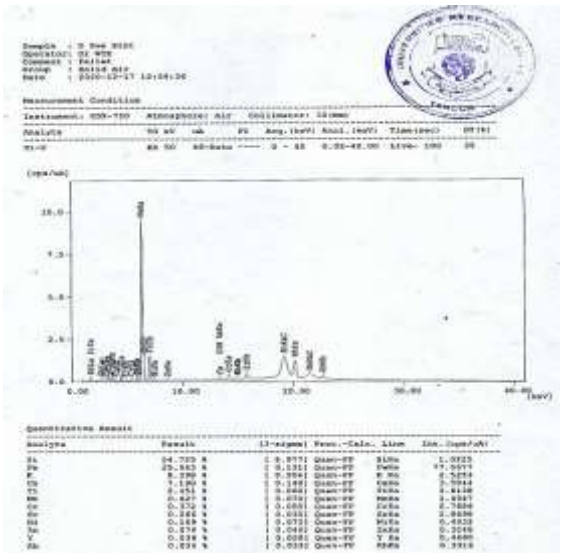

Figure 2 EDXRF spectrum of contaminated soil

The high content of Si resists the damage to crops by pathogenic microorganisms and that of other elements provide as plant nutrient. Iron (Fe) is one of the major elements present in the soil, mostly in the forms of oxide. Generally, the most dominant oxidation state is Fe^{3+} and when reducing conditions are prevailing, iron exists as Fe^{2+}. Iron oxides are very important components in most soil as they have major influence on chemical, physical, and microbial properties of soils. Because of their particles size (usually 5-200 nm), iron oxides possess large specific surface area and highly reactive surfaces. The average particle's diameter was determined to be approximately 33.423 nm. Degradation was slow in case of larger size iron oxide particles, indicating surface area dependency of the reaction. Potassium (K) is commonly supplied to the soil as farm manure and as commercial fertilizers. It is called fertilizer elements. Calcium (Ca) plays a vital role in plant growth, specifically cell wall formation, cell division and pollination. Calcium also promotes

healthy soil structure by loosening soils and stabilizing organic matter, which increases soil water-holding and nutrient-holding capacity. The more calcium is in the soil, the higher the pH of the soil can become.

Titanium (Ti) is considered a beneficial element for plant growth. When plants experience Fe deficiency, Ti helps induce the expression of genes related to Fe acquisition, thereby enhancing Fe uptake and utilization, subsequently improving plant growth. The other nutrient elements (manganese (Mn), chromium (Cr), nickel (Ni), strontium (Sr), zinc (Zn), yttrium (Y) and rubidium (Rb) are used by higher plants in very small amounts, thereby justifying the name micronutrients or trace elements. Such a designation does not mean that they are needed in small quantities. This is due to the relatively small quantities of micronutrients in sands and organic soils and to the low availability of most of these elements under very alkaline conditions.

Insecticide Residue Percent in Contaminated Soil Samples

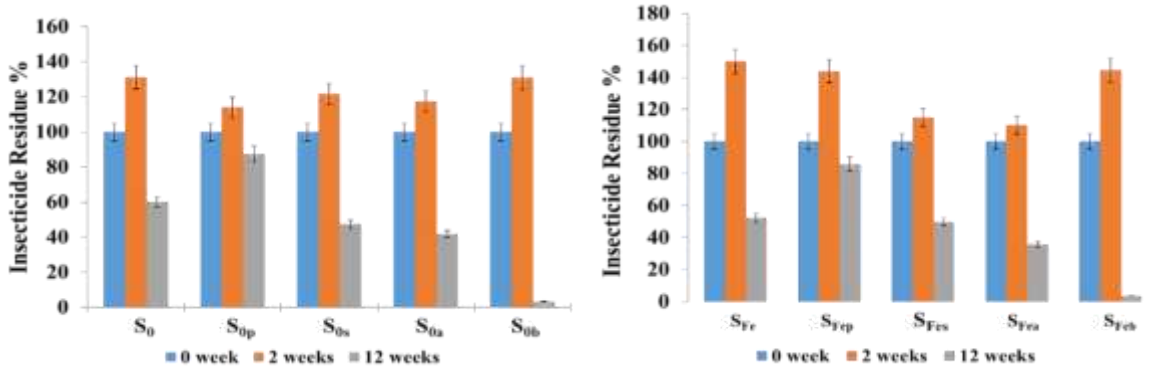

(a) (b)

Figure 3 Insecticide residue percent in contaminated soil treated with Peanut, Sesame, Aster and Bermuda grass (a) in the absence of iron oxide particles and (b) in the presence of iron oxide particles through 12 weeks experiments

The effect of iron oxide particles were prepared by using *Camellia sinesis* (Tea leaves) as reducing agent on phytoremediation has been investigated for phytoremediation of the residue of insecticides from contaminated soil by UV-Vis and GC-MS. Relative to S_0 in 0-week treatment, the percentages of insecticide residue in the S_0, S_{0p}, S_{0s}, S_{0a}, and S_{0b} treatments were found to be 131.28, 114.09, 121.76, 117.4 and 130.98 % PBA formed through 2 weeks experiments and 60.1, 87.46, 47.47, 41.87 and 3.4 % PBA formed through 12 weeks experiments (Figure 3-a). Relative to S_{Fe} in 0-week treatment, the percentage of insecticide residue in the S_{Fe}, S_{Fep}, S_{Fes}, S_{Fea}, and S_{Feb} treatments were observed as 149.94, 143.88, 114.98, 110.2 and 144.52 % PBA formed after 2 weeks experiments and 52.29, 86, 49.84, 35.81, and 3.3 % PBA formed through 12 weeks experiment (Figure 3-b). All treatments were found to possess phytoremediation efficiency for insecticide-contaminated soil. Among them, Aster and Bermuda grass with iron oxide particles phytoremediation had the best degradation efficiency.

Insecticide residue was removed more quickly in the presence of iron oxide particles than by plants alone. Soil moisture also played an important role to increase ionization and activation of iron oxide particles. During cultivation, the plants were watered regularly. This may be because soil saturation with water, decreases the oxygen levels and thus prevent the oxidation of iron oxide particles. Insecticides, which are persistent in aerobic environments, are more readily degraded under reducing conditions. The results showed that the iron oxide particles played a significant role

in the degradation of insecticide residue in the soil, compared with natural degradation in soil without them.

Cypermethrin is a relatively stable to sunlight and, though it is probable that photodegradation plays a significant role in the degradation of the product, its effects in soils are limited. The most important photodegradation product is 3-phenoxybenzoic acid (PBA) and, to some extent, the amide of the intact ester, do not differ greatly from those resulting from biological degradation. Degradation in the soil occurs primarily through cleavage of the ester linkage to give PBA, and carbon dioxide. Some carbon dioxide is formed through the cleavage of both the cyclopropyl and phenyl rings under oxidative conditions. The half-life of cypermethrin in a typical fertile soil is between 2 and 4 weeks. Cypermethrin is adsorbed very strongly on soil particles, especially in soils containing large amounts of clay or organic matter.

The excellent performance of functionalized iron oxide particles in nanomaterial and biomedical applications often relies on achieving the attachment of ligands to the iron oxide surface both in sufficient number and with proper orientation (Korpany *et al*., 2017). The results of this study could be due to relationships between the ligand chemical structure and surface binding on magnetic iron oxide particles (~30 nm) for a series of related benzoic acid derivatives. The structure of the resultant ligand-surface complex was primarily influenced by the relative positioning of hydroxyl and carboxylic acid groups within the ligand. The chemical structure of benzoic acid derivatives enables fast and stable covalent binding on the surface of magnetite (Fe_3O_4) particles, which act as catchers and carriers for magnetic removal. The results of studies have shown that, when iron oxide particles are applied, the levels of cypermethrin as its secondary metabolite PBA can be effectively lowered.

GC-MS Analysis of Cypermethrin and Its Metabolites

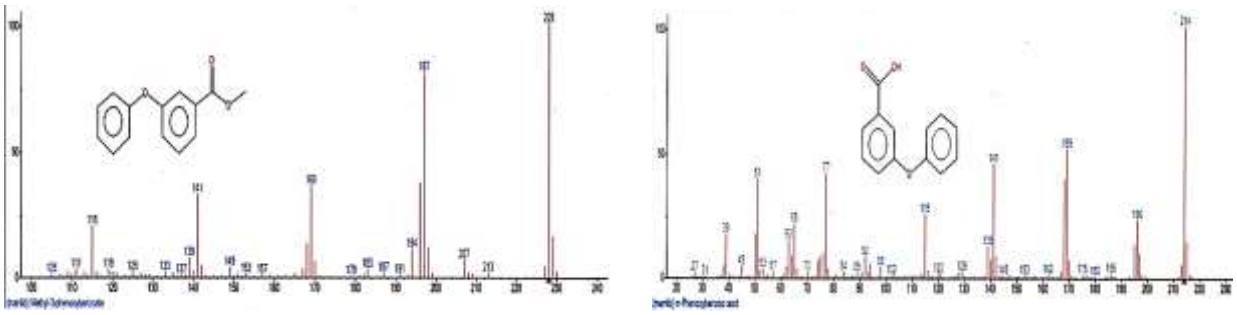

(a) **(b)**

Figure 4 MS spectra of (a) Methyl 3-Phenoxybenzoate observed sample and (b) 3-PBA (library spectrum)

Gas chromatograph-mass spectrometry (GC-MS), is a sophisticated method for identification of molecular structure of the insecticides present in the samples. Confirmatory methods for organic residues or contaminants shall provide information on the chemical structure of analyte. Figures 4 (a) and (b) are mass spectra corresponding to the observed sample Methyl 3-Phenoxybenzoate and the standard 3-PBA.GC-MS had been successfully applied for determining metabolites of cypermethrin in soil. Appearance of cypermethrin breakdown product 3-PBA was evident after 12 weeks application. GC-MS analysis of extracted solution consisting of the target compounds, was carried out and a library matching was done with the obtained mass spectrum and library spectrum. PBA was eluted at a GC retention time of 8.06 min (Figures 5 and 6) and identified by its mass spectrum (Figure 4). The percentages of insecticide residue PBA are calculated based on the peak area in gas chromatograms (Figure 3).

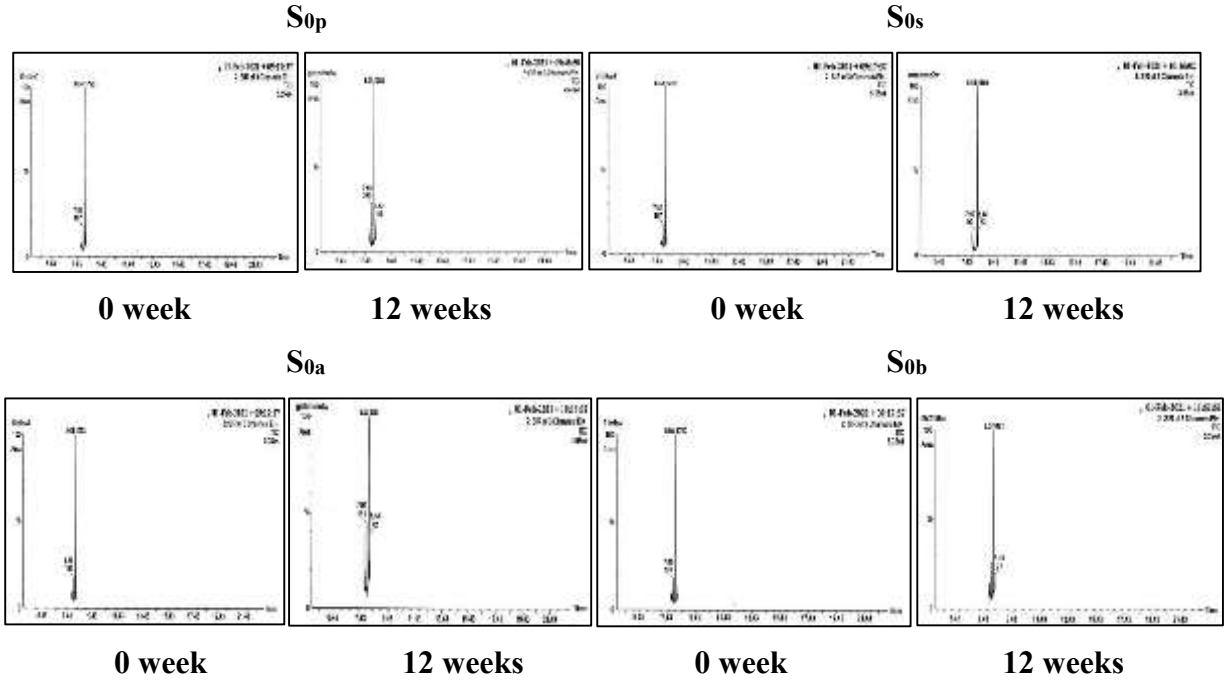

Figure 5 Gas chromatograms for insecticide residue in contaminated soil samples (S_0, S_{0p}, S_{0s}, S_{0a}, S_{0b})

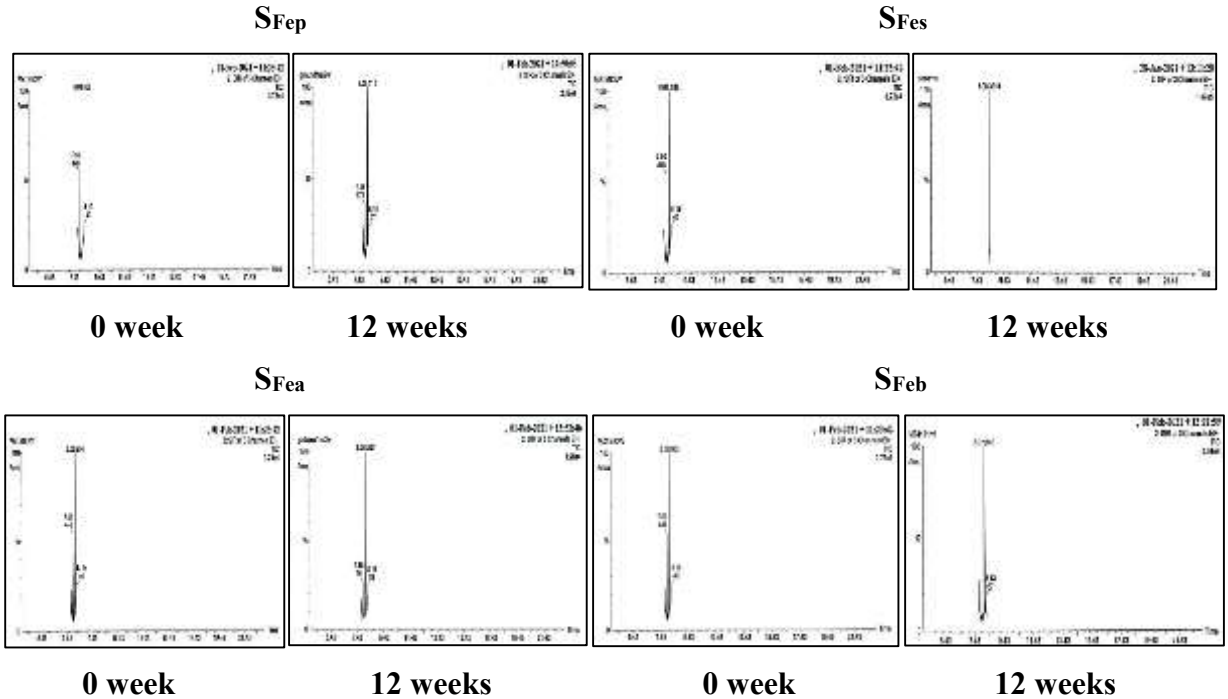

Figure 6 Gas chromatograms for insecticide residue in contaminated soil samples (S_{Fe}, S_{Fep}, S_{Fes}, S_{Fea}, S_{Feb})

Enhancement of Urease and Dehydrogenase Enzyme Activities

The effects of iron oxide particles on increasing urease and dehydrogenase activities were found to be maximum during the incubation periods (12 weeks). According to figure, the changes of urease and dehydrogenase activities depend on dosage of iron oxide particles. The degradation of cypermethrin in soil is mostly attributed to microorganisms. Urease and dehydrogenase activities are appropriate substitute biomarker of general microbial activities in soils.

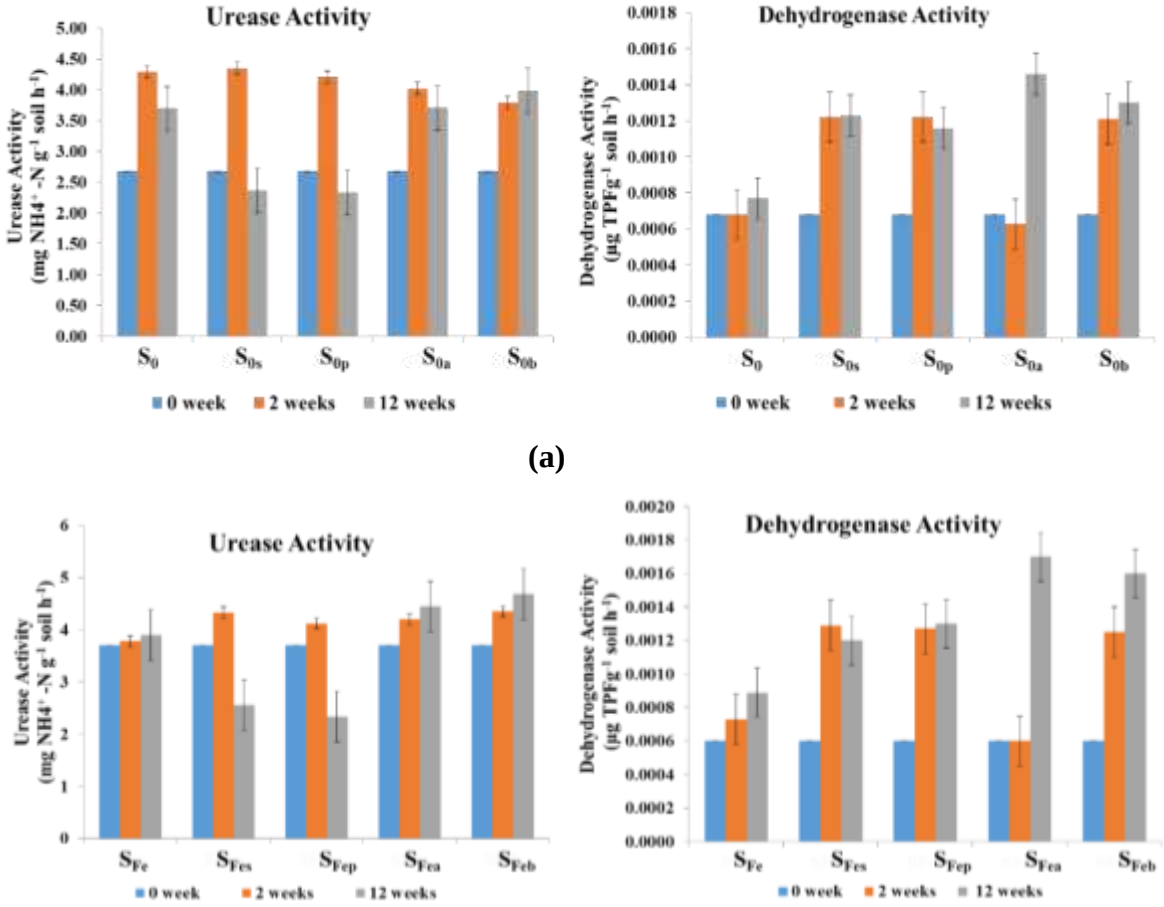

Figure 7 Soil urease and dehydrogenase activities in insecticide contaminated soil treated with Peanut, Sesame, Aster and Bermuda grass (a) in the absence and, (b) in the presence of iron oxide particles

After 12 weeks, the urease and dehydrogenase activities in the controls (or treated soil in the absence of iron oxide particles-S_0), were found to reach 3.74 mg NH_4^+-N g^{-1} soil $h^{-1}$and 0.0008 µg TPF g^{-1} soil h^{-1}, whereas 2.364 mg NH_4^+-N g^{-1} soil h^{-1} and 0.0012 µg TPFg^{-1} soil h^{-1} in Peanut plant (S_{0p}), 2.33 mg NH_4^+-N g^{-1} soil $h^{-1}$and 0.0012 µg TPF g^{-1} soil h^{-1} in Sesame plant (S_{0s}), 3.71 mg NH_4^+-N g^{-1} soil $h^{-1}$and 0.0015 µg TPF g^{-1} soil h^{-1} in Aster (S_{0a}) and 3.7 mg NH_4^+-N g^{-1} soil h^{-1} and 0.0013 µg TPF g^{-1} soil h^{-1} in Bermuda grass (S_{0b}) (Figure 7-a). The percentage of urease and dehydrogenase activities increased to 63.20 and 33.33 % plant (S_{0p}), to 62.30 and 44.44 % in Sesame plant (S_{0s}), to 65.38 and 55 % in Aster (S_{0a}), and to 77.78 and 62.5 % in Bermuda grass (S_{0b}) relative to controls (assumed as 100 %) through 12 weeks.

After 12 weeks, the urease and dehydrogenase activities in the presence of iron oxide particles (S_{Fe}) were found to reach 3.9 mg NH_4^+-N g^{-1} soil $h^{-1}$and 0.0009 µg TPF g^{-1} soil h^{-1}, 2.55 mg NH_4^+-N g^{-1} soil h^{-1} and 0.0012 µg TPF g^{-1} soil h^{-1} in Peanut plant (S_{Fep}), 2.342 mg NH_4^+-N g^{-1} soil $h^{-1}$and 0.0013 µg TPF g^{-1} soil h^{-1} in Sesame plant (S_{Fes}), 4.45 mg NH_4^+-N g^{-1} soil h^{-1} and 0.0017 µg TPF g^{-1} soil h^{-1} in Aster (S_{Fea}) and 4.68 mg NH_4^+-N g^{-1} soil $h^{-1}$and 0.0016 µg TPF g^{-1} soil h^{-1} in Bermuda grass (S_{Feb}) (Figure 7-b). The percentage of urease and dehydrogenase activities increased to 65.38 and 50 % in Peanut plant (S_{Fep}), to 60 and 50 % in Sesame plant (S_{Fes}), to

99.14 and 87.5 % in Aster (S_{Fea}) and to 98.93 and 78 % in Bermuda grass (S_{Feb}) relative to S_{Fe} (assumed as 100 %) through 12 weeks.

The present study showed that urease and dehydrogenase enzyme quantities were improved by the addition of proper iron oxide particles, showing the usefulness of iron oxide particles in phytoremediation.

Conclusion

The possibility of iron oxide particles assisted phytoremediation of four plants (Peanut, Sesame, Aster, and Bermuda grass) to remediate soil contaminated with cypermethrin was determined in this study. The results of this study suggest that addition of iron oxide particles of an adequate amount could enhance degradation of cypermethrin and its most persistent metabolite, PBA. Thus, in agricultural practice, adequate application of iron oxide particles is an efficient method to reduce the accumulation of cypermethrin and PBA in soil and significantly decrease environmental risks. Aster and Bermuda grass with iron oxide particles phytoremediation had the best degradation efficiency. The two plants also had affected on the soil microbial and biochemical properties, reflected by the increase in enzyme activity.

Acknowledgements

The authors would like to express their profound gratitude to the Myanmar Academy of Arts and Science for giving permission to submit this paper and to Professor and Head, Dr Daw Ni Ni Than, Department of Chemistry, University of Yangon, for her kind encouragement.

References

Bootharaju, M.S., and T. Pradeep. (2012). "Understanding the Degradation Pathway of the Pesticide, Chlorpyrifos by Noble Metal Nanoparticles". *Langmuir*, vol. 28, pp. 2671-2679

Casida, L.E., D.A. Klein, and T. Santoro. (1964). "Soil Dehydrogenase activity". *Journal of Soil Science*, vol. 98, pp. 371-376

Fernandez-Garcia, M., and J. A. Rodriguez. (2007). *Metal Oxide Nanoparticles.* Upton, USA: Brookhaven National Laboratory, pp. 1-60

Guo, H., J. Yao, and M. Cai. (2012). "Effects of Petroleum Contamination on Soil Microbial Numbers, Metabolic Activity and Urease Activity". *Chemosphere*, vol. 87 (11), pp. 1273-1280

Jaremko, D., and D. Kalembasa. (2014). "A Comparison of Methods for the Determination of Cation Exchange Capacity of Soils". *Ecological Chemistry* and *Engineering S. Journal*, vol. 21 (3), pp. 487-498

Korpany, K.V., D.D. Majewski, C.T. Chiu, S.N. Cross, and A.S. Blum. (2017). "Iron Oxide Surface Chemistry: Effect of Chemical Structure on Binding in Benzoic Acid and Catechol Derivatives". *Langmuir*, vol. 33 (12), pp. 3000-3013

Malachowska-Jutsz, A., and K. Matyja. (2019). "Discussion on Methods of Soil Dehydrogenase Determination". *International Journal of Science and Technology*, vol. 16 (1), pp. 1-7

Srivastava, A., K.K. Yadav, N. Gupta, J. K. Singh, R. Katiyar, and V. Kumar. (2019). "Nano-Phytoremediation of Pollutants from Contaminated Soil Environment: Current Scenario and Future Prospects". vol. 6, pp. 383-400

Xie, W.-J., Z. Jian-Min, W. Huo-Yan, and C. Xiao-Qin. (2008). "Effect of Nitrogen on the Degradation of Cypermethrin and Its Metabolite 3-Phenoxybenzoic Acid in Soil". *Pedosphere*, vol. 18 (5), pp. 638-644

SCREENING OF PHYTOCHEMICALS AND SOME BIOLOGICAL ACTIVITIES OF THE AERIAL PARTS OF *BACOPA MONNIERI* (L.) WETTST. (BYONE-HMWE)

Aye Aye Thant[1], Yi Yi Win[2], Ni Ni Than[3]

Abstract

The aim of the study was to screen some phytochemical constituents of *Bacopa monnieri* (L.) Byone-hmwe such as total phenolic and total flavonoids contents, and some biological activities such as antioxidant, antimicrobial, and antiproliferative activities. The total phenolic content was determined by Folin-Ciocalteu's assay and expressed as GAE equivalent. An aluminium chloride colorimetric assay was used to calculate the total flavonoids content, which was then expressed as QE equivalent. The antioxidant activity of ethanol and water extracts of *B. monnieri* was determined by DPPH assay. These assays found that the ethanol extract (IC_{50} = 470.15 µg/mL) was more potent than the water extract (IC_{50} =770.54 µg/mL) in antioxidant activity. The ethyl acetate extract of the plant was found to have high potent antimicrobial activities against all six tested microorganisms, with inhibition zone diameters (21-26 mm) determined by agar well diffusion method those of pet-ether, ethanol and water extracts. The *in vitro* antiproliferative activity of ethanol extract was more potent against A549 (lung) and Hela (cervical) human cancer cell lines (IC_{50} = 115.03 µg/mL and IC_{50} = 129.95 µg/mL) than the water extract determined by MTT assay.

Keywords*: Bacopa monnieri*, antioxidant, antimicrobial and antiproliferative activities

Introduction

Byone-hmwe, a member of the *Scrophulariaceae* family, is a small, creeping herb with numerous branches, small oblong leaves and light purple or white flower (Bone, 1996). It grows in grassland occurring in aquatic sites, sand and wet soil occupying the edges of freshwater or brackish pools, streams and lake beds. Flowers and fruits appear in summer, and the entire plant is used medicinally. According to World Health Organization (WHO), the majority of the World's population uses traditional medicines for their primary health care needs. Plant secondary metabolites possesses biological properties such as antiapoptosis, antiaging, antiatherosclerosis, cardiovascular protection, inhibition of angiogenesis and cell proliferation activity (Han *et al.*, 2007). It is also used in analgesic and antipyretic activity to treat asthma, insanity epilepsy, hoarseness, enlargement of spleen, snake bite, rheumatism, leprosy, eczema and ringworm. It is used as a diuretic appetitive and cardio tonic (Mishra *et al.*, 2015). Byone-hmwe contains alkaloids, glycoside, flavonoids and saponins (Saraswati *et al.*, 1996). Byone-hmwe has antianxiety, anticancer, antidepressant, antidiabetic, antihypertensive, anti-lipidemia; anti-inflammatory, antimicrobial, antioxidant, hepatoprotective, gastrointestinal protective and neuroprotective activities (Natthawut *et al*., 2016). Byone-hmwe is an important medicinal herb in Ayurveda for the treatment of a number of health problems. The purpose of the present study is to screen the antioxidant, antimicrobial and anti-proliferative activities of some crude extracts of the aerial parts of Byone- hmwe.

[1] PhD Candidate, Department of Chemistry, University of Yangon
[2] Dr, Associate Professor, Department of Chemistry, Hpa-an University
[3] Dr, Professor and Head, Department of Chemistry, University of Yangon

Botanical Aspect of *Bacopa monnieri* (L.) Wettst (Byone-hmwe)

Family : Plantaginaceae

Botanical name : *Bacopa monnieri* (L.) Wettst.

Myanmar name : Byone-hmwe

Part used : the aerial parts

Bacopa monnieri

Materials and Methods

Plant Material

The sample was collected from Yangon Region, Myanmar in the month of May 2019 and identified as *B. monnieri* by the authorized botanist at the Department of Botany, University of Yangon. The aerial parts including flowers and leaves was dried under the shade for a week, cut into very small pieces and then ground into purely fine powder using an electric grinder. The powdered sample was stored in the airtight containers.

Chemicals

95 % Ethanol, ethyl acetate, pet-ether, 2,2-diphenyl-1-picryhydrazyl (DPPH), dimethyl sulfoxide (DMSO), trypticase soy broth from Difco U.S.A, tryticase soy agar from Becton, U.S.A, Muller-Hinton agar (Hi-Media) and triple sugar iron sugar from Becton, U.S.A. phosphate buffer saline (PBS) powder, fetal bovine serum (FBS, Sigma 172012), trypsin, alcohol (70 % ethanol), Minimum Essential Medium (α MEM, Wako 135-15735), 0.1 mM non-essential amino acid (NEAA, Gibo 11140-050),1 mM sodium pyruvate (SM, Gibco-11360-070)

Instruments

Quartz cuvette (4 mL), UV-visible spectrophotometer (UV-7504), a stirrer, an autoclave (Tomy Seiko Co., Ltd, Tokyo, Japan), a constant temperature bath (Yamato Scientific Co., Ltd, Japan), sterile petri-dish, spirit burner, polyethylene plastic bag, a refrigerator and an incubator multipipette, 96 well plate, aluminum foil, centrifuge tube, Haemacytometer, microscope and vibrator.

Preparation of Extracts

Each 50 g of the dried Byone-hmwe powder was extracted with ethanol, petroleum ether, ethyl acetate and water by sonication using each solvent (100 mL,1 h) at 70 ℃. Each filtrate was evaporated under reduced pressure by a rotatory evaporator to yield different solvent extracts.

Preliminary Phytochemical Tests

Preliminary phytochemical tests on the powdered sample were carried out according to the reported methods in order to classify the types of organic constituents present in the samples such as alkaloids, α-amino acids, carbohydrates, cyanogenic glycosides, flavonoids, glycosides, organic acids, phenolic compounds, reducing sugars, saponins, starch, steroids, tannins and terpenoids by appropriate reported methods (M-Tin Wa, 1972).

Determination of Total Phenol Contents by Folin-Ciocalteu Method

Total phenolic contents of ethanol and water extracts were estimated by the Folin-Ciocalteu method as described by Kaveti. *et al* (2011). A dilute extract (1 mL) of gallic acid used as a standard was mixed with Folin-Ciocalteu reagent (5 ml, 1:10 diluted with water) and 4 mL of 1 M of

aqueous sodium carbonate. The mixture was left to stand for 30 min at 25 °C for the colour to develop. Absorbance was measured at wavelength 765 nm UV-spectrophotometer (Shimadzu, USA). Sample of extracts were evaluated at a concentration of 1000 mg/mL. The total phenolic contents were expressed in terms of gallic acid equivalent, GAE (standard curve equation: $y = 0.0177x + 1.0207$, $R^2 = 0.9918$), mg of GAE/g of dry extract. The experiment was repeated three times at each concentration.

Determination of Total Flavonoids Contents by Aluminum Chloride Colorimetric Assay

Total flavonoids contents of ethanol and water extracts were determined by using aluminum chloride colorimetric assay described by Kaveti *et al*. (2011).1 mL of samples/standard (Quercetin) was mixed with 1.5 mL of methanol. A 0.1 mL of 1 % $AlCl_3$ and 0.1 mL of 1 M potassium acetate and 2.8 mL distilled water was added to the mixture and left at RT for 30 min. The absorbance of the mixtures was measured at wavelength 415 nm. The total flavonoids contents were expressed in terms of quercetin equivalent, QE (standard curve equation: $y = 0.0039x + 0.0199$, $R^2 = 0.9986$), mg of QE/g of dry extract. The experiment was repeated three times at each concentration.

Antioxidant Action by DPPH Free Radical Scavenging Assay

Preparation of DPPH solution

DPPH (4.732 mg) was thoroughly dissolved in 95 % ethanol (100 mL). This solution was freshly prepared in the brown-coloured reagent bottle and stored in the fridge for no longer than 24 h. Each tested sample (20 mg) and 20 mL of ethanol were thoroughly mixed by shaker. The mixture solution was filtered and the stock solution (1000 µg/mL) was obtained. By adding ethanol, DPPH solutions with different concentrations of 500–62.5 µg /mL were prepared from the stock solution.

Determination of antioxidant activity

The effect of Byone-hmwe on the DPPH radical was determined by using the method of Marinova and Batchvarov (2011). The control solution was prepared by mixing 1.5 mL of 120 µM DPPH solution and 1.5 mL of 95 % ethanol using shaker. The test sample solution was also prepared by mixing thoroughly 1.5 mL of 120 µM DPPH solution (Absorbance = 0.8941 used for control) and 1.5 mL of each sample solution (1000-62.5 µg/mL). The mixture solutions were allowed to stand at room temperature for 30 min. Then, the absorbance of these solutions was measured at 517 nm by using UV-7504 spectrophotometer. Absorbance measurements were made in triplicate for each concentration and then mean values so obtained were used to calculate percent inhibition of oxidation by the following equation:

$$\% \text{ RSA} = \frac{A_{DPPH-}(A_{smaple-}A_{blank})}{A_{DPPH}} \times 100$$

where, % RSA = % radical scavenging activity

A_{DPPH} = absorbance of DPPH in EtOH solution

A_{Sample} = absorbance of sample and DPPH solution

A_{blank} = absorbance of sample and EtOH solution

The experimental results were performed in triplicate. The data were recorded as mean ± standard deviation.

Screening of Antimicrobial Activity of the Samples by Agar Well Diffusion Method

The antimicrobial activity of four crude extracts such as pet-ether, ethyl acetate, ethanol and water extracts from the aerial parts of Byone-hmwe was determined against six strains of microorganisms such as *Bacillus subtilis* (IFO 90571), *Staphylococcus aureus* (AUH5436), *Pseudomonas aeruginosa, Salmonella typhi* (AUH8465), *Candida albicans* (NITE09542) and *Escherichia coli* (AUH5436) by employing agar well diffusion method (Anibijuwon and Udeze, 2009). These tests were screened at the strains' storage facility, Sagaing University.

Preparation of nutrient agar medium

A mixture of meat extract (0.5 g), peptone (0.5 g), sodium chloride (0.25 g) and 1.5 g of agar powder was placed in a sterilized conical flask, 100 mL of sterile distilled water was added to obtain nutrient agar medium. The resulting mixture was heated to dissolve the contents. Then, the pH of this solution was adjusted to 7.2 with 0.1 M sodium hydroxide solution. It was sterilized in an autoclave at 121 ℃ for 15 min.

Determination of antimicrobial activity by agar well diffusion method

Agar well diffusion method was used to evaluate the antimicrobial activities of the extracts against bacteria and fungi. Different extracts (1 mg each) were dissolved in 1 mL of their respective solvent. After inoculation, plates were dried for 15 min. A hole with a diameter 8 mm was punched aseptically with a sterile cork or a tip and volume 0.1 mL of extract solution at desired concentration was introduced into the well. Then, agar plates were incubated under suitable conditions depending upon the microorganisms. The antimicrobial agent diffuses in the agar medium and inhibits the growth of the microbial strain tested. The plates were incubated for 24 h to allow the extract to diffuse through the agar media to form zones of inhibition. The extent of antimicrobial activity was measured by the diameter of inhibition zone.

Investigation of Antiproliferative Activity of Ethanol and Water Extracts against Human Cancer Cell Lines

Antiproliferative activity of ethanol and water extracts of Byone-hmwe was investigated by the reduction of 3-(4,5-dimethylthiazol-2-yl)-2.5-diphenyltetrazolium bromide (MTT) to formazan at Division of Natural Product Chemistry, Institute of Natural Medicine, and University of Toyama, Japan. The cell lines used were Hela (human cervix cancer) and A549 (lung cancer). Minimum essential medium with L-glutamine and phenol red (α-MEM, Wako) were used for cell cultures. All media were supplemented with 10 % fetal bovine serum (FBS, sigma) and 1 % antibiotic antimycotic solution (Sigma). From the above medium solution, 100 mL of this supplemented medium was mixed with 1 mL of non-essential amino acid (NAA) for A-549. The *in vitro* antiproliferative activity of the crude extracts was determined by the procedure described by (Win *et al.,* 2015). Briefly, each cell line was seeded in 96-well plates (2×10^3 per well) and incubated in the respective medium at 37 °C under 5 % CO_2 and 95 % air for 24 h. After the incubation, the cells were washed with PBS, serial dilutions of the tested samples were added. The sample solution in wells with cells were incubated in an incubator for 72 h. The sample solution with cell and medium was added with 100 µL MTT reagent. And then the wells were incubated in an incubator for 3 h, After the incubation, cells in the medium were aspirated with aspirator. The cell was washed with PBS (5 mL) 2 times. Then, DMSO was added about 100 µL per well and the 96 well plates were placed in the dark for 15 min. And then, the absorbance of each solution was measured at 570 nm by using UV-visible spectrophotometer. The concentrations of the crude extracts were 200, 20 µg/ mL and 20, 10, 2 mM for positive control were prepared by serial dilution. Cell viability was calculated from the mean values of the data from three wells using the

equation below and antiproliferative activity reagent was expressed as the IC_{50} (50 % inhibitory concentration) value, 5-fluorouracil (5FU) was used as a positive control.

$$(\%)\ \text{Cell viability} = \frac{A_{(\text{test sample})} - A_{(\text{blank})}}{A_{(\text{control})} - A_{(\text{blank})}} \times 100$$

where,

$A_{(\text{test sample})}$ = absorbance of test sample solution

$A_{(\text{control})}$ = absorbance of DMSO solution

$A_{(\text{blank})}$ = absorbance of MTT reagent

Results and Discussion

Phytoconstituents in Byone-hmwe

The phytochemical screening of Byone-hmwe was preliminarily carried out by the appropriate methods and the results are shown in Table 1. The phytochemical tests revealed the presence of the secondary metabolites such as alkaloids, α-amino acids, carbohydrates, glycosides, saponins, phenolic compounds, flavonoids, tannins, steroids and terpenoids but cyanogenic glycosides, starch, and reducing sugars were absent in the aerial parts of Byone-hmwe.

Table 1 Results of Preliminary Phytochemical Tests on Byone-hmwe

No.	Test	Extracts	Test Reagent	Observation	Remark
1	Alkaloids	1% HCl	(i)Wagner's	reddish brown ppt	+
			(ii) Dragendorffs'	orange ppt	+
			(iii) Mayer's	white ppt	+
			(iv) Sodium picrate	yellow ppt	+
2	α-amino acids	H_2O	Ninhydrin	violet spot	+
3	Carbohydrates	H_2O	10 % α-naphthol & conc:H_2SO_4	red ring	+
4	Cyanogenic glycosides	H_2O	Sodium picrate solution	no brick red colour	-
5	Flavonoids	EtOH	Mg ribbon & conc: HCl	pink colour	+
6	Glycosides	H_2O	10 % lead acetate	white ppt	+
7	Phenolic compounds	EtOH	1 % $FeCl_3$	green colour	+
8	Reducing sugars	H_2O	Fehling's solution A & B	no brick red ppt	-
9	Saponins	H_2O	distilled water	frothing	+
10	Starch	H_2O	iodine solution	no blue colour	-
11	Steroids	PE	acetic anhydride & conc:H_2SO_4	green colour	+
12	Tannins	EtOH	1 % gelatin	white ppt	+
13	Terpenoids	$CHCl_3$	acetic anhydride & conc:H_2SO_4	pink colour	+

(+) = presence (-) = absence (ppt) = precipitation

Total Phenolic and Flavonoids Contents

In the present study, the resulted total phenolic and flavonoids contents in ethanol and water extracts of Byone-hmwe aerial parts are shown in Table 2 and Figure 2. The aerial parts of Byone-hmwe contained significant total flavonoids contents. The ethanol extract with mean value of 7.435 mg GAE/g extract had higher potency than water extract with mean value 3.596 mg GAE/g extract and total flavonoids content expressed that ethanol extract with mean value of 24.05 mg QE/g was more potent than water extract with mean value of 15.23 mg QE/g extract, respectively.

Table 2 Total Phenolic and Flavonoids Contents of Extracts of Byone-hmwe Aerial Parts

Extracts	TPC (mg GAE/ g ± SD)	TFC (mg QE /g ± SD)
Ethanol	7.435 ± 0.029	24.05 ± 0.004
Water	3.596 ± 0.07	15.23 ± 0.002

* mg gallic acid and quercetin equivalent /g extract. each concentration

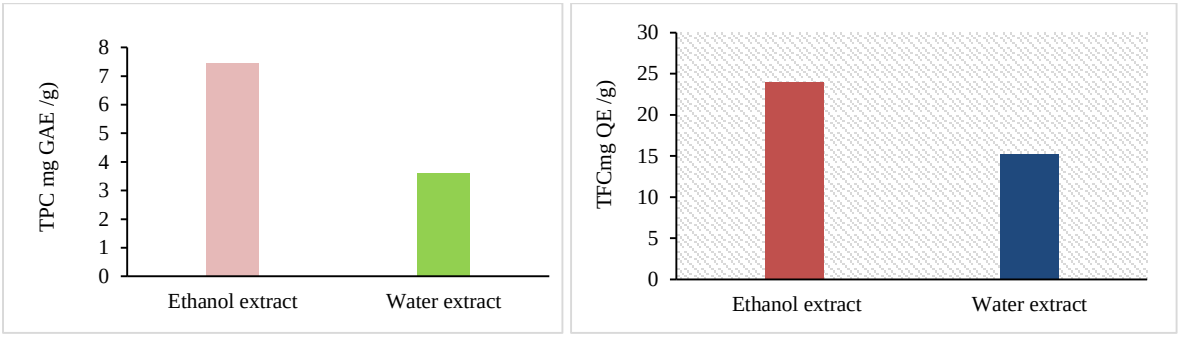

Figure 2 Total phenolic and flavonoids contents of ethanol and water extracts of the aerial parts of Byone-hmwe

In vitro Antioxidant Activity

Free radicals scavenging capacity of the extract was determined using the stable free radical containing DPPH. It can accept an electron or hydrogen radical. The odd electron in it makes the solution to appear deep violet in colour. The absorption vanishes when DPPH accepts an electron resulting in delocalization. DPPH radical scavenging ability of an antioxidant is supposed to be due to hydrogen donating property (Soares *et al*., 1997). In the DPPH free radical scavenging assay, 62.5-1000 µg/mL of ethanol and water extracts of the aerial parts of Byone-hmwe were used. A decrease in absorbance exhibits increase in radical scavenging activity. The radical scavenging activities of two crude extracts were expressed in terms of % RSA and IC_{50} (50 % inhibitory concentration). The IC_{50} values of ethanol and water extracts of the aerial parts of Byone-hmwe were found to be 470.15 µg/mL and 770.54 µg/mL, respectively. Similarly, the reference ascorbic acid (6.25-100 µg/mL) showed significant free radicals scavenging activities ranging from (26.9- 88.34 %) and IC_{50} value was 11.9 µg/mL. Since the lower the values, the greater the antioxidant activity of the samples. The ethanol extracts of the aerial parts of the plant had higher antioxidant activity than water extracts. The results are shown in Table 4 and Figure 3, 5.

Table 3 Antioxidant Activity of Crude Extracts from the Aerial Parts of Byone-hmwe

Crude extracts	% RSA ± SD at different concentrations (µg/mL)					IC_{50} (µg/mL)
	62.5	125	250	500	1000	
Water extract	11.36 ± 0.33	20.13 ± 1.12	30.13 ± 0.56	40.38 ± 0.48	58.02 ± 0.37	770.54
Ethanol extract	25.2 ± 0.57	35.75 ± 0.98	46.3 ± 0.66	57.3 ± 0.3	67.14 ± 0.26	470.15

Table 4 % RSA (Radical Scavenging Activity) of Standard Ascorbic Acid

Sample	% RSA ±SD at different concentrations (µg/mL)					IC 50 (µg/mL)
	6.25	12.5	25	50	100	
Ascorbic acid	26.9 ± 0.04	52.41 ± 0.01	70.55 ± 0.01	88.34 ± 0.01	94.62 ± 0.01	11.9

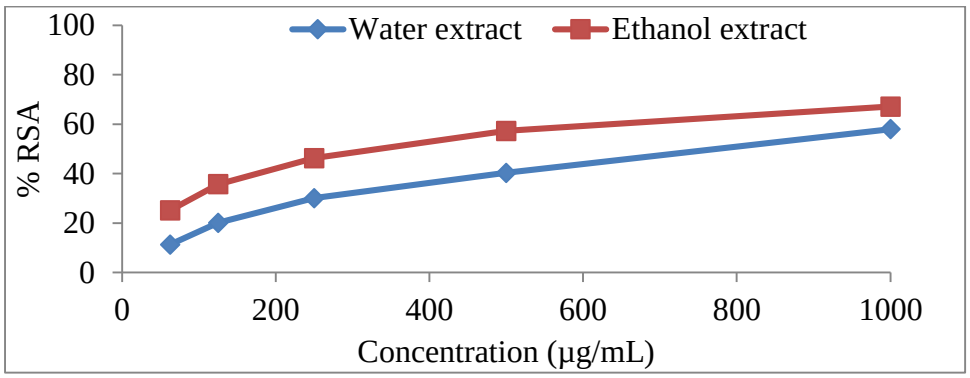

Figure 3 DPPH radical scavenging activities of crude extracts of Byone-hmwe at different concentrations

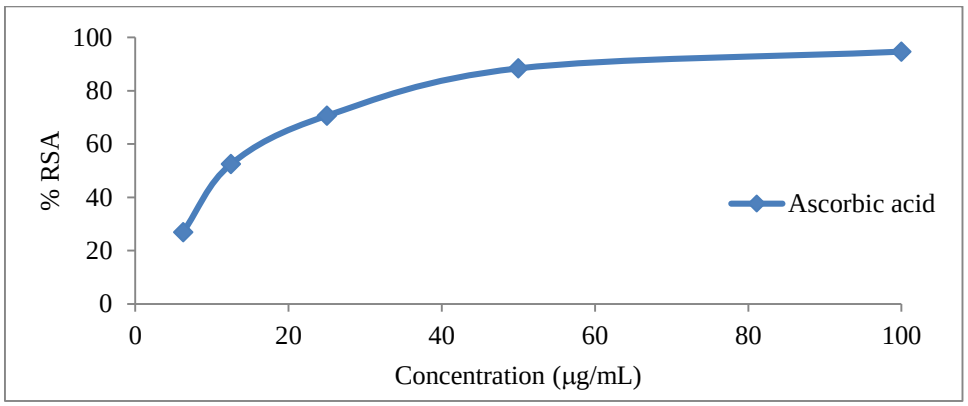

Figure 4 DPPH free radical scavenging activities of standard ascorbic acid

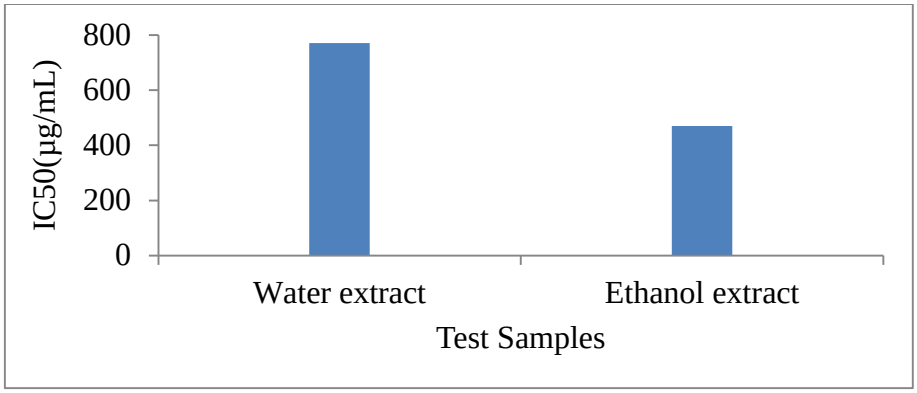

Figure 5 Comparison of percent inhibition and IC_{50} value of crude extracts of Byone-hmwe

Antimicrobial Activity

The antimicrobial activity was determined by measuring the diameter of the zone of inhibition and recording it (Table 5). According to the method described by Selvamohan *et al*. (2012), in this investigation, four extracts (pet-ether, ethanol, ethyl acetate and water of Byone-hmwe were tested against two-gram negative bacteria (*P. aeruginosa and E. coli*), three-gram positive bacteria (*B. subtilis, S. typhi and S. aureus*) and *C. albicans* fungus by agar well diffusion method. The measurable zone diameter, including the well diameter, shows the degree of completeness of the antimicrobial activity. In this experiment, the well diameter was set as 8 mm (Figures 6 and 7). The greater zone diameter, the greater the activity of the tested organisms. According to the results, it was found that water and ethanol extracts of Byone-hmwe exhibited activity against all six microorganisms, with the zone diameter inhibition range between 14-19 mm. Moreover, ethyl acetate extract (the inhibition zone diameter 21-26 nm) and pet–ether extract (the inhibition zone diameter 11-14 mm) were also tested against six microorganisms, water and ethanol extracts showed medium activity on selected microorganisms, and pet ether extract showed low activity against *B. subtilis, C. albicans, E. coli, P. aeruginosa, S. aureus and S. typhi.*

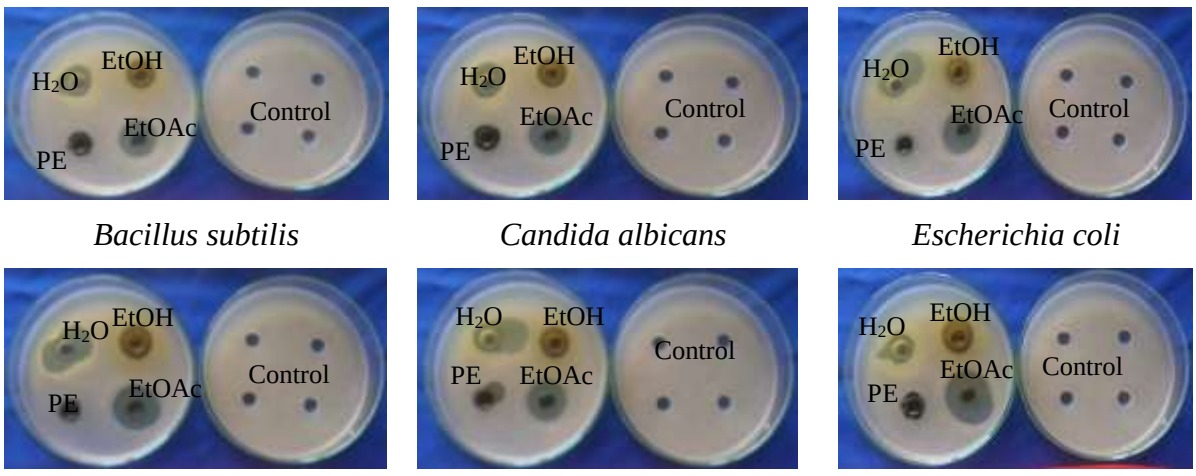

Figure 6 Screening of antimicrobial activities of the aerial parts of *Bacopa monnieri*

Table 5 Inhibition Zone Diameter of the Aerial Parts of *Bacopa monnieri* Against Six Different Microorganisms

Extracts	Inhibition zone diameter (mm) against six microorganisms					
	B. subtilis	***C. albicans***	***E. coli***	***P. aeruginosa***	***S. aureus***	***S. typhi***
Water	15 (++)	16 (++)	14 (+)	15 (++)	16 (++)	16 (++)
EtOH	15 (++)	15 (++)	14 (+)	17 (++)	16 (++)	19 (++)
EtOAc	21 (++)	22 (+++)	22 (+++)	26 (+++)	21 (+++)	26 (+++)
PE	13 (+)	14 (+)	11 (+)	11 (+)	11 (+)	14. (+)

Diameter of agar well = 8 mm
9 mm-14 mm = (+) Low activity
15 mm- 20 mm = (++) Medium activity
21 mm above = (+++) High activity

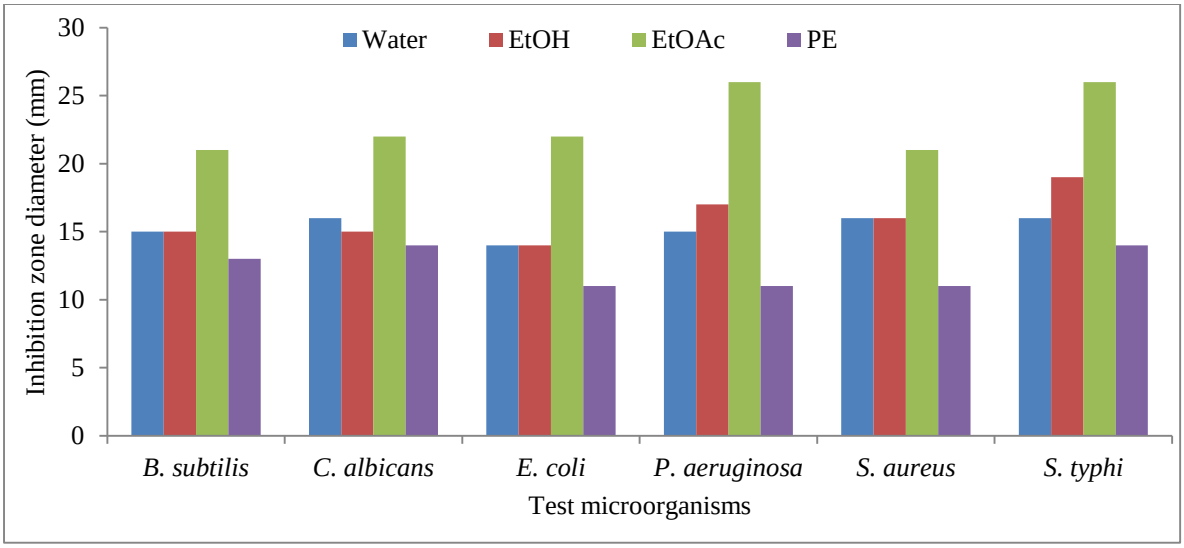

Figure 7 Inhibition zone diameters for crude extracts of the aerial parts of Byone-hmwe

Antiproliferative Activity of the Ethanol and Water Extracts Against One Human Cancer Cell lines

Antiproliferative activity is the activity relating to a substance used to prevent or retard the spread of cells, especially malignant cells, into surrounding tissues. The MTT assay was used to assess the antiproliferative activity of ethanol and water extracts of the Byone-hmwe on two cancer cell lines, A 549 (lung cancer cell line) and Hela (Cervix cancer cell line). The anticancer effect was expressed as IC_{50} values (50 % inhibitory concentration). The lower the IC_{50} values, the higher antiproliferative activity is. According to these results, the ethanol extract of the Byone-hmwe showed antiproliferative activity with the IC_{50} values of 115.03 µg/mL (for the A549 cell line) and 129.95 µg/mL (for Hela cell line). But the ethanol extracts of Byone-hmwe possessed weaker antiproliferative activity for two cancer cell lines (A 549 and Hela) which compared with water extracts because of their IC_{50} values of >200 µg/mL. The test samples had weaker antiproliferative activity when compared with standard 5 FU (Table 6 and Figure 8).

Table 6 Antiproliferative Activity of Crude Extracts of Byone-hmwe

Text Sample	Antiproliferative activity					
	Lung			Cervix		
	20 (µg/mL)	200 (µg/mL)	IC_{50} µg/mL	20 (µg/mL)	200 (µg/mL)	IC_{50} (µg/mL)
Ethanol extract	96.47 ± 17.04	8.45 ± 0.07	115.03	72.25 ± 9.19	6.59 ± 0.00	129.95
Water extract	72.23 ± 0.64	91.71 ± 7.07	>200	96.83 ± 0.64	91.29 ± 0.71	>200

Table 7 Antiproliferative Activity of Standard of 5- Fluorouracil

Positive Control	2 (µg/mL)	10 (µg/mL)	20 (µg/mL)	IC_{50} (µg/mL)
5- Fluorouracil (Lung cancer cell line)	136.24 ± 12.94	70.45 ± 5.59	47.89 ± 8.21	19.06
5- Fluorouracil (Cervix cancer cell line)	91.44 ± 24.93	85.22 ± 4.95	24.93 ± 0.28	15.84

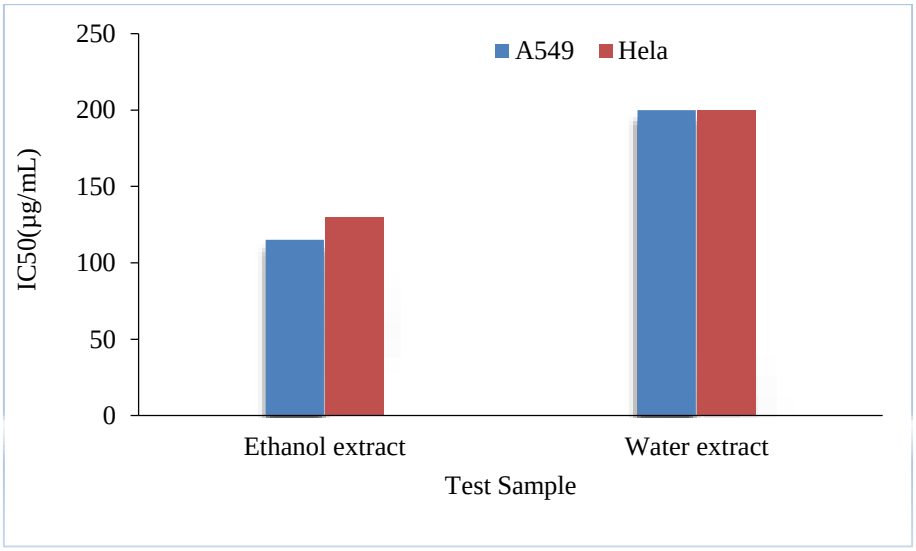

Figure 8 IC_{50} values of crude extracts of the aerial parts of Byone –hmwe

Conclusion

From the preliminary phytochemical results, the aerial parts of Byone-hmwe extracts had bioactive secondary metabolites such as alkaloids, phenolic compounds, steroids, flavonoids and terpenoids. (Jun, *et al*.,2017 and Gharech, *et al.*,2014). Therefore, ethanol, water, ethyl acetate and pet-ether extracts were examined antimicrobial activity, and water and ethanol extracts were screened for antioxidant and antiproliferative activities. The pharmacological activities based on extraction was carried out the ethanol, water, pet-ether and ethyl acetate extracts, the aerial parts of Byone- hmwe. The ethanol extract had higher phenol contents (7.435 ± 0.029 mg GAE/g) and flavonoids contents (24.05 ± 0.004 mg QE/g). The antioxidant activity of ethanol extract (IC_{50} = 470.15 µg/mL) is higher than that of water extract (IC_{50} = 770.54 µg/mL). The ethyl acetate extract of Byone-hmwe had the highest antimicrobial activity (inhibition zone diameter 21-26 mm) compared to the pet-ether, water and ethanol extracts. According to the results, the ethanol extracts was found to possess mild antiproliferative activity against human cancer cell lines such as A549 lung cancer cell line (IC_{50} = 115.03 µg/mL and Hela cervical cancer cell line (IC_{50} = 129.95 µg/mL).

Acknowledgements

The authors would like to thank the Department of Higher Education (Lower Myanmar), Ministry of Education, Yangon, Myanmar, for allowing us to carry out this research programme Thanks are also extended to the Myanmar Academy of Arts and Science for giving permission to submit this paper.

References

Bone, K. (1996*). Clinical Application of Ayuredic and Chinese Herbs Monography for the Western Herbal Practitioners Warwick*, Queenland,1st Edn, Phytotherapy Press, p.152

Gharceh, M. A., H. A. Shoeb, H. M. F. Madkour, L. A. Refahy, M.A. Mohamed and A. M. Saad. (2014).” Antioxidant and Cytotoxic Activities of Flavonoidal Compounds from Gmelina arborea Roxb.” *Global Journal of Pharmacology*.8(1),87-97

Han, X., T. Shen, and H. Lou. (2007).” Dietary Polyphenols and Their Biological Significance.” *International Journal of Molecular Science*.vol.8, p.950-988

Jun, H., W. Ma, N. Li, and K. J. Wang. (2017). “Antioxidant and Anti-Inflammatory Flavonoids from the flowers of Chuju, a Medical (ultivar of Chrysanthemum Morifolim Ramat.” *J. Mex. Chem. Soc*, 61(4), 282-289

Kaveti, B., S. A. Nedumaran, T. Devi, M. S. Sikarwar, and S. Fluoria. (2011). “Phytochemical Analysis and *vitro* Antioxidant activity of *Parkia speciosa*”. *International Journal of Green Pharmacy*, 9(4), p.51-54

Marinova, G., and V. Batchvarov, (2011)." Evaluation of the Methods for Determination of the Free Radical Scavenging Activity by DPPH ". *Bulgarian Journal of Agricultural Science*, vol.17, p.11-24

Mishra, S.K., R. N. Tiwari, P.L. Shivna, and A. K. Mishra. (2015). Micropropagation and Comparative Phytochemical Antioxidant Study of *Bacopa monnieri* (L) Pennell. *Res J Pharm Biol Chem Sci*, vol6 **(**6), p. 902-912

Nattawut, C., A. Nanthida, K. Piya, S. Kanjana, K. Niwat, and J. Wannee. (2016). "*Brahmi (Bacopa monnieri*); Up-to-date of Memory Boosting Medicinal Plant: A Review". *IndianJ.Agpric*, vol. 50, p. 1-7

Saraswati, G, B, K. O. Shashi, Y. Mahato, and Y. Kazau. (1996.)." Dammarane-type Triterpenoid Saponins from *Bacopa monnieri* Phytochemistry" vol.42, p.815-835

Selvamohan, T., V. Ramadas, and S. Kishore, (.2012**).** “Antimicrobial Activity of Selected Medicinal Plants Against Some Selected Human Pathogenic Bacteria”,3 **(**5), p.3374-3381

Soares, J. R., T. C. P. Dins, A. P. Cunha, and L. M. Ameida. (1997).” Antioxidant Activity of some Extracts of Thymas zygis.”. *Free Radical Research Journal*, vol.26, p.469-478

M-Tin Wa (1972). "Phytochemical Screening Methods and Procedures". *Phytochemical Bulietin of Botanical Society of America*, Inc, vol,5(3), p.4-10

Tripathi, N., D, S. Chouhan., N. Saini, and S. Tiwari. (2012). "Assessment of Genetic Variation Among Highly Endangered Medicinal Plant *Bacopa monnieri* (L) from central India using RAPD and ISSR analysis 3 Biotech ". *Ind. J. Exp. Biol*., vol.2, p. 327-336

Win, N. N., T. Itro, S. Aimaiti, H. Imagawa, H. Ngwe, I. Abe and H. Morita. (2015). "Kaempulchraols A–H, Diterpenoids from the Rhizomes of *Kaempferia Pulchra* Collected in Myanmar". *J. Nat. Prod*, vol. 78, p. 1113–1118

MORPHOLOGICAL, STRUCTURAL AND THERMAL PROPERTIES OF CHITOSAN/GRAPHENE OXIDE BIONANOCOMPOSITES

Aung Than Htwe[1], Naing Min Tun[1], Myo Min Soe[1], Masao Gohdo[2], Yoichi Yoshida[3], Ni Ni Than[4]

Abstract

Graphene oxide (GO) has been successfully synthesized from graphite powder using the Hummer's method. In this research, an ecofriendly bionanocomposite material has been fabricated from chitosan (CS)/graphene oxide (GO) by the casting method. The synthesized GO and CSGO were characterized by using FT IR, XRD, FESEM, TG-DTA and UV-Vis spectroscopy. Finally, the size and surface charge of synthesized nanoparticles were determined using the dynamic light scattering (DLS) and zeta potential analyzer, respectively. The results obtained from those different studies revealed that chitosan and graphene oxide could mix with each other homogeneously.

Keywords: chitosan, graphene oxide, Hummer's method, bionanocomposite

Introduction

Nanocomposites are materials which consist of two components, with one of them having dimensions in nanometers (10^{-9} m) range (Bahal *et al.*, 2019). With the worsening of environmental problems, more and more attention has been attached to green chemistry. Chitosan (CS), a widely used polysaccharide, is the second largest renewable biopolymer after cellulose (Gong *et al.*, 2009). Solubility and poor mechanical properties of chitosan limit its widespread applications. Chitosan is insoluble in water but dissolves in aqueous solutions of organic acids like acetic, formic and citric acids. It can be used as a modifier due to the abundance of $-NH_2$ and -OH functional groups which renders it ideal for a variety of chemical modifications (Pati *et al.*, 2015). The amine and two hydroxyl groups on each glucosamine monomer act as adsorption sites, especially the amine groups which are strongly reactive with metal ions. The cross-linking of chitosan is made between functional groups of chitosan and different kinds of cross-linking agents, such as glutaraldehyde, and epichlorohydrin (Liu *et al.*, 2012).

Graphene oxide is a hydrophilic carbon-based film enhancing the metal adsorption potential. The high surface area allows binding to metal oxides and the epoxy and carboxyl groups allows binding to biopolymers (Naicker *et al.*, 2019). Graphene oxide (GO), unlike graphene, has functional groups, e.g., carboxylic acid, epoxide, and hydroxyl groups, attached to a carbon sheet (Kosowska *et al.*, 2019). Graphene oxide (GO) may possess qualities for heavy metal adsorption that are superior to graphene. With all the promise and potential, relatively little is known about the safety of carbon-based nanomaterials, including nanotubes, graphene, and their derivatives (Dhawan *et al.*, 2019).

In the present study, chitosan (CS), glutaraldehyde cross-linked graphene oxide (GO) and chitosan/graphene oxide (CSGO) nanocomposites were prepared, and characterized. Finally the size and surface charge of synthesized nanoparticles were measured by dynamic light scattering and zeta potential analyzer, respectively.

[1] Lecturers, Department of Chemistry, University of Yangon, Myanmar
[2] Assistant Professor, The Institute of Scientific and Industrial Research, Osaka University, Japan
[3] Professor, The Institute of Scientific and Industrial Research, Osaka University, Japan
[4] Professor and Head, Department of Chemistry, University of Yangon, Myanmar

Materials and Methods

Chitosan, with a deacetylation degree of about 90 %, was purchased from Boao Biological Tech. Co. Ltd in China. Graphite powder, analytical grade, was purchased from BDH. The other reagents, such as CH_3COOH, NaOH, 98 % H_2SO_4, H_2O_2, HCl, $KMnO_4$, glutaraldehyde and isopropyl alcohol, were supplied by Department of Chemistry, University of Yangon, Myanmar. All of the chemicals used in this study were of analytical grade. Solutions were diluted by using deionized water and distilled water.

Preparation of Graphene Oxide (GO)Powder

The graphite powder was used to prepare GO according to the well-known Hummer's method with some modification. In brief, 3.0 g of graphite powder was placed in a beaker and then 98 % of sulphuric acid and 68 % of nitric acid were added in a 90:30 v/v ratio. During the reaction, the solution was in exothermic condition, so it must be stirred in the ice bath at 10 °C to maintain the temperature while the 9 g of $KMnO_4$ was slowly added and stirred for 15 min after the temperature was controlled in the ice bath to 9 ^oC. 150 mL of distilled water was gradually added into the above solution under stirring with 300 rpm at 90 °C for 30 min to achieve neutral conditions. Then, 30 mL of hydrogen peroxide (H_2O_2 30 %) was added to the solution, which was then stirred at 300 rpm for 1h. The resultant solution was centrifuged and washed with 600 mL hot distilled water to form a brown paste. 100 mL of 10 % hydrochloric acid was added and stirred for 30 min. Then, the precipitate was washed with 200 mL of distilled water five times at 7000 rpm for 30 min to get an acid-free mixture. The yellow-brown GO mixture was obtained. The obtained GO mixture was sonicated for 2 h and then centrifuged at 3000 rpm for 30 min. The GO dispersed mixture was purified using multiple washings with distilled water and ethanol until it reached neutrality (pH 7). After multiple washings, the solid GO was dried in oven at 80 °C to obtain dried GO.

Preparation of Chitosan/Graphene Oxide Bionanocomposite

A 1 g of chitosan powder was dissolved in 100 mL of 1 % (v/v) acetic acid solution and was stirred continuously at room temperature to form 1 % chitosan (CS) solution. The 10 g of graphene oxide (GO) powder was dispersed into 100 mL of distilled water to form 10 % GO solution. The CSGO solutions were prepared with three different ratios of CS:GO, (95:5, 90:10, 85:15 v/v) by stirring the mixed polymer composite solution at 60 °C for 2 h. The mixture was sonicated at room temperature for 2 h to ensure a homogeneous dispersion of CSGO solution, after which 0.2 mL glutaraldehyde (50 % in H_2O) was added dropwise with constant stirring. A black gel of CSGO solution was obtained. The mixed solution was cast on a glass plate and then dried in an oven at a temperature of 60 °C for 8 h. The dried CSGO films were removed from the glass plate, cut and powdered by using mortar and pestle. A series of chitosan/graphene oxide bionanocomposites coded as CSGO5 (CS/GO 95:5 %), CSGO10 (CS/GO 90:10 %), and CSGO15 (CS/GO 85:15 %) were prepared, respectively.

Characterization

The surface morphology of bionanocomposite materials was studied using FESEM (Hitachi model SU 8000). FESEM images of samples were collected under an accelerating voltage of 5 kV. Fourier transform infrared spectrophotometer (Shimadzu, Japan) was used. The resolution was 4 cm^{-1} with 64- time scanning, and the scanning was performed in the range of 4000 –500 cm^{-1}. The X-ray diffraction (XRD) measurements of CS, GO and CSGO bionanocomposites were recorded using Shimadzu 8000 X-ray diffractometer (Shimadzu, Japan) with a detector operating under a voltage of 40.0 kV and a current of 30.0 mA using Cu Kα radiation

(λ = 0.15418 nm). The recorded range of 2θ was 5–40 ◦, and the scanning speed was 6 ◦/min. The particle size distribution (PSD) of aggregates was measured using an optical microscope (Shimadzu, STZ-171 with Moticam U2.0MP, Japan), which captured the images. Dynamic light scattering (DLS) was used for the measurement of average particle size, and polydispersity index (PDI) on a high-performance particle Zetasizer Nano ZS (Model MALI034324, Malvern Instruments, UK).

Results and Discussion

Preparation and Characterization of CSGO Bionanocomposites

The CSGO bionanocomposites were successfully prepared by in situ mineralization, wherein the CSGO hydrogel was first prepared. CS is soluble in water at acidic pH, at which amine functional groups of the molecule undergo protonation.

FT IR spectroscopy

FT IR experiments were carried out to investigate the interaction between GO and CS. As shown in Figure 1, in the spectrum of GO, the peaks at 1039, 1321, and 1620 cm^{-1} correspond to C–O–C stretching vibrations, C–OH stretching, and the C–C stretching mode of the sp^2 carbon skeletal network, respectively, while peaks located at 1716 and 3208 cm^{-1} correspond to C–O stretching vibrations of the–COOH groups and O–H stretching vibration, respectively. These functional groups make GO highly hydrophilic and render it dispersible (Maleki and Paydar, 2016). In the spectrum of CS, there are two characteristic absorption bands centered at 1618 and 1581cm^{-1}, which correspond to the C=O stretching vibration of -NHCO- and the N-H bending of $-NH_2$, respectively. The GOCS spectra show peaks at 3225, 3228, 3240 cm^{-1} (O-H distortion) and 1618 cm^{-1}, as well as a superposition band assigned to the amine groups of CS and carboxyl groups of GO, 1405 cm^{-1} and 1149 cm^{-1}, indicating C-O bonds. Additionally, the characteristic signal of secondary amides (N–H bending) shifts from 1538 to 1542 cm^{-1} (between the CS and GO-CS signals) (Figueroa *et al.*, 2020). Compared with pure CS and GO, both peaks at 1581 cm^{-1} related to -NH bending vibration and at 1718 cm^{-1} belonging to C=O stretching of the carboxyl group disappear in the spectra of CSGO bionanocomposites. Moreover, the band corresponding to the C=O characteristic stretching band of the amide group shifts to a lower wavenumber. These could be ascribed to the synergistic effect of hydrogen bonding between CS and the oxygenated groups in GO and electrostatic interaction between polycationic CS and the negative charge on the surface of GO (Han *et al.*, 2011).

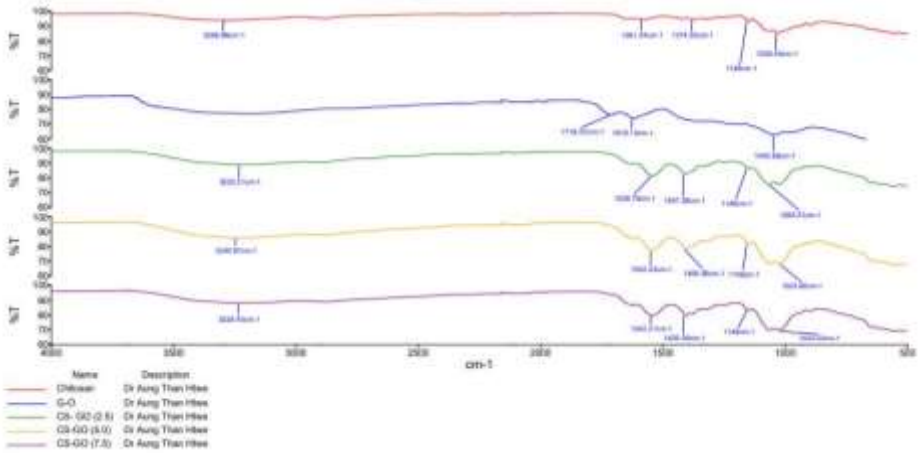

Figure 1 FT IR spectra of GO, CS and CSGO bionanocomposites

X-ray diffraction analysis

Figure 2 shows the XRD patterns of pure CS, GO and CSGO bionanocomposites. As seen in figure, the diffractive region of GO is observed at 2θ value of 11.28°. Pure chitosan showed a characteristic peak at around 2θ values 9.68° and sharp peak at 20.10°. The main diffractive region of all CSGO are found weak broad peak at 2θ value of 11.85° and weak broad peak at 21.40°. When incorporation of GO into CS chemical structure of the CS films changes due to overlap of biopolymer diffraction, it indicates that there was mainly physical interaction but scarcely chemical reaction between CS and GO (Han *et al.*, 2011).

It is noticed that incorporation of CSGO only slightly increases the intensity of the characteristic peaks of CS. The CSGO bionanocomposite exhibited a combination of amorphous and crystalline peaks (Kumar and Koh, 2014). In this particular case, the electrostatic interaction and hydrogen bonding may contribute to a relatively ordered arrangement of the attached CS chains along the rigid template offered by GO (Yang *et al.*, 2010).

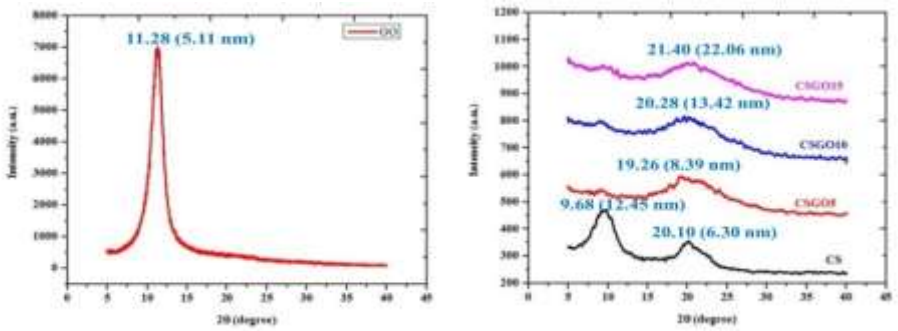

Figure 2 XRD patterns of pure GO, CS and CSGO bionanocomposites

FESEM-EDX Analysis

The morphology of the prepared CSGO5, CSGO10 and CSGO15 were investigated by field-emission-scanning electron micrographs (FESEM) technique. The surfaces of the CSGO5, CSGO10 and CSGO15 display a generally smooth morphology, as shown in Figures 3a–d, indicating that the chitosan films blending with graphene oxide are miscible. In addition, the surface of the composite films showed high homogeneity. The blending graphene oxide is wrapped in or covered by a chitosan layer. There is barely an isolated fully exfoliated graphene oxide sheet, which indicates a good adhesion between the chitosan and the graphene oxide (Figueroa *et al.*, 2020; Yang *et al.*, 2010).

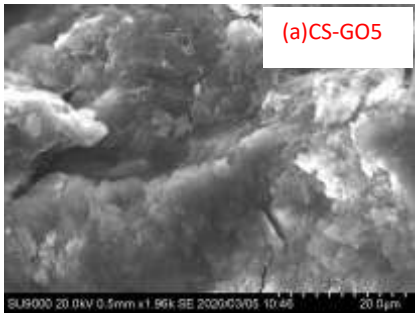

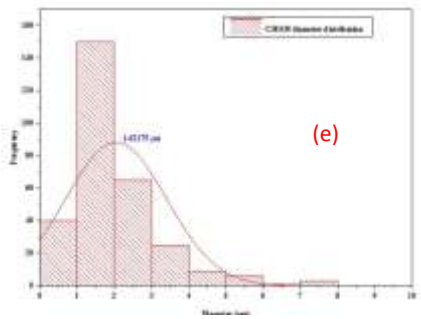

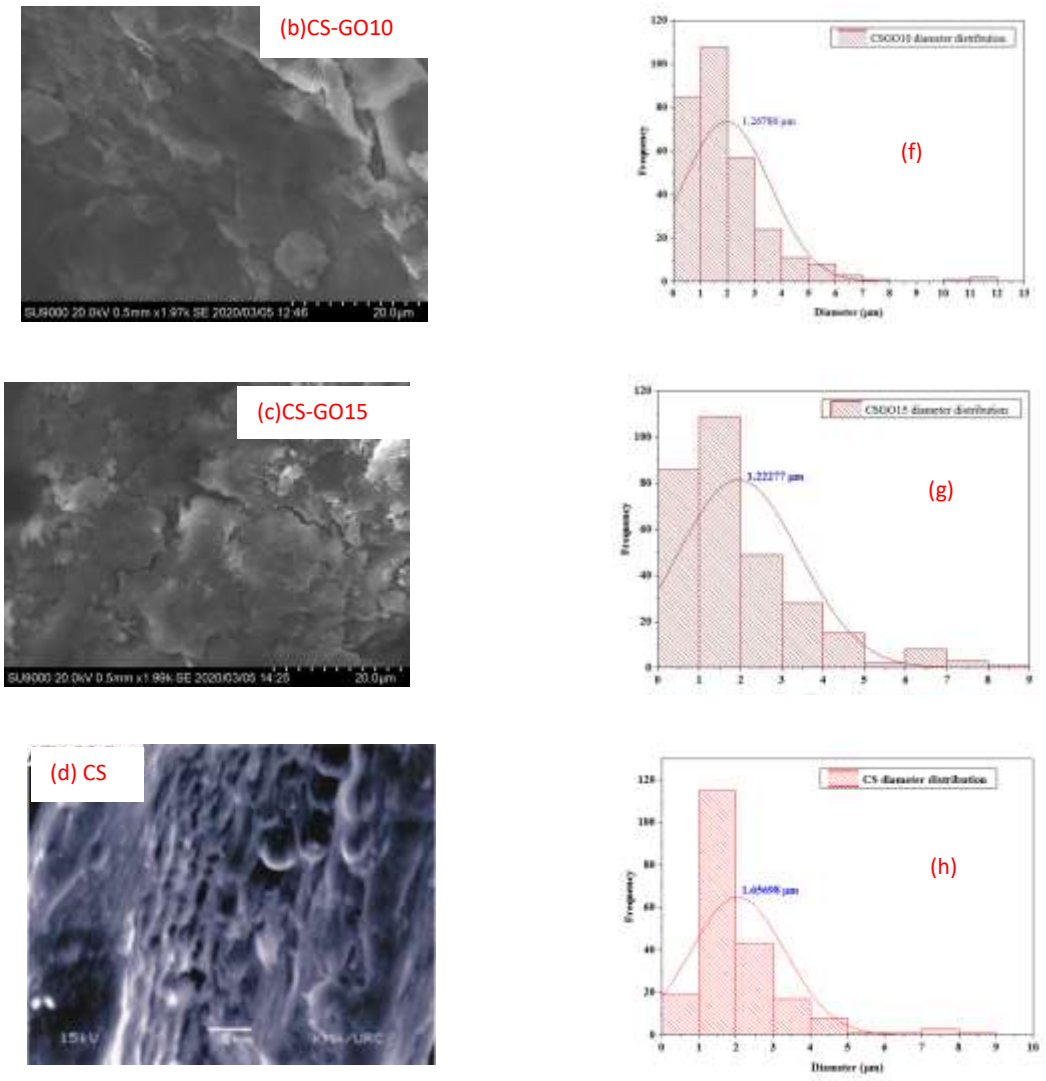

Figure 3 FESEM images of CSGO bionanocomposites (a, b, c, d) and the corresponding statistical histograms (e, f, g, h)

Size diameter distributions (Figures 3 e-h) were evaluated by measuring at least 300 particles from FESEM micrographs. The results are obtained that the average diameters of the obtained bionanocomposites are 1.65 μm for CS, 1.29 μm for CSGO5, 1.26 μm for CSGO10 and 1.22 μm for CSGO15, respectively. The resulting nanocomposite have a significant size decrease (from 1.29 μm for CSGO5 to 1.22 μm for CSGO15), as can be seen from the size diameter distribution histograms. It indicates that the produced bionanocomposite possesses narrow size distribution.

To check the chemical composition of the material, an energy dispersive X-ray (EDX) spectroscopy analysis was also presented in Figure 4 and Table 1. The EDX spectra of CSGO bionanocomposite samples which confirm the presence of C, N, and O ions in the matrix. The EDX results are also consistent with the weight percentage of C, N, and O. From quantitative analysis it is evident that bionanocomposite samples contains approximately 62.84 % C, 1.24 % N and 35.92 % O by weight in CSGO5, 57.32 % C, 4.14 % N and 38.54 % O by weight in CSGO10, and 58.62 % C, 5.30 % N and 36.07 % O by weight in CSGO15, respectively. These results were found to be consistent with the XRD data.

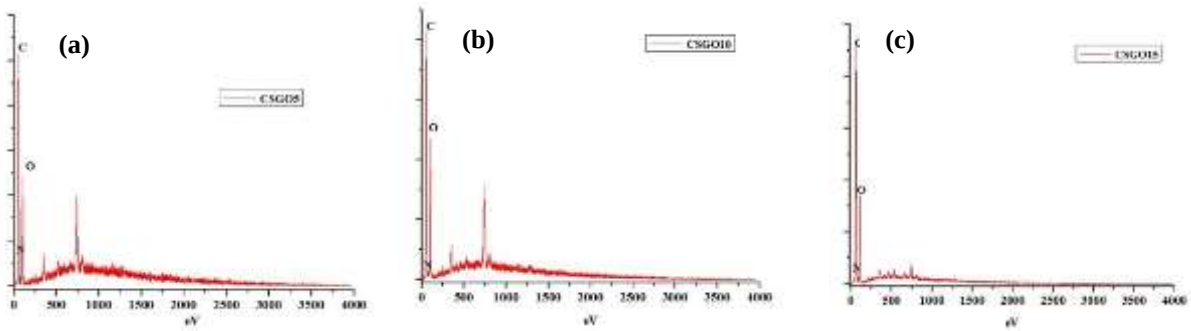

Figure 4 EDX spectra of (a) CSGO5, (b) CSGO10, and (c) CSGO15

Table 1 Compositional Analysis of the CSGO by EDX

Sample	Atomic % in bionanocomposites		
	C	N	O
CSGO5	62.84	1.24	35.92
CSGO10	57.32	4.14	38.54
CSGO15	58.62	5.30	36.07

Thermogravimetric analysis

The thermal stability of the pure GO and three different ratios of CS/GO composite powder (CSGO5, CSGO10 and CSGO15) was studied by thermogravimetric analysis as shown in Figure 5(a) and (b). As seen in Figure 5(a) and (b), the thermal stability of GO was observed because of the weight loss of 75.28 % within the temperature range of 38 °C to 218 °C. This attributes to the thermal decomposition of unstable groups containing oxygen and evolution of CO_2 gas. The thermograms of all CSGO composites are shown in Figure 5(a) and (b), with weight loss in three stages. The first stage ranges in temperature from 37 °C to 155 °C, with weight loss of 22.15 % in CSGO5, 18.85 % in CSGO10 and 19.75 % in CSGO15. There is evaporation of water. The second stage, with temperature ranging from 155 °C to 426 °C, was observed to lose 38.77 % in CSGO5, 40.06 % in CSGO10, and 39.42 % in CSGO15 corresponding to the exothermic peaks at 313 °C, 307 °C, and 282 °C, respectively. This is due to a complex process including the degradation of the saccharide ring. In the third stage, the temperature ranges from 426 °C to 600 °C, and weight loss of 33.23 % in CSGO5, 32.99 % in CSGO10, and 36.61 % in CSGO15 corresponds to the broad exothermic peaks at 527 °C, 543 °C, and 502 °C. In this stage, weight loss is due to complete degradation of polymer. The results show that the maximum weight loss percent of GO is higher than that of CSGO bionanocomposites.

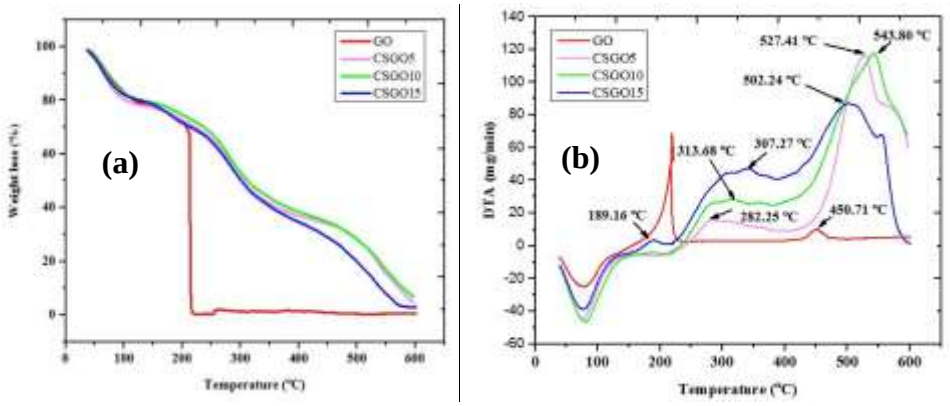

Figure 5 (a)TG curves (b) DTA curves for GO and CSGO bionanocomposites

UV-vis absorption spectra

The UV-Vis spectrum (Figure 6) of pure GO shows two absorption peaks one at 229 nm and another at 335 nm (Wong *et al.*, 2015; Xu *et al.*, 2013). The CS peaks shows at 239 nm and 246 nm. The CSGO bionanocomposite shows 226 nm, 262 nm and 363 nm for CSGO5, 225 nm, 311 nm and 349 nm for CSGO10, and 227 nm and 325 nm for CSGO15. It was found that the intensity of CSGO bionanocomposite is lower than that of CS and GO. After attachment with CS, the peaks of GO have shown a bathochromic shift. This shift in absorption maxima might be attributed to the formation of particles in the nano scale. This also indicates the strong covalent interaction between GO and CS where the active ester group of GO might have reacted with the amine groups on CS, forming an amide bond between GO and CS (Suneetha, 2018).

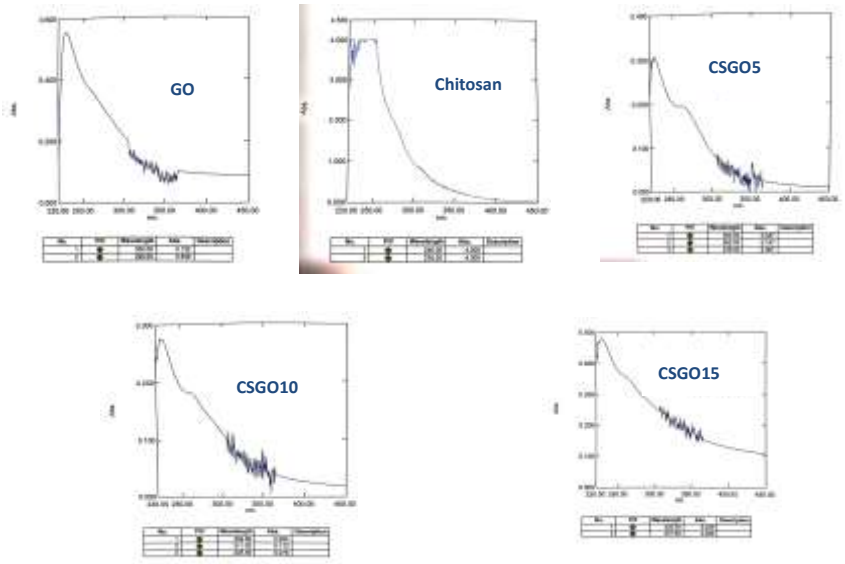

Figure 6 UV-vis spectra of GO, CS and CSGO bionanocomposites

Optical microscopy

Size data were obtained by image processing and analysis obtained from samples studied by optical microscopy. Figure 7 shows the optical micrographs captured by the camera for GO and CSGO samples. It was found that the samples of CSGO showed the lowest particle sizes prior to particle size measurement by optical microscopy (52.29 μm for CSGO5, 31.29 μm for CSGO10 and 28.39 μm for CSGO15, respectively). Among them, CSGO15 had a higher quantity of aggregates with fewer fine particles around the large aggregates. In this case, pure CSGO bionanocomposites have a higher quantity of aggregates with fewer fine particles around the large aggregates. Therefore, the image capture must be very fast. Therefore, the results obtained from image analysis captured by optical microscopy were non-invasive. These results can thereby determine more realistic particle sizes of the aggregates (Quilaqueo *et al.*, 2019).

Figure 7 Optical micrographs of pure GO and CSGO bionanocomposites

Particle Size Study of GO and CSGO by Dynamic Light Scattering

The DLS experiment was conducted at a constant temperature of 25 °C. Figure 8 shows the size distribution graphs for the GO and CSGO bionanocomposites obtained by DLS method according to size distribution data analysis. The DLS results showed the presence of CSGO nanoparticles with a size of approximately 594.6 nm for CSGO5, 686.5 nm for CSGO10, 1383.0 nm for CSGO15 and the presence of larger particles, which corresponded to the GO carrier (498.5 nm). It was found that the increasing the GO content of 5 %, 10 % and 15 %, the lower the average diameter. Therefore, it can be observed that the average diameter of all of the prepared CSGO bionanocomposite are higher than that of pure GO. These reveal that ranges of distribution of the resultant CSGO bionanocomposites were wider than that of GO. This also confirms the binding of CS and GO bionanocomposites that leads to larger-size (Zeinali *et al.*, 2016).

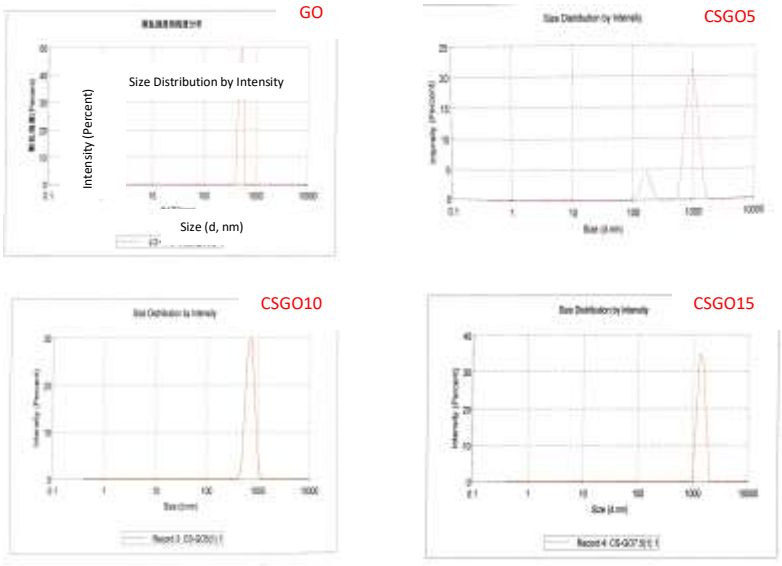

Figure 8 Particle size distribution of GO and CSGO bionanocomposites

Zeta Potential Measurement

Although ζ-potential plays a key role in colloidal stability, it does not show the true particulate state in various environments. To estimate the aggregation behaviour of GO and CSGO samples under aging conditions, visual evidence of settling was used. All the GO samples show excellent colloidal dispersity and stability in deionized water after 24 h at 37 ºC. At higher pH, the oxygenated functional groups such as hydroxyl and carboxyl of GO and CSGO could be easily deprotonated, leading to a favourable electrostatic attraction with the cationic CS. In order to further support our hypothesis, zeta potential measurements were conducted for GO and CSGO nanocomposites at neutral solutions, and the results are presented in Figure 9.

It was found that the zeta potential value of pure GO is about – 25 mV because of $–COO^-$ groups on the GO (Karimzadeh *et al.*, 2019). All the CSGO bionanocomposites showed + 37.7 mV for CSGO5, + 34.6 mV for CSGO10 and + 39.6 mV for CSGO15, respectively (Table 2). So the positive zeta potentials for CSGO were consistent with the presence of protonated amine groups of CS. It is well known that higher absolute value of zeta potential means higher stable state of colloidal systems, and potential values higher than +30 mV or lower than -30 mV permit a basically stable suspension (Sun *et al.*, 2016).

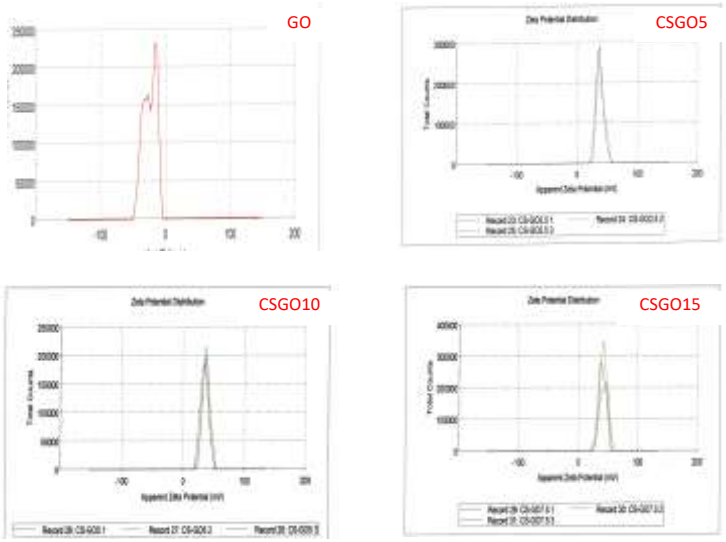

Figure 9 Zeta potential measurement of GO and CSGO bionanocomposites

Table 2 The Zeta Potential and Calculated Average Diameter of the GO and CSGO

Sample	Zeta potential (mV)	Average diameter calculated by laser particle size (nm)
GO	- 25.0	498.5
CSGO5	+ 37.7	594.6
CSGO10	+ 34.6	686.5
CSGO15	+ 39.6	1383.0

Conclusion

The bionanocomposites of chitosan/graphene oxide GO were prepared successfully by solvent casting method. It is observed that graphene oxide is dispersed on a molecular scale in the chitosan matrix and some interactions occur between chitosan and graphene. In CSGO bionanocomposites FT IR showed the existence of oxygen-containing functional groups of GO, amino groups of CS, and amide I groups forming from reaction between GO and CS. The XRD patterns implied amorphous state of CSGO. FESEM images confirmed the linking and grafting of CSGO. TG-DTA measurements indicated homogeneous dispersion of GO within the CS polymer matrix. The synthesized bionanocomposite was found to have greater thermal stability. Presence of both the components of the bionanocomposite was confirmed by UV-Vis and FT IR spectral studies. These studies also indicate the strong interaction between GO and CS in the bionanocomposites. The nanoparticles size and surface charge were measured by dynamic light scattering and zeta potential analyzer. DLS measurement was formed that the increasing the GO content, the larger will be the average diameter, All the results demonstrated that graphene oxide was well-dispersed in the chitosan matrix, and there were the strong H-bondings between hydroxy groups of the chitosan and hydroxy groups of the graphene oxide. The main contribution of the present research is that the synthesis of chitosan- graphene oxide bionanocomposite may be used for the control of wastewater pollution.

Acknowledgements

The authors would like to thank the Department of Higher Education, Ministry of Education and University of Yangon for some support to do this research. This research was supported by the KAPLAT program (JSPS Core-to-Core) Japan and Osaka University for intensive 2020. We would like to acknowledge KAPLAT Program Coordinator Professor Dr Hideaki OHGAKI, Institute of Advanced Energy, Kyoto University. Finally, we are also thankful to Nanotechnology Open Facility, Osaka University, for providing zetasizer, XRD, and FESEM facilities.

References

Bahal, M., N. Kaur, N. Sharotri, and D. Sud. (2019). "Investigations on Amphoteric Chitosan/TiO_2 Bionanocomposites for Application in Visible Light Induced Photocatalytic Degradation". *Advances in Polymer Technology*, vol. 2019, pp. 1-9

Dhawan, A. K., J. W. Seyler, and B. C. Bohrer. (2019). "Preparation of a Core-Double Shell Chitosan Graphene Oxide Composite and Investigation of Pb(II) Absorption". *Heliyon*, vol. 5(e01177), pp. 1-14

Figueroa, T., C. Aguayo, and K. Fernandez. (2020). "Design and Characterization of Chitosan-Graphene Oxide Nanocomposites for the Delivery of Proanthocyanidins". *International Journal of Nanomedicine*, vol. 15, pp. 1229-1238

Gong, Y., Y. Yu, H. Kang, X. Chem, H. Liu, Y. Zhang, Y. Sun, and H. Song. (2009). "Synthesis and Characterization of Graphene Oxide/Chitosan Composite Aerogels with High Mechanical Performance". *Polymers*, vol. 11 (777), pp. 1-12

Han, D., L. Yan, W. Chen, and W. Li. (2011). "Preparation of Chitosan/Graphene Oxide Composite Film with Enhanced Mechanical Strength in the Wet State". *Carbohydrate Polymers*, vol. 83, pp. 653-658

Karimzadeh, Z., S. Javanbakht, and H. Namazi. (2019). "Carboxymethyl Cellulose/MOF-5/Graphene Oxide Bio Nano Composite as Antibacterial Drug Nanocarrier Agent". *BioImpacts*, vol. 9 (1), pp. 5-13

Kosowska, K., P. D. Pyzik, M. K. Borkowicz, and J. Chlopek. (2019). "Synthesis and Characterization of Chitosan/Reduced Graphene Oxide Hybride Composites". *Materials*, vol. 12 (2077), pp. 1-13

Kumar, S., and J. Koh. (2014). "Physicochemical and Optical Properties of Chitosan Based Graphene Oxide Bionanocomposite". *International Journal of Biological Macromolecules*, vol. 70, pp. 559-564

Liu, L., C. Li, C. Bao, Q. Jia, P. Xiao, X. Liu, and Q. Zhang. (2012). "Preparation and Characterization of Chitosan/Graphene Oxide Composites for the Adsorption of Au(III) and Pd(II)". *Talanta*, vol. 93, pp. 350-357

Maleki, A., and R. Paydar. (2016). "Bionanostructure- Catalyzed One-Pot Three-Component Synthesis of 3,4-Dihydropyrimidim-2(^{1}H)-One Derivatives Under Solvent-Free Conditions". *React. Funct. Polym.*, vol. 109, pp. 120-124

Naicker, C., N. Nombona, and W. E. Zyl. (2020). "Fabrication of Novel Magnetic Chitosan/Graphene Oxide/Metal Oxide Nanocomposite Beads for Cr(VI) Adsorption". *Chemical Papers*, vol. 74, pp. 529-542

Pati, M. K., P. Pattojoshi, and G. S. Roy. (2015). "Fabrication and Characterization of Graphene Based Nanocomposite for Electrical Properties". *Advances in Materials Physics and Chemistry*, vol. 5, pp. 22-30

Quilaqueo, M., M. G. Krumm, R. R. Figueroa, E. Troncoso, and H. Estay. (2019). "Determination of Size Distribution of Precipitation Aggregates Using Non-Invasive Microscopy and Semiautomated Image Processing and Analysis". *Minerals*, vol. 9 (724), pp. 1-14

Sun, D., S. Kang, C. Liu, Q. Lu, L. Cui, L., and B. Hu. (2016). "Effect of Zeta Potential and Particle Size on the Stability of SiO_2 Nanospheres as Carrier for Ultrasound Imaging Contrast Agents**".** *Int. J. Electrochem. Sci.*, vol. 11, pp. 8520 – 8529

Suneetha, R. B. (2018). "Spectral, Thermal and Morphological Characterization of Biodegradable Graphene Oxide-Chitosan Nanocomposites". *J. Nanosci. Tech.*, vol. 4 (2), pp. 342-344

Wong, C. P. P., C. W. Lai, K. M. Lee, and S. B. A. Hamid. (2015). "Advanced Chemical Reduction of Reduced Graphene Oxide and Its Photocatalytic Activity in Degrading Reactive Black 5". *Sci. Tech. Adv. Mater.*, vol. 8, pp. 7118-7128

Xu, S., L. Yong, and P. Wu. (2013). "One-pot, Green, Rapid Synthesis of Flowerlike Gold Nanoparticles/ Reduced Graphene Oxide Composite with Regenerated Silk Fibroin As Efficient Oxygen Reduction Electrocatalysts". *ACS Applied Materials & Interfaces*, vol. 5, pp. 654-662

Yang, X., Y., L. Li, S. Shang, and X. Tao. (2010). "Well-Dispersed Chitosan/Graphene Oxide Nanocomposites". *ACS Applied Materials & Interfaces*, vol. 2 (6), pp. 1707-1713

Zeinali, S., S. Nasirimoghaddam, and S. Sabbaghi. (2016). "Investigation of the Synthesis Chitosan Coated Iron Oxide Nanoparticles under Different Experimental Conditions". *Int. J. Nanosci. Nanotechnol.*, vol. 12 (3), pp. 183-190

A STUDY OF SOME BIOACTIVITIES AND ISOLATION OF PURE ORGANIC COMPOUNDS FROM THE BARK OF *DOCYNIA INDICA* (WALL.) DECNE (PIN-SEIN)

Tin Myo Khaing[1], Ja Mai[2], Tint Tint Win [3], Cho Cho Win[4]

Abstract

In the research work, the bark of *Docynia indica* (Wall.) Decne (Pin-Sein) was collected from Pang Wa Village, Loi Mwe Township, Shan State. Phytochemical constituents present in the bark of Pin-Sein were investigated according to the general methods. Two kinds of nutritional values (moisture and ash) of Pin-Sein bark were determined by oven dry method and AOAC method. In addition, the elemental contents in this sample were determined by EDXRF. The antimicrobial activities of the various crude extracts were tested by agar well diffusion method on six selected microorganisms (*Bacillus subtilis, Staphylococcus aureus, Salmonella typhi, Bacillus pumilus, Candida albicans* and *Escherichia coli*). Moreover, antioxidant activity of crude extract of Pin-Sein bark was measured by DPPH free radical scavenging assay method. The pure organic compounds, TMK-1 and TMK-2 were isolated from the bark of Pin-Sein by thin layer and column chromatographic techniques. Finally, these isolated compounds were identified by phytochemical tests and their respective melting point. The functional groups of pure organic compounds were identified by FT IR spectral data.

Keywords: *Docynia indica* (Wall.) Decne, phytochemical constituents, antimicrobial activity, antioxidant activity, DPPH assay

Introduction

Pin-Sein is one of the well-known Myanmar indigenous medicinal plants. Its botanical name is *Docynia indica* (Wall.) Decne. It belongs to the genus *Docynia* and species *indica* in the family rosaceae. *D. indica* is a plant that is abundantly found in the Shan State in Myanmar. *D. indica* is an evergreen tree, which distributes widely in southwest China and Southeast Asia. The *D. indica* leaves were widely used as tea or a drug for the healing of fever, cancer, empyrosis and rheumatic disease by the local ethnic minorities in southwest China, with lipid-lowering and weight-loss effects (Deng *et al*., 2014). The fruits were consumed by the locals. Previous studies have demonstrated that the content of polyphenols and flavonoids in *D. indica* was much higher, which exhibited significant bioactivities, including antioxidant, antitumor, anti-obesity, and anti-bacterial activities (Loan *et al*., 2011). Dietary supplementation of natural substances with antioxidant activity was now regarded as a safe and effective strategy for the prevention and treatment of obesity, which could be natural active substances instead of medicine (Hogan *et al*., 2010).

Polyphenols are the biggest group of phytochemicals and many of them have been found in plant-based foods. Polyphenol-rich diets have been linked to many health benefits. Polyphenols are strong antioxidants that complement and add to the functions of antioxidant vitamins and enzymes as a defense against oxidative stress caused by excess reactive oxygen species (ROS). Polyphenols have also beneficial for health as anti-carcinogenic, anti-ulcer, anti-atherogenic, anti-thrombotic, anti-inflammatory, immune modulating, antimicrobial and for its analgesic effect (Loganayaki *et al*., 2010). Therefore, the bark of Pin-Sein was selected to investigate some

[1] Dr, Associate professor, Department of Chemistry, Kyaing Tong University
[2] MSc Candidate, Department of Chemistry, Kyaing Tong University
[3] Dr, Lecturer, Department of Chemistry, Kyaing Tong University
[4] Lecturer, Department of Chemistry, Kyaing Tong University

bioactivities and isolation of some organic compounds in this research paper. Plant, flower, fruit and bark of *D. indica* are shown in Figure 1.

Figure 1 Plant, flower, fruit and bark of *Docynia indica* (Wall.) Decne

Materials and Methods

Sample Collection and Preparation

The bark of Pin-Sein was collected from Pang Wa Village, Loi Mwe Township, Shan State, in January, 2020. The species was identified by Department of Botany, Kyaing Tong University.

The collected sample was cut into small pieces and allowed to be dried in air for 10-14 days. The air-dried samples were stored in well-stoppered bottles and used throughout the experiment.

Preliminary Phytochemical Screening of Bark of Pin-Sein

Preliminary phytochemicals tests were carried out according to the general methods (Harborne, 1984).

Determination of Moisture Content

The dry powder sample (2 g) was placed in a pre-weighed crucible. Then it was heated in an oven at 103 °C- 105 °C for 2 h. Just after being removal from the oven, the sample was allowed to cool at room temperature in desiccator for 1 h. The crucible and the dry sample were weighed again. This process of heating, cooling and weighing was repeated until a constant weight was obtained.

Determination of Ash Content

Clean porcelain crucible with a lid was heated in a Muffle furnace at 550 °C for 1 h. After cooling in desiccator for 30 min, the crucible was weighed. The dry powder sample (2 g) was weighed into pre-weighed crucible and heated at a low temperature to prevent sputtering. Then the crucible with lid were transferred to a Muffle furnace and ignited at 550 °C for about 6 h, until the residue was uniformly grayish to white. During heating, the lid was removed. The lid was put on after complete heating to prevent loss of ash. Next, the temperature of furnace was maintained at 105 °C for 20 min. It was cooled in desiccator and then weighed again. The process of heating, cooling and weighing was repeated until a constant weight was achieved.

Determination of Elemental Contents of the Sample

The air dried sample was ground to a fine powder. It was used to detect the elemental contents by EDXRF (Energy Dispersive X-ray Fluorescence) Spectrometry.

Preparation of Crude Extracts from Pin-Sein Bark

The air-dried sample (25 g) was added into separate conical flasks containing 100 mL of solvents (Pet-ether, EtOAc, EtOH and H_2O) and stand for 48 h with occasional stirring. The content of flask was filtered through sterile Whatman No. 1 filter paper and evaporated to dryness. These various solvent crude extracts of selected sample were used for the investigation of antimicrobial activity.

Screening of Antimicrobial Activity of Crude Extracts from Pin-Sein Bark

The nutrient agar medium was prepared according to the method described by Cruickshank, 1975. Nutrient agar was boiled and then 25 mL of this agar medium was poured into the test tube and plugged with cotton wool and autoclaved at 121 ºC for 15 min. Then, the tubes were cooled down to 30-35 ºC and poured into sterilized petri-dish and 0.02 mL of spore suspension was also added into the dishes. The agar was allowed to set for 2 h after which 10 mm plate agar disc was made with the help of sterilized cork borer. After that, about 0.1 mL of sample was introduced into the agar-disc and incubated at 37 ºC for 24 h. The inhibition zone (clear zone) that appeared around the agar-disc indicated the presence of antimicrobial activity.

Antioxidant Activity of Watery and Ethanol Extracts from Bark of Pin-Sein

The control solution was prepared by mixing of 3 mL of 0.002 % DPPH solution and 3 mL of 95 % ethanol using vortex mixer. Blank solution was prepared by mixing 3 mL each of crude extracts solution (25, 50, 100, 200, 400 μg/mL) and 3 mL of ethanol. Test sample solution was prepared by mixing 3 mL each of crude extracts solution (25, 50, 100, 200, 400 μg/mL) and 3 mL of 0.002 % DPPH solution. All these solutions were allowed to stand at room temperature for 30 min. The absorbance of these solutions was measured at 517 nm by UV-visible spectrophotometer and the percentage of the radical scavenging activity (% RSA) was calculated.

Isolation of Pure Organic Compounds from Pin-Sein Bark

The sample (300 g) was percolated with ethanol (1200 mL) for about one month at room temperature. During percolation, the whole mixture was frequently shaken to achieve maximum extraction of sample. After percolation time, the solution was filtered. The filtrate was evaporated to dryness at room temperature and the ethanol extract was obtained. The ethanol extract was re-extracted with ethyl acetate. The solution was filtered and then the filtrate was evaporated to dryness at room temperature. Ethyl acetate crude extract (6.02 g) was obtained. Ethyl acetate crude extract (2 g) was separated by column chromatography applying silica gel (70-230 mesh) as an adsorbent with n-hexane and ethyl acetate solvent system with various ratios from non-polar to polar. Total fractions were collected in clean containers. Each fraction was checked by TLC with suitable solvent system. The fractions with the same R_f value were combined to give total combined fractions and then evaporated at room temperature. The combined fractions were checked on TLC plate under UV detector. The R_f values of pure organic compounds (TMK-1 and TMK-2) were measured. The amounts of pure organic compounds were weighed and then the yield percent was calculated based on the ethyl acetate crude extract.

Identification of Isolated Pure Organic Compounds by TLC

Thin layer chromatography was conducted on 0.25 mm pre-coated silica gel (60 F_{254} Merck). It was cut into small plates (1×5 cm in size). The isolated pure organic compounds were checked by TLC with specified solvent systems (Stahl, 1965).

Polyphenol Test for Pure Organic Compound

A small amount of pure organic compound was tested with 1 % ferric chloride solution and then 1 % potassium ferric cyanide solution was added into the mixture. Formation of the colour of the filtrate was examined to decide the presence or absence of phenolic compounds (Marini-Bettolo *et al*., 1981).

Flavonoid Test for Pure Organic Compound

A small amount of pure organic compound was tested with three drops of concentrated hydrochloric acid and small pieces of magnesium ribbon. Observations were carried out to see whether the colour of the solution turned or not within 10 min.

Determination of Melting Point for Pure Organic Compounds

A few crystals form of pure organic compounds TMK-1 and TMK-2 were inserted into the capillary tubes and the melting points were determined by melting point apparatus.

Identification of Pure Organic Compounds by FT IR Spectroscopy

The FT IR spectral data of isolated pure organic compounds (TMK-1 and TMK-2) were recorded by Shimadzu Fourier Transform Infrared Spectrometer, at the Department of Chemistry, Taunggyi University. The resultant IR spectra were applied for the identification of functional groups for` the pure organic compounds.

Results and Discussion

Phytochemicals Present in the Bark of Pin-Sein

The respective colour indicates the presence or absence of phytochemical constituents in the Pin-Sein bark. It contains phytochemical constituents such as glycosides, reducing sugars, saponins, tannins, α-amino acids, polyphenols, flavonoids, carbohydrates and steroids. Alkaloids were not detected.

Moisture Content of Pin-Sein Bark

The moisture content of Pin-Sein bark was found to be 6.2 %. If the moisture content is greater than 10 %, the chance for growth of microorganism and the degradation of chemical compositions of nutrients will be higher.

Ash Content of Pin-Sein Bark

The ash content of Pin-Sein bark was found to be 0.54 %. So, Pin-Sein bark is a good source of mineral elements.

Elemental Contents in the Bark of Pin-Sein by EDXRF

EDXRF spectrum of the sample is shown in Figure 2. The relative elemental compositions are presented in Table 1. It was found that calcium was the highest amount (1.432 %) and potassium (0.327 %), the second highest amount the bark of Pin-Sein. According to the data, the inorganic minerals such as calcium, potassium, sulphur, barium, iron, strontium, copper and rubidium were present in this sample.

Table 1 Elemental Contents in the Bark of Pin-Sein

Symbol	Elements	Content (%)
Ca	Calcium	1.432
K	Potassium	0.327
S	Sulphur	0.042
Ba	Barium	0.009
Fe	Iron	0.005
Sr	Strontium	0.004
Cu	Copper	0.002
Rb	Rubidium	0.001

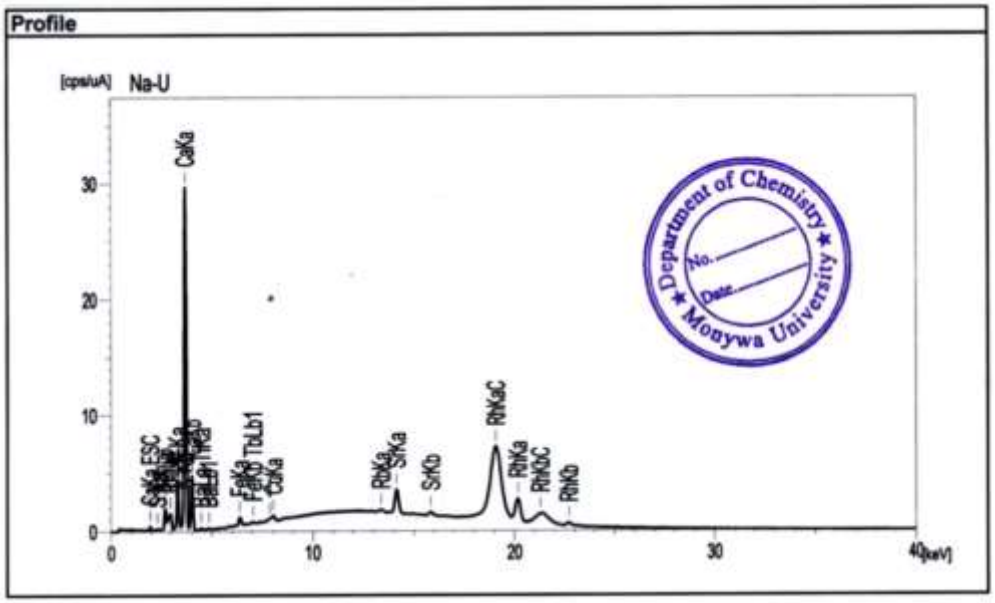

Figure 2 EDXRF spectrum of the bark of Pin-Sein

Antimicrobial Activities of Crude Extracts from Bark of Pin-Sein

The antimicrobial activities of various crude extracts from the bark of Pin-Sein are tabulated in Table 2. According to these data, the Pin-Sein bark was high in antimicrobial activity with inhibition zone diameter range, 18-31 mm in Figure 3. Three extracts of ethanol, ethyl acetate and chloroform showed high activities on six selected microorganisms. Among the various crude extracts of Pin-Sein bark, ethyl acetate extract exhibited the potent antimicrobial activity with inhibition zone diameter range, 29-31 mm. So, ethyl acetate extract of Pin-Sein bark sample was selected for the isolation of pure organic compounds by column separation method. It was observed that the Pin-Sein bark sample has a potential source of new classes of antibiotics that could be useful for infectious diseases chemotherapy and control.

Table 2 Antimicrobial Activities of the Various Crude Extracts of the Pin-Sein Bark

Microorganisms	Inhibition zone diameter (mm)				
	Pet-ether	**EtOAc**	**EtOH**	**$CHCl_3$**	**H_2O**
Bacillus subtilis	22.53	30.50	21.76	24.66	19.68
Staphylococcus aureus	23.66	29.47	24.06	26.60	21.56
Salmonella typhi	19.56	29.78	21.68	24.91	18.47
Bacillus pumilus	22.20	31.98	23.41	24.50	20.10
Candida albicans	23.35	29.43	21.22	29.64	20.50
Escherichia coli	22.98	25.40	23.11	25.97	20.68

Agar well (8 mm); 9 mm ~ 14 mm (+) -mild activity;
15 mm ~ 20 mm (++) -medium activity; 21 mm above (+++) -highest activity

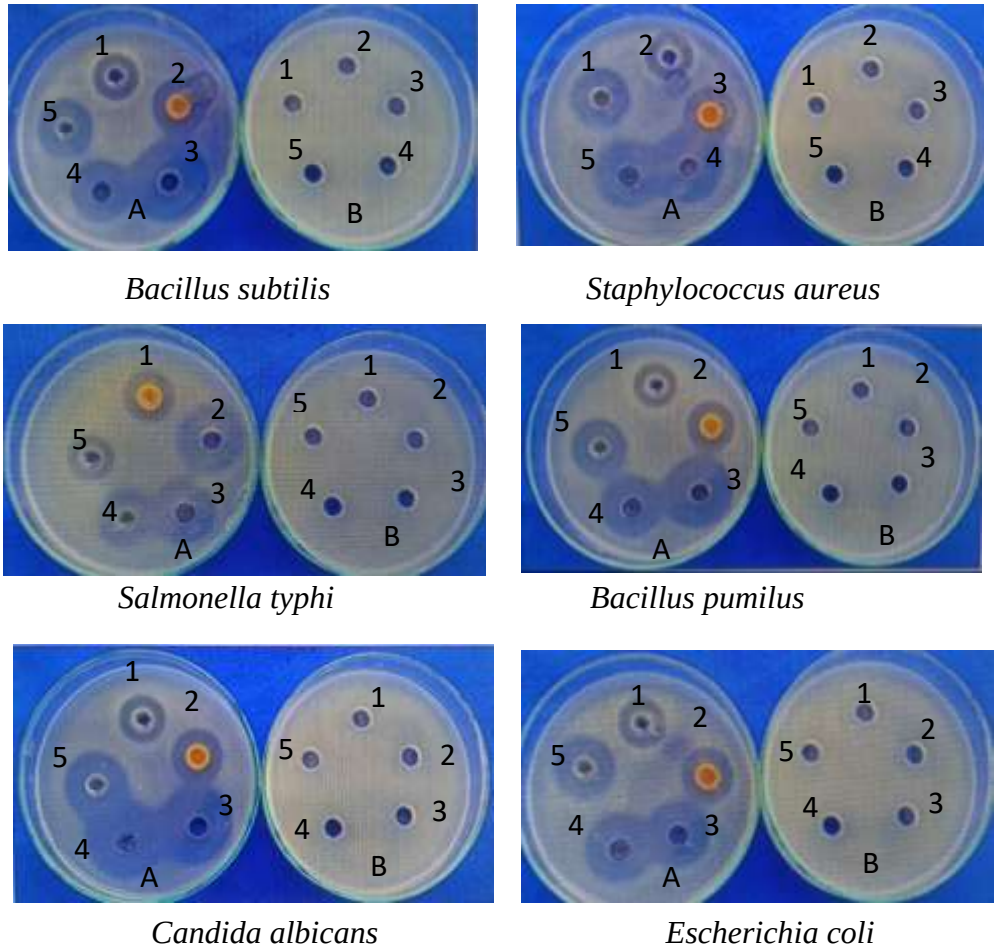

Bacillus subtilis *Staphylococcus aureus*

Salmonella typhi *Bacillus pumilus*

Candida albicans *Escherichia coli*

1- Pet-ether, 2- EtOAc, 3- EtOH, 4- $CHCl_3$, 5- H_2O, A- Sample, B- Control

Figure 3 Antimicrobial activity of the bark of Pin-Sein

Antioxidant Activity of Crude Extracts from Pin-Sein Bark

It was found that the higher the concentration of crude extract, the lower the absorbance of DPPH solution and the greater the radical scavenging activity of the extract. The results are shown in Table 3. The plot of % inhibition versus concentrations of different extracts is shown in

Figure 4. So, the lower value of IC_{50} indicates the higher antioxidant activity. Therefore, ethanol extract (IC_{50}= 95.89 µg/mL) showed more potent antioxidant activity than watery extract (IC_{50}= 226.30 µg/mL) of the sample but lower activity in compare with standard ascorbic acid (IC_{50}= 3.70 µg/mL) in Figure 5. According to these data, the Pin-sein bark sample showed good antioxidant activity.

Table 3 Percent Inhibitions and IC_{50} Values of Watery and Ethanol Extracts of Pin-Sein Bark

Extracts	Concentration (µg/mL)	Percent inhibition (%)	IC_{50} (µg/mL)
Watery	25	33.27	226.30
	50	32.05	
	100	42.68	
	200	49.65	
	400	63.06	
Ethanol	25	8.29	95.89
	50	28.94	
	100	88.13	
	200	87.18	
	400	96.74	
Ascorbic acid	3.125	41.51	3.70
	6.25	87.01	
	12.5	88.91	
	25	89.92	
	50	90.10	
	100	93.55	

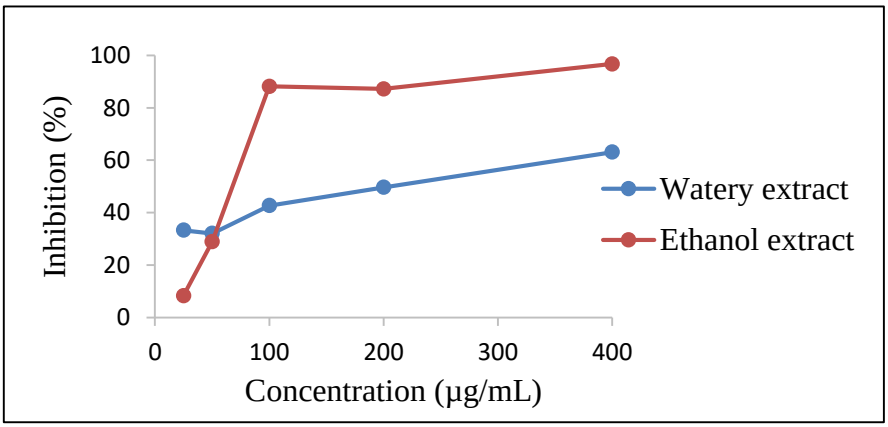

Figure 4 Plot of percent inhibition Vs different concentrations of crude extracts from the bark of Pin-Sein

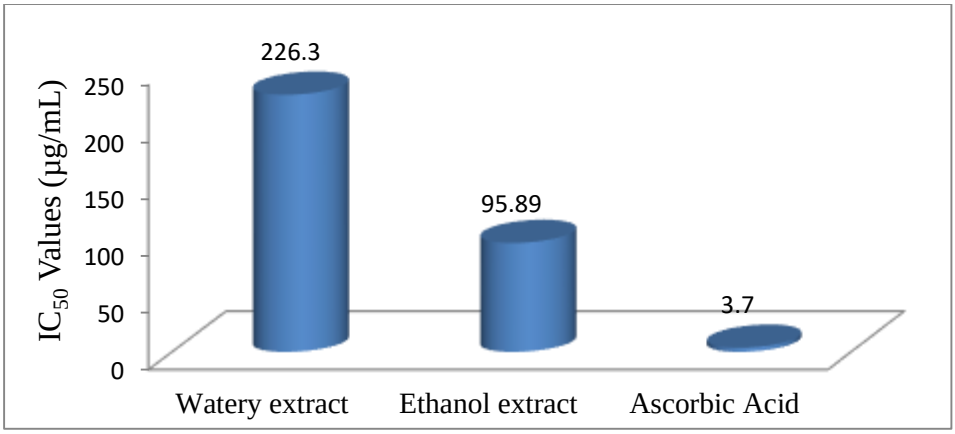

Figure 5 IC_{50} values of crude extracts of the Pin-Sein bark and standard ascorbic acid

Isolation of Pure Organic Compounds

From the column chromatographic separation of sample, totally 107 fractions were obtained. The fractions with the same R_f value were combined to give eight combined fractions. The fraction 6 gave 27 mg of pure organic compound, TMK-1, (R_f = 0.55) as a pale yellow crystal form and the yield percent was 1.35 % based on the ethyl acetate crude extract. The fraction 8 gave 31 mg of pure organic compound, TMK-2, (R_f = 0.64) as a yellow crystals form and the yield percent was 1.55 % based on the ethyl acetate crude extract.

FT IR Assignments of Pure Organic Compound, TMK-1

The FT IR spectrum of TMK-1 is shown in Figure 6, and the spectral data are tabulated in Table 4. TMK-1 consists of O-H stretching vibration of hydroxyl group, unsymmetrical and symmetrical CH stretching vibration, C=O stretching vibration, C=C stretching vibration of aromatic ring, C-O-C stretching vibration of ether group, =CH out of plane bending vibration of cis or Z and trans or E alkenic group, =CH out of plane bending vibration of aromatic ring and OH out of plane bending vibration, respectively. These functional groups are consistent with the structure of polyphenol (Silverstein e*t al.*, 2003). The occurrences of these functional groups imply that the isolated compound TMK-1 may be polyphenol.

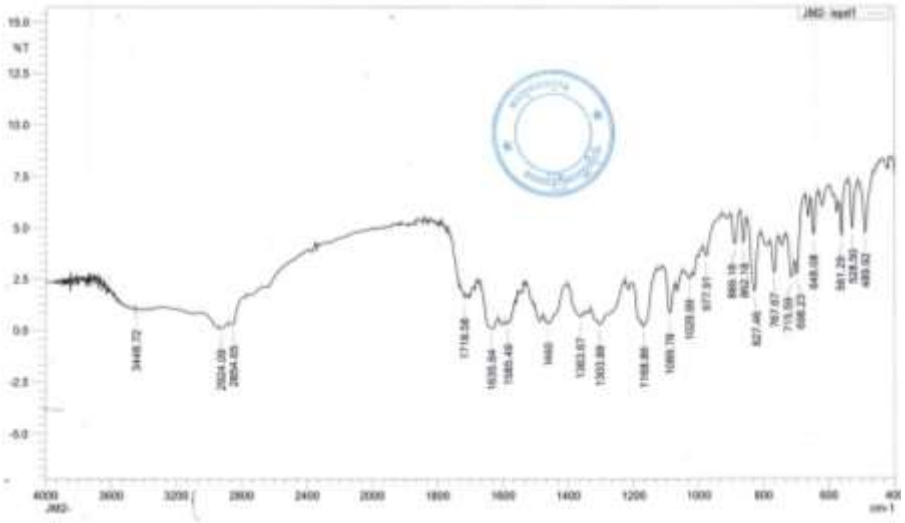

Figure 6 FT IR Spectrum of pure organic compound, TMK-1

Table 4 FT IR Assignments of Pure Organic Compound, TMK-1

Absorption band(cm^{-1})	Assignments (functional group)
3448	O-H stretching vibration of hydroxyl group
2924, 2854	unsymmetrical and symmetrical stretching vibration of sp^3 hydrocarbons
1718	C=O stretching vibration
1635, 1585	C=C stretching vibration of aromatic ring
1460, 1363	C-H in plane and out of plane bending vibration of sp^3 hydrocarbons
1303	OH in plane bending vibration
1168	C-O stretching vibration of hydroxyl group
1089	C-O-C stretching vibration of ether group
977	=CH out of plane bending vibration of trans or E alkenic group
889, 862	=CH out of plane bending vibration of aromatic ring
827	=CH out of plane bending vibration of cis or Z alkenic group
767, 715	C=C and OH out of plane bending vibration

FT IR Assignments of Pure Organic Compound, TMK-2

Figure 7 shows the FT IR spectrum of pure organic compound, TMK-2. These data are described in Table 5. The pure organic compound, TMK-2 consists of O-H stretching vibration of hydroxyl group, unsymmetrical and symmetrical stretching vibration of sp^3 hydrocarbons, C=O stretching vibrations, C=C stretching vibration of aromatic ring, C-O-C stretching vibration of ether group, =CH out of plane bending vibration of aromatic ring, =CH out of plane bending vibration of cis or Z alkenic group, C=C out of plane bending vibration and OH out of plane bending vibration, respectively. These functional groups are consistent with the structure of flavonoid (Silverstein e*t al.*, 2003). According to these functional groups, isolated pure organic compound, TMK-2 may be flavonoid.

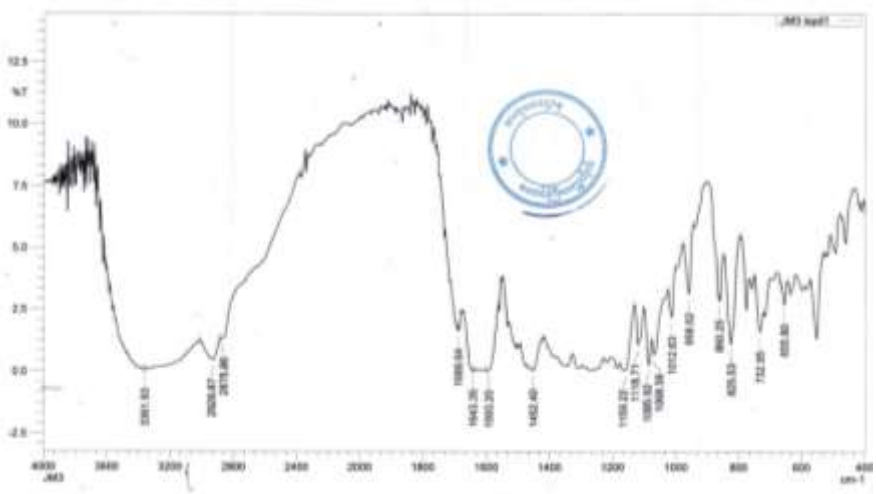

Figure 7 FT IR spectrum of pure organic compound TMK-2

Table 5 FT IR Assignments of TMK-2

Absorption band (cm^{-1})	Assignments (functional group)
3361	O-H stretching vibration of hydroxyl group
2929, 2875	unsymmetrical and symmetrical stretching vibration of sp^3 hydrocarbons
1689	C=O stretching vibration of carbonyl group
1643, 1593	C=C stretching vibration of aromatic ring
1452	C-H in plane bending vibration of sp^3 hydrocarbons
1159	C-O stretching vibration of hydroxyl group
1118, 1085	C-O-C stretching vibration of ether group
1068	O-H in plane bending vibration
1012; 958, 860	=CH in plane and out of plane bending vibration of aromatic ring
825	=CH out of plane bending vibration of cis or Z alkenic group
732	C=C out of plane bending vibration of aromatic ring
655	O-H out of plane bending vibration

Pure organic compound, TMK-1 gave the blue black colour solution for polyphenol test and TMK-2, reddish pink colour solution for flavonoid test. So, two isolated compounds may be polyphenol and flavonoid. The melting points of polyphenol (TMK-1), 253-256 ºC and flavonoid (TMK-2), 298-301 ºC, were observed, respectively.

Conclusion

In this research work, the bark of *Docynia indica* (Wall.) Decne was a good source of phytochemicals and mineral elements. It was found to contain 6.2 % moisture and 0.54 % ash. Antimicrobial activity of Pin-Sein bark was high activity on six selected microorganisms with inhibition zone diameter range of 18-31 mm. Among the crude extracts, antimicrobial activity of ethyl acetate extract was found to be the highest and water extract was the lowest in the bark of Pin-Sein. Therefore, Pin-Sein bark was less soluble in water. In addition, IC_{50} values of 95 % ethanol and watery extracts were 95.89 µg/mL and 226.30 µg/mL. So, ethanol extract had more potent antioxidant activity than watery extract of this sample. According to these data, the Pin-sein bark sample showed good radical scavenging activity and inhibition ability. It might be considered as a potential source of antioxidants. Polyphenol and flavonoid, pure organic compounds were isolated from Pin-Sein bark by column chromatography. The yield percent of polyphenol (TMK-1) was 1.35 % and of flavonoid (TMK-2), 1.55 % based upon the ethyl acetate crude extract. R_f values of polyphenol and flavonoid were 0.55 and 0.64. Melting point was found to be 253 -256 ºC of polyphenol, and 298-301ºC of flavonoid. The functional groups present in these two compounds were identified by FT IR spectral data. Due to its bioactivity and bioactive constituents: polyphenol and flavonoid, the bark of Pin-Sein may be useful as antioxidant for the treatment of oxidative stress related diseases such as diabetes, cancers, tumors, hypertension, liver diseases, inflammatory etc.

Acknowledgements

The authors wish to thank the Myanmar Academy of Arts and Science for accepting this research paper. We also thank to Professor and Head, Dr Cho Cho Nyein, Department of Chemistry, Kyaing Tong University for her kind interest and encouragement to this paper.

References

Cruickshank, R. (1975). *Handbook of Bacteriology*. London: 11th Ed., E. and S. Livingstone Ltd., pp. 888

Deng, X., X. Zhao, Z. Lan, J. Jiang, W. Yin, and L. Chen. (2014). "Anti-tumor Effects of Flavonoids from the Ethnic Medicine *Docynia delavayi* (Franch.) Schneid. and its Possible Mechanism". *J. Med. Food*, vol.17 (7), pp.787-794

Harborne, J. B. (1984). *Phytochemical Methods: A Guide to Modern Techniques of Plant Analysis.* New York: 3rd Ed., Chapman and Hall ltd, pp. 120-160

Hogan, S., **C. S.** Canning, X. Sun, and K. Zhou. (2010). "Effects of Grape Pomade Antioxidant Extract on Oxidative Stress and Inflammation in Diet Induced Obese Mice". *J. Agric. Food Chem.*, vol. 58, pp. 11250-11256

Loan, N. T. T., H. T. M. Tan, V. T. H. Tam, C. L. Luan, L. M. Huong, and D. N. Lien. (2011). "Antiobesity and Body Weight Reducing Effect of *Docynia indica* (Wall.) Decne Fruit Extract Fractions in Experimentally Obese Mice". *VNU J. Sci. Nat. Sci. Technol.*, vol. 27, pp. 125-133

Loganayaki, N., S. Perumal, and M. Sellamuthu. (2010). "Antioxidant Activity of Two Traditional Indian Vegetables: *Solanum nigrum* L. and *Solanum torvum* L.". *Food Sci. Biotechnol.,* vol.19 (1) pp. 121-127

Marini-Bettolo, G., M. Nicoletti, M. Patamia, C. Galeffi, and I. Messana. (1981). "Plant Screening by Chemical and Chromatographic Procedures under Field Conditions". *J. Ethanopharmacol*. pp. 121-123

Silverstein, R. M., F. X. Webster, and D. J. Kiemle. (2003). *Spectroscopic Identification of Organic Compounds*. New York: 7th Ed., John Wiley & Sons, Inc.

Stahl, E. (1965). "Effect of Low Temperature and Use of Gradients in Thin Layer Chromatography''. *J. Pharm. Belg.* vol. 20, pp. 159-168

PREPARATION AND CHARACTERIZATION OF ECO-FRIENDLY BIOPLASTICS FROM SAWDUST BIOMASS WASTE

Hnin Yu Wai[1], Yamin Ko[2]

Abstract

The present work is concerned with the preparation and characterization of sawdust-derived cellulose based bioplastics. Sawdust was collected from Family Saw Mill, North Okkalapa Township, Yangon Region, Myanmar. The physicochemical properties (such as moisture content, ash content, bulk density, and pH) of sawdust was determined by conventional methods and also characterized by modern techniques such as FT IR, SEM and TG DTA analyses. The cellulose in sawdust powder was prepared by using alkali treatment, bleaching process and hydrolysis method. The yield percent of the cellulose from sawdust powder was 36.6 %. Prepared cellulose was characterized by FT IR, SEM and XRD analyses. Bioplastics were prepared by mixing with various proportions (1, 2, 3, 4, 5, 6 g) of cellulose using 50 mL of water, 2 mL of acetic acid and 0.5 mL of sorbitol as plasticizer. The most favourable conditions for preparing bioplastic namely (SCB 3) was found to be 3 g of cellulose with 0.5 mL of sorbitol and 2 mL of acetic acid, was the most suitable for preparing bioplastic. It was found that the bioplastic (SCB 3) possesses tensile strength (9.40 MPa), elongation at break (45.00 %) and tear strength (56.70 kNm^{-1}). The selected bioplastic SCB 3 was characterized by FT IR, SEM and TG DTA analyses. All prepared bioplastics showed a plain, clear, smooth surface, were flexible, and pale yellow in colour. The prepared bioplastics can be used in packaging.

Keywords: cellulose, bioplastic, physicochemical properties, sorbitol

Introduction

Cellulose - based plastic has much potential in packaging applications, in transparent plastics or coatings, gel formulations, and as reinforcement in foams and composites (Henriksson *et al*., 2008). Widespread applications are currently restricted by the high cost due mainly to the difficulties in extraction of cellulose without chain cleavage during enzymic or chemical treatment. When dried, difficult to disperse lumps due to strong inter-molecular forces and entanglement of cellulose can give rise to problems in its dispersion into bioplastics (Chiellini *et al.,* 2002).Cellulose would be extracted from wood using some of the chemical and mechanical methods and they could be extracted in nano and micro forms by alkalization, bleaching and acid hydrolysis process (Piyaporn, 2015).One of such potential waste materials is sawdust which is relatively abundant and inexpensive. Sawdust is an industrial waste obtained as by-products from cutting, sawing or grinding of timber in the form of fine particle. Although sawdust consists largely of cellulose, it also contains soluble sugar, acids, resins, oils and waxes and other organic substances (Abdul Awal *et al.,* 2016). Sawdust is basically a waste of small particles available in saw-milling industries, pulp plant and paper industries as well as wood processing industries particularly, in the most of the country in a quite large volume in forms of heaps and mostly burnt off resulting in the environmental pollution (Rominiyi *et al.,* 2017). Bioplastic is form of plastic made from renewable biomass, instead of the conventional plastic derived from petroleum. It includes low accumulation of bulky plastic materials in the environment, increased soil fertility and reduced the cost of waste management. Bioplastic packaging options include bags for compost, agricultural foils, horticultural products, consumer goods, household appliances, stationery, cosmetic packaging, toys and textiles (Pramanik, *et al.,* 2015).

[1] Dr, Associate Professor, Department of Chemistry, Maubin University
[2] MSc Student, Department of Chemistry, University of Yangon

The aim of this research is to prepare and characterize the cellulose from sawdust and to prepare the bioplastic from cellulose.

Materials and Methods

The chemicals used in the experimental work were from British Drug House Chemical Ltd., England. In all the investigations, the recommended and standard procedures of both conventional and modern techniques were employed. The experiments were conducted at Physical Chemistry Research Laboratory, Department of Chemistry, University of Yangon.

Collection of Samples

In the experiment, sawdust was collected from Family Saw Mill, North Okkalapa Township, Yangon Region, Myanmar.

Preparation of Sawdust Powder

Sawdust was washed with distilled water 3 times, and cleaned samples were dried in the solar for 4 days. Then dried again at 80 °C for 2 h. They were ground by an electric grinder and sieved with 80 mesh sieve to get the fine sawdust powder.

Physicochemical Properties of Sawdust Powder

The physicochemical properties (moisture content, ash content, bulk density, and pH) of prepared sawdust powder were determined by conventional methods.

Characterization of Sawdust Powder

The sawdust powder was characterized by FT IR, SEM and TG-DTA analyses.

FT IR analysis was performed in order to characterize the functional groups of samples. A Perkin-Elmer Spectrum GX, USA was used for FT IR analysis.

The scanning electron micrograph of sawdust powder was performed by a Scanning Electron Microscope (JSM-5160, JEOL Ltd., Japan).

Thermal analysis of sawdust powder was determined by a DTA-60H (Hi-TGA 2950) thermal analyzer.

Preparation of Cellulose

Sawdust powder was washed with distilled water 3 times, and cleaned samples were dried in the solar for 4 days. Then dried again at 80 °C for 2 h. They were ground by an electric grinder and sieved with 80 mesh sieve to get the fine sawdust powder. And then cellulose was prepared by the chemical process: alkali treatment, bleaching process followed by acid hydrolysis.

Alkali treatment

Sodium hydroxide 16 g were dissolved in distilled water and the volume was made up to 100 mL with distilled water. The alkali treatment purified the cellulose by removing hemicellulose from sawdust. The sawdust powder was put in a round-bottomed flask with 16 % (w/v) sodium hydroxide solution and refluxed at 70 °C for 6 h, and then washed several times with distilled water until pH 7. Then they were filtered and dried at room temperature.

Bleaching process

The bleaching process was performed to purify the cellulose by removing lignin from sawdust. The alkali treated sawdust powder was put in a beaker with 30 % (v/v) sodium hypochlorite solution and bleached at 70 °C for 6 h, and then washed several times with distilled water until pH 7. Then they were filtered and dried at room temperature.

Acid hydrolysis

The acid hydrolysis treatment was performed on treated sample with 10 % (v/v) sulphuric acid solution at 40 °C for 30 min. The treated pulp was centrifuged at 6500 rpm for 30 min to remove acidic solution. The colloidal suspension was washed several times with distilled water until pH 7 and sonicated for 15 min. To obtain cellulose fiber, they were filtered and dried at room temperature for 3 days. The yield percent of the cellulose from sawdust powder was 36.6 %.

Characterization of the Prepared Cellulose

The prepared cellulose was also characterized by FT IR, SEM and XRD analyses.

Preparation of Bioplastics

In this research, all of bioplastics were prepared by blending casting method.

Each of 1, 2, 3, 4, 5 and 6 g of cellulose was mixed with 50 mL of water, 2 mL of acetic acid and 0.5 mL of sorbitol as plasticizer. The solution was stirred on the magnetic stirrer at 70 °C for 30 min. The solution was casted onto cleaned and dried melamine plate at room temperature. And then, allowed to air dry for 3 days.

Determination of the Physicomechanical Properties of the Prepared Bioplastics (SCB)

The physicomechanical properties (thickness, tensile strength, elongation at break, and tear strength) of the prepared bioplastics were determined by the conventional method and modern techniques.

Water uptake and degree of swelling of the prepared bioplastics were also determined.

Characterization of the Selected Bioplastic (SCB 3)

The selected bioplastic was characterized by FT IR, SEM and TG-DTA analyses.

Determination of Biodegradation by Soil Burial Test

Biodegradation of the prepared bioplastic was studied by soil burial test to examine the morphology changes.

Results and Discussion

Cellulose is a common natural polymer, so that it occupies an important position in the advancement of human civilization today. Cellulose can be used as the main material in the modern pharmaceutical industries, cosmetics, material industries, and other sectors. Table 1 shows that the physicochemical properties of sawdust determined by the conventional method.

Table 1 Physicochemical Properties of Sawdust

No.	Physicochemical Properties	Quantity
1	Moisture content (%)	8.25
2	Ash content (%)	0.96
3	Solid content (%)	91.75
4	Bulk density (g mL^{-1})	0.42
5	pH	6.32

Characteristics of Sawdust Powder

FT IR spectrum of raw sawdust powder shows that it contains cellulose which was proved by the presence of typical cellulose groups, -OH with absorption band at 3329 cm^{-1} (Figure 1 and Table 2).

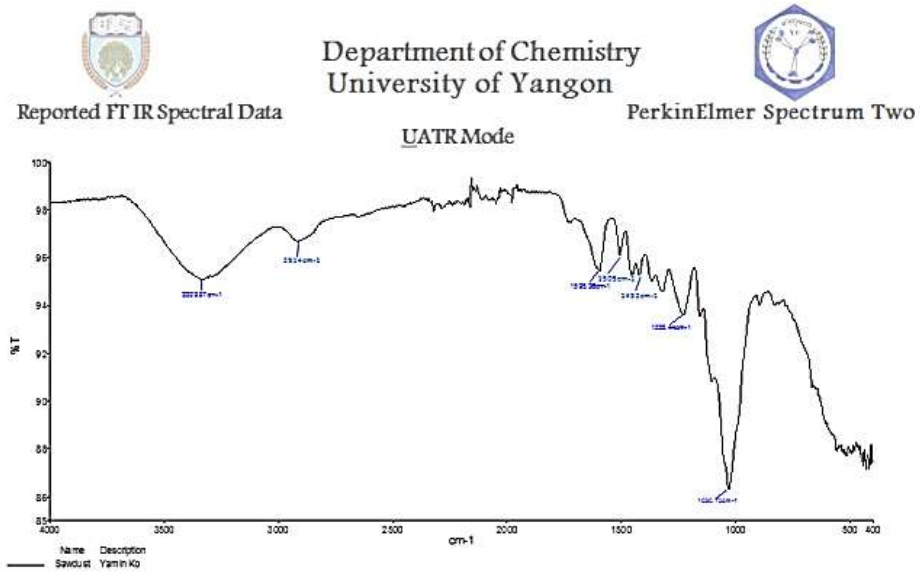

Figure 1 FT IR spectrum of sawdust powder

Table 2 FT IR Band Assignment of Sawdust Powder

Observed wavenumber (cm^{-1})	Literature wavenumber (cm^{-1}) *	Band assignment
3329	3100-3700	O-H stretching
2914	2850-2990	C-H stretching
1595, 1505, 1452	1450-1600	C=C stretching
1228, 1030	1020-1285	C-O stretching

* (Patcharaporn *et al.*, 2018)

The surface morphology of the sample was characterized by SEM analysis. From SEM image of sawdust powder, it is clearly observed that the sawdust material exhibits a dense fibrous structure (Figure 2).

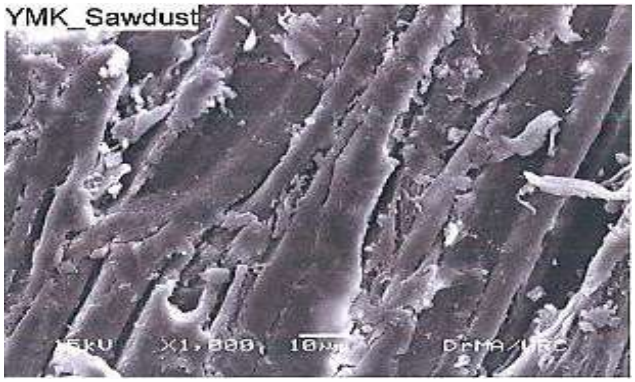

Figure 2 SEM photomicrograph of sawdust powder

Thermal stability of sawdust powder (Figure 3) and the TG-DTA Data (Table 3) are shown. The data show three distinct weight losses corresponded to the dehydration of water, the decomposition of organic residue and the carbonization of starting molecule.

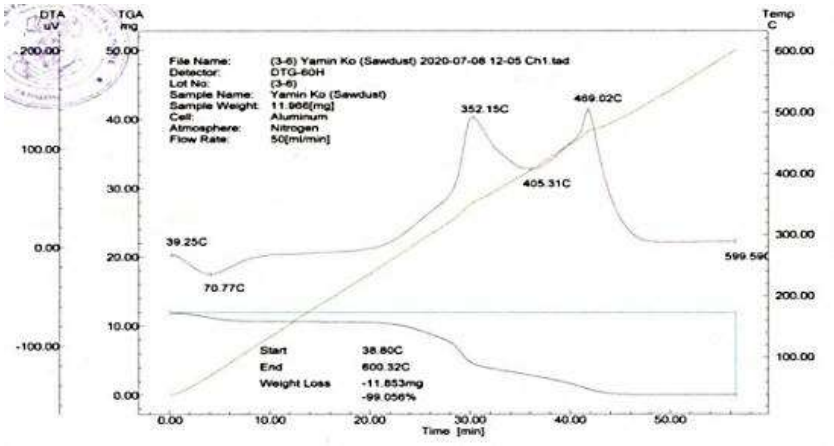

Figure 3 TG-DTA thermogram of sawdust powder

Table 3 TG-DTA Data of Sawdust Powder (SD)

Sample	TG		DTA		Remarks
	Temperature Range (°C)	Weight Loss (%)	Peak Temperature (°C)	Nature of Peak	
SD	39.25-100	13.67	70.77	endothermic	Dehydration of water
	100-360	43.55	352.15	exothermic	Decomposition of organic residue
	360-500	41.78	469.02	exothermic	Carbonization
		99.00			

Characteristics of the Prepared Cellulose

Cellulose is a very abundant polymer in nature. It can be extracted from various sources such as from plants, animals, algae, fungi, bacteria and minerals. Cellulose in nature is never found in pure form, but is always bound to other polysaccharides such as lignin, pectin, hemicellulose, wax, ash and xylan. In the present work, cellulose isolation from sawdust was conducted with chemical method using strong acid (H_2SO_4) for hydrolysis process. The yield percent of the cellulose from sawdust powder is 36.6 %.

FT IR analysis was performed in order to characterize the functional group of samples. The FT IR spectrum of cellulose (Figure 4) and the spectral data (Table 4) are given. The structural changes of each prepared (a) alkali treated sawdust powder, (b) bleached sawdust powder and (c) cellulose powder are shown in Figure 4 and band assignments are presented in Table 4. The broad peaks at 3300 cm^{-1} in all samples were due to the O-H stretching. The peak at 2894 cm^{-1} was due to stretching of aliphatic C-H on hemicelluloses and cellulose. Appearance of the band 1618-1650 cm^{-1} was owing to relative pure ring stretching mode similar to the aromatic ring C-O stretching in benzene as well as in pyrone ring. The bands at 1372 cm^{-1} and 1319 cm^{-1} were due to symmetric CH_2 bending and wagging. The weak band at 1031 cm^{-1} could be assigned to C-H bending vibration of polysaccharides. The band at 1024 cm^{-1} was due to the removal of lignin and hemicelluloses. The peak at 995 cm^{-1} also indicated stretching involving C-O-C and C-OH at C-5 and C-6 of cellulose.

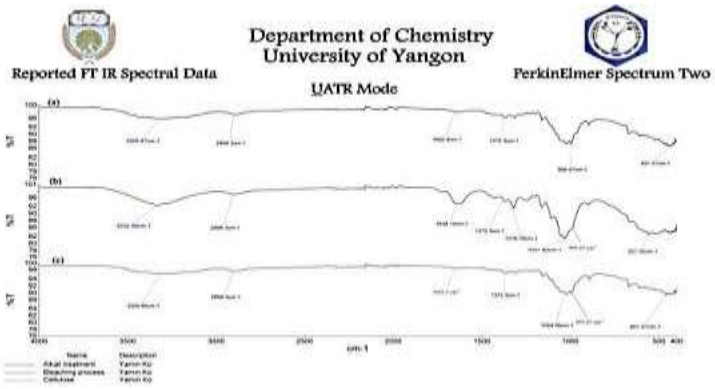

Figure 4 FT IR spectra of (a) alkali treated sawdust powder, (b) bleached sawdust powder and (c) cellulose powder

Table 4 FT IR Band Assignments of Alkali Treated Sample, Bleached Sample and Cellulose Powder

Observed wavenumber (cm^{-1})			Literature wavenumber (cm^{-1}) *	Band assignment
Alkali treated sample	Bleached sample	Cellulose powder		
3305	3332	3309	3300-3400	O-H stretching
2894	2894	2894	2820-2970	C-H stretching
1642	1638	1642	1618-1650	C-O stretching
1372	1372	1372, 1319	1300-1430	CH_2 bending
-	1031	1024	1000-1320	C-H bending
995	995	995	990-1050	C-O-C and C-OH ring stretching

* (Piyaporn, 2015)

The morphology of prepared cellulose studied by SEM analysis shows a microfibril structure (Figure 5).

Figure 5 SEM photomicrograph of cellulose

The XRD profile of the sawdust-derived cellulose shows that the characteristic peaks at 2θ values around 13.38°, 15.37° and 19.25° indicating typical semi-crystalline cellulose (Figure 6). This indicated that the sawdust powder completely transformed into cellulose through alkali treatment, bleaching and acid hydrolysis process.

The simplest and most widely used method for estimating the average crystalline size is from the full width at half maximum (FWHM) of a diffraction peak using the Scherrer equation,

$$d = K\lambda / \beta \cos\theta$$

where, d is the crystallite size, λ is the diffraction wavelength, β is the corrected FWHM,

θ is the diffraction angle and K is a constant which is close to unity.

The crystallite size of prepared cellulose calculated by this method is shown in Table 5.

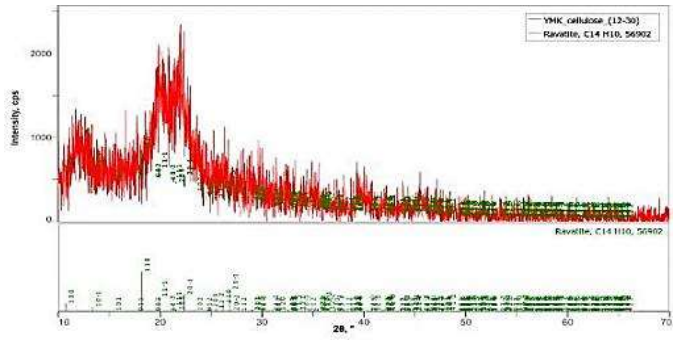

Figure 6 X-ray diffractogram of cellulose powder

Table 5 XRD Data of Cellulose Powder

No.	2θ (°)	Miller indices (h k l)	β(FWHM)	Crystallite size (nm)
1.	13.38	(1 0 $\bar{1}$)	0.4074	20.51
2.	15.37	(1 0 1)	0.4074	20.56
3.	19.25	(0 0 2)	0.4074	20.67
Average Crystallite Size (nm)				20.58

Preparation and Physicomechanical Properties of SCB Bioplastics

For all of the prepared bioplastics, physicomechanical parameters were determined. Among these parameters, tensile strength is more specific than other for determining bioplastics quality. The six types of bioplastics were prepared. The results of the physicochemical properties of prepared bioplastics are presented in Table 6 and Figures 7, 8 and 9. The effect of cellulose content on tensile strength and elongation at break of the cellulose blended bioplastics were studied. The tensile strength and elongation at break (% of cellulose-based bioplastic increased along with an increase in cellulose content. The highest tensile strength was found in bioplastic SCB 3 which contains 3 g of cellulose having tensile strength of 9.4 MPa. When the cellulose content exceeded 3 g, the tensile strength of the blend bioplastic decreased along with an increase in cellulose content, but it was still much higher than that of the unreinforced bioplastic.

Table 6 Physicomechanical Properties of SCB Bioplastics

Properties	Bioplastics					
	SCB-1	**SCB-2**	**SCB-3**	**SCB-4**	**SCB-5**	**SCB-6**
Thickness (mm)	0.15	0.16	0.18	0.19	0.10	0.10
Tensile Strength (MPa)	3.90	6.30	9.40	9.23	8.97	7.80
Elongation at Break (%)	27.00	36.00	45.00	43.20	40.70	39.60
Tear Strength (kN / m)	29.50	44.40	56.70	53.86	50.95	49.42

SCB 1 = (1 g) Cellulose + (50 mL) H_2O + (0.5 mL) sorbitol + (2 mL) acetic acid
SCB 2 = (2 g) Cellulose + (50 mL) H_2O + (0.5 mL) sorbitol + (2 mL) acetic acid
SCB 3 = (3 g) Cellulose + (50 mL) H_2O + (0.5 mL) sorbitol + (2 mL) acetic acid
SCB 4 = (4 g) Cellulose + (50 mL) H_2O + (0.5 mL) sorbitol + (2 mL) acetic acid
SCB 5 = (5 g) Cellulose + (50 mL) H_2O + (0.5 mL) sorbitol + (2 mL) acetic acid
SCB 6 = (6 g) Cellulose + (50 mL) H_2O + (0.5 mL) sorbitol + (2 mL) acetic acid

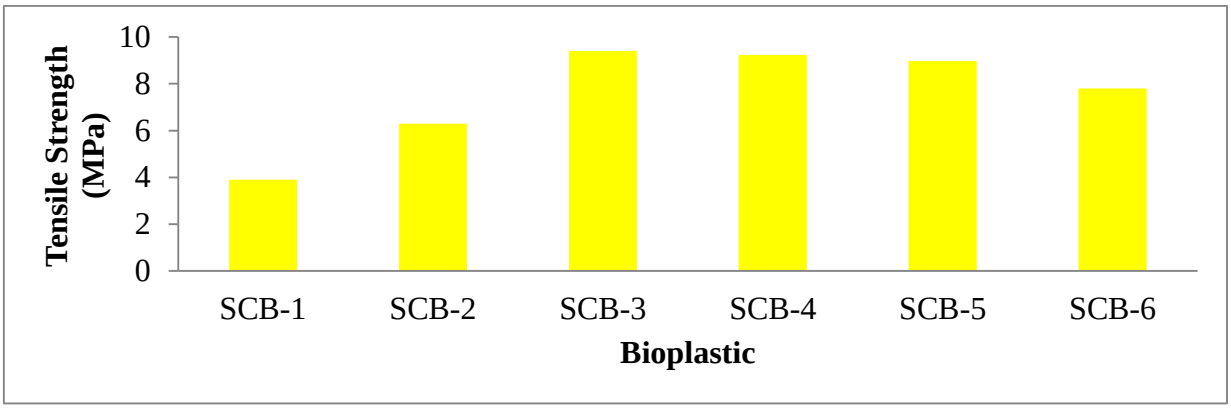

Figure 7 Tensile strength of different types of bioplastic

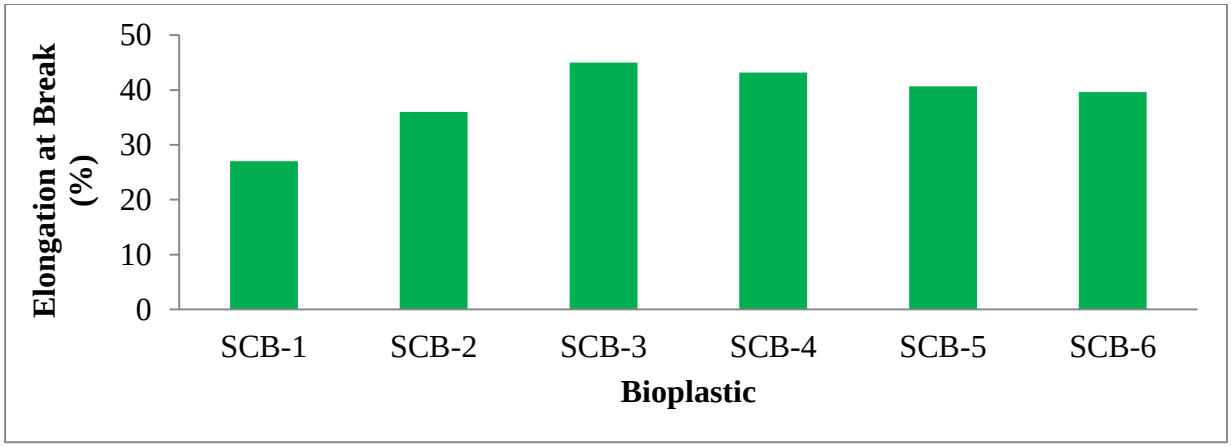

Figure 8 Elongation at break of different types of bioplastic

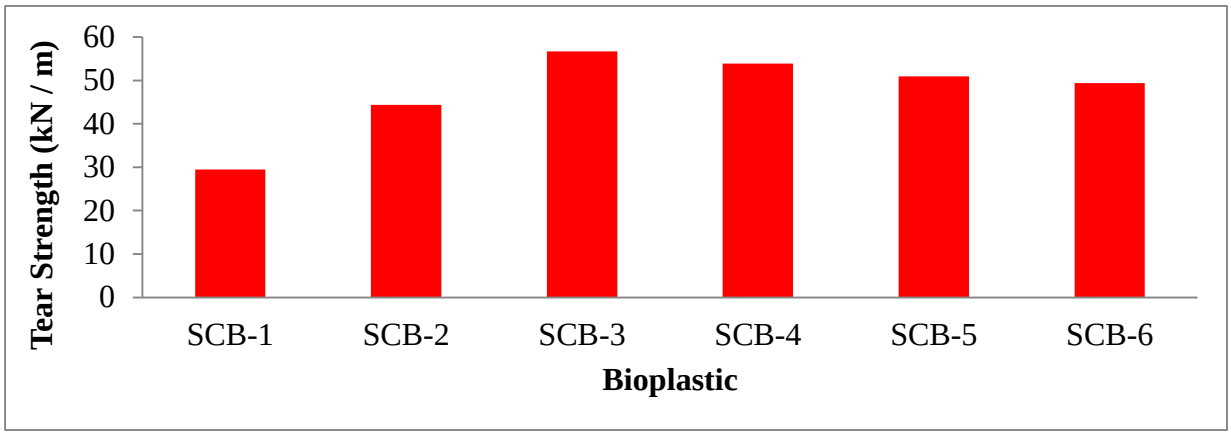

Figure 9 Tear strength of different types of bioplastic

Water Uptake Properties of SCB Bioplastics

The water uptake was investigated with increasing immersion time. The water uptake is one of the most significant parameters when a bioplastic is intended to be used as making utensils. The water uptake was the amount of water entrapped in the matrix including bound water. The water absorption properties of SCB bioplastics were studied for varying time intervals such as 5 min, 10 min, 15 min, 20 min, 25 min and 30 min. The water uptakes as a function of time for SCB bioplastics are shown in Table 7 and Figure 10. The bioplastic SCB 3 has the equilibrium water uptake percentage among them. Therefore, bioplastic SCB 3 was chosen to make the most suitable bioplastic.

Table 7 Water Uptake of SCB Bioplastics

Bioplastics / Time (min)	Water Uptake (%)					
	5	**10**	**15**	**20**	**25**	**30**
SCB-1	55.76	61.53	67.31	71.15	76.92	82.69
SCB-2	61.12	68.51	74.07	79.62	83.34	92.37
SCB-3	80.15	86.37	93.31	99.82	105.87	112.29
SCB-4	98.16	100.80	110.38	114.67	119.43	125.63
SCB-5	116.36	119.20	126.34	135.50	140.34	149.15
SCB-6	121.9	128.37	131.50	137.87	146.28	152.48

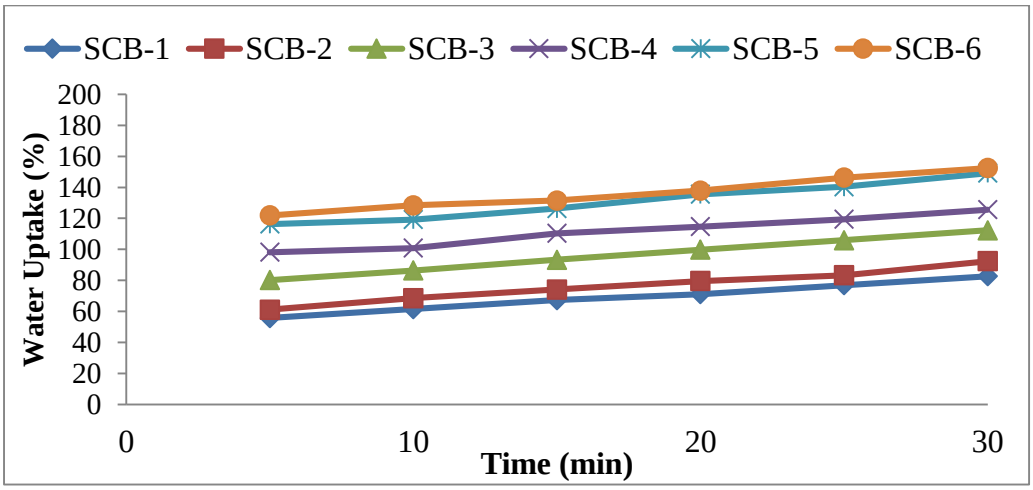

Figure 10 Water uptake of various types of bioplastic at different contact times

Degree of Swelling Properties of SCB Bioplastics

The degree of swelling of SCB bioplastic with different compositions as a function of immersion time in distilled water at room temperature is shown in Table 8 and Figure 11. For a given blend composition time, mostly the degree of swelling increased with increasing immersion time. The degree of swelling from 5 min to 30 min was slightly different for all prepared bioplastics.

Table 8 Degree of Swelling of Different Types of Bioplastic

Bioplastics / Time (min)	Degree of Swelling (%)					
	5	**10**	**15**	**20**	**25**	**30**
SCB-1	35.80	38.09	40.23	41.57	43.47	45.26
SCB-2	37.93	40.65	42.36	44.32	45.98	48.85
SCB-3	43.48	47.56	51.85	56.84	62.86	68.23
SCB-4	48.50	53.85	57.59	63.73	68.73	73.98
SCB-5	54.96	59.48	65.94	69.25	74.58	78.42
SCB-6	59.72	64.73	72.35	75.93	80.79	84.74

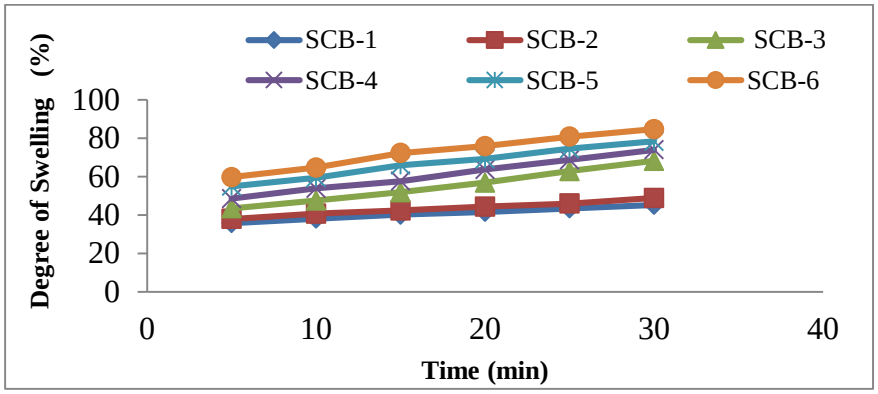

Figure 11 Degree of swelling of SCB bioplastics as a function of contact time

Characteristics of the Selected Bioplastic (SCB 3)

FT IR spectrum for SCB 3 bioplastic recorded in the range of 400-4000 cm^{-1} is shown in (Figure 12 and table 9). In the FT IR spectrum of SCB 3 bioplastic, the differences seem to be in the region 3200-3600 cm^{-1}, 1650 cm^{-1} and 1350 cm^{-1}. But there is an enhancement of OH group wavenumber from 3309 cm^{-1} at cellulose become 3275 cm^{-1} at SCB 3 bioplastic. The decrease in OH group value is due to cellulose their combined in bioplastic.

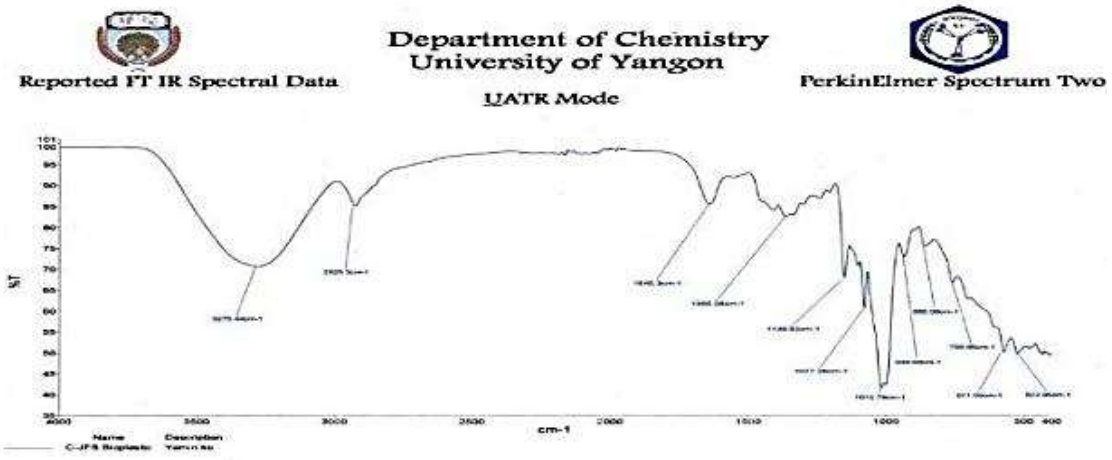

Figure 12 FT IR spectrum of SCB 3 bioplastic

Table 9 FT IR Band Assignments of SCB 3 bioplastic

Observed wavenumber (cm^{-1})	Literature wavenumber (cm^{-1}) *	Band assignment
3275	3200-3600	O-H stretching
2928	2850-2940	C-H stretching
1640	1600-1650	C-O bending
1365, 1149	1350-1380	C-H or C-O bending
1077, 1015	1000-1125	CH_2-O-CH_2 pyranose ring stretching
934, 860	800-995	C-O-C asymmetric stretching

* (Piyaporn, 2015)

Figure 13 shows the SEM microphotograph of SCB 3 bioplastic. It was observed rough and agglomerates were seen on the surface of the SCB 3 bioplastic.

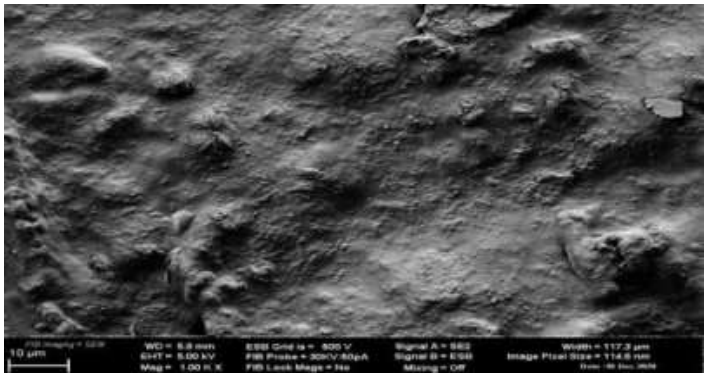

Figure 13 SEM photomicrograph of SCB 3 bioplastic

Thermal stability of SCB 3 bioplastic (Figure 14) and the interpretation (Table 10) are performed. The data show three stages of distinct weight losses. The first stage dehydration of water occurred at 280.44 ºC with weight loss of 13.05 %. The second stage started at about 348.86 ºC with weight loss of 63.24 %, which is attributed to the depolymerization with volatilization. In the third stage, the exothermic peak was found at 479.35 ºC with the weight loss percent about 22.40 % which is corresponded due to the carbonization. The TG-DTA analysis of SCB 3 bioplastic suggested that the degradation of total mass loss is 98.69 %.

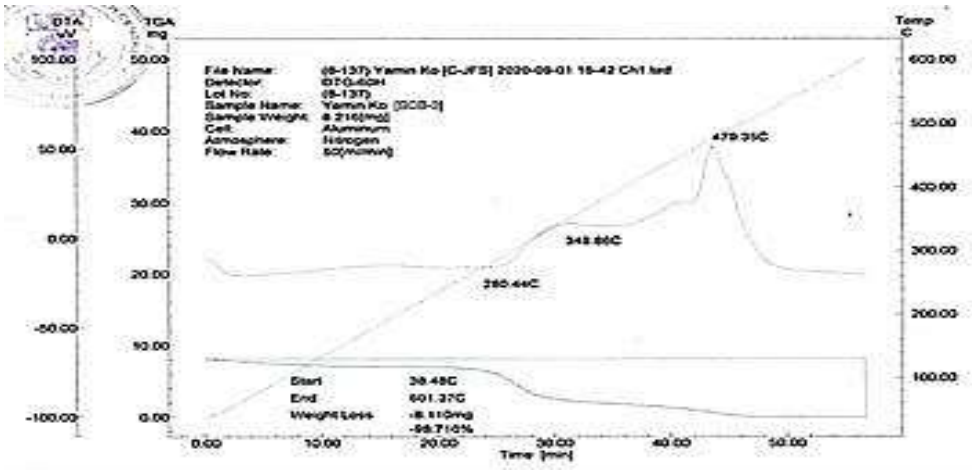

Figure 14 TG-DTA thermogram of SCB-3 bioplastic

Table 10 TG-DTA Data of SCB-3 Bioplastic

Sample	TG		DTA		Remarks
	Temperature Range (°C)	Weight Loss (%)	Peak Temperature (°C)	Nature of Peak	
SCB-3 Bioplastic	38.48-300	13.05	280.44	endothermic	Dehydration of water
	300-400	63.24	348.86	exothermic	Depolymerization with volatilization
	400-500	22.40 98.69	479.35	exothermic	Carbonization

Biodegradation of the Prepared SCB Bioplastics

These bioplastics clearly showed a slight deformation, after two days. Degradability of bioplastics is important when a polymeric system is applied in daily lives as its weight loss degree has a direct influence on the environment. The effect of different amounts of cellulose on bioplastic weight loss rate was conducted via soil burial test. Figure 15 shows the biodegradation nature of SCB 3 bioplastic for 2 days interval. The degradation rate (%) of the prepared bioplastics are presented in Table 11. It was found slightly degradation, after 2 days.

(a) (b) (c) (d) (e)

Figure 15 The physical appearances of SCB 3 bioplastic; (a) before burial test, (b) after two days, (c) after four days, (d) after six days and (e) after eight days burial

Table 11 Degradation Rate of Prepared Bioplastics by Soil Burial Test

Bioplastics / Time (day)	Degradation Rate (%)				
	0	**2**	**4**	**6**	**8**
SCB-1	0	4.008	12.84	24.65	40.98
SCB-2	0	9.65	18.46	30.78	49.26
SCB-3	0	15.2	24.58	36.14	59.62
SCB-4	0	20.96	31.62	42.27	68.46
SCB-5	0	26.02	37.02	49.18	76.35
SCB-6	0	34.02	40.28	56.58	82.48

Some Possible Application of Prepared the SCB Bioplastic

Bioplastic packaging options include bags for compost, agricultural foils, horticultural products, nursery products, toys, textiles, disposable cups, salad bowls, plates and food containers. The photographs of SCB bioplastic are presented (Figure 16) and the cup for food made from

prepared bioplastic is shown in Figure 17. Bioplastics last for 6 months at room temperature. But after 6 months, fungi are found on the surface. So, its shelf life is 6 months.

Figure 16 Photograph of SCB 3 bioplastic

Figure 17 Cup made of bioplastic

Conclusion

The physico-mechanical properties of SCB bioplastics such as thickness, tensile strength, elongation at break and tear strength were investigated. The effect of cellulose content on tensile strength and elongation at break of the bioplastics were also studied. Among them, SCB 3 bioplastic has the highest tensile strength, elongation at break and tear strength. It possesses 0.18 mm of thickness, 9.40 MPa of tensile strength, 45.00 % of elongation at break and 56.70 kN/m of tear strength respectively. All prepared bioplastics showed plain, smooth surface, flexible and pale-yellow colour. Among them, SCB 3 bioplastic is better than the other bioplastics. The prepared SCB bioplastics will be widely used in food packaging and making utensils. The use of cellulose-based bioplastic materials in the production of eco-friendly and less expensive utensils when compared to conventionally synthesized polymers.

Acknowledgments

The authors would like to express their deepest gratitude to for the provision of opportunity to do this research the Rubber Research and Development Centre for the necessary research testing and Universities' Research Center (URC) for TG-TDA, SEM, XRD and thanks are extended to Department of Chemistry, University of Yangon for FT IR.

References

Abdul Awal, A. S. M., A. A. K. Mariyana, and M. Z. Hossain. (2016). "Some Aspects of Physical and Mechanical Properties of Sawdust Concrete". *Inteternational Journal of Geomate*, vol. 10, pp. 8-23

Chiellini, E., F. Chiellini, and P. Chiellini. (2002). "Polymers from Renewable Resources in Degradable Polymers in Principle and Applications". *Journal of Applied Polymer Science*, vol. 18, pp. 16-23

Henriksson, M., L. A. Berglund, P. Isaksson, T. Lndstorm, and T. Nishino. (2008). "Cellulose Nanopaper Structure of High Toughness". *Journal of Biomacromolecules*, vol. 9, pp. 7-18

Patcharaporn, C. and. A. H. T. Duangdao. (2018). "A Study of Microcrystalline Cellulose Prepared from Parawood (*Hevea Brasiliensis*) Sawdust Waste Using Different Acid Types". *Journal of Metals, Materials and Minerals*, vol. 28, pp. 16-34

Piyaporn, K. (2015). "Extraction and Characterization of Cellulose Nanocrystals Produced by acid Hydrolysis from Corn Husk". *Journal of Metals, Materials and Minerals*, vol. 25, pp. 9-26

Pramanik, P., N. Sharma, and U. Mina. (2015). "Bioplastic: Sustainable Green Plastic". *International Journal of Applied Science*,vol 5, pp. 1-15

Rominiyi, O. L., B. A. Adaramola, O. M. Ikumapayi, O. T. Oginni, and S. A. Akinola. (2017). "Potential Utilization of Sawdust in Energy, Manufacturing and Agricultural Industry; Waste to Health". *World Journal of Engineering and Technology*, vol. **7**, pp. 9-20

DECONTAMINATION OF ARSENIC IN AQUEOUS SOLUTION BY MANGANESE FERRITES*

Cho Cho Thet[1], Aye Aye Hlaing[2] and Kobayashi Takaomi[3]

Abstract

Decontamination of pentavalent arsenic (As^{5+}) ions in aqueous solution by manganese ferrites ($MnFe_2O_4$) was presented in this paper. $MnFe_2O_4$ were prepared by sonochemical synthesis method and they were used as adsorbents for removal of arsenic. The essential parameters such as pH of the precursor and post annealing temperature based on the formation of spinel manganese ferrite were discussed. The structural properties of manganese ferrites including compound identification, the crystal structure and surface morphology were investigated by Fourier transform infrared (FT-IR), X-ray diffraction (XRD) and Scanning electron microscope (SEM). The adsorption behaviour of As^{5+} ions on the manganese ferrite has been performed by batch adsorption experiment. The concentration of arsenic adsorbed on manganese ferrite was determined by atomic absorption spectroscopy coupled with hydride vapour generation (HVG-AAS). The adsorption capacity was fitted with the *Langmuir* isotherm model. The decontamination efficiency and adsorption amount of As determined from *Langmuir* isotherm model were discussed.

Keywords: arsenic (As), adsorption, $MnFe_2O_4$, ferrite, HVG-AAS, sonochemical, spinel structure

Introduction

Most of the common materials for the decontamination of heavy metals ions include biomass-based materials, metal oxides, geopolymers, zeolites, silica, activated carbon, activated alumina and ferrites. Spinel ferrite nanoparticles have been focused on as adsorbents because their unique physicochemical properties are differ from their bulk. Besides, the shape and size as well as magnetic properties can be tuned. They also have surface versatility, high surface-to-volume ratio, long-lasting in water treatment and less aggregation. Manganese ferrite ($MnFe_2O_4$) has a face centered cubic (FCC) structure of either normal or inverse or mixed spinel-type as well as soft magnetic n-type semiconducting material. Ferrite particles have a wide variety of applications including heterogeneous catalysis (Zhang *et al*., 2019), adsorption (Durán *et al*., 2020), sensors (Vignesh *et al*., 2015) and magnetic technology (Chandunika *et al*., 2020).

Heavy metal ions in the waste water are removed by many techniques including reverse osmosis (Pires da Silva *et al*., 2016), precipitation (Alina Pohl 2020), solvent extraction (Silva *et al*., 2005), ion exchange (Hussain *et al*., 2021) and membrane filtration (Vo *et al*., 2020). Adsorption (Panda *et al*., 2020) is an alternative method by an adhesion of an adsorbate such as a fluid, liquid, or gas, by creating a thin layer on the surface of an adsorbent. Inorganic arsenic (As^{3+} and As^{5+}) elements are relatively scared to living organisms since they are toxic and carcinogenic elements. Symptoms of arsenic poisoning include vomiting, abdominal pain, encephalopathy and watery diarrhea. Long-term exposure to arsenic contaminated water could result in thickening of the skin, darker skin, abdominal pain, diarrhea, heart disease, numbness and cancer (Amighian *et al*., 2006). The permissible limit of total arsenic in drinking water is 0.01 ppm (10 ppb) by world health organization (WHO) (Agusu *et al*., 2019).

Therefore, the effective and efficient adsorbents only for selective removal of arsenic are urgently required. On the other hand, the development of new materials as well as technologies are becoming the challenges to the remediation of waste water treatment since improper separation

[1] Dr, Professor, Department of Physics, Dawei University
[2] Dr, Deputy Director, Department of Research and Innovation (DRI), Myanmar
[3] Dr, Professor, Department of Materials Science and Technology, Nagaoka University of Technology
[*] Best Paper Award Winning Paper in Physics (2021)

methods of heavy metals from aqueous solution can be spread to the living organisms and environment. In this work, the main aim is synthesis manganese ferrite by sonication method in order to use them as adsorbents for decontamination of arsenic heavy metal ions. The adsorption behavior of As by manganese ferrites was investigated by doing batch adsorption process.

Experimental Details

Synthesis of Manganese Ferrite

All reagents were of analytical grade and they were used without further purification. Briefly, 2.7 g of ferric chloride hexahydrate ($FeCl_3 \cdot 6H_2O$) and 0.845 g of manganese (II) sulfate, ($MnSO_4 \cdot H_2O$) were dissolved in 100 ml of deionized water so that the molar ratio of Mn to Fe in the solution is 1:2. The solution was then constantly stirred until completely dissolution. 9 M sodium hydroxide (NaOH) solution was used to adjust the pH of the precursor solution at 9. Then, the solution was transferred to high frequency ultrasonic bath. The sample was exposed by ultrasound irradiation at 500 kHz and 50 W for 1 h. The brownish precipitates were separated from the solution by centrifugation and washed with excess water to remove the impurities and followed by washing with acetone. Afterwards, the precipitates were dried at 50 °C for 24 h. The dry precipitates were grounded by agate motor to get the fine powders. Then, the powders were calcined at 500 °C for 6 h.

Batch Adsorption Experiment

The batch adsorption experiment were carried out by adding fixed amount 0.1 g of $MnFe_2O_4$ powders in 50 mL of As^{5+}aqueous solution having a concentration of 5 ppm. The process was continued by operating at 200 rpm for 1, 5, 10, 15, 20, 25, 30, 45, 60 and 120 min in a shaker at the room temperature (27 ºC). The solution was then filtered by using the Smith filter paper (125 mm) for the separation of the adsorbent particles from the aqueous solution and filtrate was measured by HVG-AAS. The values of initial concentration, C_i, were also varied from 0.1 to 400 ppm and measured equilibrium concentration (C_e) depending on C_i values.

Measurements and Characterization

The identification of functional group was investigated by FT-IR (IRPrestige-21 Shimadzu spectrophotometer). The crystal structure of the samples was measured by RIGAKU SmartLab XRD. Surface morphology of ferrite was revealed by JEOL-JSM 5300 LV scanning microscope. Concentrations of total As in the filtrate were determined by AAS (Shimadzu model AA-6300) coupled with a hydride generation system (HVG-1, Shimadzu). The spectrophotometer was operated at 193.78 nm with a slit width of 1.0 nm. The lamp current was 12 mA. The fuel acetylene (air-acetylene flame) flow rate was 2.0 liters per minute and the burner height of 7 mm. The flow rate of the argon carrier gas was 70 ml per minute at a pressure of 0.35 Mpa.

Results and Discussion

FT-IR spectroscopy is used to identify the functional groups of ferrites. From this investigation, it was found out that formation of spinel ferrite strongly depends on post annealing temperature. Only broad band around at 590 cm^{-1} was observed in as-synthesized ferrites. It implies that spinel structure was not obtained without treatment of post annealing. Thus, calcination is treated in order to enhance sufficient activation energy of the formation of ferrites. Complete spinel structures were formed at the band 587 cm^{-1} and 490 cm^{-1} at the annealing sample as shown in Fig. 1.

The characteristic peaks at 587 cm^{-1} and 490 cm^{-1} correspond to the metal-oxygen (M-O) bond stretching vibration at the tetrahedral sites and octahedral sites (Srinivasan *et al*., 2018). The difference between these absorption bands is due to the change in bond length (M-O) at the tetrahedral and octahedral site (Mounkachi *et al*., 2017). The other peaks at 3483 cm^{-1} corresponds to O-H bond stretching vibration revealing the presence of residual hydroxyl groups. Peak at 1122 cm^{-1} can be assigned to the vibration of groups OH. The strong peaks at 1636 cm^{-1} are corresponding to O–H bending vibrations in water.

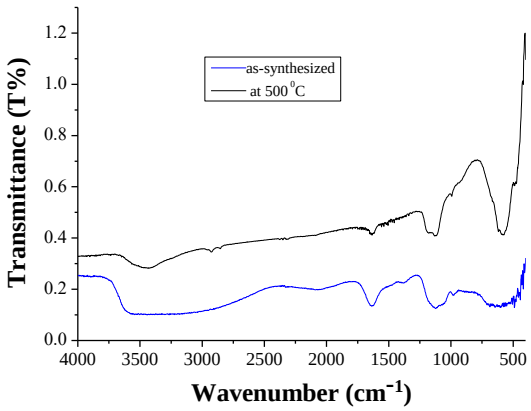

Figure 1 FT-IR spectra of (a) as-synthesized ferrite and (b) manganese ferrites calcined at 500 °C

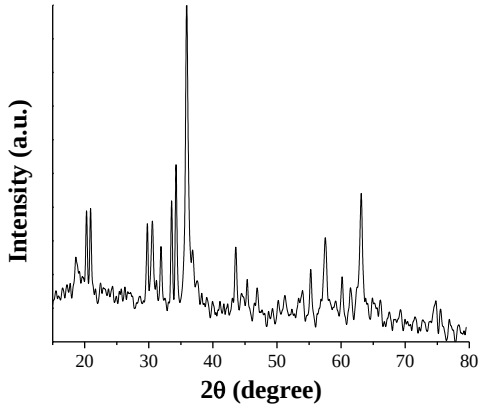

Figure 2 FT-IR spectra of manganese ferrites calcined at 500 °C

XRD measurement was performed in order to additionally confirm the formation of ferrite structure. The diffraction peaks [(220), (311), (222) (400), (422), (511), (440), (533)] in XRD pattern in Figure 2 was corresponding to the characteristic crystallographic planes of the spinel structure of ferrites (Mary Jacintha *et al*., 2017). These Miller indices indicated the single-phase $MnFe_2O_4$ with face centered cubic (FCC) crystal structure. The better crystallinity of spinel ferrite structure was observed at 500 °C by XRD result.

The SEM micrograph in Fig.3 shows that the porous structure providing the greater surface area which is an advantage for the adsorption. To evaluate the porosity, nitrogen adsorption was conducted at 25 °C. The surface area of manganese ferrite 3.6572 m^2/g was obtained according to Brunauer– Emmett–Teller (BET) method. Figure 4 showed amounts of adsorbed N_2 in the ferrite at different relative N_2 pressures.

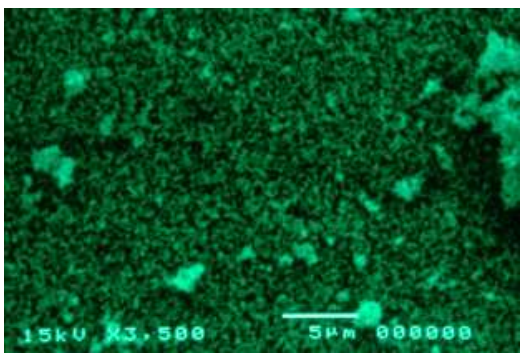

Figure 3 SEM micrograph of manganese ferrite

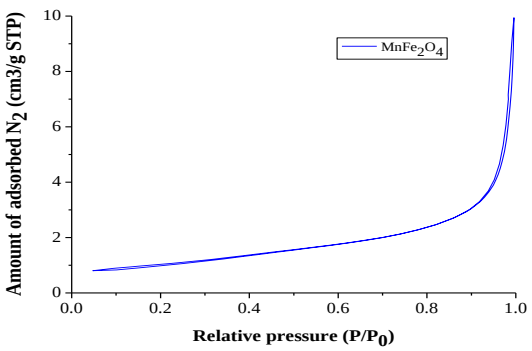

Figure 4 N_2 isotherms of manganese ferrite

To identify the possible rapidness of removal process As by Mn-ferrite, time dependence adsorption test was performed. The removal percent was calculated by the following formula:

$$\text{removal}(\%) = \frac{C_i - C_e}{C_i} \times 100 \qquad (1)$$

The adsorption amount (q_e) of As ion generally is calculated by following formula:

$$q_e = \frac{(C_i - C_e)V}{m} \qquad (2)$$

Where, q_e = equilibrium adsorption amount (mg/g)

C_i = initial concentration (mg/L or ppm)

C_e= equilibrium concentration (mg/L or ppm)

V = volume of the aqueous solution (mL)

m = mass of adsorbent (mg)

The maximum removal percent and equilibrium adsorption amount (q_e) are found out to be 57 % and 1.4256 mg/g at the shaking 25 min until to 2 h as shown in plot 5 (a) and (b).

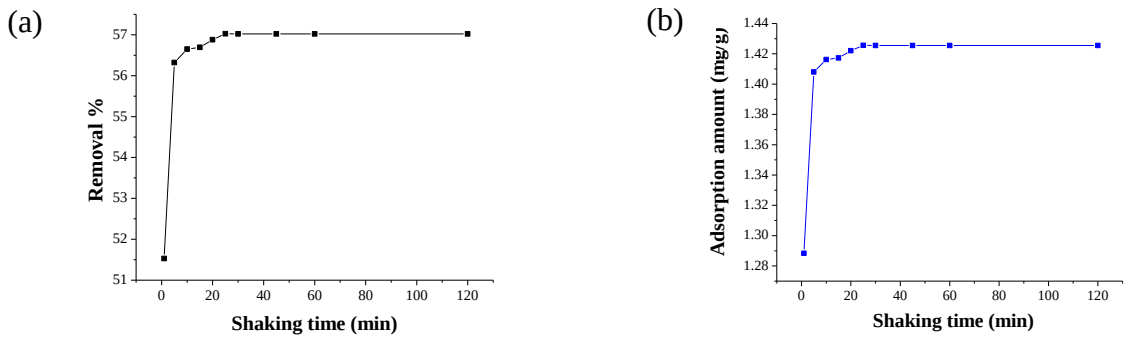

Figure 5 Time course curve of (a) removal % and (b) adsorption amounts of As ions on manganese ferrite (C_i = 5ppm)

Figure 6 (a) illustrates the graphical representation of isotherm which was subjected to sorption isotherm of *Langmuir*. Figure 7(b) represents the adsorption isotherm of As ion on manganese ferrite. The adsorption amount for each equilibrium concentrations can be observed in this plot. The adsorption amount (q_e) is gradually increased until the value of C_e is 46 ppm. Then, the q_e becomes constant beyond this concentration and it implies that adsorption amount of As has been saturated at C_e 46 ppm.

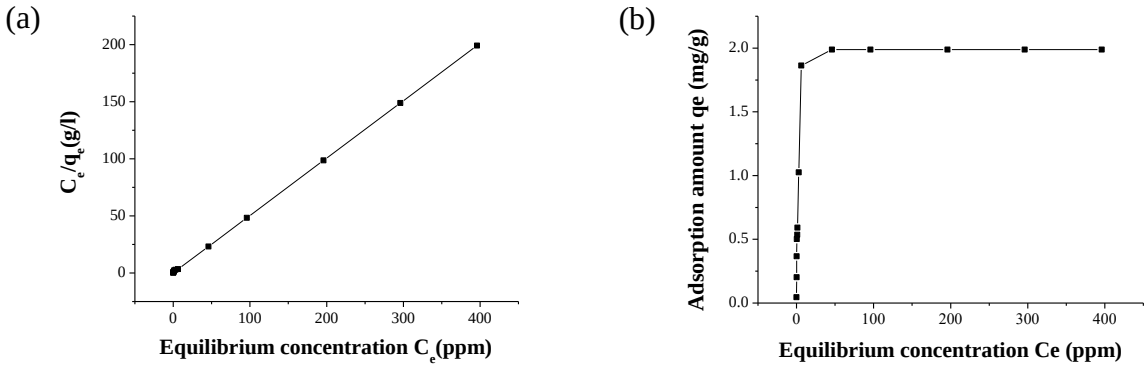

Figure 6 (a) *Langmuir* adsorption isotherm plots of As on manganese ferrite and (b) adsorption isotherm of As^{5+} ion on manganese ferrite

Conclusions

Manganese ferrites ($MnFe_2O_4$) synthesized by high frequency (500 kHz, 50 W) ultrasound method have been applied to decontaminate the arsenic (As) from aqueous solution. Annealing temperature 500 ºC plays the essential parameter in the present sonochemical synthesis system to obtain the manganese ferrite particles. The formation of cation at the tetrahedral and octahedral site in FT-IR spectrum revealed that $MnFe_2O_4$ is spinel ferrite crystal system. XRD study additionally confirmed that the final product is manganese spinel crystal phase. According to the batch adsorption experiment and measurement results by AAS, the removal efficiency of As was found out to be 92 % from the 100 ppb concentration of As^{5+} aqueous solution. Thus, the manganese ferrite synthesized at pH 9 and annealing at 500 ºC could effectively decontaminate to trace level concentration of arsenic from aqueous solution.

Acknowledgements

We would like to acknowledge to Prof Dr Theingi Shwe, Rector, Dawei University, for her encouragement and allowing us to participate in this event. We are especially thanks you to Prof Dr Cho Cho Myint, Pro-rector, Dawei University, for her kind permission to contribute this work. Our special thanks go to Dr Ye Chan, Professor and Head of Universities' Research Centre (URC) for the supporting of research facilities and excellent discussion.

References

Amighian J., M. Mozaffari and B. Nasr, "Preparation of nano-sized manganese ferrite ($MnFe_2O_4$) via coprecipitation method," ***phys. stat. sol. (c)*** 3, No. 9, 3188-3192, 2006.

Agusu L., Alimin, La Ode Ahmad, Muhammad Zamrun Firihu, Seitaro Mitsudo and Hiromitsu Kikuchi, **"**Crystal and microstructure of $MnFe_2O_4$ synthesized by ceramic method using manganese ore and iron sand as raw materials," ***J. Phys.: Conf.*** **Ser.** 1153 012056, 1-7, 2019.

Chandunika R.K., R Vijayaraghavan and Niroj Kumar Sahu, "Magnetic hyperthermia application of $MnFe_2O_4$ nanostructures processed through solvents with the varying boiling point," ***Mater. Res. Express***, 7, 064002, 1-10, 2020.

Durán S. V., Byron Lapo, Miguel Meneses and Ana María Sastre, "Recovery of neodymium (III) from aqueous phase by chitosan-manganese-ferrite magnetic beads**,"** ***Nanomaterials***, 10, 1204, 2-15, 2020.

Mary Jacintha A., V. Umapathy, P. Neeraja and S. Rex Jeya Rajkumar, "Synthesis and comparative studies of $MnFe_2O_4$ nanoparticles with different natural polymers by sol–gel method: structural, morphological, optical, magnetic, catalytic and biological activities," ***Journal of Nanostructure in Chemistry***, 7, 4, 375-387, 2017.

Mounkachi O., M. Hamedoun and A. Benyoussef, "Electronic and magnetic properties of $SnFe_2O_4$ spinel ferrites," ***Journal of Superconductivity and Novel Magnetism***, 30, 11, 3035-3038, 2017.

Panda L., Jena, S.K., Rath, S.S. "Heavy metal removal from water by adsorption using a low-cost geopolymer," ***Environ Sci Pollut Res***, 27, 24284-24298, 2020.

Pires da Silva J. R., Fábio Merçon, Claudio Manoel Guimarães Costa and Deborah Radoman Benjo, "Application of reverse osmosis process associated with EDTA complexation for nickel and copper removal from wastewater," ***Desalination and Water Treatment***, 57, 41, 19466-19474, 2016.

Pohl A., "Removal of heavy metal ions from water and wastewaters by sulfur-containing precipitation agents," ***Water, Air, & Soil Pollution***, 231, 503, 1-17, 2020.

Silva J.E., A.P. Paiva, D. Soares, A. Labrincha and F. Castro, "Solvent extraction applied to the recovery of heavy metals from galvanic sludge," ***Journal of Hazardous Materials B***, 120 113-118, 2005.

Srinivasan S.Y., Paknikar K.M, Bodas D, Gajbhiye V, "Applications of cobalt ferrite nanoparticles in biomedical nanotechnology," ***Nanomedicine (Lond).*** 13, 10, 1221-1238, 2018.

Vignesh R. H., Kalimuthu Vijaya Sankar, Samuthirapandian Amareshb, Yun Sung Lee and Ramakrishnan Kalai Selvan, "Synthesis and characterization of $MnFe_2O_4$ nanoparticles for impedometric ammonia gas sensor," ***Sensors and Actuators B***, 220, 50-58, 2015.

Vo T. S., Muhammad Mohsin Hossain, Hyung Mo Jeong and Kyunghoon Kim, "Heavy metal removal applications using adsorptive membranes," ***Nano Convergence*** 7, 36, 2-26, 2020.

Zhang Q., Xiaoyuan Yang and Jingqi Guan, "Applications of Magnetic nanomaterials in heterogeneous catalysis," ***ACS Appl. Nano Mater.***, 2, 8, 4681-4697, 2019.

DIGITAL IMAGE PROCESSING OF MYANMAR AUTOMOBILE NUMBER PLATE RECOGNITION USING MATLAB

Aung Zaw Myint[1], Aye Aye Thant[2]

Abstract

This paper presents an image processing method for recognizing a Myanmar automobile license number plate. An optical character recognition method is used to read the license plates. The boundary method is applied for characters segmentation. The implementation of the system is simulated on MATLAB software. In this paper, automobile license number plate is detected and segmented successfully.

Keywords*:* Digital image processing, MATLAB software, Image segmentation and recognition.

Introduction

An image is defined as an array or a matrix of square pixels arranged in rows and columns. Image processing is a procedure of converting an image into digital form and carry out some operation on it, in order to get an improved image and to retrieve some important information from the image [Al Faqheri.W and Mashohor.S,2009]. An image processing is a type of signal processing in which input is an image and output may be image or characteristics, features and statistical parameters associated with that image [Kumar .M, 2009]. Image processing can perform core research area within computer engineering, computer science, information systems, information technology, and software engineering which has come to be known collectively as the discipline of computing.

The field of digital image processing has experienced continuous and significant expansion in recent years [Gonzalez.R.C and Woods.R.E, 2002]. Nowadays, Myanmar automobile character plates are required for more advanced improvements in terms of modernized technologies. Myanmar automobile license plate is composed of two lines. The first line represents the division region and the second line represents vehicle numbers. Number plates are used for identification of vehicles all over the nations.

Automobile license plate identification is essential in numerous situations and implementations such as traffic control in unlimited areas, automatic payment of tolls for highways or bridges, general security systems wherever there is the need for distinguishing vehicles [Suresh.P and Suganthi.M, 2014]. In car parking, number plates are automatically recognized and stored in database to calculate duration of the parking.

Automobiles are identifying either manually or automatically. Automobile numbers identification is an image processing technique to identify vehicles of their number plates. Plate localization is accomplished to remove the unwanted background details and focusing on to the essential details in the image. Character extraction is done by segmenting the character portions from the localized number plate. A method has been proposed to remove the frame lines in the number plate followed by digital filtering. A method on image segmentation, region growing and clustering methods are described. Character recognition is an essential application, where the system is put up to deal with distorted characters in the license plate due to hazards.

[1] Dr, Associate Professor, Department of Physics, Shwebo University
[2] Dr, Pro-Rector, Myitkyina University, Ministry of Education

Materials and Method

MATLAB Software

The most important part in this process is the software model used in the image processing technology. The programs are implemented in MATLAB. The algorithm is divided into following parts: Capture image, pre-processing, plate region extraction, segmentation of character in the extracted number plate, character recognition, comparison with database and indicate result. The flow chart of license plate recognition system implementation is shown in Figure 1.

The image is captured by digital camera or webcam. The image captured is stored in JPEG (Joint Photographic Experts Group) format converted in to gray scale image in MATLAB. When the image is captured, there is a lot of disturbances and noises present in the image as shown in Figure 2. In the process, the RGB image is converted to a grayscale image. Grayscale images are obtained from color images. The process alters the color to grayscale by eliminating hue and saturation information. It eliminates unnecessary information and noise. According to the R, G, B value in the image, it calculates the value of gray value and obtains the gray image at the same time. Gray level cannot remove the noises. Media filtering is to remove the noises from the image.

Plate Region Extraction

The extraction of number plate from eroded image is the most important stage. The extraction can be done by using image segmentation method. There are numerous image segmentation methods available in various literatures. The number plate image is filtered and binarized. The set of connected components are segmented to measure the dimensions (height, width and area) of each of these segmented regions.

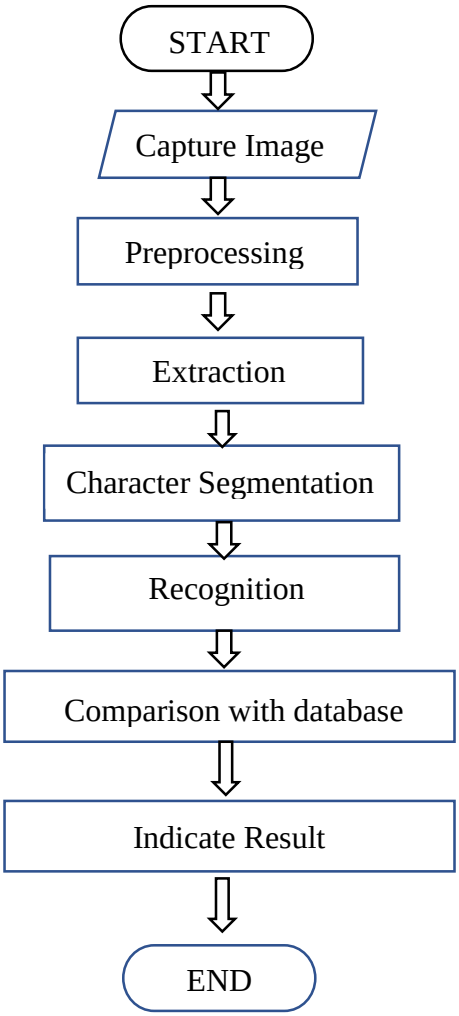

Figure 1 The flow chart of automobile number plate recognition system

Figure 2 Image noises condition of preprocessing

Character segmentation

To extract the characters from the localized number plate, the contents in that image will either be trivial noise components or characters to be identified. Only rectangular segmented regions are taken into data base file. Character segmentation separates each character in the number plate image and then finds the length of the number plate, the correlation and database using labeling components. If both values are same, it will generate the value 0-9 and A – Z. Sobel operators are used to calculate the threshold value that detects high light regions with high edge magnitude and high edge variance.

Morphological Operation

Mathematical morphology method is to detect the edges of the rectangular plate. Mathematical morphology is a part of digital image processing which is concerned with image filtering and geometric analysis by using structuring elements. Structuring element is a characteristic of certain structure and features to measure the shape of an image. The shape and size of the structuring element play an important role in image processing. Structuring elements are used in morphological operations which represent as matrices. The image is processed and changed into set and represents as matrix. The basic mathematical morphological operations namely dilation, erosion, opening, closing is used for detecting, modifying, manipulating the features which present in the images based on their shapes. Dilation and erosion are often used in combination for specific image preprocessing applications such as filling holes or removing small objects. Dilation adds pixels to the boundaries of objects in an image, while erosion removes pixels on object boundaries. After image binarization, morphological operations are performed to remove the unwanted regions.

Results and Discussion

Morphological operations are conducted for number plate localization and the structuring elements are not fixed value. The characters in the upper line of Myanmar license plate are written in smaller font size. This case can be a problem for character recognition stage. Even in the character segmentation stage, some characters in the upper line were disappeared while implementing morphological operations. License plate localization stage may fail in lighting condition. Filters can be used for lighting condition and motion blur.

The vehicle number plate image is measured by using Euler number and bounding box properties Measured characters are segmented by using binary image processing. In this system, the vehicle number plate image is tested and license plate characters are segmented successfully as shown in Figure 3. The characters are converted to string and display in edit box. These characters are stored as text file in this code as shown in Figure 4. The distance between the camera and the vehicle, illumination and orientation are still the challenges for license plate recognition.

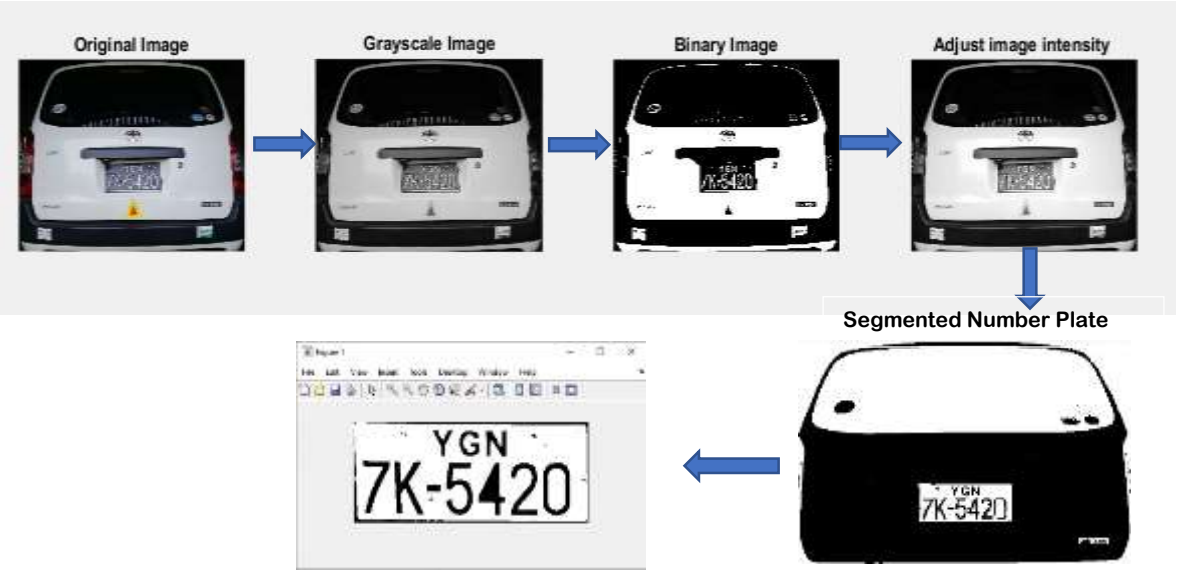

Figure 3 System design for vehicle number plate recognition

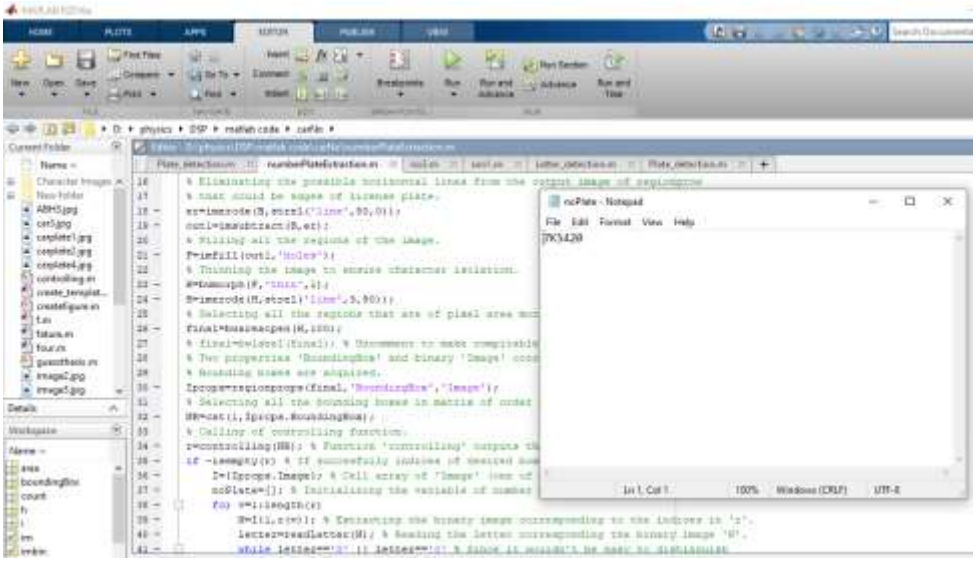

Figure 4 Display of automobile number as text file after recognition

Conclusion

This work has proposed a method for the detection and identification of automobile number plate. All the letters and numbers are simplified and segmented by using bounding box method in this approach. After segmentation of numbers and characters presented on the number plate, it is recognized the numbers and characters. The experimental results indicate that approach is applicable for the localization and recognition of a Myanmar license plate. The character recognition has been accomplished with the aid of optical characters recognition. According to the types of vehicles, the vertex of the plate from the ground varies depending on the car model. In some cases, the plate is located in the lower-left or lower right part of the vehicle. Besides these displacements of the plate position in the vehicles, the distance between the camera and the vehicles may also vary and then the localization of the number plate captured image plays a very critical role. Automobile numbers identification systems are applicable for the purpose of effective traffic control and security applications. The system in this research is developed based on digital images

and can be simply applied in toll gate, car parking systems for the use of documenting access of parking services, secure usage of parking houses and also to prevent car theft issues.

Future work

In the future work, to increase the accuracy in classification of the present work, more than one classifier and feature selection techniques can be combined to obtain a better result and to remove the false positives/negatives. Various types of automobile number plate can be classified by using digital image processing technique in the future.

Acknowledgements

The authors would like to acknowledge Dr Yin Maung Maung, Head of Department of Physics, University of Yangon, for his kind permission to carry out this research.

References

Anishiya.P. and S.Mary Joans, (1022), "Number Plate Recognition for Indian Cars Using Morphological Dilation and Erosion with the Aid of Ocrs", *International Conference on Information and Network Technology*, Vol 4, 115-119.

Al Faqheri.W and Mashohor.S, (2009), "A real-time Malaysian automatic license plate recognition(M-ALPR) using hybrid fuzzy", *IJCSNS International Journal of* Computer *Science and Network Security*, Vol. 9, 333-340.

Damayanti.F, S. Herawati, Imamah, M. Fifinb Ayu and A. Rachmad, (2019), " Indonesian license plate recognition based on area feature extraction","*TELKOMNIKA*", Vol.17, No.2,620-627.

Gonzalez.R. C and R.E.Woods, (2002), "*Digital Image Processing"*, 2nd Ed, Upper Saddle River, NJ: Prentice-Hall Senthilraja.

Kumar.M, (2009), "*A Real-Time Vehicle License Plate Recognition (LPR) System*", *THAPAR UNIVRSITY PATIALA.*

Sarfraz,M, M.J. Ahmed and S. A. Ghazi, (2003), "Saudi Arabian license plate recognition system, Geometric Modeling and Graphics Proceedings", International Conference on, IEEE 2003, 36-41.

Suresh.P and M.Suganthi, (2014),"*Noise Reduction in Computed Tomography*", International Journal of Scientific & Engineering Research, Vol-5, Issue 3.

COMPARISON OF SHIELDING STRENGTH FOR LEAD, COPPER AND ALUMINUM

Win Mar[1]

Abstract

Human safety and structural material that may be compromised from radiation exposure are vital concerns in nuclear technology. Gamma attenuation coefficient of shielding material is measured using a proper electronic system under condition of narrow beam geometry. The radiation shielding characteristics of three elemental materials were examined by using half thickness method. From the experimental data, it is found that while only 0.6cm thickness of lead is required to reduce the gamma photon intensity to half of its original value, about 1.2 cm of copper and 1.8 cm of aluminum. To achieve this goal, linear attenuation coefficient of these samples was calculated. It is cleared that lead has a far better absorber of gamma photon than copper and aluminum. In this research, comparing shielding strength of the three elemental materials, it is concluded that lead is the best as copper is the second and aluminum is the third.

Keywords*: attenuation coefficient, elemental materials, shielding materials, shielding strength.*

Introduction

Radiation is naturally present in our environment and exists since the birth of this planet. It comes from outer space (cosmic), the ground (terrestrial), and even from within our own bodies. It is present in the air we breathe, the food we eat, the water we drink, and in the construction, materials used to build our homes. Today, radiation refers to the whole electromagnetic spectrum as well as to the atomic and subatomic particles that have been discovered. One of the many ways in which different types of radiation are grouped is in terms of ionizing and nonionizing radiation. The ionizing radiations are commonly classified into two principal types. Directly ionizing radiations include radiations of energetic particles carrying an electric charge, such as beta particles, alpha particles, protons, and other recoil nuclei. They cause ionization by direct action on electrons in atoms of the media through which they pass. [2]

Another type of radiation, indirectly ionizing such as neutrons and x-ray or gamma-ray photons, are not charged and cause ionization through a more complicated mechanism involving the emission of energetic secondary charged particles which cause most of the ionization. Directly ionizing radiation interacts very strongly with shielding media and is therefore easily stopped. By contrast, indirectly ionizing radiation, may be quite penetrating and the shielding required may be quite massive and expensive. [2]

Gamma Ray Shielding as Elemental Materials

Shielding remains an important aspect of radiation physics. Radiation shielding is very pertinent in nuclear industries as well as in radioisotopes production and usage, and in particle accelerator facilities. Materials for shielding gamma rays are typically measured by the thickness required to reduce the intensity of the gamma rays by one half (the half value layer $t_{1/2}$). The knowledge of this thickness is an indication of the minimum thickness we have to use in order to ensure appreciable protection from that source. The shielding efficacy of the three metallic materials; Copper, Aluminum and Lead have equally been compared. [1]

There are some basic principles for radiation shielding. The type and amount of shielding required depend on the type of radiation, the activity of the radiation source and the dose rate that

[1] Professor & Head, Department of Physics, Kalay University.

is acceptable for outside the shielding material. However, there are other factors for choice of shielding material such as their cost and weight. The good shielding material should have high absorption cross-section for radiation and at the same time irradiation effects on its mechanical and optical properties should be small. A number of experimental and theoretical works have been performed on radiation shielding, which has large different application areas with different materials (e.g. concrete, semi-conductor, lead, copper and aluminum etc.) A study of absorption of gamma and neutron radiations in shielding materials has been an important subject in the field of radiation physics. [1]

Radiation attenuation

The attenuation coefficient of gamma rays was determined by measuring the fractional radiation intensity N_x passing through the thickness x as compared to the source intensity N_0. The linear attenuation coefficient (μ) has been obtained from the solution of the exponential form: [1]

$$N_x = N_0 e^{-\mu x} \qquad (1)$$

Half-value layer (HVL) is the thickness of an absorber that will reduce the gamma-radiation to half. This is obtained by using the following equation: [1]

$$x_{1/2} = \frac{\ell n 2}{\mu} \qquad (2)$$

Some properties of Elemental Materials

Lead had a particularly high density, 11.3gcm^{-3} compared with many other metals (e.g iron 7.8gm^{-3}, copper 8.9 gcm^{-3}, aluminum 2.7 gcm^{-3}, Lead owes its high density to two factors: Its high atomic number and hence high relative atomic mass of 207, the metal atoms (or, more precisely, ions) are arranged in a dense, close packed structure (face centered cubic structure).The high density of lead has important bearings on other properties, particularly attenuation of X-rays gamma rays and sound waves. Some properties of lead, copper and aluminum are shown in Table (1). [4]

Table 1 Some Physical Properties of Lead, Copper and Aluminum

Physical Properties	Pb	Cu	Al
Density (g/cm^{-3})	11.34	8.96	2.70
Atomic number	82	29	13
Atomic weight	207.19	63.54	26.98

Experimental setup

Source for Gamma Ray

In the present work, gamma source Cs-137 forms gamma disc shape from Nuclear Lab in University of Yangon is chosen ^{137}Cs has one energy. It has an activity of 5μCi, half-life is 30.17 years and energy of the source is 0.662 MeV.

Sample Collection and Sample preparation

Three elemental materials, aluminium, copper and lead were collected in Yangon Division. Aluminium and copper sample has a thickness of (0.1) cm and area has (5.4×5.4) cm^2. Lead sample has a thickness of (0.1) cm and area has (7.4×7.4) cm^2.

Equipment

In the present work, the equipments used in gamma ray spectrometry were described as:

- Thallium Activated Sodium Iodide detector (Model 802.5)
- High Voltage Power Supply (Model 3002)
- ST-360 Radiation Counter with Windows (Model ST-360) and Macintosh Software Electronic setup of NaI (TI) detector system for γ-ray spectrometry in the forms of narrow beam is used. Detector transforms the radiations energy into electronic pulses: the preamplifier followed up these pulses by making impedance matching and put into the main amplifier. The operation of the main amplifier is amplifying, shaping and rejecting the pulses and feeding to the analog to digital converter portion of ST-360 RC. Finally is generates number of counts.

Experimental set up and procedure

The three elemental material were used as absorbers for gamma radiation. These samples were placed midway position between the source and detector. The detector was placed horizontally and the distance between the source and detector was 20 cm. The Cs-137 source was fixed in the lead shield. First the gamma intensity I_0 (in the absence of the shield sample) was used. Then, the sample position was placed at the centre of the source and detector. The detector was located forward direction of gamma beam. The above procedures were repeated for three types of elemental shield sample.

The transmitted gamma counts collection was done for 100s. Detector working voltage is 900V(positive bias). For each thickness of elemental shield sample, the gamma intensity reaching the detector was measured and the results obtained were recorded.

Gamma Rays Transmitting Measurement

Gamma ray's transmission was measured at the direction normal to the specimen, used with 5μCi of Cs-137. The absorption type operates in such a way that the radiation source and they were usually located in the different sites of the object to be measured. The detector in the lead shield was placed 20 cm from the source. Firstly, the intensity of gamma ray which pass through (without absorber of shield sample) was collected, and then passing through with absorber. The net count was recorded and the graphs were plotted for different thickness of various elemental shield samples. From the graph, the thickness of each sample which reduces the gamma photon intensity to half of its original value was obtained. And then the linear attenuation coefficients for three types of elemental shield samples were calculated by using equation (2).

The standard error of counting rates

The determination of error associated with the measurement is a very important task. It is probably as important as the measurement. So, to reduce the error in the research work, the standard error of counting rate for different thickness of each sample are calculated by using equation (3). The calculated values are recorded in Table (2), (3) and (4). [3]

In practice, the number of counts is usually recorded in a scalar, but what is reported is the counting rate, i.e. counts recorded per unit time. The following symbols and definitions will be used for counting rates. [3]

G = number of counts recorded by the scalar in time t_G with the sample present

= gross count

B = number of counts recorded by the scalar in time t_B without the sample

= background count

$g = \frac{G}{t_G}$ = gross counting rate

$b = \frac{B}{t_B}$ = background counting rate

r = net counting rate = $\frac{G}{t_G} - \frac{B}{t_B}$ = g-b

The standard error of the counting rate,

$$\sigma_r = \sqrt{\frac{G}{t_G^2} + \sqrt{\frac{B}{t_B^2}}} \qquad (3)$$

The standard error of the average counting rate is

$$\sigma_{\bar{r}} = \frac{1}{N}\sqrt{\sum_{i=1}^{N}\sigma_{r_i}^2} = \frac{1}{N}\sqrt{\sum_{i=1}^{N}\left(\frac{G_i}{t_G^2} + \frac{B_i}{t_B^2}\right)}$$

$$= \frac{1}{N}\sqrt{\frac{G_i}{t_G^2} + \frac{B_i}{t_B^2}} \qquad (4)$$

For many the background rate is negligible compared to the gross counting rate

$$\sigma_{\bar{r}} = \frac{1}{N}\frac{\sqrt{G}}{t_G} \qquad (5)$$

Results, Discussion and Conclusion

Results

The transmission data of without absorber, with absorber and net count rate of different thickness for lead absorber is described in Table (2). The transmission data of without absorber, with absorber and net count rate of different thickness for copper and aluminum are also described in Table (3) and (4). The standard error of each counting rate for three samples are calculated by using equation (3) and then recorded in Table (2), (3) and (4).

Figure (1) shows the relationship between exponential decrease of gamma photon net count rate versus the different thickness of elemental materials (lead, copper and aluminum absorber). In the research work, from Figure (1), the thickness of lead, copper and aluminum that requires to reduce the gamma photon intensity to half its original value are obtained 0.6cm, 1.2cm and 1.8 cm. The half thickness of lead, copper and aluminum absorber are recorded in Table (5). The linear attenuation coefficient for lead absorber is calculated by using equation (2) and is obtained 1.16 cm^{-1}. The linear attenuation coefficient of copper and aluminum are also calculated by using equation (2) and are obtained 0.58 cm^{-1} and 0.39cm^{-1}. The standard error of the average counting rate for three elemental materials is calculated by using (5).

In the present work, the linear attenuation coefficient and standard errors 1.16±0.31cm^{-1} for lead, 0.58±0.23cm^{-1} for copper and 0.39±0.22cm^{-1} for aluminum and are recorded in Table (5).

From the Figure (1), the graph of lead has very sharp exponential decrease of gamma photon; the graph of copper has second and aluminum has third. In three elemental materials, lead is better shield because it requires just a few thicknesses of it to reduce the photon intensity to half its original value, then follow by copper and aluminum being the least. In comperes of linear attenuation coefficient for three elemental materials, lead is most, copper is the second and aluminum is the third. In this research, lead is far better of gamma photon when compared to copper and aluminum. Copper is a better absorber than aluminum.

Discussion

Shielding remains an important aspect of radiation physics. Radiation shielding is very pertinent in nuclear industries as well as in radioisotopes production and usage and in particle accelerator facilities.

Materials for shielding gamma rays are typically measured by the thickness required to reduce the intensity of the γ-rays by one half (the half value layer, HVL). In the improved shielding calculations, the thickness of the materials used in the shielding, the minimum thickness that could give us the maximum shielding from the emitting source, or even 99%.

The knowledge of thickness us an indication of the minimum thickness we have to use in order to ensure appreciable protection from the source. It is clearly seen that, lead that minimum thickness and most linear attenuation coefficient is the best gamma shielding strength then follow by copper and aluminum being least.

Table 2 The gross count, net count and net count rate for increasing lead absorb thickness

Sr No.	Absorber thickness (cm)	Gross count (G)	Net count	Net count rate (r) C/s
1	0	10823	7334	73.34±1.20
2	0.1	9989	6500	65.00±1.17
3	0.2	9339	5850	58.50±1.15
4	0.3	8639	5150	51.50±1.12
5	0.4	8089	4600	46.00±1.10
6	0.5	7589	4100	41.00±1.08
7	0.6	7156	3667	36.67±1.06
8	0.7	6749	3260	32.60±1.05
9	0.8	6409	2920	29.20±1.03

Table 3 The gross count, net count and net count rate for increasing copper absorber thickness

Sr No.	Absorber thickness (cm)	Gross count (G)	Net count	Net count rate (r) C/s
1	0	9078	7334	73.34±1.04
2	0.1	8644	6900	69.00±1.02
3	0.2	8244	6500	65.00±0.99
4	0.3	7894	6150	61.50±0.98
5	0.4	7544	5800	58.00±0.96
6	0.5	7244	5500	55.00±0.95
7	0.6	6914	5170	51.70±0.93
8	0.7	6614	4870	48.70±0.91
9	0.8	6394	4650	46.50±0.90
10	0.9	6124	4380	43.80±0.89
11	1.0	5864	4120	41.20±0.87
12	1.1	5664	3920	39.20±0.86
13	1.2	4689	3667	36.67±0.80

Table 4 The gross count, net count and net count rate for increasing aluminum absorber thickness

Sr No.	Absorber thickness (cm)	Gross count (G)	Net count	Net count rate (r) (C/s)
1	0	8360	7334	73.34±0.97
2	0.2	7826	6800	68.00±0.94
3	0.4	7326	6300	63.00±0.91
4	0.6	6876	5850	58.50±0.88
5	0.8	6426	5400	54.00±0.86
6	1.0	6026	5000	50.00±0.84
7	1.2	5676	4650	46.50±0.82
8	1.4	5316	4290	42.90±0.80
9	1.6	4976	3950	39.50±0.77
10	1.8	4689	3667	36.67±0.76
11	2.0	4426	3400	34.00±0.74
12	2.2	4176	3150	31.50±0.72

Table 5 The shielding strength [Atomic Mass, Half Value Layer (HVL) and Linear Attenuation Coefficient, (μ))] of three elemental materials

Sr No	Elemental Material	Atomic Mass	Half Value Layer (HVL) (cm)	Linear Attenuation Coefficient (μ) (cm^{-1})
1	Lead (Pb)	82	0.6cm	1.16 ± 0.31
2	Copper (Cu)	29	1.2cm	0.58 ± 0.23
3	Aluminum (Al)	13	1.8cm	0.39 ± 0.22

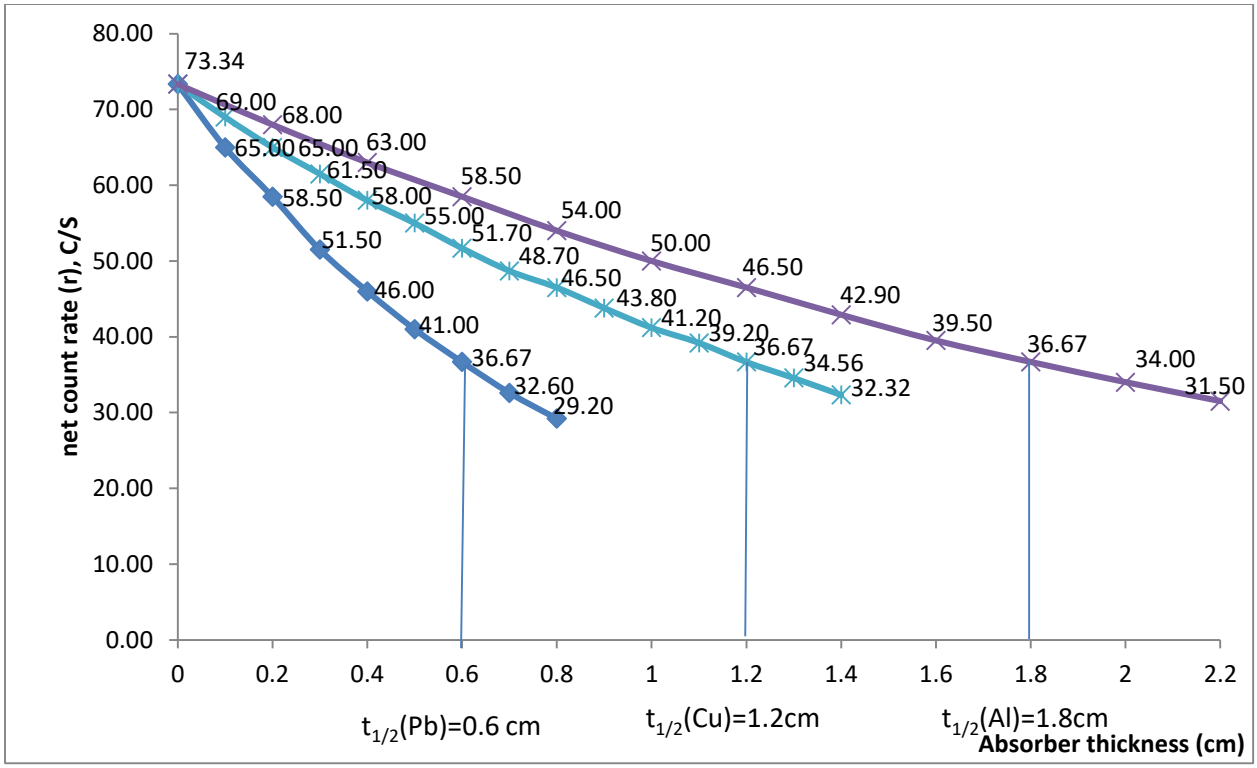

Figure 1 Exponential decrease of gamma photon net count rate versus different thickness of elemental metals

Conclusion

Radiation shielding against high energy photons is based on materials with high atomic number and high density that are known to absorb and attenuate ionizing radiation emitted from natural, human-made sources and radiation producing devices.

Effective of shield depends upon energy of radiation, thickness and type of the shielding materials. The higher atomic number and density of shielding materials, the more effective it is in reducing intensity of gamma radiation.

Lead was a very common shielding materials used to shield gamma radiation as it can reduce gamma particle. High gamma absorption cross section and high atomic number properties of lead enable it to be very effective in shielding γ and X radiations.

In this research, the half value layer and linear attenuation coefficient for three elemental materials were experimentally investigated.

It is clearly seen that the highest atomic number of leads is the best then followed by copper and aluminum being the least are remarkably effective for shielding gamma rays. It is concluded that, the shielding strength are most for lead, more for copper and less for aluminum in gamma radiation.

Acknowledgement

The author would like to express my gratitude to Ministry of Education, the department of Higher education in Myanmar, University of Yangon, and Universities' Research Centre (URC) for all necessary facilities.

References

1. Celiktas C.,2011. A method to determine the gamma-ray linear attenuation coefficient. *Ann Nucl Energ 38:5.*

2. James E M., 2004. Physics for radiation protection: A Handbook; WILEY-VCH Verlag GmbH & Co. KGaA, Weinheim.

3. Knoll G F.,2000. Radiation detection and measurements;third edition; John Wiley and sons .

4. Hubbell J H., Seltzer S M., Tables of photon attenuation coefficients and mass absorption coefficients 1keV to 20 MeV for Elements Z=1 to 92 and 48 Additional Substances of Dosimetric Interest, NIST, Gathersburg, MD.

DETERMINATION OF EFFICIENCY AND ENERGY RESOLUTION OF SCINTILLATION DETECTOR IN 511-1332 keV ENERGY RANGE

Yin Thuzar Thein[1], U Win[2]

Abstract

The most radiation detection method is based on the gamma – ray Spectrometry measurement, which is widely used in different fields. To obtain accurate analytical results in an experimental research, quality control of the detection system is important. Detection efficiency and energy resolution of NaI(Tl) scintillation detector are fundamental parameters for detection system. In this work, detection efficiency and energy resolution of 2″ x 2″ NaI(Tl) detector were experimentally measured using ^{22}Na, ^{60}Co and ^{137}Cs standard radioactive sources at the energy range of 511 keV to 1332 keV.

Keywords: Scintillation detector, Energy resolution, Detection efficiency, Gamma ray spectrometry

Introduction

In gamma ray Spectrometry measurements, NaI (Tl) scintillation detectors have been widely used in variety of different fields such as neutron activation analysis technique, nuclear reactor technology, elemental analysis of different alloys, nuclear medicine, industry, radiation protection and environmental applications [Vrkiye Akar Tarim, Orhan Gurler, 2018].

Especially, NaI (Tl) detectors used to make qualitative and quantitative analysis with various natural and artificial radionuclides. In each application, the accurate values of detection efficiency and energy resolution of NaI(Tl) detector is essential in nuclear investigations and in all experimental studies that measure radiation.

Every resolution and detection efficiency system depends on the energy of gamma rays, detector type, density and size, detector and source dimensions, detector and source geometry and different detector operating parameters [Karadeniz and Vurmaz,2017].

The necessary calibration corrections were applied to improve the quality of radioactivity measurements. In this study, efficiency and energy resolution of the 2″x2″ NaI(Tl) detector were measured experimentally at 511.0 keV, 661.66 keV, 1173.23 keV,1274.60 keV and 1332.48 keV gamma ray energies obtained from ^{22}Na,^{60}Co and ^{137}Cs standard radioactive isotopes.

Materials and Method

Experimental Procedure

In this research work, NaI(Tl) scintillation detector (Type 38B51 2″x 2″), multi-channel analyzer (13727 – 99), serial S2AA6691 and high voltage power supply 1.5 kV DC (09107 – 99) were used. By using the measure software for the spectrum analysis; peak searching, peak area calculation, energy calculation, peak evaluation and data acquisition. To reduce the background of detecting system, the detector is shielded with 3 cm thick lead on all sides.

Block diagram for γ- ray spectroscopy system with NaI(Tl) detector is shown in Figure 1. The three different standard radionuclides ^{22}Na, ^{60}Co and ^{137} Cs were used in this work. The distance between source and detector is 4 cm. Optimum voltage is 650 V and kept constant throughout the experiment. The time taken for data acquisition was 300 seconds or 5 minutes.

[1] Dr, Lecturer, Department of Physics, Dagon University
[2] Dr, Professor (Head), Department of Physics, Dagon University

Table 1 showed gamma ray emission probabilities per decay, half-life, decay fraction and present activity for all radioisotope sources used in this work. The energies, emission probabilities and decay fractions were taken from International Atomic Energy Agency (IAEA) Nuclear Data Services [Vrkiye Akar Tarim,et al,2018].

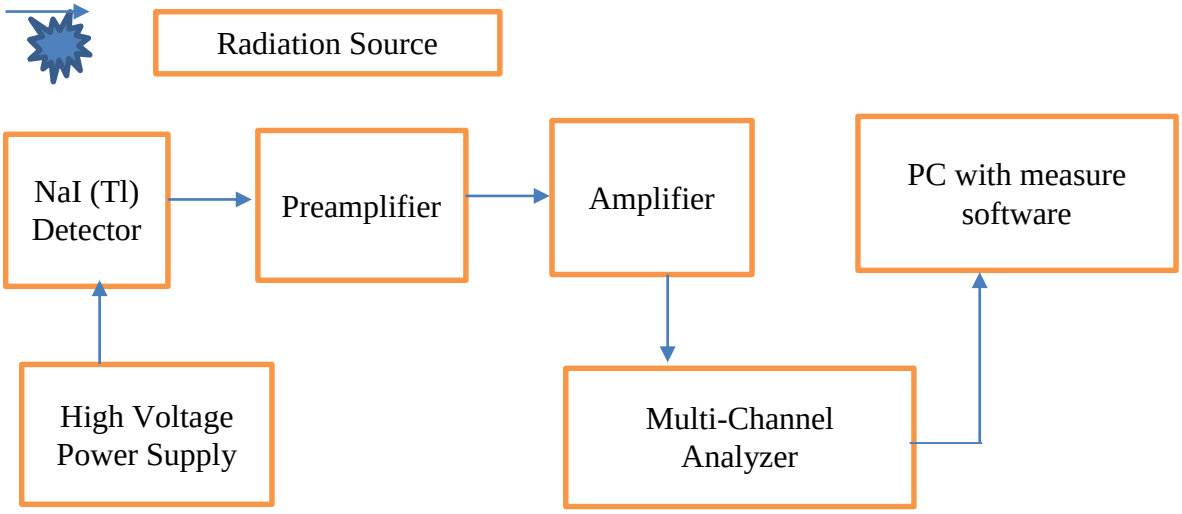

Figure 1 Schematic diagram of the experimental setup

Table 1 Specifications of the radionuclides

Nuclide	Gamma Energy (keV)	Half-life (year)	Present Activity (μ Ci)	Decay fraction (*f*)	Emission Probability (%)
^{22}Na	511	2.6	2.0114	0.99	99.00
	1275			0.9994	99.94
^{137}Cs	662	30.1	4.6218	0.851	85.00
^{60}Co	1173	5.27	0.6381	0.9985	99.85
	1332			0.9986	99.982

Energy Calibration

Firstly, the detector system was calibrated before using in measurement of gamma radiation detection. In this research work, the energy calibration is performed by measuring 661.66 keV photopeak from ^{137}Cs and the 1173.23 keV and 1332.48 keV photopeak from ^{60}Co standard sources. Acquire the spectra for both the sources for preset time is 300 seconds. For the 1024-channel setup, MCA setting gain level is 1, offset [%] is 5, interval width [channel] is 1. Do not change the calibration process of NaI(Tl) detector in the whole experiment. Energy calibration of the NaI(Tl) detector was occasionally made to establish the linking between the energy, channel number, detector efficiency, energy resolution and in order to convert channel number to energy scale. Figure 2 shows energy calibration curve which is plotted by energy of gamma – rays with the pulse – height corresponding to the photo – electrons from different gamma sources. In this diagram, the pulse – height is proportional to the energy and use to correlate channel number to energy for any source. The measured typical gamma ray spectrum for ^{137}Cs, ^{60}Co and ^{22}Na radionuclides are shown in Figure 3, 4 and 5.

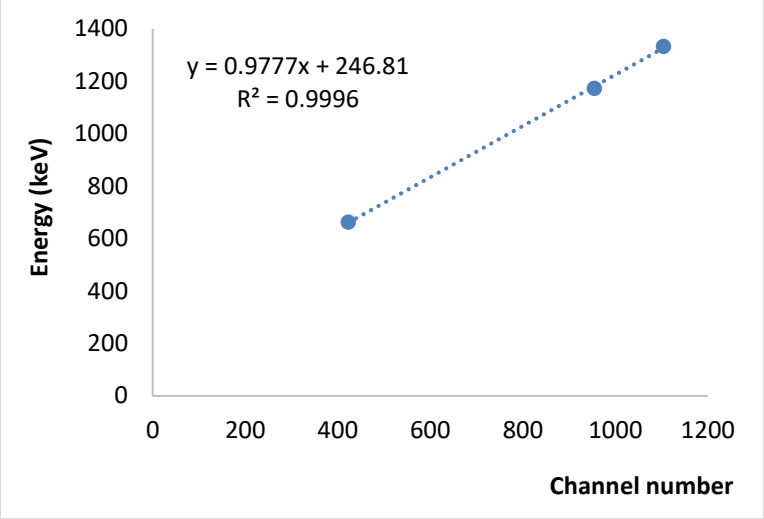

Figure 2 The energy calibration curve for NaI(Tl) using ^{60}Co and ^{137}Cs nuclides

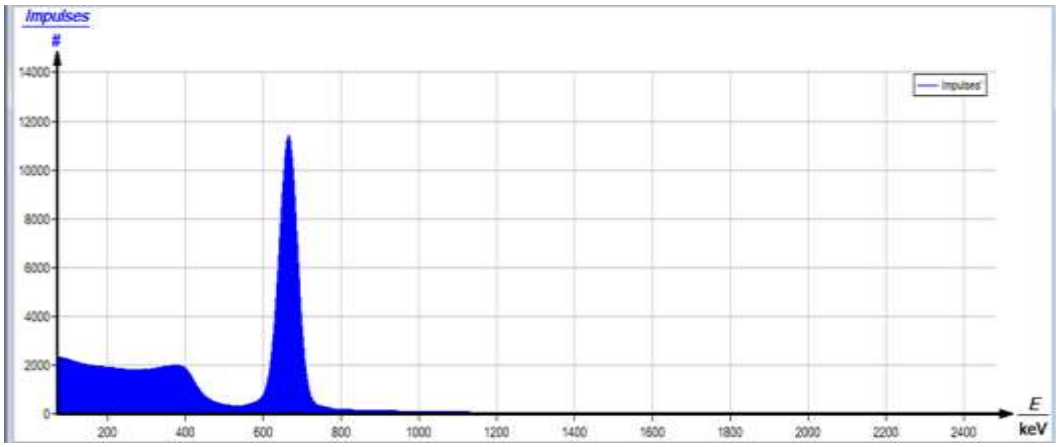

Figure 3 Typical ^{137}Cs spectrum measured using NaI(Tl) detector

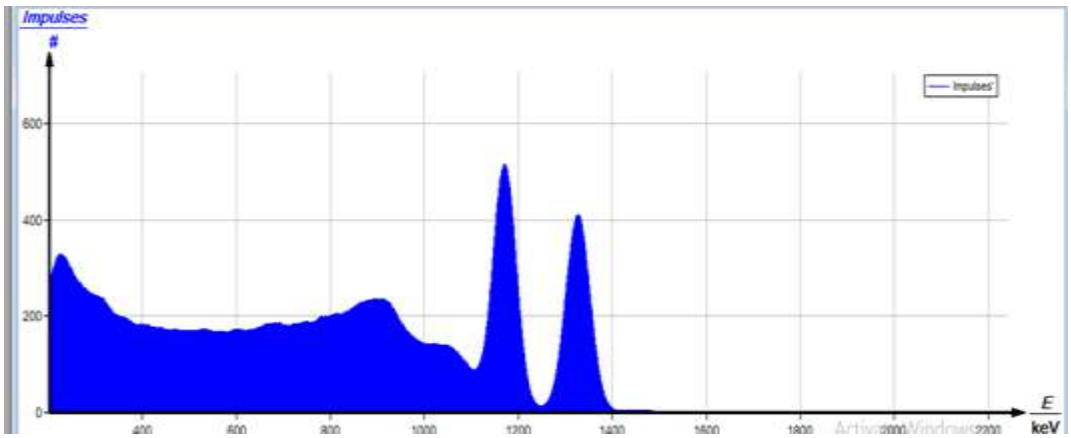

Figure 4 Typical ^{60}Co spectrum measured using NaI(Tl) detector

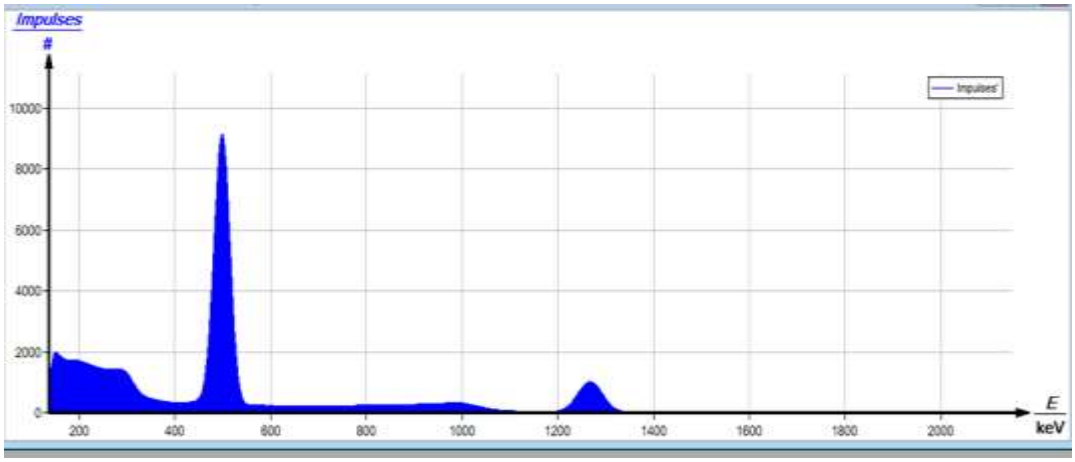

Figure 5 Typical ^{22}Na spectrum measured using NaI(Tl) detector

Energy Resolution

Energy resolution is a very important parameter to avoid the interference between two gamma ray energies from gamma source and it is the ability of the detector to accurately determine the energy incoming gamma radiation. Energy resolution depends on the detector type and the energy of gamma photons and allows a detector to differentiate between primary photons and Compton scatter photons. The experimental formula for determining the percent energy resolution is

$$\%\, Energy\ resolution = \frac{E_2 - E_1}{E_0} \times 100$$

$E_2 - E_1 = \Delta E$ is full Width Half Maximum (FWHM), E_0 is gamma energy. The FWHM is denoted by the symbol "r" and it is the width of the Gaussian distribution at half of its maximum position. The gamma ray spectrums were counted for three standard sources and from which FWHM is estimated by using measure software. The experimental data is given in table 2 [Pansare, Ansari, et al,2016].

Detector Efficiency

$$DE = \frac{D}{N} \qquad \text{(or)}$$

$$\varepsilon(\%) = \frac{A_{out}}{A_{in}} \times 100$$

DE is the detector efficiency; D is the number of pulses recorded by the detector and N is the number of radiations emitted by the source. A_{out} is the number of counts recorded by the detector and A_{in} is the number of gamma rays falling on detector. A_{in} can be calculated by using the equation,

$$\mathrm{A}_{in} = \frac{r^2}{4d^2} \times A_t.$$

$\frac{r^2}{4d^2}$ is geometrical factor, d is the distance between source and detector, r is the radius of detector, A_t is activity of radioactive nuclide and it can be calculated by using equation,

$$A_t = A_0\, e^{-\lambda t}.$$

A_0.is initial activity at t = 0, λ is decay constant and t is the time difference between experiment date and source manufacture date [Pansare, Ansari, et al,2016].

Results and Discussion

The detection efficiency of the NaI(Tl) detector was determined experimentally at 511,662,1173,1275 and 1332 keV gamma ray energy emitted by ^{22}Na, ^{60}Co and ^{137}Cs radioactive sources. The measured results were shown in Table 2 and have been displayed as a function of gamma energy in Figure 6. From Figure 6, the detector efficiency is high in the low energy region and decreases with increasing energy. This is because of decreased in the number of photoelectric events and increased Compton scattering when energy increases. In Figure 6, the experimental data points were fitted a second-degree polynomial equation using measure software. It gives a good description with the correlation between the efficiency values and the gamma ray energies, which is about $R^2 = 0.9984$.

Another important parameter for detection system is energy resolution, obtained from the full width at half its maximum (FWHM). The values of FWHM and energy resolution for the NaI(Tl) detector is listed in Table 2. Figure 7 is displayed as a function of gamma ray energy with measured energy resolution of the NaI(Tl) detector. From this figure, the energy resolution of the NaI(Tl) detector decreased with increasing in gamma energy.

Table 2 Experimental results for efficiency, FWHM and resolution of NaI(Tl) detector

Nuclide	Gamma Energy(keV)	Efficiency (%)	FWHM (keV)	Resolution (%)
^{22}Na	511	9.35	42.02152	8.22338
^{137}Cs	662	7.42	47.65	7.19788
^{60}Co	1173	3.32	59.08165	5.03679
^{22}Na	1275	2.51	58.87	4.618
^{60}Co	1332	2.458	58.329	4.37905

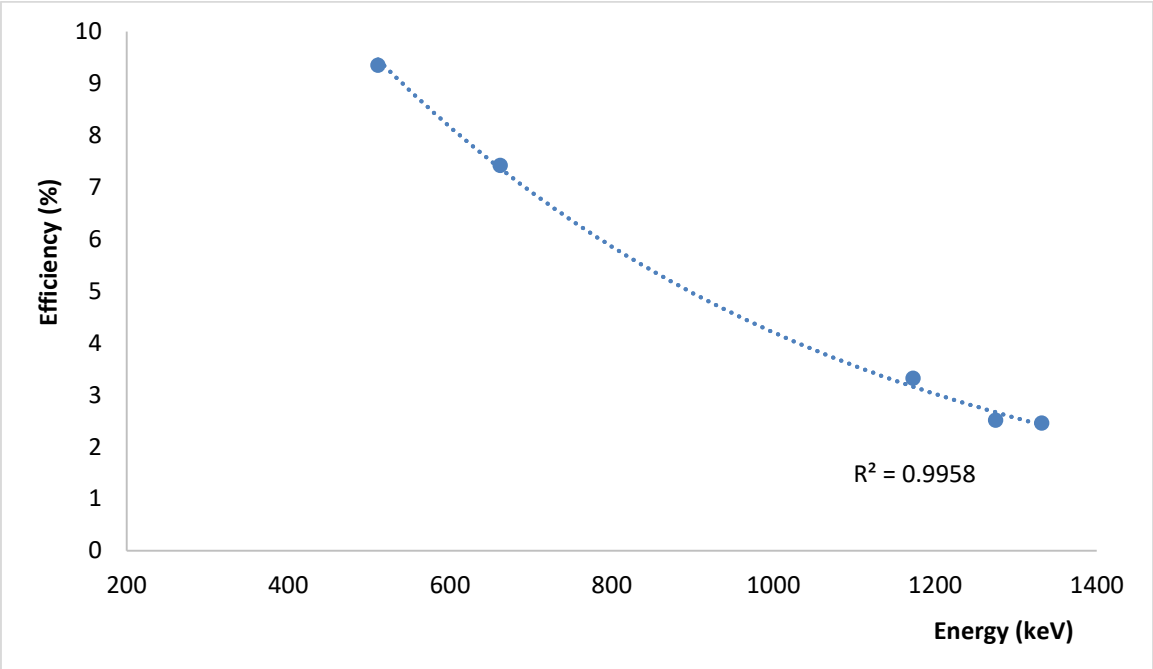

Figure 6 Variation of detector efficiency as a function of different energies

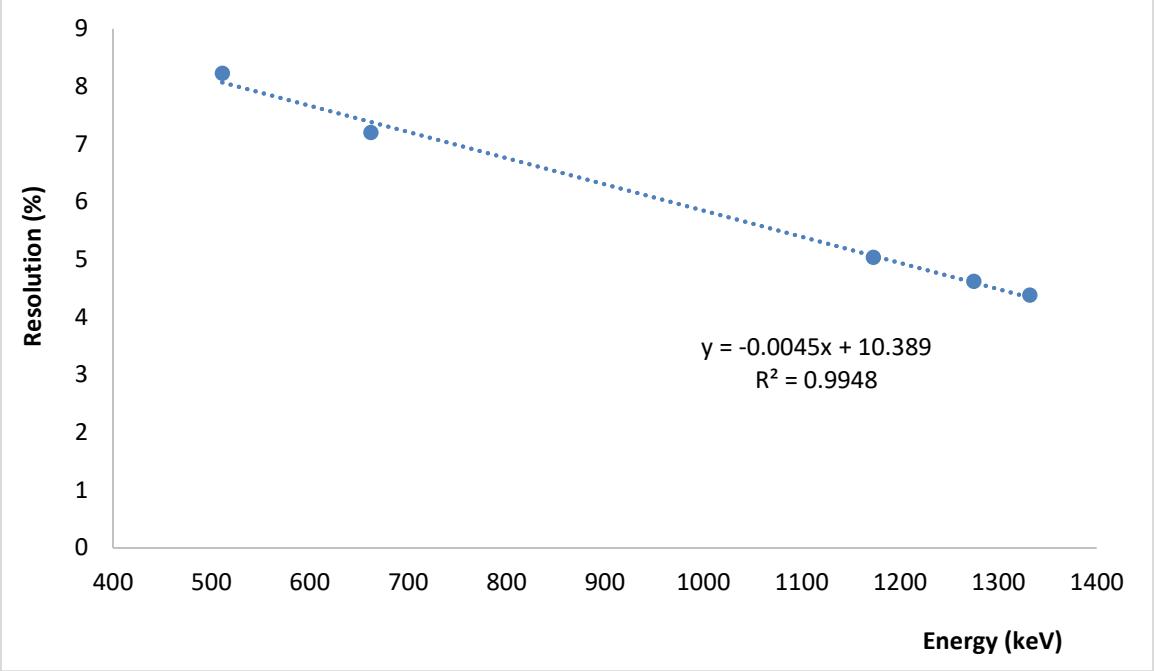

Figure 7 Energy resolution of the NaI(Tl) detector

Conclusions

In this research work, detector efficiency and energy resolution of the NaI(Tl) detector was determined experimentally by using gamma ray spectrometry measurement in 511 keV to 1332 keV energy range. The values of detection efficiencies for these energies are 9.35%, 7.42%, 3.32%, 2.51% and 2.458% respectively. The values of energy resolution for these five energies are 8.22338%, 7.19788%, 5.03679%, 4.618% and 4.37905%. The results were found that the resolution of the detector was directly proportional to the energy of gamma ray and its efficiency was exponentially proportional to the gamma ray energy. These two factors depend on the gamma ray energy, detector type, size and other detector parameters. So, determination of detector efficiency and energy resolution of the NaI(Tl) detector is essential to specify the quality for the results of gamma ray spectrometry measurements.

Acknowledgements

I would like to express my sincere gratitude to Professor Dr U Win, Head of Department of Physics, Dagon University, for his kind permission.

Many thanks are also due to my teachers, colleagues and friends from nuclear laboratory, Department of Physics, Dagon university for their advices and efforts in this research.

References

Akkurt I., K. Gunoglu, and S.S, Arda, (2014)" Detection Efficiency of NaI(Tl) Detector in 511 -1332 keV energy Range". Publishing Corporation Science and Technology of nuclear Installations, Turkey, Volume 2014, 1-5.

Casanovas R., J.J. Morant and M. Salvado. (2012)."Energy and resolution calibration of NaI(Tl) and LaBr3 (Ce) Scintillators and validation of an EGS5 Monte Carlo user code for efficiency calculation". Nuclear Instruments and Methods in Physics research A,675,78-83.

Debertin K. and R.G. Helmer, (1988)"Gamma and X-ray Spectrometry with Semiconductor Detector",North – Holand.

Karadeniz O. and S.Vurmaz,(2017) "Experimental investigation on the photopeak efficiency of a coaxial high purity Germanium detector for different geometries". Journal of Basic and Clinical Health Sciences,1 18-22.

Pansare G.R., S.J. Ansari and U.R. Kamthe,(2016)" Measurement of energy resolution and detection efficiency of NaI(Tl) scintillation gamma gay spectrometer for different gamma gay energies". Research Journal of Material Science, India, Vol.4(4), 7-12.

Su Su Win, Nyein Nyein, Nyi Nyi Tun, (2020)" Determination of Resolution and Detection Efficiency of NaI(Tl) Scintillation Gamma – Ray Spectrometer". University of Mandalay, Research Journal, Vo..11, 162-168.

Vrkiye Akar Tarim,Orhan Gurler, (2018)" Source – to – Detector Distance Dependence of Efficiency and Energy Resolution of a 3″ x 3″ NaI (Tl) Detector". European Journal of Science and Technology, Turkey, No.13,pp.103-107.

STRUCTURAL, MICROSTRUCTURAL AND NON - OHMIC BEHAVIOUR OF ZnO BASED VARISTORS WITH FIVE ADDITIVE OXIDES

Pwint Yi Thein[1], Thandar Win[2], Yin Yin Swe[3] and Mar Mar Myint[4]

Abstract

ZnO based varistors with 5 additive oxides Bi_2O_3, Cr_2O_3, Co_3O_4, MnO_2 and Sb_2O_3 are prepared and characterized in this research work. Standard varistor processes, known as weighting, ball milling, mixing with distilled water, pre heat treatment, secondary ball milling, seiving, sintering, pressing into circular shape disc, electroding and reheating processes are carried out to obtain the varistors with desired stoichiometric compositions. XRD technique is used to examine the structural features of prepared varistors. It is obvious that a little change of lattice dimensions is obtained. But there are no significant change of hexagonal, wurtzite ZnO structure after addition of additive oxides. Microstructural features of prepared varistors are characterized with the help of SEM. From the SEM images, it is noticed that irregular micro grains are uniformly distributed and there are no cracks. Further, average grain size slightly increases with increasing composition " x " in prepared varistors. Non - ohmic behaviour of prepared varistors are studied by using the high voltage DC power supply. From the ln V vs. ln I variations, non linearity factor, threshold voltage and leakage current are estimated. It is observed that non linearity factor slightly increases as composition " x " increases, on the other hand, threshold voltage and leakage current decrease when the composition " x " is raised. The transition metal oxides are involved in formation of interface states and deep traps in host matrix ZnO and both of which are contributed to high - non ohmic behaviour. Additive oxides, used in this study are known to be non - linearity enhancers and inducers. Threshold voltage is affected by the numbers of grain boundaries across the series between the two electrodes and inversely proportional to grain size. In this study, average grain size slightly increases with composition " x " in prepared varistors and that leads to lower the threshold voltage. The higher the non - linearity factor affects the lower the leakage current and the better the performance of varistor. It can be concluded that, prepared varistors can be used as transient surge voltage protection device.

Keywords: varistor, additive oxides, XRD, SEM, non - ohmic behaviour.

Introduction

Research activity in the area of ZnO based ceramics has been traditionally fueled by the need for ideal candidate as intrinsic voltage regulator in the context of circuit protection. Consequently the wide range of doped ZnO based systems have been studied. It is well known that the ZnO varistor is controlled essentially by the dopant additives, usually metal oxides and the dopants are responsible for the formation of varistor behavior. It is believed that, the dopants play an important role to modify the defect concentration at the ZnO grain and / or of grain boundary where the performance of ZnO is sensitive to the some additives even when the amount is very small [Levinson L. M. and Phillip H. R. 1975].

The structure of metal oxide varistor (MOV) consists of a matrix of conductive ZnO grains separated by the grain boundaries providing P - N junction semiconductor characteristics. These boundaries are responsible for blocking conduction at low voltages and are the source of the non - linear electrical conduction at high voltages.

Varistors are inherently polycrystalline, multi junction grain boundary devices, that can absorb transient surge voltage and serve to protect electronic and electrical circuit components. The voltage surges are induced by power switching and electromagnetic pulses. Varistors are ceramic elements whose I - V characteristics is highly non - linear [Bialek T., 1999]. The varistors are usually manufactured in the ceramic process, in which pressed zinc oxide with admixture of

[1.] Professor, Department of Physics, Nationality Youth Resources Development Degree College Yangon, Myanmar
[2,4.] Lecturer, Department of Physics, Nationality Youth Resources Development Degree College Yangon, Myanmar
[3] Associate Professor, Department of Physics, Nationality Youth Resources Development Degree College Yangon, Myanmar

other metallic oxides is sintered. A matrix made of ZnO grains enclosed by an intergranular layer composed of dissolved oxides admixtures form the obtained microstructure [Emtage P. R., 1977; Mah an G. D., 1983 ; Cao Z. C. et al., 1994 ; Sun H. T. et al., 1993].

The primary constituent of varistor is ZnO, typically 80 mol % or more. In addition to ZnO, varistor contains the smaller amounts of a numbers of other additive oxides. A typical composition contains 97 mol % ZnO, 1 mol % Sb_2O_3, and 1/2 mol % each Bi_2O_3, CoO, MnO and Cr_2O_3 [Masuoka M. et al., 1969; Masuoka M., 1971].

In this research work, ZnO based varistors with 5 additive oxides Bi_2O_3, Cr_2O_3, Co_3O_4, MnO_2 and Sb_2O_3 are prepared by solid state sintering. X - rays diffraction studies are used to examine the structural features of prepared varistors. Microstructural properties of prepared varistors are investigated with the help of SEM technique. Non – ohmic behaviour of prepared varistors are characterized by using high voltage DC power supply.

Experimental Detail

In this study, analar grade II - VI compound semiconductor ZnO and five additive oxides, Bi_2O_3, MnO_2, Co_3O_4, Cr_2O_3 and Sb_2O_3 were chosen as starting precursors. Bi_2O_3 play the essential role on varistor effect by providing the high non - linearity of current - voltage characteristics. It is also reported that Bi is located between ZnO electrically conductive granules, ensuring electrical insulation. Co_2O_3 are oxides indispensable for obtaining the strong non - linear characteristics. The role of MnO_2 and Cr_2O_3 is to dope ZnO granules and thus to remove the Fermi level and modify the ZnO structure of space load and facilitating the reduction of potential barrier height. Sb_2O_3 has a role of fixing Bi_2O_3 at high temperature and thus limit the size of ZnO granules [Frigura - Llisa F. M. et al., 2019]. In this way, the threshold voltage is set for certain height of barrier pocket. Starting precursors, ZnO and 5 additive oxides were weighted by the following stoichiometric compositions:

$$(1 - x)\ ZnO + (2.x)\ Bi_2O_3 + (2.x)\ MnO_2 + (2.x)\ Co_3O_4 + (2.x)\ Cr_2O_3 + (2.x)\ Sb_2O_3,$$

where x = 0.01, 0.02, 0.03, 0.04 and 0.05 respectively. Precursor weighting was performed with an electronic balance, which can accurately weigh more than 0.01 milligram. The weighting operation was relatively simple because of all oxides were delivered in the form of powders, for which granulometry was well determined. Homogenization of mixture of oxides, milling was necessary to facilitate. After weighting, the oxides were milled in ball milling process for each 5 hrs. The mixing operation was made much easier in liquid phase by addition of distilled water.

The resulting materials in previous step were viscous and dried over the heated plate (~ 200^{o}C) for each 3 hrs. This step was carried out with the help of thermostatic oven. After this operation, the resulting powder had a non - uniform grain size. Therefore it must be milled again by ball milling process for each 5 hrs. Ball milling process had led to acceptable granulation and sieving with 400 mesh sieve, was carried out in order to separate the granules from the powder with the size greater than 200 μm. After that, sintering process (at 1100^{o}C) was carried out to all samples for each 5 hrs.

Then a slow cooling down to ambient temperature occurred. At this high temperature, the physicochemical knowledge of processes inside the varistor was still imperfect. The variator' s heating was obviously uneven, being more important at the surface than in the center. Regardless the chemical composition of the varistors, in the industry thermal cycle parameters were the same.

After the samples were sintered, the powder samples were pressed with the 20 - tons press into circular shape disc with 20 cm in diameter and 3.5 mm in thickness. A conductive pastes, based on Ag were deposited onto both surface of the circular shape discs, where the cross sectional

area of electrode was A = 7.0695 mm^2. Cu electrodes were attached to those surfaces and the varistors were reheating at 600^oC for each 3 hrs, known as varistor reheating process. At this stage, removal of the solvent and polymerization on the surface of the electrodes were carried out.

X - rays diffraction studies were used to determine the prepared powdered samples (varistors) with the help of Rigaku Multiflux x - ray diffractometer with Cu K_α (λ = 1.5418 Å) monochromatic radiation. The powdered samples were scanned from 10° to 70° with a scanned speed of 0.01°/sec. Applied voltage and current of the x - ray diffractometer were set to be 50 kV and 40 mA. XRD is a rapid analytical technique primarily used for phase identification of crystalline material and can provide information on unit cell dimensions. X - rays diffraction is now commonly technique for the study the crystal structures and atomic spacing. It is based on constructive interference of monochromatic x - rays and a crystalline sample. These x - rays are generated by a cathode ray tube, filtered to produce monochromatic radiation, collimated to concentrate, and directed toward the sample. The interaction of the incident rays with sample produces constructive interference (and a diffracted ray) when conditions satisfy Bragg's law. This law relates the wavelength of electromagnetic radiation to the diffracted angle and the lattice spacing in the crystalline sample. These diffracted x- rays are then detected, processed and counted. By the scanning the sample through a range of 2 θ angle, all possible directions of the lattice should be attained due to the random orientation of the powdered material. Conversion of the diffracted peaks to d - spacings allows identification of the powdered mineral because each mineral has a set of unique - spacings. This is achieved by comparison of d - spacings with standard reference patterns. From the x - ray diffraction spectra of powdered materials / samples, unit cell dimensions, such as lattice parameters, lattice distortion, unit cell volume, crystalline size.

Microstructural features of powdered samples (varistors) were characterized with the assistance of (JEOL, Model No. JSM- 5610 LV). Applied voltage and current of SEM were set to be 15 kV and 68 uA, and 4000 magnification. The SEM uses a focused beam of high - energy electrons to generate a variety of signals at the surface of solid specimens. The signals that derive from electron - sample interactions reveal information about the sample including external morphology (texture), chemical composition, crystalline structure and orientation of materials making up the samples. Data are collected over a selected area of the surface of the sample and a 2 - dimensional image is generated that displays spatial variations in these properties. Area ranging from approximately 1 cm to 5 microns in width can be imaged in a scanning mode using conventional SEM technique. The SEM is also capable of performing analyses of selected point locations on the samples; this approach is especially useful in qualitatively determining chemical composition, crystalline structure and crystal orientation. From the SEM images, surface morphology of the powdered samples such as average grain size and grain growth situation were examined and lattice micro strain were studied.

Electrical characteristics, known as I vs. V variations, of prepared varistors were carried out by using (Gwinstek PFR 100 M) high voltage DC power supply. To eliminate the transient response, I -V measurements were done with the step voltage 0.5 V and delay time 1 minute in the DC voltage range from 0 V to 250 V. From the ln V vs. ln I plots, important parameters of varistor, known as non - linearity factor, threshold voltage and leakage current were examined. ZnO based variators with 5 additive oxides were listed in table 1.

Table 1 ZnO based varistors with 5 additive oxides

Sample Name	Stoichiometric composition
Sample 1	0.99(ZnO) +(0.002) Bi_2O_{3+} (0.002) MnO_2 + (0.002) Co_3O_4 + (0.002) Cr_2O_3 + (0.002) Sb_2O_3
Sample 2	0.98(ZnO) +(0.004) Bi_2O_{3+} (0.004) MnO_2 + (0.004) Co_3O_4 + (0.004) Cr_2O_3 + (0.004) Sb_2O_3
Sample 3	0.97(ZnO) +(0.006) Bi_2O_{3+} (0.006) MnO_2 + (0.002) Co_3O_4 + (0.006) Cr_2O_3 + (0.006) Sb_2O_3
Sample 4	0.96(ZnO) +(0.008)6Bi_2O_{3+} (0.008) Mn_2 + (0.008) Co_3O_4 + (0.008) Cr_2O_3 + (0.008) Sb_2O_3
Sample 5	0.95(ZnO) +(0.01) Bi_2O_{3+} (0.01) MnO_2 + (0.01) Co_3O_4 + (0.01) Cr_2O_3 + (0.01) Sb_2O_3

Flow diagram of experimental detail was presented in figure 1.

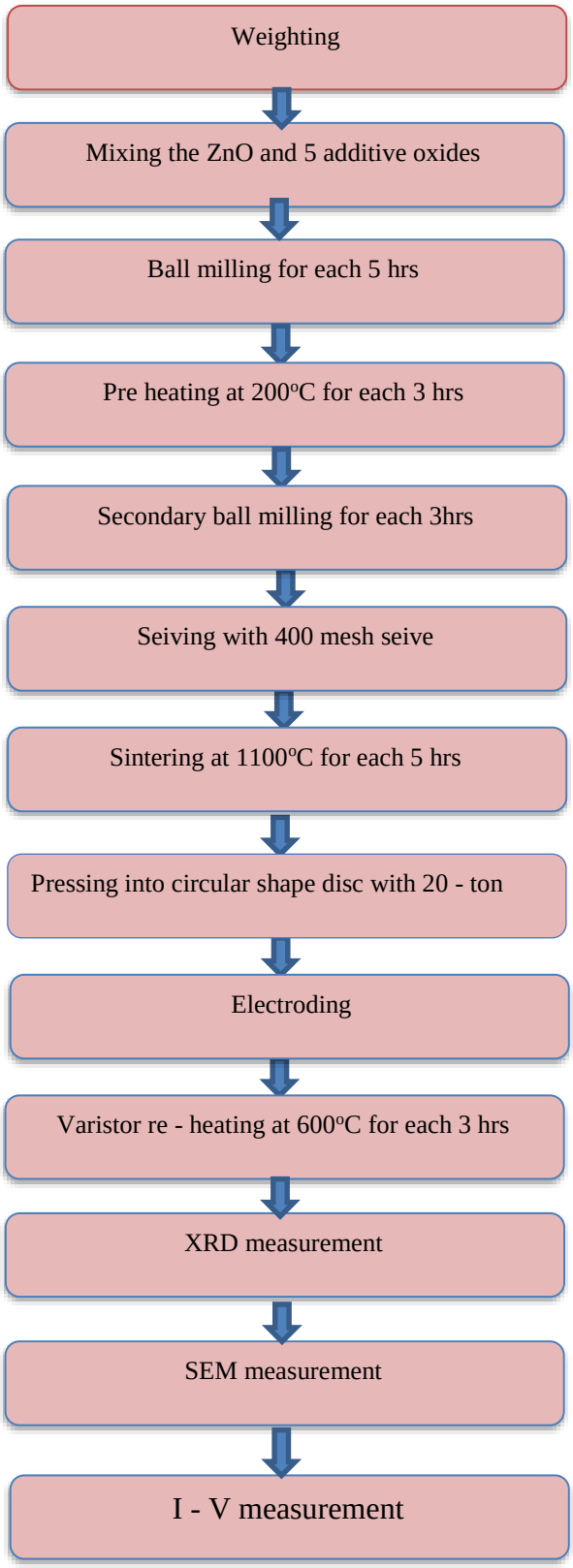

Figure 1 Flow diagram of experimental.

Results & Discussion

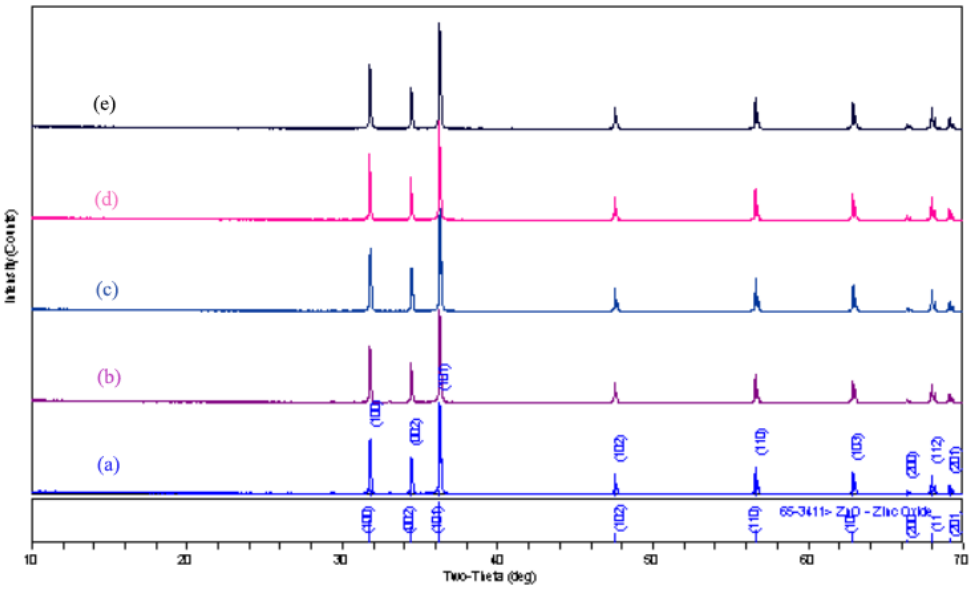

Figure 2 XRD spectra of ZnO with five additive oxides (composition 'x'= 1 mol%, 2 mol%,3 mol%,4 mol% and 5 mol%).

Figure 2 depicts the x - rays diffraction spectra of ZnO based varistors with 5 additive oxides. Peak search algorithm, known as Jade software is used to identify the unknown peaks in this study. Only x - rays diffraction peaks from single phase, hexagonal, wurtzite ZnO structures with reference (66 - 3411 > JCPDF file no.) are observed. Further, (101) peak is the most intense peak and a little shift of (101) peak, in terms of 2 - θ value is noticed in all spectra. These results indicate that, Bi, Mn, Co, Cr and Sb ions are partially occupied into Zn site in the crystal of ZnO lattice. Lattice dimensions, known as lattice constants " a " and " c " are evaluated by substituting the interplanar spacing " d " values from (101) and (110) planes in the following equation (1):

$$\frac{1}{d^2} = \frac{4}{3}\left(\frac{h^2+hk+k^2}{a^2}\right) + \frac{l^2}{c^2} \qquad (1)$$

d = interplanar spacing

h, k, l = miller indices

a, c = lattice parameters

Unit cell volume of ZnO based powdered samples are estimated by using the following equation (2):

$$V = \frac{\sqrt{3}}{4}a^2 \times 6 \times c \qquad (2)$$

V = cell volume

Lattice constants, lattice distortion and unit cell volume of ZnO based powdered samples are collected in table (2).

Table 2 List of lattice constants, lattice distortion and unit cell volume of ZnO based powdered samples.

Sample	lattice parameter "a(Å)"	Lattice parameter "c(Å)"	lattice distortion	Cell Volume $\times 10^{-30}$ (m^3)
1	3.235	5.243	1.621	142.570
2	3.238	5.241	1.618	142.761
3	3.241	5.239	1.616	142.933
4	3.244	5.236	1.614	143.147
5	3.249	5.234	1.611	143.496

Crystalline size and lattice micro strain of ZnO based powdered samples are examined by using the following Debye - Scherrer equations (3) and (4).

$$D = \frac{0.9\,\lambda}{\beta\cos\theta} \qquad (3)$$

$$\varepsilon = \frac{\beta}{4\tan\theta} \qquad (4)$$

Crystallite size, lattice micro strain and full width at half maximum (FWHM) of the most intense (101) peak are listed in table (3)

Table 3 List of crystallite size, lattice micro strain and FWHM of (101) peak of ZnO based powdered samples.

Sample	crystallize size (nm)	micro strain	β $\times 10^{-3}$ rad
1	31.46	3.567	4.635
2	31.15	3.602	4.681
3	30.87	3.635	4.724
4	30.64	3.662	4.759
5	30.39	3.692	4.798

Figure (3) depicts the variation of composition " x " with the lattice constants of ZnO structure. It is noticed that lattice constant " a " increases with decreasing lattice constant " c " when composition " x " is raised.

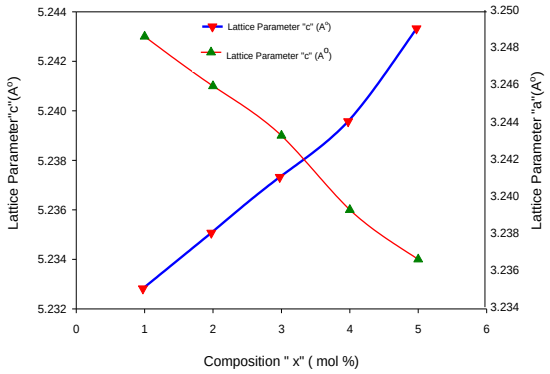

Figure 3 Variation of composition " x " (mol %) with the lattice constants of ZnO structure.

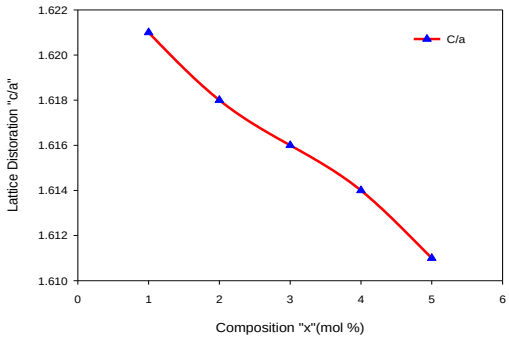

Figure 4 Influence of composition " x "(mol %) on lattice distortion " c/a " of ZnO structure.

Figure (4) shows the influence of composition " x " on lattice distortion " c/a " of ZnO structure. It is examined that lattice distortion " c/a " decreases with increasing composition " x ".

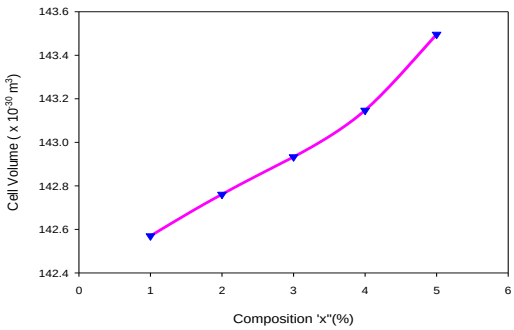

Figure 5 Effect of composition " x "(mol %) on unit cell volume of ZnO structure.

Figure (5) illustrates the effect of composition " x " on unit cell volume of ZnO structure. It is found that, unit cell volume slightly increases when composition " x " is raised.

It is believed that, there will be compress stress during the sintering process. Further, additional additive oxides create the dislocations, defects and vacancies in host ZnO structure. Those facts cause a little change of unit cell dimensions of ZnO structure and appearance of lattice micro strain. But there are no significant change of hexagonal, wurtzite ZnO structure.

Microstructural features of prepared varistors are studied with the help of SEM technique. It is found that all SEM images are not remarkly different and irregular micro grains are uniformly

distributed in all SEM images. Agglomerations of grains are formed on all images and average grain sizes are in micron scale. Further, there are crack free and no pin - hole arrangement in all images. Average grain sizes are found to be 2.8 μm, 3.32 μm, 4.16 μm, 4.6 μm and 5.2 μm respectively. It is also noticed that average grain size slightly increases as composition " x " increases in prepared varistors. Average grain sizes are found to be 2.8 μm, 3.32 μm, 4.16 μm, 4.6 μm and 5.2 μm respectively, as seen in figure (6).

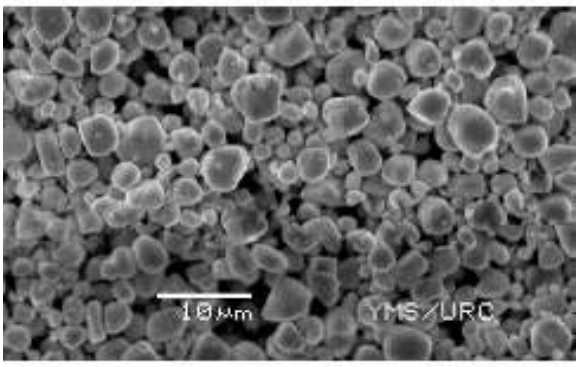

Figure 6(a) The SEM Images of ZnO based Varistor with five additive oxide (composition x = 0.01)

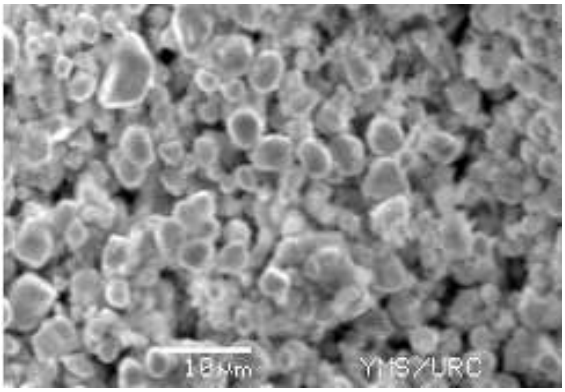

Figure 6(b) The SEM Images of ZnO based Varistor with five additive oxide (composition x = 0.02)

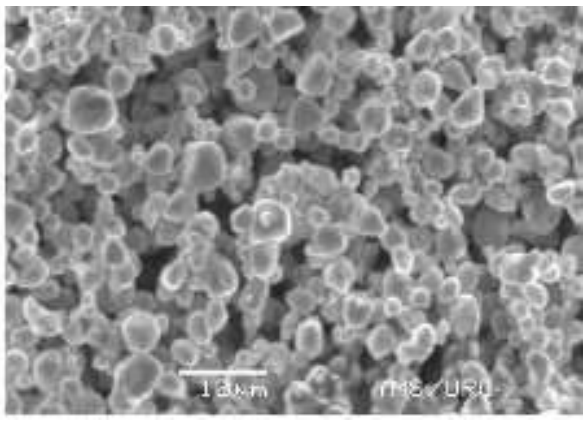

Figure 6(c) The SEM Images of ZnO based Varistor with five additive oxide (composition x = 0.03)

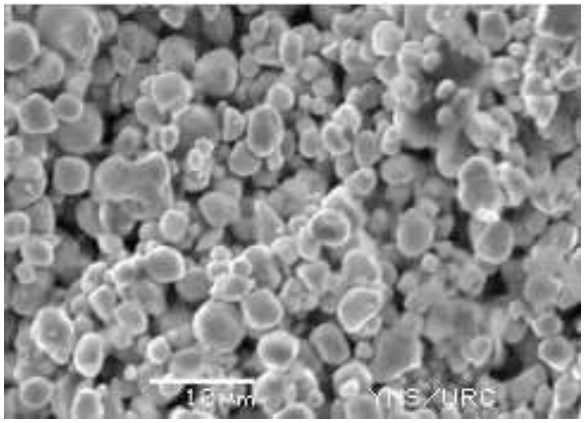

Figure 6(d) The SEM Images of ZnO based Varistor with five additive oxide (composition x = 0.04)

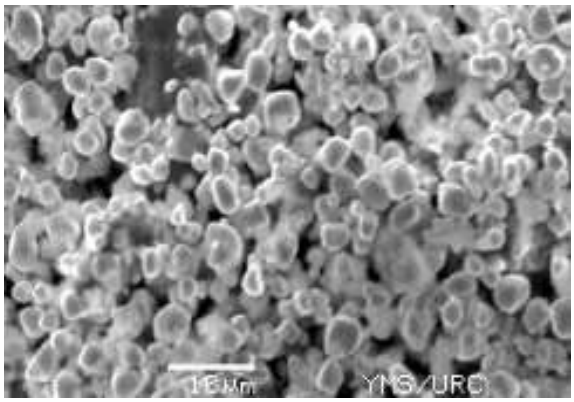

Figure 6(e) The SEM Images of ZnO based Varistor with five additive oxide (composition x = 0.05)

Varistor behaviour of prepared samples are studied from the current - voltage characteristic of the samples (ln V vs. ln I plots), as displayed in figure (7).

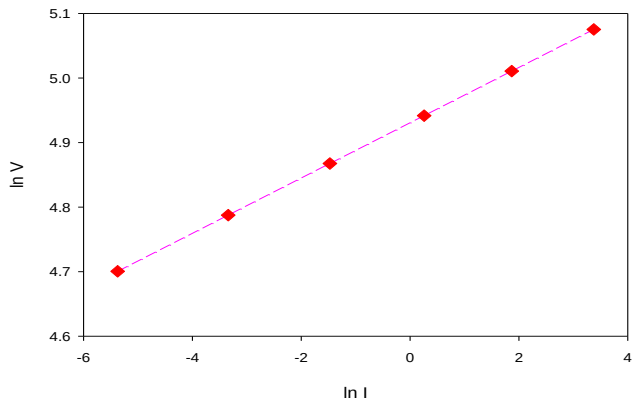

Figure 7(a) Non- linear behavior of ZnO based Varistor with five additive oxide (composition x = 0.01).

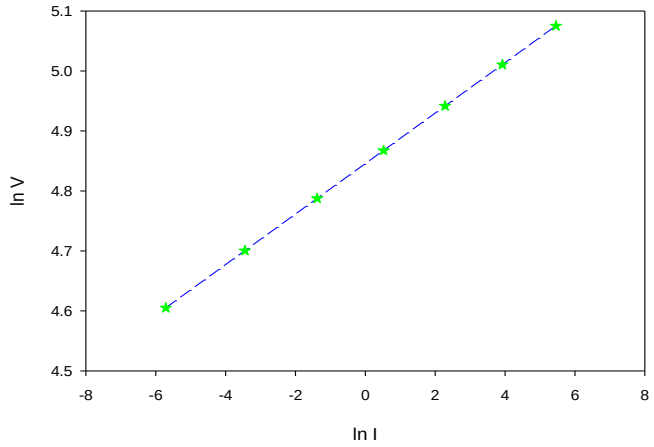

Figure 7(b) Non- linear behavior of ZnO based Varistor with five additive oxide (composition x = 0.02).

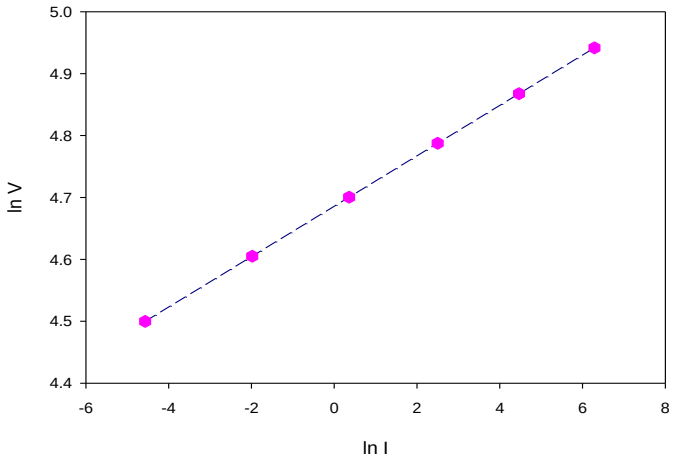

Figure 7(c) Non- linear behavior of ZnO based Varistor with five additive oxide (composition x = 0.03).

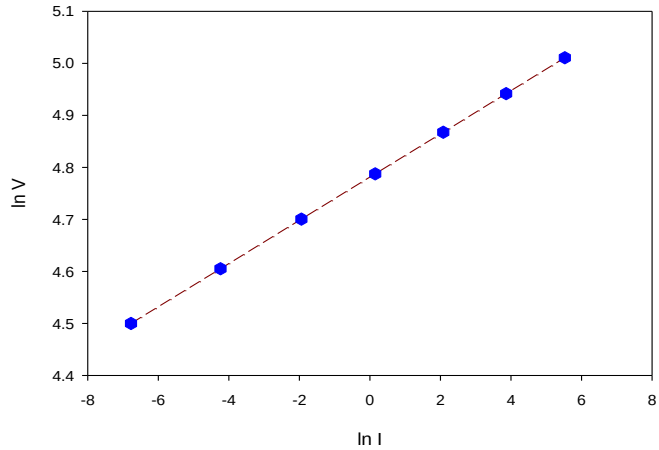

Figure 7(d) Non- linear behavior of ZnO based Varistor with five additive oxide (composition x = 0.04)

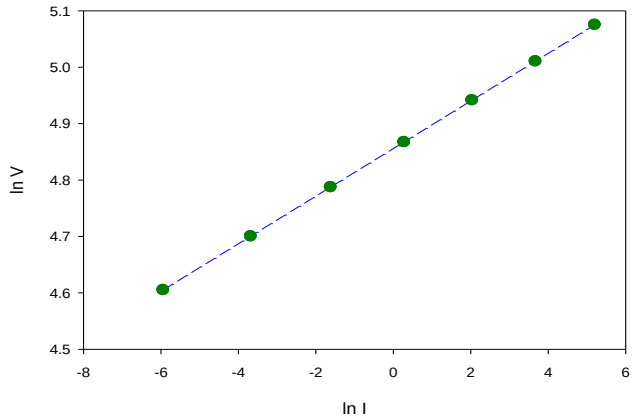

Figure 7(e) Non- linear behavior of ZnO based Varistor with five additive oxide (composition x = 0.05).

From the ln V vs. ln I plots, non - linear coefficients (α values) are examined by using the equation (5):

$$\propto = \frac{\log\left(I_2/I_1\right)}{\log\left(V_2/V_1\right)} \qquad (5)$$

where I_2 = 1 mA and I_1 = 10 mA and, V_2 and V_1 are the voltages corresponding to currents I_2 and I_1. Threshold voltages (V_{1mA}), which is measured at current 1 mA and the leakage currents are studied at 0.8 $V_{1\,mA}$. Variator properties are collected and listed in table (4).

Table 4 Varistor properties of prepared samples.

Composition x (%)	Non-linear Coefficient (α)	Threshold Voltage V_{TH}(V)	Leakage Current I_L (mA)
1	24.46	83.5	4.31
2	24.79	78.7	3.97
3	24.97	76.3	3.86
4	25.18	73.6	3.70
5	25.46	70.2	3.47

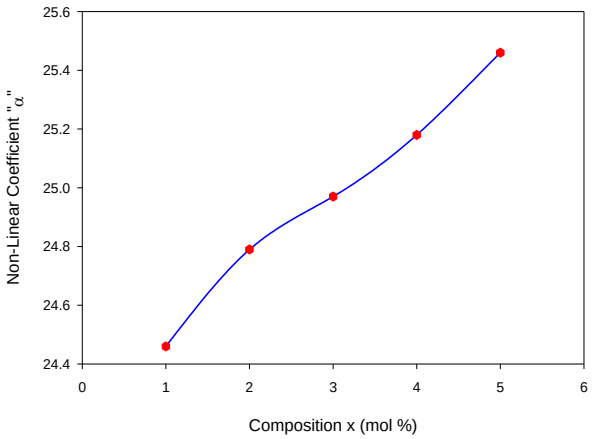

Figure 8 Influence of composition " x "(mol %) on the non - linearity factor " α " of prepared varistors.

Figure (8) represents the influence of composition " x " on the non - linearity factor " α " of prepared varistors. Figure (8) represents the influence of composition " x " on the non - linearity factor " α " of prepared varistors. It is noticed that, non - linearity factor " α " increases as composition " x " in prepared varistors. It is well known that, Bi ions are non - linearity inducer and Co, Mn, Sb, and Cr ions are non - linearity enhancers in ZnO based varistor. Further, the transition metal oxides are involved in formation of interface states and deep traps, both of which are contribute to non - ohmic behavior [Poonsuk Poosimma 2014].

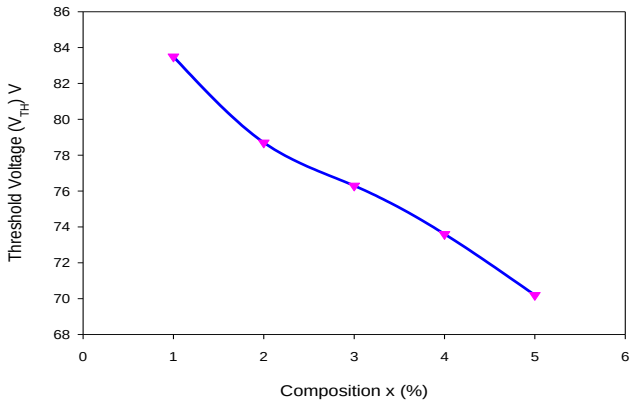

Figure 9 Variation of composition " x " (mol %) with threshold voltage (V_{TH}) of prepared varistors.

Figure (9) illustrates the variation of composition " x " with threshold voltage (V_{TH}) of prepared varistors. It is obvious that threshold voltage (V_{TH}) decreases as composition "x" increases in prepared varistors. Threshold voltage depends on the all types of stresses, such as thermal, mechanical, electrical and chemical stresses. In addition, threshold voltage is affected by the numbers of grain boundaries across the series between the two electrodes, which is inversely proportional to the grain size. In this study, increase of grain size leads to lower the threshold voltage in prepared varistors, as shown in figure (9).

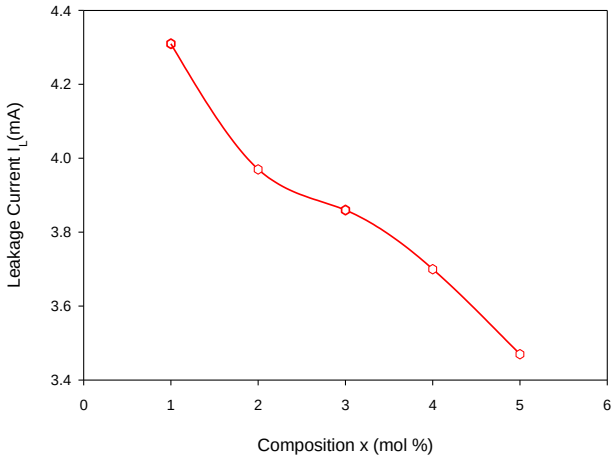

Figure 10 Effect of composition " x "(mol %) on leakage current " I_L " of prepared varistors.

Figure (10) shows the effect of composition " x " on leakage current " I_L " of prepared varistors. It is obvious that leakage current " I_L " decreases when the composition " x " is raised in prepared varistors. During the clamping of transient voltages, the non - linearity factor "α " is

required to suppression of leakage current, which is measured at nominal voltage (below 1 mA at medium and high voltage). The higher the non - linearity factor, the lower the leakage current, as listed in table (4) and the better the varistor's performance.

Conclusion

ZnO based varistors with 5 additive oxides Bi_2O_3, MnO_2, Co_3O_4, Cr_2O_3 and Sb_2O_3 are successfully prepared in this research work. The additive oxides are well known as non - linearity factor inducers and non - linearity enhancers in ZnO based varistors. Weighting, mixing, primary ball milling, drying, secondary ball milling, sieving, sintering, pressing into circular shape disc, electroding, and varistor re - heating processes are performed.

X - rays diffraction studies are carried out to examine the structural features of prepared variators. It is believed that appearance of compressive stresses during the solid state sintering processes. Further, additional Bi, Mn, Co, Cr and Sb ions doping create the dislocations, defects, and vacancies in host ZnO structures. These facts are the main reasons for the changes of unit cell dimensions of ZnO structures. But, there are no significant change of hexagonal, wurtzite ZnO structure after additive oxides doping.

Microstructural properties of prepared varistors are characterized with the help of SEM technique. It is noticed that all SEM images are not remark different. Agglomerations of grain are formed on all images.

Further, irregular micro grains are uniformly distributed in all SEM images. Average grain sizes are in micron scale, crack free and no pin hole arrangement in all images. It is also observed that average grain size slightly increases as composition " x " increases in prepared varistors.

Important parameters of prepared varistors, such as non - linearity factor " α ", threshold voltage " V_{th} " and leakage current " I_L " are examined by using the high voltage DC power supply. Non - linearity factor is estimated from the slope of ln V vs. ln I variations. It is obtained that non - linearity factor increases when the composition " x" is raised. Additive oxides, used in this study are known to be non - linearity factor inducers and enhancers. In addition, the transition metal oxides are involved in formation of interface states and deep traps, both of which are contributed to high non - ohmic behaviour.

Acknowledgement

The authors wish to acknowledge the Directorate of Education and Training, Ministry of Border Affairs, Union of Myanmar for financial support for this project. The authors also thank to Universities' Research Centre (U R C), University of Yangon for XRD and SEM examinations.

References

Bailek T. (1999); "Insulation System Protection with Zinc Oxide Surge Arresters ", IEEE Electrical Insulation Magazine, vol 15 (1), pp 5 - 10.

Cao Z. C. et al., (1994); "Ineffective Grain Boundaries and Break Threshold and Zinc Oxide Varistors ", Materials Science and Engineering, B 22, pp 261 - 266.

Emtage P. R. (1977); " The Physics of Zinc Oxide Varistor ", Journal of Applied Physics, vol 48 (10), pp 4372 - 4384.

Frigura - Llisa F. M., et al., (2019); " New Technical Parameters and Operational Improvement of Metal Oxide Varistor Manufacturing Process," Process, vol 7 (18), doi:10.3390/pr7010018.

Levinson L. M. and Phillip H. R. (1975); " Physics of Metal Oxide Varistor ", Journal of Applied physics, vol 46 (3), pp 1332 - 1341.

Mahan G. D. (1983); " Intrinsic Defects in Zinc Oxide Varistor ", Journal of Applied Physics, vol 54 (7), pp 3825 - 3832.

Masuoka M. et al., (1969); " Voltage Nonlinearity of Zinc Oxide Ceramics Doped with Alkali Earth Metal Oxides ", Japanese Journal of Applied Physics, vol 8 (10), pp 1275 - 1276.

Musuoka M. (1971); " Non - Ohmic Properties of Zinc Oxide Ceramics ", Japanese Journal of Applied Physics, vol 10 (6), pp 736 - 746.

Poonsuk Poosimma (2014); " Stability of Zinc Oxide Varistor ", PhD Dissertation, School of Materials, Faculty of Engineering and Physical Science, University of Manchester, U K.

Sun H. T. et el., (1993); " Electrical Non-uniformity of Grain Boundaries within ZnO Varistor ", Journal of American Ceramics Society, vol 76 (54), pp 1150 - 1155.

DATA SENDING FROM ONE ESP BOARD TO MULTIPLE ESP BOARDS VIA ESP_NOW PROTOCOL

Wint Shwe War Hlaing*

Abstract

In this research, the data such as temperature and humidity from one ESP board is transferred to the other two ESP boards using ESP_NOW protocol. ESP_NOW is one of the connectionless communication protocols. It can transfer data in the form of short packet transmission. Multiple devices can talk to each other in ESP_NOW protocol. In this research, data are transferred from one-to-many boards. One ESP32 board functioned as the data sender while two other ESP32 boards are used as receivers. ESP8266 boards or Wemos boards can be also used instead of ESP32 boards. DHT 11 sensor is used to obtain the data of temperature and humidity. The messages from the sender are visualized in a serial monitor or PuTTY. The receiving data are displayed on the I2C LCD as well as on the serial monitor or PuTTY. The proper data transferring range is also measured.

Keywords: ESP32, ESP_NOW, data transferring range, MAC address, PuTTY.

Introduction

Generally, the Wi-Fi routers operate with the 2.4 GHz band. Using a Wi-Fi router, the range of which data can be transferred is up to 150 feet (46 m) indoors and 300 feet (92 m) outdoors. The 802.11a routers with 5 GHz bands can reach approximately one-third of these distances [Dotdash, 2018]. The working function of ESP_NOW protocol is similar to the 2.4 GHz wireless connection which is used in wireless keyboards and mice.

Using ESP_NOW protocol, there are two main data transfers between ESP boards such as one-way and two-way communication. In one-way communication of ESP boards, two ways are categorized as (i) one ESP board transporting the data to multiple ESP boards and (ii) one ESP board receiving data from multiple ESP boards. An ESP32 (master) sends data to two ESP32 boards (slaves) in this research.

DHT 11 sensor is used to obtain the temperature and humidity. Three ESP32 boards are used; - one ESP32 for data sender and two ESP32 for data receiver. Two I2C LCDs are functioned to display the receiving data. Moreover, serial monitors and PuTTY monitoring systems are used for data visualization.

ESP32 (master) is connected to the DHT 11 sensor which data of temperature and humidity is obtained. The Media Access Control (MAC) addresses of receiver ESP32 boards (slaves) are obtained firstly. ESP32 (master) sends data to ESP32 boards (slave) via MAC address. Data sending success or failure to ESP32 (slaves) can be observed on the serial monitor or PuTTY monitoring window. Data receiving can be visualized on I2C LCD as well as serial monitor or PuTTY. And then, the range of which data are enabled to reach is determined on I2C LCD.

Experimental Procedure

Hardware, Software Equipment

In this research, three ESP32, DHT 11, and two I2C LCDs are used as the hardware components. Hardware such as the ESP32 library and DHT library are required to be included in Arduino IDE. ESP32 boards are not included in the default Arduino IDE. It can be installed in the Arduino IDE through the board manager. Master to slave communication is implemented on

* Dr, Associate Professor, Department of Physics, Yangon University of Education

ESP_NOW protocol. MAC address of each receiver ESP32 board can be determined by using software.

ESP32

ESP32 is one of the microcontroller chips fabricated by "Espressif". It consists of a microcontroller, Wi-Fi, Bluetooth, and Bluetooth low energy (BLE) for internet communication. ESP32 has upgraded the design of ESP8266 by integration with classical Bluetooth and BLE. It has a dual-core processor and it is faster than ESP8266. It can operate in sleep mode and is suitable for battery-powered applications.

In ESP32, there is eighteen 12-bit Analog to Digital converters (ADC), two 8-bit Digital to Analog converters (DAC) for signal processing. And then, there is four serial peripherals interface (SPI) channels, two inter-integrated circuits (I2C) interfaces, two inter-integrated sound(I2S) audio interfaces, and three Universal asynchronous receiver-transmitter (UART) for the peripheral interfacing. Moreover, eight channels of IR remote control and sixteen channels of pulse-width modulation (PWM) are added in ESP32. Hall- effect sensor, touch sensor, ultra-low-power preamplifier, and low-dropout (LDO) regulator are integrated into ESP32 chip. Multi-functional pin assignments of ESP32 are shown in Figure 1 [Bill, 2020].

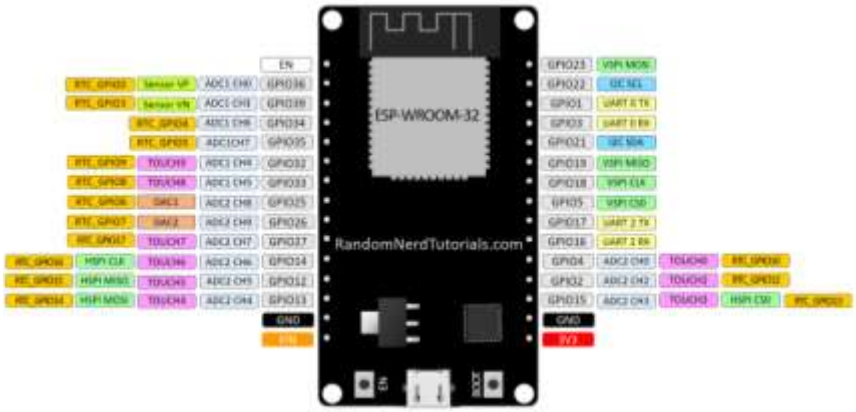

Figure 1 Pin assignment of ESP32

ESP_NOW

A wireless communication protocol is called ESP_NOW which allows ESP devices to communicate directly without connecting to a Wi-Fi network made by a router. The pairing among devices is required before their communication. After the initial pairing with the MAC address is accomplished, the connection is continuous and peer-to-peer communication is implemented without a handshake. ESP_NOW communication takes place in the low power consumption. It can send packets of messages (up to 250 bytes) between ESP boards. Any ESP board can function as either master or slave.

The following features are:

- It supports maximum 20 ESP boards.
- It sends data up to 250-bytes payload.
- Sending callback function can be set to inform the transmission whether data sending success or failure.
- Data sending range by ESP_NOW is more than that by Wi-Fi.

PuTTY

PuTTY is used as an open-source emulator, serial monitor, and network file transfer application. It is operated by connecting to the serial port. PuTTY is designed for Microsoft window. PuTTY configuration is expressed in Figure 2 [Tatham Simon, 2019].

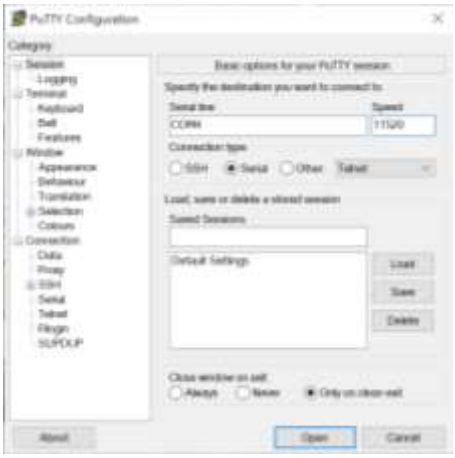

Figure 2 PuTTY configuration

MAC Address

MAC Address stands for Media Access Control address and it is a unique identifier hardware device on a network. MAC Addresses are identified by manufacturers. It can be changed optionally but it will return to its factory default MAC address when the device is reset. MAC Addresses composes of six groups of two hexadecimal digits, separated by colons like the following:

0xFF:0xFE:0XA6:0x00:0x0F:0xDD

The including "WiFi.macAddress()" in Arduino IDE can obtain MAC address. MAC address can be visualized on a serial monitor or PuTTY after uploading the sketch and pressing the reset button on ESP32. MAC address on serial monitor and PuTTY is illustrated in Figure 3 (a, b).

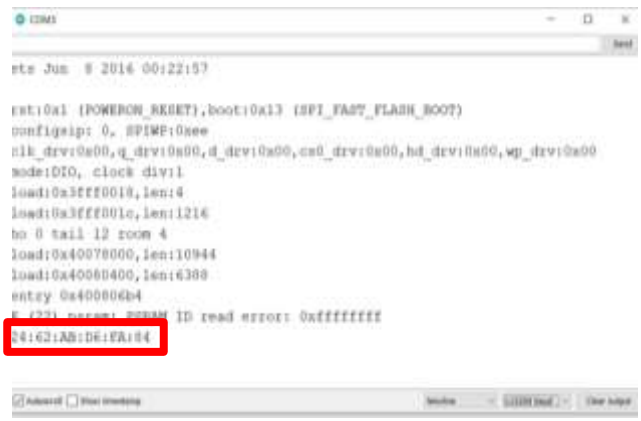

Figure 3(a) MAC on serial monitor

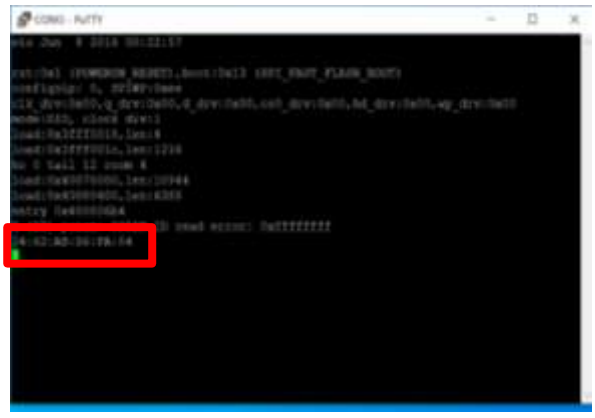

Figure 3(b) MAC on PuTTY

DHT 11 Sensor

The DHT 11 sensor is used to measure temperature and humidity. It measures humidity based on the change of capacitance and determines the temperature using a thermistor which is

built-in DHT 11. Additionally, it composes of an analog-to-digital converter. DHT 11 produces the 40-bit data output which contains the values of temperature and humidity.

Figure 4 A DHT 11 sensor

System Operation

The temperature and humidity are detected by master ESP32 and it is sent to the two slaves ESP32 boards using ESP_NOW communication. There are two main implementations: hardware and software preparation.

Hardware Preparation

There are two types of circuits. One is a master sender circuit and another circuit is a slave receiver circuit. The master sender circuit composes of ESP32 and a DHT 11 sensor. Data pin, Vcc, and ground of DHT11 are connected to D2, 3.3V, and ground of ESP32, respectively as shown in Figure 5. The schematic circuit of master sender and PCB layout are drawn by easyEDA software, and these are shown in Figure 6 (a, b).

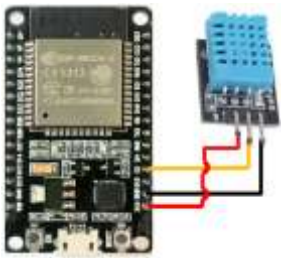

Figure 5 Circuit connection of DHT11 sensor and ESP32

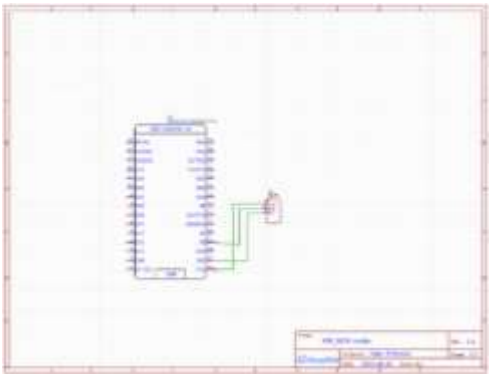

Figure 6(a) Schematic circuit of sender

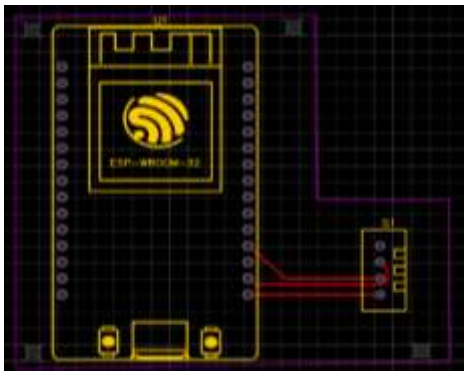

Figure 6(b) PCB layout of sender

The slave receiver circuit composes of ESP32 and I2C liquid crystal display (I2C LCD). Serial clock (SCL), serial data (SDA), Vcc, and ground of I2C LCD are connected to D22, D21, 3.3V, and ground of ESP32, respectively as shown in Figure 7. The schematic slave receiver circuit and PCB layout are drawn by easyEDA software, and these are shown in Figure 8(a, b).

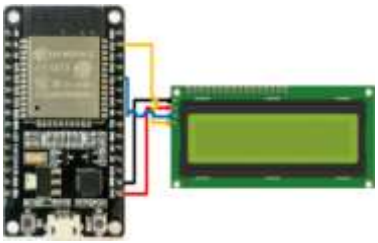

Figure 7 Circuit connection of I2C LCD and ESP32

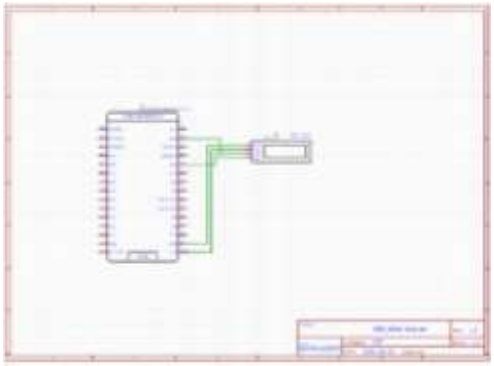

Figure 8(a) schematic circuit of receiver

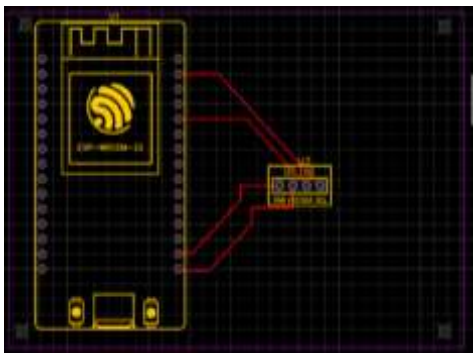

Figure 8(b) PCB layout of receiver

Software Preparation

The following syntaxes are mainly used in ESP_NOW programming.

First of all, the master ESP32 board and two slave ESP32 boards are set as the stationary mode by using the "WiFi mode (WIFI_STA)". ESP_NOW is required to initialize by calling "esp_now init()". The Wi-Fi STA mode should set before ESP_NOW is initialized. In this stage, the pair of master ESP32 board and two slave ESP32 boards will get all the information by using the calling"esp_now_deinit()". The paired ESP boards will complete after the calling "esp_now_deinit()". But the paired master ESP32 board and two slaves ESP boards are also needed that the paired devices with the broadcast MAC address be added by calling "esp_now_add_peer()" before sending data from the master ESP32 board. As soon as Wi-Fi will start, ESP_NOW data are sent to two slaves ESP32 boards. A master ESP board can send the maximum of 20 slaves ESP32 boards [Brandi Georg, 2021]. The "esp_now_send()" is included to send the ESP_NOW data and the "esp_now_register_send_cb()" is called to register the callback function in master ESP32 board. If the master ESP32 board with a pre-determined MAC address receives the sending data, it will return "ESP_NOW_SEND_SUCCESS" in the callback function. If two slaves ESP32 boards does not receive the sending data, the "ESP_NOW_SEND_FAIL" will be returned in the callback function into the master ESP32 board.

For the receiver section two slaves ESP32 boards, the "esp_now_register_recv_cb" is used to register for information on receiving a packet in the callback function.

The program flow of a master ESP32 board and that of two slave ESP32 boards are expressed in Figure 9.

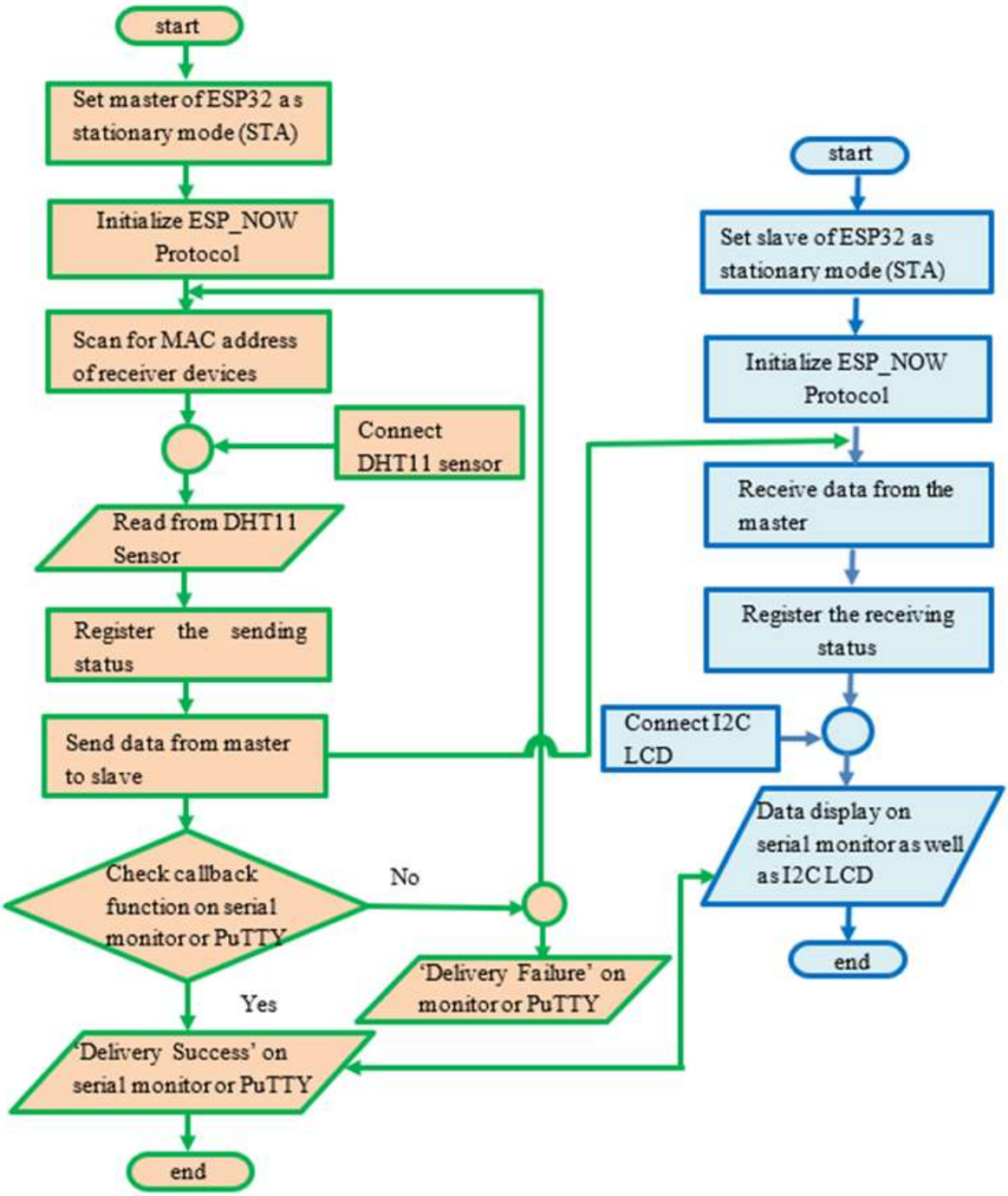

Figure 9 Flow chart of a master ESP32 board and two slave ESP32 boards

Results and Discussion

Results

Although data can be sent to 20 ESP receiver boards via ESP_NOW protocol, one ESP32 board functions as sender (master) while two ESP32 boards work as receivers (slaves). To send data to multiple ESP receiver boards, the unique MAC address of each ESP receiver board must be known. The MAC address in the ESP32 receiver boards can be determined by using software in which the "WiFi.macAddress()" is contained. Figure 10 is the MAC addresses of two receiver ESP32 boards.

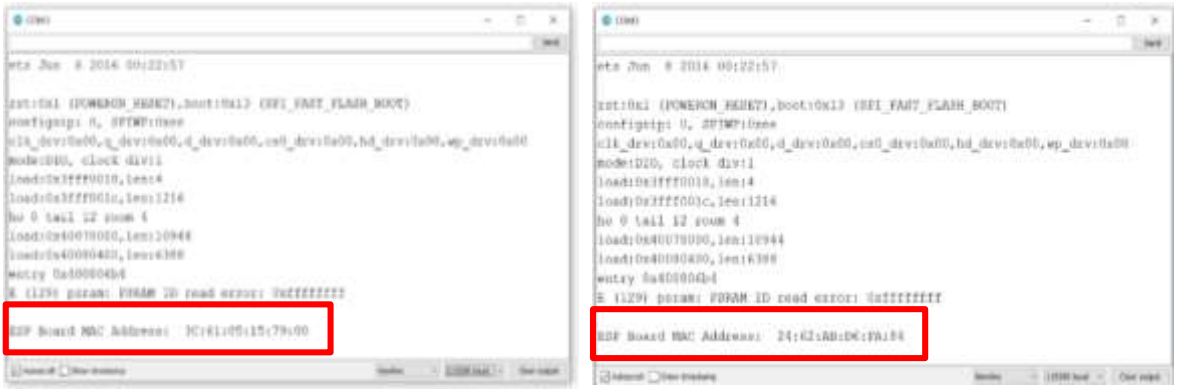

Figure 10 MAC address of two receiver ESP32 boards

As soon as the ESP32 sender (master) is powered on, it sends data to two ESP32 receiver boards whether they are powered or not. Figure 11 shows that the no power-condition of two ESP32 receiver boards. At that time, the ESP32 sender cannot receive an acknowledge message from two ESP32 receivers so that "delivery fail" for two ESP32 receivers is expressed on the serial monitor.

If one of two ESP32 receivers is activated, the ESP32 sender can receive the acknowledge message from one ESP32 receiver, and then "delivery success" and "delivery fail" are displayed as shown in Figure 12. If two ESP32 receivers are activated, the ESP32 sender gets acknowledged from each ESP32 receiver, and "delivery success" for each ESP32 receiver board is displayed on the ESP32 sender board's serial monitor as shown in Figure 13. So, the ESP32 sender can visualize which ESP32 receiver receives data and which board didn't.

In the receiver section, each ESP32 receiver is connected to I2C LCD so that data received are visualized in the serial monitor as well as the LCD screen. When the ESP32 receivers are powered on and they are in coverage range from the ESP32 sender, they receive data sent from the ESP32 sender. The data received in the serial monitor and PuTTY are shown in Figure 14 and Figure 15, respectively. The data received are displayed on I2C LCD as shown in Figure 16.

The communication range between sender and receiver is observed in Yangon University of Education campus and stable communication is observed up to 205 meters as shown in Figure 17.

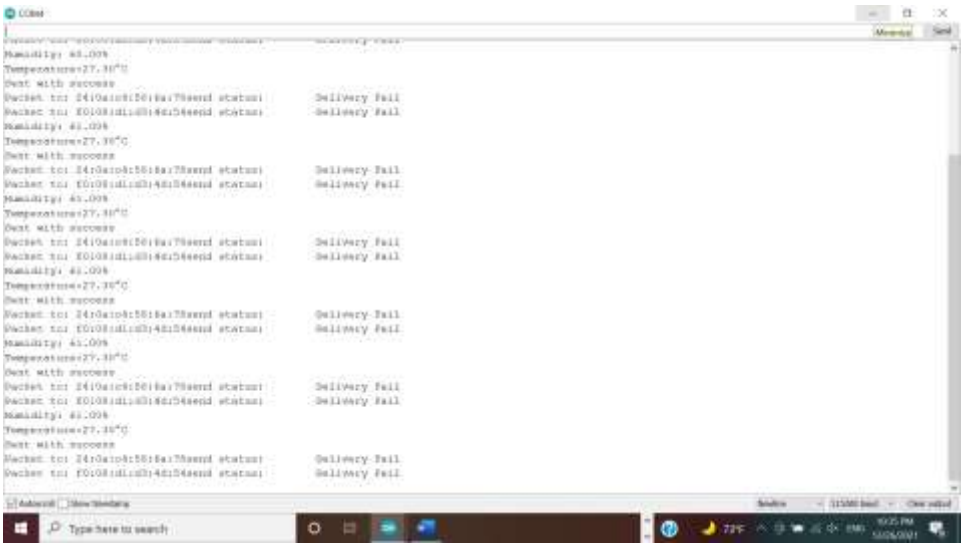

Figure 11 Sender's monitor showing two receivers being inactive

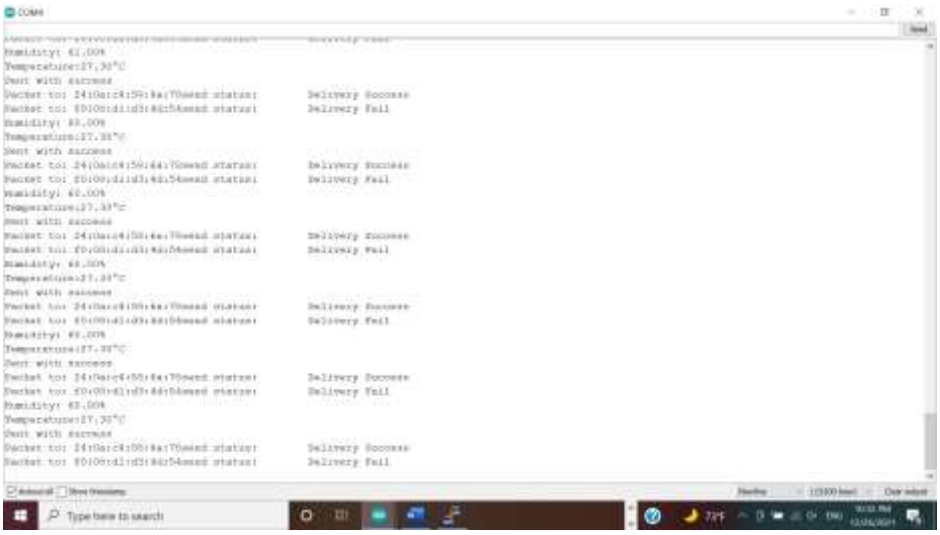

Figure 12 Sender's monitor showing one of two receivers being active

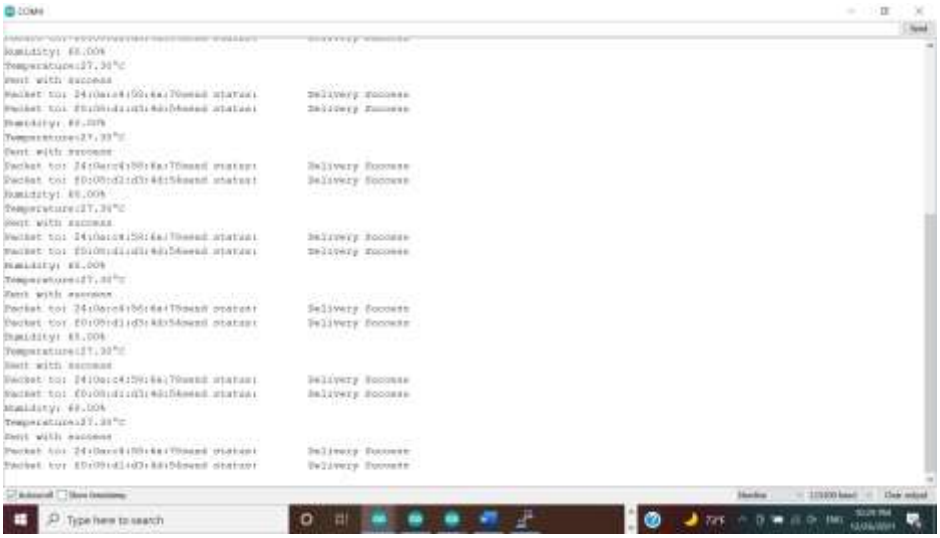

Figure 13 Sender's monitor showing two receivers being active

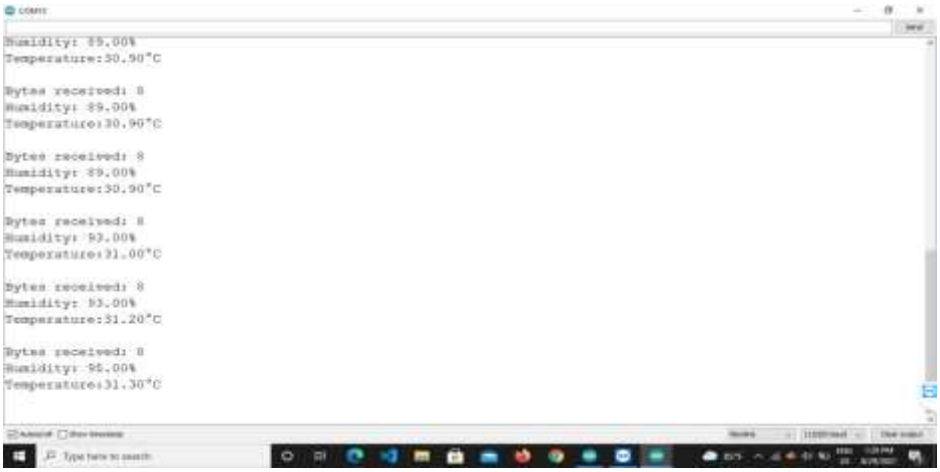

Figure 14 Data received on serial monitor

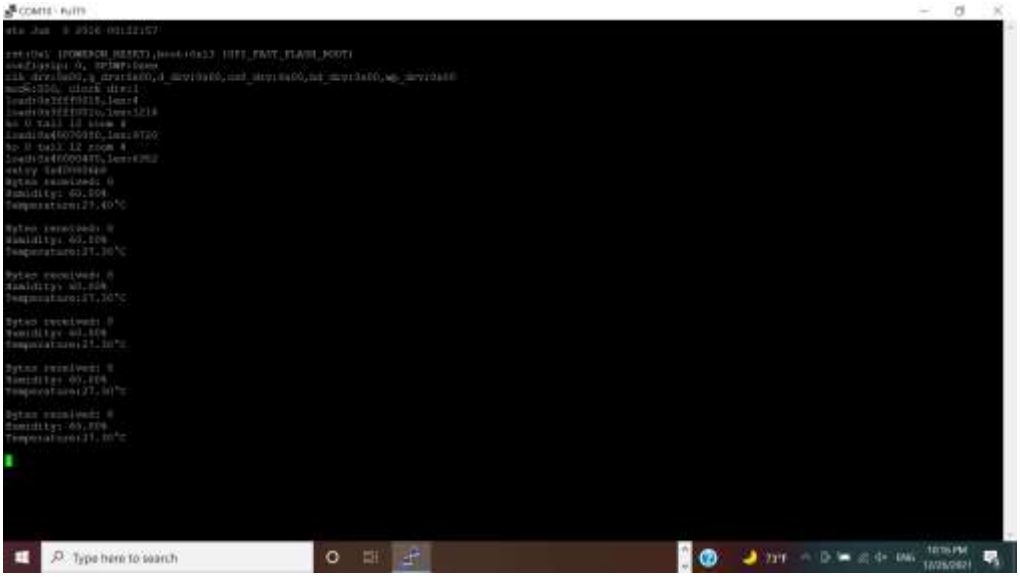

Figure 15 Data received on PuTTY

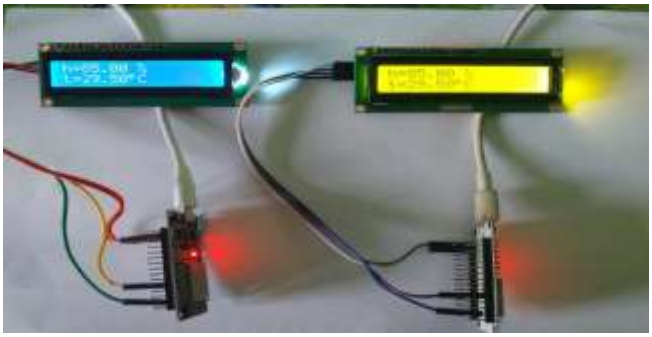

Figure 16 Data received on I2C LCD

Figure 17 Measurement of rage at stable ESP_NOW communication range

Discussion

In this research, only three ESP32 boards are used; one sender, two receivers. ESP8266, the WeMos board can be used instead of ESP32. But uploaded code must be slightly changed depending on the boards used in practice. In the determination of the stable range between sender and receiver, the on-board antenna of each ESP board should be pointed to each other. Two ESP boards can communicate and transfer data with a range of outdoor up to 220 meters (~ 722 feet). In this research, a stable communicated range is 205 meters (~ 673 feet) because the experimental site is not an open-air site.

Conclusion

ESP_NOW communication has many advantages over Wi-Fi communication but it has some weaknesses.

Advantages of ESP_NOW over Wi-Fi are:

(i) The maximum number of receiver ESP boards that can receive data from the sender in a stable communication range is 20.

(ii) By using ESP_NOW, ESP boards can communicate everywhere. Router or dynamic host configuration protocol (DHCP) is not needed in ESP_NOW communication.

(iii) Its essential feature is faster data transmission because it does not connect to Wi-Fi access points.

(iv) After pairing the master and slave devices, it communicates continuously. On the other hand, if one of the receiver ESP boards power off or reset incidentally, it will reconnect to the master ESP board automatically when it powers up again or it restarts.

Disadvantages of ESP_NOW are:

(i) It can transfer small data packets which are limited to 250 bytes.

(ii) Multiple ESP receivers are supported but it is limited to the maximum number of 20 receivers.

Acknowledgements

I would like to acknowledge Professor Dr Khin Khin Win (Retired), Head of Department of Physics, University of Yangon, and Professor Dr Yin Maung Maung, Head of Department of Physics, University of Yangon, for their kind permission to do. I sincerely thank all of Professors from the Department of Physics, University of Yangon for their kind encouragement to carry out this research.

I would like to thank Professor Dr Hla Toe, Head of Department of Physics, Yangon University of Education, for his advice, kind permission, and encouragement through the research period.

I deeply grateful to Professor Dr Ohn Than (Retired), Head of Department of Physics, Kyaukse University who supports the continuous guideline about the hardware and software of ESP32.

References

Bill, (2020) *ESp32-2*, Canada, DroneBot Workshop.

Brandi Georg, (2021) *ESP-IPF Programming Guide*, China, Espressif Systems (Shanghai) Co., Ltd.

Dotdash, (2018, *how-far-your-wifi-signal-reach*, New York, OpenWeb.

Robocraze, (2019) *Tutorial-Getting-Started-with-ESP-Now*, India, TIF Labs Pvt. Ltd.

Santos Rui, (2020) *ESP_Now-Two-Way-Communication-ESP32*, America, Random Nerd Tutorials Lab, No Starch Press.

Santos Rui, (2020) *ESP32 troublesshooting guide*, America, Random Nerd Tutorials Lab, No Starch Press.

Santos Rui, (2020) *Learn ESP32 with Arduino IDE*, America, Random Nerd Tutorial Lab, 2nd ed., No Starch Press.

Tatham Simon, (2019) *PuTTY*, United States, Wikipedia.

PREPARATION AND STRUCTURAL PROPERTIES OF $PbMnO_3$ CERAMICS BY SOLID STATE SINTERING METHOD

Win Win Yee[1], Nilar Oo[2], Nyo Nyo Myint[3] and Pwint Yi Thein[4]

Abstract

Analar grade PbO and MnO_2 are weighted by the stoichiometric compositions, (1 - x) PbO + (x) MnO_2, where x = 0.10, 0.15, 0.20, 0.25 and 0.30 respectively. Two starting materials, PbO and MnO_2 are mixed and grinded by agate mortar for each 3 hrs. Then, the mixture are heat treated at 500°C for each 3 hrs. After that, the mixture are grinded again by agate mortar. Finally, the mixture are heat treated at 700°C for each 3 hrs. All heat treatment schedules are solid state sintering processes. XRD technique is used to examine the structural properties and phase formation of the ceramic samples. From the XRD analyses, the variations of dopant concentrations with the structural properties are studied. In addition, dielectric properties of the ceramics samples are also investigated.

Keywords: solid state sintering, XRD, lattice parameter, crystallite size, lattice micro strain, dielectric properties

Introduction

Perovskite oxides with ABO_3 structure, have important properties in ferroelectricty, piezoelectricity, dielectricity, ferromagnetism and multiferronics. Most of properties of perovskite oxides are related to the network of BO_6 octahydra and the state of A/B site cations or mixture with different cations or/and vacancies. Potenial applications of perovskite oxides are uses in sensors and catalyst electrodes, certain types of fuel cells, solar cells, laser, memory devices and spintronics applications [Kuzushita et al., 2003; Misono, 2005; Goodenough and Zhou 2015].

Recently, perovskite type $PbMnO_3$ material is studied for uses in gas sensors and photocatalytic applications [Borhade et al., 2018; Borhade et al., 2018]. $PbMnO_3$ has a Goldsmith tolerance " t " factor or the geometric perovskite tolerance factor " t " is greater than 1 and form a perovskite polytype. In this study, $PbMnO_3$ ceramics is obtained by using eco - friendly solid - state sintering method and solid state sintering process. Processing parameters ae systematically investigated and optimized. X - rays diffraction studies are used to examine the phase formation and structural properties of ceramic samples. Dielectric properties of the samples are determined by using LCR meter.

Experimental Procedure

Analar grade PbO and MnO_2 were used as starting materials. PbO and MnO_2 powder were weighted and mixed by the stoichiometric compositions, (1 - x) PbO + (x)MnO_2, where x = 0.10, 0.15, 0.20, 0.25, and 0.30 respectively. The mixture were grinded by agate mortar for each 3 hrs and sintered at 500°C for each 3 hrs. Then, the mixture were grinded again by using agate mortar and sintered at 700°C for each 3 hrs. All heat treatment schedules were solid state sintering processes. X - rays diffraction studies were used to examine the phase formation and structural properties of ceramic samples, by mean of Rigaku Multiflux using Cu K_α (λ = 1.5418 Å) monochromatic radiation, as seen in figure (1). The voltage and current were 50 kV and 40 mA respectively. Specimen were scanned from 0° to 80° with step size of 0.01°/ sec. X- rays spectra

[1] Associate Professor, Natural Science Department, Technological University,Hmawbi,Yangon, Myanmar.
[2] Associate Professor, Natural Science Department, Technological University, Thanlyin, Yangon, Myanmar.
[3] Professor, Department of Physics, East Yangon University, Yangon,Myanmar.
[4] Professor, Department of Physics, Nationality Youth Resources Development Degree College Yangon, Myanmar

were recorded at room temperature From the XRD analyses, variations of molar ratios with structural properties were studied.

The mixture powder were uniaxially pressed into circular shape disc of 20 mm in diameter and 3.5 mm in thickness. Silver paste was coated onto both surfaces of the samples for electroding (area of electrode = 7.0695 mm^2). Dielectric properties of the samples were examined by using LCR meter (TH 2821). Flow diagram of experimental procedure for $PbMnO_3$ samples was depicted in figure (2).

Figure 1 Diagram of XRD Rigaku Multiflux.

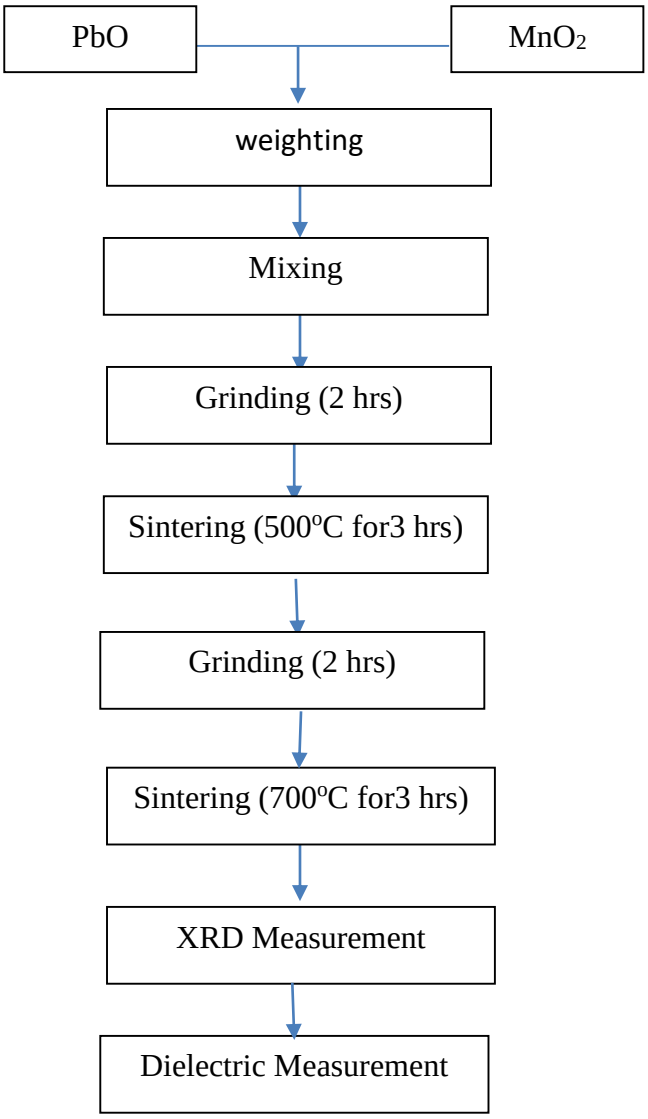

Figure 2 Flow diagram of experimental procedure for the $PbMnO_3$ ceramics.

Results and Discussion

Structural characterization of the prepared ceramic samples were examined by using XRD technique. The mixture of PbO, MnO_2 and $PbMnO_3$ structures were found in XRD patterns of Mn 10 mol % and Mn 15 mol %. In the XRD profiles of Mn 20 mol %, Mn 25 mol % and Mn 30 mol %, single phase, polycrystalline, and tetragonal $PbMnO_3$ structures were observed, as seen in figure (3).Lattice parameters are estimated by using the following equation (1):

$$\frac{1}{d^2} = \frac{h^2+k^2}{a^2} + \frac{l^2}{c^2} \qquad (1)$$

d = interplanar spacing

h, k, l = miller indices

a, c = lattice parameters

Cell volumes of the tetragonal $PbMnO_3$ specimens are studied by using the equation (2):

$$(\text{cell volume})V = a \times a \times c \quad (2)$$

Structural properties (lattice parameters, lattice distortion and cell volume) are estimated and listed in table (1). Crystallite size and micro strain are determined by using the Debye - Scherrer equations (3) and (4):

$$D = \frac{0.9\lambda}{\beta\cos\theta} \quad (3)$$

$$\varepsilon = \frac{\beta}{4\tan\theta} \quad (4)$$

In this equations, β is full width at half of the peak maximum (FWHM) and λ is the wavelength of the using X-ray and θ is the peak position which known as Bragg's angle. Structural properties such as lattice parameters, lattice distortion and cell volume are listed in table (1). Crystallite size and lattice micro strain are listed in table (2). Figure (4) shows the effect of Mn content on lattice parameters of $PbMnO_3$ ceramics. It is studied that lattice parameters increase with increasing Mn content. Figure (5) depicts the variation of Mn content with lattice distortion of $PbMnO_3$ ceramics. It is obvious that lattice distortion increases when Mn content is raised. It is due to increase of both lattice parameters a and c with increasing Mn content in $PbMnO_3$ ceramics. Influence of Mn content on unit cell volume of $PbMnO_3$ ceramics is depicted in figure (6). It is studied that unit cell volume increases with increasing Mn content. During the rapid thermal annealing, lattice micro strain, defect and dislocation appear in $PbMnO_3$ ceramics. Consequently, influence of Mn content on lattice parameter, lattice distortion and unit cell volume of the $PbMnO_3$ ceramics is observed, as seen in figures (4), (5) and (6) respectively. The results were nearly the same as others' reports. Structural optimization were done on tetragonal P4/mm (non - centrosymmetric) and P4/mm (centrosymmetric) structures [Subramanian S. S. 2014], using lattice parameters and results indicate that P4/mm structure is more stable than P4/mm structure. X - ray diffraction patterns cannot distinguish with the polar structure P4/mm versus the nonpolar structure P4/mm. Dielectric properties of ceramic samples were measured by using LCR meter (model TH 2821), and the results were listed in table (3). $PbMnO_3$ crystal structure is illustrated in figure 7 (a) and (b). Antiferromagnetic $PbMnO_3$ is a one of the potential candidates for spintronics.

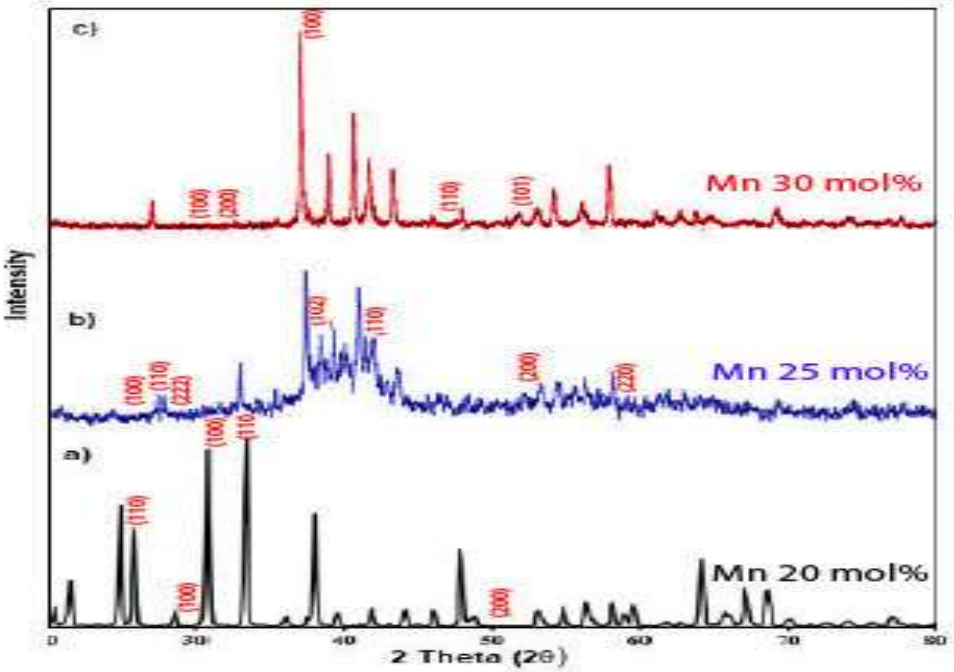

Figure 3 XRD profiles of $PbMnO_3$ ceramics with different Mn contents.

Table 1 Structural properties of $PbMnO_3$ ceramics with different Mn contents.

Molar concentration (mol %)	lattice parameter "a" (Å)	lattice parameter "c(Å)"	lattice distortion	Cell Volume $10^{-3}(m^3)$
Mn 20 mol%	3.8439	3.9114	1.0175	57.7931
Mn 25mol%	3.8481	3.9189	1.0184	58.0305
Mn 30mol%	3.8512	3.9251	1.0181	58.2160

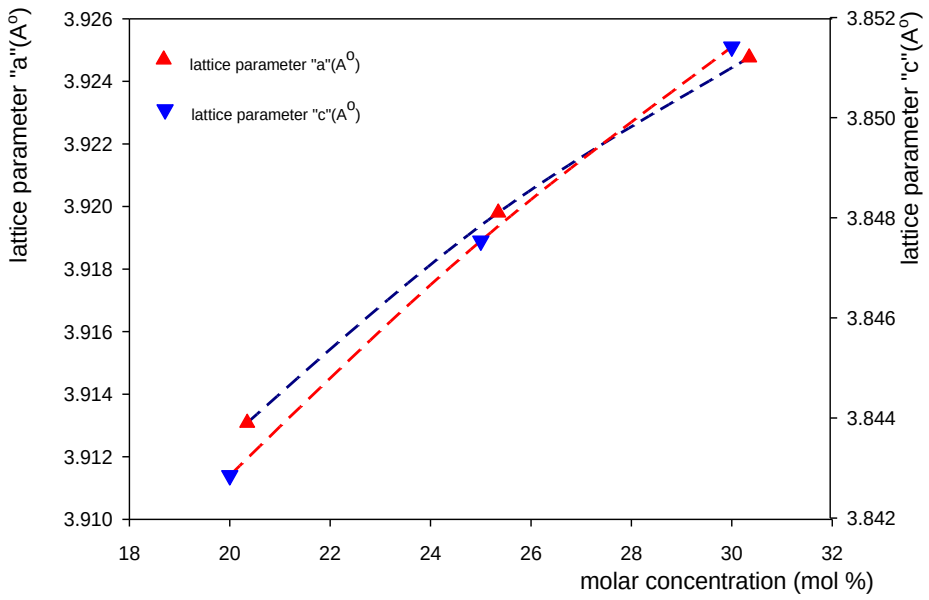

Figure 4 The effect of Mn content on the lattice parameters of the $PbMnO_3$ ceramics.

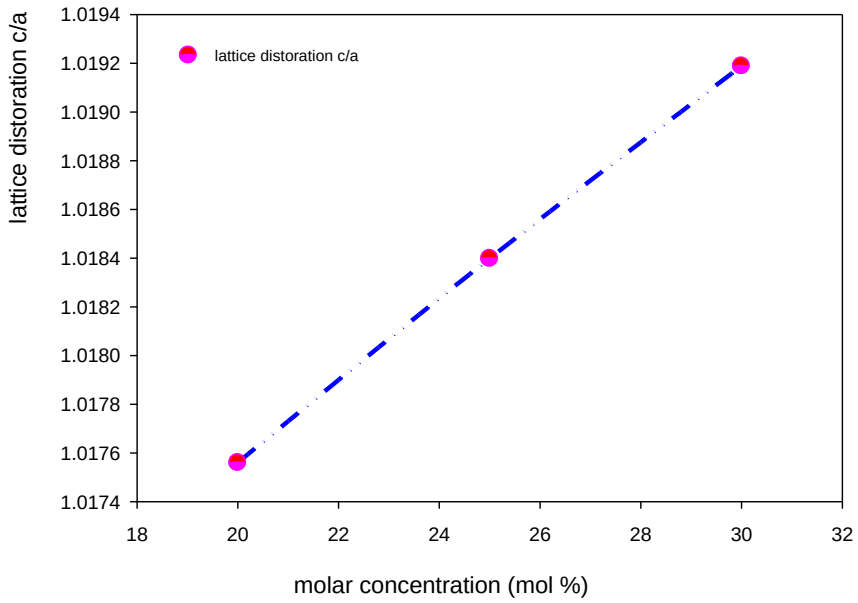

Figure 5 The variation of Mn content with lattice distortion of $PbMnO_3$ ceramics.

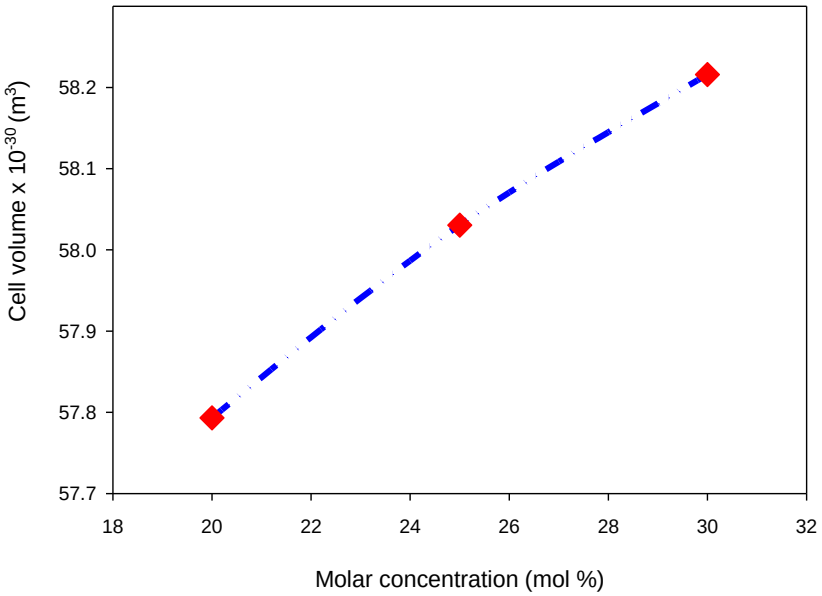

Figure 6 Influence of Mn content on unit cell volume of $PbMnO_3$ ceramics.

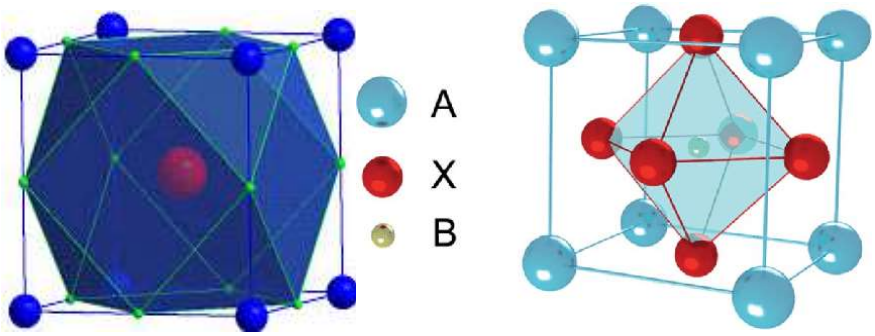

Figure 7 Crystal structure of $PbMnO_3$

Table 2 Crystallite size and lattice micro strain of $PbMnO_3$ ceramics at different Mn contents.

Molar concentration (mol %)	crystallize size (nm)	micro strain
Mn 20 mol%	31.297	4.468×10^{-3}
Mn 25 mol%	31.417	4.451×10^{-3}
Mn 30 mol%	36.941	3.778×10^{-3}

Dielectric properties of ceramic samples were measured by using LCR meter (model TH 2821), and the results were listed in table (3). The static dielectric constant is related to material's capacity of modifying electric flux density by phenomena such as polarization – a mere orientation of molecules or dissipation losses as heat,etc. One can consider as they remain approximately constant for a given temperature and frequency domain. The reported values of static dielectric constant is 37.5 ~ 41.85, and our results are agreed with reported value. [A V Borhade, et al. 2018].

Table 3 Dielectric properties of $PbMnO_3$ ceramics at different Mn contents.

Molar concentration (mol %)	Dielectric constant(ε_r) (measured at 1kHz)
Mn 20 mol%	38.91
Mn 25 mol%	38.95
Mn 30 mol%	39.46

Conclusion

$PbMnO_3$ ceramics were successfully prepared by using solid state sintering method. Processing parameters, such as sintering temperature, sintering time, grinding time and Mn concentration were optimized. Solid state reaction appears during the sintering process. It is eco - friendly, requires less times and easy to workup. The results obtained from XRD analyses are nearly the same as others ' reports. Antiferromagnetic material $PbMnO_3$ is a one of the potential candidates for gas sensor, photocatalytic and spintronic device applications. This paper provides the useful information's to the researchers, dealt with materials, chemical and electronic engineering.

Acknowledgement

The authors wolud like to acknowledge the Universities' Research Centre, University of Yangon for XRD measurements.

References

Borhade A. V. S.L. Sangle and D.R. Tope (2018); " Synthesis, Characterization and Gas Sensing Performance of $PbMnO_3$, $PbMnO_3$: SiO_2 and $PbMnO_3$: Al_2O_3 ", International Journal of Scientific Research in Science, Engineering and Technology, vol 4 (11), pp 1 - 10.

Borhade A. V. S.L. Sangle, D.R. Tope and S.S.Kushare (2018); " Eco - Friendly Synthesis of $PbMnO_3$: Its Photocatalytic Activity for Removal of Orange G Dye ", International Journal of Chemical and Physical Science, vol 7, pp 297- 304.

Goodenough J. B. and Zhou J. (2015); " Varied Role of Pb in Transition - Metals $PbMnO_3$ Perovskite (M = Ti, V, Cr, Mn, Fe, Ni, Ru)", Science and Technology of Advanced Materials, vol 16, 036003.

Kuzushita K. (2003);" Charge Disproportionation and Magnetic Properties in Perovskite Iron Oxides", Physics B Condensed Matter, vol 329, pp 736 - 737.

Misono M. (2005); " A Review of the Future of Mixed Oxides Catalysts: The Case of Heteropolyacid and Perovskites", Catalyst Today, vol 100, pp 95 - 100.

Subramania S. S. (2014); " Magnetic Ground State and Electronic Structure Calculations of $PbMnO_3$ Using Density Function Theory (DFT) ", Advanced Materials Research, vol 895, pp 420- 423.

ELECTRICAL PROPERTIES OF P(Py-2FPy)-ZnO COMPOSITE FILMS BY FOUR-POINT PROBE METHOD

Nyunt Win[1], Cho Cho Thet[2] and Ye Chan[3]

Abstract

This work focuses on the investigation of electrical properties of organic-inorganic nanocomposite films. Poly (pyrrole-2formyl pyrrole)-zinc oxide (P(Py-2FPy)-ZnO) composite films are fabricated by ex-situ chemical copolymerization through spin coating technique. Organic copolymer P(Py-2FPy) films were prepared by chemical copolymerization. For the inorganic components, ZnO nanoparticles were synthesized by room temperature solution method. P(Py-2FPy)-ZnO composite films with different concentrations of ZnO nanoparticles are fabricated in order to investigate the effects of ZnO contents on the electrical properties of films. The structural properties of copolymer and composite films were characterized by Ultraviolet-visible (UV-Vis) spectroscopy. The electrical properties of composite films including the sheet resistivity and conductivities of the composite films are measured by four-point probe method. Finally, the results of sheet resistivity and conductivity of composite films depending on concentration of ZnO nanoparticles are discussed. It was found out that the conductivities of composite films were increased with increasing the concentration of ZnO nanoparticles.

Keywords: copolymer, chemical polymerization, composite films, sheet resistivity, conductivity, *ex-situ*, spin coating.

Introduction

Metals are of great interest in industry as structural materials due to their high density and high strength to weight ratio. Some applications are limited due to their poor corrosion resistance. Corrosion is the deterioration of a metal as a result of chemical reactions between it and the surrounding environment. Anti-corrosion coatings protect metal components against degradation due to moisture, salt spray, oxidation, or exposure to a variety of environmental or industrial chemicals in a range of industries. Metal anticorrosion inhibits corrosion through physical and chemical effects which are great significance for industrial production and biomedical materials. The development of industry and science and technology such as metal chemistry, alloying effects, and the electrochemical and polymer field are improved the corrosion resistance of metals.

Coatings used for corrosion protection are mainly of three types such as metallic, organic and inorganic. The application organic coating establishes a barrier between substrate material and environment. It includes protected materials for paints, varnishes and lacquers, water-emulsion and solution finishes, organosols and plastisols. Organic corrosion inhibitors can be used alone or in combination with inorganic corrosion inhibitors for enhancing the anti-corrosive properties of a coating. Coating technology is a very common method which includes sol-gel coatings (Irina Stambolova et al., 2018), electroless coating (Fayomi *et al.,* 2019), electrochemical coating (Wenzheng Lu et al., 2020) and thermal and plasma-enhanced atomic layer deposition (Min Li *et al.,* 2019) and chemical oxidation (De Cheng *et al.,* 2021). Anticorrosive coating materials include organic polymers (ChandrabhanVerma *et al.,* 2020), metal oxide (Kalendova *et al.,* 2009) and graphene-containing composites (Hongran Zhao *et al.,* 2021).

From the observation of new fabrication strategies of organic-inorganic composite films, nanocomposites are derived from organic polymers and inorganic nanoparticles. The composites are expected to display synergistically improve the electrical properties of composite films by

[1] Associate Professor, Department of Physics, Pathein University
[2] Dr, Professor, Department of Physics, University of Yangon
[3] Dr, Professor (Head), Universities' Research Centre, University of Yangon

combining the attractive functionalities of both components. Therefore, polymer-based inorganic nanoparticle composite films will be interesting in several applications as new conductive polymeric materials. In addition, organic polymers are considered to be good hosting matrices for composite materials since they can easily be tailored to yield a variety of bulk physical properties.

Inorganic nanoparticles (TiO_2 and ZnO) possess outstanding optical, catalytic, electronic and magnetic properties which are significantly different from their bulk states. The polymer inorganic composites comprise inorganic nanoparticles like TiO2 or ZnO are uniformly dispersed in and fixed to a polymer matrix. The interfacial surface area of composite was increased due to higher surface area of nanoparticles. Besides, smaller particle size allows a much more homogeneous distribution of a composite material. In the integration of inorganic components in polymer matrix, the important criteria are (i) suitable synthetic method of inorganic nanoparticles in order to well dissolve in monomer solutions (ii) the enough stirring time is necessary for the homogeneous composite solution (iii) preparation technique of composite film formation. In this case, it is very important to consider the polymerization methods which are uncomplicated and the possibility of film formation.

In this work, inorganic ZnO nanoparticles in organic Py-2FPy copolymer were composited (Nyunt Win et al., 2020). The composite P(Py-2FPy)-ZnO film was prepared in order to study the electrical properties of films. The conductivities of composite films depending on various concentrations of inorganic ZnO are investigated by using four-point probe measurement. This work aims to investigate the enhancement of electrical conductivity from the development of organic-inorganic composite films.

Experimental Details

Preparation of the Organic Monomer Solution

(200 mg, 3 mmol) of Py and (286 mg, 3 mmol) of 2FPy were mixed and dissolved in 2 ml of chloroform ($CHCl_3$). They were stirred at the room temperature for 30 min to obtain the monomer solution (Yusuke Hoshina and Takaomi Kobayashi, 2012).

Preparation of the Inorganic ZnO Nanoparticles

ZnO nanoparticles were synthesized by room temperature solution method. Zinc acetate dihydrate ($Zn(CH_3COO)_2.2H_2O$) and ethanolamine ($NH_2CH_2CH_2OH$) and 2-methoxyethanol were used as a starting precursor, a solution stabilizer and a solvent. 1 g of $Zn(CH_3COO)_2.2H_2O$ and 0.28 g of ethanolamine in 10 mL of 2-methoxyethanol were vigorously stirring for 12 h for the hydrolysis reaction in air (Sun Y. et al., 2011).

Preparation of the Composite Films

486 mg of as-synthesized ZnO solution was added to 486 mg of monomer solution. Thus, the weight ratio of inorganic to organic is 1:1. The mixture was continuously stirred for 24 h. Then, the solution containing (995 µl, 13 mmol) trifluoroacetic acid (TFA) and (2 ml) $CHCl_3$ was additionally put to composite solution at room temperature. After that, the mixed solution was spin-coated onto the Petri dish at 20 rpm using a home-made spin coater until to complete the formation of copolymerization. After that, the film was successively washed by excess deionized water and acetone and dried in a vacuum oven for 12 h. Figure 1 illustrates the synthesis route scheme of the composite films.

Characterization Tools

The UV-Vis spectroscopy was performed in order to examine the absorbance values of all synthesized samples. The UV-Vis spectra were obtained by using the Shimadzu UV-1800 UV-Vis spectrophotometer. The electrical properties were measured by Keithley 2450 source meter.

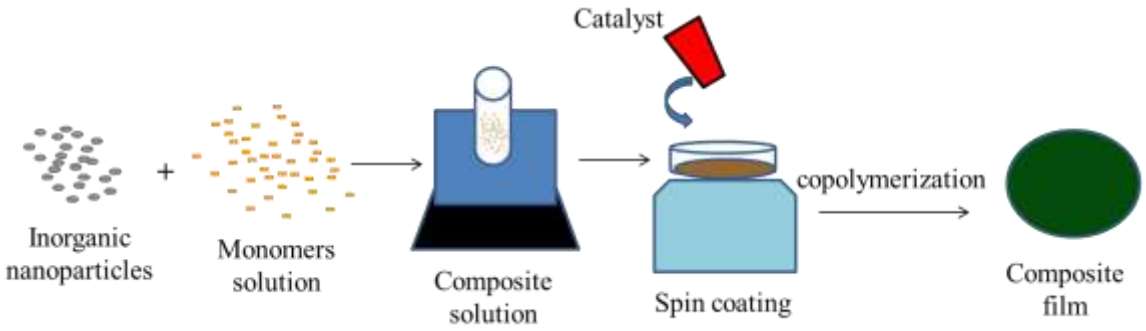

Figure 1 Schematic of *ex-situ* synthesis inorganic-organic nanocomposites films

Results and Discussion

Figure 2 shows the comparative UV-Vis spectra of ZnO, copolymer film and P(Py-2FPy)-ZnO composite films respectively. The optical absorption wavelengths of monomers, 2FPy and PPy, are found at 266 and 305 nm. However, the new copolymerization peak is formed at the wavelength 454 nm after the TFA catalyst is added. This peak indicated that the 2FPy group is incorporated into the chemical structure of the conjugated polymer chains (Yusuke and Kobayashi, 2012). When ZnO is present in the copolymer matrix of composite film, the absorption intensity of polymer chains is greatly increased. Besides, the weaker band is additionally appeared around 680 nm. This is due to strong interaction of ZnO with pyrrole segments to form bipolaron state which can enhance the electrical conductivity of composite films than pure copolymer film. The movement of polarons and bipolarons along the polymer backbone gives rise to enhanced conductivity of polymer film (Bredas and Street, 1985).

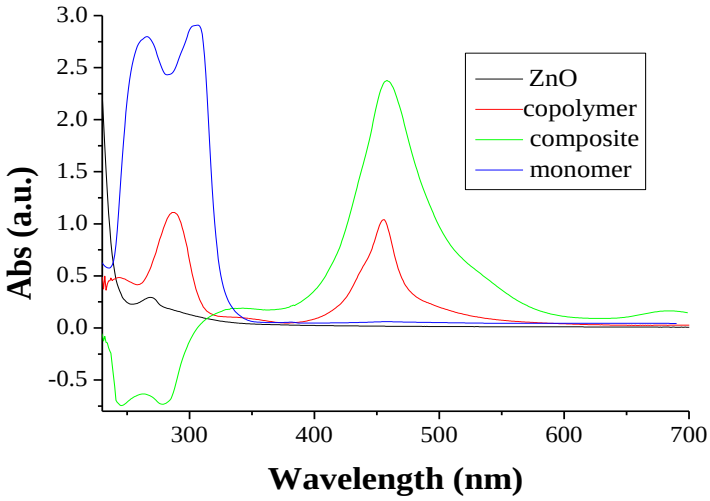

Figure 2 UV-Vis absorption spectra of ZnO, monomer, copolymer film and P(Py-2FPy)-ZnO composite films

Table 1shows the experimental parameters of films depending on concentration of ZnO nanoparticles obtained from the four-point probe measurement.

The sheet resistivity (ρ) of the conductive films is calculated by using the following formula:

The sheet resistivity (ρ) of the conductive films is calculated by using the following formula:

$$\rho = \frac{\pi}{\ln 2} \times \frac{V}{I} \times t \qquad (1)$$

where, V is voltage between the inner two probes of meter, I is current, t is the thickness of the films. Finally, the conductivity (σ) is determined by using the relationship:

$$\sigma = \frac{1}{\rho} \qquad (2)$$

Figure 3(a) and (b) illustrate the graph of sheet resistivity of pure copolymer and composite films depending on different volume of ZnO nanoparticles. As shown in these graphs, sheet resistivity of the films is decreased with increasing the volume of ZnO nanoparticles. It was found out that the values of sheet resistivity for all composite films were decreased and their conductivities were increased than pure copolymer films. The conductivity of the pure copolymer (0 mL of ZnO nanoparticles) films showed the lowest while the conductivities of composite films were enhanced with the increasing volume of ZnO. It is remarkable to note that the highest conductivity is obtained for the films composited with 0.5 mL of ZnO nanoparticles within the investigated volume limits of ZnO. This improvement of conductivity may be due to the facts that copolymers are associated with the structure of the P(Py-2FPy) and the metal oxide nanoparticles was incorporated into the polymer backbone with ionic complex formation as the dopant (Bredas and Street, 1985). Figure 4 shows comparison of decreasing sheet resistivity and increasing conductivities of pure copolymer (zero mL volume of ZnO nanoparticles) and composite films (0.1 to 0.5 mL of ZnO nanoparticles composited with copolymer solution).

Table 1 Experimental parameters of the films depending on concentration of ZnO nanoparticles

Concentration of ZnO nanoparticles (mL)	Thickness (t) ($\times 10^{-1}$ cm)	Voltage (V) (mV)	Current (I) (μA)	Sheet Resistivity (ρ) ($\times 10^{4}$ Ω-cm)	Conductivity (σ) ($\times 10^{-4}$ Scm^{-1})
0	0.0344	5.5869	0.0020	4.3550	0.2296
0.1	0.047	10.1503	0.01219	1.7736	0.5638
0.2	0.1625	0.051	0.0009	0.4173	2.3962
0.3	0.05	17.5038	0.1071	0.3703	2.7001
0.4	0.0538	0.6424	0.004942	0.3169	3.1552
0.5	0.0919	0.0053	0.000226	0.0977	10.2000

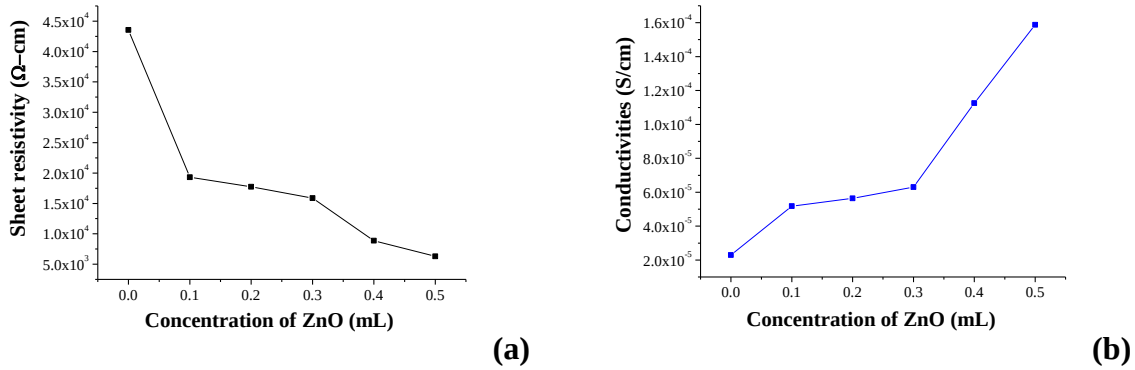

Figure 3 (a) Sheet resistivity and (b) conductivities of P(Py-2FPy)-ZnO composite films depending on concentration of ZnO nanoparticles

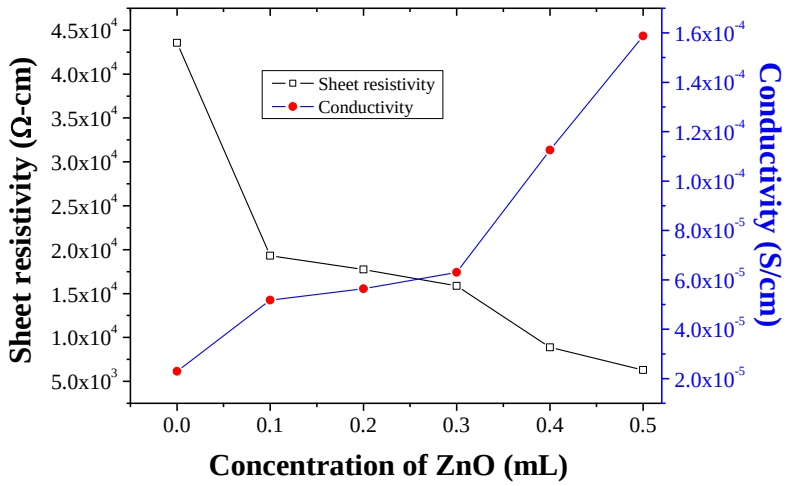

Figure 4 Sheet resistivity and conductivities of P(Py-2FPy)-ZnO composite films

Conclusions

The electrical properties of composite films depending on effects of inorganic ZnO nanoparticles in the organic matrices (copolymer) are systematically investigated by four point-probe method. It is found out that the values of sheet resistivity of the composite films are decreased and their conductivities are increased with increasing concentration of ZnO nanoparticles. This may be due to increasing concentration of charge carriers which tends to increase in doping of metal oxide nanoparticles in the copolymer backbone. This can be also explained that the delocalization effect which is associated with the doping process and that produces polarons and/or bipolarons in the composite structure which in turn enhance the conductivity. Therefore, all these results are directed to promote the conductivities of composite films for their potential applications for anticorrosion technology.In conclusion, by exploiting the physics of the inorganic nanoparticles, organic polymer and polymeric nanocomposites, a new functional composites P(Py-2FPy)-ZnO materials will lead to important coating materials due to their electrical conductivity and mechanical flexibility by the unique combination of inorganic and organic materials.

Acknowledgements

We would like to acknowledge Dr Than Tun, Rector, Pathein University, for his encouragement and allowing us to participate in this event. Our special thanks go to Dr Yin Yin Yin Myint, Professor and Head of Department of Physics, who gives me valuable suggestions for this work.

References

Bredas, J.L and G.B. Street, "Polarons, bipolarons, and solitons in conducting polymers," *Acc. Chem. Res*., 18,309-315, 1985.

ChandrabhanVerma, Lukman O.Olasunkanmi, Ekemini D.Akpan, M.A.Quraishi, O.Dagdag, M.El Gouri, El-Sayed M.Sherif and Eno E.Ebenso, "Epoxy resins as anticorrosive polymeric materials: A review" *Reactive and Functional Polymers*, 156, 10474, 2020.

De Cheng, Chen Wen, Jingying Bai, Yeshen Qin and Baocheng Jiao, "Corrosion behavior of chemical oxidation film of magnesium alloy in NaCl solution," *IOP Conf. Series: Earth and Environmental Science*, 719, 022092, 2021.

Fayomi O. S. I, I. G Akande and A. A. Sode, "Corrosion prevention of metals via electroless nickel coating: A review," *Journal of Physics: Conference Series*, Issue 2, 1378, 2019.

Hongran Zhao, Jiheng Ding**, M**in Zhou and Haibin Yu, "Enhancing the anticorrosion performance of graphene–epoxy coatings by biomimetic interfacial designs," **A**CS Appl. *Nano Mater.*, 4, 7, 6557-6561, 2021.

Irina Stambolova, Stancho Yordanov, Lyuben Lakov, Sasho Vassilev, Vladimir Blaskov, and Bojidar Jivov, "Preparation of sol-gel SiO_2 coatings on steel and their corrosion resistance," *MATEC Web of Conferences*, 145, 05011, 2018.

Kalendova A., D. Vesely and P. Nemec, "Study of corrosion inhibition properties of metal oxide based core shell pigments in organic coatings," *Materials Research Innovations*, 13, 3, 288-290, 2009.

Min Li, Zhi-Xian Jin, Wei Zhang, Yu-Hang Bai, Yan-Qiang Cao, Wei-Ming Li, Di Wu and Ai-Dong Li "Comparison of chemical stability and corrosion resistance of group IV metal oxide films formed by thermal and plasma-enhanced atomic layer deposition," *Scientific Reports*, 9,10438, 2019.

Nyunt Win, Cho Cho Thet, Lwin Ko Oo and Ye Chan, "Development of P(Py-2Fpy)/ZnO composite fims and investigation of their electrical properties" J. Myanmar Acad. Arts Sci. 2020 Vol. XVIII.No.2A, 51-58.

Sun Y., J. H. Seo, C. J. Takacs, J. Seifter and A. J. Heeger, "Inverted polymer solar cells integrated with a low-temperature-annealed sol-gel-derived ZnO film as an electron transport layer," *Adv. Mater*., 23, 1679-1683, 2011.

Wenzheng Lu, Tsz Him Chow, Yao Lu and Jianfang Wang, "Electrochemical coating of different conductive polymers on diverse plasmonic metal nanocrystals," Nanoscale, 12, 21617-21623, 2020.

Yusuke Hoshina and Takaomi Kobayashi "Electrically conductive films made of pyrrole-formyl pyrrole by straightforward chemical copolymerization" *Ind. Eng. Chem. Res.* 51, 5961-5966, 2012.

DETECTION OF MYXOSPOREAN PARASITES INFECTED IN THE KIDNEYS OF *CIRRHINUS MRIGALA* (HAMILTON, 1822)*

Yu Yu Aye[1], Thant Zin[2], Kay Lwin Tun[3]

Abstract

Cirrhinus mrigala, Mrigal carp was sampled monthly and examined myxosporean parasitic infection in kidneys of fish, over 12 months of study period. *Myxobolus* sp. under the phylum Cnidarian was recorded. Spores of *Myxobolus* sp. elongated and ellipsoid in valvular view, measurement 11.6µm±1.1µm in length and 7.6µm±0.8µm in width. The highest prevalence of *Myxobolus* sp. infection were recorded in August (82%) with highest mean intensity of infection (3) when the fish was one year old. Among the infected fish, only 16.7% of infected fish showed cysts formation on the kidneys through the study period. The histology slides of infected tissues were examined under light microscope to understand the histopathological changes of infested tissues. Histopathological changes such as abnormalities of convoluted tubules, dilation of blood vessels, hypertrophy and deformities of glomerulus, and congestion of blood cells caused by *Myxobolus* infection were observed. Dilation in the capillaries and vacuolar degeneration in the epithelium of renal tubules were observed. The infested kidney tissue showed the prominent circular vacuolar spaces filled with damaged cells necrosis in the tissue. To improve quality fish fry production and successful harvesting, therefore, management practices and pond hygiene should be adopted in nursery operation systems and grow-out ponds.

Introduction

Disease has a serious impact on fish in both captive and natural environments in worldwide. In cultured fish population, the parasites may involve in the serious outbreak of disease (Kayis *et al*., 2009). It is a major problem that carrying heavy load of parasites in cultured fishes, out of which myxosporean parasites are emerging as a major group in aquaculture. In order to increase the production and to get the profits, application of the knowledge in the control of diseases is essential in fisheries sector (Snieszko, 1983).

Examination of parasitic infections in *Cirrhinus mrigala* is still required to improve production for local market. Among the fish parasites, myxosporeans are diverse and widely distributed metazoan parasites known both marine and freshwater fish (Kent *et al*., 2001; Canning and Okamura, 2004; Lom and Dykova, 2006). They are small parasites (< 100 µm) and more than 2200 species are reported across the world (Liu. 1981).

The complex life cycle of myxozoa requires a tubificid worm as an alternative host, in which the ingested spore further develops as actinospores. When actinospores were released from the tubificid, they enter into the fish and life cycle is completed (Lom and Dykova, 1992). Myxospoean parasites are one of the economically important groups of parasites as they infect the fish and most commonly parasitize invertebrates (Lom and Dykova, 2006). They are common in nursery ponds and high mortality rates caused by their infections. These parasites infested in the organs of fish, where they may cause serious structural changes depend on the intensity of parasites. Myxosporean parasitic infestations caused economically losses in the carp nursery ponds (Sanaullah and Ahmed, 1980). Parasitic diseases are the most serious limiting factors because fish pathogens can easily be transmitted in a restricted water body in fish ponds.

Different myxosporeans infect various organs of fish. *Myxidium* species infection abundantly found in gallbladder and intestine while *Myxobolus* and *Thellohanellus* species occur

[1] Lecturer, Fisheries and Aquaculture, Department of Zoology, University of Yangon
[2] Professor and Head, Department of Zoology, University of Mandalay
[3] Professor and Head, Department of Zoology, University of Yangon
[*] Best Paper Award Winning Paper in Zoology (2021)

in gills and skin (Kay Lwin Tun, 2016). Infections of Myxosporea to internal organs of fish show more serious damage than those to external organs such as skin and scale (Tun *et al.*, 2017). The kidneys are one the important organs in excretion and regulation of the water balance within the fish body. Myxosporean infection in kidney of fish has been reported in marine and freshwater fish. Severe lesion of the glomeruli capsules and fat deposits on the kidney tubules of *Hypophthalmicthys molitrix* (Yu and Wu, 1992). Similarly, diffused histozoic myxidian parasite in the caudal kidney of cultured eel in Taiwan (Liu, 1981). Degenerative and necrotic changes in the kidney tubules in carps caused by enzootic nature of myxosporeans (Mishra, *et al*., 1982). Moe Kyi Han (2006), Sein Sein Myint (2007), Pa Pa Win (2007) and Shwe Sanda, *et al*. (2020) reported incidence of Myxosprean in Manadaly environs. However, the classification of myxosporean parasites is currently based on morphology of spore.

Infections with myxozoa have recently been described as a cause of clinically significant kidney disease in two species of anurans (Kayis *et al*., 2009). Histopathological changes were glomerular shrinkage, increased spaces between glomerulus and Bowman's capsule, increased tubular lumen in the kidneys of some carps (Ullah, *et al*., 2017). Examination of parasitic infections in kidneys of *Cirrhinus mrigala* in Myanmar is still required to improve production of mrigal fish. The present study was therefore undertaken to detect the myxozoan parasites infected to the kidneys of *Cirrhinus mrigala* in Yezin fishery station, one of the biggest *C. mrigala* hatchery in Myanmar and to evaluate the histopathological alterations caused by Myxosporean parasitic infestation in kidneys of *Cirrhinus mrigala*.

Materials and Methods

Study Area

Yezin Fishery Station is a government owned fish seed multiplication center, carrying out research and documentation of fish species in Zayarthiri Township, Nay Pyi Taw Region. It is situated at 19° 50' 14.9" N and 96° 16' 36.8" E about 19 km away from Pyinmana city, and it is located near the Yezin Dam and beside the Yangon-Mandalay Highway Main Road. One of the biggest *Cirrhinus mrigala* hatchery in Myanmar and also distributes fry/fingerling *C. mrigala* through the country.

Study Period

The research work was carried out from August 2018 to September 2019.

Sample Collection and Examination of Parasites

Cirrhinus mrigala fingerlings were cultured in experimental pond (8.3mx33.3m) at Yezin Fishery Station as extensive culture system. Thirty fish were collected monthly to examine the occurrence of parasites. A total of 30 fish samples were carried to the laboratory of Department of Aquaculture and Aquatic Diseases, University of Veterinary Science or laboratory Aquatic Bioscience, University of Yangon with oxygen filled plastic bags. The total length, standard length and body weight of each specimen were immediately measured and recorded. Fish were dissected and kidneys were collected to examine the parasites. The kidney is divided into 2 parts. One part was used for smear slide preparation and other for histological slides preparation. For smear slide preparation, the kidneys of fish were checked under stereomicroscope for the cyst formation of myxosporean. Kidneys were squeezed with cover slip with 1 drop of normal saline (0.9%). Occurrence of parasites was examined under light microscope, Olympus – CX 31.

Identification of parasites

Identification myxosporean parasites was conducted on the various morphological structures of spore such as shape, size, number of polar capsules, length and number of coils of polar filaments, intercapsular process presence or not, number of nuclei and iodinophilous vacuole in the sporoplasm, etc. according to the guidelines of Lom and Dykova (1992) and Kalavati and Nandi (2007). They were measured and photographed using the light microscope (Olympus CX 31) under x100 magnification.

Data analysis for parasites

Prevalence of parasitic infection was calculated in accordance with the following methods (Bush *et al*., 1997).

$$\text{Prevalence (\%)} = \frac{\text{Number of infected host}}{\text{Total number of host examined}} \times 100$$

Mean intensity of infection was classified four stages according to Culloty *et al*. (1999).

Stage (I): 1-20 parasites observed within five minutes of screening under x40 magnification

Stage (II): 21-40 parasites observed within five minutes of screening under x40 magnification

Stage (III): 41-60 parasites observed within five minutes of screening under x40 magnification

Stage (IV): 1-10 parasites in all field of region observed immediately in screening under x40 magnification

$$\text{Mean Intensity} = \frac{\text{Total Number of parasites recovered}}{\text{Total number of infected fishes}}$$

Fish were divided into three groups according to their total length and prevalence of infection among the group was compared. Fish sizes will group as 0-4 Cm, 4-8 Cm and 8 and above.

Preparation of Histopathological Slides

To understand the histological changes of infested tissues of kidneys, infected tissue with cyst formation were fixed 10% neutral buffered formalin. After fixation for 48 hours, the tissues were cut in order to obtain a size of 1 cm^3. The prepared tissues were dehydrated through a graded series of ethanol, cleared in xylene, and infiltrated in the paraffin. Sections were cut at 5µm in thickness on a microtome (TBS SHUR/Cut 2500) fitted with a sharpened microtome knife. These sections were then stained with Hematoxylin-Eosin. The permanent mounting of the slides was made by DPX (distyrene, plasticizer and xylene). Histopathological lesions were examined and photographed at different magnifications with the help of binocular microscope with digital camera and attached monitor (Olympus – CX 31).

Results

Myxobolus sp. infection in the kidney of *Cirrhinus mrigala*

Myxobolus sp. was recorded in the kidneys of *Cirrhinus mrigala* collected from Yezin Fisheries Station. *Myxobolus* sp. was identified and according to Lom and Arthur (1989), Lom and Dykova (1992) and Kalavati and Nandi (2007).

Morphometry of *Myxobolus* parasites

Spores of *Myxobolus* sp., measured 11.6µm±1.1µm in length and 7.6µm±0.8µm in width and appeared elongated ellipsoidal in valvular view. Two polar capsules were slightly pyriform and unequal in shape with 4 to 6 filaments, larger 5.0µm±1.1µmx3.3µm±0.5µm and smaller 3.5µm±0.8µmx3.3µm±0.5µm in size (Plate 1). Sporoplasm was finely granular and occupied most of the extracapsular cavity of spore. Spores elongated and ellipsoid in valvular view with mucus envelope around the posterior end. Two polar capsules were slightly pyriform and unequal in shape with 4 to 6 filaments. Sporoplasm was finely granular and occupied most of the extracapsular cavity of spore.

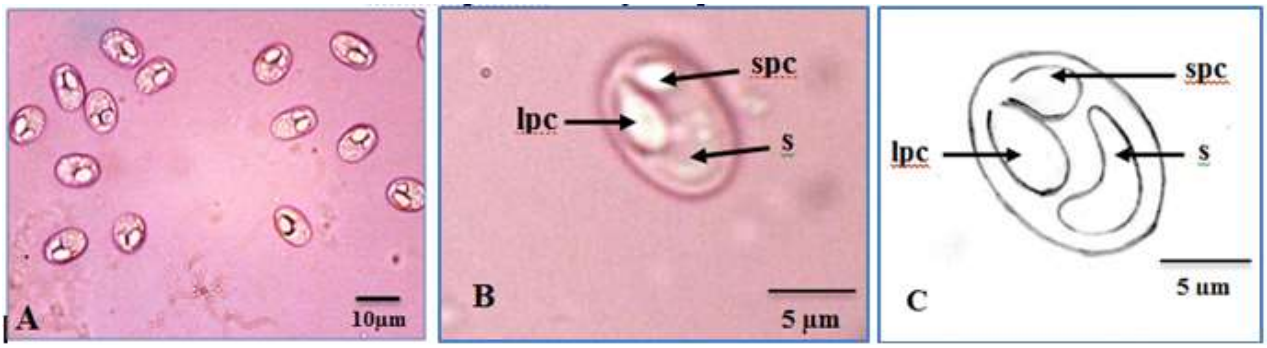

Plate 1 *Myxobolus* sp. recorded in the kidneys of *Cirrhinus mrigala* (A) *Myxobolus* sp. infected in the kidneys of *Cirrhinus mrigala* (B) Detail morphology of *Myxobolus* sp. (C) Diagramatic presentation of *Myxobolus* sp. (lpc = large polar capsule, spc = small polar capsule, s = sporoplasm)

Prevalence and mean intensity of *Myxobolus* sp. infections

The white nodule, cyst, was found on the surface of the kidney. The size of the cysts was 0.5 ± 0.08 mm (n=10). Only 16.7% of infected fish showed cysts on the kidney through the study period. Prevalence of *Myxobolus* sp. infection was examined 8%, 2%, 14%, 6% and 26% in December 2018, January, February, March and April 2019, respectively (Fig.1). The highest prevalence of *Myxobolus* sp. was 82% in August and followed by 64% in July, 54% in June and 62% in May 2019. The mean intensity of *Myxobolus* sp. was Stage 3 in July and August and the remaining months fluctuated between Stage 1 and Stage 2 respectively (Fig. 2). The total highest prevalence infection (51.6%) was observed on fish over 8.1cm group. The total lowest prevalence infection was observed on fish, under 4cm group in the present study (Fig. 3).

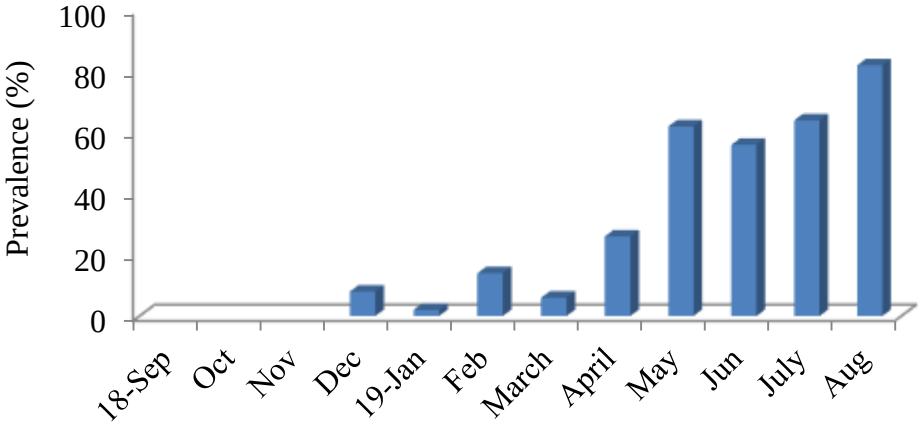

Figure 1 Prevalence of *Myxobolus* sp. in the kidneys of *Cirrhinus mrigala* during the study period, from September 2018 to August 2019.

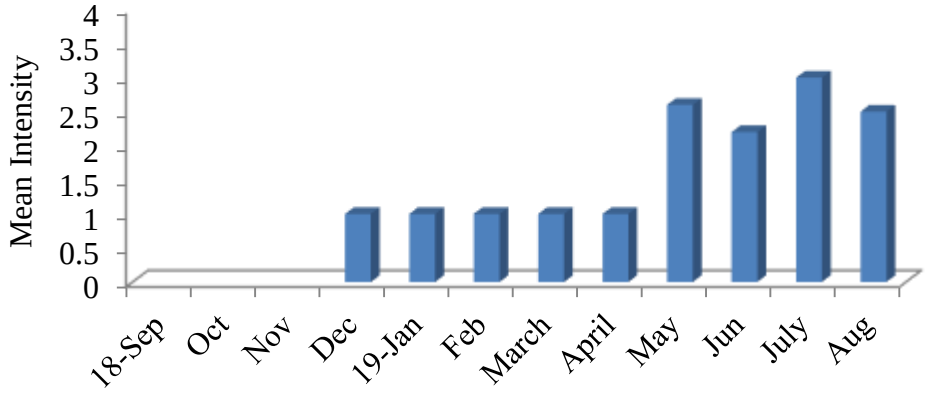

Figure 2 Mean intensity of *Myxobolus* sp. in the kidneys of *Cirrhinus mrigala* during the study period, September 2018 to August 2019.

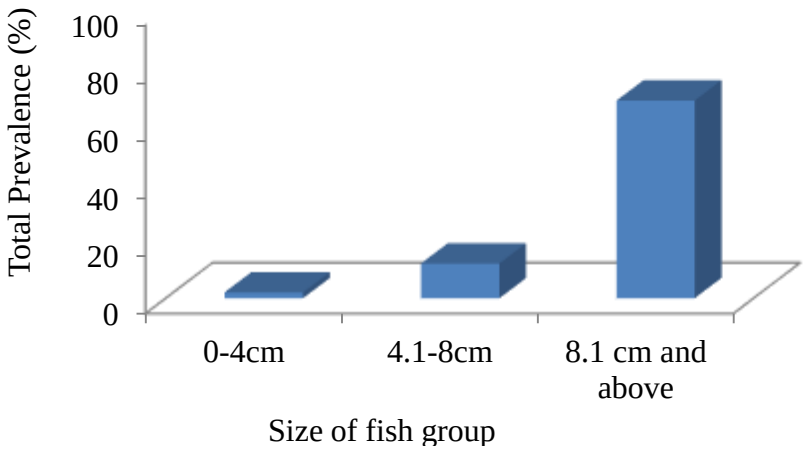

Figure 3 Total prevalence of *Myxobolus* sp. infection in the kidneys of *Cirrhinus mrigala* in relation to fish sizes.

Histopathological study of the kidneys

Pathogenesis in kidneys caused by *Myxobolus* sp. included black pigmentation, deformity of Bowman's capsule, necrotic in renal tubules and cysts of *Myxobolus* sp. in the infested kidneys of the fish (Plate 2, A). Most of the large plasmodia including mature spores and pathological lesions were also encountered in the fish kidneys. Aggregations of inflammatory cells were seen between renal tubules and the inflammatory response is indicated by the red colored tissue because of the effect of excessive erythrocytes (Plate 2, B). Pronounced change in the kidneys of fish included increasing gap between glomerulus and Bowman's capsule and shrinking of tubular lumen were observed under microscope in cross sections (Plate 2, B). The myxosporean infested kidneys showing distinct canalculi within the tissue, proliferation of Bowman's capsule and in some places necrotic renal tubules were also noted (Plate 2, C). In infested kidney cells, nucleus looks blurred due to *Myxobolus* sp. infestations so the membrane cannot be seen clearly. Dilation in the capillaries and vacuolar degeneration in the epithelium of renal tubules were observed (Plate 2, C). The infested kidney tissue showed the prominent circular vacuolar spaces filled with damaged cells necrosis in the tissue. The necrotic in kidney cells caused by parasitic infestations and abnormal increasing the haematophoitic tissue were seen in the kidney of fish (Plate 2, D). The kidney tissue showing deformity of Bowman's capsule and distal and proximal renal tubules were observed. In renal tubules, swelling of epithelial cells and large vascular formation were observed.

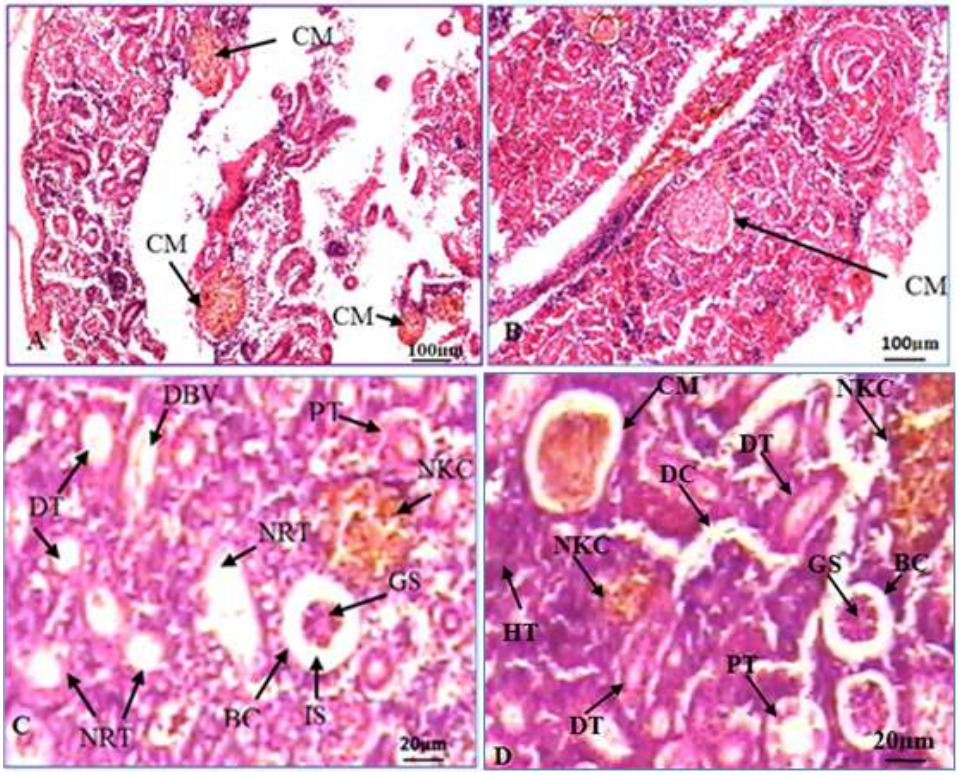

Plate 2 Pathogenesis in kidneys of *Cirrhinus mrigala* showing infested conditions under histopathological finding

(A) Fish kidney attached by *Myxobolus* sp. cyst and aggregations of inflammatory cells (CM=Cyst of *Myxobolus* sp.)

(B) Cyst in the kidneys tissue containing mature spores of *Myxobolus* sp. (CM=Cyst of *Myxobolus* sp.)

(C) Dilation in the capillaries of renal tubules (NRT=Neurotic renal tube, DBV=Degenerative blood vessels, DT=disorganized tubules, NKC=Necrotic kidney cell, GS=Glomerular Shrinkage, IS=Increase Space between glomerulus and Bowman's capsule, BC=Bowman's capsule, PT=Proximal tube)

(D) Deteriorated and necrotic kidney caused by *Myxobolus* sp. infestations (DT=disorganized tubules, PT=Proximal tube, NKC=Neurotic Kidney cell, GS=Glomerular Shrinkage, BC=Bowman's capsule, HT=Hematopoietic tissue, DC=Distinct canalculi, CM=Cyst of *Myxobolus* sp.)

Discussion

The present study was conducted to assess the incidence and parasite infestation in the kidneys of *Cirrhinus mrigala* with respect to different months. *Myxobolus* sp. was isolated and identified from the fish samples collected from Yezin Fishery Station, Nay Pyi Taw Region. *Myxobolus* sp. is the predominant species group within the phylum Cnidarian. Most of the species infect primarily fish, both freshwater and marine species and a few numbers of species were found in amphibians (Lom and Dykova, 2006).

Myxobolus species were recorded in the kidneys of *Cirrhinus mrigala.* A total of 112 nominal species were described for *Myxobolus sp.* (Butschli, 1882). The shape and dimension of *Myxobolus* sp. recorded in the present study is similar to *Myxobolus eirasi* infected in caudal fin of *Cirrhinus mrigala* and *Myxobolus guangzhouensis* infected in scales of *Cirrhinus mrigala* (Eiras *et al*., 2014). However, length of polarcapsules was slightly different. The shape and size of *Myxobolus* sp. detected in this study is similar to *Myxobolus* sp. 7 infected in gills and kidney of *Cirrhinus mrigala* cultured in Mandalay, Kantawgyi Lake which is reported by (Pa Pa Win, 2007).

Yokoyama *et al.*, 2014 discussed that although of Myxosporean are simlar, the species are assumed to be different if the host fish species and infection sites are different. *Myxobolus* can be identified by the morphological characters of the spores and the location and size of plasmodia. However, this technique is inconsistent due to many other biological features, such as life cycle, morphology of myxospores and actinospores or host and tissue preferences. Moreover, the morphological classification is artificial and does not reflect phylogenetic relationships reacquired from molecular data according to recent analyses (Fiala, 2006). The classification of myxosporeans recorded in the present study should be expended to phylogenetic analyses because molecular biological methods have become increasingly applied in parasitological studies.

High prevalence infection was found from August 2019 when the fish was about 1year old. Tun *et al*. (2014) reported the prevalence of gallbladder myxosporean parasite, *Zschokella honjoi* infection in *Labeo rohita* and they found that the infection decreased when the size of fish increased. However, their finding is based on the Myxozoan parasites recorded in the external organs such as skin, gills and fins. For internal organs, Myxosporeans parasite should need infection time to penetrate to the target organs. Gastrointestinal myxosporeans, *Enteromyxum* spp., known to cause severe disease in numerous species of cultured marine fishes globally showed high prevalence of infection when the fish are more than 1year old (Yanagida *et al*., 2006). It is assume that Myxospreans infection in internal organs takes time.

In the present study, the kidneys showed distinct black melanin pigmentation, necrosis of nephric tubules, vacuole formation and enlargement of Bowman's capsule. Similar, small early developmental stages of the myxosporean parasites, dilation of blood vessel and hyperplasia of blood cells were observed in the kidneys of mrigal collected in Kantawgyi Lake (Pa Pa Win, 2007). The necrosis of the renal tubules affects the metabolic activities and promotes metabolic abnormalities in fish (Yokote, 1982). Therefore, it is a target organ in many diseases due to the

affinity of the organ for circulating particulate antigens. Kidneys are important organs in excretion and regulation of water and salt concentrations within the fish body. Pathological signs in kidneys such as necrotic kidney tubules, hemorrhage and vacuolation were observed. In this finding, the kidneys showed the prominent circular vacuolar spaces filled with damaged cells and necrosis of the tissue.

Since the fish in Yesin Fishery Station was cultured in earthen pond, it is difficult to estimate the mortality due to infection. However, according to the damage of kidney reveled in the histological studies of the present finding indicated the negative effect of *Myspobolus* sp. to Marigal fish cultured in Yezin Fishery Station. Therefore, *Myxobolus* sp. recorded in the present study are threatening species for fish hatcheries. In addition it can have impact on natural population of *Cirrhinus mrigala* in near future. *Cirrhinus mrigala* is important aquaculture species in Myanmar for both local consumption and export market. They have been cultured in earthen ponds which will be one of the factors for disease transmission of Myxosporean since Tubifex in the earthen pond acts as an alternative host in the lifecycle species of Myxozoa. The present finding will support the fishery sector for the management of parasitic infection in earthen pond culture system for *Cirrhinus mrigala.* Management practices and pond hygiene should be adopted in operation systems of Yezin Fishery Station.

Conclusion

The kidneys of *Cirrhinus mrigala* collected from Yezin Fishery Station is infected with *Myxobolus* species. High prevalence of infection was recorded from May to August, 2019. Black pigmentation, distinct canalculi within the tissue, proliferation of Bowman's capsule and in some places necrotic renal tubules were noted in the infected tissue. Therefore, management practices and pond hygiene should be adopted in operation systems of Yezin Fishery Station for the production of more hygienic and successful yield.

Acknowledgements

I would like to thank Dr. Win Ohnmar Kyaw, Professor and head of Department of Aquaculture and Aquatic Diseases, University of Veterinary Science for her encouragements to carry out this study. Profound indebtedness are due to U Khin Maung Maw, Director General, Department of Fisheries, for allowing me to conduct the study at Yezin Fishery Station; U Soe Paing, Assistant Director, Yezin Fishery Station, Department of Fisheries, for supporting fish specimens and fish pond to conduct this work at Yezin Fishery Station, Nay Pyi Taw.

References

Bush, A.O., Lafferty, D.K., Lotz, J.M., and Shostak, A.W., (1997). Parasitology meets ecology on its own terms: Margolis *et al*. revesited. *J. of Parasitology*. 83(4): 575-583.

Butschli, O., (1882). Myxosporidea. *In: Bornn's Klass Ordn., des Tierreiches, Protozoa*. 1: 590-603.

Canning, E.U., and Okamura, B., 2004. Biodiversity and evolution of the Myxozoa. *Adv Parasitol*, 56: 43-131.

Culloty, S.C., Novoa, B., Pemas, M., Longshaw, M., Mulcahy, M.F., Fieist, S.W., and Figueras, A., (1999). Susceptibility of a number of bivalve species to the protozoan parasite *Bonamia ostera* and their ability to act as vector for this parasite. *Disease of Aquatic Organisms*. 37: 73-80.

Eiars, J.C., Monar, K., and Lu, Y.S., (2005). Synopsis of the species of Myxobolus Butschli, 1882 (Myxozoa: Myxosporea: Myxobolidae). Systematic Parasitology 61: 1-46.

Eiras, J.C., Zhang, J., and Molnar, K., (2014). Synopsis of the species of Myxobolus Butschli, 1882 (Myxozowa: Myxosporea, Myxobolidae) described between 2005 and 2013. *Syst Parasitol*. 88: 11-36.

Fiala, I., (2006). The phylogeny of myxosporea (Myxozoa) based on small subunit ribosomal RNA gene analysis. *Int. J. Parasitol.* 36: 1521-1534.

Kalavati, C., and Nandi, N.C., (2007). The *Handbook on Myxosporean Parasites of Indian Fishes*. Department of Zoology, Andhra University, Vishakhapatnam Zoological Survey of India, M-Block, New Alipore, Kolkata 700 053 Edited by the Director, Zoological Survey of India, Kolkata.

Kay Lwin Tun, (2016). Parasitic infection in fresh water cultivated fishes in Myanmar. Myanmar Aquaculture Science and Technology Symposium, Myanmar. Page-9.

Kay Lwin Tun, Hnin Hnin Htay, July Maung Maung, Yokoyama, H., Yoshinaga, T., (2014). Seasonal fluctuation of Myxozoan infection in Rohu, *Labeo rohita* (Cypriniformes: Cyprinidae), in Myanmar. ISAAH 7. Oregon, United States. pp. 34.

Kay Lwin Tun, Hnin Hnin Htay, Yaung Naung, Yokoyama, H., and Yoshinaga, T.,(2017). Morphology, phylogeny and seasonal fluctuation of Zschokkella sp. (Myxozoa: Myxosporea) infecting the gallbladder of *Labeo rohita* (Cypriniformes: Cyprinidae) HISF 20th Anniversary International Symposium, Tokyo, Japan. Page-40.

Kayis, S., Ozceplep, T., Capkin, E., and Altinok, I., (2009). Protozoan and metazoan parasites of cultured fish in Turkey and their applied treatments. *The Israel Journal of Aquaculture* – Bamidgeh, 61: 93-102.

Kent, M.L., Andree, K.B., Bartholomew, J.L., Matbouli, M., and Desser, S.S., (2001). Recent advances in our knowledge of the Myxozoa. *J. Eukaryot Microbiol.,* 48: 395-413.

Liu, C.I., (1981). *The pathology of major diseases of eel in Taiwan*. Proceedings of the Republic of China-United States Cooperative Science Seminar on Fish Diseases. Science Council, Taipei, Taiwan, Republic of China.

Liu, Y., Hu, G., Cao, L., Wang, X., and Chen, M., (2019). A comparison of Monte Carlo methods for computing marginal likelihoods of item response theory models. *Journal of the Korean Statistical Society*. 48(4): 503-512.

Lom, J., and Arthur, 1.R., (1989). A guideline for preparation of species descriptions in Myxosporea. *Journal of Fish Diseases*. 12: 151-156.

Lom, J., and Dykova, I., (1992). *Protozoan Parasites of Fishes*, Developments in Aquaculture and Fisheries Science, *Elsevier Science, Amsterdam*. 26: 315.

Lom, J., and Dykova, I., (2006). Myxozoan genera: Definition and notes on taxonomy, life cycle, terminology and pathogenic species. *Folia Parasitological*. 53: 1-36.

Mishra, B.K., Kumar, D., Dey, R.K., and Suresh, K., (1982). Observation on renal myxosporidiasis in Indian major carps. *Abst Proc Symp on Diseases of Finfish and Shelfish*. Mangalore, Karnataka: College of fisheries. 1-3.

Moe Kyi Han, (2006). Study on the myxosporean infection in Rohu, *Labeo rohita* (Halminton, 1822). *PhD Thesis*. Department of Zoology, University of Mandalay.

Pa Pa Win, (2007). Effect of some feeds on Myxosporean infection in Mrigal, *Cirrhinus mrigala* (Hamiltion, 1822). *PhD Thesis*, Department of Zoology, Univsesity of Mandalay.

Sanaullah, M., and Ahmed, A.T.A., (1980). Gills myxoboiasis of major carps in Banladesh. *Journal of Fish Disease*, 3: 349-354.

Sein Sein Myint,(2007). Study on the myxosporean infection in common carp, *Cyprinus carpio* (Linneaus, 1785), *PhD Thesis*, Department of Zoology, Universityof Mandalay.

Shwe Sanda, Myint Myint Win and Thant Zin, (2020).Occurrence of Parasites in Some Freshwater Fish Species from Taungthaman Lake, Amarapura Township, Mandalay Region. Pinlong University Research Journal. 12(2): 254-260.

Snieszko, S.F., (1983). *Diseases of fishes: Research and Control*. *Fisheries* 8(1): 20-22.

Ullah, F., Sultana, T., Khan, L., Feroz, K., Ahmad, Q.A., and Hussain, S., (2017). Histopathological alteration in Gill, Kiney and Liver of *Cirrhinus mrigala*, *Catla catla*, *Hypophthalmichthys molitrix* and *Labeo rohita* due to sub-lethal exposure of textile industries effluents in Faisalabad, Pakistan. *Journal of Entomology and Zoology Studies*, 5(2): 54-62.

Yanagida T., Sameshima M., Nasu H., Yokoyama H., and Ogawa K., (2006). Temperature effects of the development of Enteromyxum spp. (Myxozoa) in experimentally infected tiger puffer, Takifugu rubripes (Temminck & Schlegel). *Journal of Fish Diseases*. 29: 561-567.

Yokote, M., (1982). Vascular system. In: Hibiya T. (ed.) An atlas of fish histology normal and pathological features, Gustav Fischer Verlag, Stuttgart, pp. 58-73.

Yokoyama, H., Suzuki, J., and Shirakashi, S., (2014). *Kudoa hexapunctata* n. sp. (Myxozoa: Multivalvulida) from the somatic muscle of Pacific bluefin tuna *Thunnus orientalis* and re-description of *K. neothunni* in yellowfin tuna *T. albacares*. Parasitol Int. 63(4): 571-579.

Yu, Y., and Wu, B., (1992). Histological studies on the twist diseases of *Hypophthalmicthys molitrix*. *J. Zhejiang Coll Fish*. 11: 95-97.

SOME BEHAVIORAL ACTIVITIES OF *GALLINULA CHLOROPUS* (COMMON MOORHEN) IN MEIKTILA UNIVERSITY CAMPUS

San San Htay[1], Myin Zu Minn[2], Ni Ni Yin[3]

Abstract

In the study period from January 2019 to December 2019, five behavioral activities of Common Moorhen were studied under four different diurnal periods. Concerning different diurnal periods, the relative percentage of time spent on locomotion and foraging was highest in the early morning. Grooming and reproductive behavior were highest in the late morning. The relative percentage of time spent resting behavior was highest in the mid-day. The time spent on locomotion varied among four different diurnal periods ($P<0.05$). Grooming activity differed among four different diurnal periods ($P<0.05$). Diurnal time spent on foraging activity varied among four different diurnal periods ($P<0.05$). No significant differences were found in resting activity in the time blocks of the day ($P>0.05$). Reproduction activity was not varied in the time blocks of the day ($P>0.05$). Throughout the study period, the dominant behavior was foraging and the contrary was reproduction. The next to foraging was locomotion and grooming because after the feeding peak in a place they usually change feeding place to search for more foods which increases their movement. Moving peak at next hour of foraging and feeding peak could be the reason for this. The minimum activity throughout the study period was reproductive behavior. Although Common moorhen breed all year, it breeds three broods in one year during the study period were recorded. Thus reproductive behavior among the behavioral activities was minimized. Among five behavioral activities of Common Moorhen throughout the study period was varied ($P<0.05$).

Keyword: behavioral activities, four different diurnal periods, *Gallinula chloropus*

Introduction

Bird's activity study is significant in understanding its life history, physical condition, food availability, social structure, as well as ecological condition (Sultana and Sarker, 2016). Behavior is also believed to be consisting of various expressions of a bird in response to the internal stimuli mainly related to the physiological needs. Bird's visual signals are communicated by the movements of the head, body, tail, wings and body feathers (Najafi *et al.,* 2012). Calls are vocal displays of birds whereas the extrinsic stimuli depend on the biotic and abiotic factors of the habitat (Quader, 2003). Behaviors may be regarded either as events or as states. Events are instantaneous and states have appreciable durations (Altmann, 1974). Activity pattern studies quantify the time allocation of animals performing behavioral activities (Rave and Baldassarre, 1989).

The amount of time allocated to various behaviors is therefore critical in understanding the ecological needs of a species and the pressures acting upon individuals of that species. The patterns of daily activity and behavior often vary among and within species (Jeschke and Tollrian, 2005); as a result, these activity patterns help us to study the life history and ecological adaptations of birds (Hamilton *et al*. 2002). The time-activity patterns of birds vary greatly according to the type of habitats they inhabit and the food they eat (Ali and Asokan, 2015).

The common moorhen (*Gallinula chloropus*) is a medium-sized member of the rail family found in aquatic environments. It has gray-black feathers and a red bill with a yellow tip. It has white stripes on its sides. They live in freshwater and brackish marshes and ponds with cattails and other aquatic vegetation. They are omnivorous and feed while walking on plants or on the edge of the water or while floating on the water (Robson, 2015).

[1] Lecturer, Department of Zoology, Meiktila University
[2] Pro-Rector, Mohnyin University
[3] Professor and Head, Department of Zoology, Meiktila University

A man-made pond on the Meiktila University Campus is a favorable habitat with emergent vegetation and various food resources for Common Moorhen, so that they are found throughout the year as common resident and breeds in this pond. Therefore, Common Moorhen was selected as a target species for behavioral study, and the present study was carried out with the following objectives:

- to study the different behavioral activities of the Common Moorhen (*Gallinula chloropus*)
- to assess the relative monthly percentage time spent in different diurnal periods and throughout the study period

Materials and Methods

Study Design

Behavioral activities of Common Moorhen (*Gallinula chloropus*) in a man-made pond on Meiktila University Campus were observed once a week. Observations were carried from a vantage point on the bank of the pond and consisted of four different diurnal periods at two hours sessions per period following the focal animal sampling method (Altmann, 1974). The four period consisted of two periods in the morning and two in the afternoon and commenced from early morning (6:00-8:00 am), and late morning (9:00 -11:00 am), followed by mid-day (12:00-2:00 pm) and afternoon (3:00-5:00 pm) respectively.

Focal animal sampling means all occurrences of behaviors of interest are recorded for a particular individual during an entire sample period. This method was chosen because it allows the observer to record the time in minutes of each behavioral act. This sampling was carried out at intervals of fifteen minutes for a total observation period of 192 hours from January 2019 to December 2019 involving 48 different days and resulting in 768 focal samples.

A particular bird was followed and its activities were noted down. The duration of each activity was recorded using a stopwatch. When the bird under the observation was moved out of sight another bird was focused. The birds were observed with the camera or binoculars or naked eyes and photographic record and video were taken as much as possible. Activities were categorized as locomotion, grooming, foraging, resting, and reproduction followed by Wallau *et al*., 2010.

Time spent for each behavioral category recorded was pooled for predetermined each of the diurnal periods and converted into the proportion of time spent in all behavior for each diurnal period, monthly and throughout the study period.

Statistical analysis

Statistical analysis was done using Statistical Package for the Social Science (SPSS), version 26. Normality tests were done before the analysis. Non-parametric ANOVA test (Kruskal-Wallis test) was used to find the significant differences among the activities.

Identification

The identification of Common Moorhen was conducted with reference to Robson, 2015. The identification of behavioral categories of Common Moorhen was based on Wallau *et al*., 2010.

A map of Meiktila University Campus showing the study site (Google Earth, 2007)

Results

The behavior of Common Moorhen (*Gallinula chloropus*) was observed from January 2019 to December 2019. A total of 15 behavioral acts were described, grouped into five categories: locomotion (N=5 acts; walking, running, jumping, flying, and swimming), grooming (N=4 acts; Bathing, shaking the feathers, preening the feathers, and cleaning the beak), foraging (N=2 acts; eating and drinking), resting (N=2 acts; sprawling and wings open/half-open/beating) and reproduction (N=2 acts; courting and copulating) (Table 1, Plate 1). Weekly diurnal activity budgets of Common Moorhen were pooled into monthly and then throughout the study period.

Relative percentage time spent of Common Moorhen in different diurnal periods throughout the study period

Concerning predetermined four different diurnal periods, the maximum percentage time spent evaluated for locomotion was 33.62 % in the early morning and the minimum was 19.76 % in the mid-day (Table 2). There was a significant difference among four different diurnal periods in locomotion ($P<0.05$). The highest percentage time spent for grooming in the late morning indicates 29.75 % and the lowest was 20.63 % in the afternoon (Table 3). Grooming activity differed among four diurnal periods ($P<0.05$). Foraging was highest in the early morning 31.77 %, and then decreased in late morning 17.56 % (Table 4). Diurnal time spent on foraging activity varied among four different diurnal periods ($P<0.05$). The observed birds that spent most of the time resting were mid-day 33.55 % and least in the early morning 19.35 % (Table 5). No significant differences were found in resting activity in the time blocks of the day ($P>0.05$). The evaluated dominant time spent in reproduction was 10.31 % in the early morning and increased to 35.05 % in the late morning. It was found to be gradually decreased to 27.84% and 26.8% in the mid-day and afternoon respectively (Table 6). Reproduction activity was not varied in the time blocks of the day ($P>0.05$).

Total percentage time spent for different behavioral activities of Common Moorhen throughout the study period

The five behavioral activities observed for Common Moorhen throughout the study period were also varied. During the study period, the evaluated dominant behavior was foraging which

indicates 34.34 %, and the contrary was reproduction at 1.77% (Table 7, Fig. 1). Five behavioral activities of Common Moorhen throughout the study period were varied ($P<0.05$).

Table 1 Behavior activities of *Gallinula chloropus* (Common Moorhen)

Behavior categories	Behavior acts
Locomotion	1. walking 2. running 3. jumping 4. flying 5. swimming
Grooming	6. bathing 7. shaking the feathers 8. preening the feathers 9. cleaning the beak
Foraging	10. eating 11. drinking
resting	12. sprawling 13. wing open/ half-open/ beating
Reproduction	14. courting 15. copulating

Table 2 Relative percentage time spent of *Gallinula chloropus* for locomotion in different diurnal periods throughout the study period

Month	Early morning (min)	Late morning (min)	Mid-day (min)	Afternoon (min)	Total (min)
January	51	34	33	44	162
February	44	24	28	22	118
March	41	31	34	41	147
April	36	20	12	25	93
May	58	38	37	53	186
June	58	38	36	56	188
July	39	24	23	36	122
August	55	20	27	32	134
September	42	23	17	23	105
October	52	35	41	44	172
November	57	45	39	48	189
December	59	31	21	34	145
Total	**592**	**363**	**348**	**458**	**1761**
%	33.62	20.61	19.76	26.01	

Table 3 Relative percentage time spent of *Gallinula chloropus* for grooming in different diurnal periods throughout the study period

Month	Early morning (min)	Late morning (min)	Mid-day (min)	Afternoon (min)	Total (min)
January	30	44	59	37	170
February	42	34	5	39	120
March	14	39	28	12	93
April	20	28	30	27	105
May	30	33	35	26	124
June	31	44	40	37	152
July	28	49	34	18	129
August	36	41	52	27	156
September	45	49	46	21	161
October	29	54	48	40	171
November	23	31	40	21	115
December	15	24	24	21	84
Total	343	470	441	326	1580
%	21.71	29.75	27.91	20.63	

Table 4 Relative percentage time spent of *Gallinula chloropus* for foraging in different diurnal periods throughout the study period

Month	Early morning (min)	Late morning (min)	Mid-day (min)	Afternoon (min)	Total (min)
January	49	27	45	55	176
February	45	7	33	48	133
March	55	20	48	49	172
April	58	58	40	57	213
May	53	18	27	47	145
June	49	35	39	42	165
July	45	31	33	39	148
August	41	21	31	38	131
September	36	14	21	33	104
October	50	24	29	44	147
November	57	44	35	47	183
December	59	31	28	44	162
Total	597	330	409	543	1879
%	31.77	17.56	21.77	28.9	

Table 5 Relative percentage time spent of *Gallinula chloropus* for resting in different diurnal periods throughout the study period

Month	Early morning (min)	Late morning (min)	Mid-day (min)	Afternoon (min)	Total (min)
January	1	3	13	2	19
February	2	3	7	0	12
March	1	1	0	1	3
April	2	1	2	1	6
May	1	1	1	2	5
June	5	9	4	4	22
July	4	4	7	8	23
August	4	2	5	7	18
September	2	1	7	5	15
October	3	3	2	2	10
November	3	5	3	5	16
December	2	1	1	2	6
Total	30	34	52	39	155
%	19.35	21.94	33.55	25.16	

Table 6 Relative percentage time spent of *Gallinula chloropus* for reproduction in different diurnal periods throughout the study period

Month	Early morning (min)	Late morning (min)	Mid-day (min)	Afternoon (min)	Total (min)
January	5	10	4	3	22
February	0	0	0	0	0
March	0	0	0	0	0
April	0	7	4	5	16
May	0	5	6	4	15
June	0	0	0	0	0
July	0	0	7	5	12
August	0	0	0	0	0
September	0	0	0	0	0
October	0	7	6	4	17
November	0	0	0	0	0
December	5	5	0	5	15
Total	10	34	27	26	97
%	10.31	35.05	27.84	26.8	

Table 7 Total percentage time spent for different behavioral activities of *Gallinula chloropus* throughout the study period

Month	Locomotion (min)	Grooming (min)	Foraging (min)	Resting (min)	Reproduction (min)	Total (min)
January	162	170	176	19	22	549
February	118	120	133	12	0	383
March	147	93	172	3	0	415
April	93	105	213	6	16	433
May	186	124	145	5	15	475
June	188	152	165	22	0	527
July	122	129	148	23	12	434
August	134	156	131	18	0	439
September	105	161	104	15	0	385
October	172	171	147	10	17	517
November	189	115	183	16	0	503
December	145	84	162	6	15	412
Total	1761	1580	1879	155	97	5472
%	32.18	28.87	34.34	2.83	1.77	

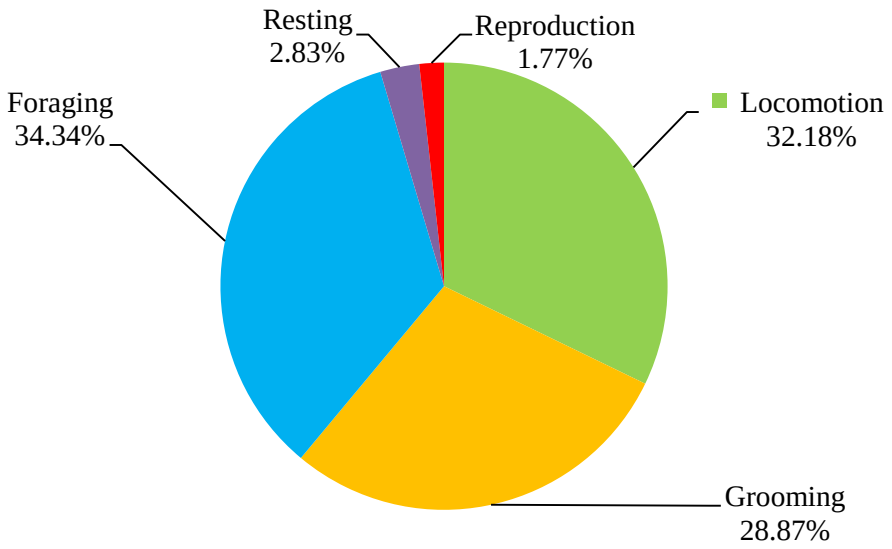

Figure 1 Overall activity budget of *Gallinula chloropus* (Common Moorhen)

A. Walking

B. Running

C. Jumping

D. Flying

E. Swimming

F. Bathing

G. Shaking the feathers

H. Preening the feathers

I. Cleaning the beak

J. Eating

K. Drinking

L. Sprawling

M. Wing open/ half-open/ beating

N. Courting

O. Copulating

Plate 1 Behavioral acts of *Gallinula chloropus* (Commom Moorhen)

Discussion

The activity budget is defined as the proportion of time an animal spent in different activities that are important for its survival in reproduction. In the present study, the diurnal time spent of Common Moorhen was evaluated for four different diurnal periods and throughout the study period. With regard to different diurnal periods throughout the study period, the relative percentage of time spent on Common Moorhen showed that locomotion and foraging were found to be highest in the early morning because, most of the feeding activities were usually found in the early morning due to the lack of human disturbance and low temperature. Thus, both of these behaviors were found to be highest in the early morning. After overnight fasting, they try to maximize foraging, feeding, and locomotion during the early morning as reported in Akhtar *et al*.,

2013. A similar result found in the behavior of the Common Moorhen reported by Wallau *et al*., 2010. On the other hand, minimum foraging activity was found in the late morning and locomotion was in the mid-day. Therefore locomotion and foraging were mainly concentrated in the morning and decreased as the day proceeded. This may be due to the rising temperature in the late morning and they gradually go back to the shelter in the mid-day and is similar to the finding of Acquarone *et al*., 2001. Evaluated grooming and reproductive behavior (courting and copulating) were highest in the late morning. The reason for grooming is that Common Moorhen made the grooming just after most of the activities of foraging and locomotion. Akhtar *et al*., 2013 described that grooming is usually found to increase after swimming and it is one of the important body-maintenance activities of birds. Bathing and preening, scratching with the claws, help allay itching, remove ectoparasites, and clean the feathers. Preening with oil from the uropygial gland helps them to maintain their feather very well. Minimum time spent for grooming activity was found in the afternoon for that they spent much time for grooming in the late morning.

Moorhen devoted the most time to reproductive behavior was in the late morning because reproductive activities are energetic and assumed to make after feeding. A similar concept was found in the research reported by Frost, 2008 that continuous breeding is realized as a consequence of a primarily favorable and availability of food supply and is the ultimate factor in triggering opportunistic breeding. Akhtar *et al.*, 2013 stated that after the first bout of feeding, they were found to use their energy in breeding activities. The contrary was found in the early morning.

Common Moorhen spent less time in resting behavior. The peak of resting activity was evaluated in the mid-day. This can be assumed that Moorhen became dormant and take a rest most of the time in the mid-day. It could be also explained as to minimize their energy expenditure at the mid-day when the temperature became higher. Akhtar *et al.*, 2013 reported that the resting peak was at mid-day and on the mid-day to avoid hot weather especially during summer. On the other hand, minimum resting and reproduction activities were found in the early morning. This may be due to actively foraging in the early morning.

Throughout the study period, five behavioral activities observed for Common Moorhen were also varied. The evaluated dominant behavior was foraging and the contrary was reproduction. The next to foraging was locomotion because after the feeding peak in a place they usually change feeding place to search for more foods which increases their movement. Moving peak at next hour of foraging and feeding peak could be the reason for this. A similar result was found in the activity pattern of white-breasted waterhen reported by Akhtar *et al*., 2013. The minimum activity throughout the study period was reproductive behavior. Although Common moorhen breed all year, it breeds three broods in one year during the study period. Thus reproductive behavior among the behavioral activities was minimized.

The present finding showed that Common Moorhen spent a different proportion of time in different activities and activity patterns significantly varied in different hours of the day as well as in different months which help them to avoid interspecific conflicts with other wetland birds in the same feeding and breeding habitats.

Conclusion

The behaviors of Common Moorhen were observed from a pond on Meiktila University Campus. Throughout the study period, 15 behavioral acts under five behavior categories were recorded. The time-activity patterns of birds vary greatly according to the type of habitats they inhabit and the food they eat. Time-budget studies quantify the time animals allocate to different activities, and the resulting information can increase our understanding of strategies in different activities and habitat needs of common moorhen. The present finding will play an important role for the management and conservation of this bird as well as other wetland birds.

Acknowledgements

I would like to grateful to Rector Dr Ba Han for his permission for doing research. I would like to express my deep gratitude to Dr.Myin Zu Minn, Pro-Rector, Mohnyin University for her supervision and invaluable suggestions. I also thank to Professor (Head) Dr Ni Ni Yin, Department of Zoology, Meiktila University for her co-supervision and moral support.

References

Altmann, J., (1974). Observational study of behavior: Sampling methods. Behavior 49(3-4): 227-267

Acquarone, C., Cucco, M. and Malacarne, G., (2001). Daily and seasonal activity of Moorhens studied by motion-sensitive transmitters. *Waterbirds*, 24(1):1-7.

Akhtar, S., Kabir, M.M., Begum, S. and Hasan, M.K., (2013). Activity patterns of White-breasted Waterhen (*Amaurornis phoenicurus*) at Jahangirnagar University Campus, Savar, Dhaka, *Bangladesh. J. Zool*., 41(2): 189-198.

Ali A.M.S. and Asokan S., (2015). Diurnal-activity patterns of the small bee-eater (*Merops orientalis*) in Southern India. *Tropical Life Sciences Research*, 26(1): 9-20.

Frost, P., (2008). Continuous breeding and associated behaviour in the Moorhen *Gallinula chloropus*. Available from https://www.research.net/publication.

Hamilton, A. J., Taylor, I. R., and Hepworth, G., (2002). Activity budgets of waterfowl (Anatidae) on a waste-stabilisation pond. *Emu Volume* 102: 171-179.

Jeschke, J. M. and Tollrian, A. D., (2005). Predicting herbivore feeding times. *Ethology* 111 (2): 187-206

Najafi, N. N., Kahrom, E., and Karami, M., 2012. Preliminary Survey of the Breeding Biology of the Purple Swamphen *Porphyrio porphyrio* in Anzali wetland, Southwest Caspian Sea. Podoces, (2012), 7(1/2): 9-15, Journal homepage, www.wesca.net.

Quader, S., (2003). Nesting and mating decisions and their consequences in the Baya weaverbird *Ploceus philippinus*. Doctorate thesis submitted to university of Florida.

Rave, D. P., and Baldassarre, A., (1989). Activity budget of Green Winged Teal wintering in coastal wetlands of Louisiana. *Journal of Wildlife Management* 53(3): 753-759.

Robson, C., (2015). *A field guide to the birds of South-East Asia*. New Holland Publishers Ltd. London. 324 pp.

Rana, S., (2018). Habitat selection and behavior of purple moorhen (*Porphyrio porphyrio*) in district Ambala, Haryana, India. *International Research Journal of Biological Sciences*, 7(3): 41-45.

Sultana, M. and Sarker, N.J., (2016). Patterns of daily activities frequencies of Common Kingfisher (*Alcedo atthis*) in Nikunja-1, Dhaka. *International Journal of Fauna and Biological Studies*, IJFBS. 3(5): 23-28.

Wallau, G.L., Della- flora, F., Bueno, A. S., Corso, J., Ortiz, M.F. and Caceres, N.C., (2010). *Behavior of the Common Moorhen in Rio Grande do Sul, Brazil*. 5 pp

A FAUNISTIC SURVEY ON THE GASTROINTESTINAL PARASITES OF SOME MARKETABLE BIRDS IN MEIKTILA TOWNSHIP, MANDALAY REGION

Chaw Su Hlaing[1], Toe Nyunt[2]

Abstract

Local resident around Meiktila environs enjoy selling wild birds as protein sources at Pauk Chaung markets of Meiktila Township, Mandalay Region. In the present study, some specimens of birds were purchased from Pauk Chaung market, Meiktila Township and freshly dead specimens were transported to laboratory of Zoology Department, Meiktila University. The goal of research investigated helminth species that harboured in the gastrointestinal tracts of five marketable bird species. Helminths collected as alive or dead and lactophenol was used as cleaning agent. Parasites were identified by using morphometric measurements and morphological descriptions. During the study period fifty gastrointestinal tracts from five species of birds were examined. Thirty-two birds out of 50 examined birds, showed infestation with eight species of cestodes, four species of nematodes and one species of acanthocephalans. The highest infected rate was observed in cestodes (51.16%), followed by nematodes (46.88%), and acanothocephalans (1.96%). The prevalence of helminths was (50.09%) in small intestine, however single helminths was incidence in the oesophagus plus crop and proventriculus plus gizzard. Not a single trematode was encountered throughout the study period. A high percentage of heiminthiasis was observed in the studied birds.

Keywords: bird helminth, Gastrointestinal parasites, prevalence, Meiktila

Introduction

Poultry acts as an important source of animal protein (meat and egg) for man (Ola-Fadunsin *et al.,* 2019). Helminth parasites appear in many birds, usually without causing much damage. There were often heavy intestinal infestations in birds which died of disease or which died of starvation during hard weather (Clapham, 2009). Presence of gastrointestinal parasites in birds causes severe economic losses in terms of reduced body weight gain, decreased egg production, sometime even mortality and affects the quality and quantity of meat production also (Sivakumar *et al.,* 2017).

Vertebrates are parasitized by four major groups of helminths (worms). Two of the groups, trematodes, or flukes, and cestodes, or tapeworms, fall within the Phylum Platyhelminthes. The other two groups are the nematodes, or roundworms, (Nematoda) and the acanthocephalans, or thorny-headed worms (Acanthocephala) (Sepulveda and Kinsella, 2013).

Helminthiasis was considered to be important problems in chickens. Avian cestodiasis constitutes one of the most common endoparasitism causing serious troubles in chicken production (Shahin *et al*., 2011). Multiple gastrointestinal tract (GI tract)) parasitic infection is a common phenomenon in poultry, affecting their normal activities which is manifested mainly by severe pains (Ola-Fadunsin *et al.,* 2019). This study was undertaken to determine the prevalence and incidence of different helminth parasites that occurred in gastrointestinal tract of the bird species.

[1] Associate Professor, Department of Zoology, Meiktila University
[2] Lecturer, Department of Zoology, Meiktila University

Materials and Methods

Host and collection of the parasitic specimens

A total of 50 birds which included four terrestrial bird species *Gallus domesticus*, *Turnix tanki*, *Streptopelia chinensis*, *Ploceus manyar* and a single water bird species of *Gallinula chloropus* were purchased from Pauk Chaung market in Meiktila during study period from December 2018 to August 2019. Ten gastrointestinal tracts including caecum from each species of birds were examined. The dead specimens were placed in wooden tray and dissected with a pair of scissors along midventral line. And then the entire tract was excised and divided into four parts that is (1) the oesophagus plus crop, (2) the proventriculus plus gizzard, (3) the small intestine and (4) the caeca plus the rectum and cloaca. Each part was cut opened longitudinally with a pair of scissors in a wax tray containing tap water. The contents were poured into petri-dish and processed by method of sedimentation and decantation to find parasites.

Preparation for identification of parasite

The freshly collected worms were cleaned in normal saline and then in distilled water to remove mucous and undesirable particles that attached to the body. Lactophenol was also used as cleaning agent to give better result in observing the specimen. After which the specimens were photographed and examined under microscope. Worms were then preserved and stored in five percent formalin with five percent glycerine added.

Data analysis

Prevalence is defined as the percentage of hosts infected with one or more individuals of a particular parasite species out of the total number of hosts examined for that parasite species.

The percentage of parasites and prevalence of infestation were calculated using the following formula (Thrusfield, 2007).

$$\text{Percentage of parasites} = \frac{\text{Number of specific parasites}}{\text{Total number of parasites}} \text{ X } 100$$

$$\text{Estimated prevalence of infestation} = \frac{\text{No. of animals infested with parasites species}}{\text{Number of examined animals}} \text{ X } 100$$

Location map of the study area (Google Earth, 2019)

Results

Occurrence of helminth parasites

A total of 50 gastrointestinal tracts from five species of birds were examined for endoparasitic helminthes. Among the studied specimens, 64 % (32/50) prevalence found gastrointestinal helminthic infection in Paukchaung market. Helminth parasites included eight species of cestodes, four species of nematodes and only one species of acanthocephalans were recorded in the study.

The identified cestodes were *Raillietina echinobothrida, R. tetragona, R. cesticillus, R. georgiensis, Davainea spiralis, Choanotaenia infundibulum, Hymenolepis nana and Cloacotaenia megalops.* Birds infected with cestodes were 51.16 %. In spite of the eight species of cestodes recovered, the largest number of total parasites count was found in cestodes especially in *Hymenolepis nana*. In this study birds infected with nematodes were 46.88 %. The recorded nematodes were *Gongylonema ingluvicola,Heterakis gallinarum, Ascaridia galli* and *Subulura brumpti*. *Moniliformis moniliformis,* an acanthocephalan, with the infection of 1.96 % was found in this study (Table 1, Fig. 2)

The prevalence of parasites

In this study, *Raillietina echinobothrida* infection was (12%), *R. tetragona* (18%), *R. cesticillus* (6%), *R. georgiensis* (4%), *Davainea spiralis* (10%), *Choanotaenia infundibulum* (4%), *Hymenolepis nana* (30%) and *Cloacotaenia megalops* (12%) were recorded.

In nematodes, *Gongylonema ingluvicola* revealed (8%), *Heterakis gallinarum* (4%), *Ascaridia galli* (12%) and *Subulura brumpti* (10%). Acanthocephalan, *Moniliformis moniliformis* showed (6%). However, the incidence of *R. georgiensis, C. infundibulum* and *H. gallinarum* were rare.

The most prevalent helminth was *H. nana*, a cestode (30%) and the least percentage of (4%) was those of *R. georgiensis* and *C. infundibulum*, and *H. gallinarum*, a nematode (4%) (Table 1, Fig 1).

Organ-wise infection of parasites

Four parts of gastrointestinal tract in each specimen, i.e, oesophagus plus crop (first part), proventriculus plus gizzard (second part), small intestine (third part), and the caeca plus rectum and cloaca (fourth part) were examined for the detection of helminth parasites. *Gongylonema ingluvicola* was encountered in first part (oesophagus plus crop) was 5.17% (29 individuals) and *Heterakis gallinarum* in second part (proventriculus plus gizzard) was 0.53% (three individuals). Most of the cestode, *Raillietina echinobothrida, R. tetragona, R. cesticillus, R.georgiensis, Davainea spiralis, Choanotaenia infundibulum, Hymenolepis nana, Cloacotaenia megalops* and one of the nematodes the *Ascaridia galli,* and an acanthocephalan species *Moniliformis moniliformis,* (altogether 10 species and 281 in number) were found in third part (small intestine) was 50.09%. In fourth part (caeca plus rectum and cloaca) the cestodes encountered were *Raillietina echinobothrida, R. tetragona, Davainea spiralis, H. nana, C. megalops* and the nematode were *H. gallinarum* and *Subulura brumpti* contributed to 44.21% (seven species and 248 in number) (Table 2).

Number of helminth in specimens recorded

With regard to the host specimens examined, twelve species of parasites were encountered in *Gallus domesticus* (Domestic chicken), three species in *Turnix tanki* (Yellow-legged Buttonquail), four species in *Streptopelia chinensis* (Spotted dove) only one species each in

Ploceus manyar (Streaked weaver) and *Gallinula chloropus* (Common moorhen) respectively (Table 3).

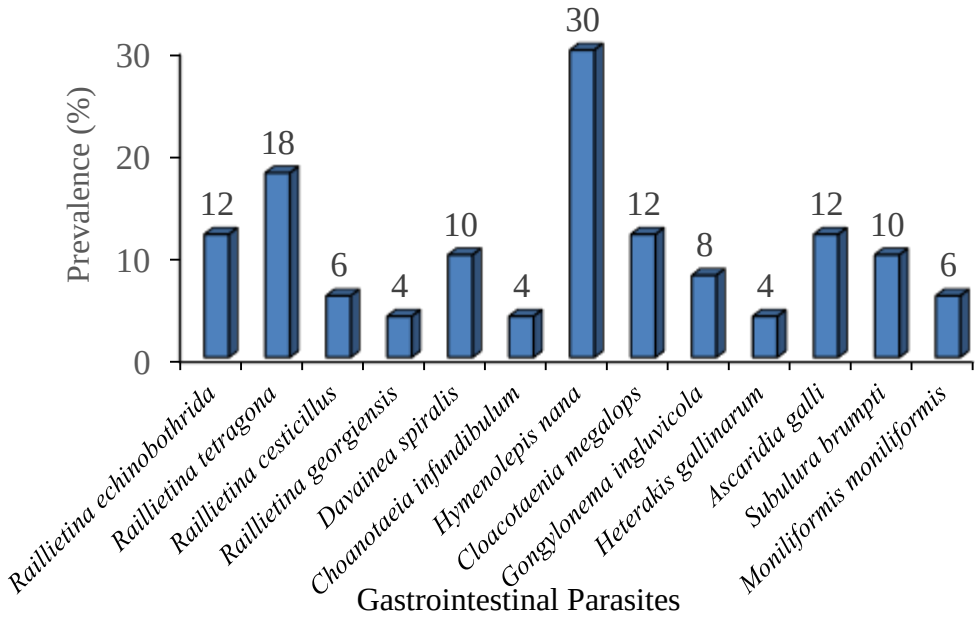

Figure 1 Prevalence of helminth infection

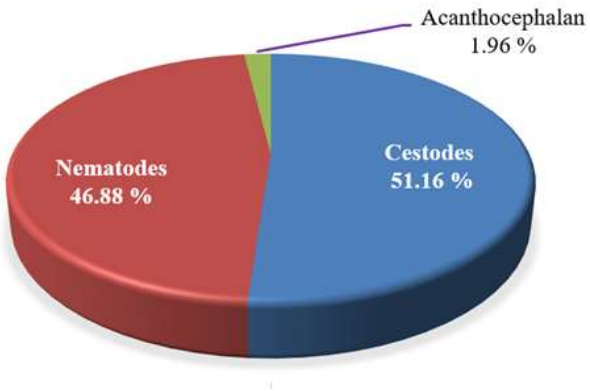

Figure 2 Occurrence of cestodes, nematodes and acanthocephalan

Table 1 Overall prevalence percentage of helminths and regions of incidence in birds examined (N = 50)

Types of helminths	Species	Regions of incidence	No. of birds infected	No. of Parasite count	Prevalence (%) N = 50	Percentage of parasites
Cestodes	*Raillietina echinobothrida*	small intestine / caeca, rectum & cloaca	6	27	12	51.16
	Raillietina tetragona	small intestine / caeca, rectum & cloaca	9	46	18	
	Raillietina cesticillus	small intestine	3	24	6	
	Raillietina georgiensis	small intestine	2	7	4	
	Davainea spiralis	small intestine / caeca, rectum & cloaca	5	21	10	
	Choanotaeia infundibulum	small intestine	2	7	4	
	Hymenolepis nana	small intestine / caeca, rectum & cloaca	15	108	30	
	Cloacotaenia megalops	small intestine / caeca, rectum & cloaca	6	47	12	
Nematodes	*Gongylonema ingluvicola*	Oesophagus / crop	4	29	8	46.88
	Heterakis gallinarum	Proventriculus / gizzard caeca, rectum & cloaca	2	5	4	
	Ascaridia galli	small intestine	6	15	12	
	Subulura brumpti	caeca, rectum & cloaca	5	214	10	
Acanthocephalan	*Moniliformis moniliformis*	small intestine	3	11	6	1.96

Table 2 Organ-wise infection rate of the recorded parasites

Organ	Parasites	Parasite count	Total	Percentage of infection (%)
Oesophagus & crop	*Gongylonema ingluvicola*	29	29	5.17
Proventriculus & gizzard	*Heterakis gallinarum*	3	3	0.53
Small intestine	*Raillietina echinobothrida*	20	281	50.09
	Raillietina tetragona	38		
	Raillietina cesticillus	24		
	Raillietina georgiensis	7		
	Davainea spiralis	12		
	Choanotaeia infundibulum	7		
	Hymenolepis nana	105		
	Cloacotaenia megalops	42		
	Ascaridia galli	15		
	Moniliformis moniliformis	11		
Caeca, rectum & cloaca	*Raillietina echinobothrida*	7	248	44.21
	Raillietina tetragona	8		
	Davainea spiralis	9		
	Hymenolepis nana	3		
	Cloacotaenia megalops	5		
	Heterakis gallinarum	2		
	Subulura brumpti	214		

Table 3 Incidence of parasitic helminth species in the examined bird species

Sr. No.	Species Examined	Cestodes								Nematodes				Acanthocephalan
		Raillietina echinobothrida	*Raillietina tetragona*	*Raillietina cesticillus*	*Raillietina georgiensis*	*Davainea spiralis*	*Choanotaenia infundibulum*	*Hymenolepis nana*	*Cloacotaenia megalops*	*Gongylonema inglrvicola*	*Heterakis gallinarum*	*Ascaridia galli*	*Subulura brumpti*	*Moniliformis moniliformis*
1	*Gallus domesticus* Domestic chicken	✔	✔	✔	✔	✔	✔	✔	✔	✔	✔	✔	✔	
2	*Turnix tanki* Yellow-legged Buttonquail										✔		✔	✔
3	*Streptopelia chinensis* Spotted dove	✔	✔					✔	✔					
4	*Ploceus manyar* Streaked weaver		✔											
5	*Gallinula chloropus* Common moorhen							✔						

Raillietina echinobothrida

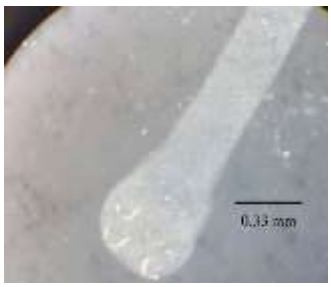

Raillietina tetragona

Raillietina cesticillus

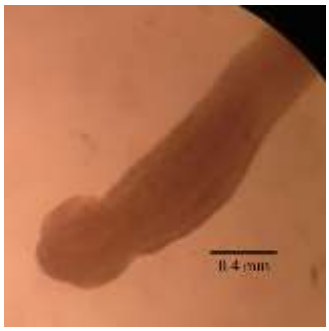

Raillietina georgiensis

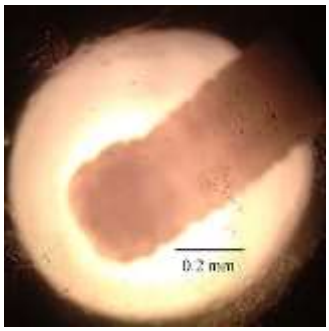

Davainea spiralis

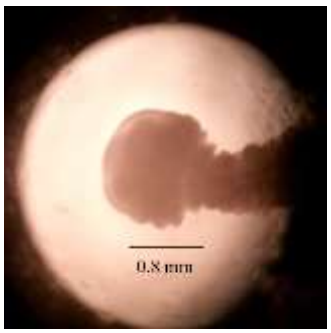

Choanotaenia infundibulum

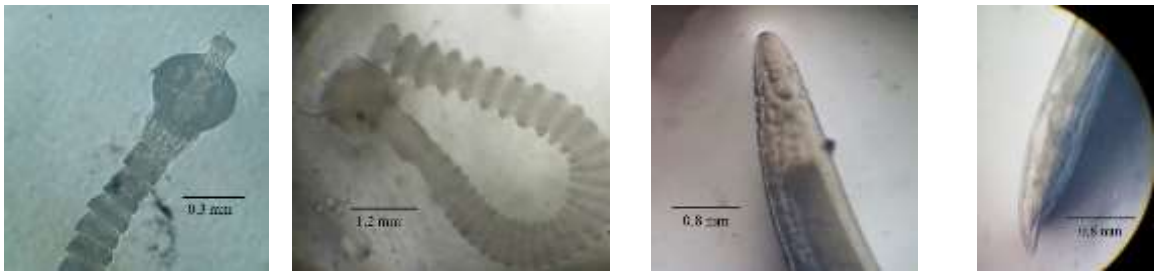

Hymenolepis nana *Cloacotaenia megalops* Anterior end Posterior end

(*Gongylonema ingluvicola*)

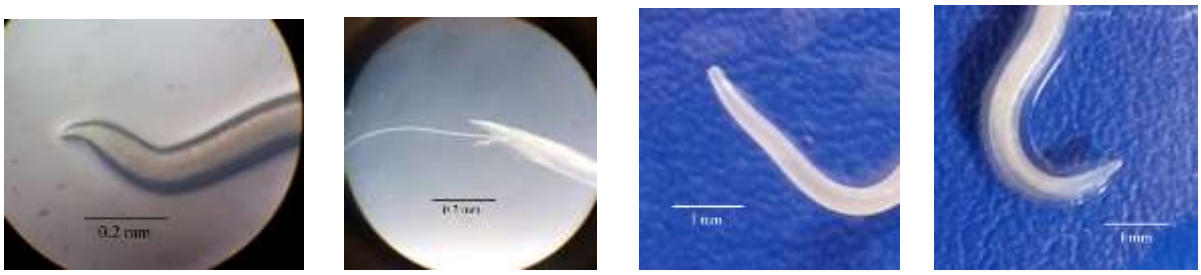

Anterior end Posterior end Anterior end Posterior end

(*Heterakis gallinarum*) (*Ascaridia galli*)

Entire body (male) Entire body (female) *Moniliformis moniliformis*

Subulura brumpti *Subulura brumpti*

Plate 1 Parasitic helminths in the bird species examined

Discussion

In the present study, 50 gastrointestinal tracts from five different species of birds, *Gallus domesticus, Turnix tanki, Streptopelia chinensis, Ploceus manyar* and *Gallinula chloropus* were examined for the endoparasitic helminths infection. GI tract was divided into four parts and then screenings for the parasites were carried out. The least infection was found in *Ploceus manyar*.

In this study, 64% (32/50) of birds examined were infected with species of parasites, which was lower than the result of Le‘ Le‘ Aye Hlaing (2011) she recorded 80% and 36% (18/50) were free of parasites.

The recorded parasitic helminths in the study were eight cestodes, four nematodes and a single acanthocephalan species. A feature of this survey was the complete absence of trematodes. The absence of these worms could be due to their complex life cycle requiring at least an intermediate host which is aquatic. Le‘ Le‘ Aye Hlaing (2011) also recorded no trematode infestations in Meiktila environs. So, the result were consistent with that observed by Le‘ Le‘ Aye Hlaing (2011).

The eight species of cestodes, included *Raillietina echinobothrida* (12%), *R. tetragona* (18%), *R. cesticillus* (6%), *R. georgiensis* (4%), *Davainea spiralis* (10%), *Choanotaenia infundibulum* (4%), *Hymenolepis nana* (30%) and *Cloacotaenia megalops* (12%) and four species of nematodes; *Gongylonema ingluvicola* (8%), *Heterakis gallinarum* (4%), *Ascaridia galli* (12%) and *Subulura brumpti* (10%) and only one species of acanthocephalans, *Moniliformis moniliformis* (6%) were recorded.

Although eight species of cestodes were recorded during this study, infection with this worms was 51.16% and followed by the nematodes 46.88% with four species identified. This incidence percentage disagreed with the result obtained by Le‘ Le‘ Aye Hlaing (2011) she investigated the highest nematode species. Among the helminthes, *Moniliformis moniliformis*, an acanthocephalan appeared as a rare parasite (1.96%), only one species of acanthocephalans was encountered during the present study.

The most prevalent cestode was *Hymenolepis nana* and the least were *Raillietina georgiensis*, *Choanotaenia infundibulum* and *Heterakis gallinarum*. Among the cestodes, the poultry tapeworm *Hymenolepis nana* was represented by the highest number of (108) individual parasites. They are small to medium-sized worms and inhabit the small intestine and caeca plus rectum and the cloaca.

The highest number of total parasite count among the nematode was that of *Subulura brumpti* with (214) individual *Gongylonema ingluvicola* (29), *Ascaridia galli* (15) and *Heterakis gallinarum* (5) individual.

The highest number of helminths amounting to (50.09%) was recorded from (small intestine), followed by those in the caeca plus rectum and cloaca (44.21%) and single helminth was encountered in the oesophagus plus crop and proventriculus plus gizzard (5.17% and 0.53%) during the present study

From these result it appeared that prevalence of different helminth parasites depend upon the physico-chemical nature of the region of the gastrointestinal tract in which they inhabit and the dimension of the different regions.

It was noted that, among the five host species studied, the highest incidence of 12 species of helminths parasites recorded in *Gallus domesticus*, followed by four species of parasites in *Streptopelia chinensis* and three species in *Turnix tanki* and a single species each in *Gallinula chloropus* and *Ploceus manyar*. From these results, it is alluded that, the more closer to human habitation, the more chance of getting infected by the parasites and vice-versa.

Conclusion

GI parasites are endemic among different avian species with *Hymenolepis nana* been the most prevalent. Knowledge on the epidemiology of these parasites is important for achieving fruitful preventive and control measures against GI parasites. There is a need for an improved veterinary medical attention and education of poultry farmers on the need to regularly and periodically treat their flock against GI parasites, as this will improve the economic value of the poultry industry. Finally, more surveys are needed to be done on different birds of Meiktila environs to gain more informations on the parasitic infection. Lack of surveillance studies and health care for backyard birds is the major factor and hence periodical deworming of backyard birds for preventing occurrence of infections can reduce the economic losses for poor people and small farmers.

Acknowledgements

We would like to grateful thanks to Rector Dr Ba Han for his permission for doing research. We also thank to Professor and Head of Zoology Department Dr Ni Ni Yin, Meiktila University for her moral support.

References

Clapham, P.A. (2009). Helminth parasites in some wild birds. *Bird Study*, 4(4), pp. 193-196.

Leʻ Leʻ Aye Hlaing. (2011). Helminths burden of backyard chicken *Gallus gallus domesticus* (Lin., 1758) in Meiktila environs. *MSc Thesis*. Meiktila University.

Ola-Fadunsin, S.D., Uwabujo, P.I., Sanda, I.M., Ganiyu, I.A., Hssain, K., Rabiu, M., Elelu, N. and Alayande, M.O. (2019). Gastrointestinal helminthes of intensively managed poultry in Kwara Central, Kwara State, Nigeria: Its diversity prevalence, intensity, and risk factors. *Journal of Veterinary World*, 12(3), pp. 389-396.

Sivakumar, M., Krishnakumar, S., Yogeshpriya, S., Venkatesan, M., Vijayasarathi, M.K. and Selvaraj, P. (2017). Multiple gastrointestinal nematodal and custodial parasitoses in a backyard fowl. *Journal of Entomology and Zoology Studies*, 5(5), pp. 1425-1427.

Sepulveda, M.S. and Kinsella, J.M. (2013). Helminth collection and identification from wildlife. *Journal of Visualized Experiments*, (82) e51000, doi: 10.3791/51000, pp. 1-5.

Shahin, A.M., Lebdah, M.A., Abu-Elkheir, S.A. and Elmeligy, M.M. (2011). Prevalence of chicken cestodiasis in Egypt. *New York Science Journal*, 4(9), pp. 21-29.

Thrusfield, M. (2007). *Veterinary Epidemiology*. Blackwell Science Limited, U.S.A, pp. 626.

TAXONOMIC STUDY ON TWENTY-THREE SPECIES OF FAMILY ASTERACEAE FROM KANBALU AND KATHA DISTRICTS*

Tin Win Kyi[1] and Thi Thi Htun [2], Nu Nu Yee[3]

Abstract

The taxonomic studies on the family Asteraceae from Kanbalu and Katha Districts in Sagaing Region were undertaken. In the present study, 23 species belonging to 15 genera of family Asteraceae were collected, studied and identified during December 2019 to October 2020. One species each from the genera *Acilepis, Cosmos, Dichrocephala, Elephantopus, Gnaphalium, Parthenium, Tithonia, Sonchus,* two species from genera *Acmella, Blumea, Conyza, Pseudognaphalium, Sphaeranthus* and *Youmgia,* three species from the genus *Emilia* were collected. From various habitats. Homogamous discoid capitula are found in 8 species. Heterogamous capitula are found in 15 species. Among them, 10 species possess disciform capitula and 5 species were radiate capitula. The characteristics of the family and detail descriptions of individual species are described with relevant photographs.

Keywords: Asteraceae, discoid, disciform, radiate, Capitulas.

Introduction

Asteraceae or Compositae (commonly referred to as the aster, daisy, composite or sunflower family) is a very large and widespread family of flowering plants. Asteraceae is an important economical, horticultural and ornamental family. The family Asteraceae has many distinct characters such as various shapes of leaves, capitula, anthers, achenes and pappus.

The Asteraceae is known by the aggregated flowers often occurring at the ends of branches or stems. Aggregation of flowers occurs on usually flat surface called receptacle. It is also referred to as the banner of the family Asteraceae. Useful characters about the receptacle may be derived by studying texture, shape (flat, convex, conical, color), presence/ absence of bracts these often observed by removing a few florets, bract size, shape, pubesence and sometimes color (Tadesse 2015).

Parthenium hysterophorus L. commonly called as congress grass is among the top ten worst weeds of the world. It is widely occurring and occupied almost all the parts of world such as in Asia, Africa, Australia and the Pacific (Monika 2014).

There are very few research paper concerning the family Asteraceae in Sagaing Region. Therefore, research on the morphological characters of this family from Sagaing Region was carried out.

The aim is to fulfill the information of taxonomical distinct characters found in Asteraceae for future research works. The objectives of the present study are to classify and identify the members of Asteraceae from Kanbalu and Katha Districts, to examine and record the differences between morphological characters of collected species.

Materials and Methods

Some species of Asteraceae were collected from Kanbalu and Katha Districts during December 2019 to October 2020. Plant parts including leaves, inflorescence, flowers and fruits

[1] Lecturer, Department of Botany, Kalay University
[2] Dr, Associate Professor, Department of Botany, University of Mandalay
[3] Dr, Professor and Head, Department of Botany, University of Mandalay
[*] Best Paper Award Winning Paper in Botany (2021)

were collected and recorded in field notes. Habit and distinctive parts of the specimens were recorded by photographs and the specimens were kept immediately into the plastic bags for further study.

Identification of genera and species were carried out by referring to Backer (1965), Dassanayake (1980), Hooker (1881), Jeffery and Kadereit (2007), Qi-ming and De-hin (2009), Wu *et al.* (2013), Monika (2014), Titiek *et al.* (2015). Myanmar names were checked by Hundley and Chit Ko Ko (1987) and Kress *et al.* (2003).

All the collected specimens were identified and described with their characters. The tribe, genera and species of Asteraceae are arranged according to Jeffery and Kadereit (2007).

The present research work deals with the taxonomic study on Asteraceae growing in Sagaing Region. The species were collected from Kanbalu and Katha Districts during December 2019 to October 2020 and 23 species belonging to 15 genera of family Asteraceae were recorded. Kanbalu District is located between 23° 12' 0" North Latitudes and 95° 30' 0" East longitude. Katha District is extended between N 24° 10' 56" North Latitudes and 96°19' 50" East longitude.

The collected species of this family were classified and identified according to the type of capitula, shape of involucres, phyllaries, receptacles, type of florets and stamens. The genera and species of this family Asteraceae have been arranged tribes.

Results

In this present study, 23 species belonging to 15 genera of the family Asteraceae have been recorded, studied and identified.

1. Taxonomic Description

1.1 ***Elephantopus scaber*** L., Sp.Pl.2: 814. 1753. (Figure 1)

E. cernuus Vell., Fl. Flum.8: t. 148. 1825.

Myanmar name : Sae ta pin, sin ta zi

English name : Unknown

Flowering period : September to December

Perennial erect herbs densely hirsute stems from woody rootstock, dichotomously branched at the upper portion. Leaves simple, alternate, petiolate; lower leaves in a radical rosette, blades oblong-obovate, cauline leaves sessile, attenuate at the base, crenate- serrulate along the margin, obtuse or rounded at the apex. Inflorescence cluster of heads, axillary or terminal, all stalks surrounded by 3 broadly ovate bracts or 4 leaf- like bracts. Capitula homogamous, discoid, purple, sessile; involucre cylindric- oblong, 2 seriate, green. Receptacle flat, epaleaceous. Florets all tubular, about 4 florets per capitulum, bisexual, corolla linear- lanceolate, 5- lobed; pale purple. Stamens 5, exserted; anthers pale yellow, Ovary oblong- conical, whitish spreading hairs, style exserted; stylar arms linear with obtuse tip. Achenes oblanceolate, ribbed, brown. Pappus 5 or 6, dirty- white, dilated and scaly at base, persistent.

1.2 ***Acilepis squarrosa*** D. Don, Prodr. Fl. Nepal.169.1825. (Figure 2)

Vernonia squarrosa (D. Don) Less., Linnaea 6:627.1831.

Myanmar name : Pan ta tae

English name : Unknown

Flowering period : December to March

Perennial erect herbs; stems terete, hardly, branched, tough. Leaves simple, alternate, petiolate, blades linear- oblong, attenuate at the base, serrate to serrulate along the margin, gradually acuminate at the apex, vines prominent. Inflorescence in the terminal solitary. Capitula terminal, homogamous, discoid, light purple, sessile; involucre many seriates, light green. Receptacle flat, epaleaceous. All florets, many florets per capitula, bisexual, 5 lobed, corolla tube infundibuliform, of peripheral florets curved outside, pale purple. Stamens 5, exserted; anthers whitish, Ovary cylindrical, distinctly ribbed; style exserted, pubescent; stylar arms branches elongate curved with acute tip. Achenes oblong with basal acute end, ribbed, brown. Pappus many, dirty white, bristle.

1.3 *Youngia conjunctiva* Babc. & Stebbins Publ.Carnegie.Inst.Wash.484:37.1937. (Figure 3)

Lactuca erythrocarpa Vaniot, Bull. Acad. Int. Geogr. Bot. 12:319. 1903.

Myanmar name : Unknown

English name : Unknown

Flowering period : February to August

Annual erect herbs; stem leaves none or few, similar to rosette leaves, branched apically or from near base. Leaves simple, basal leaves oblanceolate, base attenuate into a petiole- like portion, lateral lobes 1 to 3 pairs, blades lyrate pinnatisect; 4 lobes, obtuse at the base, dentate along the margin, acute at the apex. Inflorescence terminal paniculiform corymbose. Capitula homogamous, ligulate, yellow, pedunculate; involucre cylindric to campanulate, 2- seriate, green; outer phyllaries triangular, inner phyllaries 6 to 8, linear, dark to blackish green, apex acute. Receptacle small flat, epaleaceous. All ligulate, bisexual, ligules 4 lobed, yellow; style exserted. Stamens 5, exserted; anthers brown. Ovary ovoid, stylar arms linear, hairy, yellow. Achenes fusiform, slightly compressed, brown. Pappus few, white.

1.4 *Youngia japonica* (L.) DC., Prodr.7(1):194.1838. (Figure 4)

Lactuca erythrocarpa Vaniot, Bull. Acad. Int. Geogr. Bot. 12:319. 1903.

Myanmar name : Unknown

English name : Unknown

Flowering period : February to August

Annual erect herbs; stem terete, solitary, and branched from base. Leaves simple, basal leaves oblanceolate, base attenuate into a petiole- like portion, lateral lobes 1 to 3 pairs, elliptic to narrowly elliptic, upper lobe largest, blades lyrate pinnatisect; 4-5 lobes, obtuse at the base, dentate along the margin, acute at the apex. Inflorescence terminal paniculiform corymbose. Capitula homogamous, ligulate, yellow, pedunculate; involucre cylindric, 2-seriate, pale green; outer phyllaries triangular- ovate, inner phyllaries 6 to 8, linear, thickened at the base, green. Receptacle small flat, epaleaceous. All ligulate, bisexual, ligules, 5 lobed, yellow, style exserted, stylar arms with acute tip. Stamens 5, exserted; anthers brown. Ovary ovoid; style exserted, pubescent; stylar arms linear, hairy, yellow. Achenes fusiform, ribbed, slightly compressed, brown. Pappus few, white.

1.5 *Sonchus arvensis* L., Sp.Pl. 2: 793.1753**.** (Figure 5)

S. wightianus DC. Prodr.187. 1753.

Myanmar name : Unknown

English name : Unknown

Flowering period : June to December

Annual, erect herbs; stem erect and branched above, terete, hairs, hollow, milky latex present. Leaves simple, alternate, sessile, lower leaves runcinate-spinous- toothed cauline with a large terminal lobe, upper leaves all oblong, sagittate the base, acutely shortly dentate along the margin, acuminate at the apex. Inflorescence terminal, combined into widely branched corymbs. Capitula homogamous, ligulate, yellow, pedunculate; involucres campanulate, many seriate. Receptacle slightly concave, epaleaceous. Florets all ligulate bisexual; corolla liguliform, 4 lobed, yellow. Stamens 5, exserted, anther yellow, Ovary oblong, style exserted, stylar arms curved with acute tip, white. Achene oblong, 5-ribbed. Pappus numerous, white.

1.6 ***Emilia fosbergii*** Nicolson. Phytologia 32:34. 1975. (Figure 6)

Myanmar name : Unknown
English name : Unknown
Flowering period : November to March

Annual, erect ascending herbs; stem and no branches, terete. Leaves simple, alternate, petiolate; blade broadly ovate to oblanceolate, upper leaves smaller, elliptic- oblong, sessile, cordate at the base, dentate or entire along the margin, obtuse at the apex. Inflorescence terminal, few capitula, branched with 2-3 capitula. Capitula homogamous, discoid, pedunculate, purple; involucre linear or cylindrical; bracts 1 seriate, green. Receptacle concave, epaleaceous. Floret tubular, bisexual, corolla tube narrowly, filiform-funnel shaped, 5 lobed, purple. Stamens 5, inserted, anther pale yellow without the top purple. Ovary oblong, style, inserted, stylar arms linear with obtuse tip. Achene oblong, 5 ribbed, the ribs grooved, brown. Pappus many, white, capillary hairs.

1.7 ***Emilia prenanthoidea*** DC. Prodr. 6. 303; (1837) (Figure 7)

Myanmar name : Unknown
English name : Unknown
Flowering period : September to December

Annual, erect ascending herbs; stem, terete, slender and no branches. Leaves simple, alternate, sessile; blade broadly ovate to oblanceolate, upper leaves smaller, linear- oblong, sessile, broadly auricled at the base, entire along the margin, obtuse or acute at the apex. Inflorescence terminal, few capitula, branched with 1-2 capitula. Capitula homogamous, discoid, pedunculate; purple; involucre linear or cylindrical; bracts 1 seriate, green. Receptacle concave, epaleaceous. Floret tubular, bisexual, corolla tube narrowly, filiform-funnel shaped, lower half filiform, upper half gradually widen, 5 lobed, purple. Stamens 5, inserted, anther pale white, with the top purple. Ovary oblong; style, inserted, stylar arms linear with obtuse tip. Achene oblong, 5 ribbed, the ribs grooved, brown. Pappus many, white, capillary hairs.

1.8 ***Emilia sonchifolia*** (L.) DC., var. Scabras, Hook. f. 3:336.1881. (Figure 8)

E. scabra DC. Prodr. (A.P.de Candolle) 6 303: 1838.

Myanmar name : Unknown
English name : Unknown
Flowering period : September to December

Annual, erect herbs; stem, terete, slender. Leaves simple, alternate, sessile, blade lyrate-pinnatifid, upper leaves smaller, elliptic- oblong, lower leaves all radical scaberulous, basal lobed 2 to 4 irregular pairs, forming winged petiole, cordate at the base, dentate or entire along the margin, obtuse at the apex. Inflorescence terminal, few capitula, branched with 3-4 capitula.

Capitula homogamous, discoid, cylindrical, pedunculate; purple; involucre campanulate, 1 seriate, green. Receptacle flat, epaleaceous. Floret tubular, bisexual, corolla tube narrowly, filiform-funnel shaped, 5 lobed, purple. Stamens 5, inserted, anther white with a purple top. Ovary oblong, style, inserted, stylar arms linear with obtuse tip. Achenes prismatic, 5 ribbed, the ribs grooved. Pappus many, white, soft.

1.9 *Gnaphalium pulvinatum* Delile, Descr. Egypte, Hist. Nat.266, Pl. 44, f. 1. 1813. (Figure 9)

Filago prostrata DC. in Wight, Contrib.22.1837.

Myanmar name : Unknown

English name : Unknown

Flowering period : December to March

Annual decumbent herbs, woolly; stem very many spreading from the root and branches, terete, glandular whitish pubescent. Leaves simple, alternate, sessile; blades oblanceolate, attenuate at the base, entire along the margin, acute at the apex. Inflorescence axillary or terminal cyme. Capitula very small, globose, in the terminal short spike or sessile, heterogamous, disciform, immersed in wool, yellow; involucre campanulate, 2 seriate, green. Receptacle convex, epaleaceous. The outer florets, numerous, female, filiform, yellow; ovary oblong, style exserted, stylar arms with obtuse tip, yellow. Disc florets, few, bisexual, corolla narrowly infundibuliform, 5-lobed; yellow. Stamens 5, inserted; anthers yellow, Ovary elliptic, style exserted, stylar arms short and flat with truncate tip. Achenes elliptic, brown, minutely curved hairy. Pappus few, denticulate.

1.10 *Pseudognaphalium hypoleucum* (DC.) Hilliard & B.L. Burtt, Bot. J. Linn. Soc. 82(3):205.1981. (Figure 10)

Gnaphalium hypoleucum DC., Contr. Bot. India 21. 1834.

Myanmar name : Unknown

English name : Unknown

Flowering period : December to March

Annual decumbent herbs, woolly; stem and branches, terete. Leaves simple, alternate, sessile; blades linear to oblong, auriculate at the base, entire along the margin, acute at the apex. Inflorescence numerous in dense terminal corymbose clusters. Capitula very small, globose, in the terminal short spike or sessile, heterogamous, disciform, immersed in wool, yellow; involucre campanulate, 3-4 seriate, green. Receptacle convex, epaleaceous. The outer florets, numerous, female, filiform, yellow. Disc florets, few, bisexual, corolla narrowly infundibuliform, 5- lobed; yellow. Stamens 5, inserted; anthers yellow. Ovary oblong; style inserted, stylar arms short and flat with truncate tip. Achene oblong, yellowish brown, minutely curved hairy. Pappus few, denticulate, pale yellow.

1.11 *Pseudognaphalium biolettii* Anderb., Opera Bot. 104:147.1991**.** (Figure 11)

Dichrocephala latiflolia DC.in Guill., Archiv. Bot. 2: 518. Et. Prod.5: 372. 1836.

Myanmar name : Unknown

English name : Unknown

Flowering period : January to May

Perennial erect herbs; stem woody near base and usually stout branched, terete, spreading finely whitish pubescent. Leaves simple, alternate, sessile and widely clasping the stem at the base with ear-shaped appendages; blades lanceolate-oblong, clasping at the base, crisped along the

margins, acute at the apex. Inflorescence corymbs on terminal branchlets. Capitula small, terminal panicles, heterogamous, disciform, globose, immersed in wool, sessile, white; involucre bell-shaped, 4-5 seriate, white. Receptacle convex, epaleaceous. The outer florets, numerous, female, filiform, yellow. Disc florets, bisexual, corolla tubular funnel-shaped, 5 lobed; green or greenish-yellow. Stamens 5, inserted; anthers yellow, Ovary oblong, pale brown; style inserted, stylar arms linear. Achene oblong, pale yellow. Pappus many, fine, hairs.

1.12 ***Dichrocephala bicolor*** Schltdl., Linnaea 25(4):209. 1853. (Figure 12)

Dichrocephala latiflolia DC.in Guill., Archiv. Bot. 2: 518. Et. Prod.5: 372. 1836

Myanmar name : Unknown

English name : Unknown

Flowering period : February to July

Annual erect herbs; stem and usually branched, terete, creeping at the base. Leaves simple, alternate, petiolate, with narrowly winged, blades lyrate- pinnatifid, attenuate at the base, irregularly serrate or crenate-dentate along the margins, acute at the apex. Inflorescence axillary or terminal solitary. Capitula small, in terminal panicles, heterogamous, disciform, globose, pedunculate; involucre campanulate, 2 seriate, green. Receptacle obconical, elevate and flattened at the apex, epaleaceous. The outer florets, numerous, female, corolla tube curved with 3 lobed, greyish- white. Disc florets, few, bisexual, corolla tubular funnel-shaped, 4 lobed; green or greenish-yellow. Stamens 4, inserted; anthers yellow, Ovary obovate, pale brown; style exserted, stylar arms linear. Achenes obovate pale brown. Pappus lacking or bearing 2minute hairs.

1.13 ***Conyza adenocarpa*** Dalzell. & A. Gibson., Bombay. Fl. 125. 1861. (Figure 13)

Conyza adnata HBK., Nov. Gen.et Sp.4: 74. Mexic. 1832.

Myanmar name : Unknown

English name : Unknown

Flowering period : December to February

Annual erect aromatic herbs, stem sometime woody below and no branched, terete. Leaves simple, alternate, sessile; blades oblong, ovate-spatulate, semi-amplexicaul at the base, irregularly serrate and spinescent along the margin, acute or apiculate at the apex. Inflorescence axillary or terminal solitary. Capitula arranged in corymbose cymes at terminal or in upper leaf- axils, heterogamous, disciform, pedunculate; yellow; involucre campanulate, 3-4 seriate. Receptacle convex, epaleaceous. The outer florets, numerous, female, filiform, 2- 3 lobed, yellow. Disc florets, bisexual, corolla narrowly infundibuliform, 5 lobed, yellow. Stamens 5, exserted; anthers yellow. Ovary obovate, style exserted, stylar arms linear, yellow. Achene obovate, brown. Pappus white, deciduous.

1.14 ***Conyza japonica*** (Thunb.) Less. Prod.5:383.1386. (Figure 14)

Erigeron japonica Thunb. 754.1784.

Myanmar name : Unknown

English name : Unknown

Flowering period : December to February

Annual erect herbs; stems usually branched at the very base, terete, spreading finely whitish pubescent. Leaves simple, alternate, sessile; blades oblong- ovate, petiolate, attenuate at the base, crenate- dentate along the margin, obtuse and apiculate at the apex, dark green above, pale green below. Inflorescence terminal cyme. Capitula few together in shortly compactly corymbose

terminal cyme, heterogamous, disciform, purple; pedunculate; involucre urceolate, 2- 3 seriate, green. Receptacle flat, epaleaceous. The outer florets, numerous, female, filiform, pale purple. Disc florets, 5 to 15 florets per capitulum, bisexual, corolla tubular narrowly infundibuliform, 5 lobed; pale purple. Stamens 5, inserted; anthers pale yellow. Ovary oblaceolate, white; style inserted, stylar arms linear, yellow. Achene oblanceolate, with few white hairs, pale brown. Pappus few, white.

1.15 ***Blumea junghuhniana*** (Miq.) Boerl. Handl. Fl. Ned. Ind. 2(1):2391891 (Figure 15)

Blumea balsamifera DC. var. macrocephala Kitam. 344. 1941.

Myanmar name : Unknown

English name : Unknown

Flowering period : December to February

Annual erect subshrub; stem woody at base and upper branches of panicles sparsely, terete. Leaves simple, alternate, more or less petiolate; blades oblong -ovate to oblong- lanceolate, pinnatifid- lobed, attenuate at the base, coarsely dentate along the margin, apiculate at the apex. Inflorescence in dense terminal pyramidal panicles. Capitula aggregated in axil or at branch terminal, heterogamous, disciform, pale purple, pedunculate; involucre campanulate, 5 seriate, pale green. Receptacle flat, except the center slightly concave, epaleaceous, glabrous. The outer florets, tubular, female, corolla tube filiform, 2-3 lobed, yellow. Disc florets, few, bisexual, corolla narrowly funnel-shaped, 5 lobed, yellow. Stamens 5, exserted; anthers pale yellow. Ovary oblong, pale white; style exserted, stylar arms linear, yellow. Achenes oblongoid, brown. Pappus hair numerous, white.

1.16 ***Blumea paniculata*** (Wall.) M. R. Almeida. Fl. Maharashta 3A:83 2001. (Figure 16)

Conyza paniculata Wall. 200 1831.

Myanmar name : Unknown

English name : Unknown

Flowering period : February to April

Annual erect herbs; stem and no branches, slender, terete. Leaves simple, alternate, petiolate; blades oblong-elliptic or ovate, attenuate or decurrent at the base, dentate along the margin, acute or obtuse at the apex, upper leaves and inflorescence bracts smaller, broadly ovate. Inflorescence large, loose, axillary or terminal panicle. Capitula aggregated in axil or at branch terminal, heterogamous, disciform, white, pedunculate; involucre campanulate, 5 seriate, green. Receptacle flat or slightly convex, epaleaceous, glabrous. The outer florets, numerous, filiform, female, corolla slender tubular, 3 lobed, yellow. Disc florets, bisexual, corolla infundibuliform, 5 lobed, yellow. Stamens 5, inserted; anthers yellow. Ovary oblong style exserted, stylar arms long, linear, bifid, white. Achene oblong, brown. Pappus numerous, whitish.

1.17 ***Sphaeranthus indicus*** L., Sp.Pl. 2: 927. 1753; Moon, Cat. 59. 1824. (Figure 17)

Sphaeranthus hirtus Willd., Sp. 3: 2395. 1804.

Myanmar name : Da- naung

English name : Unknown

Flowering period : September to March

Annual erect aromatic herbs; stem and divaricately branches, strongly scented with 4 winged. Leaves simple, alternate, sessile; blades obovate-oblong, attenuate at the base, coarsely serrate- dentate along the margin, acute at the apex. Inflorescence ellipsoid, axillary or terminal

solitary. Capitula ovoid- globose, heterogamous, disciform, pedunculate; with deeply crenate 3 wings; each capitulum sessile, purple; involucre lanceolate, 2 seriate. Receptacle solid conical, paleaceous, flat. The outer florets, female, corolla tubular filiform, 2 lobed, pale yellow. Disc florets bisexual, corolla infundibuliform, 5 lobed; yellow. Stamens 5, exserted; anthers pale yellow. Ovary oblong, brown; style exserted, stylar arms linear, purple. Achene oblong or elliptic- oblong, pale brown. Pappus absent.

1.18 ***Sphaeranthus peguensis*** Kurz ex C.B. Clarke, Compos., Ind. 97. 1876. (Figure 18)

Myanmar name : Kadu
English name : Unknown
Flowering period : October to March

Annual erect aromatic herbs; stem and branches winged. Leaves simple, alternate, sessile; blades linear- oblong, decurrent at the base, dentate obtuse coarsely serrate along the margin, acute at the apex. Inflorescence axillary or terminal solitary. Capitula clusters of broadly ovoid- globose, heterogamous, disciform, pedunculate; purple; involucre campanulate, 2-3 seriate. Receptacle conical, fistular, paleaceous, flat. The outer florets, female, corolla tubular filiform, 3 lobed, pale yellow. Disc florets bisexual, corolla infundibuliform, 5 lobed, yellow. Stamens 5, exserted; anthers purple. Ovary oblong, pale yellow; style exserted, stylar arms linear, purple. Achene oblong, brown. Pappus absent.

1.19 ***Parthenium hysterophorus*** L. FI. Andhra Pradesh 2:533. 1997. (Figure 19)

Myanmar name : Unknown
English name : Unknown
Flowering period : June to October

Annual erect herbs; stem and branches angular. Leaves simple, alternate, pinnatifid, petiolate; blades oblong- lanceolate, decurrent at the base, entire along the margin, acute at the apex. Inflorescence axillary or terminal solitary. Capitula heterogamous, radiate, white or creamy white; involucre hemispheric, ovoid- oblong, 5 series, green; phyllaries oblong. Receptacle small, convex, paleaceous. Ray florets, female, tubular 2 lobed, white or creamy white. Disc florets, male, corolla narrowly tubular, 4 lobed, creamy white. Stamens 4, inserted; anthers white. Ovary oblong, white; style inserted, stylar arms curved, white. Achenes 2 spiny, oblong or elliptic-oblong, flattened, triangular and dark brown- black with two thin, white, spoon- shaped appendages, pale brown. Pappus pale brown, persistent.

1.20 ***Cosmos caudatus*** Kunth. Nov. Gen, Sp. (Folio ed.) 4: 188.1820. (Figure 20)

Cosmos bipinnatus auct. NonCav: Trimen, Handb. Fl. Ceylon 3:40.1895.

Myanmar name : Unknown
English name : Unknown
Flowering period : January to August

Annual erect herbs with long branches; stems and branches, sub-quadrangular. Leaves compound, opposite, petiolate; blade segments linear- elliptic at the base, lateral segments 2 or 3 pairs, entire along the margin, apiculate at the apex. Inflorescence axillary or terminal solitary on long penduncles. Capitula solitary, heterogamous, radiate, pale purple, pedunculate; involucre campanulate, 2 seriate, green. Receptacle convex, epaleaceous. Ray florets, neuter, ligulate, 3- lobed; purple. Disc florets many, bisexual, corolla tube infundibuliform, 5 lobed, yellow. Stamens 5, inserted; anthers black. Ovary linear; style exserted, pubescent; stylar slender arms

linear, thickened upwards, with hairy, yellow. Achenes linear fusiform, ribbed, with hairy, dark brown or black. Pappus awns 2, divergent, linear 3, green.

1.21 ***Tithonia diversifolia*** (Hemsl.) A. Gray, Proc. Amer. Acad. Arts 19:5.1883**.** (Figure 21)

Mirasolia diversifolia Hemsl., Bot. Centr. Amer. 2: 168, t.47. 1881.

Myanmar name : Taung nay kya; Nay kya yaing

English name : Unknown

Flowering period : November to January

Perennial erect, suffruticose herbs, large and shrub; stem and branches, striate. Leaves simple, alternate, petiolate; broadly winged almost to the base; blades 3-5 lobed, trinerved and cuneate at the base, crenate-serrate along the margin, acuminate at the apex. Inflorescence axillary or terminal solitary. Capitula on long peduncles, heterogamous, radiate, pedunculate; involucre broadly campanulate, 3-4 seriate, green. Receptacle conical, paleaceous. Ray florets, neuter, 2- 3 lobed, ligulate, bright yellow. Disc florets numerous, bisexual, corolla tube cylindrical, 5 lobed, yellow. Stamens 5, inserted; anthers brown with the top yellow. Ovary oblong; style exserted, stylar arms coiled, yellow. Achene oblong, dark brown. Pappus of ligulate florets minutely scaly, those of tubular florets, 2 awns with about 6 short broad scales connate ate the base, linear- lanceolate, white.

1.22 ***Acmella paniculata*** (Wall. ex DC.) R.K. Jansen, Syst. Bot. Monoger. 8.67.1985. (Figure 22)

Spilanthes acmella var. *paniculata* (Wall. ex DC.) C. B. Clarke ex Hook. f, Fl. Brit. Inda 3: 307. 1881.

Myanmar name : Japan ne gya

English name : Unknown

Flowering period : December to March

Annual erect herbs; stem and branches, erect or prostate, green or purple, rooting at the nodes. Leaves simple, opposite, subsessile or petiolate; blades broadly ovate to ovate- triangular, attenuate at the base, dentate to coarsely dentate along the margin, acute to acuminate at the apex. Inflorescence axillary or terminal solitary. Capitula solitary, terminal, heterogamous, radiate, pedunculate; involucre ovate or elliptic, 2 seriate. Receptacle oblong, paleaceous. Ray florets, neuter, 2 lobed, yellow. Disc florets many, bisexual, corolla funnel- shaped, 5 lobed; yellow. Stamens 5, inserted; anthers black. Ovary oblong, style exserted, stylar arms curved, yellow. Achene oblong, compressed with ciliate edges, black. Pappus consisting of 2 short hairs.

1.23 ***Acmella uliginosa*** (Sw.) Cass., Dict. Sci. Nat. (ed.2)24:331.1822 (Figure 23)

Spilanthes uliginosa Sw., Prodr. (Swartz) 110.1788.

Myanmar name : Unknown

English name : Unknown

Flowering period : Throughout the year

Perennial erect herbs; stems erect or ascending bright green, branches, usually decumbent and rooting from the lower nodes, terete. Leaves simple, opposite, subsessile or shortly petiolate; blades narrowly ovate or elliptic, with long petiole, attenuate cuneate at the base, subentire or undulate along the margin, obtuse or subacute at the apex, vines prominent. Inflorescence axillary or terminal solitary. Capitula terminal or subterminal, heterogamous, radiate, pedunculate; involucre broadly campanulate, 1 seriate, green. Receptacle highly conical, paleaceous. Ray florets, neuter, 3 lobed, yellow. Disc florets many, bisexual, corolla funnel- shaped, 4 lobed;

yellow. Stamens 5, inserted; anthers black. Ovary ovate, style exserted, pubescent; stylar arms, curved, broader, hairy, yellow. Achene oblong- ovate, densely ciliate on margins, no ribbed, black. Pappus 2-4 very short fine bristles from marginal cilia, pale brown.

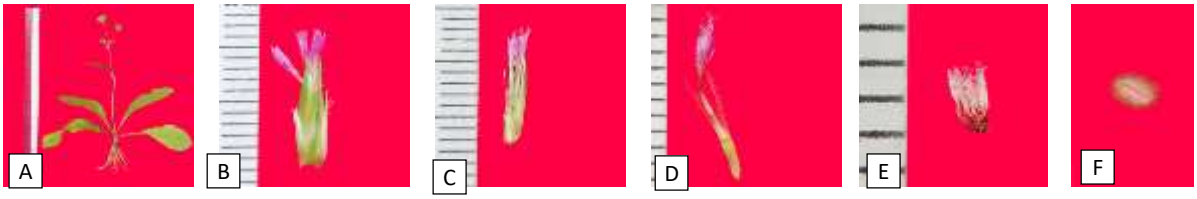

A. Inflorescence B. Capitulum C. L.S of capitulum D. Disc floret E. Stamens F. T.S of ovary

Figure 1 *Elephantopus scaber* L.

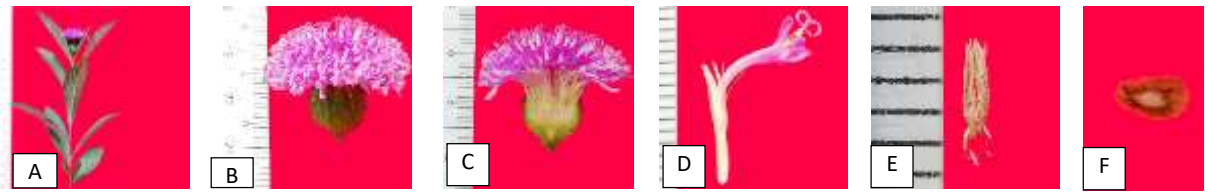

A. Inflorescence B. Capitulum C. L.S of capitulum D. Disc floret E. Stamens F. T.S of ovary

Figure 2 *Acilepis squarrosa* D. Don**.**

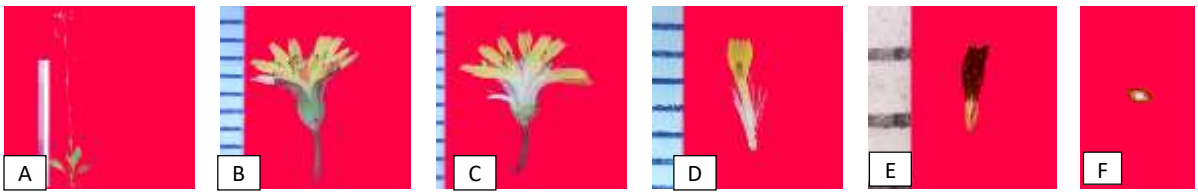

A. Inflorescence B. Capitulum C. L.S of capitulum D. Ligulate floret E. Stamens F. T.S of ovary

Figure 3 *Youngia conjunctiva* Babc. & Stebbins

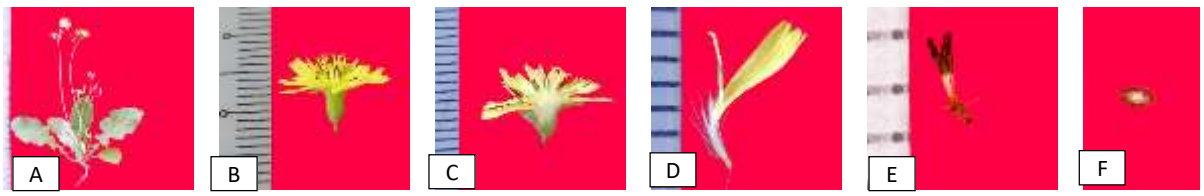

A. Inflorescence B. Capitulum C. L.S of capitulum D. Ligulate floret E. Stamens F. T.S of ovary

Figure 4 *Youngia japonica* (L.) DC.

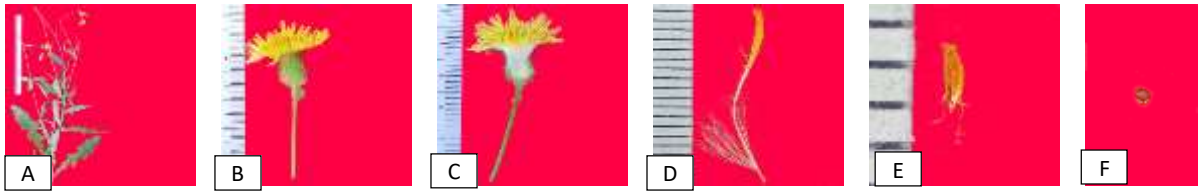

A. Inflorescence B. Capitulum C. L.S of capitulum D. Ligulate floret E. Stamens F. T.S of ovary

Figure 5 *Sonchus arvensis* L.

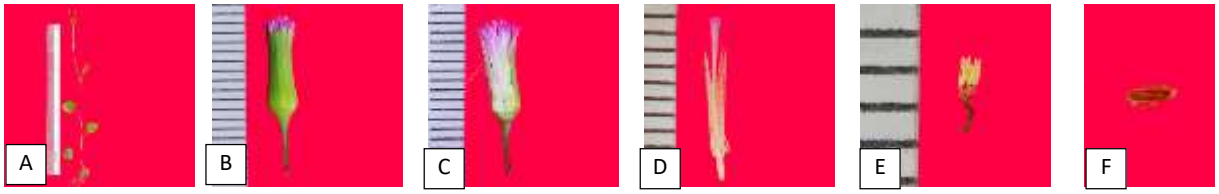

A. Inflorescence B. Capitulum C. L.S of capitulum D. Disc floret E. Stamens F. T.S of ovary

Figure 6 *Emilia fosbergii* Nicolson

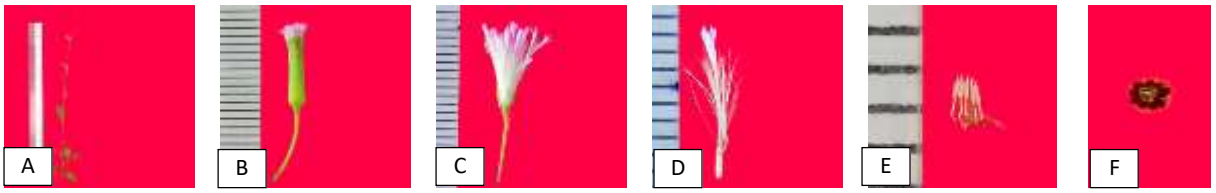

A. Inflorescence B. Capitulum C. L.S of capitulum D. Disc floret E. Stamens F. T.S of ovary

Figure 7 *Emilia prenanthoidea* DC.

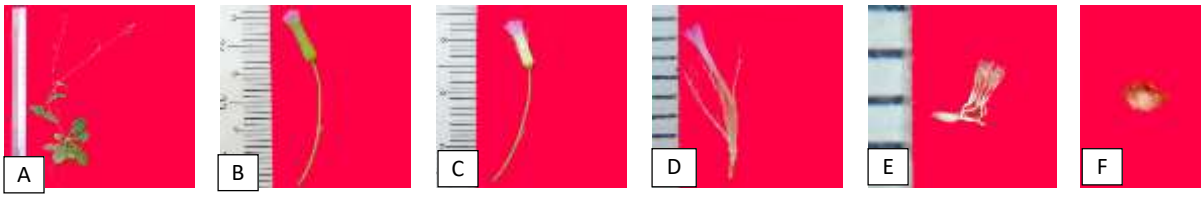

A. Inflorescence B. Capitulum C. L.S of capitulum D. Disc floret E. Stamens F. T.S of ovary

Figure 8 *Emilia sonchifolia* (L.) DC. var. Scabra

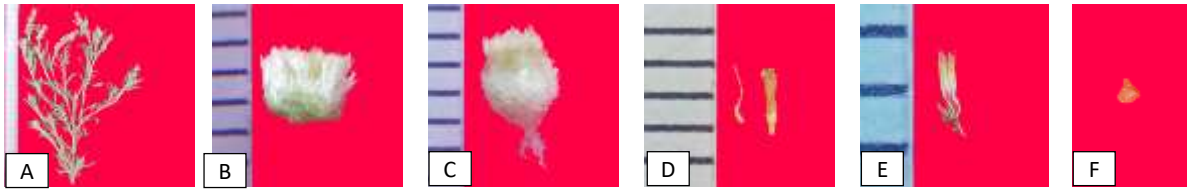

A. Inflorescence B. Capitulum C. L.S of capitulum D. Filiform & Disc floret E. Stamens F. T.S of ovary

Figure 9 *Gnaphalium pulvinatum* Delile.

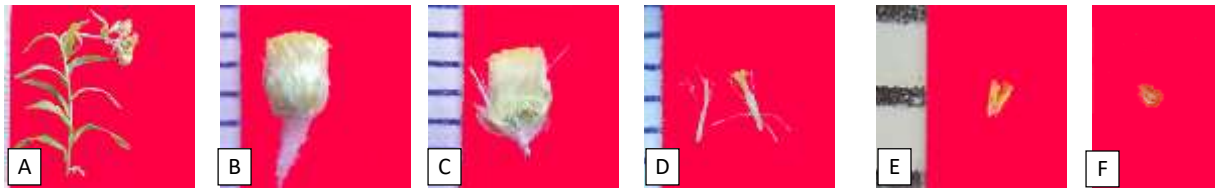

A. Inflorescence B. Capitulum C. L.S of capitulum D. Filiform & Disc floret E. Stamens F. T.S of ovary

Figure 10 *Pseudognaphalium hypoleucum* (DC.) Hilliard & B.L. Burtt.

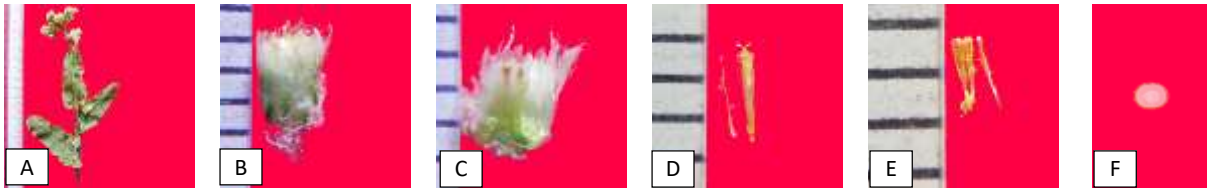

A. Inflorescence B. Capitulum C. L.S of capitulum D. Filiform & Disc floret E. Stamens F. T.S of ovary

Figure 11 *Pseudognaphalium biolettii* Anderb.

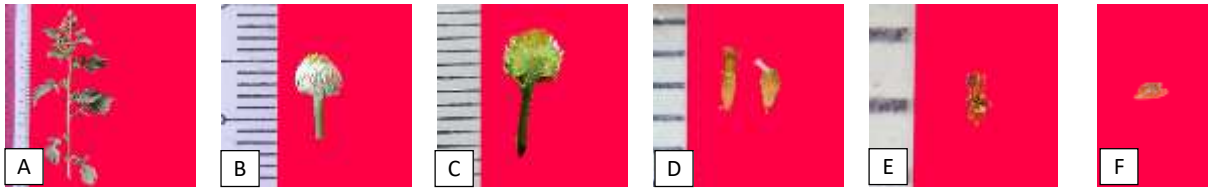

A. Inflorescence B. Capitulum C. L.S of capitulum D. Disc & Filiform floret E. Stamens F. T.S of ovary

Figure 12 *Dichrocephala bicolor* Schltdl

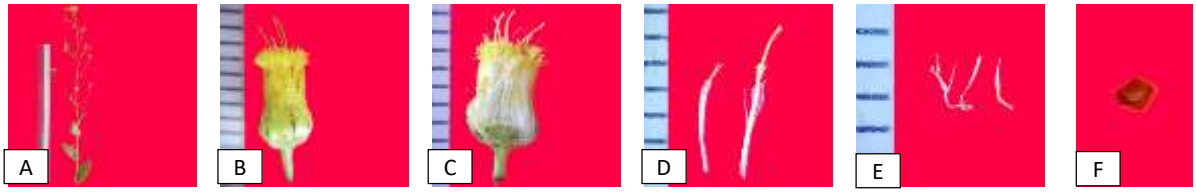

A. Inflorescence B. Capitulum C. L.S of capitulum D. Filiform & Disc floret E. Stamens F. T.S of ovary

Figure 13 *Conyza adenocarpa* Dalzell & A. Gibson.

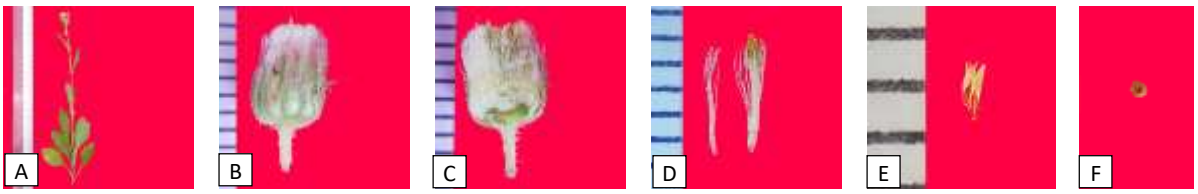

A. Inflorescence B. Capitulum C. L.S of capitulum D. Filiform & Disc floret E. Stamens F. T.S of ovary

Figure 14 *Conyza japonica* (Thunb.) Less.

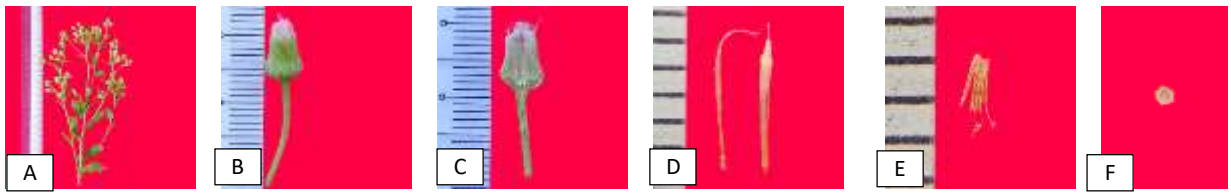

A. Inflorescence B. Capitulum C. L.S of capitulum D. Filiform & Disc floret E. Stamens F. T.S of ovary

Figure 15 *Blumea junghuhniana* (Miq.) Boerl.

A. Inflorescence B. Capitulum C. L.S of capitulum D. Filiform & Disc floret E. Stamens F. T.S of ovary

Figure 16 *Blumea paniculata* (Wall.) M. R. Almeida.

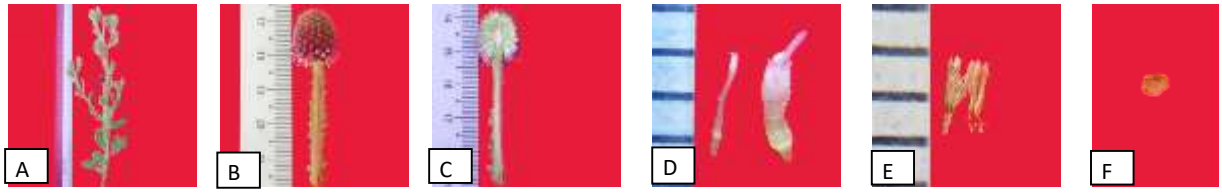

A. Inflorescence B. Capitulum C. L.S of capitulum D. Filiform & Disc floret E. Stamens F. T.S of ovary

Figure 17 *Sphaeranthus indicus* L.

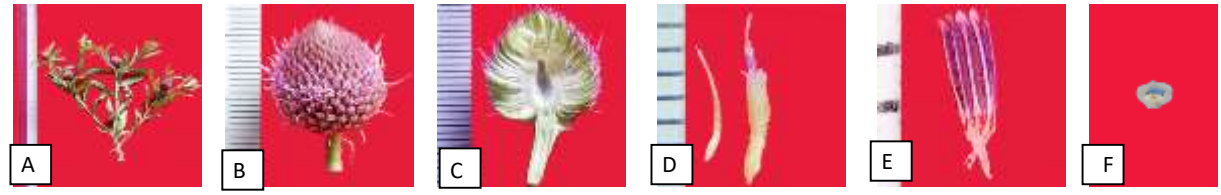

A. Inflorescence B. Capitulum C. L.S of capitulum D. Filiform & Disc floret E. Stamens F. T.S of ovary

Figure 18 *Sphaeranthus peguensis* Kurz ex C. B. Clarke

A. Inflorescence B. Capitulum C. L.S of capitulum D. Ray & Disc floret E. Stamens F. T.S of ovary

Figure 19 *Parthenium hysterophorus* L.

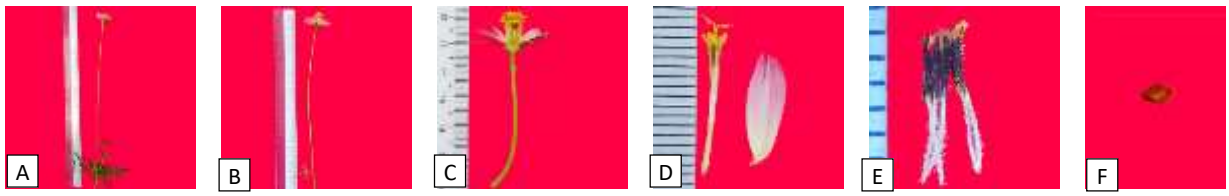

A. Inflorescence B. Capitulum C. L.S of capitulum D. Disc & Ray floret E. Stamens F. T.S of ovary

Figure 20 *Cosmos caudatus* Kunth.

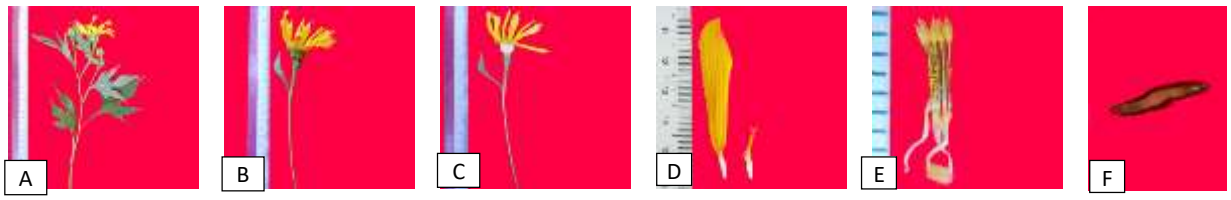

A. Inflorescence B. Capitulum C. L.S of capitulum D. Ray & Disc floret E. Stamens F. T.S of ovary

Figure 21 *Tithonia diversifolia* (Hemsl.) A. Gray

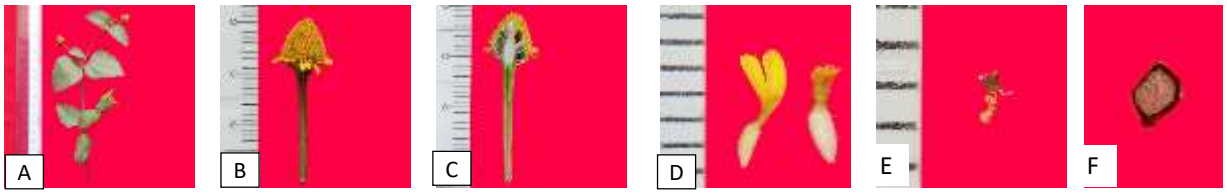

A. Inflorescence B. Capitulum C. L.S of capitulum D. Ray & Disc floret E. Stamens F. T.S of ovary

Figure 22 *Acmella paniculata* (Wall.ex.DC.) R. K. Jansen

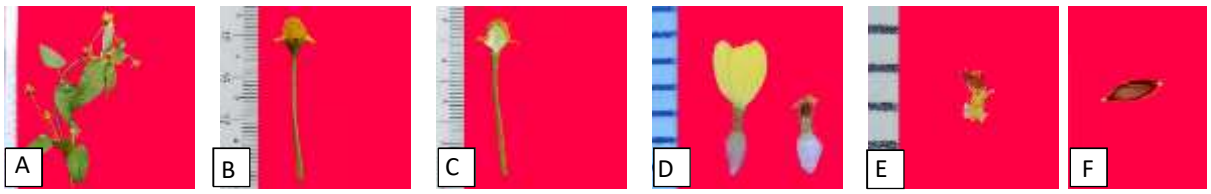

A. Inflorescence B. Capitulum C. L.S of capitulum D. Ray & Disc floret E. Stamens F. T.S of ovary

Figure 23 *Acmella uliginosa* (Sw.) Cass.

An artificial key to the studied species

1. Capitula having male and female florets in the same capitula, white ---------- 19. *Parthenium hysterophorus*

1. Capitula having bisexual and female florets in the same capitula, purple, yellow ----------2

2. Capitula homogamous ----------3

2. Capitula heterogamous ----------10

3. Florets yellow color ----------4

3. Florets purple color----------6

4. Involucre bright many seriate, stamen yellow----------5. *Sonchus arvensis*

4. Involucre bright 2 seriate, stamen black ----------5

5. The outer phyllaries triangular, dark to blackish green ----------3. *Youngia conjunctiva*

5. The outer phyllaries triangular-ovate, green ----------4. *Youngia japonica*

6. Leaves without lobes ----------7

6. Leaves with lobes ----------8

7. Leaves base cordate; anther pale yellow without the top purple----------6. *Emilia fosbergii*

7. Leaves base obtuse; anther pale white with the top purple----------7. *Emilia prenanthoidea*

8. Leaves blade lyrate; capitula pedunculate----------8. *Emilia sonchifolia*

8. Leaves blade ovate to oblanceolate, linear-oblong; capitula sessile----------9

9. Leaves in a radical rosette; 4 florets per capitula ----------1. *Elephantopus scaber*

9. Leaves alternate; many florets per capitula ----------2. *Acilepis squarrosa*

10. Capitula radiate----------11

10. Capitula disciform ----------14

11. Leaves compound; capitula pale purple ----------20. *Cosmos caudatus*

11. Leaves simple; capitula pale yellow ----------12

12. Leaf with lobes; receptacle convex ----------21. *Tithonia diversifolia*

12. Leaf without lobes; receptacle conical ----------13

13. Annual; leaves blade broadly ovate to ovate-triangular ----------22. *Acmella paniculata*

13. Perennial; leaves blade narrowly ovate or elliptic----------23. *Acmella uliginosa*

14. Receptacle obconical; stamen 4----------12. *Dichrocephala bicolor*

14. Receptacle convex, concave or flat; stamen 5----------15

15. Capitula sessile----------16

15. Capitula pedunculate ----------18

16. Inflorescence axillary or terminal, involucre 2 seriate---------- ----------9. *Gnaphalium pulvinatum*

16. Inflorescence terminal, involucre 3-5 seriate----------17

17. Annual; leaves blade linear to oblong ----------10. *Pseudognaphalium hypoleucum*

17. Perennial; leaves blade lanceolate-oblong ----------11. *Pseudognaphalium biolettii*

18. Leaves sessile----------19

18. Leaves petiolate ----------22

19. Capitula yellow color ----------13. *Conyza adenocarpa*

19. Capitula purple color ----------20

20. Receptacle flat, capitula terminal ----------14. *Conyza japonica*

20. Receptacle conical, capitula axillary or terminal ----------21

21. Peduncle with wing; receptacle solid conical; anther yellow--------17. *Spharanthus indicus*

21. Peduncle without wing; receptacle fistular conical; anther purple----------18. *Spharanthus peguensis*

22. Stem branched; capitula purple color ----------15. *Blumea junghuhniana*

22. Stem no branched; capitula yellow color----------16. *Blumea paniculata*

Discussion and Conclusion

Homogamous capitula are found in 8 species. Among 8 species, 5 species have discoid capitula and 3 species possessed ligulate capitula. Heterogamous capitula are found in 15 species. Heterogamous type can also be subdivided into disciform and radiate capitula. Among them, 10 species possess disciform capitula and 4 species have radiate capitula.

Sphaeranthus indicus L. has stems with strongly scented 4 winged, the peduncule with deeply crenate 3 wings and yellow anther. The conical receptacle of *Sphaeranthus indicus* L. are absent fistular. These characters were in agreement with previous findings.

The leaves of *Emilia prenanthoidea* DC. and *E. fosbergii* Nicolson. were absent lobes and those of *E. sonchifolia* (L.) DC. var. Scabra were present lobes. The different characters were in agreement with Hooker (1881), Backer (1965) and Dassanayake (1980) Jeffery (2007).

In this study, the three genera were found different characters of leaves shape, anther and capitula color. The leaves of *Acmella paniculata* (Wall. ex DC.) R.K. Jansen were broadly ovate to ovate-triangular and then the stems of this species were green or purple in color. The leaves of *Acmella uliginosa* (Sw.) Cass. were found narrowly ovate or elliptic and the stems of this species were bright green. The distinct characters were agreed to those mentioned by Dassanayake (1980), Jeffery (2007), Titiek (2015) and Wilson (2015).

The capitula of *Conyza adenocarpa* Dalzell & Gibson were arranged in corymbose cymes at terminal or in upper leaf-axils and yellow color. The capitula of *Conyza japonica* (Thunb.) Less. were arranged few together in shortly compactly corymbose terminal cymes and purple color. The characters of two species including tribe Asteraceae were similar to Hooker (1881), Backer (1965), Qi-ming (2009).

Sphaeranthus peguensis Kurz. ex C.B Clarke. included tribe Inuleae has the peduncle without wings and yellow florets and purple anthers. The conical receptacle of this species is present fistular. The characters of *Sphaeranthus peguensis* Kurz ex C.B Clarke were in agreement with Naidu (2012) and Aye Aye Thin. (2017).

Parthenium hysterophorus L. have female ray florets and male disc florets, achene having spoon-shaped appendages. The species that possess these characters are similar to Naidu (2012).

The involucres of *Youngia conjunctiva* Babc. & Stebbins. were found 2 seriate and then the outer bracts of this species were triangular and dark to brackish green. The outer bracts having involucres of *Y. japonica* (L.) DC. were triangular-ovate and green in color. The characters of these two species were agreed with those mentioned by Dassanayake (1980), Wu *et al.* (2013).

The species of family Asteraceae are seed dispersal, they grow rapidly and distribute enormously. According to the field studies, members of the family Asteraceae can grow on the climate of the research from the present study. The present study can give valuable information about some member of the family Asteraceae.

Acknowledgements

We would like to thank to all persons who supported in various ways and special thanks to Dr Tint Khaing Aye Professor and Head, Department of Botany, Kalay University, for her encouragement.

References

Aye Aye Thin. (2017). Pollen morphology of Asteraceae found in Mandalay Region. PhD Dissertation, Department of Botany, University of Mandalay.

Backer, C.A. (1965). Flora of java Vol II. Nordhoff. groningen. the Netherlands.

Dassanayake, M. D. (1980). A revised handbook to the flora of Ceylon Volume I. University of Peradeniya, Department of Agriculture, Peradeniya, Sri Lankaand the Smithsonian Institution, Washington, D. C., U. S. A.

Hooker, J. D. (1881). Flora of British India. Reeve & Co., 5 Henrietta Street, Convent Garden, London.

Hundley, H.G & Chit Ko Ko. (1987). List of trees, shrubs, herbs, and principal climbers, etc. Fourth Revised Edition Mayangon, Rangoon, Burma.

Jeffery and Kadereit. (2007). The family and genera of vascular plants. Vol. VIII. New York.

Kress, J., Robert. A. Defilipps. Ellen Farr & Yin Yin Kyi. (2003). A Checklist of

the trees, shrubs, herbs and climbers of Myanmar. Department of Systematic Biology-Botany. National Museum of National History, Washington DC. USA.

Monika, K. (2014). *Parthenium hysterophorus* L. a noxious and rapidly spreading weed of India. Department of Botany, k. l. p. College, Rewari, Haryana. India.

Naidu, V. S. G. R. (2012). Weed identification. Directorate of weed science Research, Jabalpur, India.

Qi-ming, H.U. and W. U. De-lin. (2009). Flora of Hong Kong, Volume 3, Hong Kong Herbarium & South China Botanical Garden.

Tadesse. (2015). How to study Asteraceae. Department of Evolution, Ecologyand Organismal Ohio State University, Ethiopia.

Titiek, S., N., Sari, P. B. Indra and Galang, T. R. (2015). A guide book to invasive alien plant species in Indonesia. Removing Barriers to Invasive Species Management in production and protection floret in Southeast Asia- Indonesia program (Foris Indonesia)

Wu, Z. Y. Raven, P. H. & Hong D.Y., eds. (2013). Flora of China Volume 20-21 (Asteraceae) Science Press (Beijing) & Missouri Botanical Garden Press (St. Louis).

MITOTIC CHARACTERS OF *ZEA MAYS* L. cv. SHAN PYAUNG AND LAY TAN PYAUNG IN SHAN STATE

Su May Naung[1] & Thi Thi Htun[2]

Abstract

The two cultivars of *Zea mays* L., Shan pyaung and Lay tan pyaung were observed to determine the karyotype analysis. These samples were supported by Seed Bank; Department of Agricultural Research, Nay Pyi Taw, Yezin. The somatic chromosome number of studied cultivars was 2n=20. The karyotype formulae were varied, 1 ST +1 SM* + 1 SM + 7 M was found in cv. Shan pyaung and 10 M in cv. Lay tan pyaung. A pair with secondary constriction or satellite submedian chromosome was observed in chromosome number 1 (SM1) of cv. Shan pyaung. In cv. Shan pyaung, the longest chromosome with 4.71 µm and the smallest chromosome with 2.18 µm, while the 4.40 µm of longest chromosome and 2.25 µm of smallest chromosome were observed in cv. Lay tan pyaung. The two studied cultivars were significantly different in morphology, karyotypic formula, chromosome group and size. The present study was elucidated to understand the number, morphology of chromosomes, and also beneficial for further research in cytogenetics concern with *Zea mays* L.

Keyword: Karyotype, somatic chromosome, secondary constriction, submedian chromosome

Introduction

Zea mays L., commonly known as maize is annual crop that belongs to the family of grass i.e Poaceae. It is also recognized by different synonyms such as Zea, Corn, silk corn etc. It is native of South America but extensively cultivated in various other countries as well like Myanmar. It is considered as staple article of food in some islands and provinces. It is widely grown in temperate and tropic regions with well drained and fertile soil (Kumar & Jhariya 2013).

Most of the world's food comes from 6 species of grasses: rice, wheat, corn, barley, oats and sorghum. After wheat, corn is the most cultivated cereal in the world because it is a basic component in the diet of the population, as it is a cereal of high nutritional value because it's containing carbohydrates, proteins, oils, vitamins and minerals. This is the reason why large areas are sown on all continents, except in Antarctica (Hipp 2004).

Maize is a tropical grass, well adapted to many climates and hence has wide ranging maturities from 70 days to 210 days (Khan *et al.* 2017). The main corn producing areas in Myanmar are primarily found in the hilly and dry zones of the country with smaller production taking place in the delta and coastal regions. According to government sources, Shan State which is located in the central part of country, accounts for 52 percent of Myanmar's total corn production area while the Ayeyarwady (delta regions), Magwe, and Sagaing regions make up the balance (Anonymous 2016).

Genetically diverse high yielding varieties and hybrids from local and exotic germplasms are used as source materials in the extraction of inbred lines in New Plant Variety Protection Unit Department of Agricultural Research (DAR), Yezin. Hybrid maize research activities are conducted with the primary aim of maize productivity and production in Myanmar to meet and overcome the export demand, and thereby full fill the domestic needs of the country, and to increase productivity and total production of maize in Myanmar. There is a strong need to develop high yielding hybrid maize. A long – term hybrid maize research and development program was

[1] Assistant Lecturer, Department of Biology, Monywa Education Degree College
[2] Dr, Associate Professor, Department of Botany, University of Mandalay

therefore initiated at Department of Agricultural Research (DAR), Yezin in 1974 (Phyu Phwe 2016).

The karyotype, is the typical chromosomal map of a species, which allows us to analyze the chromosome number and the morphology of the chromosomes (shape, size and position of the centromere), information of great value since the chromosomes are guides of phylogenetic affinities and indicators of the systematic classifications (Agreda *et al*. 1991; González *et al*. 2003; Poggio *et al*. 2005).

As well as carrying out studies of populations that are in the process of selection or improvement, with the objective of showing evidence about the frequency changes that occur in maize populations. Similary is important to propose broader karyotypic studies that include a greater number of native races, as well as more exhaustive studies such as fluorescent chromosome bands and genome size estimation (Acosta 2009).

According to Teodoro-Pardo *et al*. (2007), the different karyotypic formula for a species can occur due to genetic variations among the populations, originating from the genome response to the different environments, enlarging the genetic variability for the genus.

In Myanmar, cytogenetic analysis was done by various researchers on many species. More comprehensive studies are needed and in particular a thorough examination of chromosome distribution among some local cultivars of *Zea mays* L. Thus, it is needed to be carried out this research work.

The aim and objectives of this research are to study on karyotype of the two *Zea mays* L. cultivars; to analyze the obtained mitotic chromosome data and to compare their morphological differences of two *Z. mays* L. cultivars.

Materials and Methods

The two cultivars of *Zea mays* L. Shan pyaung (Accession No. 009486) and Lay tan pyaung (Accession No. 011438) were used for this study. The seed samples were obtained from Seed Bank, Department of Agricultural Research, Nay Pyi Taw, Yezin.

The meiotic analysis was done in Department of Biology, Taunggyi Education Degree College. The seeds were germinated on moist filter paper in Petri dishes, kept at room temperature in the dark. After two days, when root lengths were about 1.0 − 1.5 cm the roots were cut and placed in small bottle filled with pre cooled distilled water. Pretreatment was done ice water 0^{o}C to 4^{o}C for 24 hours. The root tips were then transferred into labeled fixation bottles filled with Carnoy's (1889) I solution (1:3 acetic acid and 95% alcohol) for three days.

The root tips were then removed from the fixative and were stained in 2% aceto-carmine for 24 hours at room temperature. The somatic chromosomes were observed using the squash technique (Belling 1921). The two root tips from each seed were used for mitotic analysis. The number of chromosomes was counted from 10 – 15 cells of each root tip. Good plates with well spread chromosomes were photomicrography while measurement of chromosomes was done with an ocular micrometer.

Measurement of (a) length of long arms, short arms and the whole length of chromosome, (b) arm ratio were recorded. Satellites were included in total length to calculate arm ratios. Karyological data were obtained from the ten most definitive cells in each genotype. Arm ratios, centromeric and relative length of each chromosome were calculated according to the following formulae.

(1) Arm ratio = Length of long arm/ Length of short arm

(2) Centromeric index = Length of short arm/ Total length of chromosome

(3) Relative length = Total length of each chromosome /Total complementary length of chromosome × 100

Mean value of short arm length, long arm length and satellite were used to prepare the ideograms. The ideogram was prepared by arranging the chromosomes in such a way that the largest chromosome is placed on the extreme left at number 1 position and the smallest one is placed on the extreme right position in each group of median and submedian (Stebbins 1971).

Results

The morphological characters, diploid somatic chromosome number, karyotype and idiogram of two *Zea mays* L. (maize) cultivars were described in Table 1 to 2 and Figure 1 to 9.

Taxonomic Description

Family	-	Poaceae
Scientific Name	-	*Zea mays* L.
English Name	-	Maize
Myanmar Name	-	Pyaung

Annual erect herbs, monoecious; stems 1.22 – 2.24 m high, solid, well defined nodes and internodes, 10 – 12 jointed swollen nodes; internode 9 – 20 cm in length, the last node end with tassel. Leaves simple, alternate and distichous, exstipulate, sessile; blades linear-lanceolate, 34 – 71 cm long and 4.0 – 9.0 cm wide, the margin entire, hairy, the apex acuminate, scarcely strigose on both surfaces; ligule 0.5 – 1.0 cm long, auriculate. Male inflorescences or tassels terminal paniculate, 27 – 44 cm long, 5 – 16 branched. Female inflorescences or ears axillary, usually 1, sometime 3 – 4, series of paired spikelets in longitudinal rows, the rows usually even number, 4 – 14. Male spikelets paired, one sessile and other pedicellate, with paired glumes; glumes overlapped, bracteate, outer lemma 3-nerved, inner palea 2-nerved, unisexual, zygomorphic; perianth modified into 2 fleshy lodicules, opposite the lemma and alternate the stamens; stamens 3; filaments free, short; anthers versatile, dithecous, dehiscent by longitudinal slit, pale yellow; gynoecium absent. Female spikelets paired, arranged in rows on the central axis or cob, sessile, with paired glumes, thick near the base of ovary, bracteate, represented by lemma and palea, unisexual, zygomorphic; perianth usually absent, sometimes 2, scaly lodicules; androecium absent; gynoecium monocarpellary, unilocular; ovary superior, dome shaped, ovary single ovuled, basal placentation; style long, silky, filiform; stigma long, hairy; fruits or kernels caryopsis, various coloured.

Tasseling Period: Varied according to cultivars.

Outstanding characters of cv. Shan pyaung

Plant height 1.22 – 1.60 m; ear height 0.38 – 0.51 m; jointed swollen nodes 10 – 12 and internodes 9 – 14 cm long. Leaf blades 37 – 69 cm long and 4 – 9 cm wide. Male inflorescences or tassels 35 – 44 cm long with 5 to 7 branches. Female inflorescences or ears only one per plant; silk color pale yellow; ears 21 – 29 cm long and 14 – 15 cm in diameter; female florets arranged in 12 – 14 rows per ear; cobs diameter 11 – 13 cm; kernel rainbow color (mixed with yellow, white, pale purple).

Tasseling Period: 40 – 58 days

Outstanding characters of cv. Lay tan pyaung

Plant height 2.13 – 2.24 m; ear height 0.78 – 0.89 m; jointed swollen 11 – 12 and internodes 9 – 20 cm long. Leaf blades 34 – 71 cm long and 4 – 9 cm wide. Male inflorescences or tassels 27 – 34 cm long with 11 to 16 branches. Female inflorescences or ears 3 - 4 per plant; silk color red; ears 22 – 25 cm long and 8 – 9 cm in diameter; female florets arranged in 4 rows per ear; cobs diameter 6 – 8 cm; kernel white in color.

Tasseling Period: 35 – 50 days

Mitotic characters

The chromosome status of the two *Zea mays* L. cultivars was determined. At the cytological level, both cultivars had 2n = 20 diploid chromosome (Figure 2 and 4). The basic structure of these chromosomes was significantly different. The karyotypic formula of cv. Shan pyaung was 1 ST +1 SM* + 1 SM + 7 M, while in cv. Lay tan pyaung, it was 10M (Table 2).

On observing the size and morphology of somatic chromosomes were classified into three groups in two cultivars, median, submedian and subterminal chromosome. In the cv. Shan pyaung, the median group consisted of 7 chromosome (chromosome number 3 to7, 9 and 10) and regarded as M_1, M_2, M_3, M_4, M_5, M_6 and M_7). The median chromosomes were ranged from mean length of 3.53 ± 0.32 to 2.18 ± 0.09 µm. The centromeric index ranged from 0.49 ± 0.01 to 0.47 ±0.01 and the relative length ranged from 11.26 ± 0.63 to 6.99 ± 0.39. The chromosome no. 1 and 2 were submedian and recorded as SM_1* and SM_2. The submedain chromosomes were ranged from mean length of 4.71 ± 0.41 to 3.84 ± 0.11µm. The centromeric index ranged from 0.34 ± 0.05 to 0.41 ± 0.01 and the relative length ranged from 15.07 ± 1.88 to 12.27 ± 0.32. Chromosome number 8 belonged to subterminal (ST_1) (Table 2).

In cv. Lay tan pyaung, chromosome number 1to 10 were median, regarded as M_1, M_2, M_3, M_4, M_5, M_6, M_7, M_8, M_9 and M_{10} respectively. All members were ranged from 4.40 ± 0.67 to 2.25 ± 0.20 µm. The centromeric index ranged from 0.49 ± 0.01 to 0.47 ± 0.01. The relative length ranged from 15.10 ± 2.25 to 7.74 ± 1.09 µm (Table 1).

Comparison on Chromosome Group

Median Group

The cultivars Shan pyaung had seven median chromosomes, while the cv. Lay tan pyaung possessed ten median chromosomes. The total length of median group of cultivars Lay tan pyaung was found the longest being (4.40 ± 0.67) while that of cultivar Shan pyuang was considered the shortest with (2.18 ± 0.09) in length. The arm ratios were ranged from 1.15 to 1.06. All the median chromosomes of the two maize cultivars studied ranged from 15.10 to 6.99 in relative lengths (Table 1 and Figure 2 to 9).

Submedian Group

The satellite was attached to the chromosomes number one of cv. Shan pyaung, which was submedian type and the longest chromosome. The cv. Shan pyaung was possessed two submedian chromosome. The total length of two submedian chromosomes were observed (4.71 ± 0.41) and (3.84 ± 0.11). The arm ratios were ranged from 1.44 to 1.42. The two submedian chromosomes of the cv. Shan pyaung ranged from 15.07 to 12.27 in relative lengths (Table 1 and Figure 2 and 9)

Subterminal Group

The cultivar Shan pyaung had only one subterminal chromosome. The total length, arm ratio and relative length of the subterminal chromosome were 2.54 ± 0.23, 1.51 and 8.10 (Table 1 and Figure 2 and 9).

Table 1 Somatic chromosome characters (total, ratio and designation) of *Zea mays* L. cultivars

	Characters	Chr. No. 1	Chr. No. 2	Chr. No. 3	Chr. No. 4	Chr. No. 5	Chr. No. 6	Chr. No. 7	Chr. No. 8	Chr. No. 9	Chr. No. 10
Shan pyaung	Total length	4.71 ± 0.41	3.84 ± 0.11	3.53 ± 0.32	3.26 ± 0.27	3.10 ± 0.26	2.91 ± 0.17	2.76 ± 0.06	2.54 ± 0.23	2.45 ± 0.19	2.18 ± 0.09
	L	2.24 ± 0.16	2.26 ± 0.10	1.83 ± 0.14	1.70 ± 0.13	1.60 ± 0.13	1.54 ± 0.09	1.45 ± 0.05	1.53 ± 0.18	1.28 ± 0.09	1.16 ± 0.06
	S	1.58 ± 0.11	1.58 ± 0.06	1.70 ± 0.18	1.56 ± 0.17	1.50 ± 0.14	1.40 ± 0.09	1.31 ± 0.03	1.01 ± 0.05	1.18 ± 0.11	1.02 ± 0.03
	Satellite	1.09 ± 0.12	-	-	-	-	-	-	-	-	-
	Arm ratio	1.42 ± 0.02	1.44 ± 0.09	1.09 ± 0.03	1.10 ± 0.05	1.07 ± 0.03	1.10 ± 0.05	1.11 ± 0.04	1.51 ± 0.10	1.09 ± 0.03	1.15 ± 0.02
	Designation	SM1*	SM2	M1	M2	M3	M4	M5	ST1	M6	M7
	C.I	0.34 ± 0.05	0.41 ± 0.01	0.48 ± 0.01	0.48 ± 0.01	0.49 ± 0.01	0.48 ± 0.01	0.48 ± 0.01	0.40 ± 0.02	0.48 ± 0.01	0.47 ± 0.01
	R. L	15.07±1.55	12.27±0.32	11.26±0.63	10.40±0.58	9.91 ± 0.54	9.37 ± 0.25	8.82 ± 0.29	8.10 ± 0.44	7.83 ± 0.51	6.99 ± 0.39
Lay tan pyaung	Total length	4.40 ± 0.67	3.96 ± 0.45	3.62 ± 0.36	3.31 ± 0.21	3.25 ± 0.20	3.17 ± 0.25	2.93 ± 0.28	2.75 ± 0.25	2.54 ± 0.18	2.25 ± 0.20
	L	2.26 ± 0.34	2.07 ± 0.25	1.91 ± 0.17	1.74 ± 0.14	1.71 ± 0.12	1.66 ± 0.13	1.54 ± 0.18	1.42 ± 0.13	1.33 ± 0.11	1.19 ± 0.10
	S	2.14 ± 0.32	1.89 ± 0.21	1.71 ± 0.20	1.57 ± 0.08	1.55 ± 0.09	1.51 ± 1.13	1.39 ± 0.11	1.33 ± 0.12	1.23 ± 0.09	1.07 ± 0.11
	Satellite	-	-	-	-	-	-	-	-	-	-
	Arm ratio	1.06± 0.03	1.10 ± 0.04	1.13 ± 0.05	1.11 ± 0.05	1.11 ± 0.05	1.11 ± 0.07	1.12 ± 0.07	1.07 ± 0.03	1.08 ± 0.05	1.12 ± 0.06
	Designation	M1	M2	M3	M4	M5	M6	M7	M8	M9	M10
	C.I	0.48 ± 0.02	0.48 ± 0.01	0.47 ± 0.01	0.48 ± 0.01	0.48 ± 0.01	0.48±0.001	0.48 ± 0.02	0.49±0.004	0.49 ± 0.01	0.48 ± 0.01
	R. L	15.10±2.25	13.70±2.78	12.49±2.16	11.48±2.31	11.21±1.86	10.94±1.93	10.24±1.94	9.48 ± 1.67	8.77 ± 1.46	7.74 ± 1.09

L=Long arm, S = Short arm, ST = Subterminal, SM= Submedian, M = Median, C.I = Centromeric index, R. L = Relative Length, Chr. = Chromosome

Table 2 Comparison of karyotypic formula of *Zea mays* L. cultivars

No.	Cultivars	Karyotypic formula
1	Shan pyaung	1 ST + 1 SM*+ 1 SM + 7 M
2	Lay tan pyaung	10 M

ST = Subterminal chromosome, SM = Submedian chromosome, M = Median chromosome, * = Satellite

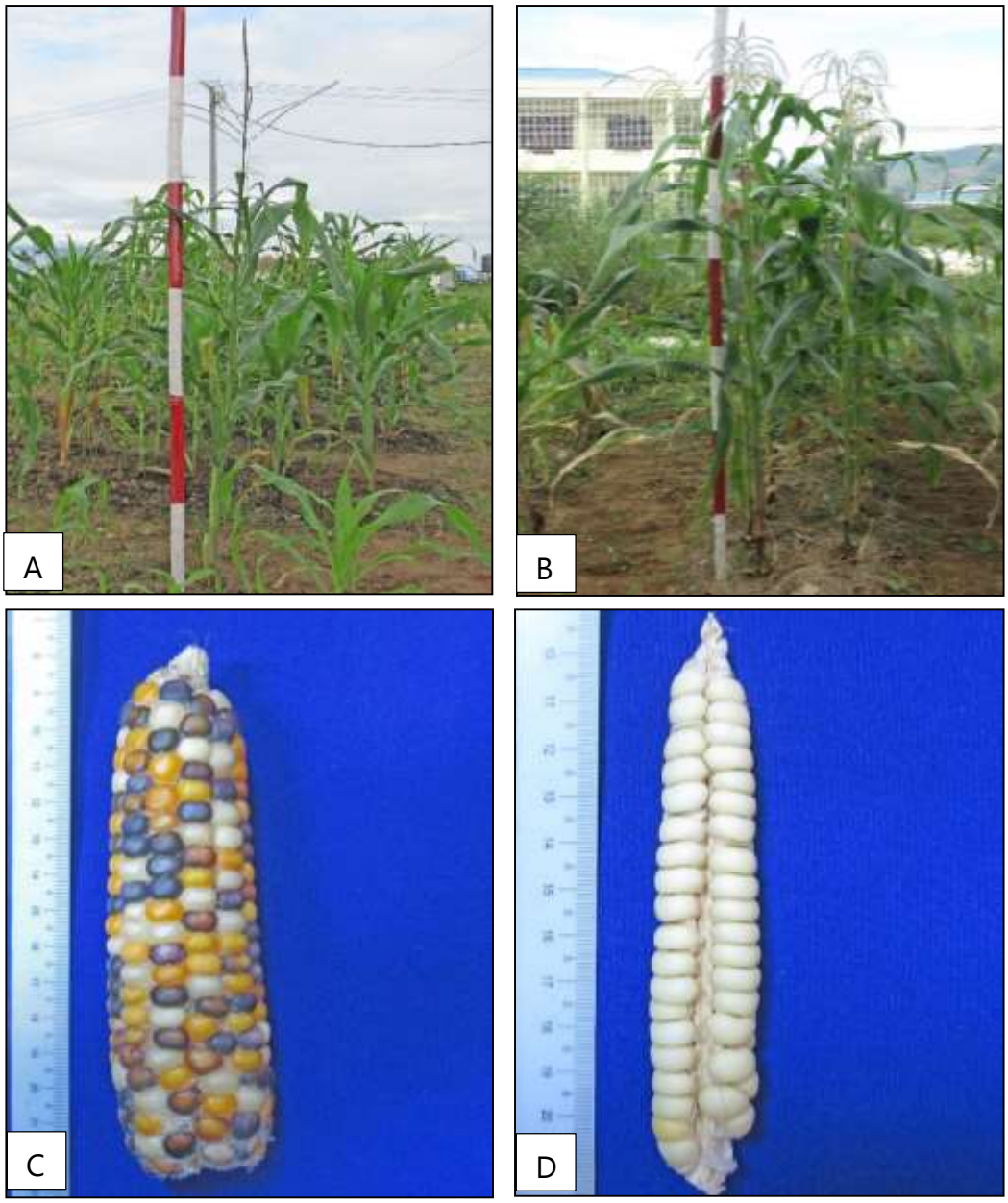

Figure 1 Morphological characters of *Zea mays* L. cv. Shan pyaung and Lay tan pyaung
A. Habit of cv. Shan pyaung B. Habit of cv. Lay tan pyaung
C. Cob of cv. Shan pyaung D. Cob of cv. Lay tan pyaung

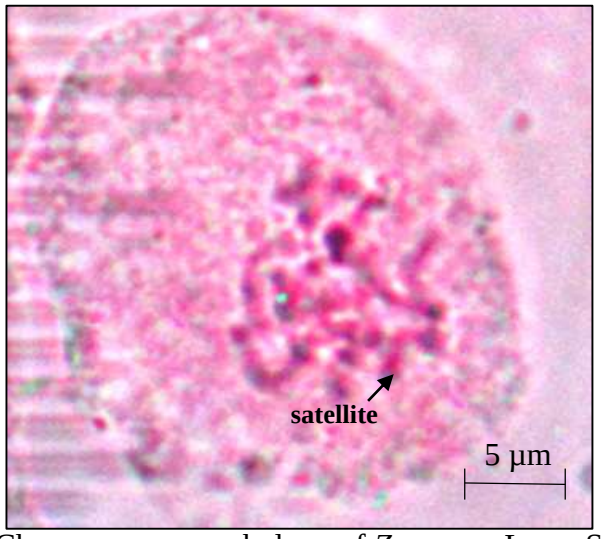

Figure 2 Chromosome morphology of *Zea mays* L. cv. Shan pyaung

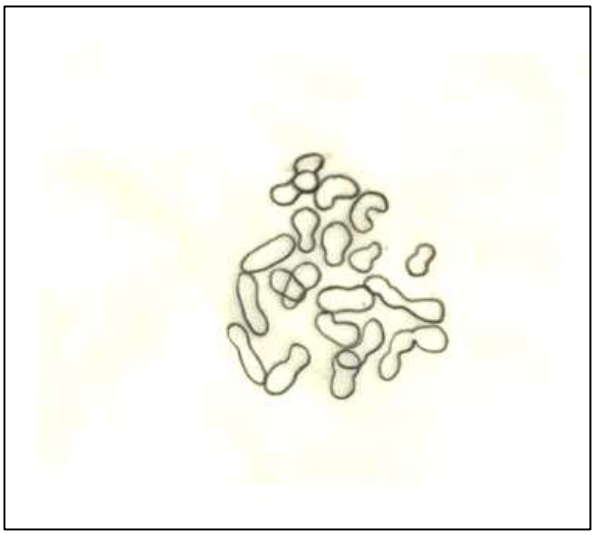

Figure 3 Chromosome outline of *Zea mays* L. cv. Shan Pyaung

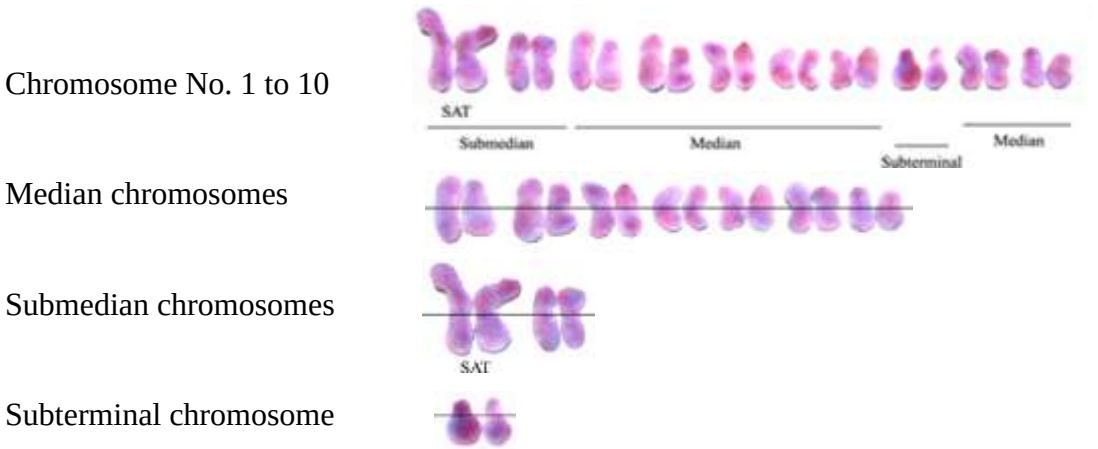

Figure 4 Karyotype of *Zea mays* L. cv. Shan pyaung

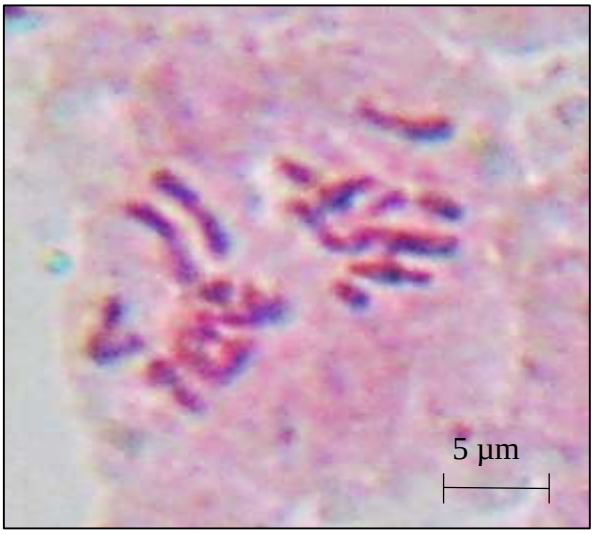

Figure 5 Chromosome morphology of *Zea mays* L. cv. Lay tan pyaung

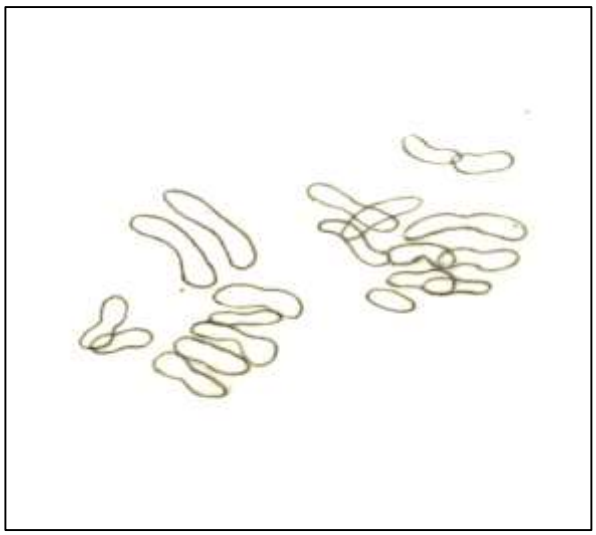

Figure 6 Chromosome outline of *Zea mays* L. cv. Lay Tan Pyaung

Chromosome No. 1 to 10

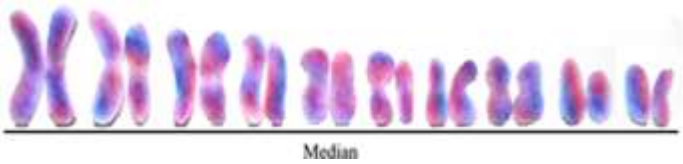

Median chromosomes

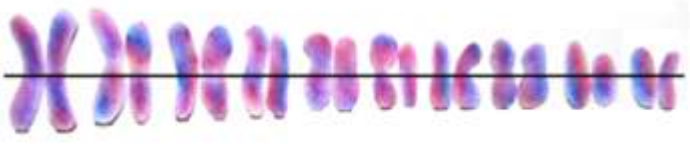

Figure 7 Karyotype of *Zea mays* L. cv. Lay tan pyaung

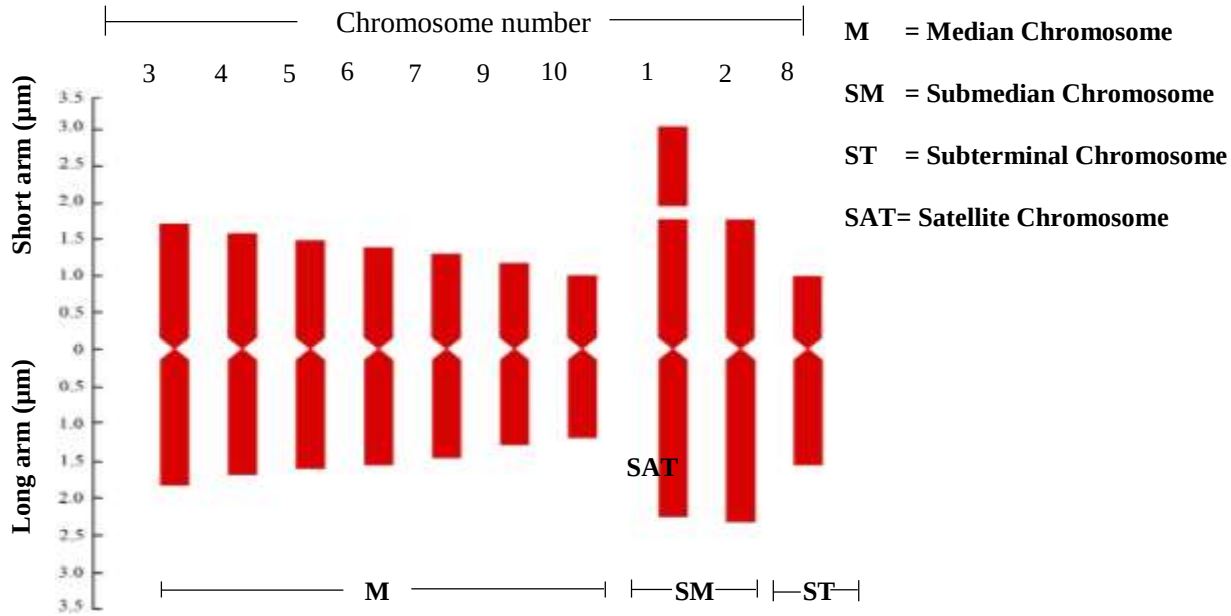

Figure 8 Idiogram of *Zea mays* L. cv. Shan pyaung

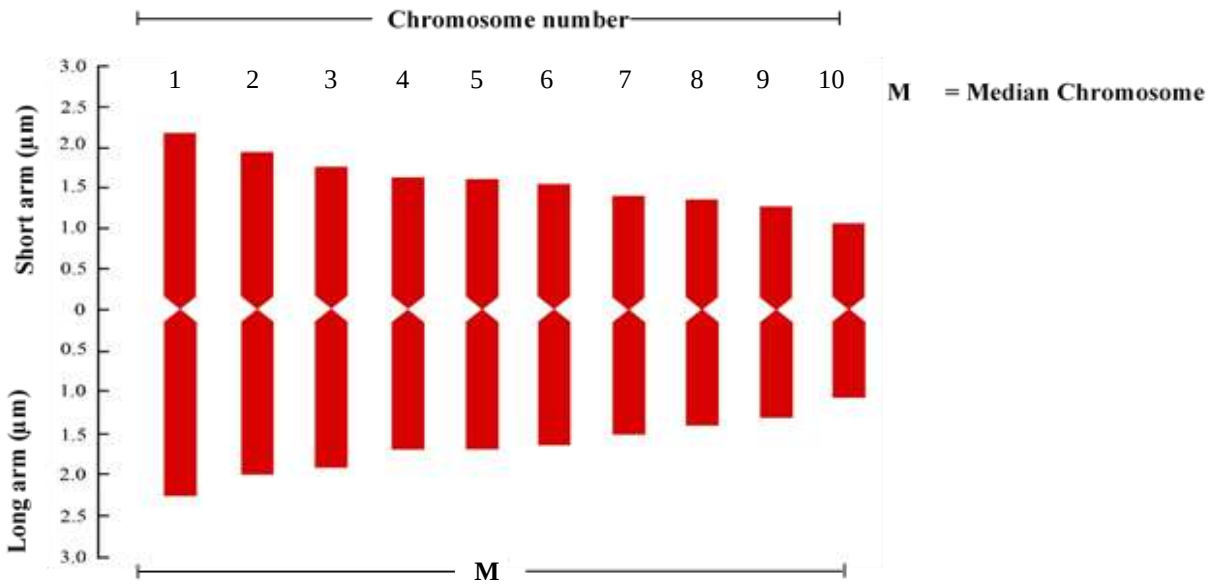

Figure 9 Idiogram of *Zea mays* L. cv. Lay tan pyaung

Discussion and Conclusion

Maize is an annual grass growing up to 4 m tall and monoecious. The female inflorescences, the ears, develop in leaf axils on the stalk; which terminates in the male inflorescence, the tassel. The broad leaf sheaths are overlapping around the stalk and the leaves are arranged in two opposing rows along the stalk, Maize has a multitude of uses and is used in the preparation of food or drinks, as animal feed or for industrial purposes.

The morphology and mitotic chromosome behavior of the two cultivars were studied in this study. The varied morphological characters were observed in this research. The cultivar Lay tan pyaung had significant mean number of plant height, ear height, node per plant, internode length and ear per plant among the two cultivars. The range of tassel length in cv. Shan pyaung was longer

(35 – 44 cm) than the cv. Lay tan pyaung (27 – 34 cm), while the cv. Shan pyaung was possessed low branch per tassel (5-7) than cv. Lay tan pyaung (11-16). The kernel color of the two studied cultivars were also significantly different. These finding were agreement with Goodman & Brown 1988, many varieties or "races" of maize differ in physical properties.

The shortest tasseling period was observed in cv. Lay tan pyaung (35 – 50 days) and the longest period was in cv. Shan pyaung (40 – 58 days). This result was agreed with the finding of Kuleshov & Am (1993), who stated that the flowering time reflects the adaptation of a plant to its environment to local climatic effects. Maize landraces vary widely, from 2 to 11 months, for the time required to mature.

Mitotic chromosome counts for the two cultivars showed 2n = 20. The chromosomes were generally different in their size and centromeric position. This result was agreed with McClintock *et al.* 1981, who reported that the maize has 10 chromosomes (n =10) with relatively large differences in size. The ten chromosomes are all morphologically distinguishable by their structural characteristics, such as relative length, centromere position, satellite, numbers and positions of chromosomal knobs.

In cv. Shan pyaung, one pair of subterminal chromosomes, two pairs of submedian chromosomes and seven pairs of median chromosomes. The SM1 possessed the satellite chromosomes and 1.09 ± 0.12 µm in length. The karyomorphological formula of cv. Shan pyaung was 1 ST+ 1 SM* + 1 SM + 7 M. This is an agreement with the previous mitotic study Silva *et al.* (2018), who studied that the satellite chromosome in submedian chromosome while 0.053 ± 0.009 µm in length was observed. Ten pairs of median chromosomes and 10 M of karyomorphological formula were found in cv. Lay tan pyaung. This result was agreed with Gonzales and Poggio (2011), there was not found satellite chromosomes in their studied maize cultivars.

The median chromosomes (M) were found in chromosome no. 3 to 7 and 9 to 10 in cv. Shan pyaung, while no.1 to 10 in cv. Lay tan pyaung. The mean of total length for median chromosomes were ranged from 4.40 ± 0.67 (cv. Lay tan pyaung) to 2.18 ± 0.09 µm (cv. Shan pyaung). Medina *et al.* (2018) proposed the mean total length of median chromosomes were 4.16 ± 2.04 µm to 2.04 ± 0.09 µm.

The submedian chromosomes (SM) were observed in chromosome no. 1 and 2 of cv. Shan Pyaung, while there was not found submedian chromosome in cv. Lay tan pyaung. The mean total length of SM chromosomes was ranged between 4.71 ± 0.41 µm to 3.84 ± 0.11µm. Medina *et al.* (2018) observed the mean total length of submedian chromosomes were 3.23 ± 0.14 µm to 1.88 ± 0.04 µm. The subterminal chromosomes (ST) were only occurred in chromosome no. 8 of cv. Shan pyaung and the mean total length 2.54 ± 0.23 µm. Ehbucha *et al.* (2016), they reported the mean total length of subterminal chromosome was 2.28 µm.

The total length of the chromosomes was different among the two maize cultivars, as observed in some other studies (Egbucha *et al.* 2016; Medina *et al.* 2018). The present study showed that total length of chromosomes of maize cultivars were ranged between 4.71 to 2.18 µm in cv. Shan pyaung and 4.40 to 2.25 µm in cv. Lay tan pyaung. Therefore, total length of chromosomes found in this study were longer than those reported earlier. Variation in the degree of chromosome condensation may be well due to the use of different root tip pretreatment methods (Tayyar *et al.* 1994). The significant differences of chromosome sizes between two maize cultivars were seen in chromosome no. 1 and 6. A few differences of chromosome sizes were found in chromosome no. 2, 3, 4, 5, 7, 8, 9 and 10.

In the present study, cv. Shan pyaung possessed nucleolus organizer (satellite chromosomes) body. Sears and Sears (1979) stated from five years studied on wheat cytogenetics chromosomes (i.e. having nucleolus organizers) are stable in chromosome segregation as well as adapted to their growing conditions. Therefore, it seems that the cv. Shan pyaung well adapted to their growing conditions.

Karyomorphology and chromosome number of a variety or species are useful in its identification and also in establishing the relationships among related species (Lavania & Srivastava 1999; Liu *et al.* 2000). The importance of cytological information to crop improvement cannot be over emphasized. Cytological studies have helped a lot in resolving the origin and evolution of plant species (Aliyu & Awopetu 2007).

In conclusion mitosis chromosome number of the studied cultivars 2n = 20 were observed, while they were different in morphological characters, karyomorphological formulae, chromosome group and size. The present data of karyology of the two maize cultivars will be assisted to classify the maize cultivars grown in Shan State and more helpful to identify the cytogenetic and cytotaxonomic characters.

Acknowledgements

I would like to mention my appreciation to Dr Nu Nu Yee, Professor and Head, Department of Botany, University of Mandalay for her kind permission to carry out this research. My special thanks to my supervisor, Dr Thi Thi Htun, Associate Professor, Department of Botany, University of Mandalay for her invaluable guidance and advice in this research.

References

Acosta, R. (2009). El cultivo del maiz, su origen y clasificación. El maiz en Cuba. Cultivos Tropicales. 30(2):113-120.

Agreda, S., E. Ferres and M. Montesinos. 1991. Manual de embryologia Y anatomia general. Valencia, Espana: Editorial Universitat de Valencia.

Albert, P.S., Z. Gao, T.V. Danilova and J.A. Birchler. (2010). Birchler. Diversity of chromosomal karyotypes in maize and its relatives. Cytogenet. Genome Res. 2010; 129 (1–3):6–16.

Aliyu, O. M. and J. A. Awopetu. (2007). Chromosome studies in Cashew (*Anacardium occidentale* L.) African Journal of Biotechnology. Vol. 6 (2): pp.131 – 136.

Anonymous. (2016). Corn Production, Supply and Demand Update 2016, USDA Foreign Agricultural Service, Global Agricultural Information Network, GAIN Report Number: BM 6014, Approved by: Rey Santella, Agricultural Attaché.

Belling, J. (1921). On counting chromosomes in pollen mother cells. Am Nat 55: 573- 574.

Bonamico, N., J. Aiassa, M. Ibáñez, M. Di Renzo, D. Díaz and J. Salerno. (2004). Characterization and classification of single cross hybrids of maize with SSR markers. Revista de Investigaciones Agropecuarias. 33(2), 129-144.

Bonamico, N., J. Aiassa, M. Ibáñez, M. Di Renzo, D. Díaz and J. Salerno. (2004). Characterization and classification of single cross hybrids of maize with SSR markers. Revista de Investigaciones Agropecuarias. 33(2), 129-144.

Carnoy's, J. B., (1886). "La cytodierese I" ocuf. Cellule, 3, I.

Egbucha, K., C. A. Duke and I. Hawau. (2016). Karyotype Analysis in *Zea mays* L. Var. Everta (Popcorn) Cultivated Within Owerri, Southeast Nigeria. International Journal of Research in Applied, Natural and Social Sciences (IMPACT: IJRANSS) ISSN (P): 2347-4580; ISSN (E): 2321-8851 Vol. 4, Issue 7, Jul 2016, 127-132 © Impact Journl patterns in the annual species of Cicer. Genome, 37: 656-663.

Gonzales, G.E. and L. Poggio. (2011). Karyotype of *Zea luxurians* and *Z. mays* ssp. *mays* using FISH/DAPI, and analysis of meiotic behavior of hybrids. Genome. 2011; 54(1):26–32

Gonzales, P., M. Caballero, A. Santisteban and P. Serrano. (2003). Prácticas de laboratorio y de aula. Madrid, España: Editorial Narcea S.A.

Goodman, M. M. and W. L. Brown. (1988). Corn and Corn Improvement, edited by Sprague, G. F. & J. W. Dudley. American Society of Agronomy, Madison, WI. Races of corn, pp. 39– 74.

Hipp, A. (2004). El maíz, por dentro y por fuera. New York, United States of America: Editorial the Rosen Publishing Group.

Khan, M., K. Khan, S. U. Afzal, N. Ali, M. M. Anjum, H. Usman and M. O. Iqbal. (2017). Seed Yield Performance of Different Maize (*Zea mays* L.) Genotypes under Agro Climatic Conditions of Haripur. International Journal of Environmental Sciences & Natural Resources.

Kuleshov, N. N. and J. Am. Soc. Agron. 25, 688 (1993).

Kumar, D. and N.A. Jhariya. (2013). Nutritional, medicinal and economical importance of corn. Research journal of Pharmaceutical Sciences,2,7-8.

Lavania, U.C. and S. Srivastava. (1999). Quantitative declination of karyotype variation in Papaver as a measure of phylogenetic differentiation and origin. Curr. Sci. 1999; pp: 429- 435.

Liu, J.H.T., S. Chen and A. Lu. (2000). Karyomorphology of *Biebersteinia Stephan* (Geraniaceae) and its systematic and taxonomic significance, Bot. Bull. Acad. Sin., 425: 61- 66.

McClintock, B., T.A. Kato-Y and A. Blumenschein. (1981). Chromosome constitution of races of maize. Colegio de postgraduados, Chapingo, Mexico.

Medina, S. E. L., J. M. Léon, C. H. Q. Jara, A. E. G. Rivero and M. F. R. C. Leon. (2018). Karyotype of native *Zea mays* ssp. *mays* Proto-Confite morocho. Biological Sciences Faculty, National University of Trujillo, Peru.

Phyu Phwe. (2016). Situation of corn in Myanmar, New Plant Variety Protection Unit. Department of Agricultural Research (DAR).

Poggio, L., G. Gonzalez, V. G. Confalonieri, C. Comas and C. Naranjo. (2005). The genome organization and diversification of maize and its allied species revisited: evidences from classical and FISH-GISH cytogenetic analysis. Cytog. Gen. Res. 109(13):259–267.

Sears, E.R. and M. S. Sears. (1979). The telocentric chromosome of common wheat. In Ramamujan ed. Proc. Fifth Intl. Wheat Gent Symp. New Delhi. India. Pp. 389- 407.

Stebbins, G.L. (1971). Chromosomal evolution in higher plants. London: Edward Arnold `Puplishers.

Tayyar, R. I., A. J. Lukaszewski and J. G. Waines. (1994). Chromosome banding patterns in the annual species of *Cicer*. Genome, 37: 656 – 663.

Teodoro-Pardo, C. V., A. Garcia-Velazqez, and T. Corona-Torres. (2007). Polimorfismo cromossômico en *Capsicum annuum* L. (Solanaceae) em recolectas de Puebla, Morelosy Quartenário, México. Agrociencia, v.41, p.873-881, 2007.

TAXONOMIC STUDY ON FIFTEEN SPECIES OF TREES FOUND IN TAMU DISTRICT OF SAGAING REGION

Tin Myo Khaing[1], Nwè Nwè Yi [2]

Abstract

The present research deals with diagnostic characters on fifteen species of trees found in Tamu District of Sagaing Region. This area lies between 23° 20´ and 24° 40´ North latitude, 94° 00´ and 94° 40´ East longitude. All the specimens were collected from Tamu District in Sagaing Region from 2017 to 2019. The fifteen species were collected, classified, identified and preserved. In this paper, 15 species belonging to 11 genera of 10 families were presented. The economically valuable timber species are *Pterocarpus macrocarpus* Kurz, *Lagerstroma speciosa* (L.) Pers., *Shorea obtusa* Wall, *S. siamensis* Miq., *Tectona grandis* L.f and *T. hamitoniana* Wall.. The individual species of taxonomic information were presented with relevant photographs. An artificial key to the species was constructed.

Keywords: Taxonomy, Trees, Tamu District

Introduction

The forest of Myanmar is one of its greatest natural resources because they cover large areas and many of the trees and other plants in them have been used for timber, fire wood, and many other products. The forests are also useful because many of them are important in the conservation of water, soil and animals life resources (Davis 1960).

In fifteen species of valuable timber trees, *Pterocarpus macrocarpus* Kurz, *Lagerstroemia speciosa* (L.) Pers., *Shorea obtusa* Wall., *Tectona grandis* L.f are very popular species in the world. Therefore, a research on the timber trees was selected and studied.

The Sagaing Region is the largest one in Myanmar. Tamu District is located in North West part of Sagaing Region in Myanmar. It lies between 23° 20' and 24° 40' North latitude and 94° 00' and 94° 40' East longitude. The total area of Tamu District is 677.2 sq km and the elevation is about 180m.

The aim and objectives of this research are to identify and classify the natural timber tree species of Tamu District, to record the list of collected plants from Tamu district; to describe the taxonomical characteristics of Angiosperms from study area.

Materials and Methods

Plant collection were made June 2018 to December 2019. A Taxonomic identification of the collected specimens were determined by referring to available literature such as Hooker (1875-1897), Backer & Brick (1963-1968), Dassanayake (1980-2001), and Qi-ming & De-lin (2007-2009). All of nomenclatural studies were recognized by referring to the website of International plant Names Index (IPNI) and Online Botanical Database of Tropical plants (TROPICOS). Myanmar names and their distribution of the studied species were referred to Hundley and Chit Ko Ko (1987) and Kress *et al*. 2003. The studied species were systematically arranged into families according to (APG IV) system of Byng *et al.* (2016). The arrangement of genera and species under the families were placed alphabetically.

[1] Lecturer, Department of Botany, Sagaing University
[2] Professor & Head, Department of Botany, Mandalay University of Distance Education

Results

List of collected species from Tamu District

Diagnostic characters on fifteen species of trees from Tamu District in Sagaing Region.

Table 1 List of the collected species from Tamu District in Sagaing Region

Group	Order	Family	Scientific name	Myanmar name
Rosides	Fabales	Fabaceae	*Millettia leucantha* Kurz	Thinwin aphyu
			Millettia peguensis Ali.	Thin win
			Pterocarpus macrocarpus Kurz	Thit padauk
	Fagales	Fagaceae	*Castanopsis indica* A.DC.	Thit e
	Myrtales	Combretaceae	*Terminalia chebula* Retz.	Phan kha
		Lythraceae	*Lagerstroemia speciosa* (L.) Pers.	Pyinma
			Lagerstroemia villosa Wall. ex Kurz.	Zaung bale
		Myrtaceae	*Syzygium grande* (Wight) Walp.	Tha byae gyi
	Sapindales	Anacardiaceae	*Buchanania latifolia* Roxb.	Lunbo : Thisi bo
		Meliaceae	*Chukrasia tabularis* A. Juss.	Taw Yin ma
	Malvales	Dipterocarpaceae	*Shorea obtusa* Wall.	Thit ya
			Shorea siamensis Miq.	Ingyin
Asterids	Lamiales	Bignoniaceae	*Fernandoa adenophylla* (Wall.ex G. Don) Steenis	Phet than
		Lamiaceae	*Tectona grandis* L.f	Kyun
			Tectona hamiltoniana Wall.	Dahat

1. *Millettia leucantha* Kurz, J. Asiat. Soc. Bengal, Pt. 2, Nat.Hist.42 (2): 68.1873. (Figure 1 A-F)

Flowering period : March to April

Perennial trees, scandent, up to 9.0 m high. Leaves unipinnately compound, imparipinnate, alternate; stipules linear. Inflorescences axillary or terminal pseudo-raceme, many-flowered. Flowers bisexual, zygomorphic, hypogynous, white. Calyx campanulate, 5- tooth. Corolla papilionaceous; standard broadly orbicular; wings ovate; keel oblong. Stamens 10, monadelphous; anthers dithecous, basifixed. Carpel 1; ovary superior, oblong, unilocular with 3-4 ovules in the locule on the marginal placentae; stigmas simple. Fruit simple, Pods, flat, woody, obtuse at the apex, beaked, brown tomentose.

† ⚥ $K_{(5)}$ $C_{1+2+(2)}$ $A_{(10)}$ $\underline{G_1}$

2. *Millettia peguensis* Ali., Kew Bull. 21: 489. 1968. (Figure 1 G-L)

Flowering period : March to May

Perennial small trees, up to 10.0 m high. Leaves unipinnately compound, imparipinnate, alternate; stipules caducous. Inflorescences axillary and terminal racemes, many flowered. Flowers bisexual, zygomorphic, hypogynous, purple. Calyx campanulate, 5-lobed. Corolla papilionaceous; standard obovate; wings oblong; keel obtuse. Stamens 10, monadelphous; anthers dithecous, basifixed. Carpel 1; ovary superior, unilocular with many ovules in the locule on the marginal placentae; stigma capitate. Fruits simple, pods, many-seeded, flat, woody, green, glabrous.

† ⚥ $K_{(5)}$ $C_{1+2+(2)}$ $A_{(10)}$ $\underline{G_1}$

3. *Pterocarpus macrocarpus* Kurz, J. Asiat. Soc. Bengal, Pt. 2, Nat. Hist. 43 (2): 187. 1874. (Figure 1 M-R)

Flowering period : April to May

Perennial, large trees, up to 30.0 m high. Leaves unipinnately compound, imparipinnate, alternate; stipules lanceolate, caducous. Inflorescences terminal and axillary paniculate racemes, many-flowered. Flowers bisexual, zygomorphic, hypogynous, bright yellow. Calyx campanulate, 5- lobed. Corolla papilionaceous; standard obovate; wings fulcate; keel oblong. Stamens 10, diadelphous; anthers dithecous, dorsifixed. Carpel 1; ovary superior, oblong, unilocular with few ovules in the locule on the marginal placenta; stigmas simple. Fruits samaroid, orbicular.

† ☿ $K_{(5)}\ C_{1+2+(2)}\ \underline{A}_{1+(9)}\ G_1$

4. *Castanopsis indica* A. DC., J. Bot. 1: 182. 1863. (Figure 2 A-F)

Flowering period : April to August

Perennial, evergreen trees, monoecious, up to about 20.0 m high. Leaves simple, alternat, glabrous on both surfaces. Inflorescences terminal paniculate spike. Flowers unisexual, actinomorphic, epigynous. Male flowers in spike, densely clustered; stamens 5, free; anthers dithecous, basifixed. Female flowers solitary spike. Carpels 3, fused; ovary inferior, trilocular with two pendulous ovules on the apical placenta; stigmas puncate. Fruits capsule, dehiscent, ovoid, yellowish green, covered with dense stout spines.

⊕ ☿ $P_{5-6}\ A_5\ \overline{G_0}$ ⊕ ♀ $P_{5-6}\ A_0\ \overline{G_{(3)}}$

5. *Terminalia chebula* Retz., Obs. 5 : 31. 1788. (Figure 2 G-L)

Flowering period : March to August

Perennial trees, up to 12.0 m high. Leaves simple, opposite, exstipulate. Inflorescences terminal and axillary paniculate spike, many-flowered. Flowers bisexual, actinomorphic, epigynous. Calyx campanulate, 5-lobed. Corolla 5- lobed. Stamens 10, free; anthers dithecous, basifixed. Carpel 1; ovary inferior, unilocular with one ovule in the locule on the pendulous placenta; stigma simple. Fruits simple, drupaceous, indehiscent, ellipsoid to subgloboid, green, glabrous.

⊕ ☿ $K_{(5)}\ C_5\ A_{10}\ \overline{G_1}$

6. *Lagerstroemia speciosa* (L.) Pers., Syn. Pl. 2.72. 1806. (Figure 2 M-R)

Flowering period : March to June

Perennial trees, up to 10.0 m high. Leaves simple, opposite and decussate, exstipulate. Inflorescences terminal, paniculate cymes, many-flowered. Flowers bisexual, actinomorphic, hypogynous, purple. Calyx campanulate, 6-lobed. Petals 6, free, orbicular. Stamens numerous, free; anthers dithecous, dorsifixed. Carpels 6, fused; ovary superior, hexalocular, with numerous ovules in each locule on the axile placenta; stigma capitate. Fruits loculicidal capsule, subgloboid, woody, greenish brown, glabrous, splitting by 6-valves.

⊕ ☿ $K_{(6)}\ C_6\ A_\infty\ \underline{G_{(6)}}$

7. *Lagerstroemia villosa* Wall. ex Kurz, J. Asiat. Soc. Bengal. Pt. 2, Nat. Hist. 42: 234.1873. (Figure 3 A-F)

Flowering period : March to May

Perennial, small tree, up to 8.0 cm high. Leaves simple, opposite and decussate, exstipulate. Inflorescences axillary, dichotomous cymes, many-flowered. Flowers bisexual, actinomorphic, cyclic, hypogynous, white. Calyx campanulate, 6-lobed. Petals 6, free. Stamens numerous, free; anthers

dithecous, dorsifixed. Carpels 6, fused; ovary superior, hexalocular, three ovules in each locule on the axile placenta; stigma capitate. Fruits loculicidal capsule, oblongoid, brown, glabrous.

$\oplus$ ☥ $K_{(6)}\ C_6\ A_\infty\ \underline{G_{(6)}}$

8. *Syzygium grande* (Wight) Walp., Repert. Bot. Syst. 2:180.1843. (Figure 3 G-L)

Flowering period : March to May

Perennial, large tree, up to 20.0 m high. Leaves simple, opposite, exstipulate. Inflorescences terminal or axillary branched paniculate, cymose, many-flowered. Flowers bisexual, actionomorphic, epigynous, cream-yellow. Calyx funnel-shaped, 4-5 lobed. Petals 5, free. Stamens numerous, spreading; anthers dithecous, basifixed,. Carpels 2 to 3, fused; ovary inferior, ovoid, many ovules in each locule on the axile placenta; stigma simple. Fruits baccate, subgloboid, violet, with prominent crown of persistent calyx segments.

$\oplus$ ☥ $K_{(4\text{-}5)}\ C_5\ A_\infty\ \overline{G_{(2\text{-}3)}}$

9. *Buchanania latifolia* Roxb., Fl. Ind. 2: 285. 1832. (Figure 3 M-R)

Flowering period : February to April

Perennial trees. Leaves simple, alternate, exstipulate. Inflorescences terminal or axillary paniculate racemes with crowded flowers rusty-velvety. Flowers bisexual, actinomorphic, hypogynous. Calyx campanulate, 5-lobed. Petals 5, free, linear. Stamens 10, in two series, inserted at the base of the disc; anthers dithecous, dorsifixed. Carpels 5, free; ovary superior, unilocular with one ovule on the basal placenta; stigmas truncate. Fruits drupaceous, small, compressed.

$\oplus$ ☥ $K_{(5)}\ C_5\ A_{5+5}\ \underline{G_5}$

10. *Chukrasia tabularis* A. Juss. in Mirb. & Cass, Apud Guillemin, Bull. Sci. Nat. Geol. 23. 241. 1830. (Figure 4 A-F)

Flowering period : July to September

Perennial, tree, up to 15.0 m high. Leaves unipinnately compound, paripinnate, alternate, exstipulate. Inflorescences terminal and axillary, many-flowered. Flowers bisexual, actinomorphic, hypogynous. Calyx capsular, 5-lobed. Petals 5, free, narrowly. Stamens 10, adnate at the base; anthers dithecous, basifixed. Carpels 2-3, united; ovary superior, numerous ovules in each locule on the axile placenta; stigmas capitate. Fruits capsular, septicidal, ellipsoid, dark brown.

$\oplus$ ☥ $K_{(5)}\ C_5\ A_{(10)}\ \underline{G_{(2\text{-}3)}}$

11. *Shorea obtusa* Wall., Cat. n. 966. 1829. (Figure 4 G-L)

Flowering period : March to June

Perennial, deciduous tree, up to 10.5 m high. Leaves simple, alternate; stipules linear. Inflorescences axillary, short raceme, many-flowered. Flowers bisexual, actinomorphic, hypogynous, creamy. Calyx cup-shaped, 5-lobed, connate at the base,. Petals 5, free, linear-lanceolate. Stamens numerous, free; anthers dithecous, basifixed. Carpels 3, fused; ovary superior, ovoid, trilocular, one ovule in each locule on pendulous placenta; stigma simple. Fruits drupaceous, samara, 5-winged; 3 larger and 2 shorter.

$\oplus$ ☥ $K_{(5)}\ C_5\ A_\infty\ \underline{G_{(3)}}$

12. *Shorea siamensis* Miq., Ann. Mus. Bot. Lugd - Bat. 1 :214.1864. (Figure 4 M-R)

Flowering period: March to May

Perennial deciduous tree, up to 16.0 m high. Leaves simple, alternate; stipules lanceolate. Inflorescence terminal and axillary paniculate raceme, many-flowered. Flowers bisexual, actinomorphic, hypogynous, yellow. Calyx cup-shaped, 5-lobed. Petals 5, free, ovate. Stamens 15,

free; anthers dithecous, basifixed. Carpels 3, fused: ovary superior, trilocualr with one ovule in each locule on the axile placenta; stigmas trifid. Fruits nutlets, ovoid, 5-winged, unequal, 3 larger and 2 smaller.

$\oplus$ ☿ $K_{(5)}$ C_5 A_{15} $G_{\underline{(3)}}$

13. *Fernandoa adenophylla* (Wall. ex G. Don) Steenis, Blumea 23: 135. 1976.
(Figure 5 A-F)

Flowering period : April to June

Perennial trees, up to 10.0 m high. Leaves unipinnately compound, imparipinnate, opposite and decussate, exstipulate. Inflorescences terminal dichasial cymes. Flowers bisexual, zygomorphic, hypogynous, yellowish-white. Calyx campanulate, 5-lobed. Corolla broadly funnel-shaped, 5-lobed. Stamens 4, free; anthers dithecous, basifixed. Carpels 2, fused; ovary superior, oblongoid, bilocular with many ovules in each locule on the axile placenta; stigmas bifid. Fruits capsular, cylindrical, pendulous, brownish hairy.

† ☿ $K_{(5)}$ $C_{(5)}$ A_4 $G_{\underline{(2)}}$

14. *Tectona grandis* L.f., Suppl. 151.1782. (Figure 5 G-L)

Flowering period : July to September

Perennial, large woody tree, up to 20.0 m high. Leaves simple, opposite and decussate, exstipualte. Inflorescences uppermost leaf axils and terminal, large panicles, many-flowered dichasial cymes. Flowers bisexual, actinomorphic, hypogynous, white. Calyx campanulate, 5-7 lobed; Corolla funnel-shaped, 6-7 lobed. Stamens 6, free; anthers dithecous, basifixed. Carpels 2, fused; ovary superior, tetralocular with one ovule in each locule on the axile placenta; stigmas bifid. Fruits drupaceous, subgloboid or tetragonally flattened, densely tomentose.

$\oplus$ ☿ $K_{(5\text{-}7)}$ $C_{(6\text{-}7)}$ A_6 $G_{\underline{(2)}}$

15. *Tectona hamiltoniana* Wall., Pl. As. Rar. 3 : 68. t -294. 1832 (Figure 5 M-R)

Flowering period : April to July

Perennial, small trees, up to 6.0 m high. Leaves simple, opposite and decussate, exstipulate. Inflorescences terminal paniculate, dichasial cyme, many-flowered. Flowers bisexual, actinomorphic, hypogynous, pale blue. Calyx campanulate, 5-to7- lobed. Corolla funnel-shaped, 5-6 lobed. Stamens 5-6, free; anthers dithecous, basifixed. Carpels 2, fused; ovary superior, tetralocular with one ovule in each locule on the axile placenta; stigmas bifid, unequal. Fruits drupaceous, rounded, enveloped by fruiting-calyx.

$\oplus$ ☿ $K_{(5\text{-}7)}$ $C_{(5\text{-}6)}$ $A_{5\text{-}6}$ $G_{\underline{(2)}}$

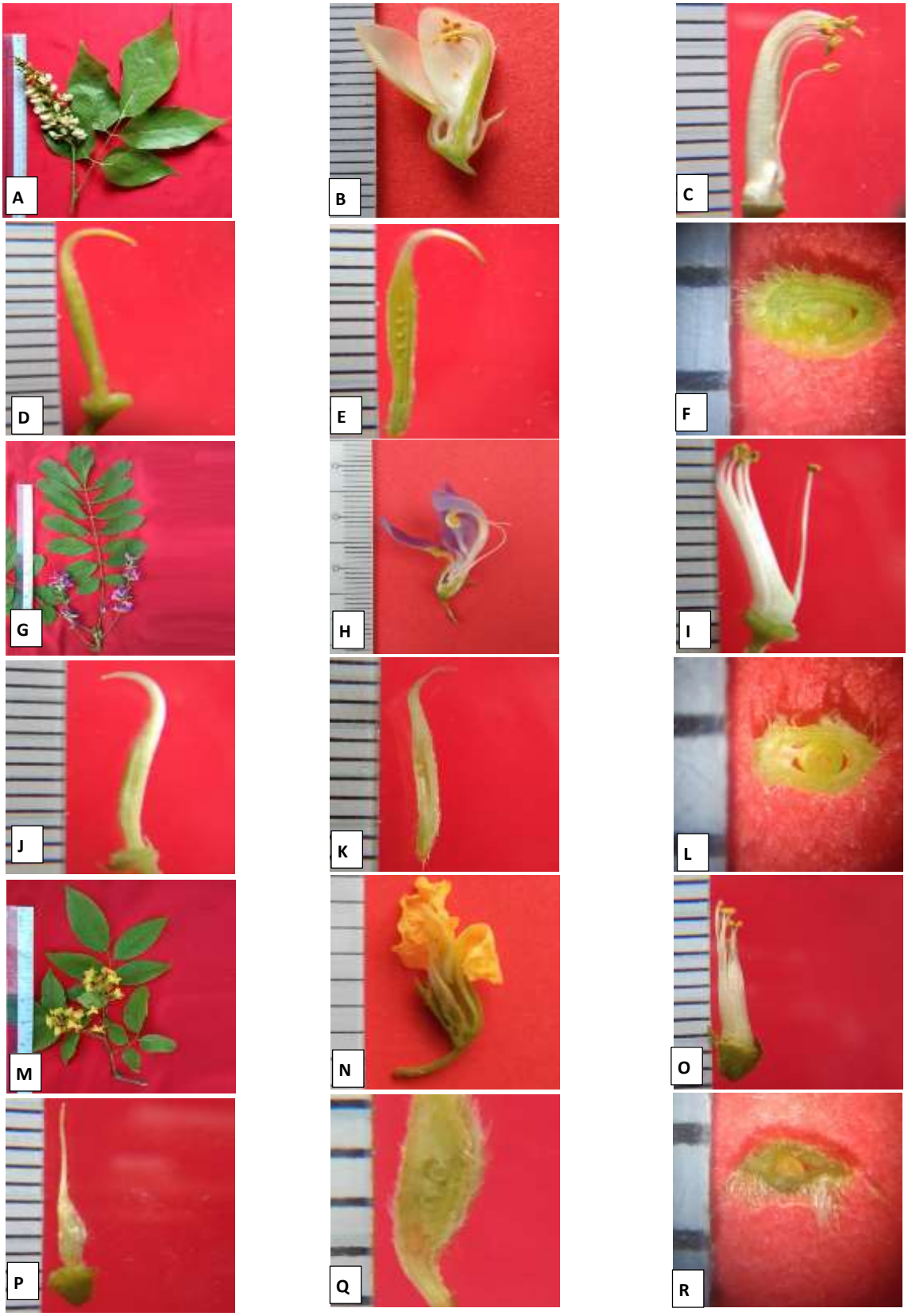

Figure 1 ***Millettia leucantha*** **Kurz**, **A.** Inflorescence, **B.** L.S of flower, **C.** Stamens, **D.** Pistil, **E.** L.S of ovary, **F.** T.S of ovary; ***Millettia peguensis*** **Ali., G.** Inflorescence, **H.** L.S of flower, **I.** Stamens, **J.** Pistil, **K.** L.S of ovary, **L.** T.S of ovary; ***Pterocarpus macrocarpus*** **Kurz**, **M.** Inflorescence, **N.** L.S of flower, **O.** Stamens, **P.** Pistil, **Q.** L.S of ovary, **R.** T.S of ovary

Figure 2 ***Castanopsis indica*** **A.DC., A.** Inflorescence, **B.** L.S of flower, **C.** Stamens, **D.** Pistil, **E.** L.S of ovary, **F.** T.S of ovary; ***Terminalia chebula*** **Retz., G.** Inflorescence, **H.** L.S of flower, **I.** Stamens, **J.** Pistil, **K.** L.S of ovary, **L.** T.S of ovary; ***Lagerstroemia speciosa*** **(L.), M.** Inflorescence, **N.** L.S of flower, **O.** Stamens, **P.** Pistil, **Q.** L.S of ovary, **R.** T.S of ovary

Figure 3 ***Chukrasia tabularis*** **A. Juss., A.** Inflorescence, **B.** L.S of flower, **C.** Stamens, **D.**Pistil, **E.** L.S of ovary, **F.** T.S of ovary; ***Shorea obtusa*** **Wall., G.** Inflorescence, **H.** L.S of flower, **I.** Stamens, **J.** Pistil, **K.** L.S of ovary, **L.** T.S of ovary; ***Shorea siamensis*** **Miq., M.** Inflorescence, **N.** L.S of flower, **O.** Stamens, **P.** Pistil, **Q.** L.S of ovary, **R.** T.S of ovary

Figure 4 ***Fernandoa adenophylla*** **(Wall.ex G. Don) Steenis, A.** Inflorescence, **B.** L.S of flower, **C.** Stamens, **D.**Pistil, **E.** L.S of ovary, **F.** T.S of ovary; ***Tectona grandis*** **L.f, G.** Inflorescence, **H.** L.S of flower, **I.** Stamens, **J.** Pistil, **K.** L.S of ovary, **L.** T.S of ovary; ***Tectona hamiltoniana*** **Wall., M.** Inflorescence, **N.** L.S of flower, **O.** Stamens, **P.** Pistil, **Q.** L.S of ovary, **R.** T.S of ovary

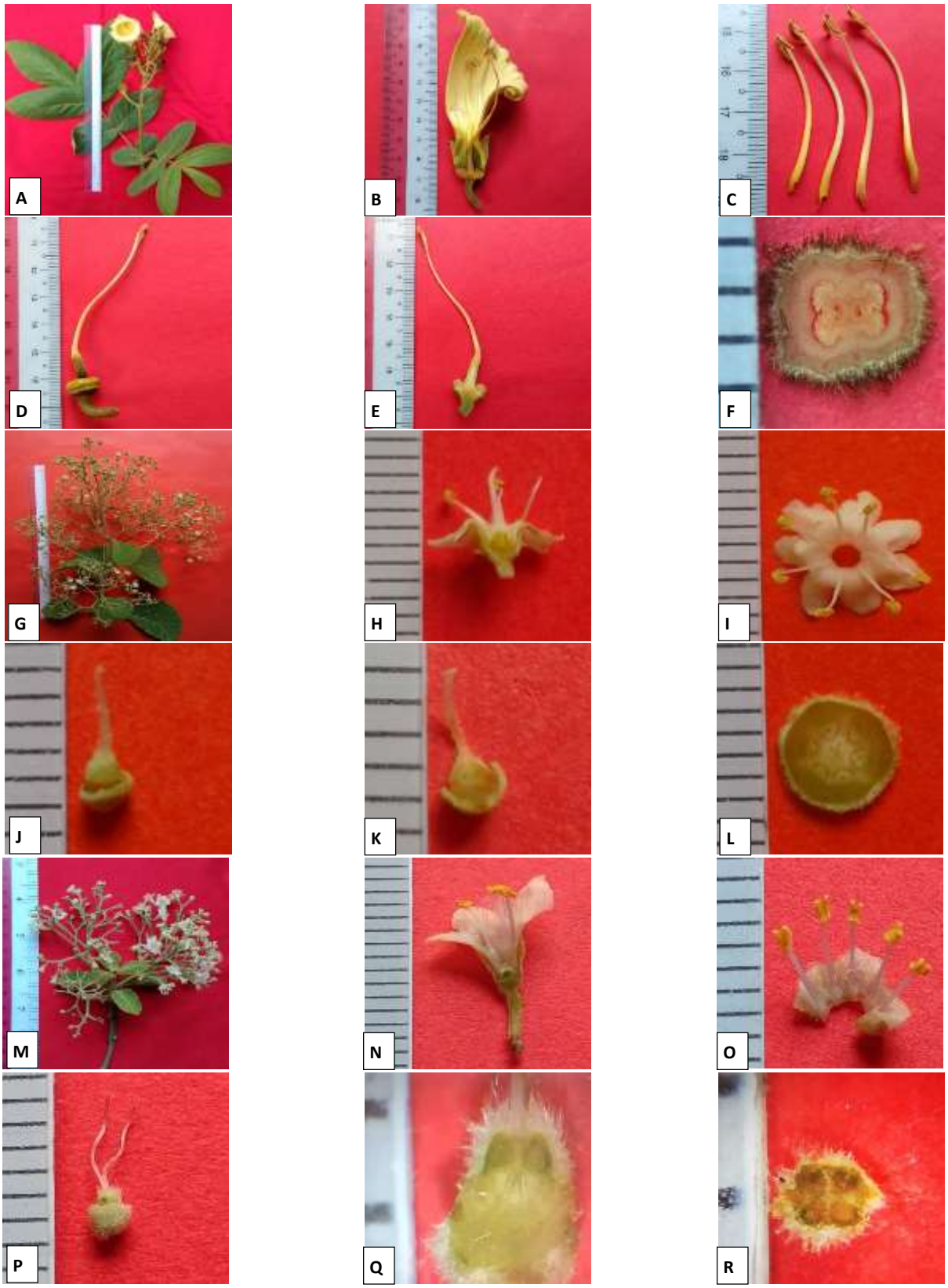

Figure 5 ***Fernandoa adenophylla*** **(Wall.ex G. Don) Steenis, A.** Inflorescence, **B.** L.S of flower, **C.** Stamens, **D.**Pistil, **E.** L.S of ovary, **F.** T.S of ovary; ***Tectona grandis*** **L.f, G.** Inflorescence, **H.** L.S of flower, **I.** Stamens, **J.** Pistil, **K.** L.S of ovary, **L.** T.S of ovary; ***Tectona hamiltoniana*** **Wall., M.** Inflorescence, **N.** L.S of flower, **O.** Stamens, **P.** Pistil, **Q.** L.S of ovary, **R.** T.S of ovary

An Artificial key to the studied species

1. Leaves compound ---------- 2
1. Leaves simple ---------- 6
    2. Flower actinomorphic; calyx capsular ---------- 10. *Chukrasia tabularis*
    2. Flower zygomorphic; calyx campanulate ---------- 3
3. Stamens 4, free ---------- 13. *Fernandoa adenophylla*
3. Stamens 10, united ---------- 4
    4. Flower purple; stigma capitate ---------- 2. *Millettia peguensis*
    4. Flower bright yellow or white; stigma simple ---------- 5
5. Stipules linear, persistent; leaf blades oblong-lanceolate ---------- 1. *Millettia leucantha*
5. Stipules lanceolate, caduceus; leaf blade ovate ---------- 3. *Pterocarpus macrocarpus*
    6. Plant monoecious, flower unisexual ---------- 4.*Castanopsis indica*
    6. Plant diecious, flower bisexual ---------- 7
7. Carpel 6; ---------- 8
7. Carpel 1-2 to 3 or 5 ---------- 9
    8. Inflorescences axillary, dichotomous cymes; flowers white ---------- 7. *Lagerstroemia villosa*
    8. Inflorescences terminal, paniculate cymes; flower purple ---------- 6. *Lagerstroemia speciosa*
9. Stamens 5 to 7; ---------- 10
9. Stamens 10 or numerous, ---------- 11
    10. 6.0 m high; leafblades 15.5-18.5 cm by 8.0-12.0 cm ---------- 15. *Tectona hamiltoniana*
    10. 20 m high; leaf blades 20-45 cm by 15-30 cm ---------- 14. *Tectona grandis*
11. Placentation axile ---------- 12
11. Placentation basal or pendulous ---------- 13
    12. Stipules present; flower hypogynous ---------- 12. *Shorea siamensis*
    12. Stipules absent; flower epigynous ---------- 8. *Syzygium grande*
13. Anther dorsifixed; stigma truncate ---------- 9.*Buchanania latifolia*
13. Anther basifixed; stigma simple ---------- 14
    14. Flower colour creamy; ovary superior ---------- 11. *Shorea obtuse*
    14. Flower colour greenish white; ovary inferior ---------- 5. *Terminalia chebula*

Discussion and Conclusion

The present research deals with the taxonomic study on fifteen species of trees in Tamu District of Sagaing Region. The types of vegetation found in the study area are Indaing Forest and mixed deciduous Forest (Nyi Nyi Kyaw 2015).Tamu District area in Myanmar is one of the valuable interesting area for floristic studies.

All together 15 species belonging to 11 genera of 10 families were recorded.The member of 15 species were dominant distributed in the study area. In the 15 species, simple leaves are 9 species as well as compound leaves are 6 species. The actinomorphic flowers are found in 11 species and zygomorphic flowers are in 4 species. 12 species of superior ovaries and 3 species of inferior ovaries were studied.

The fruit types are variable in the studied species. The capsules are found in *Lagerstromea speciosa* (L.), *L. villosa* Kurz., *Chukrasia tabularis* A. Juss. *Fernandoa adenophylla* (Wall.ex G. Don). The deupaceous are *Castanopsis indica* A.DC., *Terminalia chebula* Retz., *Buchanania latifolia* Roxb., *Shorea obtusa* Wall., *Tactona grandis* L.f, *T. hamiltoniana* Wall. and pod in the species of genus *Mellettia.* The baccate is found in *Syzygium grande* (Wight) Walp. and *Shorea siamensis* Miq. is nutlets. *Pterocarpus macrocarpus* Kurz is samaroid fruit.

In the study area, *Mellettia leucantha* Kurz, *Pterocarpus macrocarpus* Kurz, *Terminalia chebula* Retz., *Lagerstromea specisa* (L.), *L. villosa* Kurz., *Shorea obtusa* Wall., *S. siamensis* Miq., *Tectona grandis* L.f and *T. hamiltoniana* Wall. were commonly found.

Among the 15 studies species, *Pterocarpus macrocarpus* Kurz, *Lagerstroema speciose* (L.), *Shorea obtusa* Wall., *Tactona grandis* L.f and *T. hamiltoniana* Wall. are economically important timber plants. *Terminalia chebula* Retz. is valuable medicinal plant of Myanmar.

In the research studied, many valuable timbers species not only can be recorded but also various forest products can be found. It is hope that the valuable timber trees are distributed as wild type in Tamu District and the natural plant resources will also be useful for further studies.

Therefore, the valuable economically timber species should be conserved as the programme of natural vegetation of Tamu District, Sagaing Region.

Acknowledgements

I would like to express my deepest gratitude to Dr Nu Nu Yee, Professor and Head, Department of Botany, University of Mandalay, for permission to do this research paper. I would like to express my sincere gratitude to Dr Nwè Nwè Yi, Professor and Head, Sagaing University of Education, for valuable suggestions and guidance. I would to offer my thanks to Dr Yu Yu Tin, Professor and Head, Department of Botany, Sagaing University for advice.

References

Backer, C.A. and R.C.B. V. D. Brink, In (1963-1968). **Flora of Java**. Vol 2. Rijksherbarium, Leyden. N.V.P. Noordhoff.

Dassanayake, M.D., (1980-2001). **A Revised Handbook to the flora of Ceylon**. Vol. I, II, III, IV, VII, IX, University of Peradeniya, Department of Agriculture, Peradeniya, Srilanka.

Davis, H.J. (1960). The forests of Burma. Department of Botany, University of Florida, U.S.A.

Hooker, J.D. (1879). **The Flora of British India**. Vol. 1-7, L. Reeve and Co, 5. Henrietta Street, Convent Garden, London.

Hundley, H.G. and Chit Ko Ko. (1987). **List of trees, shrubs, herbs and principle Climbers**; etc. Fourth Revised Edition Shwe Daw Oo Press, Mayangon, Yangon, Myanmar.

Kress, W.J., R. A. Defilipps, E. Farr and Yin Yin Kyi. (2003). **A checklist of the trees, shrubs, herbs and climber of Myanmar**. Department of systematic biology-botany. National museum of Natural history Washington D.CUSA.

Ng, P.K.L & Y.C. Wee. (1994). **The Singapore red data book. A community service project by Asia Pacific Breweries**. The Nature Society, Singapore.

Nyi Nyi Kyaw. (2015). Forest and Forestry in Myanmar: Meeting the Challenges in the 21st Century. Forest Department, Ministry of Environmental Conservation and Forestry, Nay Pyi Taw.

Qi-ming, H.U. & W.U. De-lin. (2009). **Flora of Hong Kong**. Vol 2, 3, Hong Kong Herbarium South China Botanical Garden, Chinese Academy of Sciences.

Subrahmanyam, N.C. (1997). **Preface Books of Morden Plant Taxonomy**. University of Delhi, Western India.

ANTIMICROBIAL ACTIVITY OF EXTRACTS FROM *ENHYDRA FLUCTUANS* LOUR. (KA-NA-HPAW)

Win Win Mar[1], Khin Min Min Phyo[2]

Abstract

Three selected medicinal plants grown in Pathein were collected on June, 2019. These plants are *Clitoria ternatea* L. (Aung-me-nyo) belonging to Fabaceae, *Melastoma malabathricum* L. (Say-o-boke) belonging to Melastomataceae and *Enhydra fluctuans* Lour. (ka-na-hpaw) belonging to Asteraceae. The fresh samples of these plants except flowers were air-dried and powdered for extraction. The powder of each plant (5 g) was extracted with 50 mL of acetone, ethanol, methanol and water on water-bath at 80℃. These extracts were tested the antimicrobial activity on eight different test organisms using the paper disc diffusion assay method. According to their antimicrobial activity, the ethanol extract of *Enhydra fluctuans* Lour. (20.74 mm of inhibitory zone) was selected for further investigation.

Keywords: medicinal plants, extracts, antimicrobial activity

Introduction

The use of medicinal plants all over the world predates the introduction of antibiotics and other modern drugs. The flora is rich in medicinal plants which are usually exploited by herbal doctor otherwise called "native doctor". Some of the plant collections are used against a variety of diseases such as typhoid, fever, gastroenteritis, dysentery, malaria and others which are typical diseases of tropical countries (Akinyemi *et al*, 2006).

The bioactivity of plant extracts is attributed to phytochemical constituents present in the extracts. However, the constituents of a plant extracts are extremely dependent on the polarity of solvents, solvent to plant material ratio, particle size of plant material, temperature and extraction method (Kannamba, *et al*, 2017).

The aim and objectives of this research are to apply the extract as substituent crude compound in practical, to study the outstanding characters of some medicinal plants, to investigate the extraction from some medicinal plants with different solvents, to study the antimicrobial activity with different test organisms by paper disc diffusion assay method.

Materials and Methods

Collection of plants materials

Three selected medicinal plants grown in Pathein were collected on June, 2019. The fresh samples of except flowers were air-dried for 45 days and ground to fine powder using a blender. The outstanding characters of these three medicinal plants are checked by Hooker (1897).

Extraction of the three selected plants (M. M. Nyein, 1976)

The polar solvents like acetone, ethanol, methanol and water were selected as extraction solvents. Exactly 5 g of each three selected plants powder were extracted with 50 mL of acetone, ethanol, methanol and water separately on water-bath at 80℃ . The extracts were filtered and the filtrate was undertaken to be semi-solid.

[1] Professor, Department of Sciences, Pathein Education Degree College
[2] Dr, Professor, Department of Botany, University of Yangon

Table 1 Three Medicinal Plants for Extraction

No	Scientific Name	Myanmar Name	Family
1.	***Clitoria ternatea* L.**	**Aung-me-nyo**	**Fabaceae**
2.	***Melastoma malabathricum* L.**	**Say-o-boke**	**Melastomataceae**
3.	***Enhydra fluctuans* Lour.**	**Ka-na-hpaw**	**Asteraceae**

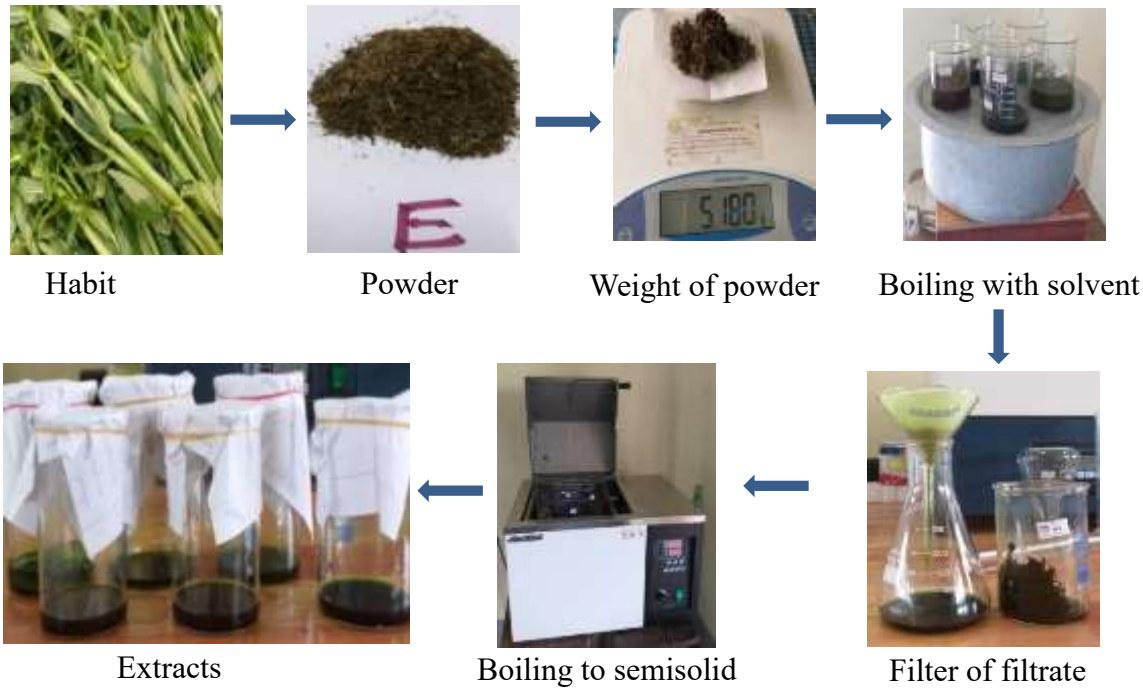

Figure 1 Extraction procedure of *Enhydra fluctuans* Lour. (M.M.Nyein, 1976)

Paper disc diffusion assay method (NITE, 2004)

Paper disc diffusion assay method was followed to determine the antimicrobial activity by the paper discs (6 mm in diameter) soaked with the respective extracts. The culture (Glucose 1 g, peptone 0.3 g, DW 100 mL) was used for respective bacteria and fungi as 8 different test organisms.

Testing the antimicrobial activities (Hassawi, and Kharma 2006)

Nutrient agar medium (Glucose 1 g, peptone 0.3 g, Agar 1.8 g, DW 100 mL) was prepared and autoclaved at 121℃ under pressure for 30 min. After cooling about 65℃, 100 mL of medium before solidification was added the test organism broth (1 mL) and poured into petri-dish. The plates were kept at room temperature for solidification and then the paper discs soaked with the respective extracts were put on agar plate for testing the antimicrobial activity. The zone of clearance around the paper disc was measured for indication of the antimicrobial activity of the extract.

Table 2 Test organisms for antimicrobial activity

No.	Test organisms	Causes of Diseases
1	***Agrobacterium tumefaciens* NITE 09678**	**Crown gall diseases**
2	***Bacillus subtilis* IFO 90571**	**DNA topoisomerase I**
3	***Bacillus pumilis* IFO 12092**	**Wound and burn infection, Fever**
4	***Candida albicans* NITE 09542**	**Candidiasis**
5	***Escherichia coli* AHU 5436**	**Diarrhoea**
6	***Malassezia furfur* AVU0255**	**Danddruff, Seborrhoeic dermatitis**
7	***Pseudomonas fluorescens* IFO 94307**	**Rice disease**
8	***Staphylococcus aureus* AHU 8465**	**Food poisoning, Methicillin Resistance**

Results

Outstanding Characters of *Enhydra fluctuans* Lour. (ka-na-hpaw) (Asteraceae)

Herbs; serrate leaves 1-3 inches variable in breadth with opposite sessile, linear oblong, base narrowed; stem elongated, hollow, thinly glabrous, rooting at the nodes; inflorescence heads terminal and axillary, heterogamous, obscurely radiate, ray florets numerous, seriate, fertile ligule minute broad 3-4 toothed and disk florets numerous, fertile, tubular, limb campanulate 5-fid, epigynous, flowers tipped with glandular hairs; corolla greenish white, two forms; anther basifixed; ovule solitary, style-arms obtuse, tip hispid; fruit dry, indehiscent.

Figure 2 Habit and inflorescence of *Enhydra fluctuans* Lour**.**

In the extraction procedure, acetone, ethanol, methanol and watery extracts from *Clitoria ternatea* L., *Melastoma malabathricum* L. and *Enhydra fluctuans* Lour. were utilized for the antimicrobial activity on 8 test organisms. All extracts of *Melastoma malabathricum* L. and *Clitoria ternatea* L. showed no antimicrobial activity. All extracts of *Enhydra fluctuans* Lour. showed antimicrobial activity on 7 test organisms except *Staphylococcus aureus.* Then, watery extract of *Enhydra fluctuans* Lour. gave the less antibacterial activity on *Bacillus pumilis.* Ethanol extract of *Enhydra fluctuans* Lour. exhibited the best antibacterial activity (20.74 mm of inhibitory zone) on *Bacillus subtilis.*

Table 3 Antimicrobial activity (inhibitory zone) of all extracts on different test organisms

Collected Plants	Extracts	*Agrobacterium tumefaciens*	*Bacillus subtilis*	*Bacillus pumilis*	*Candida albicans*	*Escherichia coli*	*Malassezia furfur*	*Pseudomonas fluorescens*	*Staphylococcus aureus*
Clitoria ternatea L.	Acetone	-	-	-	-	-	-	-	-
	Ethanol	-	-	-	-	-	-	-	-
	Methanol	-	-	-	-	-	-	-	-
	Water	-	-		-	-	-	-	-
Melastoma Malabathricum L.	Acetone	-	-	-	-	-	-	-	-
	Ethanol	-	-	-	-	-	-	-	-
	Methanol	-	-	-	-	-	-	-	-
	Water	-	-	-	-	-	-	-	-
Enhydra fluctuans Lour.	Acetone	14.33 mm	-	15.14 mm	12.41 mm	-	15.63 mm	14.58 mm	-
	Ethanol	16.24 mm	20.74 mm	10.74 mm	15.97 mm	14.21 mm	13.01 mm	11.47 mm	-
	Methanol	12.16 mm	+	10.74 mm	11.56 mm	20.71 mm	12.32 mm	10.00 mm	-
	Water	-	-	+	-	-	-	-	-

Paper disc is 6 mm in diameter, - is no activity, + is <10 mm

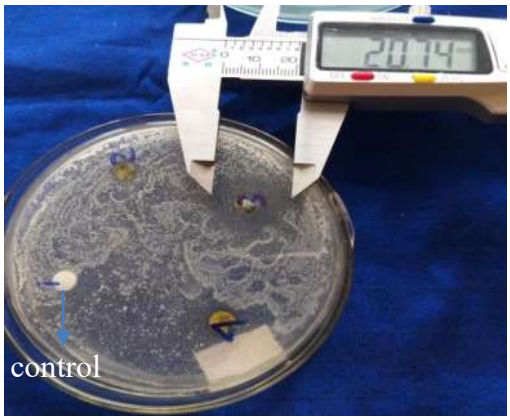

Figure 3 The best antibacterial activity of ethanol extract from *Enhydra fluctuans* Lour. on *Bacillus subtilis*

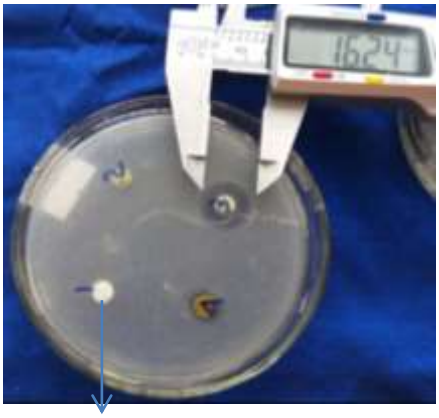

Figure 4 Antibacterial activity of ethanol extract on *Agrobacterium tumefaciens*

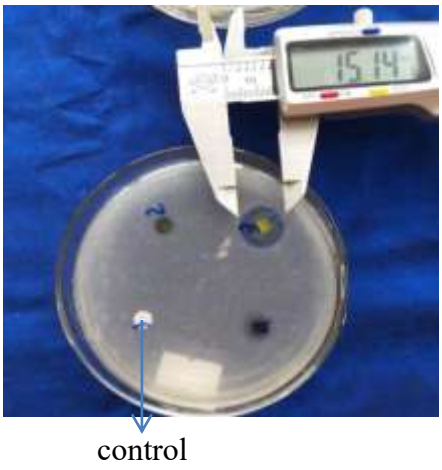

Figure 5 Antibacterial activity of acetone extract on *Bacillus pumilis*

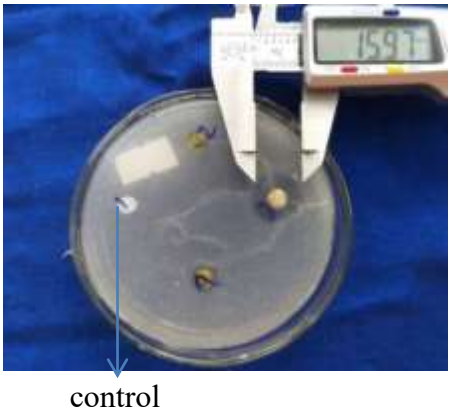

Figure 6 Antifungal activity of ethanol extract on *Candida albicans*

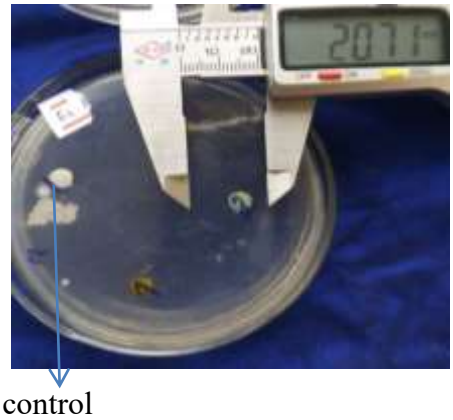

Figure 7 Antibacterial activity of methanol extract on *Escherichia coli*

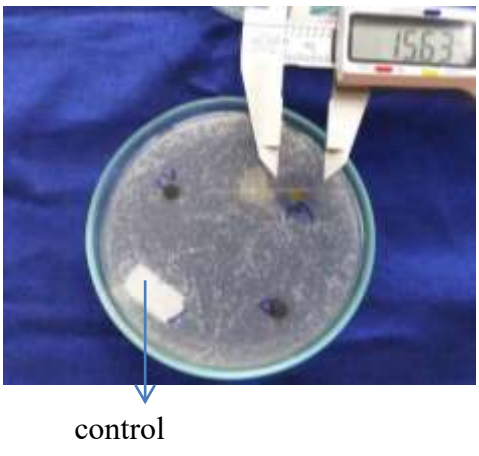

Figure 8 Antibacterial activity of acetone extract on *Malassezia furfur*

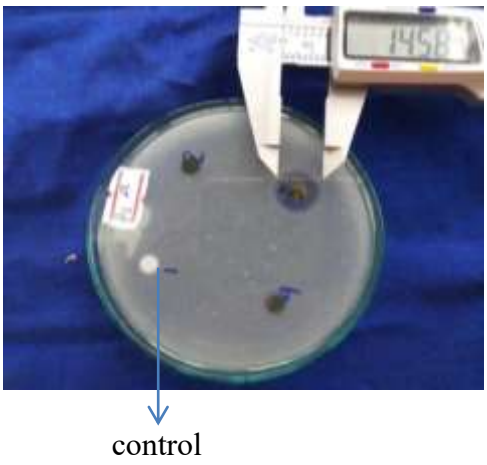

Figure 9 Antibacterial activity of acetone extract on *Pseudomonas fluorescens*

Discussion and Conclusion

This study is reported for the antimicrobial activity. Some of the medicinal plants are potentially effective antimicrobial agents. The resulting information will contribute to a better understanding of antimicrobial activity of the plant.

The plant species could have an antimicrobial agent that caused the antimicrobial activity. Also, they could have the different concentrations that cause high variations in their antimicrobial activity (Hassawi and kharma, 2006).

The possible phytochemical constituents, thrombolytic and membrane stabilizing activities of the crude ethanolic extract of *Enhydra fluctuans* (CE) were investigated along with the antimicrobial, antioxidant and cytotoxic potentials of its petroleum ether (PESF), carbon tetrachloride (CTCSF), chloroform (CSF) and aqueous (AQSF) soluble fractions (Kamal *et al*., 2019).

Enhydra fluctuans is one such plants which is available abundantly in India especially in the North-Eastern states. It has immense potential as a medicinal plants and also has many beneficial effects such as anticancer, antioxidant, antidiabetic, anti-inflammatory, antimicrobial, anti-diarrheal, hepatoprotective and even neuropharmacological effects, These activities can be attributed mainly to the presence of phytochemicals such as flavonoids, alkaloids, saponins, tannins, phenols and carbohydrates (Sarma *et al.*, 2014).

Screening of extracts from *Enhydra fluctuans* Lour. with acetone, ethanol, methanol and water were utilized. These semi-solid extracts were used for testing of antimicrobial activity by paper disc diffusion assay method on eight different test organisms.

Among three medicinal plants, almost extracts of *Enhydra fluctuans* Lour. showed the antimicrobial activity on seven test organisms. According to these activity, 20.74 mm of inhibitory zone of ethanol extract from *Enhydra fluctuans* Lour. showed the best antibacterial activity on *Bacillus subtilis.* Other two medicinal plant extracts showed no antimicrobial activity.

The second-best antibacterial activity of methanol extract is 20.71 mm of inhibitory zone on *Escherichia coli.* The acetone, ethanol and methanol extracts also showed the antibacterial activity on *Agrobacterium tumefaciens* (14.33 mm, 16.24 mm and 12.16 mm of inhibitory zones), *Bacillus pumilis* (15.14 mm, 10.74 mm and 10.74 mm of inhibitory zones), *Malassezia furfur* (15.63 mm, 13.01 mm and 12.32 mm of inhibitory zones) and *Pseudomonas fluorescens* (14.58 mm, 11.47 mm and 10.00 mm of inhibitory zones) and then the antifungal activity on *Candida albicans* (12.41 mm, 15.97 mm and 11.56 mm of inhibitory zones). The watery extract showed the less antibacterial activity on *Bacillus pumilis* but the acetone extract showed no antibacterial activity on *Bacillus subtilis* and *Escherichia coli.* Moreover, all extracts of *Enhydra fluctuans* Lour. showed no antibacterial activity on *Staphylococcus aureus.*

Acknowledgements

Firstly, I wish to express our gratitude to Professor Dr Than Tun, Rector, Pathein University for providing me an opportunity to do this work. I also extended my thank to Professor Dr Myint Myint Khaing and Dr Nay Aung, Pro-Rectors, Pathein University, for their valuable instruction and guidance. I would like to express my thank to Daw Than Than Naing, Vice Principle, Pathein Education Degree College for her encouragement and suggestions. I would like to record my deep thank to Professor Dr Min Min Soe, Head of Botany Department, Pathein University for her valuable instructions, encouragement of this research paper.

References

Akinyemi K. O, O. K. Oluwa, E. O. Omomigbehin, (2006) **Antimicrobial activity of crude extracts of three medicinal plants used in south-west Nigerian folk medicine on some food borne bacterial pathogens,** Department of Microbiology, Lagos State University, (LASU), Nigeria.

Ali M., M. Billah, M. Hassan, M. R. Dewan and A. Emran (2013) ***Enhydra fluctuans*** **Lour. A Review,** Department of Pharmacy, Noakhali Science and Technology University, Sonapur, Noakhali, Bangladesh. Backer C.A. and R. C. Bakhuizen (1963); **Flora of Java**, Vol. I, N.V. P., Netherlands.

Hassawi D. and A. Kharma (2006) **Antimicrobial Activity of Some Medicinal Plants Against Candia albicans**, Department of Biotechnology, Faculty of Agricultural Technology, Al-Balqa Applied University, Al-Salt, 1917, Jordan.

Hooker J. D. (1897); **Flora of British India,** Vol. V, L. Reeve and Co. Ltd., England.

Kamal S. S. R. Rony, S. Sharmin, F. R. Laboni and M. H. Sohrab (2019) **Phytochemical and Pharmacological Potential of *Enhydra fluctuans* Available in Bangaladesh,** Journal of Pharmaceutical Research International**,** Department of Pharmacy, World University of Bangladesh.

Kannamba B, T. D. Winnie, M. Surekha, B. Lavanya, (2017) **Effect of Extraction Methods and Solvent on Phytochemical Composition of Medicinal Plants Extracts,** P.G Department of Chemistry, Andhra Loyola College, Vijaywada, 52008, India.

Mar Mar Nyein (1976) **The antibacterial actions of some indigenous plant extract *in vitro* and *in vivo*,** MSc Thesis, University of Rangoon, Myanmar.

NITE (National Institute of Technology and Evaluation) (2004) **Surface sterilization and Baiting method,** Kizarazu, Japan.

Sarma U. Vedant V. Borah, Kandarpa KR. Saiki and N. K. Hazarika (2014) ***Enhydra fluctuans*****: A Review on its Pharmacolgical importance as a Medicinal Plants and Prevalence and Use in North-East India,** International Journal of Pharmacy and Pharmaceutical Science, Department of Microbiological, Srimanta Sankaradeva University of Health Science, Guwahati-781032, Assam.

SOME OPTIMAL PARAMETERS FOR FUNGAL LIPASE ACTIVITY

May Barani Shu Shu Tan[1], Nu Yin Aye[2], Bay Dar[3]

Abstract

Lipolytic fungi were isolated from different sources. Soil sample was collected from the car workshop as fuel oil contaminated soil, Thuwana Township, Yangon Region, Myanmar. Other samples were collected from pork sausage and cheese. Fungal strains were directly isolated from 2 different sources. Diluted soil (concentration - 10^{-3}, 10^{-5}, 10^{-6}, 10^{-7}, 10^{-8}, 10^{-9}) was used to culture fungi. Fungal strains were cultured on Potato Dextrose Agar (PDA) medium. Lipolytic fungi were screened using Tributyrin Agar (TBA) medium. The isolated fungi were identified by their pure colony morphology and spore formation according to the references. In the present study, three different types of lipolytic fungi were observed from three different sources. Some optimal parameters such as fermentation period, substrate, incubation temperature and initial pH were investigated for lipase activity. Lipase from *Aspergillus* sp. (1) (isolated from pork sausage source) showed the maximum lipase activity at pH 6.0 and 40ºC. Lipase produced from *Penicillium* sp. (isolated from cheese source) exhibited the greatest lipase activity at 45 ºC and pH 8.0, while the highest lipase activity from *Aspergillus* sp. (18) (isolated from fuel oil contaminated soil) was at 50 ºC and pH 8.5.

Keywords: Lipolytic fungi, Lipase, Parameter

Introduction

Lipase enzymes (Triacylglycerol acyl-hydrolase; EC 3.1.1.3) hydrolyze triacylglycerols which are the major constituents of fats and oils. Lipases and esterases catalyze both hydrolysis and synthesis of ester (Griebeler *et al.*, 2011). Lipase enzymes hydrolyze the ester bonds of insoluble substrates in water at the substrate-water interface (Colla *et al.*, 2015).

Fungi are the best microbial sources for commercial lipase production because these can be easily extracted from fermentation processes in short time. Fungal lipases are high productivity, low costs, safe and easy handling. Lipase production by filamentous fungi mainly depends on various factors such as oil substrates, optimum pH and temperature. Optimum parameters are crucial for the best production of extracellular enzyme (Wadia and Jain, 2017 & Kotogan *et al.*, 2014).

Industrial attention has particularly increased in microbial lipases due to their substrate specificity, stability, and various industrial applications like detergent, food, pharmaceutical, dairy, cosmetic, perfumes, biodiesel, paper, and leather (Shukla and Desai, 2016). Lipases play an important role in numerous industrial applications. It is need to study their characteristics because lipases obtained from different sources may have different properties (Colla *et al.*, 2015).

This study was undertaken to observe the best fermentation period, substrate, and the effect of temperature and pH on the maximum activity of lipase enzyme.

[1] PhD student, Department of Botany, University of Yangon
[2] Associated Professor, Department of Botany, Dawei University
[3] Professor, Head of Botany Department, Sittway University

Materials and Methods

Sample preparation from different sources

1. Collection and isolation of lipolytic fungi from pork sausage (PS)

Small pieces of pork sausage sample were kept in a plastic bowl. Pork sausage in the plastic bowl was incubated for two weeks until fungal growth was observed.

2. Collection and isolation of lipolytic fungi from cheese (CH)

Cheese was incubated in the plastic cup for eight days until fungal growth was observed.

3. Collection and isolation of lipolytic fungi from fuel oil contaminated soil (OS)

Fuel oil contaminated soil sample was taken from the car workshop, Thuwana Township, Yangon Region, Myanmar. Soil sample was dried in the air. A ten-fold dilution series of soil was prepared according to Alexander and Strete (2001).

Cultivation of Fungi

Fungal strains were directly collected from pork sausage, cheese, and diluted soil contaminated with fuel oil. Fungi were cultivated and isolated on Potato Dextrose Agar (PDA: Mash Potato 200 g, Peptone 3 g, Dextrose 20 g, Agar 20 g, Distilled water 1000 mL, pH 6.5 ± 2 according to Atlas, 1993) medium at room temperature for 5 - 7 days old. The pure fungal strains were maintained in test tubes with PDA medium. PDA medium was also used as stock culture medium or sub-culture medium for maintenance of fungus according to Atlas, 1993. All stock cultures were stored at 4 ºC. Chloramphenicol was added for antibacterial activity.

Screening of lipolytic fungi using Tributyrin Agar (TBA) medium

Screening of lipase producing fungi was done using tributyrin as a substrate on agar plates. Two different percentages (0.1 % and 1 %) of Tributyrin were used in this study. Lipolytic fungi were screened using Tributyrin Agar medium with 0.1 % tributyrin (Composition %/mL: Peptone 0.5 g, Yeast extract 0.3 g, Tributyrin (HiMedia) 0.1 mL, Agar 2.0 g, pH 6.0) according to Kotogan *et al.*, (2014) and Griebeler *et al.*, (2011). In addition, Tributyrin Agar (TBA) medium with 1 % tributyrin (composition %/mL: Peptone 0.5 g, Yeast extract 0.3 g, Agar 2.0 g, Tributyrin (HiMedia) 1.0 mL, pH 7.5 ± 0.2) was also used for screening of lipolytic fungi according to Wadia and Jain (2017). Clear hydrolytic halo regions occurred around colonies, it indicated that lipase enzyme was produced. All the isolated fungal cultures were inoculated on TBA plates and incubated at room temperature for 2 - 17 days.

Identification of lipolytic fungi

Fungi were identified according to Barnett (1960) and Dube (1983).

Preparation of inoculum and optimization of culture medium

Four different media were prepared for production of lipase by submerged fermentation. Seven days old fungal culture, which was already grown in Czapek-Dox Agar slant test tube, was used for preparation of inoculum. The spores were scratched with sterile inoculating loop and mixed with 10 ml of sterile distilled water in a tube. Spore suspension was transferred into 500 ml conical flask containing 200 ml of fermentation medium (Pandey *et al.*, 2016). The optimal density of fermentation broth was taken and examined the lipase production in different time intervals such as 1 day, 2 day, 3 day, 4 day, 5 day, 6 day, 7 day, etc. The composition of four different fermentation

media (g/L) was as; medium 1 (M1) (Glucose 10 g, Peptone 20 g, NaCl 5 g, Yeast extract 5 g, pH 6.0 ± 0.2 and Coconut oil 10 mL) (Prabhakar *et al.*, 2002); M2 (KH_2PO_4 0.25 g, KCl 0.5 g, $MgSO_4.7H_2O$ 0.5 g, Peptone 8.0 g, Glucose 8.0 g, pH 8 ± 0.2 and Sunflower oil 15 ml) (Pandey *et al.*, 2016); M3 (KNO_3 3.0 g, KH_2PHO_4 1.0 g, $MgSO_4.7H_2O$ 1.0 g, pH 6.5 ± 0.2 and Olive oil 20 ml) (Brooks and Asamudo, 2011); M4 (KNO_3 2.5 g, KH_2PO_4 1 g, $MgSO_4$ 0.5g, NaCl 5 g, pH 8 ± 0.2 and Olive oil 15 ml) (Lanka and Trinkle, 2017).

Extraction of enzyme from fermentation broth

All media were examined by taking optimal densities on 1 day, 2 day, 3 day, 4 day, 5 day, 6 day and 7 day of fermentation to observe the best medium for lipase production. The filtrates were centrifuged at 10,000 rpm, 4˚C for 10 minutes to obtain supernatant. The clear supernatant was considered as crude enzyme. The resulting supernatant was evaluated for lipase activity by using p-nitrophenyl palmitate (pNPP, Sigma) as a substrate as described by Winkler and Stuckmann, 1979 (Massadeh and Sabra, 2011, Pandey *et al.*, 2016, and Rodrigues *et al.*,2016).

Lipase activity assay

The extracellular lipase activity was determined by using p-nitrophenyl palmitate (p-NPP) (Sigma, USA) as substrate according to Winkler & Stuckmann (1979). The pNPP substrate solution was prepared by freshly mixing solution A (3 mg of pNPP in 1 ml of isopropanol) with solution B (10 mg of gum Arabic and 40 ml of Triton X-100 in 9 ml of Tris-HCl buffer, pH 8.0) while stirring until all was dissolved. Freshly prepared 1 ml of p-NPP solution was incubated in a water bath at 37ºC for 10 minutes. After 10 min, 0.5ml of crude enzyme sample and 0.5 ml distilled water was added and the reaction mixture was further kept in the water bath for 30 min at 35 - 37ºC. After that, the enzymatic reaction was stopped by adding 0.1 ml of 100 mM $CaCl_2.2H_2O$. The formation of yellow color due to release of p-nitrophenol indicated lipase activity. The absorbance of yellow color was measured by spectrophotometry at 410 nm against a control without enzyme (Massadeh and Sabra (2011), Pandey *et al. (*2016), Rodrigues *et al.* (2016)). The concentration of liberated yellow color compound (p-nitrophenol) in the reaction mixture was determined by using standard curve of p-nitrophenol (4 to 20 µg ml^{-1} in 0.05 M Tris HCl buffer, pH-8.0) (Kanwar *et al.*, 2005). One unit (U) of lipase activity was defined as micromole (µM) of p-nitrophenol liberated from the hydrolysis of p-nitrophenyl ester by one ml of soluble enzyme per minute under standard assay conditions.

Preparation of p-nitrophenol standard curve

Standard curve of p-nitrophenol was prepared using the concentration range of p-nitrophenol (4, 8, 12, 16 and 20 µg ml^{-1}) in 0.05 M Tris HCl buffer, pH-8.0 according to Kanwar *et al.*, 2005 and www.Shodhganga.inflibnet. ac>bitstream.com.

Effect of different lipid substrates on lipase activity

The substrate of fermentation medium was replaced with various lipid substrates such as coconut oil, sunflower oil, olive oil, peanut oil and lard (rendered pig fat) (Basheer, 2007 and Sirisha *et al.*, 2010).

Effect of Temperature on lipase activity

The effect of temperature on lipase activity was investigated at temperatures ranging from 25 to 50˚C by keeping the remaining parameters same (Sirisha *et al.*, 2010, Basheer, 2007 and Niaz *et al.*, 2014).

Effect of pH on lipase activity

The optimum pH for lipase activity was examined by varying from pH 5.0 to 9.0. The remaining parameters were unaltered (Basheer, 2007 and Sirisha *et al.*, 2010).

Results

Isolation of lipolytic fungi from different sources

Lipolytic fungi were isolated from different sources. In this study, some optimal parameters of three different types of lipolytic fungi as shown in Table 1 such as *Aspergillus* sp. (1) (was selected from 3 strains) from pork sausage (Figure 1), *Penicillium* sp. (was selected among 5 strains) from cheese (Figure 2), and *Aspergillus* sp. (18) (was selected from 8 strains) from fuel oil contaminated soil (Figure 3) were observed. Each lipolytic fungus was identified based on their characters of pure colony morphology and spore formation according to Barnett (1960) and Dube (1983).

Table 1 Lipolytic fungi from different sources

No.	Fungal sources	Lipase producing fungi	Code of isolated strains	Showed clear zone (Halo region)	
				0.1%TBA	1% TBA
1.	Pork sausage	*Aspergillus* sp. (1)	PS-1	After 2-5 days	After 5- 17 days
2.	Cheese	*Penicillium* sp.	CH-1	‖	‖
3.	Fuel oil contaminated soil	*Aspergillus* sp. (18)	OS-8	‖	‖

Identification of isolated lipolytic fungi

Characteristics of mycelium and spore formation of *Aspergillus* sp. isolated from Pork Sausage (PS)

Aspergillus sp. (1) colony was yellow color inside and white color periphery. Mycelia were scattered in culture.

(A) **(B)** **(C)** **(D)**

Figure 1 Lipolytic fungus *Aspergillus* sp. (1) from pork sausage

(A) Fungal growth on pork sausage (B) Fungal colony (5 - 7 days old) (yellow color inside and white color periphery) (PS) (C) Clear zone (halo) around fungal colony (2 days old) on 1 % TBA medium (D) Micrograph of *Aspergillus* sp. (1) (X 200)

Characteristics of mycelium and spore formation of *Penicillium* sp. isolated from cheese (CH)

Penicillium sp. colony was green color inside and white color periphery. Mycelia were scattered in culture.

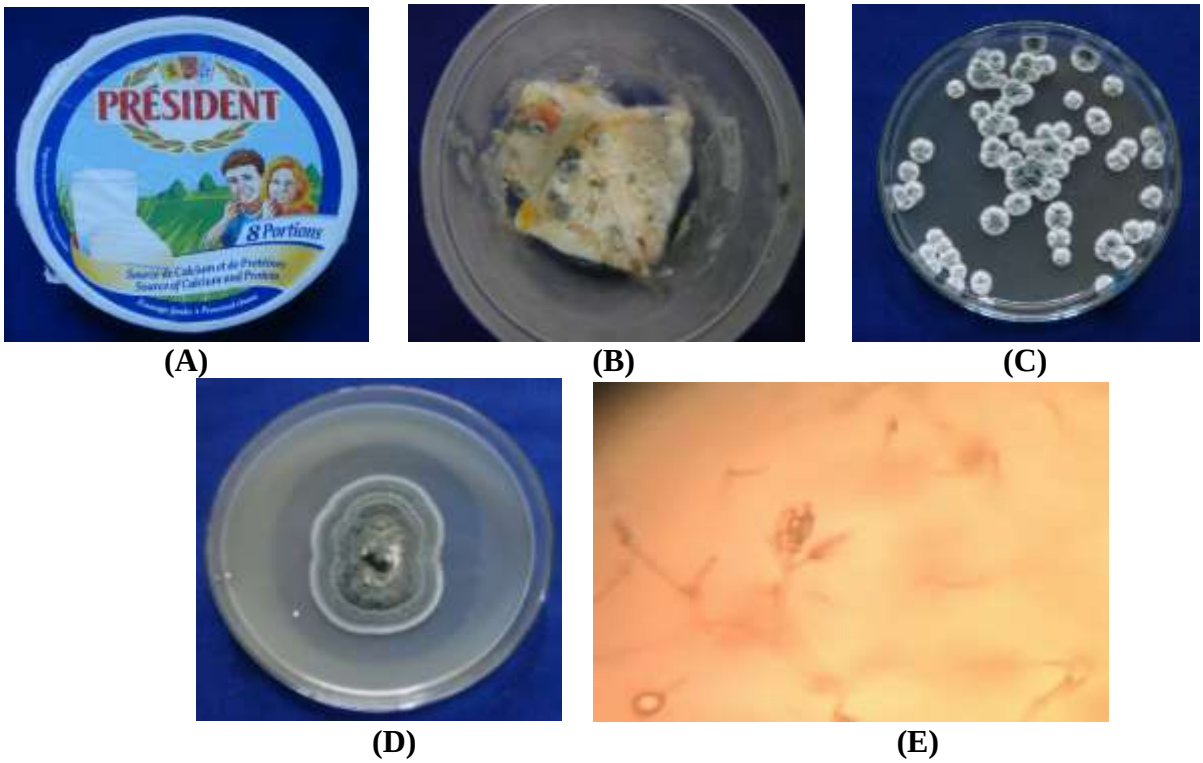

Figure 2 Lipolytic fungus *Penicillium* sp. from cheese

(A) Collected cheese source (B) Fungal growth on cheese (C) Pure fungal colony (5 - 7 days old) (green color inside and white color periphery) (CH - 1) (D) Clear zone (halo) around fungal colony (12 days old) on 1 % TBA medium (E) Micrograph of *Penicillium* sp. (X 400)

Characteristics of mycelium and spore formation of *Aspergillus* sp. isolated from fuel oil contaminated soil (OS)

Aspergillus sp. (18) colony was black color inside and white color periphery. Mycelia were scattered in culture.

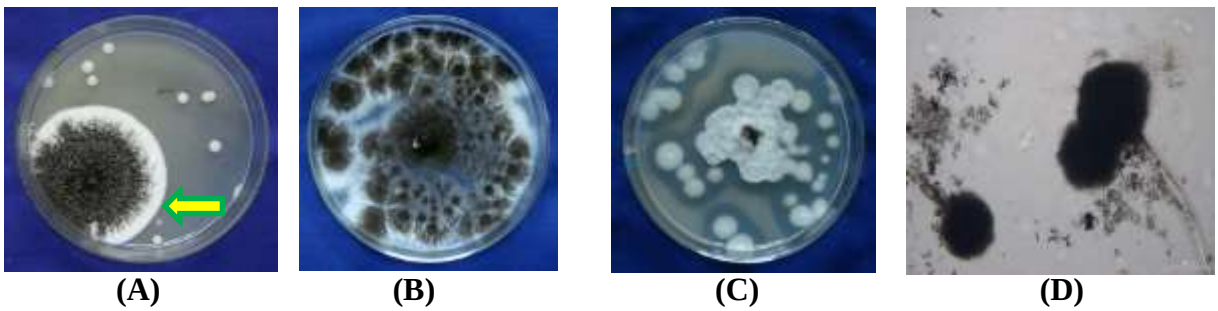

Figure 3 Lipolytic fungus *Aspergillus* sp. (18) from fuel oil contaminated soil

(A) Fungus isolated from soil sample (10^{-8}) (B) Pure fungal colony (5 - 7 days old) (black color inside and white color periphery) from soil sample (10^{-8}) (C) Clear zone (halo) around fungal colony (6 days old) on 1% TBA medium (D) Micrograph of *Aspergillus* sp. (18) (X 200)

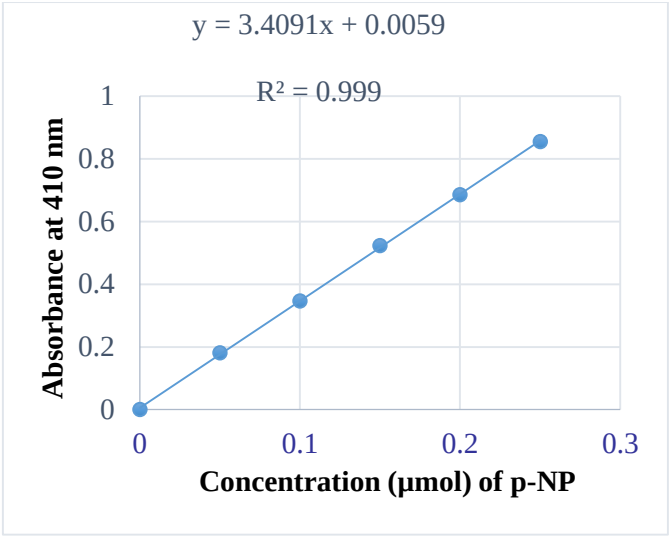

Figure 4 p-nitrophenol (p-NP) standard curve

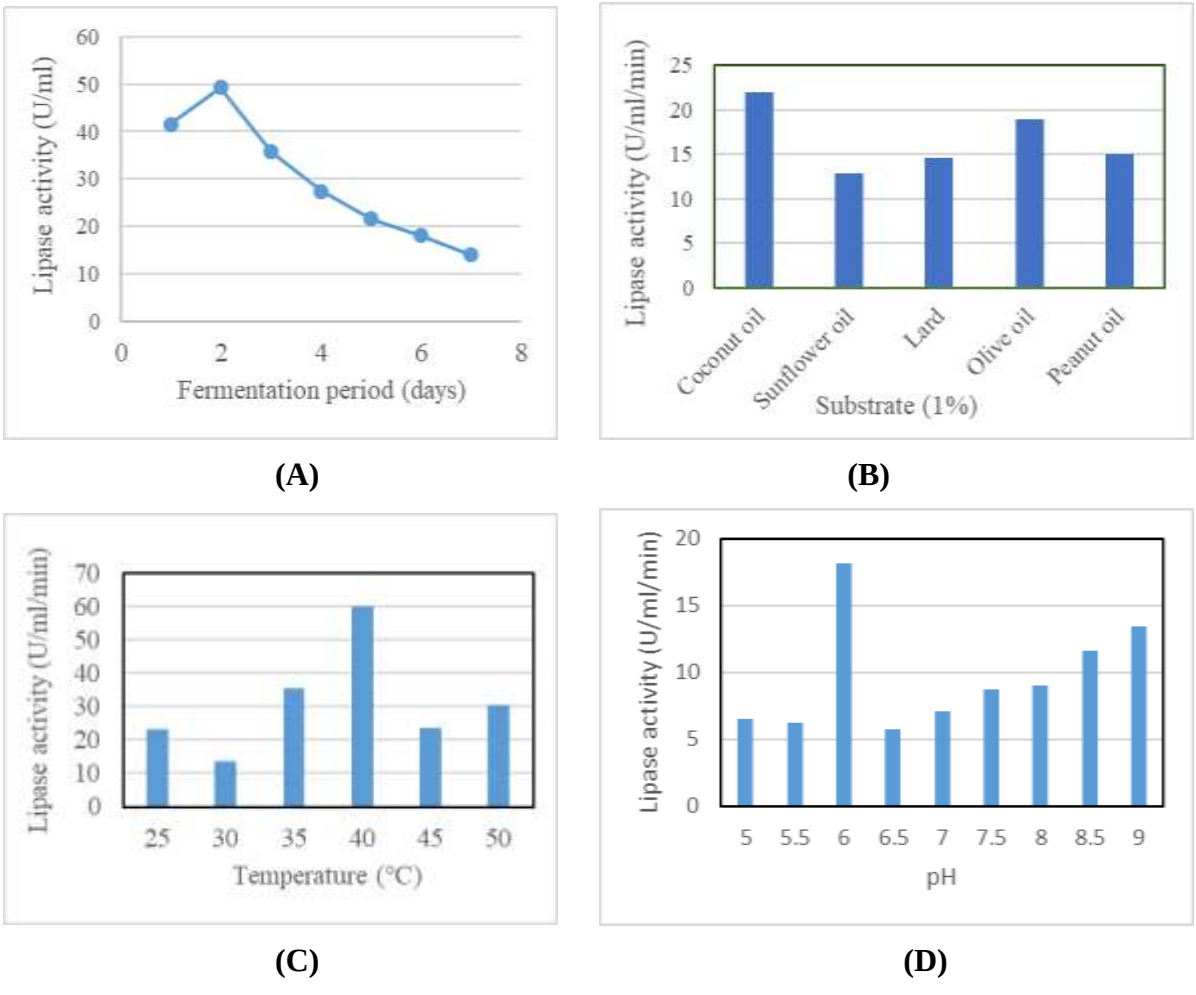

Figure 5 Effect of incubation period, substrate, temperature and pH on lipase activity by *Aspergillus* sp. (1) from pork sausage

(A) Effect of incubation period on lipase activity, (B) Effect of different oil substrates on lipase activity, (C) Impact of temperature on lipase activity, (D) Effect of pH on lipase activity

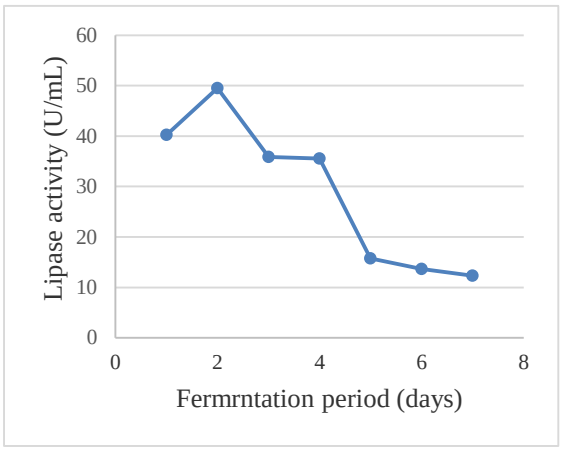

(A)

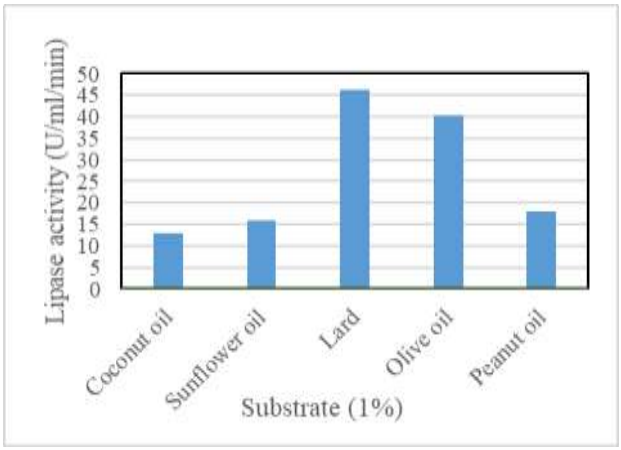

(B)

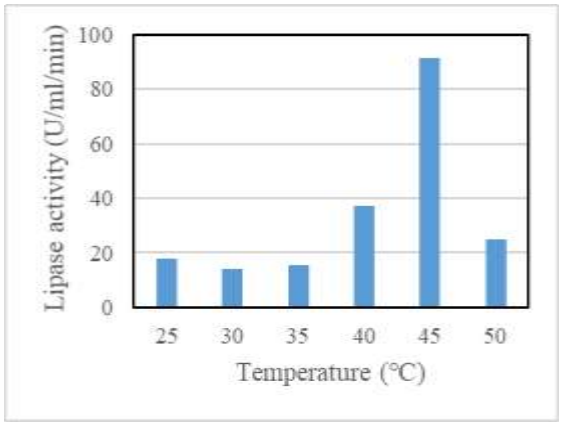

(C)

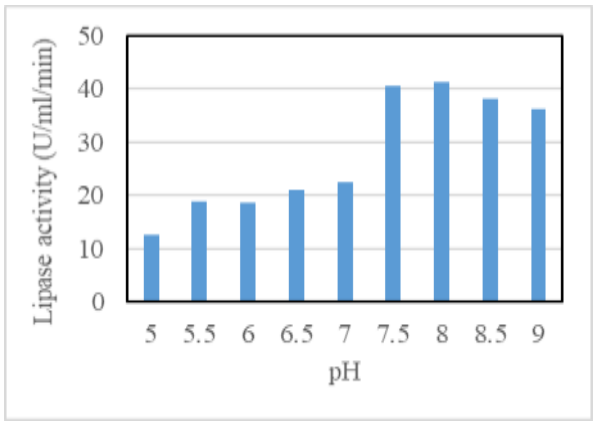

(D)

Figure 6 Effect of incubation period, substrate, temperature and pH on lipase activity by Penicillium sp. from cheese

(A) Effect of fermentation period on lipase activity, (B) Effect of various lipid substrates on lipase activity, (C) Impact of temperature on lipase activity, (D) Effect of pH on lipase activity

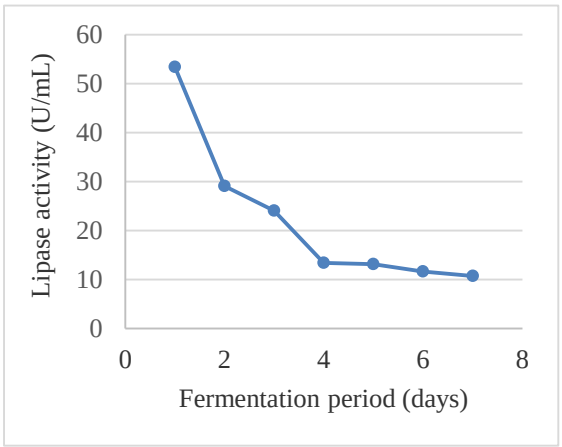

(A)

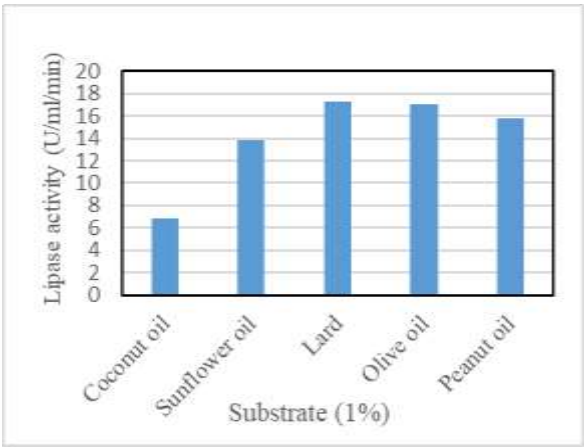

(B)

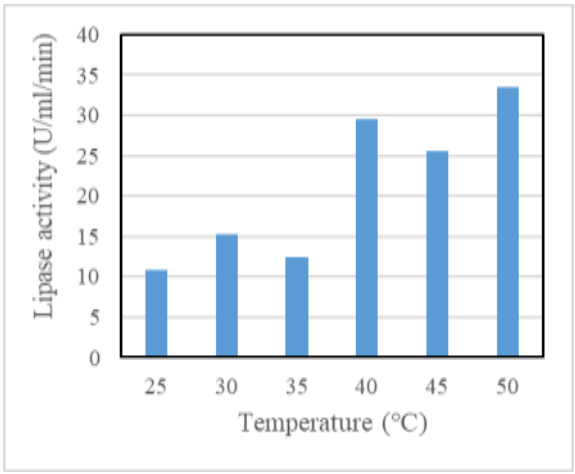

(C)

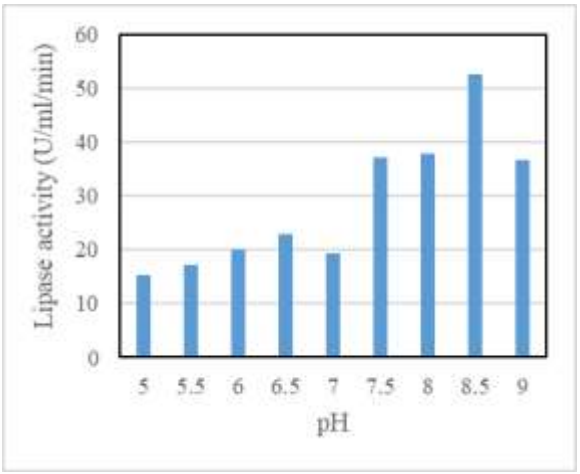

(D)

Figure 7 Effect of incubation period, substrate, temperature and pH on lipase activity by *Aspergillus* sp. (18) from fuel oil contaminated soil

(A) Effect of fermentation period on lipase activity, (B) Impact of different lipid substrates on lipase activity, (C) Effect of temperature on lipase activity, (D) Impact of pH on lipase activity

Discussion and Conclusion

In this research work, three different lipolytic fungi were selected and inoculated through four different submerged fermentation media to obtain the best lipase production. Some optimal experimental conditions such as effect of incubation period, substrate, temperature and pH were studied for production of lipase enzyme after medium optimization. The lipase activity was estimated by spectrophotometric method using p-NPP substrate solution.

In the present investigation, isolated *Aspergillus* sp. (1) from pork sausage and isolated *Penicillium* sp. from cheese produced the maximal lipase activity on second day. Lipase from *Aspergillus* sp. (1) exhibited the highest activity at 40 °C. Brooks and Asamudo (2011) reported that optimum temperature of lipase activity was 40 °C for *Aspergillus niger* AC-5 and 45 °C for *A. niger* AC-7 which were isolated from contaminated body creams.

In this study, *Aspergillus* sp. (1) produced the greatest lipase activity (18.13 U/ml/min) at pH 6.0. Prabhakar *et al.,* (2002) reported that *Aspergillus japanicus* and isolated *Aspergillus* sp. from contaminated ghee showed the best lipase activity at pH 6.0. The highest activity of crude lipase from *A. japanicus* was 34 U/ml and the isolated *Aspergillus* sp. was 36 U/ml under the optimized conditions.

In the present study, *Penicillium* sp. and isolated *Aspergillus* sp. (18) from fuel oil contaminated soil showed maximum activity at 45 °C and 50 °C. Bakir and Metin (2017) reported that lipase enzyme which shows maximum activity at 45, 50 and 55 °C may be useful for various processes such as detergent, leather, medical, cosmetic, textile and food industries.

In this study, lipase from *Aspergillus* sp. (18) showed the maximum activity at pH 8.5 while *Penicillium* sp. produced the best lipase activity at pH 8. The present results proved that the enzyme under investigation is an alkaline lipase. Colla *et al.* (2015) stated that a lipase obtained from *A. fumigatus* presented optimum pH of 8.5.

In the present study, lipase produced by *Penicillium* sp. through submerged fermentation showed the maximum activities at 45 °C and pH 8.0, while lipase from *Aspergillus* sp. (18)

exhibited at 50 °C and pH 8.5. The pH was higher in alkaline pH. Lipase produced through Smf with *Aspergillus* sp. (1) had optimum temperature and pH at 40 °C and pH 6.0.

In conclusion, fungal lipases are one of the enzymes having huge market demand. Optimization studies on media parameters for maximum lipase activity were done on selected lipolytic fungi. Total three lipolytic fungi have shown a broad range of pH and temperature. For a maximum lipase production, carbon and nitrogen sources are also important.

Acknowledgements

I would like to express my sincere gratitude to Professor Dr. Aye Pe, Professor and Head of Botany Department, University of Yangon, for his permission to carry out this research and invaluable advice.

References

Atlas, R. M., (1993). **Handbook of Microbiological Media.** CRC Press, London.

Alexander, S. K. and D. Strete, (2001). **Microbiology: A Photographic Atlas for The Laboratory.** U.S.A.

Barnett, H. L., (1960). **Illustrated Genera of Imperfected Fungi.** Second Edition. Printed in the United States of America.

Basheer, S. M., (2007). **Lipase production by marine fungus aspergillus awamori nagazawa.** Kerala, India.

Brooks A. A. and N. U. Asamudo, (2011). **Lipase production by strains of Aspergillus species isolated from contaminated body creams.** Nigeria. Journal of Toxicology and Environmental Health Sciences Vol. 3(11), pp. 311-316.

Bakir, Z. B and K. Metin, (2017). **Production and characterization of an Alkaline lipase from Thermophilic *Anoxybacillus* sp. HBB16.** Turkey. Biochem. Eng. Q., 31 (3) 303-312.

Colla, L. M., A. M. M. Ficanha, M. J. Rizzardi, T. E. Bertolin, C. O. Reinehr and J. A. V. Costa, (2015). **Production and characterization of lipase by two new isolates of Aspergillus through solid-state and submerged fermentation.** BioMed Research International, ID 725959.

Dube, H. C., (1983). **An Introduction to Fungi. Second Revised Edition.** Printed at Vishal Printers, Delhi.

Griebeler, N., A. E. Polloni., D. Remonatto, F. Arbter., R. Vardanega, J. L. Cechet, M. D. Luccio, D. d. Oliveira, H. Treichel, R. L. Cansian, E. Rigo and J. L. Ninow, 2011. **Isolation and screening of lipase-producing fungi with hydrolytic activity.** Food Bioprocess Technol 4: p. 57-586.

Kanwar, S. S., R. K. Kaushal, A. Jawed, R. Gupta and S. S. Chimni, (2005). **Methods for inhibition of residual lipase activity in colorimetric assay: A comparative study.** Indian Journal of Biochemistry and Biophysics, Vol. 42, pp. 233-237.

Kotogan, A., B. Nemeth, C. Vagvolgyi, T. Papp and M. Tako, (2014). **Screening for extracellular lipase enzymes with transesterification capacity in Mucoromycotina strains.** ISSN (FTB-3455), p. 1330-9862.

Lanka. S and T. Trinkle, (2017). **Screening and Isolation of Lipase Producing Fungi from Marine Water Obtained from Machilipatnam Costal Region.** International Journal of Pharmacognosy and Phytochemical Research; 9 (7); 928 - 932, India.

Massadeh, M. I., and Sabra, F. M., (2011). **Production and characterization of lipase from *Bacillus sterarothermophillus*.** Jordan. African Journal of Biotechnology, Vol. 10(61), pp. 13139-13146.

Niaz, M., T. Iftikhar, F.F. Qureshi and M. Niaz, (2014). **Extracellular lipase production by *Aspergillus* nidulans (MBL-S-6) under submerged fermentation**. Pakistan. Int. J. Agric. Biol., 16: 536_542.

Prabhakar, T. K. A. Kumar and P. Ellaiah, (2002). **The effect of cultural conditions on the production of lipase by fungi.** Journal of Scientific and Industrial Research, Visakhapatnam. Vol. 61, pp- 123-127.

Pandey. H., A. Kestwal, D. Chauhan, S. Kumari, V. Dhalwal, G. J. Singh, P. Singh, Parul Mann, A. Sharma, G. Saxena, A. Kapoor and B. Giri, (2016). **Isolation and screening of potential fungi and standardization of a process for the production of exracellular lipase.** DU Haurnal of undergraduatae Research and Innocation (Delhi, 2016): p. 116-122.

Rodrigues. C., S. T. A. Cassini, P. W. P. Antunes, L. M. Pinotti, R. P. Keller and R. F. Goncalves, (2016)**. Lipase producing fungi for potential wastewater treatment and bioenergy production.** Academic journal of biotechnology. Vol. 15(18), pp. 759-767. Africa.

Sirisha, E., N. Rajasekar and M. L. Narasu, (2010). **Isolation and optimization of lipase producing Bacteria from Oil contaminated soils.** India. Advances in Biological Research 4 (5): 249-252.

Shukla, B. N and P. V. Desai, (2016). **Isolation, characterization and optimization of lipase producing *Pseudomonas* spp. from oil contaminated sites.** India. Int.J.Curr.Microbial.App.Sic. 5(5): 902-909.

Winkler, U. K and M. Stuckmann, (1979). **Glycogen, hyaluronate, and some other polysaccharides greatly enhance the formation of exolipase by Serratia marcescens.** Journal of Bacteriology, 138, 663-670.

Wadia, T. and S. K. Jain, (2017). **Isolation, screening and identification of lipase producing fungi from oil contaminated soil of Shani Mandir Ujjain.** Int. J. Curr. Microbiol. App. Sci (2017) 6(7): p. 1872-1878.

Websites

www.Shodhganga.inflibnet. ac>bitstream.com

SOME ECOLOGICAL ASPECTS OF ROCKY SHORE MARINE GASTROPODS IN BO RON GA ISLAND, NORTHERN RAKHINE COASTAL REGION*

Naung Naung Oo[1]

Abstract

Rakhine Coastal Region is known in terms of biodiversity since it is dubbed by the local and international scientists as ecologically and biologically significant marine area. This research is an attempt to investigate the zonal distribution, influencing factors and faunal responses, habitat preference, abundance and determine the species diversity of molluscan species in rocky shore area of Bo Ron Ga Island, Northern Rakhine Coastal Region. This study was carried out from January to December 2020 in five study sites of Bo Ron Ga Island. There were a total of 1548 individuals of macrobenthic fauna collected encompassing 33 known species of molluscs groups. Most of the number of gastropod shells was found in Bo Ron Ga Island which constitutes about 96% of the entire collection and contributed by *Nerita costata* (21.22%), *Nassarius globosus* (17.2%), *Morula nodicostata* (16.11%), *Nerita albicilla* (12.51%) and *Littoraria undulata* (6.88%). In the present study, Hnget Gaung Taung was harboured with the highest species (49 spp.), followed by Pan Nantha Kyun (36 spp.), Lin Noh Kyun (34 spp.), San Taw Shin (33 spp.) and the lowest was observed at Pyin Gyi (25 spp.). In addition, maximum diversity index, equitability and correlation of habitats and species preferences of gastropods were also presented.

Keywords: Rocky shore habitats, species diversity, faunal assessment, molluscs, anthropogenic activity.

Introduction

The rocky shore is an intertidal area of seacoasts where solid rock predominates, still it is considered as a part of marine ecosystem. Rocky shores are biologically rich in terms of the number and variety of species they support, and are a useful 'natural laboratory' for studying intertidal ecology and other biological processes.

The ecological habitat structure may affect the species diversity and abundance in several systems (Connell 1961; Underwood and Chapman 1989). It has been difficult to understand the effects of habitat structure on assemblages because the different elements of habitat structure are often puzzled. The complexity of habitats positively affects the density and richness of molluscs (Beck 2000).

Marine invertebrates and algae living in rocky habitat are alternatively affected by physical forces such as waves and temperature, desiccation and exposure to tidal periods (Denny and Gaines 2007). As a result, the sharp physical gradient and spatially clustered community has made the rocky intertidal zone as an ideal place to study the role of physical and biological factors in determining the abundance and distribution of organisms (Connell 1972 and Paine 1966).

Among different habitats of the islands, the rocky shore ecosystem is physically harsh environment on the earth but supports a wide variety of fauna. This high species diversity is attributable to the existence of a large number of ecological niches. Several studies have accounted the detailed structure of flora and fauna of intertidal zone (Colman 1933; Fletcher and Frid 1996). This zone is one of the hotspots of biodiversity within the marine coastal ecosystem as well as an island ecosystem. In recent times, these rocky shore habitat is under increasing threat as a consequence of anthropogenic activity and climate change. Further, many of these areas are still unexplored and the threat is unexplained to pave the way for its conservation. The objectives of

[1] Dr, Lecturer, Department of Marine Science, Mawlamyine University

[*] Best Paper Award Winning Paper in Marine Science (2022)

current study are 1) to know factors influencing rocky shore habitats and adaptation; and 2) to investigate the habitat preference and species diversity of Bo Ron Ga Island.

Materials and Methods

A study was conducted to assess the present status of rocky shores of Bo Ron Ga Island (Lat. 19˚47′ N and 20˚25′ N, Long. 92˚54′ E and 93˚15′ E), Northern Rakhine Coastal Region as they are known to support more ecological niches. The locations were selected based on the accessibility for sampling, exposure of rocky stretch during low tide, harbouring of different micro-habitats, namely, tide pools, loose boulders, rock on rock, surface of substrata (hard/smooth), vertical surface, flat, phytal cover, etc. Five sampling sites were chosen along the rocky coast of Bo Ron Ga Island (Fig. 1).

Sampling site	Position
	Western Bo Ron Ga Island
1. Hnget Gaung Taung (= Mye Ngu Kyun)	(Lat. 19˚55′ N, Long. 92˚58′ E)
2. San Taw Shin	(Lat. 19˚51′ N, Long. 93˚00′ E)
	Middle Bo Ron Ga Island
3. Pan Nantha Kyun	(Lat. 19˚35′ N, Long. 93˚12′ E)
	Eastern Bo Ron Ga Island
4. Pyin Gyi	(Lat. 19˚50′ N, Long. 93˚13′ E)
5. Lin Noh Kyun	(Lat. 19˚45′ N, Long. 93˚16′ E)

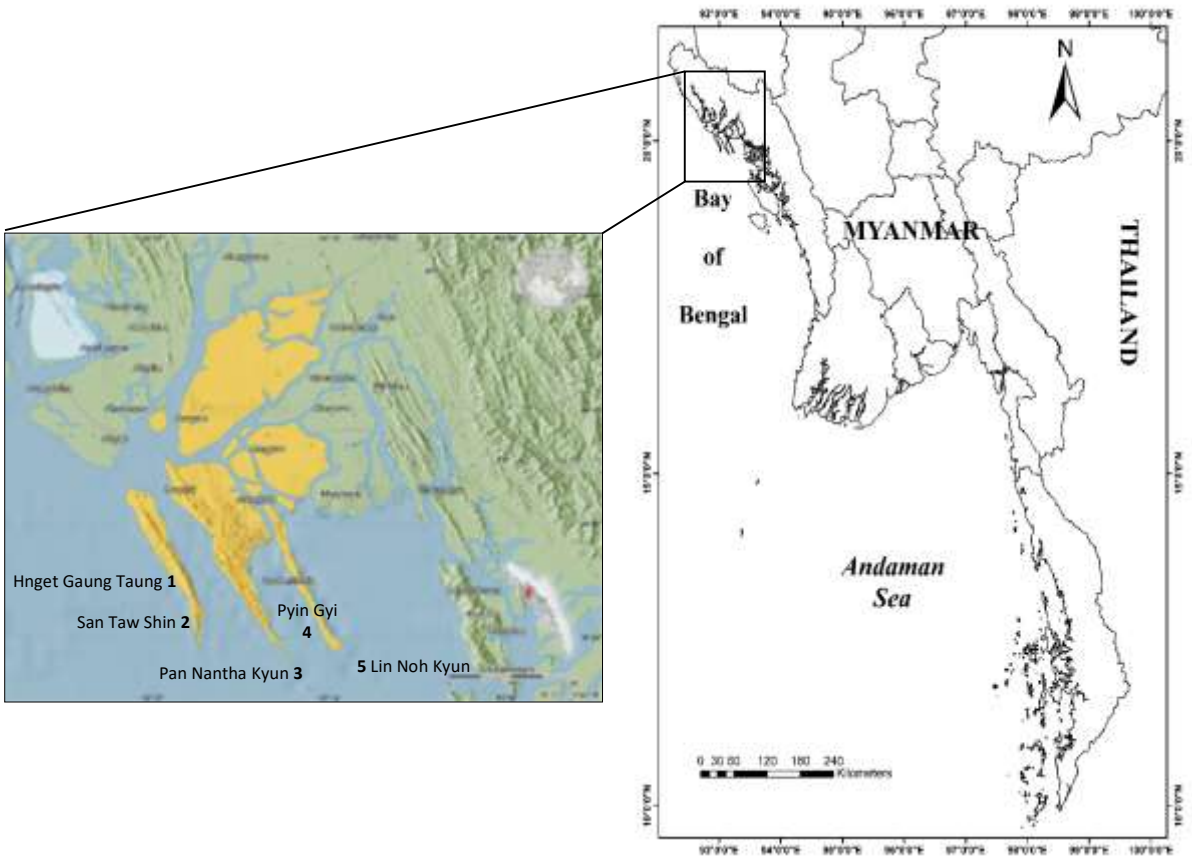

Figure 1 Map showing the sampling sites in Bo Ron Ga Island, Northern Rakhine Coastal Region

Quantitative samples were collected during low tides by adopting quadrat method, with a frame size of 50 × 50 cm. At each station, three replicate samples were collected. Altogether six replicate samplings were made during the study period spread from January to December 2020 during lowest low tides. A total of 90 (18 samples × 5 locations) quantitative samples and several qualitative samples were collected during the study. Samples were first kept in seawater for some time and then transferred to laboratory where they were washed to remove sediments or debris. After narcotising the samples were transferred to 5% buffered formaldehyde. The collected fauna were taxonomically identified up to the lowest possible taxonomic units, for example, species/ or a genus using standard taxonomic literature (Subba Rao 2003; Subba Rao and Dey 2000).

Results and Discussion

Zonal distribution of some rocky shore molluscan faunas in study areas

Based on the amount and type of inundation the rocky shores of Bo Ron Ga Island are generally classified into the following zones: High tide zone, Mid tide zone and Low tide zone. Although some overlap does occur, plants and animals are adapted to live in certain zones on the shore and each zone contains its own unique complement of organisms (Table 1).

High tide zone: It is also known as the upper zone or the dry upper-beach zone. Organisms are exposed to the drying heat of the sun during daytime and cool and low temperature during night. Because of these severe conditions, only a few resistant organisms live here (Table 1). The most characteristic organisms of this zone are the perwinkles (*Littoraria* sp.) and neritids (*Nerita* sp.). Periwinkles are so common in this zone that it is frequently referred to as the Littorina-zone. At the lower edge of the splash zone, rough snails (periwinkles) graze on various types of algae. These snails are well adapted to life out of the water by trapping water in their mantle cavity or hiding in cracks of rocks. Other common animals are isopods, barnacles and limpets.

Mid tide zone: This zone is known as the middle zone or the middle beach zone. It is the true intertidal zone, subjected to daily ebb and flood of the tides. As such, the animals living in this zone are immersed in water during high tide and exposed to air and drying during low tide. Animals in this zone are more abundant than the above one. Several groups of animals live attached to rocks, hiding in their crevices or in the tide pools. Chitons, limpets, neritids, top shells and turban shells are some of the important molluscs that inhabit this zone (Table 1). Another characteristic feature of this zone is the formation of tidal pools. This is rocky pools in the intertidal zone that are filled with seawater. In low located pools, whelks, mussels, sea urchins and *Littoraria littorea* are common.

Low tide zone: This is the lowest zone and bared only by the ebbing spring tides. This zone is much more stable than above two zones. As such, exposure to air is not as frequent as in the case of mid-littoral. In the study areas, the upper distribution is set by their ability to survive exposure to the air and the lower distribution is controlled by predation and competition with other species for a space on the rock. Tritons (*Cymatium* sp.), distorsios (*Distorsio* sp.), crustaceans and rock boring worms like sipunculids are common in this zone (Table 1). Some of the forms such as limpets, oysters and mussels have developed thick shells and strong power of attachment to withstand the force of battering waves. There are others which have developed soft and flexible bodies, such as seaweeds and hydroids.

Table 1 Zonal distribution of some molluscan faunas on rocky shore in study areas

Dominant species	High Tide	Mid Tide	Low Tide
Polyplacophora			
Chiton shells (*Acanthopleura* sp.)	+		
Chiton shells (*Ischnochiton* sp.)	+		
Gastropoda			
Lottiid limpets (*Patelloida* sp.)	+		
Patellid limpets (*Patella* sp.)	+	+	
Patellid limpets (*Cellana* sp.)	+		
Pyramid tops (*Tectus* sp.)	+	+	
Maculated top (*Trochus* sp.)	+	+	
Turban shells (*Turbo* sp.)	+	+	
Neritids (*Nerita* sp.)	+	+	
Perwinkles (*Littoraria* sp.)	+	+	
Vermetid worms (*Thylacodes* sp.)	+	+	
Clusterwinks (*Planaxis* sp.)	+	+	
Cowries (*Cypraea* sp.)		+	+
Moon snails (*Natica* sp.)		+	
Triton shells (*Cymatium* sp.)			+
Distorsios (*Distorsio* sp.)			+
Firebrand murex (*Chicoreus* sp.)		+	+
Rock shells (*Thais* sp.)		+	
Rock shells (*Drupa* sp.)	+	+	+
Rock shells (*Morula* sp.)	+	+	+
Spider conchs (*Lambis* sp.)			
Nassa mud snails (*Nassarius* sp.)		+	
Miter shells (*Mitra* sp.)		+	+
Whelks (*Cantharus* sp.)		+	
False limpets (*Siphonaria* sp.)	+		
Bivalvia			
Decussate arks (*Barbatia* sp.)		+	+
Horse mussels (*Brachidontes* sp.)	+	+	
Yellowbanded horse mussels (*Modiolus* sp.)		+	
Box mussels (*Septifer* sp.)		+	
Common file shells (*Lima* sp.)			+
Hooded oysters (*Saccostrea* sp.)	+	+	+
Leaf oysters (*Dendostrea* sp.)			+
Jewel box shells (*Chama* sp.)		+	+
Total	17	23	12

Factors influencing on some rocky shore molluscan faunas and their adaptation

The continuously changing environment in the rocky shores demands that the organisms have to be tolerant for these changes and adjust to the factors that influence the survival and distribution of rocky shore species. An adaptation is a characteristic that helps an organism survive.

Adaptations are either structural (body form), functional (physiological), and behavioural. The following are the parameters which influence the distribution of rocky shore organisms in Bo Ron Ga Island (Table 2).

Table 2 Influencing factors and faunal responses in study areas

Influencing factors	Responses
Wind	Molluscs fauna developed an adaptation to heating and windy condition by vaporization of internal water reserves
Sunlight	When free radicals are produced from an excess of light, they can be scavenged and deactivated
Temperature	Heat stress can be avoided by evaporative cooling
Salinity stress	Regulate intercellular osmotic pressure by actively excreting salts or water
Desiccation	Avoid the desiccation by migrating to a region that is more moist and cool and attach more firmly to the substrate
Predation	Reacted by visual camouflage and chemical camouflage
Wave action	Move to shelters, permanent attachment use byssal threads or cementation
Platform and composition	One rock platform can support many different kinds of plants and animals, because some sections are almost always under water, while other parts are usually dry
Rock pools	Certain plants and animals can survive in rock pools where sheltered for a big wave washes the boulder out

Habitat preference of some rocky shore molluscan faunas in study areas

To study the habitat preference of macrobenthic rocky shore molluscan faunas, samples were collected from different microhabitats of the five locations in Bo Ron Ga Island. The following characteristics and correlation of rocky shore environment were considered to the study of habitat preference of macrobenthic molluscs fauna (Fig. 2, Table 3 A & B).

Table 3 A Classify rocky shore habitats and faunal preferences in study areas

Habitats	Preferences
Hardness of substratum (smooth and rough)	The most preferred substrata of the rocky shore fauna included rough substrata (accounted more than 30 species during sampling, for example, *Cellana radiata*, *Nerita costata*, *Nassarius globosus*) followed by smooth substrata on 15 species (type species: *Turbo bruneus*).
Vertical surface (sloping and flat)	It was evident that the rocky shore fauna preferred flat surface (type species: *Lambis lambis*) rather than sloping.
Wave action (protected and exposed)	Protected areas from the wave actions have highly diversified macrofaunal population (type species: *Planaxis sulcatus*).
Crevices	Some of the species preferred to live on the rock crevices (type species: *Ischnochiton bouryi*, *Natica severa*).
Rock-on-rock	*Drupa ricinus ricinus*, *Morula nodicostata* and *Littoraria undulata* preferred to live in this rocky micro-habitat.
Loose boulders	Few species were recorded in this region (type species: *Littoraria undulata*).
Tide pools	Organisms living in this habitat have high tolerant capacity to withstand this harsh condition, for example type species such as *Nerita*, *Cypraea* sp., *Trochus* sp., *Lambis* sp. in addition to these benthic invertebrates, fishes namely gobies, damsels, stone fish and blennies were also noted.
Symbiotic association	This category covers close associations of two species. It includes mutualism (both are of beneficiaries), parasitism (harmful to the host) and commensalism (neither obviously harmful nor beneficial to the host). In this habitat, *Desmospongia*, *Holothuria atra*, *Metridium* and *Tridacana* were recorded as symbiotic associations during the period of study.
Phytal association	In the present study, gastropods *Distorsio kurzi* and *Mitra stictica* were observed as phytal (seaweed/seagrass) associated fauna. Among the 12 different habitats, the Flat Vertical Surface (FVS) and Protected from Wave Action (PWA) harboured highest number of species and the epiphytic being the lowest.

Table 3 B Correlation between habitats and species preferences in study areas

	Hardness	Vertical surface	Wave action	Crevices	Rock-on-rock	Loose boulders	Tide pools	Symbiotic	Phytal
Hardness	1.000								
Vertical surface	0.876	1.000							
Wave action	-0.089	0.144	1.000						
Crevices	-0.400	-0.233	-0.042	1.000					
Rock-on-rock	-0.172	0.013	0.043	0.645	1.000				
Loose boulders	-0.049	0.247	0.169	0.073	0.611	1.000			
Tide pools	-0.288	-0.448	0.319	0.233	0.249	-0.268	1.000		
Symbiotic	-0.237	0.138	0.366	0.580	0.762	0.695	0.095	1.000	
Phytal	0.418	0.189	0.357	-0.579	-0.549	-0.295	0.281	-0.520	1.000

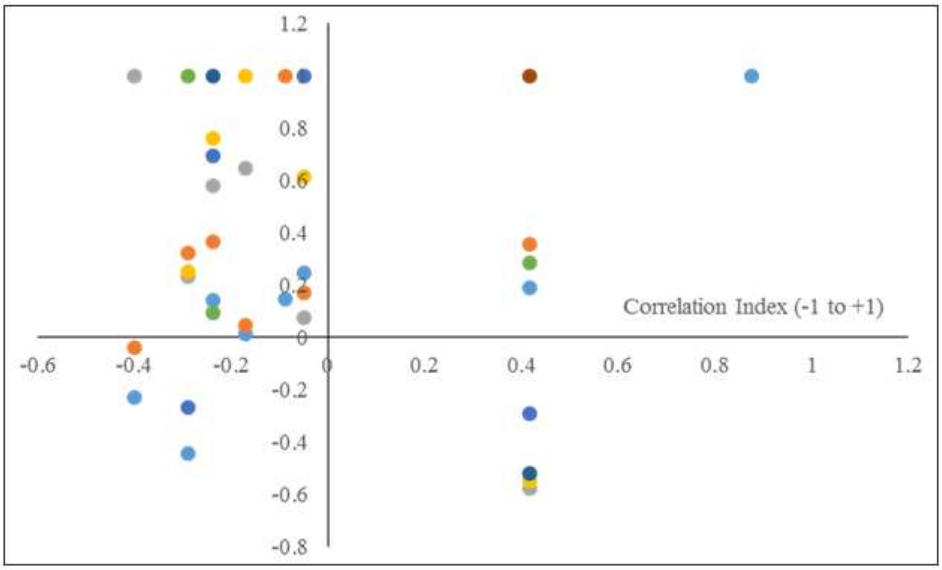

Figure 2 Correlation between habitats and species preferences in study areas

Abundance of some rocky shore molluscan faunas in study areas

From the Bo Ron Ga Island in Northern Rakhine Coastal Region, 1548 individuals of macrobenthic fauna represented by diverse phyla, namely, Porifera, Cnidaria, Annelida, Arthropoda, Mollusca, Echinodermata and Chordata, were collected.

Table 4 Numerical abundance (Mean no/m^2) of molluscan fauna in study areas

Species	HGT	STS	PNTK	PG	LNK	Total	%
Acanthopleura sp.	2	1			1	4	2.26
Ischnochiton sp.	1		1			2	1.13
Patelloida sp.	2	2		1		5	2.82
Patella sp.	1	1	1		1	4	2.26
Cellana sp.	4	2	2	1	2	11	6.21
Tectus sp.	2				1	3	1.69
Trochu sp.	2	1	2	1	1	7	3.95
Turbo sp.	1	2	2	1	1	7	3.95
Nerita sp.	1	1	1		1	4	2.26
Littoraria sp.	5	4	3	4	4	20	11.30
Thylacode sp.	2					2	1.13
Planaxis sp.	1		1			2	1.13
Cypraea sp.	1		1	1	1	4	2.26
Natica sp.	5	3	2	2	4	16	9.04
Cymatium sp.	2	1	1			4	2.26
Distorsio sp.	1		1	1		3	1.69
Chicoreus sp.		1	1		1	3	1.69
Thais sp.	4	1	3	4	4	16	9.04
Drupa sp.		1	1		1	3	1.69
Morula sp.					2	2	1.13
Lambis sp.			1	1		2	1.13
Nassarius sp.	1	1	2	2	2	8	4.52
Mitra sp.	2			1		3	1.69
Cantharus sp.	1	1	2	1	1	6	3.39
Siphonaria sp.	1	1	1		1	4	2.26
Barbatia sp.	1	1	1	1		4	2.26
Brachidontes sp.	1	1	1		1	4	2.26
Modiolus sp.	1	2	2			5	2.82
Septifer sp.	2	2				4	2.26
Lima sp.	1	1			1	3	1.69
Saccostrea sp.	1	1	1	1	3	7	3.95
Dendostrea sp.		1	1	1		3	1.69
Chama sp.			1	1		2	1.13
Total	49	33	36	25	34	177	
% contribution	27.68	18.64	20.34	14.12	19.21		
Mean	1.81	1.43	1.44	1.47	1.70		

Symbols: HGT = Hnget Gaung Taung, STS = San Taw Shin, PNTK = Pan Nantha Kyun, PG = Pyin Gyi, LNK = Lin Noh Kyun.

Among all the major taxonomic groups considered, Polyplacophora, Gastropoda and Bivalvia of phylum Mollusca significantly contributed the highest (33 species) number of species, followed by Echinodermata (4 species), Crustacea (3 species), Annelida (2 species) and the least represented phyla were Porifera, Cnideria and Chordata (each 1 species). Overall, molluscs were the dominant taxa accounted about 96% of total population and contributed by *Nerita costata*

(21.22%), *Nassarius globosus* (17.2%), *Morula nodicostata* (16.11%), *Nerita albicilla* (12.51%) and *Littoraria undulata* (6.88%). Spatially, there were considerable differences in number of species among locations (Fig. 3). In present study, Hnget Gaung Taung was harboured with highest species (49 spp.), followed by Pan Nantha Kyun (36 spp.), Lin Noh Kyun (34 spp.), San Taw Shin (33 spp.) and lowest was observed at Pyin Gyi (25 spp.) (Table 4).

Overall, Hnget Gaung Taung showed highest percentage contribution (27.68 no/m^2) followed by Pan Nantha Kyun (20.34 no/m^2) whereas the lowest contribution was observed at Pyin Gyi (14.12 no/m^2) (Table 4). Among the five locations, Hnget Gaung Taung recorded highest mean abundance (1.81 no/m^2) followed by Lin Noh Kyun (1.70 no/m^2), Pyin Gyi (1.47 no/m^2), Pan Nantha Kyun (1.44 no/m^2) and San Taw Shin (1.43 no/m^2) (Table 4).

Hnget Gaung Taung: *N. costata* registered the highest abundance (84 no/m^2) followed by *N. albicilla* (45 no/m^2) and *M. nodicostata* (22 no/m^2).

San Taw Shin: In this location, the species were more or less evenly distributed. *N. albicilla* was the dominant species (32 no/m^2) followed by *M. nodicostata* (23 no/m^2) and *N. costata* (22 no/m^2).

Pan Nantha Kyun: *N. globosus* observed as the dominant fauna (7 no/m^2) followed by *M. nodicostata* (5 no/m^2) and *N. albicilla* (4 no/m^2).

Pyin Gyi: The highest contribution at this location was by *N. costata* (28 no/m^2) followed by *N. globosus* (24 no/m^2) and *N. albicilla* (14 no/m^2).

Lin Noh Kyun: In this location, the highest contribution was recorded by *M. nodicostata* (28 no/m^2) followed by *N. albicilla* (24 no/m^2) and *N. globosus* (14 no/m^2).

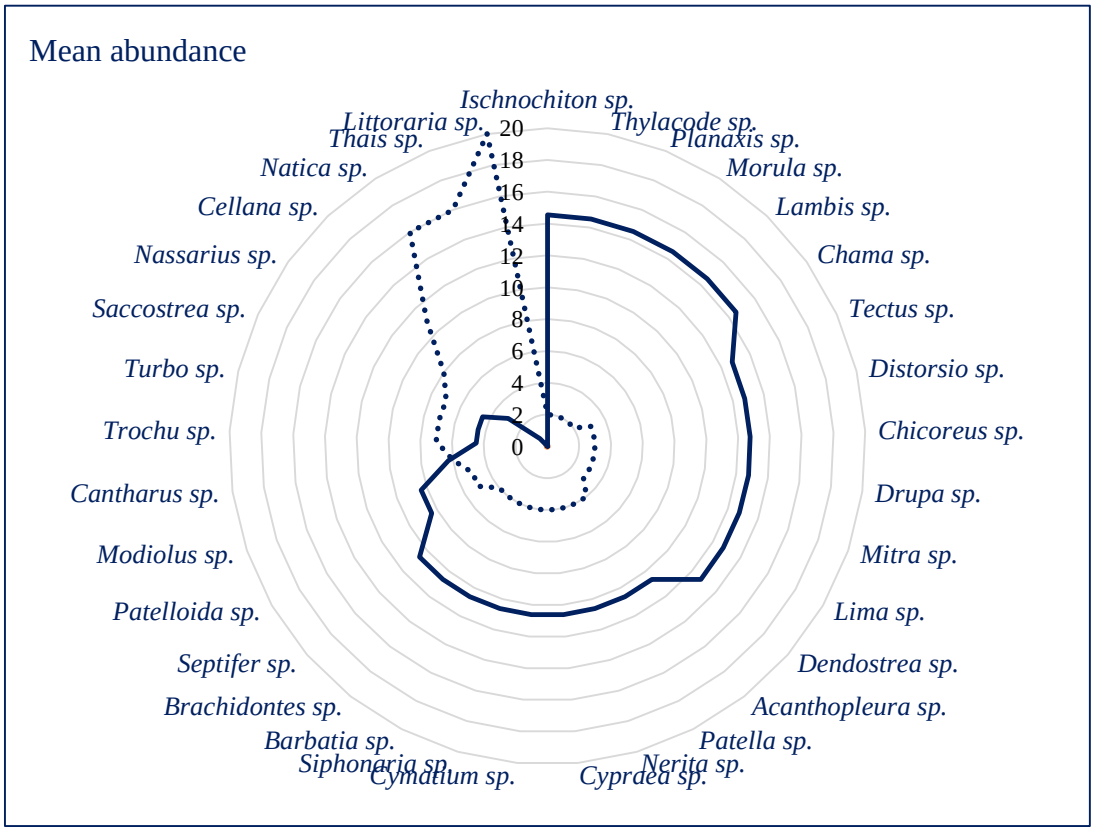

Figure 3 Mean abundance of some rocky shore molluscan faunas in study areas

Species diversity of some rocky shore molluscan faunas in study areas

Tropical shoreline is interspersed with the variety of habitats and thus the susbstrate heterogeneity is an inherent feature of the tropic (Hillebrand 2004). Rocky shores are known for their great diversity of animals and plants. The benthic communities of the intertidal habitats are largely shaped by the prevailing physical forces such as wave action, tidal range and tidal inundation, submergence, exposure to the light, temperature and the monsoon mediated variability in physico-chemical parameters. In this study, the intertidal zone tends to be colonized by algae in wave-sheltered conditions, and by limpets, barnacles and mussels as wave-exposure increases. Comparison of station-wise species diversity of molluscan faunas in study areas were shown in figure 4.

Table 5 Species diversity measures of some molluscan faunas in study areas

Sampling sites	Diversity (*H'*)	Evenness (*J'*)	Richness (*R'*)	H_{max}	Equitability
Hnget Gaung Taung	3.111	0.944	6.681	3.296	0.944
San Taw Shin	3.019	0.963	6.292	3.135	0.963
Pan Nantha Kyun	3.131	0.973	6.697	3.219	0.973
Pyin Gyi	2.664	0.940	4.971	2.833	0.940
Lin Noh Kyun	2.818	0.941	5.388	2.996	0.941

Diversity (*H'*): The highest value of *H'* was recorded at Pan Nantha Kyun (3.131), followed by Hnget Gaung Taung (3.111). The lowest value of *H'* was recorded at Pyin Gyi (2.664) (Table 5).

Evenness (*J'*): Pan Nantha Kyun showed the highest value of Pielou's Evenness (*J'*: 0.973), whereas the lowest value was recorded at Pyin Gyi (*J'*: 0.940) (Table 5).

Richness (*R'*): Over all, the third sampling at Pan Nantha Kyun showed the highest Margalef's diversity value (*R'*: 6.697), followed by first sampling of Hnget Gaung Taung (*R'*: 6.681). On the other hand the lowest value (*R'*: 4.971) was recorded at Pyin Gyi (Table 5).

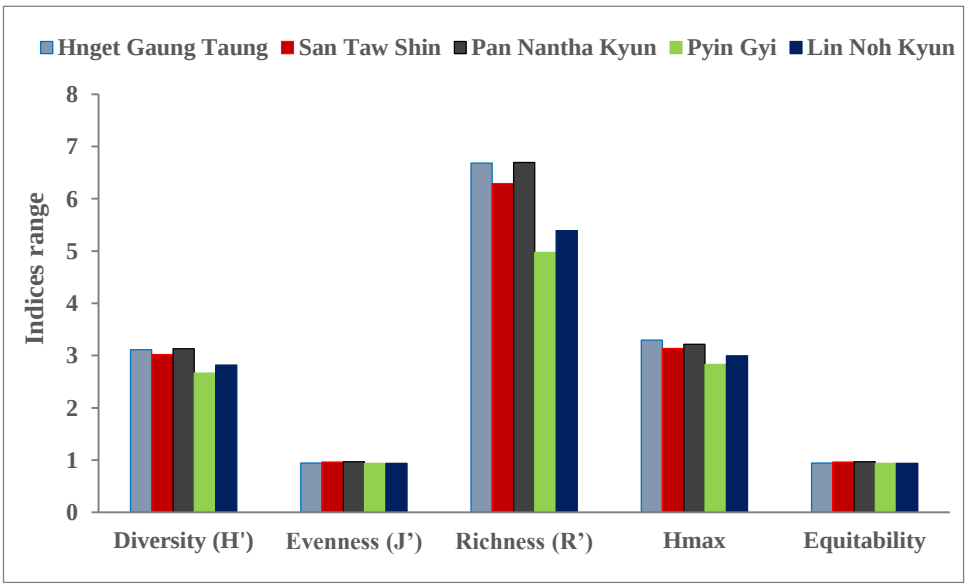

Figure 4 Diversity of some rocky shore molluscan faunas in study areas

Conclusion

A rocky shore is an intertidal area that consists of mostly solid rocks but the rocky shores are not all the same. It is often a biologically rich environment and can include many different habitat types such as steep rocky cliffs, platforms, rock pools and boulder fields. Together with the wind, sunlight and other physical factors it creates a complex environment in different places. Organisms that live in this area experience temporal fluctuations in their environment; consequently they have developed adaptation characters during the evolutionary development to survive. A study of Bo Ron Ga Island in Northern Rakhine Coastal Region revealed a total number of 47 species/taxa belonging to 30 families under 7 diverse phyla namely Porifera, Cnidaria, Annelida, Arthropoda, Mollusca, Echinodermata and Chordata. Among the seven phyla the Mollusca was the more diverse and constituting 33 species. Overall, molluscs were the dominant taxa accounted about 96% of total population and contributed by *Nerita costata*, *Nassarius globosus*, *Morula nodicostata*, *Nerita albicilla* and *Littoraria undulata*. Spatially, there were considerable differences of species composition between locations. At all locations, diversity of gastropods was recorded highest, followed by echinoderms. Based on the correlation matrix analysis different habitats can be studied to understand the habitat preference of rocky shore macrofauna. Some of the rocky shore communities are naturally unstable. This may be due to frequent physical disturbance caused either by anthropogenic activities or as a result of climate change and natural calamities as well. In general severe disturbance to the rocky shore habitat can shift community composition to an alternate state dominated by low profile algae, and fewer mussels. Eventually this could result in the local extinction of the displaced species.

Acknowledgements

I would like to express my gratitude to Dr. Aung Myat Kyaw Sein, Rector of Mawlamyine University; Dr Khine Khine San, Dr Myint Thida and Dr Mar Lar Aung, Pro-rectors of Mawlamyine University for their permission to undertake this research work. I would like to express my sincere thanks to Dr Nyo Nyo Tun, Professor and Head of Department of Marine Science in Mawlamyine University and Dr Soe Pa Pa Kyaw, Professor and Head of Department of Marine Science in Pathein University, for their advices and needful assistance. My final thank goes to local people from my study areas, for their assistance in the sample collections and Daw Lwin Lwin who has put in back breaking hours studying seashells but more importantly has kept me focused.

References

Beck, M. W. (2000). Separating the elements of habitat structure: independent effects of habitat complexity and structural components on rocky intertidal gastropods. J. Exp. Marine Biol. Ecol. vol. 249, pp. 29-49.

Colman, J. (1933). The nature of the intertidal zonation of plants and animals. *J. Marine Biol. Assoc*. vol. 18, pp. 435-476.

Connell, J. H. (1961). Effects of competition, predation by *Thais lapillus*, and other factors on the distribution of the barnacle *Balanus balanoides*. *Ecol. Monogr*. vol. 31, pp. 61-104.

Connell, J. H. (1972). Community interactions on marine rocky intertidal shores. *Annu. Rev. Ecol. Evol. Syst*. vol. 3, pp. 169-192.

Denny, M. W. and Gaines, S. D. (2007). *Encyclopedia of Tide pools and Rocky Shores*. University of California Press, Berkeley.

Fletcher, H. and Frid, C. L. J. (1996). Impact and management of visitor pressure on rocky intertidal algal communities. *Aquatic Conserv: Mar. Freshw. Ecosyst*. vol. 6, pp. 287-297.

Hillebrand, H. (2004). Strength, slope and variability of marine latitudinal gradients. *Marine Ecol. Prog. Ser*. vol. 273, pp. 251-267.

Paine, R. T. (1966). Food web complexity and species diversity. *Am. Nat*. vol. 100, pp. 65-75.

Subba Rao, N. V. (2003). Indian Seashells (Part 1): Polyplacophora and Gastropoda. *Zoological Survey of India*. Kolkata. no. 192, pp. 1- 416.

Subba Rao, N. V. and Dey, A. (2000). Catalogue of Marine Molluscs of Andaman and Nicobar Islands. *Zoological Survey of India*, Kolkata. pp. 1-323.

Underwood, A. J. and Chapman, M. G. (1989). Experimental analyses of the influences of topography of the substratum on movements and density of an intertidal snail, *Littorina unifasciata*. *J. Exp. Marine Biol. Ecol*. vol. 134, pp. 175-196.

STUDY ON THE DISTRIBUTION AND ABUNDANCE OF MANGROVE CRABS FROM MON COASTAL AREA

Nyunt Sandar Aung*

Abstract

The present study was conducted in six mangrove areas of Mon State (Bilukyun (Sabelar), Setse, Tarokpi, Kalegauk, Kaudut and Zeephyuthaung) from June 2012 to April 2017. During the study period, a total of 24 species of brachyuran crabs under 4 families (Portunidae, Grapside, Ocypodidae and Dorippidae) were recorded. Among the recorded species, *Scylla serrata, Scylla olivacea*, *Sesarma anderosorii*, *S. bidens*, *S. intermedium*, *Varuna littera*, *Gelasimus acutus*, *G. annulipes*, *G. dessumieri*, *G. marionis var nitidus*, *Uca chloropthalmus*, *Uca hesperiae*, and *Uca tetragonon* were observed at almost all the study areas. Almost all species were collected from Kalegauk and Kaudut mangrove areas representing 24 species and followed by Zeephyuthaung representing 17 species. *Scylla serrata, S. olivacea* and *Metaplax elegans* were the most abundance and also collected in every month in all stations. *Dorippe dorsipes* and *Ocypoda sp.* were only observed in Kalegauk and Kaudut mangrove areas. Seasonally, the highest species diversity of crabs was observed in hot months and the highest number of individuals of crab species was observed in the wet season.

Keywords: Abundance, brachyuran crabs, Dorippidae, Grapsidae, mangrove areas, Portunidae, Ocypodidae.

Introduction

Myanmar has extensive mangrove forests along the Rakhine, Ayeyarwaddy and Tanintharyi Coasts. The regions provide many mangroves and coastal habitats, and also serve as the breeding sites and the development of shrimps, prawns, crabs and fish culture. Mon Coast is situated at the southern part of Myanmar and have the long coastline more than thousand kilometers. It is famous for its inland and offshore. Crabs are one of the most commercial function in Mon coastal areas.

Mangroves are unique inter-tidal ecosystem of tropic and subtropics which support genetically diverse group of aquatic and terrestrial organisms. They provide the most important sources of fisheries and livelihoods of people living in the coastal zone. The products come from marine fisheries, freshwater and aquaculture of shrimp, crabs and fishes from marine, brackish and freshwater. Mangrove ecosystems are also known to be the areas of high biodiversity since which provide home for many marine and fresh water species. Crabs are one of the important species in the mangrove ecosystem.

Brachyuran crabs are the most predominant and abundant species in many mangrove forests. Some of the crabs are resident species where some others are visiting species within the mangrove areas. The crabs depend directly on mangrove areas for survival by feeding on leaves and litter. The complex structure of prop roots, pneumatophores and main trunks provides living spaces for numerous organisms and cover from the predation of large populations of small fishes, nektonic and benthic crustaceans, annelids, mollusks and invertebrates. Occurrence of crab species are related to habitat condition, community types, and nature of substrate. *Sesarma biden* and *Sesarma intermedium* prefer to live in the mangrove areas of *Avecinnia - Excoecaria* forest types. *Scylla serrata* species prefer to live in muddy substrate in deep forest. The groups of *Uca* and *Gelesimus* species seem to have preference for high tide regions of the mangrove forest.

At present, an attempt has been made on the study of distribution and abundance of mangrove crabs along the Mon Coasts including Bilukyun, Tarokpi, Setse, Kaudut, Kalegauk and

* Dr, Associate professor, Department of Marine Science, Mawlamyine University

Zeephyuthaung. The aim of the present study is to know the distribution and abundance of mangrove crabs within the study areas.

Materials and Methods

The study of distribution and abundance of crabs was carried out along the mangrove areas of Mon coast from June 2012 to April 2017. Monthly field trips were conducted on six designated places where mangrove crabs are landed including Bilukyun (Sabelar) (Lat. 16° 14′N, Long. 97°32′ E), Setse (Lat. 15° 54′N, Long. 97°35′ E), Tarokpi(Lat. 15° 55′N, Long. 97°34′ E), Kaudut(Lat. 16° 29′N, Long. 97°23′ E), Kalegauk (Lat. 15° 31′N, Long. 97°51′ E) and Zeephyuthaung (Lat. 15° 11′N, Long. 97°47′ E). The locations of study areas were shown in Fig.1. The specimens were collected mainly by hand and locally made traps during day time in almost all the habitats within the mangrove and surrounding areas. The colorations, localities and date of collection of the crabs were noted immediately after they have been caught. All specimens were first preliminarily examined on the day of collection and then preserved in 10% formalin for further examination. Species identification was largely based on the F.A.O species identification sheets and some identification guide books. Diagnostic characters of the specimen followed after De Man (1888), Alcock (1896,1900), Chhapgar (1956), Sakai (1965), Barens (1967), Crane (1975), Motoh (1980), Carpenter and Niem (1998), Keenan (1998), Peter (2008) and Naser (2011) and some previous workers. Local name of the studied species was informed by the local fishermen.

Figure 1 Map showing the samples collected areas: Bilukyun (Sabelar); Setse; Tarokpi; Kaudut; Kalegauk and Zeephyuthaung

Results

A total of 24 species, 15 genera, 4 families belonging to order Decapoda under the class crustacea and the Phylum Arthropoda was recorded during the study period comprising 3 species of Portunidae, 12 species of Grapsidae, 8 species of Ocypodidae and 1 species of Dorippidae. The classified list of mangrove crab species was presented in Fig.2 and Table 1. The distribution and abundance of mangrove crabs was observed monthly at the six stations, namely, Bilukyun (Sabelar), Setse, Tarokpi, Kaudut,

Kalegauk and Zeephyuthaung within the study period. Kalegauk and Kaudut mangrove areas were represented as the most diverse crab species representing 24 species and followed by Zeephuthaung representing 17 species. Among the recorded species, *Dorippe dorsipes* and *Ocypoda sp.* were only observed in Kalegauk and Kaudut mangrove areas. The distribution of the crab species among the study areas were presented in Table 2.

Table 1 The Classified list of Brachyuran Crabs from the study areas of Mon Coast.

Phylum	Class	Order	Family	Genus	No.	Species
Arthropoda	Crustacea	Decapoda	Portunidae	*Scylla*	1	*Scylla serrata*
					2	*S. olivacea*
				Charybdis	3	*Charybdis riversandersoni*
			Grapsidae	*Metopograpsus*	4	*Metopograpsus messor*
				Grapsus	5	*Grapsus tenuicrustatus*
				Pachygrapsus	6	*Pachygrapsus minutus*
					7	*P. planifons*
				Pseudograpsus	8	*Pseudograpsus intermedia*
				Varuna	9	*Varuna littera*
				Metasesarma	10	*Metasesarma obesum*
				Sesarma	11	*Sesarma anderosorii*
					12	*S. bidens*
					13	*S.intermedium*
				Parasesarma	14	*Parasesarma plicatum*
				Metaplax	15	*Metaplax elegans*
			Dorippidae	*Dorippe*	16	*Dorippe dorsipes*
			Ocypodidae	*Ocypoda*	17	*Ocypoda sp.*
				Gelesimus	18	*Gelasimus annulipes*
					19	*G. niarionis var nitidus*
					20	*G. acutus*
					21	*G. dessumieri*
				Uca	22	*Uca chloropthalmus*
					23	*U. hesperiae*
					24	*U.tetragonon*

Table 2 Distribution of branchyuran crabs among study areas of Mon coast.

No.	Species	Bilukyun	Setse	Tarokpi	Kalegauk	Kaudut	Zeephyuthaung
1	*Scylla serrata*	+	+	+	+	+	+
2	*S. olivacea*	+	+	+	+	+	+
3	*Charybdis riversandersoni*	-	-	-	+	+	+
4	*Metopograpsus messor*	-	+	+	+	+	+
5	*Grapsus tenuicrustatus*	-	-	+	+	+	+
6	*Pachygrapsus minutus*	-	-	-	+	+	-
7	*P. planifons*	-	-	-	+	+	-
8	*Pseudograpsus intermedia*	-	-	-	+	+	-
9	*Varuna littera*	+	+	+	+	+	+
10	*Metasesarma obesum*	-	-	-	+	+	-
11	*Sesarma anderosorii*	+	+	+	+	+	+
12	*S. bidens*	+	+	+	+	+	+
13	*S.intermedium*	+	+	+	+	+	+
14	*Parasesarma plicatum*	-	-	-	+	+	-
15	*Metaplax elegans*	+	+	+	+	+	+
16	*Dorippe dorsipes*	-	-	-	+	+	-
17	*Ocypoda sp..*	-	-	-	+	+	-
18	*Gelasimus annulipes*	+	+	+	+	+	+
19	*G. niarionis var nitidus*	+	+	+	+	+	+
20	*G. acutus*	+	+	+	+	+	+
21	*G. dessumieri*	+	+	+	+	+	+
22	*Uca chloropthalmus*	+	+	+	+	+	+
23	*U. hesperiae*	+	+	+	+	+	+
24	*U. tetragonon*	+	+	+	+	+	+
	Total	**14**	**15**	**16**	**24**	**24**	**17**

Abbreviation; + present; - absent

Figure 2 Brachyuran crabs: a) *Scylla serrata*; b) *S. olivacea*; c) *Charibdis riversandersoni*; d) *Metopograpsus messor*;e) *Grapsus tenuicrustatus*; f) *Pachygrapsus minutus*; g) *P. planifons*; h) *Pseudograpsus intermedius*; i) *Varuna litterata*; j) *Metasesarma obesum*; k) *Sesarma anderosorii*; l) *S. bidens*; m) *S. intermedium*; n) *Parasesarma plicatum*; o) *Metaplax elegans*; p) *Dorippe dorsipes*; q) *Ocypoda sp.*; r) *G. annulipes*;s) *G. marionis var nitidus*; t**)** *G. acutus*; u) *Gelasimus dussumieri*; v) *Uca chlorophthalmus*; w**)** *Uca hesperiae*; x) *Uca tetragonon*.

Monthly occurrence of crab species in the study areas

Scylla serrata, S. olivacea and *Metaplax elegans* were collected in every month in all stations. Monthly occurrence of mangrove crabs was presented in Fig. 3.

In Bilukyun (Sabelar), *Scylla serrata, S. olivacea, Sesarma bidens, S. anderosorii* and *Metaplax elegans* were the most common species where as others species were frequently observed. The highest species number of crabs was found in February. The least number was found in December.

In Setse, *Scylla serrata, S. olivacea, Sesarma bidens, S. anderosorii, S. intermedium, Varuna littera* and *Metaplax elegans* species were collected in every month within the study period. *Uca* and *Gelesimus* species were recorded as the most abundance. The highest species number of crabs was found in April but smallest number in November.

In Tarokpi, *Scylla serrata, S. olivacea, S. anderosorii, Sesarma bidens, S.intermedian* and *Metaplax elegans* species were collected in every month within the study period. *Uca* and *Gelesimus* species were recorded as the most abundance species in observation. Other species are frequently observed. The highest species diversity of crabs was found in March and the lowest in April.

In Kalegauk, *Scylla serrata, S. olivacea, Sesarma bidens, S. intermedian, S. anderosori, Metaplax elegans* and *Gelasimus acutus* species were collected in every month within the study period. *Uca* and *Gelesimus* species were recorded as the most abundance species in observation. Other species are frequently observed. Among the collected species *Pachygrapsus planifons, P. minutes, Metopograpsus thukuhar, M. messor, Parasesarma plicatum, Dorippe dorsipes* and *Ocypoda sp.* were rarely observed. The highest species diversity of crabs was found in June and least amount in August.

In Kaudut, *Scylla serrata, S. olivacea, Sesarma bidens, S. anderosorii, S. intermedium, Varuna littera, Metaplax elegans* species were collected in every month within the study period. *Uca* and *Gelesimus* species were recorded as the most abundance species. Other species are frequently observed. Among the collected species, *Pachygrapsus planifons, Grapsus tenuicrustatus, Metopograpsus messor, Pseudograpsus intermedia, Parasesarma plicatum, Metasesarma obesum, Dorippe dorsipes and Ocypoda sp.* were rarely observed. The highest species of crabs was found in May and July. In the month of August, they were found in very few numbers.

In Zeephyuthaung *Scylla serrata, S. olivacea, Varuna littera* and *Metaplax elegans* species were collected in every month within the study period. *Uca* and *Gelesimus* species were recorded as the most abundance species. The predominated month of crab occurrence was in March, in contrast the least accounted number had been recorded in February.

Seasonal occurrence of crabs in study areas

Number of individual crabs with related to species were collected monthly and compared to determine their abundance seasonally at each study sites. (Fig. 4, Fig.5 and Table.3) The study revealed that the dominant numbers of crab species had been collected from Kalegauk and Kaudut. In Kalegauk equal number of crab species was observed in all three seasons (summer, wet and winter). In Kaudut, species dominance occurred in summer and equal numbers of crab species had been recorded in wet and winter. And also, dominant number of crabs had been found during summer months in Setse, Tarokpi and Zeephyuthaung, but in Bilukyun, equal numbers of crab species could be collected during summer and wet months.

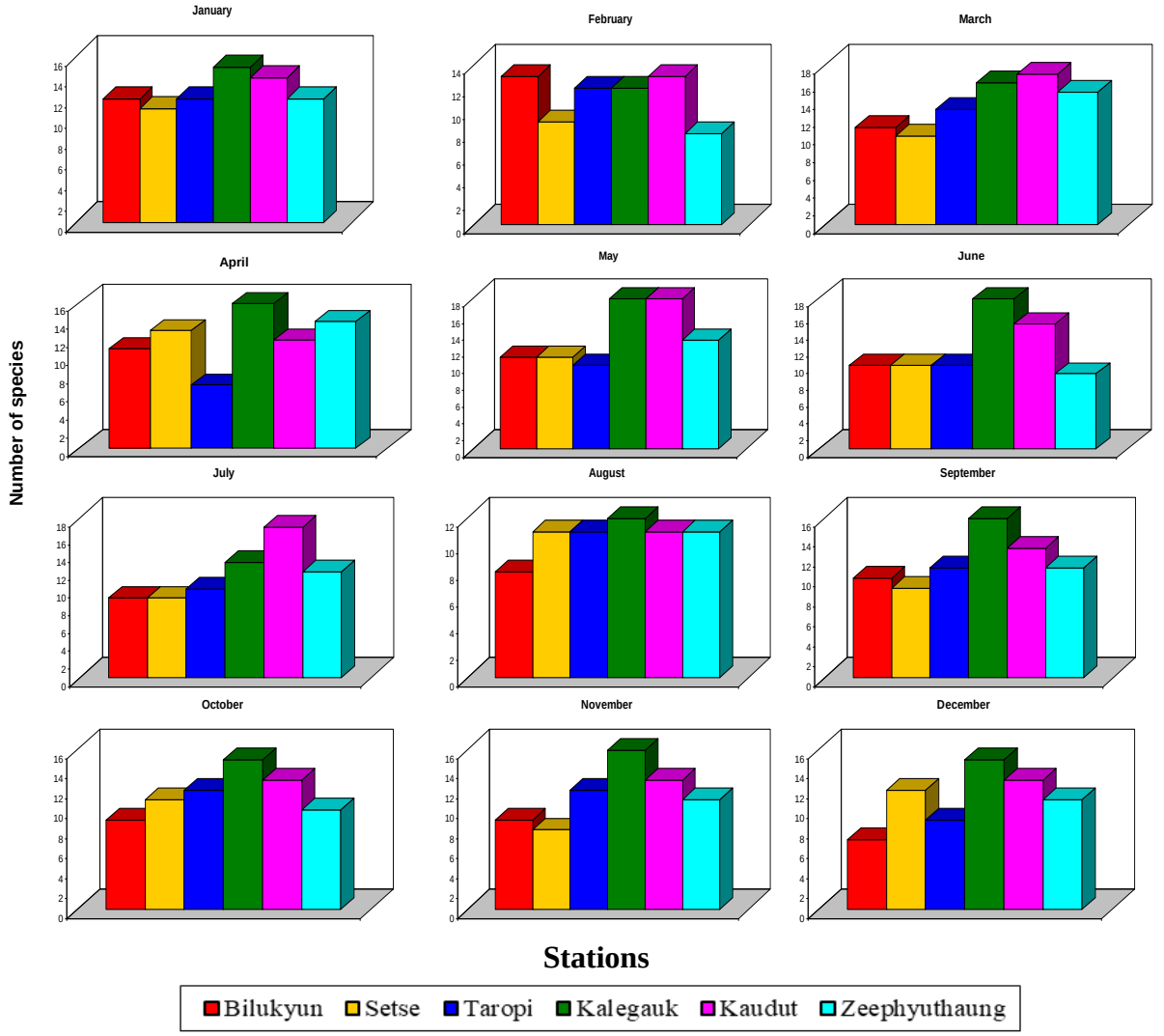

Figure 3 Monthly occurrence of crab species in the study areas of Mon Coast.

In relation to the seasonally dominant individual species, totalling 928 individuals and 14 species, belonging to 6 genera, under 3 families were recorded in Bilukyun station. Among these, 228 individuals, 456 individuals and 244 individuals were observed from summer, wet and winter, respectively. A total of 6 genera were recorded in summer and wet but in winter only 5 genera were recorded. Among the recorded species, *Varuna littera* was most abundance in summer and wet seasons. In winter, *Sesarma bidens* was occurred as dominant species.

In Setse, a total of 944 individuals and 15 species, belonging to 7 genera under 3 families were recorded. Among these, 192 individuals, 476 individuals and 276 individuals were recorded in summer, wet and winter respectively. During the study period, *Varuna littera* and *Sesarma intermedium n* were dominant during the summer months, *Sesarma bidens* was most abundance in wet season. In summer season, *Varuna littera* and *Metopograpsus messor* were dominated. In Tarokpi, a total of 1164 individuals, 16 species, belonging to 7 genera, under 3 families were recorded. Among those, 232 individuals, 520 individuals and 304 individuals were collected summer, wet and winter, respectively. During the study period, *Varuna littera* and *Sesarma intermedium n* were dominant in the summer months. In wet and winter season, *Sesarma intermedium n* was found dominance.

In Kalegauk, a total of 1960 individuals and 24 species belonging to 15 genera, under 4 families were recorded. Among those, 412 individual, 976 individuals and 580 individuals were collected in

Table 3 Seasonal composition of crab species from the study areas

Species	Bilukyun			Setse			Tarokpi			Kalegauk			Kaudut			Zeephyuthaung		
	Hot	Wet	Cool	Hot	Wet	Cool	Hot	Wet	Cool	Hot	Wet	Cool	Hot	Wet	Cool	Hot	Wet	Cool
Scylla alivacea	8	12	8	4	12	8	4	12	12	8	16	4	8	16	12	8	12	12
S. serrata	8	4	4	12	12	8	12	20	8	8	20	12	12	20	8	12	12	8
Charibdi riversandersoni	0	0	0	0	0	0	0	0	0	20	28	12	4	16	8	12	12	8
Metopograpsus messor	0	0	0	20	20	32	24	48	36	12	40	32	12	48	36	0	0	0
Grapsus tenuicrustatus	0	0	0	0	0	0	0	0	0	16	36	28	20	32	12	0	0	0
Pachygrapsus minutus	0	0	0	0	0	0	0	0	0	12	44	32	8	60	32	0	0	0
P. planifons	0	0	0	0	0	0	0	0	0	16	64	28	16	112	0	0	0	0
Pseudograpsus intermedia	0	0	0	0	0	0	0	0	0	16	52	0	8	28	20	0	0	0
Sesarma anderosorii	12	36	32	12	44	28	8	20	16	36	64	48	28	72	36	12	16	8
S. bidens	28	44	36	16	60	24	24	48	32	52	76	60	36	68	40	16	36	24
S.intermedium	12	32	24	24	44	28	28	60	40	32	48	44	16	40	24	20	32	28
Parasesarma plicatum	0	0	0	0	0	0	0	0	0	24	64	36	16	0	24	8	32	12
Metasesarma obesum	0	0	0	0	0	0	0	0	0	0	56	24	20	48	24	0	0	0
Varuna littera	44	72	0	24	44	32	28	60	36	44	84	36	24	52	28	32	44	36
Dorippe dorsipes	0	0	0	0	0	0	0	0	0	0	0	12	0	56	20	0	0	0
Ocypoda sp.	0	0	0	0	0	0	0	0	0	12	0	0	36	20	0	0	0	0
Metaplax elegans	20	28	16	12	32	24	16	44	24	20	44	28	24	48	36	12	36	20
Gelasimus acutus	12	32	20	16	36	24	8	40	24	12	44	20	12	36	20	8	24	16
G. annulipes	8	20	0	0	28	16	12	36	16	8	32	24	8	44	12	32	56	0
G. dessumieri	20	32	12	12	32	16	12	24	12	12	24	16	20	48	28	12	40	24
G. niarionis var nitidus	16	28	20	12	24	20	8	28	16	12	36	28	12	32	24	8	40	28
Uca chloropthalmus	12	36	20	8	44	16	12	44	16	8	44	20	12	0	12	16	0	0
Uca hesperiae	12	44	32	8	0	0	12	36	16	12	24	12	16	32	24	12	0	24
Uca tetragonon	16	36	20	12	44	0	24	0	0	20	36	24	12	44	16	0	32	20
Total number of crabs	228	456	244	192	476	276	232	520	304	412	976	580	380	972	496	220	422	286
Total number of species	14	14	12	15	14	13	16	15	15	22	22	22	23	22	22	15	14	14
Total number of genera	6	6	5	7	7	7	8	7	7	13	13	13	14	14	14	7	7	7
Total number of families	3	3	3	3	3	3	3	3	3	3	3	4	3	4	4	3	3	3

summer, wet and winter, respectively. According to genera, 13 genera were recorded in summer and winter periods but in wet season 14 genera were recorded. *Sesarma bidens* was the most abundant species in winter and summer season. The dominant species during the wet season was *Varuna littera*. In Kaudut, a total of 1848 individuals and 24 species belonging to 15 genera under 4 families were recorded. Among those, 380 individuals, 972 individuals and 496 individuals were recorded during summer, wet and winter, respectively. *Sesarma bidens* was the most abundant species in the winter and summer season. In the wet season, *Pachygrapsus planifons* was the most abundant speies. In Zeephyuthaung, a total of 928 individuals and 15 species belonging to 7 genera under 3 families were recorded. Among those, 220 individuals, 422 individuals and 286 individuals were recorded summer, wet and winter, respectively. In summer, *Varuna littera* and *Gelasimus annulipes* were dominant and only *Gelasimus annulipes* was the most abundant species during the wet season and only *Varuna littera* was the most abundant in the winter months.

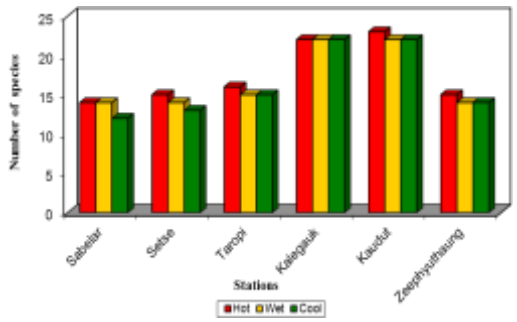

Figure 4 Stations wise seasonal occurrence of crab species.

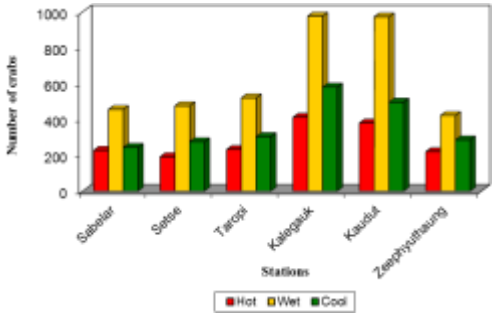

Figure 5 Stations wise seasonal occurrence of total crabs.

Discussion

During the study period, a total of 24 species, 15 genera under 4 families could be collected. Of all the collected species of crabs, 3 species such as *Scylla serrata*, *Scylla olivacea* and *Charybdis riverandersonii* were included under the family Portunidae, 12 species, *Metopograpsus messor*, *Grapsus tenuicrustatus*, *Pachygrapsus minutes*, *P. planifons*, *Pseudograpsus intermedia*, *Varuna littera*, *Metasesarma obesum*, *Sesarma anderosorii*, *S. bidens*, *S.intermedium* and *Parasesarma plicatum*, *Metaplax elegans* were included in the family Grapsidae; and 8 species, *Ocypoda sp.*, *Gelasimus annulipes*, *G. niarionis var nitidus*, *G. acutus*, *G. dessumieri*, *Uca chloropthalmus*, *Uca hesperiae* and *Uca tetragonon*were in the family Ocypodidae; and the only one species, *Dorippe dorsipes* was included in the family Dorippidae. Alcock (1896) mentioned that the common mud species of *S. serrata, and S. olivacea* had been recorded from Myanmar coastal waters. In the present study these two species were also recoded. Chhapgar (1956) recorded that one of the Potunid crab, *Charybdis annulata*, was collected by Myanmar coastal waters particular in the mangrove region and rocky shore. It was observed that Sesarmid crabs were the most abundance in the muddy substrate of mangrove regions apart from Potunid crabs. The genus *Charybdis* as mentioned by Alcock (1900) included six species *namely Charybdis orientalis, C. merguiensis, C. affanis, C.rosrom, C. ornata* and *C. hoplites*. According to Sandar Win (1997) three species were recorded from Mon State. Among the recorded crab species, the species *Charybdi. river andersori* was recorded from Zeephyuthaung, Kalegauk, Kaudut areas. According to Alcock (1896), the genus *Metopograpsus* included two species such as *M. messor* and *M. maculatus* which has been recorded from Myanmar Coastal Waters. Khin Khin Than (1986) has been studied one species, *M. latifrons* from Myanmar Coastal Waters and Khin Mar Wai (1995) recorded three species such as *M. messor, M. latifrons* and *M. maculatus* from Rakhine Coastal Area. Sandar Win (1997) recorded *M. messor* from Mon Coastal area. Only one species of genus

Metopograpsus, *M. messor* was recorded from Setse, Tarokpi, Kalegauk, Kaudut and Zeephyuthaung areas.

Another common mangrove Sesarmid crabs is the genus Grapsus. Most of the Grapsid crabs are resident in the mangrove region and they have bright and distinct color. The genus Grapsus was recorded by Alock (1900) included one species *G. strigosus* which had been recorded from Myanmar coastal waters. Khin Khin Than (1986) and Thida Soe (2014) also recorded *G. strigosus* from Myanmar coastal waters and Chaungtha areas. According to Zin Moh Moh Tun (2014) included two *species G. albolineatus and G. tenuicrustatus* which had been recorded in Ye coastal areas. According to Zin Moh Moh Tun (2014) included two species *Grapsus albolineatus* and *G. tenuicrustatus* which had been recorded in Ye coastal areas. In the present study *Grapsus tenuicrustatus* was recorded from Tarokpi, Kalegauk, Kaudut and Zeephyuthaung study areas. The genus *Pachygrapsus* discovered by Alcock (1896) included one species *P. minutus* which has been recorded from Myanmar Coastal Waters. Bronchard (2011) discovered three species**,** *P. minutus, P. planiforns* and *P. plicatus* from Mayotte region. In the present study two species, *P. minutus* and *P. planiforns* are recorded from Kalegauk and Kaudut.

No species of the genus *Varuna* had been recorded from Myanmar coastal waters in the record of Alcock (1968). But the species *Varuna littera* had been recorded by Sandar win (1997) from Mon coastal area. Thida Soe (2014) recorded this species from Chaungtha and Zin Moh Moh Tun (2014) also recorded *Varuna littera* from and Ye coastal area. In the present study the species *Varuna littera* also recorded from all stations. The genus *Metasesarma* discovered by Alcock (1896) included one species *M. rousseauxii* which had been recorded from Myanmar Coastal Waters. Khin Mar Wai (1994) also found this species from Rakhine coast. Bronchard (2011) discovered *M. obesum* from Mayotte region. In the present study *M. obesum* was recorded from Kalegauk and Kaudut. The genus *Parasesarma* mentioned by Bronchard (2011) discovered *P. plicatum* from Mayotte region. In the present study *P. plicatum* was collected from Kalegauk and Kaudut. Alcock (1900) recorded six species of genus *Sesarma* such as *S. pictum*, *S. taeniolatum*, *S. edwardsi*, *S. andesoni* and *S. pilotum* under the genus *Sesarma* from Myanmar coastal waters. In the present study, the three species *S. bidens, S. intermedian* and *S. anderosori* were recorded from all stations. The genus *Metaplax* discovered by Thet Su Mar (2010) included three species *Metaplax dentipes*, *M. elegans* and *M. distinct* which had been recorded from Ayeyawady Delta. In the present study only one species *Metaplax elegans* was recorded from Kalegauk and Kaudut. Alcock (1900) recorded five species of *Dorippe* including *D. dorsipes*, *D. astute*, *D. facchino*, *D. granulate* and *D. polota* from Myanmar coastal waters. In the present study, *D. dorsipes* was recorded from Kalegauk and Kaudut mangrove.

The genus *Ocypoda* recorded by Alcock (1900) included one species *O. cordimana* which had been recorded from Myanmar coastal waters. *O. certopthalma* had been recorded by Khin Khin Than (1986) and Khin Mar Wai (1995). *O. certopthalma, O. stimposon* and *O. roundata* were recorded by San San Lwin (1986) from Chaungtha area. Sandar Win (1997) recorded three species such *as O. certopthalma, O. cordimanus, O. roundata and O. stimpsoni* were recorded from Mon coastal area. Thida Soe (2014) also discovered three species: *O. certophthalma, O. cordimanus, O. stimposon* from Chaungtha coastal areas. Moreover, Zin Moh Moh Tun (2014) also recorded *O. certopthalma* from Ye coastal areas. In the present study *Ocypoda* sp. was recorded from Kalegauk and Kaudut. The genus *Gelasimus* included.

Alcock (1896) recorded three spceis namely, *G. annulipes, G. acutus and G. dussumieri* and Chhapgar (1956) recorded one species of *G. marionis var nitidus*. The genus *Gelasimus*, Khin Khin Than (1986) recorded four species such as *G. lacteal, G. annulipes, G. marionisnitidus* and *G. marionis* from Myanmar coastal waters. In the present study, the above mentioned four species were collected from all stations.

The genus *Uca* mentioned by Bronchard (2011) also included six species, *U. annulipes*, *U. inversa*, *U. hesperiae*, *U. tetragonon*, *U. chlorophthalmus* and *U. urvillie* were collected from Mayotte region. Thida Soe (2014) also discovered three species *G. annulipes*, *G. tetragonan* and *G. marionis* from Chaungtha coastal areas. In the present study *U. chlorophthalmus*, *U. hesperiae* and *U. tetragonon* were collected from all stations. According to the distribution and occurrence of collected species, it was recorded that 14 species under 3 families from Bilukyun (Sabelar); 15 species under 3 families from Setse; 16 species under 3 families from Tarokpi; 24 species under 4 families from Kalegauk and Kaudut and 17 species under 3 families from Zeephyuthaung.

Khin Khin Than (1986) oberserved 66 species 10 families (Calappidae, Leucosidae, Maiidae, Parthenopidae, Portunidae, Xanthidae, Pinnotheridae, Grapsidae and Ocypodidae) from Myanmar coastal waters. Sanda Win (1997) recorded 29 species under 7 families (Calappidae, Parthenopidae, Portunidae, Xanthidae, Ocypodidae, Grapsidae and Potomonidae) from Setse coastal areas. Thet Su Mar (2010) observed 27 species 3 families (Portunidae, Grapsidae and Ocypodidae from the Pyindaye reserved forest, Ayeyarwaddy Delta. Myint Myint Aye (2013) recorded 24 species under 7 families (Dorippidae, Calappidae, Portunidae, Xanthidae, Geocarcinidae, Ocypodidae and Grapsidae) from U-TO creek Chaungtha coastal area. Thida Soe (2014) recorded 65 species 14 families (Dromiidae, Dorippidae, Leucosidae, Calappidae, Majidae, Pisidae, Parthenopidae, Portunidae, Xanthidae, Galenidae, Goneplacidae, Ocypodidae, Grapsidae and Porcellanidae) from Chaungtha coastal areas. And also, Zin Moh Moh Tun (2014) recorded 34 species 9 families of brachyuran crabs (Portunidae, Xanthidae, Calappidae, Ocypodidae, Xenophthalmidae, Dotillidae, Parthenopidae, Ozidae and Grapsidae) from Ye coastal area. In the present study, 24 species of brachyuran crabs under 4 families (Portunidae, Grapside, Ocypodidae and Dorippidae) were recorded.

Among the study area, Kalegauk and Kaudut mangrove region were recorded as the most diverse species areas and are followed by Zeephyuthaung. Accordance to the crab families' occurrence, the family Ocypodidae were represented as the most abundance group in Bilukyun (Sabelar), Setse and Zeephyuthaung. Whereas the family Grapsidae dominated in Kaudut and Kalegauk and the family Grapsidae and Ocypodidae were found abundantly in Tarokpi. As record the monthly occurrence of mangrove crabs among study areas in Mon, the most common species in Bilukyun (Sabelar) area were *Scylla serata*, *S. olivacea*, *Sesarma bidens*, *Sesarma anderosorii* and *Metaplax elegans*. The predominant period of those species was February. The common species found in Setse area were *Scylla serata*, *Scylla olivacea*, *Sesarma bidens*, *Sesarma anderosorii*, *Varuna littera* and *Metaplax elegans*. All those species were found throughout the year and the highest occurrence of them was in April. The common species found in Tarokpi were *Scylla serata*, *S. olivacea*, *Sesarma bidens*, *Sesarma anderosorii* and *Metaplax elegans*. The highest abundance period was in March. In Kalegauk, *Scylla serata*, *S. olivacea*, *Sesarma bidens*, *Sesarma anderosorii*, *Metaplax elegans* and *Gelasimus acutus* were common species and the highest abundance period of these species was noticed in June. In Kaudut, *Scylla serata*, *Scylla olivacea*, *Sesarma bidens*, *Sesarma anderosorii*, *Varuna littera* and *Metaplax elegans* were common species and peaked in May. The common species found in Zeephyuthaung were *Scylla serrata*, *S. olivacea*, *Varuna littera* and *Metaplax elegans*. The highest abundant period was in March. This result showed that two species under genus *Scylla* had been observed in all study areas and it may be said that these two species have a wide range in distribution.

In the observation of seasonal occurrence of collected species in Mon study areas, the crab species abundantly occurred during wet months. In Bilukyun area, the dominant species during summer and wet months was *Varuna littera* and *dominant* species in winter months was *Sesarma bidens*. In Setse, the dominant periods of crabs were found during wet season and the dominant species of this period was *Sesarma bidens*. *Sesarma intermedium n* dominated during summer time, and *Metopograpsus messor* in winter months. *Varuna littera* was found in abundance both during

summer and winter months. In Tarokpi, the most dominant period of crab species was noticed in wet months. The dominat species observed in summer months were *Varuna littera* and *Sesarma intermedium n* which were found throughout the wet and winter months. For the remaining three study areas in Mon, the period dominated by crab species had also been noticed during wet months and the most common species in that season were *Varuna littera* in Kalegauk, *Pachygrapsus planifons* in Kaudut, *Gelasimus annulipes* in Zeephyuthaung. According to these results, it may be considered that wet season was regarded as the most abundant periods of crab species. Recording to seasonal occurrence of crabs, Thet Su Mar (2010) observed 8 genera (*Scylla*, *Episesarma*, *Sesarma*, *Metaplax*, *Metopograpsus*, *Clistocoeloma*, *Varuna*, *Ilyoplex* and *Gelasimus*) in the hot, wet and cool season respectively from the Pyindaye reserved forest, Ayeyarwaddy Delta.

In the present study, especially in Bilukyun (Sabelar) station, 6 genera (*Scylla*, *Sesarma*, *Varuna*, *Metaplax*, *Gelesimus* and *Uca*) were recorded in hot and wet season and 5 genera (*Scylla*, *Sesarma*, *Metaplax*, *Gelesimus* and *Uca*) were recorded in the cool season. In Setes station, 7 genera (*Scylla*, *Grapsus*, *Sesarma*, *Varuna*, *Metaplax*, *Gelesimus* and *Uca*) were observed in dry, wet and cool seasons. In Tarokpi station, 8 genera (*Scylla*, *Metopograpsus*, *Grapsus*, *Sesarma*, *Varuna*, *Metaplax*, *Gelesimus* and *Uca*) in hot season and 7 genera (*Scylla*, *Metopograpsus*, *Sesarma*, *Varuna*, *Metaplax*, *Gelesimus* and *Uca*) were recorded in wet and cool seasons. In Kalegauk station, during hot, 13 genera (*Scylla*, *Charybdis*, *Metopograpsus*, *Grapsus*, *Pachygrapsus*, *Pseudograpsus*, *Varuna*, *Sesarma*, *Parasesanna*, *Metaplax*, *Ocypoda*, *Gelesimus*, *Uca*) were recorded and also (*Scylla*, *Charybdis*, *Metopo grapsus*, *Grapsus*, *Pachygrapsus*, *Varuna*, *Metasesarma*, *Sesarma*, *Parasesanna*, *Metaplax*, *Dorippe*, *Gelesimus*, *Uca*) were recorded in wet and cool seasons. In Kaudut station, during hot season (*Scylla*, *Charybdis*, *Metopograpsus*, *Grapsus*, *Pachygrapsus*, *Pseudograpsus*, *Varuna*, *Metasesarma*, *Sesarma*, *Parasesarma*, *Metaplax*, *Ocypoda*, *Gelesimus*, *Uca*); in wet season (*Scylla*, *Charybdis*, *Metopograpsus*, *Grapsus*, *Pachygrapsus*, *Pseudograpsus*, *Varuna*, *Metasesarma*, *Sesarma*, *Metaplax*, *Dorippe*, *Ocypoda*, *Gelesimus*, *Uca*); in cool season (*Scylla*, *Charybdis*, *Metopograpsus*, *Grapsus*, *Pachygrapsus*, *Pseudograpsus*, *Varuna*, *Metasesarma*, *Sesarma*, *Parasesanna*, *Metaplax*, *Dorippe*, *Gelesimus*, *Uca*) were recorded. In Zeephyuthaung station, 7 genera (*Scylla*, *Charybdis*, *Varuna*, *Sesarma*, *Metaplax*, *Gelesimus*, *Uca*) were recorded in hot, wet and cool seasons.

Conclusion

Among the recorded species, the genus *Scylla* particular *Scylla serrata* and *S. olivaceae* species are the most economically important species for both exports and local consumption. It is seemed to be suggested that the most abundantly occurrence of these crabs was between Decembers to March according to the monthly distribution data from the study areas within the study period. Among the study areas, Kalegauk and Kaudut mangrove region were represented as the highest diversity of crabs, however, Bilukyun (Sabelar) and Setse areas a smaller number of crab species were recorded.

Acknowledgements

Special thanks go to Rector and Pro-rectors of Mawlamyine University for encourage to do the research and complete the work. My deepest thanks are due to Dr. Soe Pa Pa Kyaw, Professor & Head of Marine Science Department, Mawlamyine University, for his kind guidance, constant encouragement and permitting me to continue and complete this work. Finally, I would like to thank my beloved family for their encouragement and providing various supports during this work.

References

Alcock, A. (1896-1900). *Materials for a Carcinological Fauna of India.* Wheldon& Wesley ltd. Stechert-hafner service agency, inc.codicote, herts.New York.

Barnes, R. S. K. (1967). *Studies on the Australasian species of the genus Macropthalmus and of other related genera (Crustacea: Brachyura)*. University of Queensland.

Bouchard, J. M. (2011). Land, Mangrove and Freshwater Decapoda Crustaceans of Mayotte Region (Crustacean Decapoda). *National museum of natural history Smithsonian Institution Washington D.C, U.S.A.* no**.** xxx, pp. 1-96.

Carpenter, K. E and Niem, V. H. (1998). *The living marine resources of the Western Central Pacific.* Food and agriculture organization of the United Nations Rome.

Chhapgar, B. F. (1956). On the Marine Crabs (Decapoda: Brachyura) of Bombay State. *Journal Bombay Natural Hist. Society*. vol. 54. part I, no.2, pp. 399-439.

Crane, J. (1975). *Fiddler crabs of the world Ocypodidae: Genus Uca*. Princeton University Press, Princeton, New Jersey.

De Man. (1888). Report on the Podophthalmous Crustacean of the Myeik Archipelago. *Journal of the Linnaean Society*. vol. XXII, part 5, pp.1-305.

Keenan, P. (1998). A revision of the genus *Scylla* De Haan, 1833 (Crustacea: Decapoda: Brachyura: Portunidae). *National University of Singapore*. vol. 46, no. 1, pp. 217-245.

Khin Khin Than. (1986). *Taxonomy and distribution of Myanmar marine crabs (Decapoda; Brachyura)*. M.Sc. Thesis. Department of Zoology, University of Yangon. (Unpublished).

Khin Mar Wai. (1995). *The taxonomic study of crabs in Gwa Area.* M.Sc. Thesis. Department of Zoology, University of Yangon. (Unpublished).

Motoh, H. (1980). *Field guide for the edible crustacean of the Philippines Southeast Asia Fisheries Development Centre (SEAFDEC).* Iloilo, Philippines.

Myint Myint Aye. (2013). *Occurrence of crab species in mangrove area of U-To creek, Chaungtha, Pathein Township, Ayeyawady Region.* PhD Thesis. Department of Zoology, Yangon University, Yangon, Myanmar. (Unpublished).

Naser, D. M. (2011). The Sesarmid crab *Parasesarma pericum* Naderloo and Schubart, 2010 (Crustacea: Decapoda: Brachyura: Sesarmidae), New to the Iraqi Coastal Waters of Khor Al-Zubair and Shatt Al-Basrah Canal, Basrah, Iraq. *Department of marine biology, Marine Science Centre, University of Basrah, Basrah, Iraq*. vol.4, no. 3, pp.185-190.

Peter, K. L. (2008). Systema Brachyurum: Part 1. An annotated checklist of extent Brachyuran crabs of the world. *The Raffles Bulletin of Zoology, National University of Singapore*, vol.17, pp.1-286.

Sakai, T. (1965). *The crabs of Sagami Bay.* East West Center-Press Honolulu. Maruzen Co., ltd., New York.

San San Lwin. (1986). *A Taxonomic study of marine crabs of Chaungtha area.* M.Sc. Thesis. Department of Zoology, Yangon University, Yangon, Myanmar. (Unpublished).

Sandar Win. (1997). *The Taxonomic study of some crabs in Mon State*. M.Sc. Thesis. Department of Zoology, Mawlamyine University, Mawlamyine, Myanmar. (Unpublished).

Thet Su Mar. (2010). *Community structure of brachyuran crab species in mangrove area of Pyindaye Forest, Ayeyarwaddy Delta.* PhD Thesis. Department of Zoology, Yangon University, Yangon, Myanmar. (Unpublished).

Thida Soe. (2014). *Diversity of crabs along Chaungtha coastal area with emphasis on habitat preference of Ocypoda ceratophthalma (Phallus,1772).* PhD Thesis. Department of Zoology, Yangon University, Yangon, Myanmar. (Unpublished).

Zin Moh Moh Tun. (2014). *A study on the Branchyura crabs in Ye coastal areas, Mon State.* M.Sc Thesis, Department of Marine Science Mawlayine University, Mawlamyine. (Unpublished)

STOMACH CONTENT ANALYSIS OF SILVER POMFRET FROM MON COASTAL AREA

Zarni Ko Ko*

Abstract

Stomach content analysis of the silver pomfret, *Pampus argenteus* was examined from March 2019 to February 2020. A detail investigation of food items of the *P. argenteus* was undertaken from Mon Coastal Areas. Copepods were the main food item in the diet of *P. argenteus* followed by the other zooplankton and crustacean appendages. The fish was a carnivore feeding mainly on zooplanktonic organisms while phytoplankton was a minor part of the diet. The semi-digested food was highly macerated and pulpy. Empty stomachs appear in very high percentages within study period. The highest value of gastrosomatic index (GaSI) was observed in February (4.09±1.22) and lowest in November (1.41±0.2) with an annual average of 2.15±0.9. The highest level of vacuity index (VI) was observed in pre-monsson and the lowest in post-monsoon with an annual value was 67%.

Keywords: *P. argenteus*, food content analysis, feeding intensity, gastrosomatic index, vacuity index, Mon Coastal Area.

Introduction

Food is one of the essential requisites of living beings in nature for persistence of their vital needs viz., growth and reproduction for survival and thus maintain their kind. The importance of the knowledge of food and feeding habits of a fish in understanding its biology has been well established. Some times the rate of feeding has an influence the spawning rate of fish. The nature of food composition of a fish species will also throw light on the possible habits it frequents.

Fishes directly depend upon their surrounding aquatic environment for their food requirements and are highly adapted in their food and feeding habits, utilizing most of the readily available food. Studies on the food and feeding habits, an important aspect in the biology of fishes, have shown that the requirements at different stages in their life cycle differ with space and time (Krishna, *et. al.*, 2016).

In general, the growth of a fish is influenced by the quality and quantity of food materials available and consumed. Thus, any variation in quality and quantity of food materials will affect the growth rate of the fish. The qualitative and quantitative variations of natural food materials in a water body are under the influence of several abiotic and biotic factors. These variations could be known by qualitative and quantitative analysis of gut contents of a fish and/or by the estimation of gastrosomatic index (Lalit *et. al.*, 2015).

The study of food and feeding habits of fish attracted the attention of fishery biologists from the beginning of the present century in view of the recognized importance of food and feeding habits as an environmental factor influencing the growth and distribution of fishes and success of their fishery. Therefore, knowledge of the food and feeding habits of various fishes is advantageous in their proper management and exploitation (Qasim, 1973).

There were several investigations that mentioned the feeding biology of the silver pomfret from abroad. There was no information on detail feeding biology of silver pomfret from Mon Coastal Area except some taxonomic information and some biological measures of pomfret fish from Mon Coastal Area.

The objectives of this study are; 1) to identify the food items and to determine the percentage of prey items in the diet of *Pampus argenteus*, 2) to estimate the feeding intensity of

* Lecturer, Department of Marine Science, Mawlamyine University

P. argenteus from Mon Coastal Area and 3) to investigate Gastrosomatic index and Vacuity Index of *P. argenteus* from Mon Coastal Area.

Materials and Methods

Sample Collection Sites

The samples of silver pomfret, *Pampus argenteus* were collected from Kyaikkhami fish landing centre (16°05'N and 97°34'E) and Asin fish landing centre (15˙19′ N and 97˙76′ E) of Mon Coastal Area from March 2019 to February 2020 (June 2019 to August 2019 was closing season).

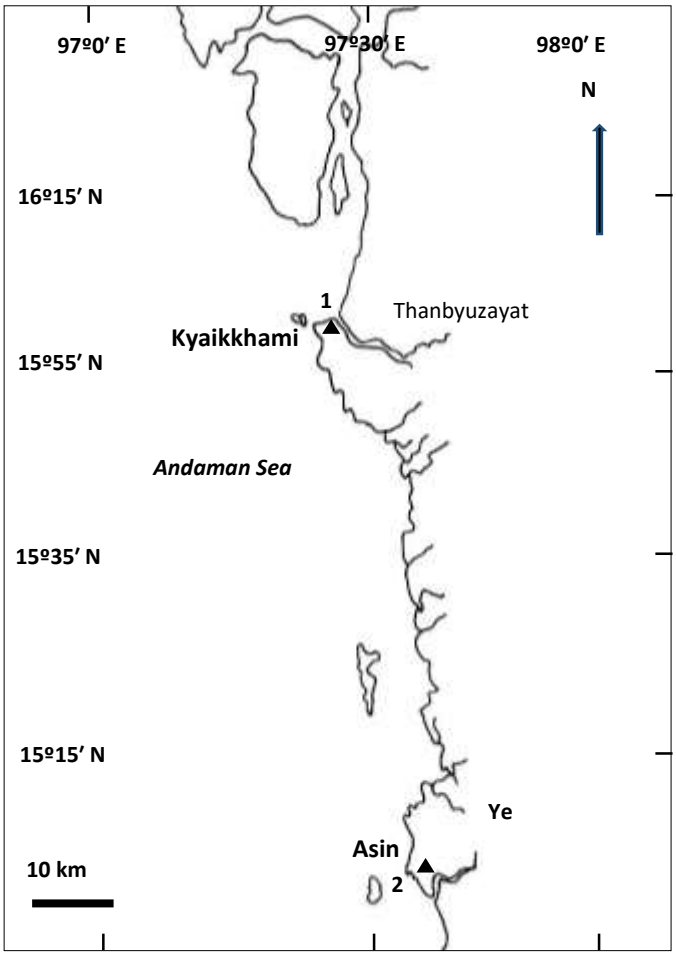

Figure 1 Map showing the fish landing centers during the present study.

Gastro-Somatic Index (GaSI)

The specimens collected were properly cleaned in the laboratory, dissected and the stomachs were removed. The total weight of the stomach with its contents was measured to the nearest 0.01 g. The contents of stomach and foregut were examined under a microscope and further identification within each taxonomic group was done following appropriate taxonomic identification guides. Gastro-Somatic Index **(**GaSI) based on monthly and seasonal calculation was obtained as described by Biswas (1993):

GaSI = (Total weight of stomach / Bodyweight) × 100

Stomach contents are analyzed both qualitatively and quantitatively. The volume of food in each gut of fish was measured and various food items are identified. The food content found in the stomach was divided into four groups.

1. Full : Stomach was full with food

2. ½ Full : Stomach was ½ full and slightly distended

3. ¼ Full : Stomach was ¼ food

4. Empty : Stomach without food

Point's method: The degree of apparent fullness of the stomach was determined and point's was assigned. Gorged (1.25), Full (1.00), ½ Full (0.50), ¼ Full (0.25), Empty (0.00) (as cited in Khrisha, *et al.*,, 2016).

Vacuity Index (VI)

Vacuity Index or the stomach emptiness index determines the amount of fish appetite for food. VI was calculated using the equation given by Euzen, 1987 (as cited in Norouzi, *et al.*, 2012).

VI= (The number of empty stomachs / total number of the stomachs examined) × 100.

The intensity of feeding as indicated by the VI is interpreted as:

- Edacious species $0 \leq VI \leq 20$
- Relatively edacious species $20 \leq VI \leq 40$
- Moderate feeder $40 \leq VI \leq 60$
- Relatively abstemious $60 \leq VI \leq 80$
- Abstemious $80 \leq VI \leq 100$

Results

In the present study, the stomach contents of *Pampus argenteus* were conducted by using during the number and occurrence methods. A total of 296 specimens of *P. argenteus* were collected during March 2019 to February 2020 except closing reason (June, July and August). The stomach contents found in *P. aegenteus* were grouped into nine categories, namely; copepod, other zooplankton, crustacean appendages, molluscan larvae, fish scales, small fish, diatoms, algal filaments and semi-digested pulp. The stomachs of fish contained largely quantities of whitish pulp semi-digested matter and copepod dominated in the diet of *P. argenteus* during present study period.

Copepods were found to be an important food items which occurred throughout the different months. Contribution of copepod as food for the fish was highest in the months of February (19.22%); followed by November (18.12%). The lowest value was in the month of September (5.88%). Other zooplankton was found commonly in the stomachs with peaks in the months of February (4.85%) and November (3.29%). The low percentage was in January (1.14%). The months of March to October was not recorded in the stomachs during present study. Crustacean appendages were also found commonly with the maximum percentage in number (5.88%) in September and the minimum number (0.22%) in February. The remaining zooplanktons were encountered in small quantities in diet and found occasionally. Molluscan larvae and algal filaments were found in the stomach of *P. argenteus* only in February and small fish was only found in September. Diatomss were occurred in small amount of percentage in the months of December (0.85%), January (0.72%) and February (0.45%). Fish scales were recorded in the

stomach in September and October but formed the largest portion (35.3% and 33.33%) among all food items in both months. The sizes of scales were very small. So, these scales may belong to different species of fish. Among food items, copepod was the most abundant with the percentage (13.46%) followed by fish scales (10.77%), other zooplankton (1.86%) and crustacean appendages (1.26%) (Table 1 and Figure 2).

According to the natural stomach condition, fishes were categorized as high feeding (full), moderate feeding (¾ and ½ full), low feeding (¼ full) and empty. Monthly fluctuations were also witnessed in the presence of occurrence of stomachs with different degrees of fullness. It is evident that higher percentage of empty of the stomach was recorded in the months of March to May and lowest percentage in the October. The lowest percentage was due to non-availability of food organisms.

In this study, percentage of high feeding was in the months of November (7.69%) followed by February (16.67%). In moderate feeding category, the highest percentage (16.67%) was recorded in September followed by November (11.54%), January (11.43%) and February (11.11%). Low feeding was observed to be more in December (38.09%) followed by January (37.14%), September (36.66) and November (34.62%). The occurrence of fishes with empty stomach was recorded during most of the months. The highest percentage (100%) of empty stomach was in the months of March, April and May and the lowest percentage of empty stomach was in the month of February (38.89%) (Table 2 and Figure 3).

Monthwise Gastro-somatic index (GaSI) of *P. argenteus* ranged from 1.41 to 4.09 and fluctuated over months. The lowest value (1.41±0.2) was found in November while the highest value (4.09±1.22) was in February (Table 3 and Figure 4). Lengthwise GaSI values for *P. argenteus* were not significantly differed with the range between 1.3 and 3.35. The maximum value was recorded in 10.0-12.9cm length group and the minimum value was found in 19.0-21.9cm length group (Table 4 and Figure 5).

The results of vacuity index (VI) showed random monthly variation in the values. The percentage range of VI was from 39% to 100%. The most abstemious fish ($80 \leq VI \leq 100$) were found in the months March, April and May. And then the relatively abstemious fishes were found in October ($60 \leq VI \leq 80$) while the moderate feeder fishes were in months of September, November, December and January ($40 \leq VI \leq 60$). Moreover, the relatively edacious fish was observed in February ($20 \leq VI \leq 40$) (Table 3 and Figure 6).

Table 1 Monthwise percentage of food composition in *Pampus argenteus* from March 2019 to February 2020.

	Months								
Food Items	**Mar. 2019**	**Apr.**	**May**	**Sept.**	**Oct.**	**Nov.**	**Dec.**	**Jan. 2020**	**Feb.**
Copepod	-	-	-	5.88	11.11	18.12	16.84	15.35	19.22
Other zooplankton	-	-	-	-	-	3.29	2.7	1.14	4.85
Crustacean appendages	-	-	-	5.88	-	1.32	-	0.66	0.22
Molluscan larvae	-	-	-	-	-	-	-	-	0.33
Fish scales	-	-	-	35.3	33.33	-	0.63	-	-
Small fish	-	-	-	5.88	-	-	-	-	-
Diatoms	-	-	-	-	-	-	0.85	0.72	0.45
Algal filaments	-	-	-	-	-	-	-	-	0.15
Semi-digested pulp	-	-	-	70.10	75.45	77.27	78.98	82.13	74.78

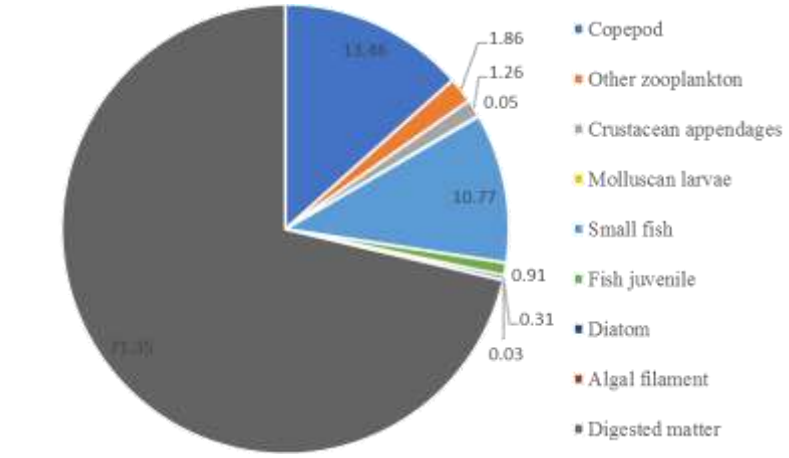

Figure 2 Percentage composition of food items in stomach of *Pampus argentus* from March 2019 to February 2020

Table 2 Monthwise percentage of feeding intensity in *Pampus argenteus* from March 2019 to February 2020.

Months	**March (2019)**	**April**	**May**	**Sept.**	**Oct.**	**Nov**	**Dec**	**Jan (2020)**	**Feb**
	n=34	n=31	n=30	n=30	n=32	n=26	n=42	n=35	n=36
Empty	100	100	100	46.67	75	46.15	52.38	45.71	38.89
¼ full				36.66	25	34.62	38.09	37.14	33.33
½ full				16.67		11.54		11.43	11.11
¾ full							9.53	5.72	
full						7.69			16.67

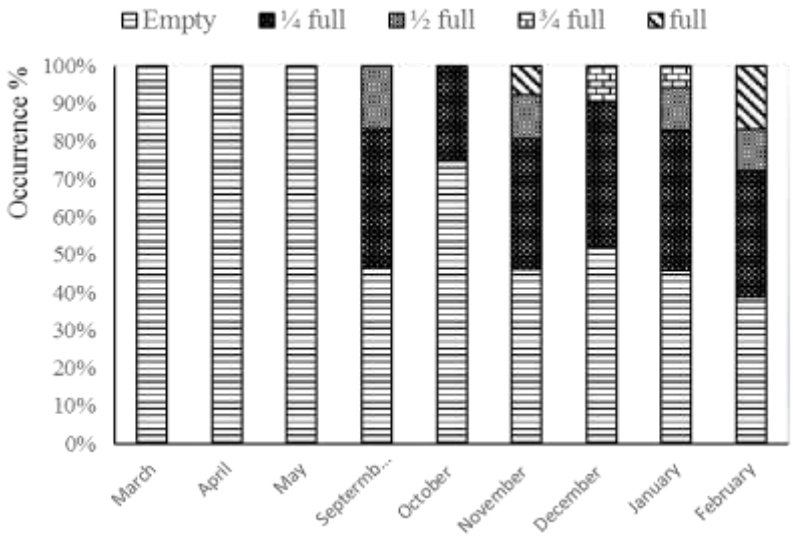

Figure 3 Month-wise percentage composition of stomach fullness of *Pampus argentus* from March 2019 to February 2020.

Table 3 Monthwise Gastrosomatic index and visceral mass index of *Pampus argenteus* from March 2019 to February 2020.

Months	Specimen examined	GaSI±SD	VMI±SD
March	34	2.24±0.91	7.57±1.78
April	31	3.18±1.15	8.5±2.56
May	30	1.91±0.77	4.87±0.94
September	30	2.1±0.49	6.25±0.81
October	32	1.58±0.24	6.37±2.1
November	26	1.41±0.2	6.56±3.57
December	42	1.56±0.32	4.17±1.38
January	35	1.6±0.19	5.35±0.46
February	36	4.09±1.22	11.02±3.66

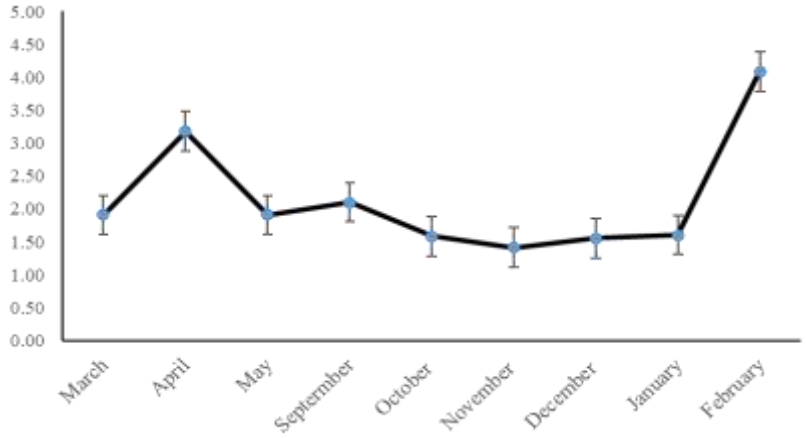

Figure 4 Month-wise Gastrosomatic index of *Pampus argenteus* from March 2019 to February 2020.

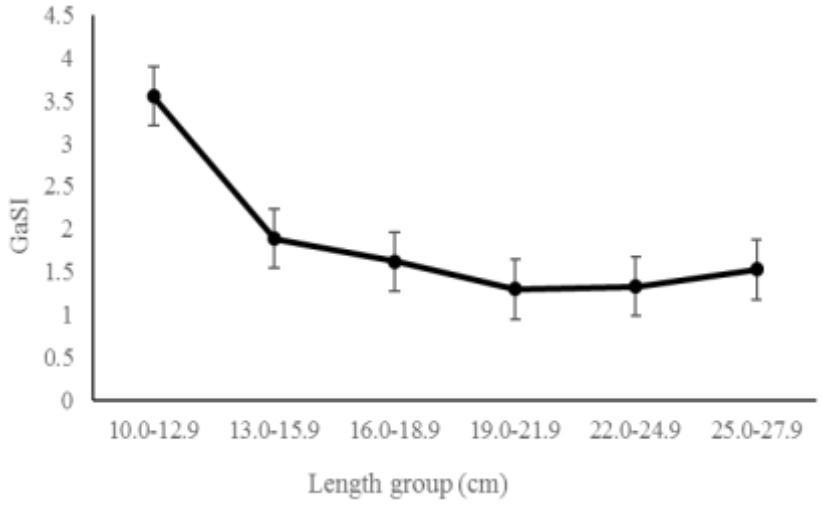

Figure 5 Length-wise Gastrosomatic index of *Pampus argenteus* from March 2019 to February 2020.

Table 4 Lengthwise Gastrosomatic index of *Pampus argenteus* from March 2019 to February 2020.

Length group	Specimen examined	GaSI±SD
10.0-12.9	71	3.55±1.31
13.0-15.9	144	1.89±0.64
16.0-18.9	65	1.62±0.39
19.0-21.9	5	1.3±0.21
22.0-24.9	9	1.33±0.46
25.0-27.9	2	1.53±0.43

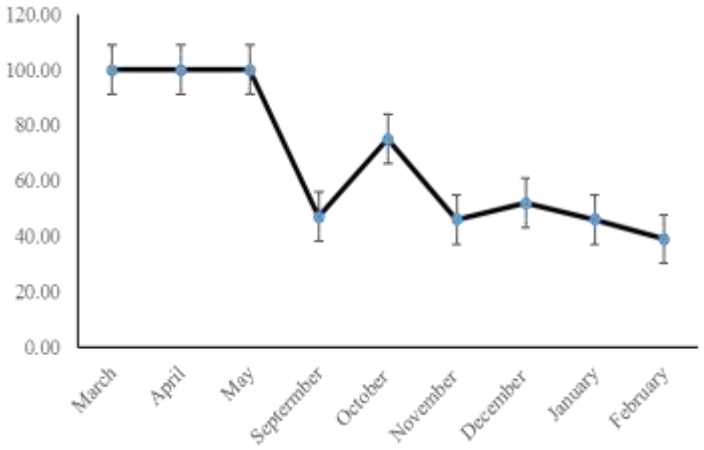

Figure 6 Month-wise percentage of vacuity index of *Pampus argenteus* from March 2019 to February 2020.

Discussion

Fishes feed on wide range of materials of plant and animal origin. They convert part of the organic materials ingested into living biomass; this process is influenced by quantity, quality of the food material and surrounding environment. Understanding fish nutrition habits requires extensive field and laboratory studies to infer the main sources of nutrition for a species. Even then, feeding studies can identify the prevalence of food items but it is not possible to assess the diet preferences of fish without detail complementary studies to estimate the range and abundance of potential food items available in their natural environment (Valinassab, *et al.*, 2011).

In the present study, *Pampus argenteus* feed largely on copepod because more copepods were found than other food items in the stomach content. Similarity, Abdu Rahiman (2006) reported that *P. argenteus* was an omnivore which fed mainly on copepod and detritus. Then the mean weight of detritus gradually decreased with increasing length but in the largest length class, it again increased. The number of copepods fluctuated without a clear pattern between length groups. The present study is agreement with his result.

Pati (1978) investigated the food of fish and stated that copepods play an important food items throughout the year, the peak occurrence found during the early southwest monsoon months of April-May and the post-monsoon months of August-November. Therefore, copepods are very important part of diet both in Pre-monsoon and post-monsoon seasons in Bay of Bengal. Moreover,

Rao (1964) observed a high percentage of copepods along with amphipods, ostracods, other crustacean zooplankton, gastropod larvae and fish remains in the stomachs of *P. argenteus*.

Abdurahiman, Zacharia, Nayak and Mohamed (2006), also observed copepods formed the largest proportion in the stomachs of *P. argenteus* from the Southeast Arabian Sea. Rao (1964) also reported that copepods were important food items in the stomachs of *P. argenteus* in the Bay of Bengal. Similarity, Thangavelu *et. al,* (2012) also reported that copepods were important food items in the stomachs of *P. argenteus* in Gujarat of Indian.In the present study, other zooplankton and crustacean appendages were found second most abundance food items in the stomachs of *P. argenteus*. Similarity, Rao (1964) observed other zooplankton (other than copepod) and crustacean remain were found second most components of food items in the stomachs.

In the present study, molluscan larvae, algal filamentss and small fishs were found occasionally in the stomachs of *P. argenteus*. Similarity, molluscan larvae and algal filamentss were recorded occasionally in fish stomachs from the Bay of Bengal (Pati, 1978). Pati (1978) described that the pomfret fishes possess tooth pharyngeal sac which acts as grinding mill to convert the food into pulpy mass and hence making the identification of food components very difficult. Therefore, the fishes in the foos component could not be identified but fish scale frequently encountered which remain undigested in the gut.

Fish scales were found in most of the months throughout the study period (Pati,1978) but only recorded in September and October with the largest percentage (35.3% and 33.33%) among all food items in both months in the present study. Occurrence of fish scales though in less quantities, indicated that small fishes formed diet of *P.* argenteus. In Rao (1964), fish scales were found occasionally in the stomachs of *P. argenteus* with a small proportion (0.8%). During the present study, diatomss were occurred in small quantities of percentage which was similar to the findings by Abdurahiman, *et al.,* (2006). Basheeruddin and Nayar (1961) investigated semi-digested pulp with fish scales, bones of fish, copepods, *Acetes* spp. and other crustacean that were entangled in the gut of pomfret fishes. Abdurahiman, *et al.,* (2006) reported that the copepods were significance in the diet of *P. argenteus* and that was also greatly emphasized in other studies such as Kuthalingam (1967), Dadzie *et al* (2000).

In a closely related species (*Parastromateus niger*, black pomfret), Sivaprakasam (1967) observed that food was present in highly macerated and in advanced state of digestion. Crustacean was main food items for *P. niger*. Dadzie (2007) also stated that crustaceans were the most common food items in the stomachs of *P. niger*. Among crustaceans, copepods were found to be higher than another crustacean group. Moreover, copepods were highly distinct components in the seasonal variation of prey items in pomfret fishes (Chinese pomfret and black pomfret) as mentioned by Abdurahiman, *et al.,* (2006). Moreover, Chinese pomfret, *Pampus chinensis* fed mainly on zooplankton in which proportion of copepod was higher than that of other zooplankton (Pati, 1977)

During the present study, the stomach contents of silver pomfret were examined from 296 samples collected from March 2019 to February 2020. On the average in length range of 10.0-26.6cm were examined. Regarding the feeding habits, the degree of fullness in stomach was occurred as full, ¾ full, ½ full, ¼ full and empty in which full was regarded as high feeding, ¾ full and ½ full was moderate feeding and ¼ full was low feeding and empty. In the present study, empty stomach was found throughout the year while the highest was found in the pre-monsoon season. Similarity, fishes with poorly fed stomach condition were dominant in all seasons and the highest proportion occurred in pre-monsoon followed by monsoon season was reported by Abdurahiman, *et al.,* (2006).

In present study, high feeding was recorded to be more in post-monsoon season and moderately feeding and low feeding also found to be high in post-monsoon seasons. Abdurahiman,

et al., (2006) found proportion of empty stomachs was higher in large fishes and the diet changed with body size as well as with season. Abdu Rahiman (2006) reported that the poor feeding condition of *P. argenteus* was found throughout the year in which the highest proportion occurred in pre-monsoon followed by the monsoon season. Moreover, empty stomachs fishes with high proportion were found in the post-monsoon season. The percentage of empty stomach was high in April to July while high feeding intensity was from August to November. The occurrence of high feeding coincides with the abundance of copepods (Pati, 1978).

Size-wise feeding intensity analyzed revealed that in all the size groups (150-549 mm TL) higher percentage of empty stomach was observed and no full and gorged stomachs of *P. argenteus* was observed during the study period (Thangavelu *et. al*, 2012). In the pomfret fish, *P. niger*, fishes with empty stomachs were recorded throughout the year except December though the maximum proportion of stomachs occurred in March and April and the minimum values in January and February (Dadzie, 2007).

During the present study, monthly gastro-somatic index of *P. argenteus* ranged from 1.41 to 4.09. The minimum value of GaSI (1.41±0.2) was found in November while the maximum value (4.09±1.22) was in February. And then Lengthwise GaSI values for *P. argenteus* were differed with the range between 1.3 and 3.35. The highest value was reported in 10.0-12.9cm length group and the lowest value was in 19.0-21.9cm length group. The GaSI value slightly varies with size group which indicated that fish feed at the same rate. The relationship between mean body weight and mean gastro-somatic index (GaSI) differed significantly. Although the body of fish increased, the weight of stomach in fish did not significantly increased. The stomach of *P. argenteus* was very small so the food contained very little in the stomach.

In the present study, the results of vacuity index (VI) indicated random monthly variation in the values. The abstemious fishes (80≤VI ≤100) and relatively edacious fishes (20≤VI≤40) occurred in pre-monsoon. And then the relatively abstemious fishes (60≤VI≤ 80) were found in post-monsoon while the moderate feeder fishes (40≤VI≤60) were in months of post-monsoon season. Hashemi and Taghavimotlagh (2013) described that vacuity index (VI) indicated moderately feeding and the fluctuation in fullness of stomach show correlation with temperature and fish with empty stomachs occurred at mature fish during spawning season. Thomas *et al* (2018) observed the highest vacuity index (VI) found at the mature fish within the spawning season. Similarity, the high VI values were also observed at the mature fish in present study.

Conclusion

In the present study, it was noticed that copepods are present in substantial quantities in the stomachs of *P.* argenteus. From the results of this study, it could be concluded that silver pomfrets, *Pampus argenteus* is a specialized feeder on semi-digested pulp and copepods. *P.* argenteus was a carnivore feeding mainly on zooplanktonic organisms especially copepods. The fishes with empty stomachs were found to be higher than high feeding during present study period. The monthly GaSI values was differed and lengthwise GaSI varies slightly with size group which indicated that fish feed at the same rate.

Acknowledgements

I sincerely thank Dr Aung Myat Kyaw Sein, Rector of Mawlamyine University and special thanks are to Dr Khaing Khaing San, Dr Myint Thida and Dr Marlar Aung, Pro-Rectors, Mawlamyine University, for providing facilities and encouragement. I am very thankful to Dr Soe Pa Pa Kyaw, Professor and Head of the Department of Marine Science, Mawlamyine University, for her encouragement and supports in preparing this work. I also am greatful to my colleagues; Dr Naung Naung Oo, Lecturer, Dapartment of Marine Science, Mawlamyine University for his valuable suggestions and constructive criticisms on this study. I wish to thank my beloved brother and my students, Department of Marine Science, Mawlamyine University, for their helps and advices during the field trips, and who are always willingiy helpful to me. I also would like to express my gratitude to all staff of Than Lwin Aye Co. Ltd, Ye Township, Mon State. Finally, my infinite thanks are to my beloved family for their kind and financial support throughout this study period.

References

Abdu Rahiman, K.P. (2006). Studies on food and feeding of marine demersal finfishes with special reference to trophic interactions. Unpublished PhD Thesis, Molluscan Fisheries Division, Central Marine Fisheries Research Institute, Marine Science of the Cochin University of Science and Technology. Indian.

Abdurahiman, K.P., Zacharia, P.U., Nayak, T.H. and Mohamed, K.S. (2006). Diet and trophic ecology of silver pomfret, *Pampus argenteus* (Euphrasen, 1788) exploited from the Southeast Arabian Sea. *J. Mar. Biol. Ass. India.* vol. 48, no**.**2, pp 206-212.

Basheeruddin. S and K.N. Nayar. (1961). A preliminary study of the juvenile fishes of the coastal waters of Madras City. *Indian. J. Fish***.** vol**.**8, pp 169-188.

Biswass, S. P. (1993). *Manual of methods in fish biology*. South Asia publishers PVT Ltd., New Delhi.

Dadzie, S. (2007). Food and feeding habits of the black pomfret, *Parastromateus niger* (Carangidae) in the Kuwaiti waters of the Arabian Gulf. *Cybium.* vol. 31, no.1, pp 77-84.

Dadzie, S., Abou-Seedo, F. and Al-Qattan, E. (2000). The food and feeding habits of the Silver pomfret, *Pampus argenteus* (Euphrasen), in Kuwait waters. *J.Appl. Ichthyol*. vol.16, pp 61-67

Hashemi, S. and Taghavimotlagh, S. (2013). Diet Composition of Bartail Flathead (*Platycephalus indicus*) in Nortwest of Persian Gulf. *World Journal of Fish and Marine Sciences*. vol. 5, no**.** 1, pp 35-41.

Krishna, P.V., Panchakshari, V. and Prabhavathi, K. (2016). Feeding Habits and Stomach Contents of Asian seabass Lates calcarifer from Nizampatnam Coast, Andhra Pradesh, India. *International Journal of Advanced Research*. vol.4, no. 4, pp 168-172

Kuthalingam, M.D.K. (1967). Observations on the fishery biology of the silver pomfret, *Pampus argenteus* (Euphrasen) from the Bay of Bengal. *Indian J. Fish*. vol.10, pp 59-74

Lalit, K., Sharma, B.K., Sharma, S.K., Upadhyay, B. and Mishra, V. (2015). Food and Feeding Habits of *Catla Catla* (Hamilton) From Lake Udai Sagar, Udaipur. *International Journal of Fauna and Biological Studies*. vol.2, no.5, pp 06-08

Norouzi, H., Valinssab, T., Kamali, A., Kaymaram, F. and Shamsaei, M. (2012). Evaluation of some feeding indius of *Saurida tumbil* in the Northern Persian Gulf and Oman Sea. *Ecology. Environment and Conservation*. vol.18, no.14, pp 53-57.

Pati.S. (1978). Food and feeding habits of the Silver pomfret: Pampus argenteus (Euphrasen) from the Bay of Bengal with a note on its significance in Fishery. Proce5th Indian Science Congre Part III.244-256.

Pati.S. (1977). Food and feeding habits of the Chinses pomfret: *Pampus chinensis* Euphrasen from the Bay of Bengal. *J. amri. Bilo.Ass India*.vol.19, no.1, pp 44-49.

Qasim, S.Z. (1973). The dynamics of food and feeding habits of some marine fishes. *Indian Journal of Fisheries*.vol.19, pp 29-34.

Rao, K.S. (1964). Food and feeding habits of fishes from trawl catches in the Bay of Bengal with observations on diurnal variation in the nature of the feed**.** *Indian Journal of Fisheries*. vol.11, pp 277-314.

Sivaprakasam, T.E. (1967). Observations on the food and feeding habits of *Parastromateus niger* (bloch) of the Saurashtra coast. *Indian Journal of Fisheries*. vol.10, pp 140-147.

Thangavelu, M.A., Hakimelahi, M., Ghodrati, S.M., Vahabnezhad, A., Taheri, M.A. (2012). Food and feeding habits of commercially important demersal finfishes off Veraval coast. *Indian Journal of Fisheries*. vol.59, no.4, pp 77-87.

Thomas, S. M., Chadha, N. K., Purayii, S. B. P., Kandiyil, A. P., Kavungal, V., Joseph, I., Sawant, P. B. and Abhijith, R. (2018). The Food and Feeding Habits of Goldsilk Seabream, *Acanthopagrus berda* (Forsskal, 1775). *Turkish. Journal of Fish. and Aquatic Sciences.* vol.19, no.7, pp 605-614.

Valinassab, T., Jalali, S., Hafezieh, M. and Zarshenas, G. A. (2011). Evaluation of some feeding indices of Pomadasys kaakan in the Northern Persian Gulf. *Iranian Journal of Fisheries Sciences*. vol. 10, no. 3, pp 497-504.

VEIN TYPES, VEIN TEXTURES AND QUARTZ TEXTURES OF THE GOLD-QUARTZ VEINS IN THE TAUNG NI GOLD PROSPECT AREA, MADAYA TOWNSHIP, MANDALAY REGION, MYANMAR*

Aung Ye Ko[1], Day Wa Aung[2] and Ohn Thwin[3]

Abstract

Taung Ni area is situated in Madaya Township, Mandalay Region, Myanmar. The mineralization style of the study area is the vein type deposit hosted by quartzite jointed and brecciated interbedded with phyllite. Two main types of quartz veins were observed within the Taung Ni gold-bearing quartz veins system: primary gold-bearing sulphide quartz veins and secondary auriferous deformed / remobilized quartz veins. The quartz veins have generally segmented structure with typically brecciated and laminated/banded textures. Mineralogically quartz dominates in all the mineralized veins and a variety of textures, such as massive quartz, comb quartz, mosaic textures quartz, sheared quartz, and mechanical breakdown of quartz are present. Three generations of quartz based on morphology have been identified: the coarse-grained quartz (first quartz generation), fine-grained to ribbon quartz due to recrystallization (second quartz generation), and sheared and comb structure quartz (third quartz generation). The distinct alteration processes are silicification, chloritization, sericitization, pyritization and hematization. Gold- bearing sulphide quartz veins show a stockwork structure with chalcopyrite filled fractures. Gold occurs as inclusions in chalcopyrite and hematite. Auriferous deformed/remobilized quartz veins show the crushed and fractured characteristics with hematite filled fractures. The hematite quartz bands offer the best potential for significant gold concentration. Fluid inclusion data indicated that the gold-bearing mineralized quartz veins were developed within mesothermal environment. On the basic of those discovered genetic characteristics, quartz veins and textures of quartz, the Taung Ni gold prospect is a orogenic (mesothermal) gold type.

Keywords –Vein types, vein textures, quartz textures, quartz generations, Orogenic (Mesothermal) gold, Taung Ni area**.**

Introduction

Taung Ni area is situated in Madaya Township, Mandalay Region, Myanmar. It is located approximately 35 km northwest of Pyin-Oo-Lwin and about 37 km NE of Mandalay. It lies between Mogok Metamorphic Belt (MMB) (Searle et al., 1964) in the east and the Sagaing Fault (Win Swe, 2013) in the west. The area occupies the western marginal zone of Shan Plateau and to the east of the Central Myanmar Basin. Location map of the study area is shown in Figure.1.

Methods of Study

This study consists of two main stages, field investigations and laboratory work. During the field work, more than fifty (50) rock samples containing of ore and quartz vein materials were collected from Taung Ni gold prospect area. These samples were prepared as thin sections, and polished sections to conduct several types of analysis. Thin sections were examined petrographically to study textural relationships. Mineralization vein textures were carefully noted during the field observation, but some were interpreted from thin sections by optical microscopy using transmitted light. Alternatively, polished sections of ores were studied using reflected light under ore microscope to identify ore mineral assemblages. Furthermore, some of the ore minerals were confirmed by scanning electron microscopy with energy-dispersive X-ray (SEM-EDX). All

[1.] Dr, Lecturer, Defence Services Science and Technology Research Centre (Pyin Oo Lwin), Myanmar
[2.] Dr, Professor & Head, Department of Geology, University of Yangon, Myanmar
[3.] Dr, Part-Time Professor, Department of Geology, University of Yangon, Myanmar
[*] Best Paper Award Winning Paper in Geology (2021)

laboratory methods were performed at the Department of Geology, University of Yangon, Myanmar and Defence Services Science and Technology Research Centre, Pyin Oo Lwin, Myanmar.

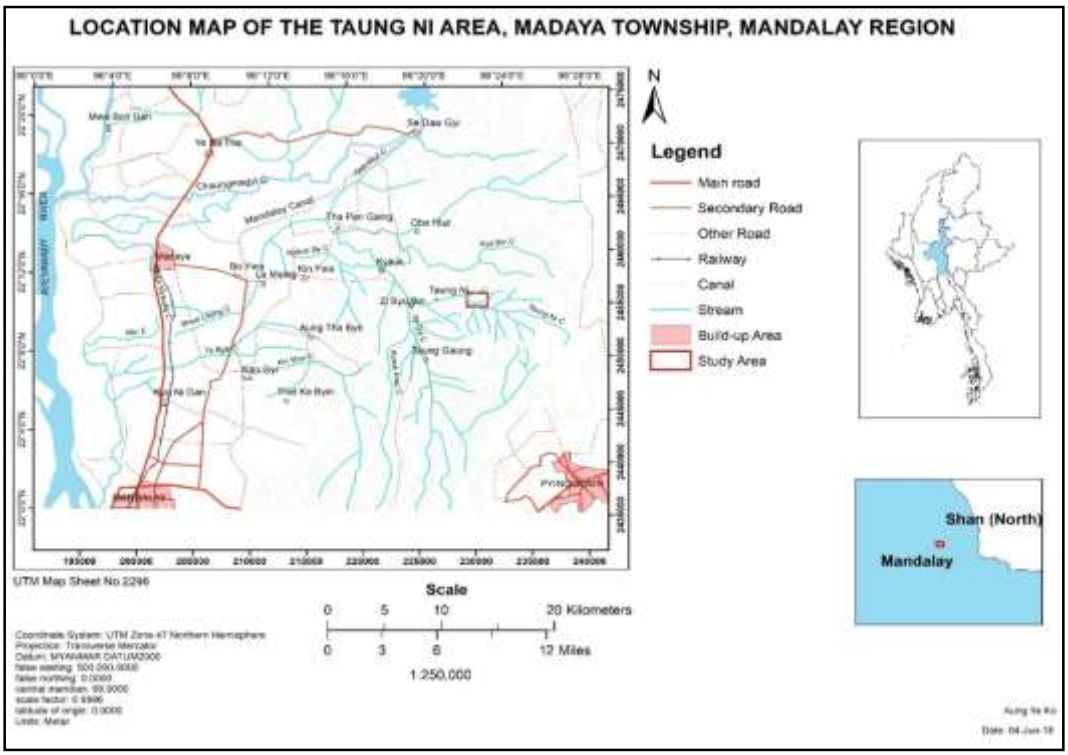

Figure 1 Location Map of the Study Area, Madaya Township, Mandalay Region

Geological Background

With increased knowledge in plate tectonics, it is now generally accepted that Myanmar is geologically built up of two main parts, the Eastern Part or Shan-Thai Block (Bunopas et al., 1983) or Sibumasu Terrane (Metcalfe, 1984) (Kachin Highlands, Shan Plateau, Tenasserim Ranges, East Himalayan Syntaxis, Mogok Metamorphic Belt, etc.) and the Western Part or Burma Platelet or Burma Microplate (Curray et al., 1979) or West Burma (Searle et al.,) with its accretionary prism of Indo-Burman Ranges or Western Ranges (Naga and Chin Hills and Arakan Yoma). Sagaing Fault, a major right lateral strike-slip fault of 1500 km length (Win Swe, 2013 and Soe Thura Tun et al., 2017) geotectonically separates these two parts along the middle. Both parts belong to the larger Asian Plate. India Plate is subducting beneath Burma Microplate, and thus, in the Andaman Sea, forms an east-dipping curvilinear oblique subduction zone that continues onshore along the Western margin of the Indo-Burman Ranges.

The study area, falling in the Shan -Thai Block, lies on the eastern margin of Mogok Metamorphic Belt (MMB), between the Sagaing Fault in the west and the Shan Scarp Fault in the east (Figure 2. a). The MMB consists of Metamorphosed Sedimentary sequences of Precambrian to Carboniferous age. Basement sediments are intruded by Jurassic to Tertiary granitoids (Searle et al., 2007). Regional stratigraphy of the study area and its environs are shown in Figure 2. b. Stratigraphic rock units include Mogok Group, Chaungmagyi Group, Molohein Group, Pindaya Group, Mibayataung Group and Upper Plateau Limestone Group (Maung Thein, 2014).

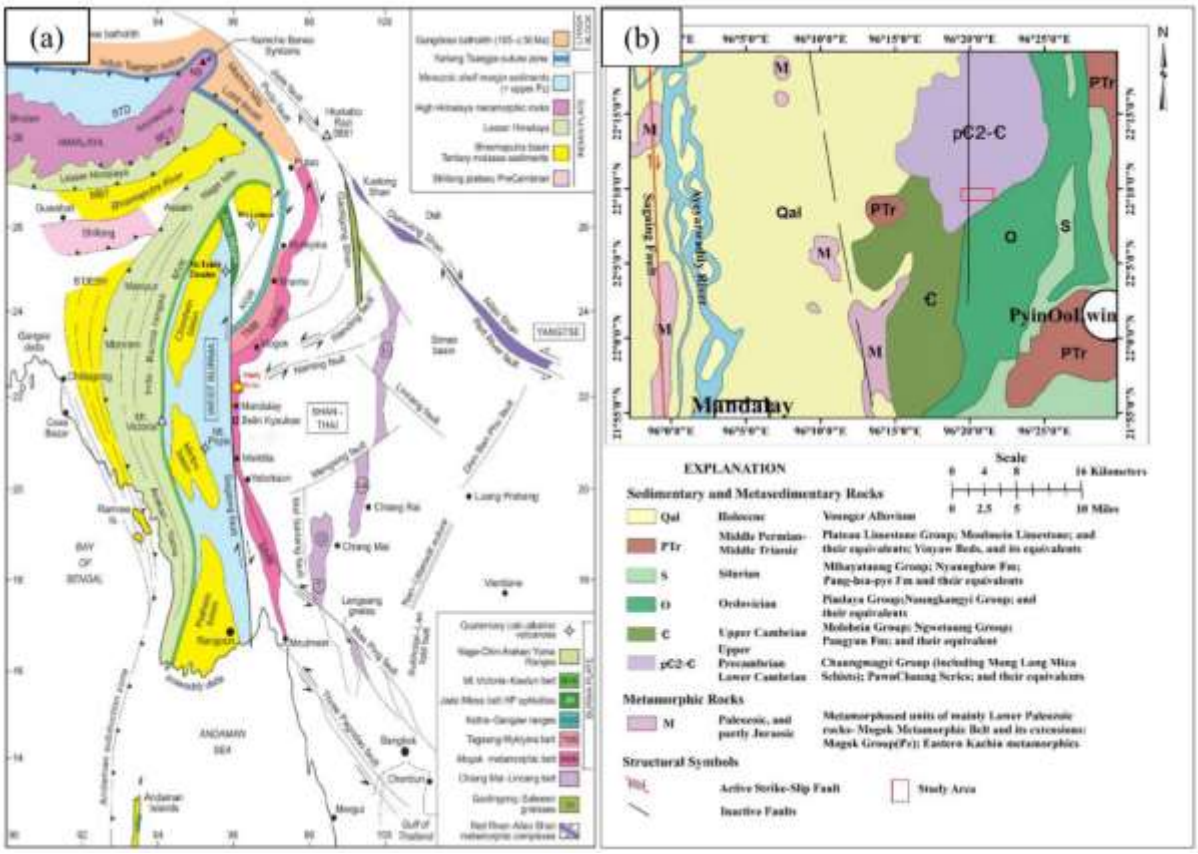

Figure 2 (a) Geological map of Myanmar and surrounding areas showing major structures, faults and Terrane boundaries (Searle et al., 2007). Study area is located within the Mogok Metamorphic Belt (MMB), marked by a star, (b) Regional geological map of the study area and its environs (Maung Thein, 2014).

Geology of Study Area

The geology of the Taung Ni area is quite simple. There is only one stratigraphic rock unit in this area. It is Late Precambrian to Early Cambrian age of Chaungmagyi Group, consisting of **Mauk Kaw Quartzite and Kin Sandy Phyllite** (Khin Maung Swe, 1973) (Figure 3)**.** From microscopic study and XRD results, quartzite and phyllite were found to be composed of low-grade metamorphic minerals such as albite, quartz, chlorite, sericite, epidote, muscovite, actinolite, and biotite. Opaque minerals were often found as disseminations especially observed in phyllite with foliations resulting from the sub-parallel to parallel orientation of minerals such as chlorite or micas due to strong pressure conditions of metamorphism. This rock type has been evidently formed by low grade regional metamorphism. The common occurrence of chlorite and sericite suggest the low pressure and low temperature. Thus, this rock type belongs to the greenschist facies (Aung Ye Ko et al.,2019a).

From field observation, major anticlinal structure was found near the gold deposit which is an asymmetrical anticline of E-W dipping. The east dip with 60° is steeper than that of the west, 42°. Based on measurement of joint sets (N=69) in the field, it shows trends of NNE - SSW, ENE - WSW and NE-SW. The prominent joint set is NE-SW. Fault criteria (slickensides) were usually formed on quartzite. A main foliation that dips steeply towards SE and NW, a stretching lineation that plunges gently NE and SW and a top-to-SW sense of ductile shearing were obsearved. Mineralized vein systems formed on the crest of anticline and synclines. These mineralized veins were complex and found in shear zones, indicating structural control (Aung Ye Ko, 2020).

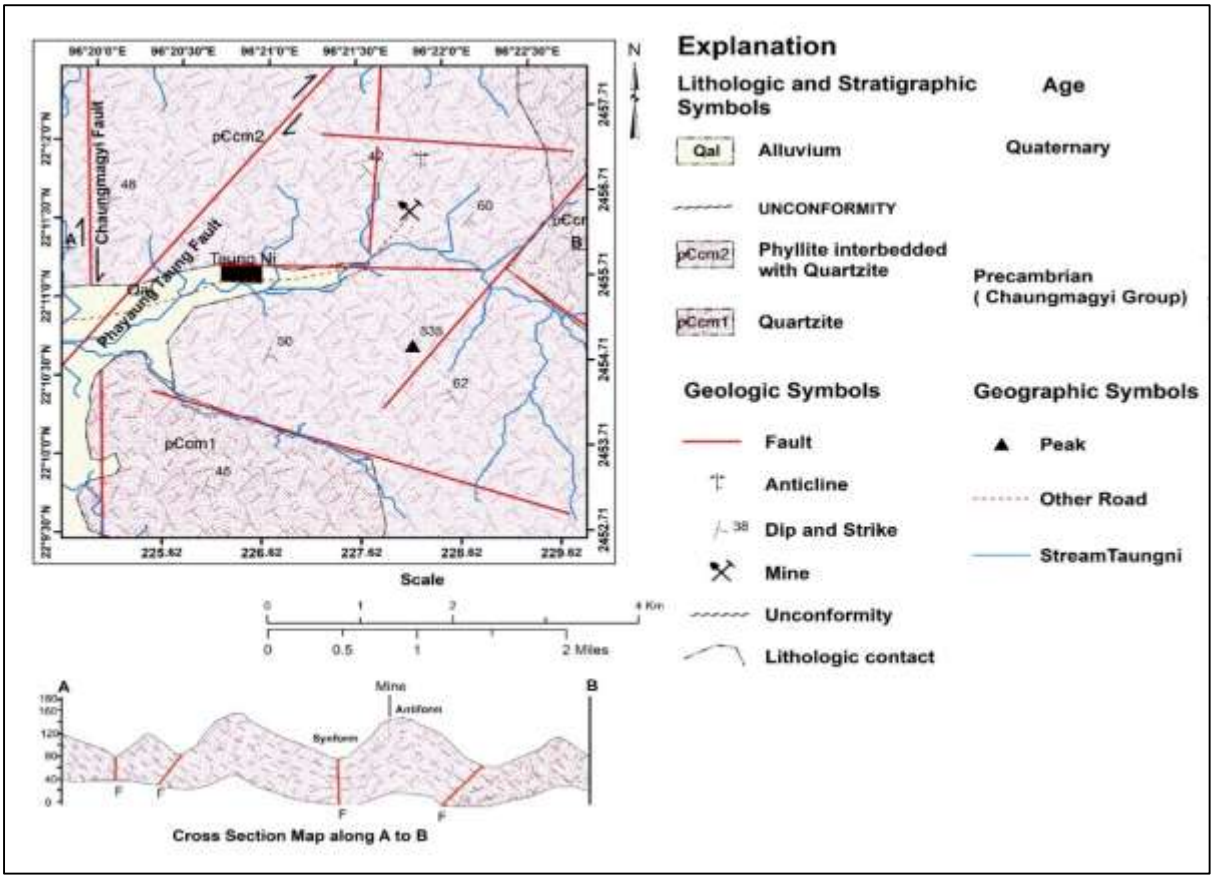

Figure 3 Geological Map of the Taung Ni Area, Madaya Township, Mandalay Region

Vein Types

The mineralization style of the study area is the vein type deposit hosted by deformed, jointed and brecciated quartzite interbedded with phyllite. The gold mineralization is associated with quartz veins occurring along the fractures of the host rock. Regionally, Taung Ni gold mineralization lies within the shear zone between Sagaing Fault and Shan Scarp Fault. The main controlling factor is the regional structure that nearly trends NE-SW and possibly formed by the activity of Phayaung Taung Fault causing the deformation like, shearing, brecciation favourable for mineralization. The gold-bearing quartz veins/ veinlets filled NE-SW and E-W structure lineaments of dilational fault zone. In the field, gold-bearing mineralized veins were observed mostly brecciated and crushed. The deposit profile suggests that the gold mineralization is most possibly related to orogeny because strong compressional and transpressional (shear) environment (Groves et al., 1998) were clearly developed indicating the strong structural control.

Two main types of quartz veins were observed within the Taung Ni gold-bearing quartz veins system: primary gold-bearing sulphide quartz veins and secondary auriferous deformed/ remobilized quartz veins. Gold-bearing sulphide quartz veins were more abundant than auriferous deformed/remobilized quartz veins in the gold prospect. Veins occurs mostly as veinlets and stringers, and stockwork veins (Figure 4. a & b).

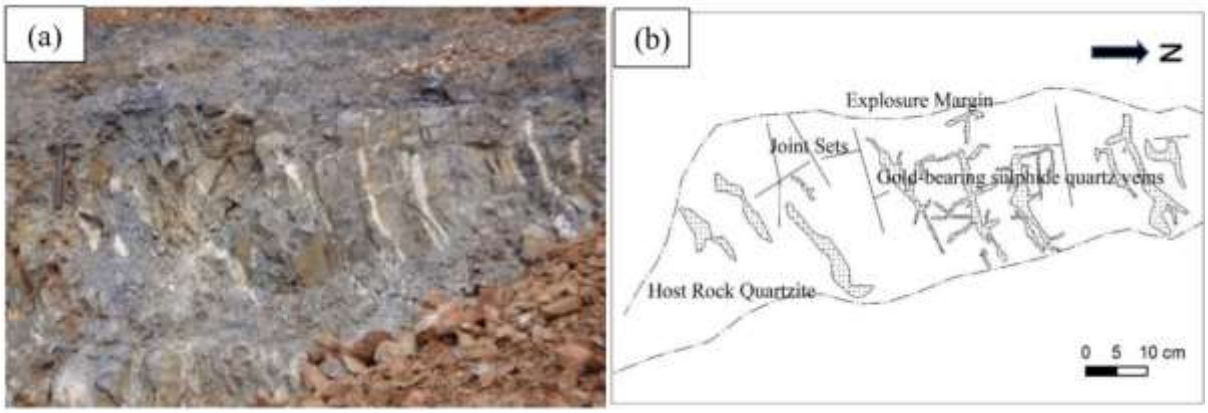

Figure 4 (a) & (b) Stockwork vein system of sulphide quartz veins hosted in quartzite

The thickness of primary gold-bearing sulphide quartz veins range from 1 to 10 cm. Veins are hosted in quartzite. Mostly, veins are steep dipping and vein direction range NNE-SSW/60°-75°vertical within host rocks (Figure 5. a & b). Secondary auriferous deformed / remobilized quartz veins are commonly developed near the E-W post-mineralization structures and they are much brecciated, deformed in oxidized zone (Figure 6. a & b). The thickness of veins is from 0.5cm to 4cm. Visible gold associated with secondarily formed hematite, Fe- hydroxides are rich in deformed quartz veins filling in micro fractures and at the crest of the vein and brecciated quartzite zone.

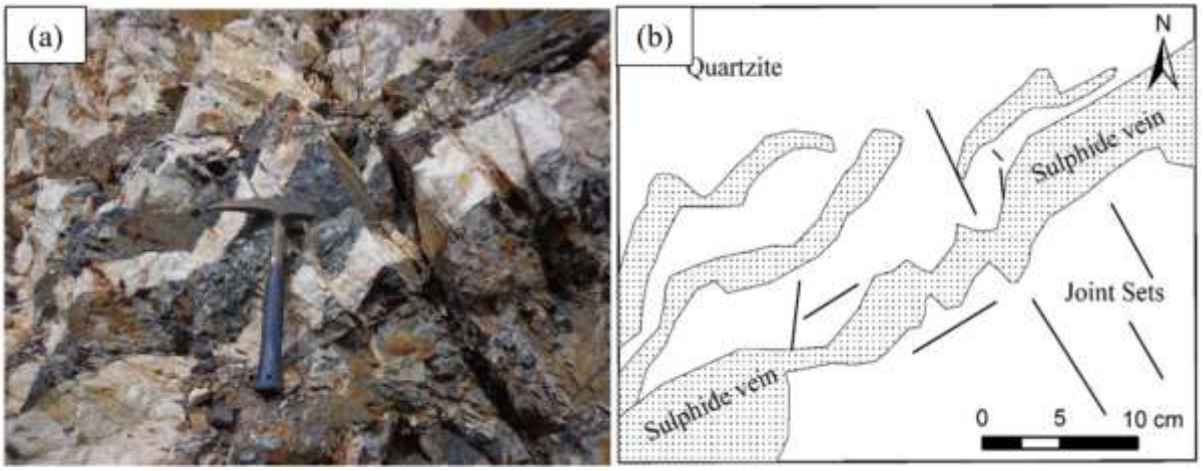

Figure 5 (a) & (b) Individual vein system of sulphide quartz veins hosted in quartzite

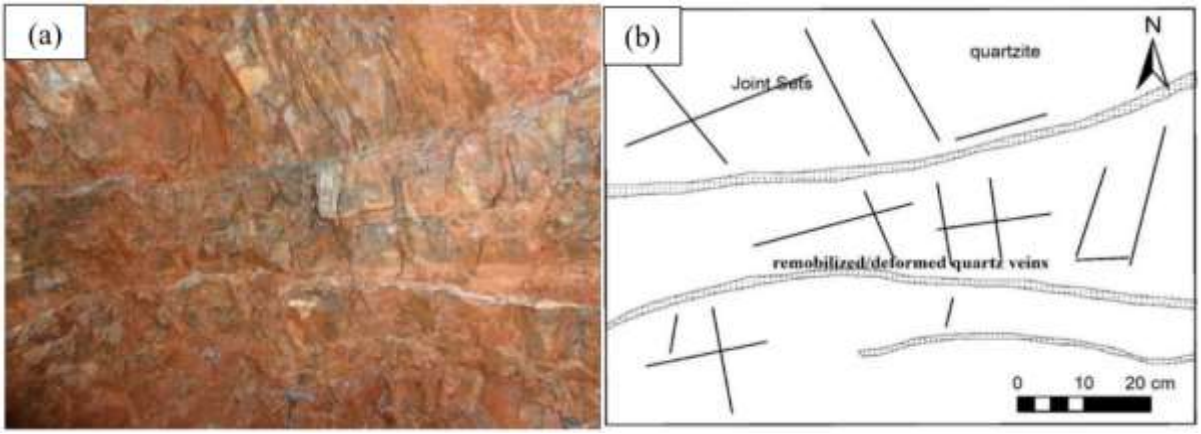

Figure 6 (a) & (b) Individual vein system of deformed /remobilized quartz veins hosted in quartzite

Vein Textures

Most of the hydrothermal veins are formed from silica-bearing fluids that originated from (1) igneous intrusions; (2) deep convection of meteoric fluids; (3) metamorphic devolatilization; (4) mantle-derived fluids (Jia et al., 2000). Quartz veins are commonly found in low-grade metamorphic rocks, typically within or above the brittle-ductile crustal stress field, forming around 2-3 kbar and 200-350°C. Hydrothermal veins can be syn-tectonic to post-tectonic (Bons, 2001). The texture has been grouped into three major classes (primary, recrystallization, and replacement) to aid interpretation of their origin and environment of formation. Primary growth textures represent initial open-space vein fill. Recrystallization textures reflect the transformation of amorphous silica or chalcedony to quartz. Replacement textures represent partial or complete pseudomorphs of other minerals by silica minerals within veins.

In the study area, the primary gold-bearing sulphide quartz veins are commonly segmented with massive, brecciated and laminated/banded textures (Figure 7. a, b, c & d). They are composed predominantly of reddish-brown to milky whitish quartz. Auriferous deformed/remobilized quartz veins developed in brecciated and oxidized zone. Vein internal texture is dissimilar to primary veins and composed crystals were of irregular form, containing much micro-fracture/ crack in which filled by secondary oxidized minerals. The mineralized veins are composed of old rose to milky white quartz. Most quartz veins show the crushed and fractured characteristics (Figure 8. a, b, c & d).

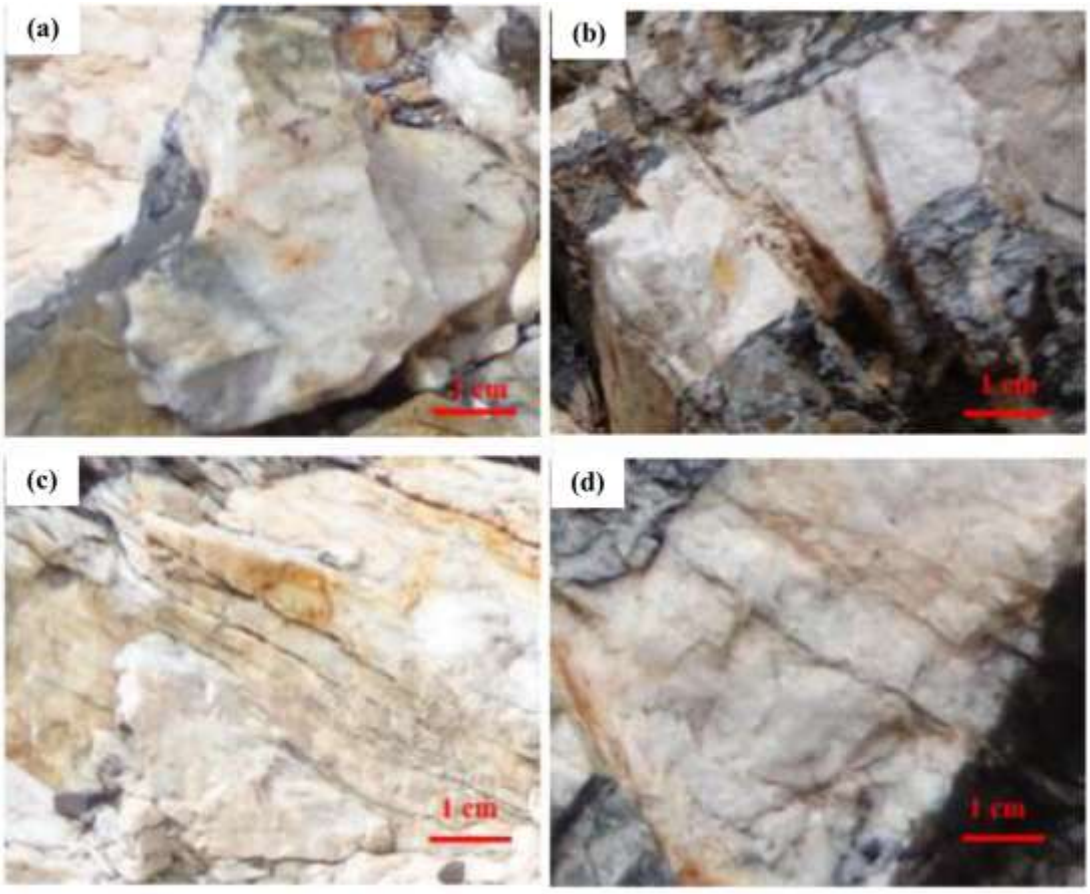

Figure 7 (a) & (b) Massive quartz veins (c) Laminated quartz vein, and (d) Banded quartz veins

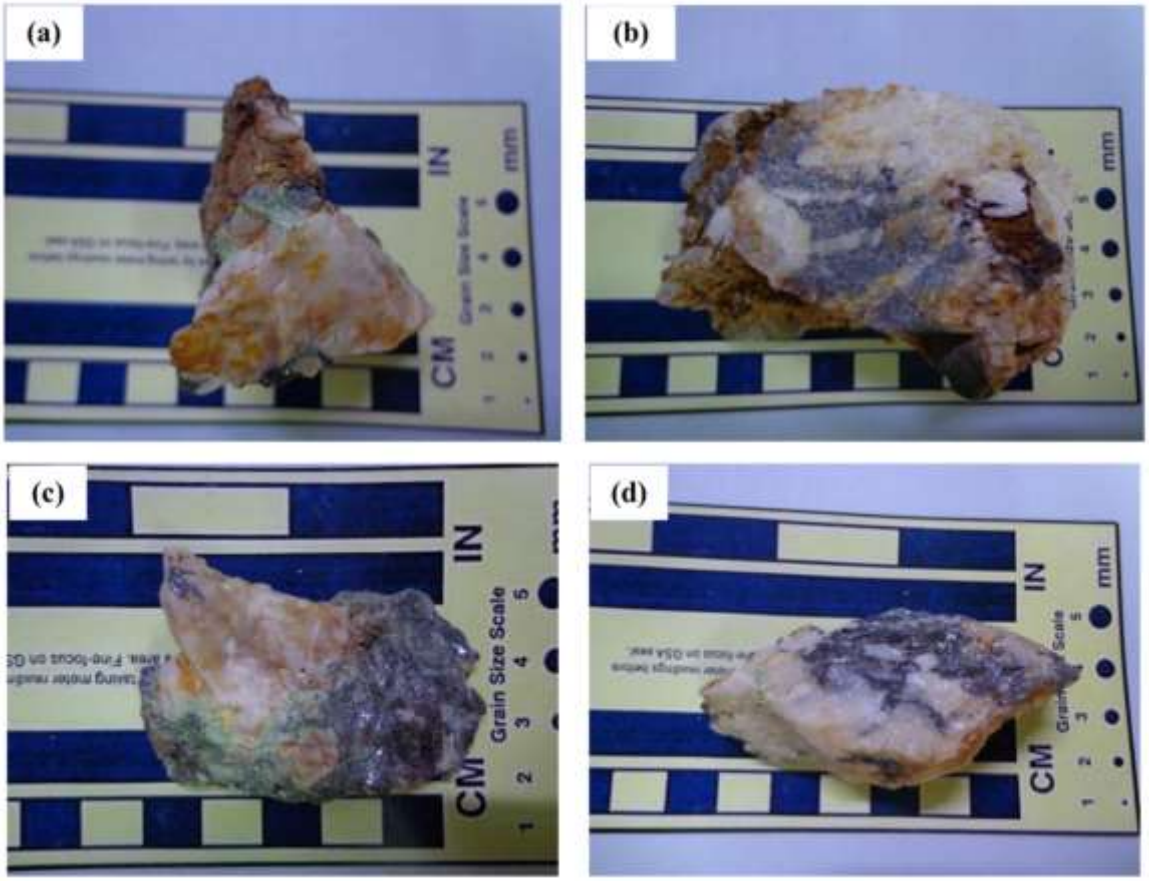

Figure 8 (a), (b), (c) & (d) Brecciated and oxidized quartz veins

Quartz Textures and Alteration Mineralogy

Quartz textures are excellent indicators of the nature and intensity of deformation prevailing during vein formation (Jébrak,1992, Vearncombe,1993 and Bouchot et al,1994). Mineralogically, quartz dominates in all the mineralized veins and commonly displays multiple growth stages and a variety of textures, such as comb quartz, recrystallized quartz (mosaic texture quartz), crushed and fractured characteristics of quartz (sheared quartz) and mechanical breakdown of quartz (Figure 9, 10 and 11). Quartz grains boundary are closely interlocked with irregular margins probably due to recrystallization and pressure effect. All quartz grains show wavy extinction and size equality is very poor. Little amounts of sericite are found along the marginal granulation and fractures of quartz grains. The mechanical fractures and marginal granulations are also common. All these fractures indicate the pre or syn-tectonic crystallization of quartz veins (Bons, 2001). Sheared and comb structure quartz indicate the formation of veins accompanied by intense stress and shearing (Folk,1974).

In the mineralized quartz veins, three generations of quartz based on morphology have been identified (Fig. 12). They include coarse-grained quartz with deformed grain boundaries (Qtz1, Fig. 12 a& b), incipient recrystallized quartz (Qtz2) defined by small polygonal quartz grains, sub-grains occupying inter-grain planes mainly parallel to the grain boundaries and vein margins (Figure 12 a, b, c, d & e) and deformed-elongated (stretched) quartz ribbons (Qtz3 Fig. 12 c, d, e & f). The quartz crystals display undulate extinction. The coarse-grained quartz regarded as the first generation and fine-grained to ribbon quartz due to recrystallization (second generation) resulting from multiple episodes of deformation and fluid circulation (Kurz et al., 2000, Oliver, 2001 and White, 2001).

Sheared and comb structure quartz (third generation) indicate the formation of veins accompanied by intense stress and shearing (Folk,1974).

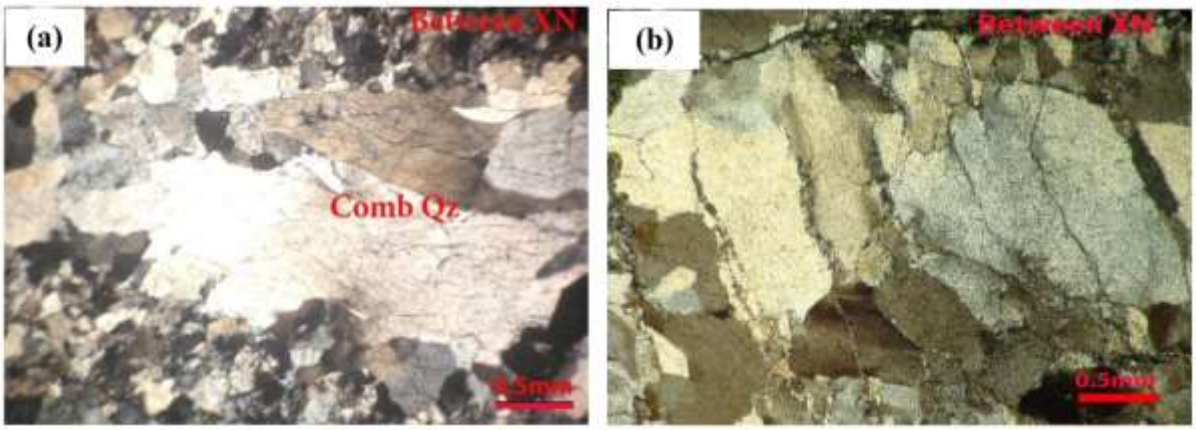

Figure 9 (a) & (b) Comb texture of quartz in quartz vein (Thin-section) (Between XN)

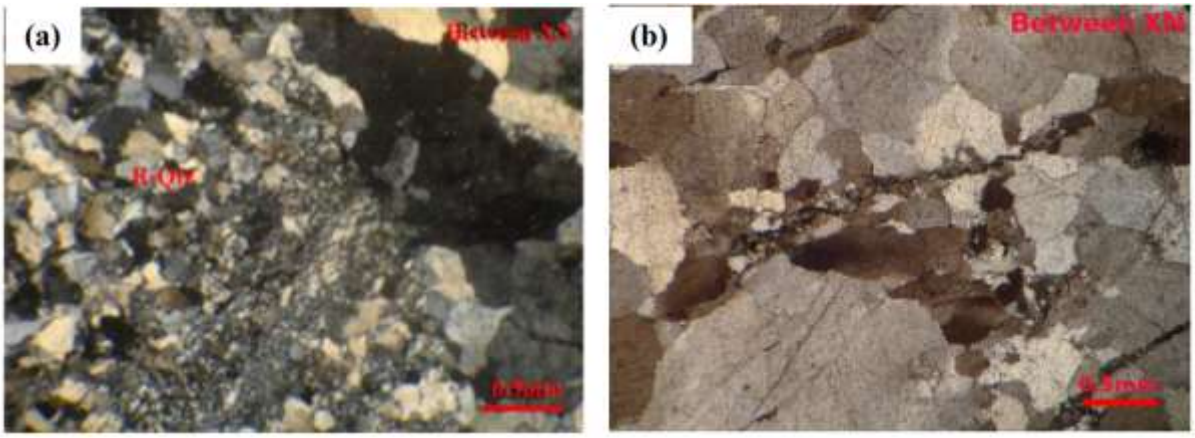

Figure 10 (a) & (b) Recrystallized quartz (R-Qtz) (Mosaic texture) in quartz vein (Thin-section) (Between XN)

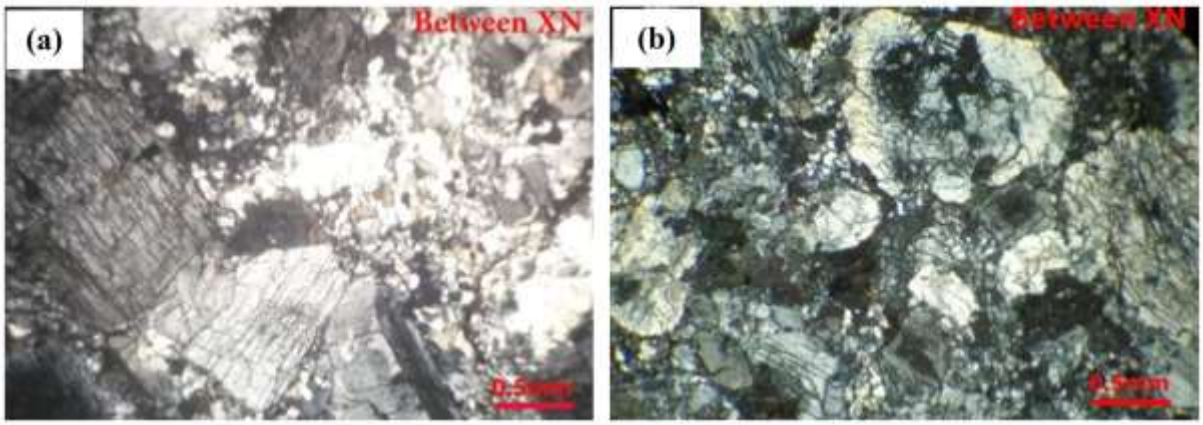

Figure 11 (a) Crushed and fractured characteristics of quartz (Sheared quartz) (b)Mechanical breakdown of quartz grains (Sheared quartz) (Thin-section) (Between XN)

Hydrothermal alteration was restricted to narrow zone around veins overlapping regional metamorphism that occurred in the study area. Sericite is abundant along the contact with the quartzite wallrock. The formation of sericite in the altered wallrock increases the permeability along the shear zone since sericite enhances permeability and facilitates ductile deformation (Kurz

et al., 2000, Oliver, 2001 and White, 2001). Generally, the vein related alteration is characterized by silicification, sericitization, chloritization and pyritization and carbonization from inner to outermost zones. Hematization and kaolinitization are found in oxidized/ supergene and strongly brecciated zones of post-mineral structural controlled wallrocks. From the microscopic study and XRD results, three distinct alteration mineral assemblages were formed; quartz + sericite + chlorite ± kaolinite, quartz + sericite + chlorite ± kaolinite ± carbonate and iron oxide + quartz + sericite + chlorite. According to the field observation, microscopic study and XRD results, the distinct alteration processes occurred in the study area are silicification, chloritization, sericitization, pyritization and hematization (Aung Ye Ko, 2020).

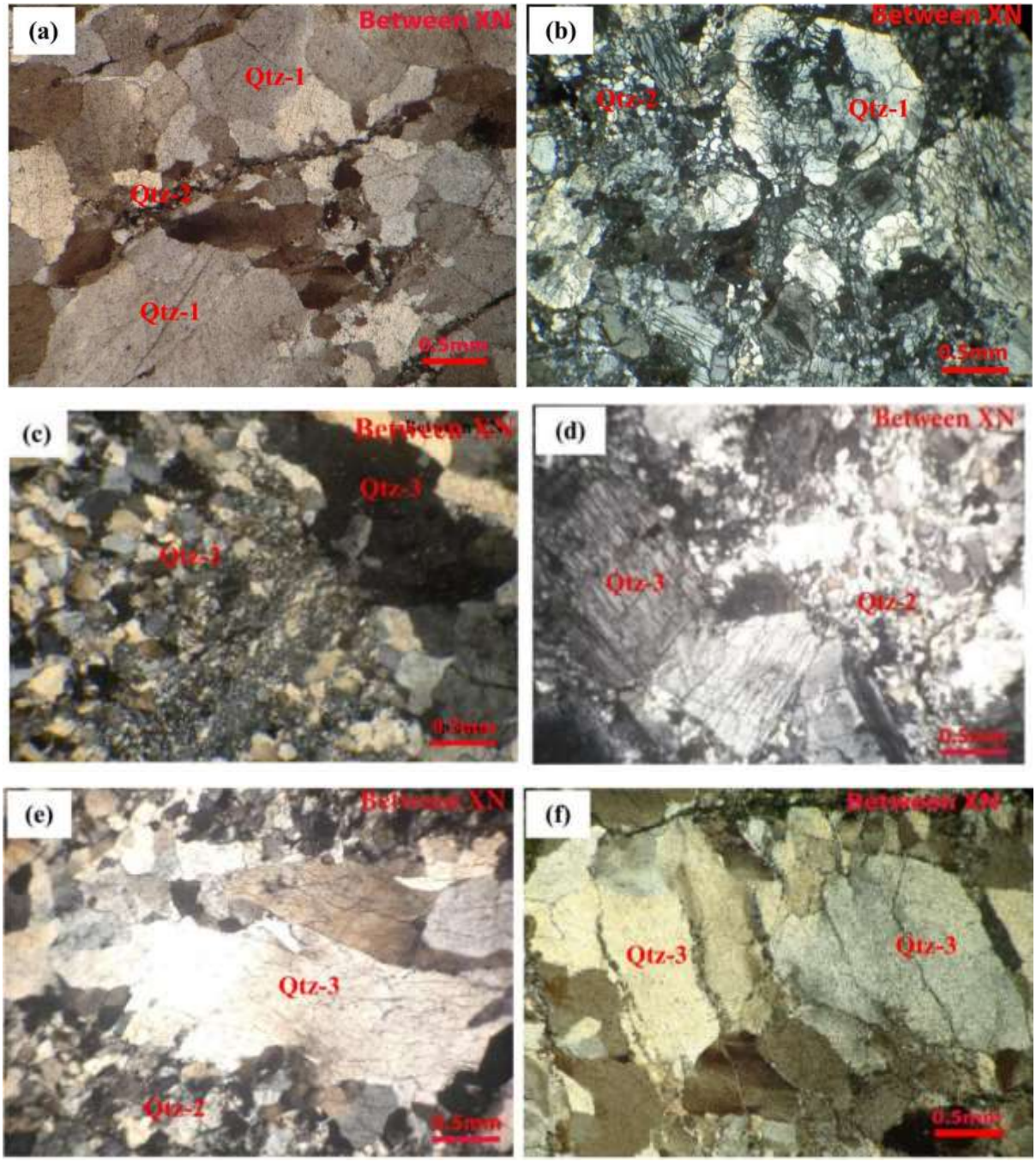

Figure 12 Photomicrograph showing generations of quartz in the mineralized quartz vein in Taung Ni area (Abbreviations: Qtz1=first quartz generation, Qtz2=second quartz generation, Qtz3=third quartz generation).

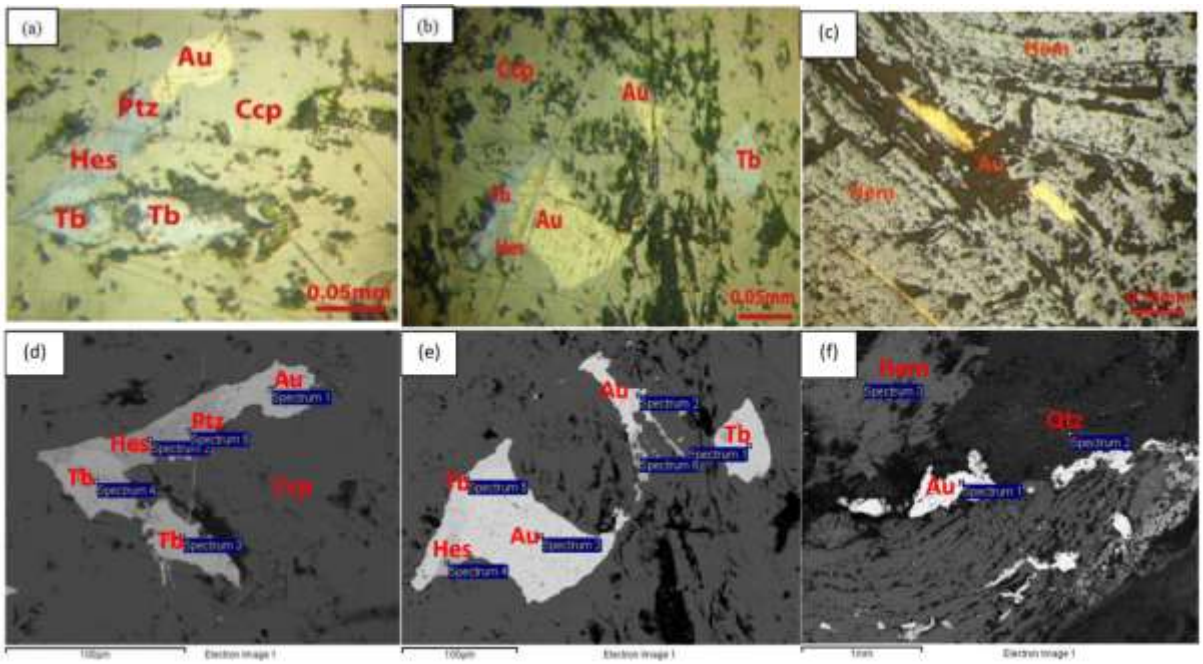

Figure 13 (a), (b) & (c) Gold associated with petzite, hessite, chalcopyrite, tellurobismuthite, hematite and quartz (Polished Section), (d), (e) &(f) Back Scattered images of gold, petzite, hessite, chalcopyrite and tellurobismuthite, hematite and quartz (Au = Gold, Ptz = Petzite, Hes = Hessite, Ccp = Chalcopyrite and Tb= Tellurobismuthite, Hem = Hematite Qtz=quartz).

The gold-bearing sulphide quartz veins mainly contain gold, electrum, petzite, hessite, chalcopyrite, tellurobismuthite and quartz dominated gangue minerals. Gold could be observed in chalcopyrite and closely associated with rare tellurium and bismuth compound minerals. Electrum grains were also found especially in sulphide quartz veins. Electrum grains are associated with gold in chalcopyrite grains and some are in quartz. In secondary veins, native gold occurs either as isolated free grain in the matrix of quartz as well as closely associated with hematite and bismuth. Its grains are strongly related to deformed, remobilized quartz veins in the brecciated zone (Figure 13). They were found together with hematite in micro-fractures of quartz. That indicates supergene origin at least in part for the native gold in Taung Ni gold prospect.

From fluid inclusion data of mineralized quartz veins, it can be deduced that there are two different mineralization phases marked by difference of homogenization temperature and salinity. Fluid inclusion microthermometry data of selected samples is shown in Table.1 Temperature-salinity diagram for various types of ore deposits (Wilkinson, 2001) is shown in Figure 14 (Aung Ye Ko, 2020).

Table 1 Fluid inclusion microthermometry data of selected samples

Sample ID	Host Rock	Host Mineral	Inclusion Type	No. of Inclusion	Homogeni-zation Tem, Range (°C)	Ice Melting Tem (°C)	Salinity (wt% NaCl.)	Remarks
PYT-1	quartzite	quartz	L-V	11	340-403	-1.7 to -2	3.01 to 3.53	Sulphide quartz vein (Early Stage)
PYT-2	quartzite	quartz	L-V	10	320-396	-1.3 to -1.6	2.31 to 2.83	Deformed quartz vein (Later Stage)

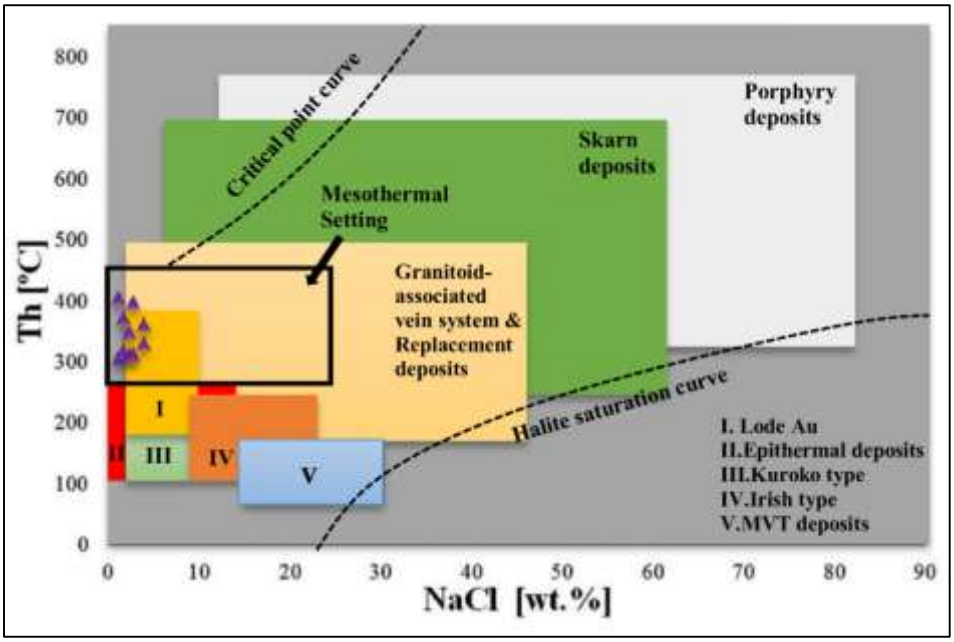

Figure 14 Temperature-salinity diagram for various types of ore deposits (Wilkinson, 2001)

Discussion

The mineralization style of the study area is the vein type deposit hosted by quartzite which is deformed, interbedded with phyllite, jointed and brecciated. Mineralized vein systems formed on the crest of anticlines and synclines. These mineralized veins were complex and found in shear zones, indicating structural control. The gold-bearing quartz veins/ veinlets filled NE-SW and E-W trending dilational fault zone. Gold-bearing mineralized veins are mostly brecciated and crushed. These deformation structures focused and enhanced crustal fluid circulation and mineralization. The deposit profile suggests that the gold mineralization must be related to orogeny because strong compressional and transpressional (shear) environment (Groves et al., 1998) were clearly developed.

Faults and shear zones are major fluid conduits in crustal basement (Kerrich, 1986 and (Knipe, 1993). Breccias are a common product in the highest, most fluid-saturated part of crustal fault zones where the potential for dilation strain increases the range of breccias formation processes (Woodcock et al., 2008). Brecciation is an excellent precursor to mineralization, as circulating hydrothermal fluids will readily interact with the fractured rocks. Enhanced permeability created in breccia zones provides pathways for crustal fluids that are sometimes metal- or hydrocarbon-rich (Woodcock et al., 2008). Thus, breccias are associated with numerous types of ore deposits both in surface and subsurface environments (Jebrak, 1997).

Gold mineralization in Taung Ni shear zone system is associated with brecciated quartz veins in steeply dipping brittle-ductile shear zones. Here brecciation is enhanced by transgranular fracturing. The quartz veins breccias show a characteristic stockwork structure with a network of discontinuous and closely spaced fractures that host mineralization. As such, the breccias act as a matrix for hydrothermal deposits. Gold-bearing quartz veins are commonly segmented, occasionally brecciated and laminated and has massive texture. In fact, gold- bearing quartz veins in the prospect area exhibit orogenic/mesothermal gold type (Groves et al., 2003).

By field evidence and fluid inclusion, it has been found that data, later stage veins were formed at around 1 km depth and early-stage mineralization were developed at 3km below the paleo water table. As indicated by mineralization with different depth conditions, it can be assumed that the MMB was uplifted between (Late Oligocene–Early Miocene, 26 and 21 Ma, Li et al., 2013

and Late Eocene–Early Miocene, 31-24 Ma, Searle et al., 2017) due to sustained subduction and collision. There was an uplift deformation occurring before later phase mineralized veins system. In view of geological conditions, fluid inclusion data, host rock mineralogy and ore mineral assemblages, gold-bearing mineralized quartz veins were found to be developed under mesothermal conditions. Figure 15 depicts interpretation mineralized system based on field evidence and fluid inclusion data.

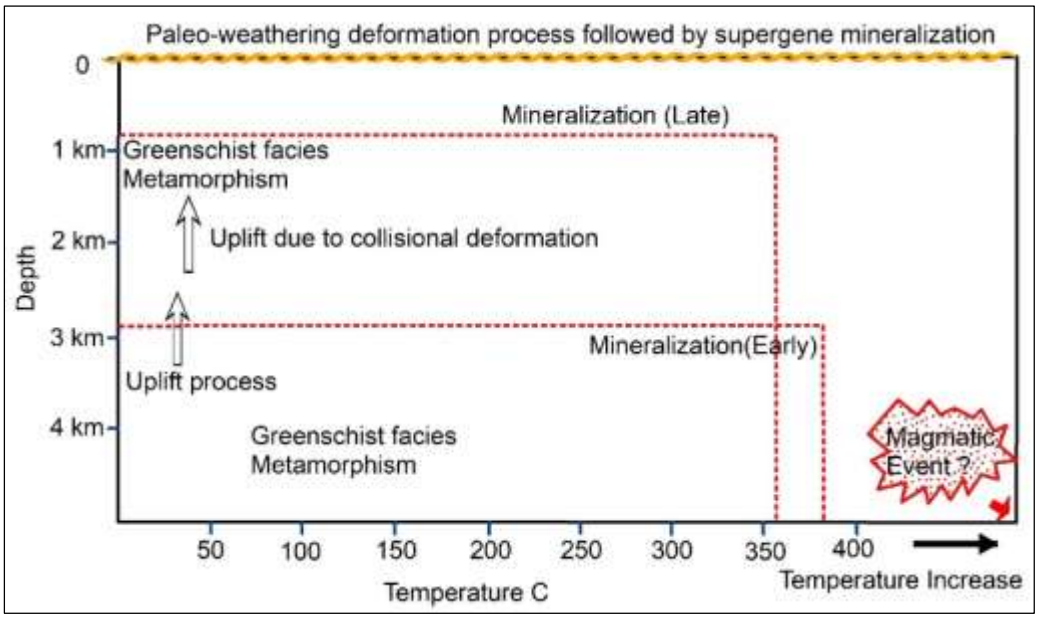

Figure 15 Schematic diagram of mineralization depth based on field evidence and fluid inclusion data showing possible two mineralization events (late mineralization developed during uplift due to collisional deformation) (Adapted from Win Phyo, 2017)

Mineralogically, quartz dominates in all the mineralized veins commonly displaying multiple growth stages and a variety of textures. Especially, primary growth texture such as massive quartz and comb quartz, and recrystallized texture such as mosaic texture quartz are found in all the quartz veins. Sheared quartz, and mechanical breakdown of quartz also dominate in all the mineralized veins. Sheared and comb structure quartz indicate the formation of veins accompanied by intense stress and shearing (*Folk*, 1974).

By morphology, three generations of quartz have been identified. They include coarse-grained quartz with deformed grain boundaries (Qtz1), incipient recrystallized quartz (Qtz2) defined by small polygonal quartz grains and sub-grains occupying inter-grain planes mainly parallel to the grain boundaries and vein margins and deformed-elongated (stretched) quartz ribbons (Qtz3). The coarse-grained quartz regarded as the first generation and fine-grained to ribbon quartz due to recrystallization (second generation) resulting from multiple episodes of deformation and fluid circulation (Kurz et al., 2000, Oliver, 2001 and White, 2001). Sheared and comb structure quartz (third generation) indicate the formation of veins accompanied by intense stress and shearing (*Folk*, 1974).

The distinct alteration processes are silicification, chloritization, sericitization, pyritization and hematization. Sericite is abundant at the contact with the quartzite wallrock. The formation of sericite in the altered wallrock increases the permeability along the shear zone since sericite enhances permeability and facilitates ductile deformation (Kurz et al., 2000, Oliver, 2001 and White, 2001).

Gold- bearing sulphide quartz veins show a stockwork structure with chalcopyrite filled fractures. Gold occurs as inclusions in chalcopyrite and hematite. Auriferous deformed /remobilized quartz veins show the crushed and fractured characteristics with hematite filled fractures. Hydrothermal hematite quartz bands offer the best potential for significant gold concentration Suh et al. (Suh et al., 2006). It is true at Taung Ni gold prospect.

Conclusions

Taung Ni vein system is structurally controlled by a dominant NE-SW trending shear zone and gold mineralization is most possibly related to orogeny. Quartz vein textures exhibit criteria of mesothermal (orogenic) gold type. All of quartz textures are indicative of orogenic gold mineralization. The generations of quartz also imply that the gold prospect is orogenic gold type. Fluid inclusion data indicated that the gold-bearing mineralized quartz veins were developed under mesothermal environment. According to the deposit profile, and the characteristics of the vein type, vein textures, and quartz textures, Taung Ni gold prospect is orogenic gold mineralization formed under mesothermal conditions.

References

Aung Ye Ko, Day Wa Aung and Ohn Thwin., (2019a) "Petrography and Mineralogical, Geochemical Investigations of Metamorphic Rocks in Taung Ni Area, Madaya Township, Mandalay Region". *Universities Research Journal 2018*, Vol.11. No.11. P 203-224. August, 2019.

Aung Ye Ko., (2020) *Gold and Lead Mineralizations in the Taung Ni-Taung Gaung area, Madaya Township,Mandalay Region*, PhD Dissertation, University of Yangon, Myanmar, (Unpublished).

Bons, P. D., (2001) "The formation of the large quartz veins by rapid ascent of fluids in mobile hydrofractures". *Tectonophysics* 336:1-17.

Bouchot, V, Gros, Y., and Piantone, P., (1994) "Dynamics of shallow late Varis can gold mineralization:The Le Châtelet Au-arsenopyrite quartz veins, Massif Central, France:" *Mineralium Deposita,* v. 29, p. 461–473.

Bunopas, C. & Vella, P., (1983) "Tectonic and geologic Evolution of Thailand. Proceedings on a Workshop on Stratigraphic Correlation of Thailand and Malaysia". *Geological Society of Thailand*. *Bangok/ Geological Society of Malaysia, Kuala Lumpur*, I, 307-322.

Curray J.R., Moore D.G., Lawver L.A., Emmel F.J., Raitt R.W., Henry M. & Kieckhefer R., (1979*) "*Tectonics of the Andaman Sea and Burma". *In:* Watkins J.S., Montadert L. *& Dickerson* P.W. *(eds)* Geological and Geophysical Investigations of Continental Margins. *AAPG, Memoirs,* 29, 189-198.

Folk, R.L., (1974) Petrology of Sedimentary Rocks, Hemphills Austin, Texas. Pub. Co, 1980. Print.

Groves, D.I., R.J., Goldfarb, M., Gebre-Mariam, S.G., Hagemann, F., Robert., (1998) "Orogenic gold deposits. A proposed classification in the context of their crustal distribution and relationship to other gold deposit types". *Ore Geology Reviews* 13,7–27.

D. I. Groves, R. J. Goldfarb, and F. Robert., (2003) "Gold deposit in metamorphic belts: Overview or current understanding, outstanding problems, future research, and exploration significance," *Economic Geology* 98: 1-29,

Jébrak, M., (1992) "Les textures intra - filoniennes, marqueurs des conditions hydrauliques et tectoniques". *Chronique de la Recherche Minière*, v. 506, p. 25–35.

Jebrak, M., (1997) "Hydrothermal breccias in vein - type deposits; a review of mechanisms, morphology and size Distribution". *Ore Geology Reviews,* v.12, pp. 111–134.

Jia, Y.F., Kerrich R., (2000) "Giant quartz vein systems in accretionary orogenic belt: the evidence for a metamorphic fluid origin from $\delta^{15}N$ and $\delta^{13}C$ studies". *Earth Planet Sci Lett* 184:211-224.

Kerrich, R., (1986) "Fluid infiltration into fault zones: chemical isotopic, and mechanical effects". *Pure Applied Geophysics,* v. 124, pp. 225–268.

Khin Maung Shwe., (1973) *The Geology of Sedaw –Taung Gaung Area, Mandalay District*. M.Sc Thesis, Department of Geology, University of Mandalay (Unpublished).

Knipe, R.J., (1993) "The influence of fault zone processes and diagenesis on fluid flow". In: Horbury, A.D., Robinson, A.G. (Eds.), Diagenesis and Basin Development. *American Association of Petroleum Geologists studies in Geology,* v. 36, pp. 112–126.

Kurz, W., Unzog, W., Neubauer, F., and Genser, J., (2000) "Evolution of quartz microstructures and textures during polyphase deformation within the Tauren window (Eastern Alps)". *International Journal of Earth Science,* v. 90, pp. 361–378.

Li, R., Mei, L., Zhu, G., Zhao, R., Xu, X., Zhao, H., Zhang,P., Yin, Y., Ma, Y., (2013) "Late Mesozoic to Cenozoic tectonic events in volcanic arc, West Burma Block: Evidences from U-Pb zircon dating and apatite fission track data of granitoids". *Journal of Earth Science.* Volume24, pages 553-568.

Maung Thein, (2014) "Geological Map of Myanmar," Complied and Updated by *Myanmar Geosciences Society*, Yangon, Myanmar.

Metcalfe, I., (1984) "Stratigraphy, palaeontology and palaeogeography of the Carboniferous of Southeast Asia". *Mem. Soc. Geol. France* No. 147, pp. 107–118.

Oliver, N.H.S., (2001) "Linking of regional and local hydrothermal systems in mid - crust by shearing and Faulting". *Tectonophysics,* v. 335, pp. 147– 161.

Searle, D.L. and Haq, B.T., (1964) "The Mogok Belt of Burma and Its Relationship to the Himalayan Orogeny," *In: Proceedings of the International Geological Congress,* Vol. 22, pp. 132–161.

Searle, M. P., Noble S. R., Cottle, J. M., Waters, D. J., Mitchell, A. H. G., Tin Hlaing, Horstwood, M. S. A., (2007) "Tectonic evolution of the Mogok metamorphic belt, Burma (Myanmar) constrained by U-Th-Pb dating of metamorphic and magmatic rocks". *Tectonics,* Vol. 26, https://doi.org/10.1029/2006TC002083.

Searle, M. P., Morley, C.K., Waters, D.J., Grdiner, N.J., Kyi Htun, U.,Than Than Nu & Robb, L.J., (2017) " Tectonic and metamorphic evolution of the Mogok Metamorphic and Jade Mines belts and ophiolitic terranes of Burma (Myanmar)". *Geology, Resources and Tectonics, Geological Society, London, Memories,* 48,261-293, https://doi.org/10.1144/M48.12.

Soe Thura Tun & Watkinson, I. M., (2017) "The Sagaing Fault, Myanmar" In: *Myanmar: Geology, Resources and Tectonic,* A.J. Barber, Khin Zaw and M.J. Crow, ed(s).: *Geological Society, London, Memories,* 48, 413-441, https://doi.org/10.1144/M48.19. 2017.

Suh, C.E., Lehmann, B., and Mafany, G.T., (2006) "Geology and geochemical aspects of lode gold mineralization at Dimako - Mboscorro SE Cameroon". *Geochemistry: Exploration, Environment, Analysis,* v. 6, pp. 295–309.

Vearncombe, J.R., (1993) "Quartz vein morphology and implications for formation depth and classification of Archaean gold-vein deposits". *Ore Geology Reviews,* v. 8, p. 407–424.

White, S.R., (2001) "Textural and microstructural evidence for semi - brittle flow in natural fault rocks with varied mica content". *International Journal of Earth Sciences,* v. 90, pp.14–27.

Wilkinson, J.J., (2001) Fluid inclusions in hydrothermal ore deposits. Lithos 55: 229–272.

Win Swe, (2013) "The Sagaing Fault of Myanmar: a brief overview. Geology of Sagaing Fault in Commemoration of 9th Anniversary of MGS". *Myanmar Geosciences Society,* Yangon, Myanmar, p.1-20.

Woodcock, N.H., and Mort, K., (2008) "Classification of fault breccias and related fault rocks". *Geological Magazine,* v. 145, pp. 435–440.

GRANULOMETRIC ANALYSIS OF DEPOSITIONAL ENVIRONMENT FROM YAW FORMATION EXPOSED IN PIN DAUNG TAUNG – THA LAUK AREA, CHINDWIN BASIN

Htay Maung[1], Tin Zaw Oo [2], Theingyi Oo[3], Kay Thi Myint Swe [4]

Abstract

The research area lies within the Chindwin Basin, which is filled by the Cretaceous to Miocene clastic sedimentary rocks which are deposited between the marine to fluvial conditions. The Yaw Formation mainly consists of thin to medium-bedded, grey to bluish-grey carbonaceous silty shale and nodular clay with some intercalated buff-yellowish sandstones. Coal seams are also inter-layers with silty clay and sandstones. The Yaw Formation fall litharenites and the textural parameter shows unimodal, moderately to poorly sorted, nearly symmetrical to very positive skewness, mesokurtic to leptokurtic values that indicate fine to medium grains which are low to medium energy of current velocity condition. Bivariate plot of the standard deviation & median diameter distinguished between the river/wave and quiet water condition. Moreover, The PQ/OP segments of the CM pattern describe graded suspension with some rolled sediments as well as the segments QR point to saltation population and the grains size analysis as three populations. The log-probability curve of Yaw Formation sediments also supports the segments of the CM pattern. This indicates that the sediments of the Yaw Formation were transported and deposited in the different modes of saltation/suspension. According to petrography and grain size distribution, the sandstones of the Yaw Formation may be deposited at the low to medium energy state of the deltaic condition in shallow marine environments.

Keywords: Segment,Log probability,Yaw Formation,Chindwin Basin

Introduction

The research area is situated about 58 miles northwest of Monywa Township, Sagaing Region within the Chindwin Basin which was filled with Cretaceous–Eocene clastic sedimentary rocks (Wang *et al.*, 2014). This area lays one-inch topographic map 84J/12 (UTM-2294/07,08, 11&12) (Fig. 1 & 2). This basin was deposited in the continental environment in the northern part and shallow marine environment in the southern part at the time of Eocene (Chhibber.H.L.,1934). The mechanical analysis is to obtain numerical data about the sediment particle size. Moreover, to describe the significance of the transportation and depositional environment of the Yaw Formation in each sample.

Figure 1 Location map of the research area

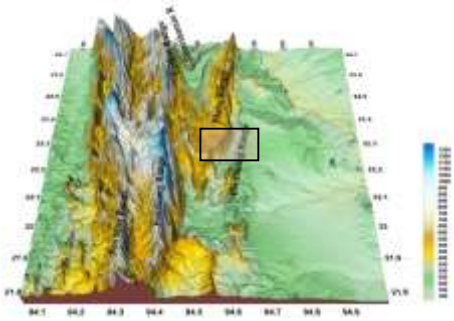

Figure 2 3-D map of the research area

[1] Lecturer, Department of Geology, University of Monywa
[2] Dr, Associate Professor, Department of Geology, University of Monywa
[3] Dr, Associate Professor, Department of Geology, University of Monywa
[4] Assistant Lecturer, Department of Geology, University of Monywa

Method of Study

Firstly, loose sand samples were collected from Yaw Formation in the study area. The 100 grams of sand were sieved for 10 minutes. Sand samples in each formation were obtained by straight sieving method, using B.S screams that are spaced at one phi. The sieves are used for size determination in sand ranges between 0.625 mm and 2 mm (Folk, 1957). The results of the grain-size distribution of the sediments of the study area are shown in the form of a Histogram, Frequency, and Cumulative curve. The statistical parameter values of grain-size distribution calculated from phi values are drawn on the probability paper.

The results of the granulometric analysis were plotted as cumulative curves on arithmetic probability paper to obtain the value of the 5^{th}, 16^{th}, 25^{th}, 50^{th}, 75^{th}, 84^{th}, and 95^{th} percentile. The statistical parameter values of grain-size distribution analysis calculated from phi values are drawn on the probability paper. A study of grain size distribution thus results from the physical effect of the depositional environment conditions existing at the time of granulometric analysis.

The following formula proposed by Folk and Ward, 1957 represents the graphic mean size;

$$\text{Medium } M_d = \phi 50$$

$$\text{Mean } M_Z = \frac{\phi 16 + \phi 50 + \phi 84}{3}$$

$$\text{Sorting } \delta_I = \frac{\phi 84 - \phi 46}{4} + \frac{\phi 95 - \phi 5}{6.6}$$

$$\text{Skewness } Sk_I = \frac{\phi 16 + \phi 84 - 2\phi 50}{2(\phi 84 - \phi 16)} + \frac{\phi 5 + \phi 95 - 2\phi 50}{2(\phi 95 - \phi 5)}$$

$$\text{Kurtosis } K_G = \frac{\phi 95 - \phi 5}{2.44(\phi 75 - \phi 25)}$$

The value of C = one percentile and the value of M = 50ø (median). The baselines C-M was plotted along the co-ordinate and abscises respectively in a log-log graph paper.

Sedimentary Units

General Statement

The sedimentary units exposed in the area from descending order are the Pondaung Formation, Yaw Formation, Letkat Formation and Natma Formation from ranging Eocene to Pleistocene ages. The geological map of the study area is shown in (Fig. 3).

Yaw Formation

The term ‘Yaw stage’ was first applied by Cotter (1912) for an argillaceous sequence exposed at the Yaw Chaung at Pokakku District and the term ‘Yaw Formation’ by Aung Khin and Kyaw Win (1969).

The Yaw Formation is dominated by the sequence of thin to medium bedded, grey to bluish-grey, greenish grey, chocolate brown, purple, thinly laminated carbonaceous silty shale and nodular shale. These variegated silty shale and clay are intercalated with buff yellowish-colored, fine-grained sandstones (Fig.4). In some places, the intraformational conglomerates occurred in this Formation. Coal seams are also observed ranging in thickness from about 3 to 4 ft (Fig.5). The occurrence of grey to bluish-grey, greenish grey, chocolate brown, purple clays, carbonaceous silty shale and nodular shale with layers of coal seams (Reineck and Singh,1980) that the depositional site was influenced by shallow brackish and swampy conditions.

The lithofacies of the Yaw Formation with evidence for marine intervals, freshwater gastropod, and lignites are various yielding continental vertebrates (Licht et al., 2013) in the Chindwin Basin.

The *Nummulites yawensis*, *Discocyclina sella*, *Operculina* sp. as microforaminifera; *Velates perversus* as grastropod; and mollusca are collected from Yaw Formation and are assigned as Late Eocene age (Bender, 1983; Aye Ko Aung, 1999).

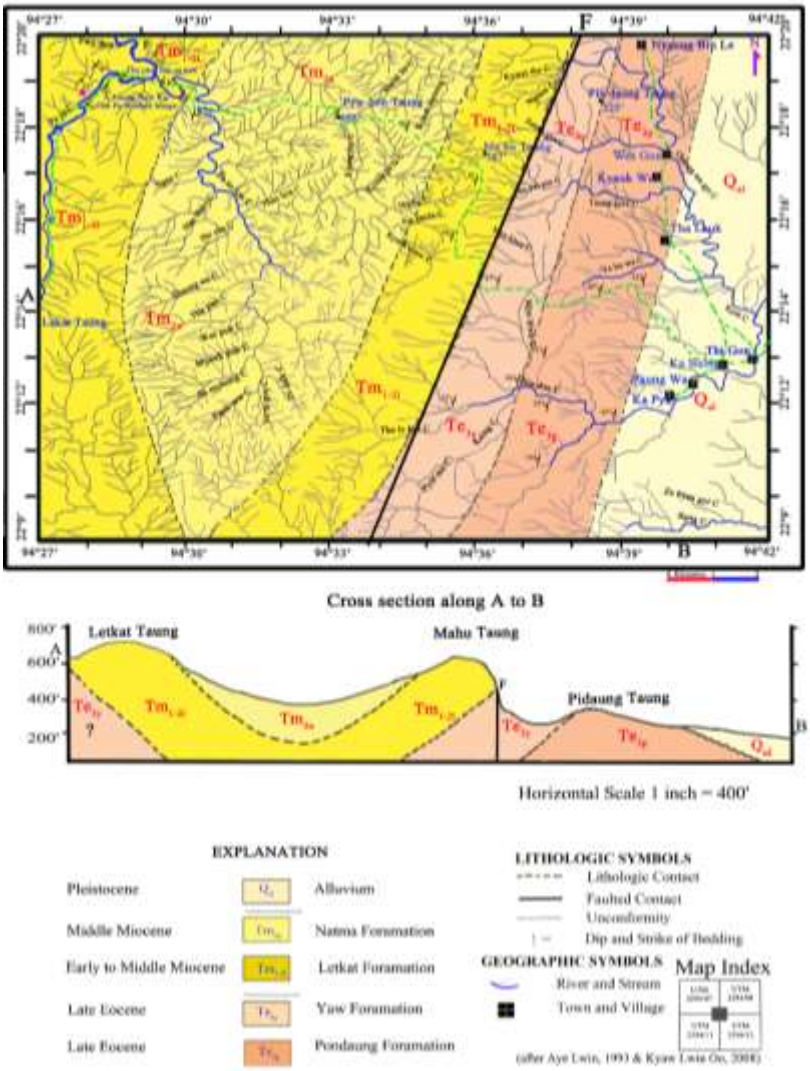

Figure 3 Geological Map of the Research Area

Figure 4 Sandstones are intercalated between the variegated clay of the Yaw Formation (22°12'07"N,94°37'10 "E)

Figure 5 Coal seams found wedge shape within the silty clay in the Yaw Formation (22°15' 40"N, 94°36'30"E)

Petrography

The sandstone of the Yaw Formation is mainly composed of about 95 % detrital grains and 5 % of chemical cement. They are poorly to moderately sorted, angular to subangular which textural maturity of this sandstone is immature.

Quartz comprises 49 to 55% of total rock volume in which monocrystalline quartz grains are more commonly than polycrystalline quartz grains (Fig.6). Generally, monocrystalline quartz shows prominent characteristics such as subrounded to angular, unique extinction, mineral inclusions and fractures.

Feldspar constitutes 19 to 24 % of the total detrital fraction. Alkali feldspar is more abundant than plagioclase feldspar. Alkali feldspar shows cross-hatched twin, lamellae twin and Carlsbad twin (Fig.7). Some plagioclase show complex twinning and is replaced by calcite cement.

Rock fragments occurred 26 to 35 % of the detrital volume (Fig. 8). Igneous rock fragments are more abundant than metamorphic and sedimentary rock fragments. Mica is composed of 3 to 5 % of the detrital fraction. Micas are frequently distorted and split apart by calcite cement.

Quartz is less than 75%, the total feldspars exceed rock fragments, and the matrix is less than 15%. So it may be termed as "Lithic arenite" (Fig. 9) condition (Pettijohn et al.,1975) in which sandstones were deposited in the deltaic environment (Tucker, M.E., 2001).

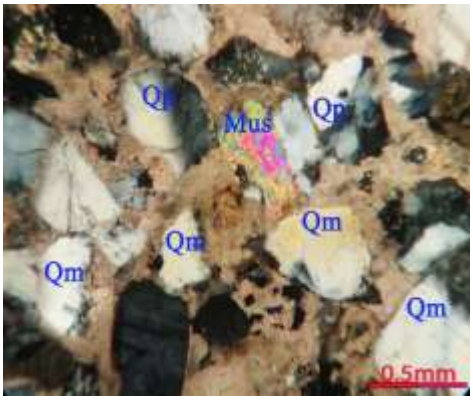

Figure 6 Showing polycrystalline quartz (Qp), monocrystalline quartz (Qm) and Muscovite (Mus) in the sandstone of the Yaw Formation under XN (10X).

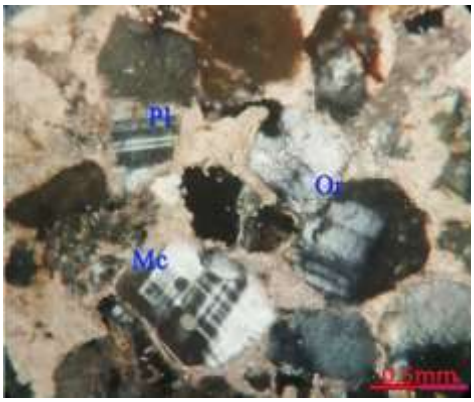

Figure 7 Showing orthoclase feldspar (Or) and plagioclase feldspar (Pl) in the sandstone of the Yaw Formation under XN (10X).

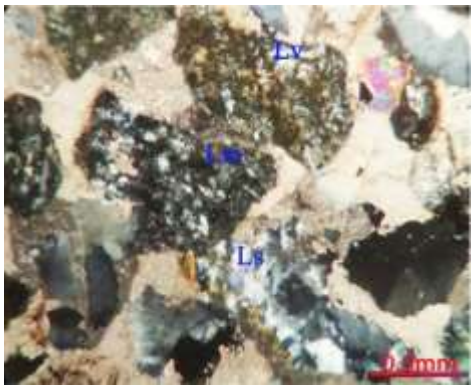

Figure 8 Showing Lv- volcanic lithic fragments, Lm- metamorphic lithic fragments, Ls- Sedimentary lithic fragments in the sandstone of the Yaw Formation under XN (10X).

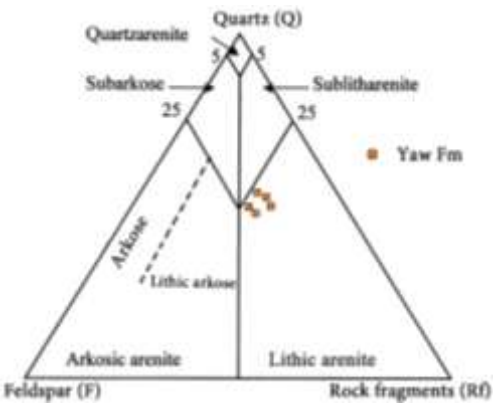

Figure 9 The samples of Yaw Formation plotted in the QFL diagram for the classification of sandstone after Dott (1964) and Pettijohn (1975).

Grain Size Distribution

The six representative samples were collected from the Yaw Formation in the research area. The C-M diagram and the analysis of log-probability size distribution curves are together used by the source of supply, depositional processes and environment (Passega 1964 & Visher 1969).

Histograms were drawn on a graph paper using the result data obtained from mechanical analysis of sands (Fig.10), which are simple bar diagrams showing the distribution of weight percent of grains in each size class in the Yaw Formation.

The shape of histograms indicates that the size distribution of the Yaw Formation's samples collected is unimodal. The unimodal sands are the result of uniformity in the force of transporting and depositing. Draw a line graph, cumulative frequency curve of the sediments that show the presence of grains coarser to finer grain size to cumulative percentage on the ordinate for each sample of the Yaw Formation (Fig.10).

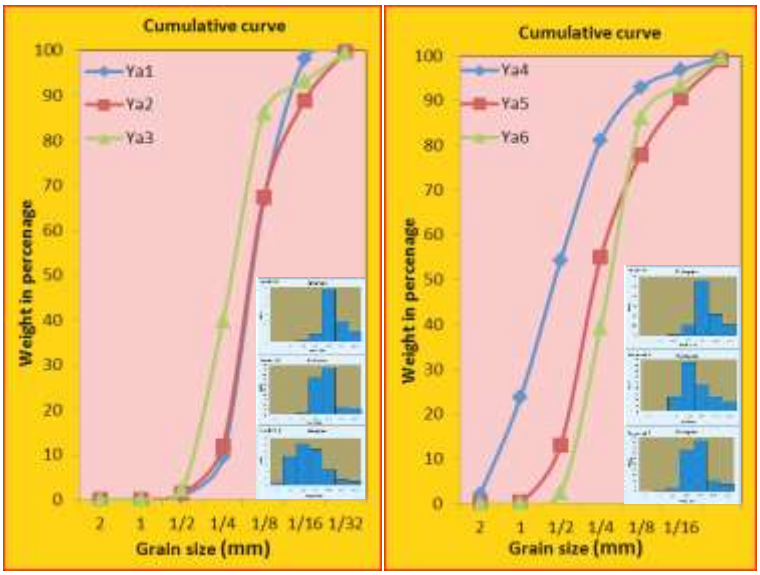

Figure 10 Representative histograms and cumulative curves of the size frequency distribution of the Yaw Formation

Statistical Calculation

The mode of Yaw sandstones is the highest midpoint on the histogram. Median indicates the corresponding 50 ø of the cumulative curve. It is significant that the median and mean diameter of the Yaw Formation range from 0.9 ø to 2.8ø and 0.9 ø to 2.9ø (Tab.1).

Table 1 Grain size distribution parameter values calculated from phi value on probability paper of the Yaw Formation

Grain size distribution parameters	**Ya_1**	**Ya_2**	**Ya_3**	**Ya_4**	**Ya_5**	**Ya_6**
Median diameter (Md)	2.8	2.6	2.5	0.9	1.9	2.4
Mean diameter (Mz)	2.8	2.9	2.3	0.9	2.1	2.3
Inclusive graphic (Sorting) standard deviation (σ_1)	0.8	0.9	0.9	1.2	1.0	0.9
Inclusive graphic Skewness (S_{KL})	0.09	0.5	0.07	0.2	0.5	0.06
Graphic Kurtosis (Kg)	1	1	1.1	1.1	1.4	1.2

Standard deviation describes the degree of scattering of the grain particles. The standard derivation varies from 0.8ø to 1.2ø (Fig. 11) which is moderate to poorly sorted in Yaw Formation. This sorting is about 20% moderate sorted and 80% poorly sorted that indicated the low to medium energy condition which will be recognized as minor variability in current velocity (Folk and Ward., 1957). The Yaw Formation is no longer transported agents as well as deposition agents due to the distribution of different grain sizes.

Skewness measures the asymmetry of the grain size frequency. The skewness ranges from 0.06ø to 0.5ø (Fig. 12) of the Yaw Formation indicating nearly symmetrical (33%) to very positive skewness (66%). In the positively skewed distribution, the mean is always higher or greater than the median or mode, supporting that both the median and mean are shifted toward finer grains size (Fig. 12). So that many medium to fine sand, silt and clay are not removed by current, but trapped between large grains distribution (Friedman. 1967). Most of the samples are strongly fine skewed and the rest are nearly symmetrical. These sediments show a tendency for more material in the fine tail.

Kurtosis shows the peakedness of a grain size-frequency distribution curve. The kurtosis value of the samples ranges from 1ø to 1.4ø (Fig. 13) representative of mesokurtic to leptokurtic kurtosis in the Yaw Formation. About 67% mesokurtic, and 33 % leptokurtic value shows that in major cases, tails and the central portion are equally sorted which has a better sorted central portion (Folk and Ward, 1957).

Statistical parameters obtained by the method were plotted in different bivariate diagrams to confirm prevailing environment conditions (Stewart, 1958). In the case of statistical parameters obtained by the graphic method as a river, wave, deltaic and quiet water condition subenvironments. The plot between standard deviation and median diameter is also absorbed by proportions of two size modes in the mixture. According to Stewart (1958), most of all Yaw sediments were plotted in the research area between the quiet water and wave water processes (Fig.14). The bivariate shows that most of the samples clustered in the deltaic environment.

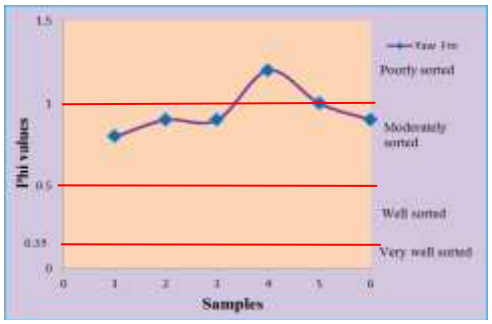

Figure 11 Sorting values of the Yaw Formation (Folk and Ward, 1957)

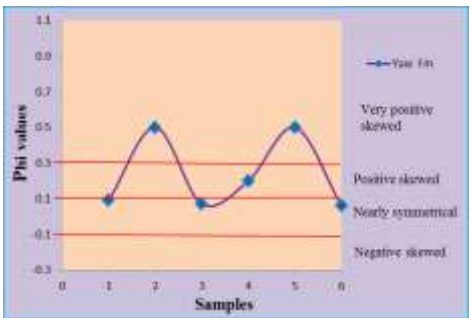

Figure 12 Skewness values of the Yaw Formation (Folk and Ward's,1957)

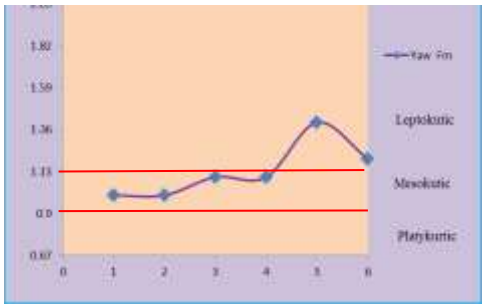

Figure 13 Kurtosis values of the Yaw Formation (Folk and Ward, 1957)

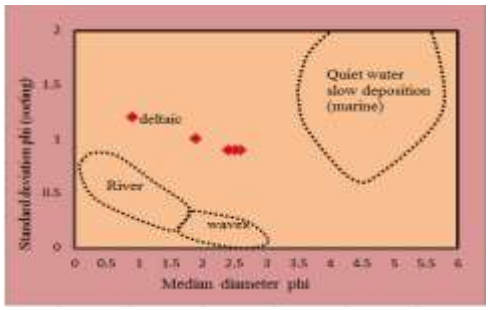

Figure 14 Bivariate plot showing standard deviation & median diameter of Yaw Formation (Stewart,1958)

C-M Pattern

Passega (1964) suggested the use of C-M diagrams for environmental analysis. The relationship between the C and M pattern of Yaw Formation is the effect of sorting by bottom confusions (Tab.2). It helps to establish a relationship between the depositional environment and prevailing hydrodynamic conditions. The plotted result of Yaw sediment samples are transported by suspension and rolling (PQ), rolling and suspension (OP) and graded suspension, mainly saltation (QR) sector supply (Fig.15). The PQ/OP segments express graded suspension with some rolled sediments as well as the segments QR point to the saltation population. Yaw sediments are predominantly rolling, saltation and suspension population because some deposits to be formed in the deltaic condition (Passega,1964).

Therefore, the C-M pattern may be interpreted that the sediments of the Yaw sandstones being deposited by the tractive current through graded suspension processes in the deltaic condition.

Table 2 Result of the percentiles, C-M pattern of the Yaw Formation

Sample No.	ø 1 (one phi percent)	ø50 (Median)	**C-M** values	
			C in micron	**M** in micron
Ya1	1	2.8	500	144
Ya2	0.8	2.9	572	134
Ya3	0.5	2.3	710	203
Ya4	0.4	0.9	752	536
Ya5	2	2.1	250	234
Ya6	0.6	2.3	662	203

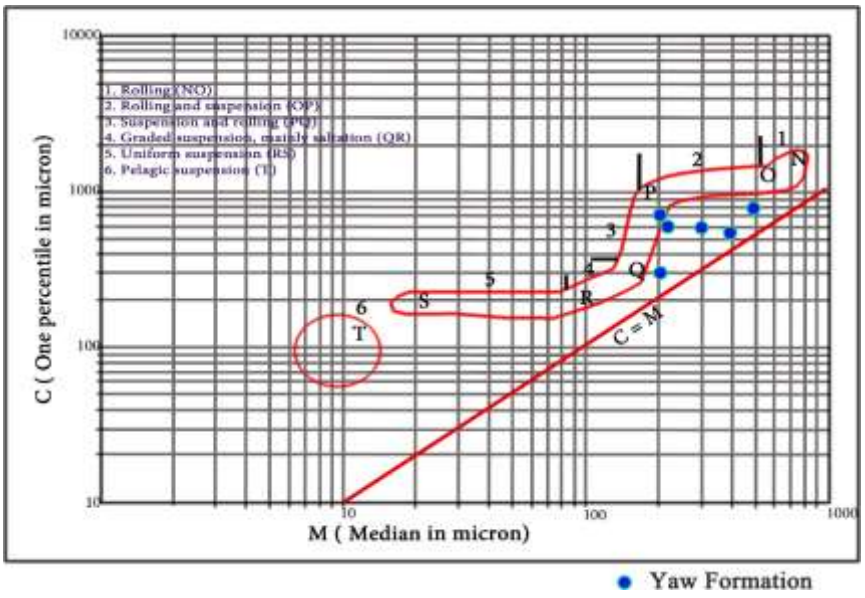

Figure 15 C-M pattern of the Yaw Formation

Log-Probability Curve

The grain sizes of the frequency curves to separate the populations are aided by the use of log probability plots (Visher, 1969). Visher plot for sediments from the Yaw Formation shows the dominance of double saltation suspension with single suspension and traction population (Fig.16). The saltation and suspension populations may range up to 29% and 95% respectively. The saltation populations are fairly better sorted than the suspension population. However, one of the samples indicates around 0.8ø values and the other samples show around 3.4ø values of the traction population. The break population of the log-probability curves for the Yaw Formation could be due to the mixing of detritus carried by tractive currents with different energy. Three and four segments of the population, truncation and saltation population are related to the traction that was confirmed by coarse truncation and fine truncation in the study area. From above the log probability data, the samples of the Yaw were deposited in the deltaic environment (Visher, 1969).

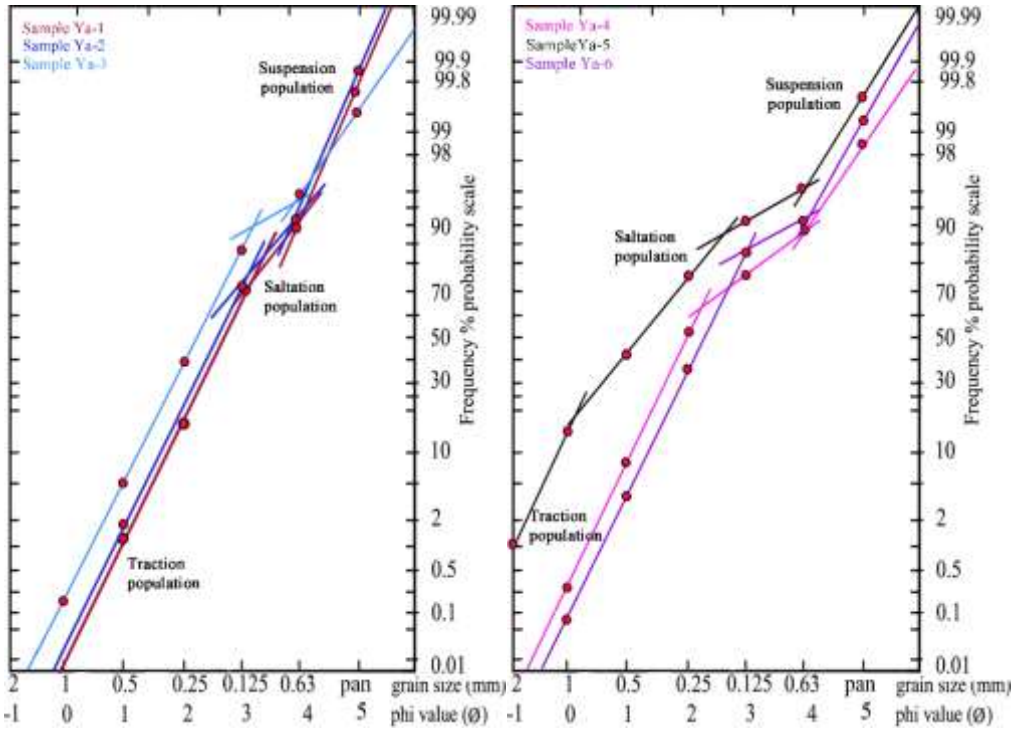

Figure 16 Log-probability curve of the Yaw Formation

Discussion and Conclusion

The research area is placed within the Chindwin basin which was deposited by continental to shallow marine sediments. According to the sequence stratigraphy (Myo Thant, 2006 & Kyaw Linn Oo, 2008), the sedimentary facies (Licht et al., 2013) in the Kalewa-Mawleik Area, at the Chindwin basin was deposited in the delta front to delta plain environment condition.

Thus, various approaches were made to interpret grain size analysis for depositional environments in the research area. The lithic arenite sandstones of the Yaw Formation were deposited from deltaic environmental conditions. The grain size distribution of the Yaw Formation is moderate to poorly sorted, nearly symmetrical to positive skewed and mesokurtic to leptokurtic kurtosis that is not removed by current, but trapped between large grains distribution indicated a relatively low to medium energy condition. Furthermore, PQ, OP and OR segments of the C-M pattern of the Yaw sediments indicate they were deposited mostly from suspension, rolling/ saltation and graded suspension. Then, the saltation and suspension population from the log probability curve ranges about nearly 29% and 95% that suggesting a different mode of transport and deposition which is deposited in deltaic conditions.

The basis of facies description, petrology and grain size analysis, it can be determined and interpreted that all sediments of the Yaw Formation have been deposited by the low to medium energy state in a deltaic condition which lies between the marginal marine and the shallow marine environment.

Acknowledgments

We are thankful to Dr. Thura Oo, Rector and University of Monywa for his kind permission to carry out this research work. We would like to thank Dr. Than Than Win, Dr. Tun Min and Dr. Khin Ngwe Aye, Pro-Rector, Monywa University, for their constructed comment and suggestion for this paper. We would like to deeply acknowledge Associate Professor Dr. Theingyi Oo and Dr. Tin Zaw Oo, Department of Geology, University of Monywa, for their invaluable guidance and suggestion.

References

Aung Khin & Kyaw Win, (1969) *Preliminary Studies of the Paleogeography of Burma during the Cenozoic;* People's Oil Industry.

Aye Ko Aung, (1999) Revision of the stratigraphy and age of the primate-bearing Pondaung Formation.In; Tun.T(ed.), *Proceedings of the Pondaung Fosssils Expedition Team*.

Aye Lwin, (1993) The sedimentology of the sandstones of the Mahudaung area, Kani and Mingin Townships. *M.Sc Theiss*, unpub. University of Mandalay.

Bender. F, (1983) *Geology of Burma,* Gebrunder Borntraeger Berlin.

Chhibber. H.L, (1934) *The Geology of Burma,* Macmillan & Co.Ltd., London.

Cotter, G.D.P, (1912) Pegu-Eocene succession in the Minbu District near Ngape, Rec, *Geology Survey Inida*, vo.41.

Dott, R.H, (1964) Wacke, grewacke and matrix. What approach to immature sandstone classification? *Journal of Sedimentary Petrology*, 34. pp. 625-632.

Folk, R.L., and Ward, M.C, (1957) Brazos river bars; a study in the significance of grain size parameters, *Journal Sediment Petrology*, 27, pp. 3-27.

Friedman, G.M, (1967) Dynamic processes and statistical parameters compared for size frequency distribution of beach and river sands. *Journal of Sedimentary Research*, 37(2): pp.327-354.

Kyaw Lwin Oo, (2008) Sedimentology of Ecoene-Miocene clastic strata in the southern Chindwin Basin, Myanmar. *Ph.D Thesis*, unpub. University of Yangon.

Licht, A., France-Lanord, C., Reisberg, L., Fontaine, C., Aung Naing Soe, and Jaeger,J, (2013) A palaeo Tibet–Myanmar connection? Reconstructing the Late Eocene drainage system of central Myanmar using a multi-proxy approach: *Journal of the Geological Society*,v. 170, no.6, pp. 929–939, https://doi.org/10.1144/jgs2012-126.

Myo Thant, (2006) The sedimentology and sequence stratigraphy of the Upper Cretaceous to lower Tertiary units of the Kalaywa-Mawlaik area, Kalaywa and Mawlaik Township. *Ph.D Thesis*, unpub. University of Yangon.

Passega, R, (1964) Grain size representation by CM patterns as a geologic tool, *Journal of Sedimentary Research,* 34 (4): pp. 830-847.

Pettijohm, F.J., Potter,P.E.,(1975). *Sedimentary rocks* 3rd edit.New York,Harper and Row, pp.628.

Reineck, H. E., and Singh, I. B, (1980) *Depositional sedimentary environment*. Springer-Verlag, New York.

Stewart, H.B .Jr, (1958) Sedimentary reflection on depositional environments in San Migue Lagoon, Baja, California, Mexico.*Bull. Am.Ass.Petrology. Geol* 42, pp.2567-2618.

Tucker, M.E., (2001). *Sedimentary Petrology*, An introduction to the origin of sedimentary rocks. 2nd Edit, Blackwell Science Ltd., UK.

Visher, G.S, (1969) Grain size distribution and depositional process; *Journal of Sedimentary Petrology* 34, pp.1074-1106.

Wang, J.G., Wu, F.Y., Tan, X.Y., Liu., C.Z, (2014) Magmatic evolution of the Western Myanmar Arc documented by U-Pb and Hf isotopes in detrital zircon. *Tectonophysics*, pp. 97-105.

MYANMAR ACADEMY OF ARTS AND SCIENCE
EXECUTIVE COMMITTEE

President : Dr Thet Lwin

Vice-Presidents: Dr Daw Kyi Kyi Hla, Dr Maung Kyaw

Secretary : Dr Win Tun

Joint Secretaries: Dr Tin Maung Tun, Dr Aye Aye Khaing, Dr Tin Tin Htwe

Executive Members

U Thi Ha
Dr Myo Thant Tyn
Dr Tin Nyo
Dr Khin Than Oo
Dr Hla Pe
Dr Maung Thin
U Kyaw Myint Oo
Dr Daw Than Nwe
Daw Carole Ann Chit Tha
Daw Khin Lat
Dr U Win

Publication Committee

Dr Thet Lwin	(Chairman)	Dr Maung Kyaw	(Vice-Chairman)
U Thi Ha	(member)	Dr Daw Than Nwe	(member)
Dr Tin Nyo	(member)	Daw Carole Ann Chit Tha	(member)
Daw Khin Lat	(member)	Dr Hla Pe	(member)
Dr U Win	(member)	Dr Maung Thin	(member)
Dr Myo Thant Tyn	(Secretary)	Dr Khin Than Oo	(Joint Secretary)

Editorial Board

Dr Maung Kyaw	(Chairman)	U Thi Ha	(member)
Dr Myo Thant Tyn	(member)	Dr Daw Than Nwe	(member)
Dr Tin Nyo	(member)	Dr Daw Khin Than Oo	(member)
Daw Khin Lat	(member)	Dr Hla Pe	(member)
Dr Maung Thin	(member)	Dr Aye Aye Khaing	(member)
Dr U Win	(Secretary)	Daw Carole Ann Chit Tha	(Joint Secretary)

Coordinators for International Academies

Daw Carole Ann Chit Tha
Dr Myo Thant Tyn
Dr Tin Nyo
Dr Tin Tin Htwe
Dr Maung Kyaw
Dr Daw Than Nwe
Dr Tin Maung Tun

INSTRUCTIONS TO AUTHORS

Presentation: Manuscripts (MS) should be typed on one side of **quarto or A4 size paper**. Typing should be single spaced, with a one-inch margin all around. A CD of the paper should be submitted together with two print-outs. In general, the text should be organized according to the following outline:

(i) Title
(ii) Abstract
(iii) Materials & Methods/ Premises / Hypotheses
(iv) Results / Findings
(v) Discussion
(vi) Summary/ Conclusion
(vii) Acknowledgements
(viii) References

The body of the text should be printed in **font size 12**, and those of the Abstract, Acknowledgement and References should be printed in **font size 10.** The relative importance of the **headings** in the text should be indicated as follows:

First Order	-	CENTRE HEADING, All Capitals
Second Order	-	Centre Heading, Capitals & lower case
Side Heading	-	Capitals & lower case, not indented (bold – faced)
Run-in heading	-	Capitals & lower case, indented (bold-faced)

Title. The title should describe the contents of the article adequately and concisely and should be typed in **font size 14.**

Author's name. Capital & lower case. The designation of the first author (where the number of authors is more than two) and the name of the institution where the work was carried out should be given at the bottom of the title page.

Abstract. The main points of the paper, including its findings and conclusions, should be highlighted in the abstract. It is not a summary, and should not contain more than 300 words; if more than 300 words, further publication will not be considered. The entire abstract should be indented and typed in **font size 10**.

Key words: Between 3-7 key words highlighting the main points should be listed below the abstract.

References. References should be presented in alphabetical order, beginning with the surname first for the senior author and surname last for the other authors, followed by the year of publication. Examples of references are given below:

To a paper: Rabinowitz, A., Than Myint, email, Tun Khaing, and S. Rabinowitz, (1999)"Description of the Leaf Deer (*Muntiacus Putaoensis),* a New Species of Muntjac from Northern Myanmar" *Journal of Zoology,* London, vol.249, pp.427-435.

To a book: Corbet, G.B., & J.E. Hill, (1992) *The mammals of the Indomalayan Region.* Oxford, Oxford University Press.

To a thesis: May Soe Thu (1995) *Taxonomy of Offshore Fishes Caught by Bottom Trawl Operations in Myanmar Waters.* M.Sc. Thesis Zoology Department, Yangon University (Unpublished).

N.B. If the manuscript submitted is from a thesis, its format should be revised to conform to the instructions of the Myanmar Journal of Arts & Science presented here. **Pagination** should commence from the title page except when they are used to identify the affiliated instructions, and cite unpublished material. F**ootnotes** should be avoided wherever possible. The MS, including illustrations and references, should not exceed **15 pages** for Arts and related subjects and **10 pages** for Science in length. Please kindly follow this limit in your final manuscript.